Tyre models for vehicle handling analysis under steady-state and transient manoeuvres

Tyre Models for Vehicle Handling Analysis under Steady-State and Transient Manoeuvres

By

Georgios Mavros

Dipl.-Eng.

A Doctoral Thesis

submitted in partial fulfilment of the requirements

for the award of

The Degree of Doctor of Philosophy of Loughborough University

July 2005

Loughborough University

This thesis is dedicated to

the memory of my beloved uncle

Giorgos

Abstract

The work presented in this thesis is devoted to the study of mechanism of tyre force generation and its influence on handling dynamics of ground vehicles. The main part of the work involves the development of tyre models for use under steady-state and transient operating conditions. The general capability of these models is assessed in a full vehicle simulation environment. The interaction between tyre and vehicle dynamics is critically evaluated and the observed vehicle behaviour is related to the inherent characteristics of different tyre models.

In the field of steady-state tyre modelling, two versions of a numerical tyre model are developed. The modelling procedure is carried out in accordance with the viscoelastic properties of rubber, which influence the mechanical properties of the tyre structure and play a significant role in the determination of friction in the tyre contact patch. Whilst the initial simple version of the tyre model assumes a parabolic pressure distribution along the contact, a later more elaborate model employs a numerical method for the calculation of the actual normal pressure distribution. The changes in the pressure distribution as a result of variations in the rolling velocity and normal load influence mainly the levels of self-aligning moment, whilst the force characteristics remain practically unaffected. The adoption of a velocity dependent friction law explains the force generating behaviour of tyres at high sliding velocities.

The analysis is extended to the area of transient tyre behaviour with the development of a tyre model appropriate for the study of transient friction force generation within the contact patch. The model incorporates viscoelasticity and inertial contributions, and incorporates a numerical stick-slip law. These characteristics are combined together for the successful simulation of transient friction force generation. The methodologies developed for the modelling of transient friction and steady-state tyre force generation are combined and further extended in order to create a generic transient tyre model. This final model incorporates a discretised flexible viscoelastic belt with inertia and a separate fully-dynamic discretised tread, also with inertia and damping, for the simulation of actual prevailing conditions in the contact patch. The generic tyre model appears to be capable of performing under a variety of operating conditions, including periodic excitations and transient inputs which extend to the non-linear range of tyre behaviour.

For the evaluation of the influence of the aforementioned tyre models on the handling responses of a vehicle, a comprehensive vehicle model is developed, appropriate for use in handling simulations. The two versions of the steady-state models and the generic transient model are interfaced with the vehicle model, and the response of the vehicle to a step-steer manoeuvre is compared with that obtained using the Magic Formula tyre model. The comparison between the responses is facilitated by the definition of a new measure, defined as *the non-dimensional yaw impulse*. It is found that the transience involved in tyre behaviour may largely affect the response of a vehicle to a prescribed input.

Keywords: Tyre forces, viscoelastic contact mechanics of tyres, vehicle handling, transient manoeuvres, combined lateral and longitudinal slip

Acknowledgements

Firstly I would like to thank my supervisors, Professor Homer Rahnejat and Mr. Paul King for their invaluable advice and encouragement throughout the course of my research.

I would also like to acknowledge Wolfson School of Mechanical and Manufacturing Engineering in Loughborough University for trusting me with a departmental studentship and supporting my work with all available resources.

I would like to thank my mother for consistently and tirelessly supporting my learning throughout my school and University years in Greece.

I wish to express my deepest gratitude to Stephanos Theodossiades and Stella Georgiadou for their hospitality and support during the final and most stressful days of my PhD.

Special thanks go to all my friends who made the whole PhD experience much more interesting and rewarding.

Finally, more than anyone, I wish to thank Elena Georgiadou for standing by me patiently and sharing my worries during the final year of my research. She has been my inspiration and she helped me keeping my spirit high when everything seemed to go wrong.

Contents

List of figures

Chapter 2

Chapter 3

Chapter 4

Chapter 5

List of tables

Nomenclature

Chapter 2

C_{af}	cornering stiffness of the front tyres
C_{ar}	cornering stiffness of the rear tyres
g	acceleration of gravity
l	wheelbase
K_{us}	under-steer coefficient
R	radius of turn
U	forward velocity
W_f	front vehicle weight
W_r	rear vehicle weight

Greek letters

a_f	slip angle of front tyre
a_r	slip angle of rear tyre
δ_f	front steer-angle

Chapter 3

a	half length of the tyre contact patch
$a_0 - a_{13}$	Magic Formula coefficients for the cornering characteristic
$b_0 - b_{10}$	Magic Formula coefficients for the braking characteristic
b	width of the tyre
B	stiffness factor of the Magic Formula

C	shape factor of the Magic Formula
C	mass per unit length of the contact patch
$c_0 - c_{17}$	Magic Formula coefficients for the self-aligning torque characteristic
c_r	coefficient of rolling resistance
C_z	vertical stiffness of the tyre
D	peak value of the Magic Formula
D_r	damping per unit length in the radial direction
D_t	damping per unit length in the tangential direction
D_x	longitudinal damping per unit length along the contact patch
D_y	lateral damping per unit length along the contact patch
D_z	damping per unit length in the vertical direction
E	curvature factor of the Magic Formula
E^*	complex relaxation modulus
E_c	storage modulus
E_L	loss modulus
f	friction force applied on a tread segment
$F_{friction}$	generic friction force
$F_{adhesion}$	friction force component due to adhesion
$F_{external}$	external force applied on a specimen involved in a frictional contact
$F_{hysteresis}$	friction force component due to hysteresis
F_r	rolling resistance force
$F_{vertical}$	vertical load at a point along the contact patch
F_x	longitudinal tyre force
f_x	longitudinal component of friction force on a tread segment

F_y	lateral tyre force
f_y	lateral component of friction force on a tread segment
F_z	normal load on the wheel-hub
g	acceleration of gravity
I	polar moment of inertia of the wheel
k	longitudinal slip ratio
$K_{1,2}$	coefficients for the calculation of viscoelastic friction
K_r	stiffness per unit length in the radial direction
K_t	stiffness per unit length in the tangential direction
K_x	longitudinal stiffness per unit length along the contact patch
K_y	lateral stiffness per unit length along the contact patch
K_z	stiffness per unit length in the vertical direction
l	length of the tyre contact patch
l_h	height of the centre of a loaded rolling wheel from the ground
M	mass of the quarter vehicle
M_f	moment about the wheel spin axis due to the pressure distribution along the front part of the contact patch
M_r	moment about the wheel spin axis due to the pressure distribution along the rear part of the contact patch
M_x	overturning couple
M_y	rolling resistance moment
M_z	self-aligning moment
M_{zr}	residual self-aligning moment (Magic Formula)

n	index for the calculation of hysteresis friction
$Ob_b(\mathbf{P})$	objective function for the identification of the longitudinal tyre properties
$Ob_c(\mathbf{P})$	objective function for the identification of the lateral tyre properties
p	tyre pressure
p	apparent normal pressure
p_v	normal pressure distribution
$\mathbf{P}$	vector of optimisation parameters
qx	longitudinal friction reduction rate coefficient
qy	lateral friction reduction rate coefficient
$\mathbf{r}(x, y)$	position vector of the bristle tip in the global frame of reference
R	stiffness coefficient of rubber
R	radius of loaded – inflated tyre outside the contact patch
R_C	instantaneous radius of the path of the wheel
R_e	effective tyre radius
s	effective shear stress of sliding interface
S	distance of travel of the wheel corresponding to an angle of rotation ϑ_r about its axis, for the calculation of the rolling resistance work
S_H	horizontal shift of the Magic Formula
S_{Ht}	horizontal shift of the pneumatic trail (Magic Formula)
S_{Hf}	horizontal shift of the residual torque (Magic Formula)
S_V	vertical shift of the Magic Formula
t	pneumatic trail
T	operating temperature of rubber
$T_{d,b}$	driving – braking torque on the wheel

T_0	reference temperature of rubber
threshold	velocity threshold for the stick-slip transition
t_r	horizontal shift of the vertical reaction
t_{travel}	total time of travel of the bristle base
u	velocity of the bristle tip (small mass) in the global frame of reference
u_x	longitudinal component of the bristle tip (small mass) velocity in the global frame of reference
u_y	lateral component of the bristle tip (small mass) velocity in the global frame of reference
u_z	vertical component of the bristle tip (small mass) velocity
V_r	linear velocity of rolling
V_x	forward velocity of the wheel centre
V_{sx}	longitudinal velocity of the bristle base due to longitudinal sliding of the tyre
V_{sy}	lateral velocity of the bristle base due to lateral sliding of the tyre
V_{syc}	lateral velocity of the bristle base due to camber and turn-slip
V_{syr}	resultant lateral velocity of the bristle base due to combined lateral sliding, camber and turn-slip
V_{vx}	forward velocity of the vehicle
W_f	work done by moment M_f over a rotation angle ϑ_r of the wheel
W_L	work lost due to hysteresis over a rotation angle ϑ_r of the wheel
W_r	work done by moment M_r over a rotation angle ϑ_r of the wheel

x	longitudinal displacement of the bristle tip (small mass) in the global frame of reference
x_L	position of the bristle base along the contact patch in the SAE moving frame of reference
x_r	radial deflection of the tyre segment with respect to the un-deformed state (positive for compression – negative for extension)
x_s	longitudinal displacement of the bristle base in the the global frame of reference
x_t	tangential deflection of the tyre segment with respect to the un-deformed state (positive for compression – negative for extension)
y	lateral displacement of the bristle tip (small mass) in the global frame of reference
y_s	lateral displacement of the bristle base in the global frame of reference
y_{sc}	lateral displacement of the bristle base in the global frame of reference due to camber and turn slip
z	normal displacement of the bristle tip (small mass) in the global frame of reference (equal to zero when the tip first enters the contact)

Greek letters

a	slip angle
a_T	horizontal shift calculated by the WLF equation
γ	camber angle
δ	vertical deflection of the tyre
ε	strain
η	damping coefficient

ϑ	angle of travel of a tyre segment through the contact arc
ϑ_0	contact angle at the leading edge of the contact patch
ϑ_r	angle of rotation of the wheel about its spin axis for the calculation of the hysteresis losses
λ	pressure saturation parameter
μ	coefficient of friction
$\mu_{adhesion}$	coefficient of friction due to adhesion
$\mu_{hysteresis}$	coefficient of friction due to hysteresis
μ_k	coefficient of kinetic friction
μ_{kx}	coefficient of kinetic friction in the longitudinal direction
μ_{ky}	coefficient of kinetic friction in the lateral direction
μ_s	coefficient of static friction
μ_{sx}	coefficient of static friction in the longitudinal direction
μ_{sy}	coefficient of static friction in the lateral direction
μ_{xm}	coefficient of friction used in the braking characteristic of the Magic Formula
μ_{xred}	total longitudinal friction reduction coefficient
μ_{ym}	coefficient of friction used in the cornering characteristic of the Magic Formula
μ_{yred}	total lateral friction reduction coefficient
σ	stress
φ	phase angle of strain response
φ	spin angle (angular displacement about the wheel's spin axis)
Φ	spin slip

Φ_C	camber slip
Φ_T	turn slip
ψ	yaw angle of the wheel
Ω	rotational velocity of the wheel about its spin axis
$\vec{\omega}$	rotational velocity of the wheel (vector)
ω	frequency of excitation

Chapter 4

a	half length of the contact patch
p	tyre pressure
$\mathbf{Atr}_x$	Inertia-damping matrix for the longitudinal degree of freedom of the tread elements
$\mathbf{Atr}_y$	Inertia-damping matrix for the lateral degree of freedom of the tread elements
$\mathbf{A}_x$	Inertia-damping matrix for the longitudinal degree of freedom of the belt elements
$\mathbf{A}_y$	Inertia-damping matrix for the lateral degree of freedom of the belt elements
$\mathbf{Btr}_x$	stiffness matrix for the longitudinal degree of freedom of the tread elements
$\mathbf{Btr}_y$	stiffness matrix for the lateral degree of freedom of the tread elements
$\mathbf{B}_x$	stiffness matrix for the longitudinal degree of freedom of the belt elements
$\mathbf{B}_y$	stiffness matrix for the lateral degree of freedom of the belt elements
c	mass per unit length of the belt
C	mass per unit length
C_a	cornering stiffness of the tyre

C_k	braking stiffness of the tyre
c_{tr}	mass per unit length of the tread
C_x	longitudinal stiffness of the tyre
C_y	lateral stiffness of the tyre
D	damping per unit length
$D_{\text{int}\,er}$	damping per unit length of lateral interconnections between adjacent tyre segments
Dlat	lateral damping per unit length of the carcass
Dlong	longitudinal damping per unit length of the carcass
D_r	damping per unit length in the radial direction
Dtrlat	lateral damping per unit length between belt and tread
Dtrlong	longitudinal damping per unit length between belt and tread
Dtry	lateral damping per unit length between adjacent tread elements
D_x	longitudinal damping per unit length along the contact patch
Dy	lateral damping per unit length between adjacent belt elements
D_y	lateral damping per unit length along the contact patch
D_z	damping per unit length in the vertical direction
f	friction force applied on a tread segment
$\mathbf{f}_{btx}$	vector of longitudinal forces between belt and tread
$\mathbf{f}_{bty}$	vector of lateral forces between belt and tread
f_x	longitudinal component of friction force on a tread segment

f_{xi}	longitudinal component of friction force applied on the i^{th} tread element
f_y	lateral component of friction force on a tread segment
f_{yi}	lateral component of friction force applied on the i^{th} tread element
$\mathbf{F}_x$	vector of longitudinal friction forces
$\mathbf{F}_y$	vector of lateral friction forces
F_{xi}	longitudinal force applied by the belt on the i^{th} tread element
F_{yi}	lateral force applied by the belt on the i^{th} tread element
F_{zi}	normal force applied on the i^{th} tread element
$\mathbf{I}_{trx}$	vector of longitudinal degrees of freedom of the tread
$\mathbf{I}_{try}$	vector of lateral degrees of freedom of the tread
$\mathbf{I}_{bx}$	vector of longitudinal degrees of freedom of the belt
$\mathbf{I}_{by}$	vector of lateral degrees of freedom of the belt
k'	transient longitudinal slip ratio
K	stiffness per unit length
$K_{\text{int } er}$	stiffness per unit length of lateral interconnections between adjacent tyre segments
Klat	lateral stiffness per unit length of the carcass
Klong	longitudinal stiffness per unit length of the carcass
Ktrlat	lateral stiffness per unit length between belt and tread
Ktrlong	longitudinal stiffness per unit length between belt and tread

Ktry	lateral stiffness per unit length between adjacent tread elements
K_x	longitudinal stiffness per unit length along the contact patch
Ky	lateral stiffness per unit length between adjacent belt elements
K_y	lateral stiffness per unit length along the contact patch
K_z	stiffness per unit length in the vertical direction
l_h	height of the loaded rolling wheel centre from the ground
p	tyre pressure
qx	longitudinal friction reduction rate coefficient
qy	lateral friction reduction rate coefficient
n	number of discrete tyre segments
n	number of discrete belt elements
n_{tr}	number of discrete tread elements
R_b	radius of the tyre belt
threshold	velocity threshold for the stick-slip transition
t_{travel}	total time of travel of the bristle base
u	longitudinal velocity of the tyre centre in the SAE frame of reference
u	velocity of the bristle tip (small mass) in the global frame of reference
$\mathbf{U}_{belt}$	vector of lateral velocities of belt segments in interaction with the tread segments
$\mathbf{U}_{rim}$	vector of lateral velocities of the rim
Urx_j	circumferential excitation velocity imposed by the rim on the j^{th} belt segment
Ury_j	lateral excitation velocity imposed by the rim on the j^{th} belt element

Ux_j	circumferential velocity of the j^{th} belt element
$Uxtr_i$	longitudinal (circumferential) velocity of the i^{th} tread element
Uy_j	lateral velocity of the j^{th} belt element
$Uytr_i$	lateral velocity of the i^{th} tread element
u_x	longitudinal component of the bristle tip (small mass) velocity in the global frame of reference
u_y	lateral component of the bristle tip (small mass) velocity in the global frame of reference
v	lateral velocity of the tyre centre in the SAE frame of reference
$\mathbf{V}_{belt}$	vector of longitudinal velocities of belt segments in interaction with the tread segments
$\mathbf{V}_{rim}$	vector of longitudinal velocities of the rim
V_s	sliding velocity (generic)
V_{sx}	longitudinal sliding velocity
V_{sy}	lateral sliding velocity
Vy	lateral component of the velocity of the centre of the wheel
x	longitudinal displacement of the bristle tip (small mass) in the global frame of reference
x_j	displacement of the j^{th} belt segment in the longitudinal (circumferential) direction
$\mathbf{X}_{belt}$	vector of longitudinal displacements of belt segments in interaction with the tread segments
x_r	radial deflection of the tyre segment with respect to the un-deformed state (positive for compression – negative for extension)
$\mathbf{X}_{rim}$	vector of longitudinal displacements of the rim

x_{rimj}	circumferential displacement imposed by the rim on the j^{th} belt segment
x_s	longitudinal displacement of the bristle base in the global frame of reference
y	lateral displacement of the bristle tip (small mass) in the global frame of reference
$\mathbf{Y}_{belt}$	vector of lateral displacements of belt segments in interaction with the tread segments
y_j	displacement of the j^{th} belt segment in the lateral direction
$\mathbf{Y}_{rim}$	vector of lateral displacements of the rim
y_{rimj}	lateral displacement imposed by the rim on the j^{th} belt segment
y_s	lateral displacement of the bristle base in the global frame of reference
ytr_i	lateral displacement of the i^{th} tread element
z	normal displacement of the bristle tip (small mass) in the global frame of reference (equal to zero when the tip first enters the contact)

Greek letters

α'	transient slip angle
γ	camber angle
η	lateral tyre deflection
ϑ	angle of travel of a tyre segment through the contact arc
ϑ_0	contact angle at the leading edge of the contact patch
θ	initial angle of the 1^{st} belt segment
ϑs	angular separation of tyre belt segments
λ	pressure saturation parameter

μ_k	coefficient of kinetic friction
μ_{kx}	coefficient of kinetic friction in the longitudinal direction
μ_{ky}	coefficient of kinetic friction in the lateral direction
μ_s	coefficient of static friction
μ_{sx}	coefficient of static friction in the longitudinal direction
μ_{sy}	coefficient of static friction in the lateral direction
μ_{xred}	total longitudinal friction reduction coefficient
μ_{yred}	total lateral friction reduction coefficient
ξ	longitudinal travel of the corresponding un-deformed segment of the tyre tread during braking
σ_x	longitudinal relaxation length
σ_y	lateral relaxation length
Ω	rotational velocity of the wheel about its axis
Ωst	angular steering velocity

Chapter 5

a	distance between the front axle and the origin of the local frame of reference
b	distance between the rear axle and the origin of the local frame of reference
c	half front wheel track
C_{af}	cornering stiffness of the front tyres
C_{ar}	cornering stiffness of the rear tyres
d	half rear wheel track
$D_{f,r}$	damping coefficient of front/rear suspension

$F_{d1} - F_{d4}$	suspension damping forces
$F_{k1} - F_{k4}$	suspension spring forces
F_{xityre}	projection of the forces of the i^{th} tyre on the x-axis of the local frame of reference
F_{yityre}	projection of the forces of the i^{th} tyre on the y-axis of the local frame of reference
$F_{z1roll} - F_{z4roll}$	additional vertical reactions on the four wheels due to the front anti-roll bar
F_{zi}	total vertical force on the i^{th} wheel
F_{zd}	sum of suspension damping forces
F_{zk}	sum of suspension spring forces
F_{zkd}	overall suspension forces
g	acceleration of gravity
$\mathbf{G}$	vector of gravitational forces
h	height of the origin of the local frame of reference from the ground with the vehicle at rest
I_{xx}	roll moment of inertia
I_{yy}	pitch moment of inertia
I_{zz}	yaw moment of inertia
I_{xy}	product of inertia
I_{yz}	product of inertia
I_{zx}	product of inertia
$K_{f,r}$	stiffness coefficient of front/rear suspension springs
K_{froll}	front anti-roll bar stiffness
K_{rroll}	rear anti-roll bar stiffness
k_{susp}	stiffness coefficient of the suspension spring (quarter car model)
k_{tyre}	vertical stiffness of the tyre

c_{susp}	damping coefficient of the suspension damper (quarter car model)
c_{tyre}	vertical damping of the tyre
ℓ	wheelbase
$\mathbf{L}$	transformation matrix
L	sum of moments about the vehicle (local) x-axis
M	sum of moments about the vehicle (local) y-axis
m	mass of the vehicle
m_{wheel}	mass of the wheel
$m_{quarter}$	mass of the quarter car body
M_x	roll moment about the vehicle (local) x-axis
$M_{xkdroll}$	overall roll moment by the suspension
M_{xfroll}	roll moment by front anti-roll bar
M_{xrroll}	roll moment by rear anti-roll bar
M_{xd}	roll moment due to damping forces
M_{xk}	roll moment due to spring forces
M_{xtyre}	roll moment due to tyre forces
M_{ytyre}	pitch moment due to tyre forces
M_{ztyre}	yaw moment due to tyre forces
M_y	pitch moment about the vehicle (local) y-axis
M_{yd}	pitch moment due to damping forces
M_{yk}	pitch moment due to spring forces
M_{ykd}	overall pitch moment by the suspension
M_z	yaw moment about the vehicle (local) z-axis
M_{xG}	roll moment due to gravity about the vehicle (local) x-axis
M_{yG}	pitch moment due to gravity about the vehicle (local) y-axis

M_{zG}	yaw moment due to gravity about the vehicle (local) z-axis
N	sum of moments about the vehicle (local) z-axis
p	roll velocity
q	pitch velocity
r	yaw velocity
R_I	global frame of reference
R_J	local frame of reference
U	forward velocity
V	lateral velocity
W	normal velocity
X	sum of forces along the vehicle (local) x-axis
x	forward displacement; x-coordinate of a point in the local frame of reference
x_G	longitudinal distance of the c.g. from the origin of the local frame of reference
x_{body}	vertical displacement of the quarter-vehicle body
x_{road}	height of the road profile
x_{wheel}	vertical wheel displacement
Y	sum of forces along the vehicle (local) y-axis
y	lateral displacement; y-coordinate of a point in the local frame of reference
y_G	lateral distance of the c.g. from the origin of the local frame of reference
Z	sum of forces along the vehicle (local) z-axis
z	normal displacement; z-coordinate of a point in the local frame of reference
z_G	vertical distance of the c.g. from the origin of the local frame of reference

Greek letters

$a_1 - a_4$	slip angles of the four tyres
a_f	slip angle of front tyres
a_r	slip angle of rear tyres
Γ	non-dimensional yaw impulse
$\Gamma_{\Delta t}$	integrated non-dimensional yaw impulse
$\delta_1 - \delta_4$	steer angles of the four wheels
θ	roll angle; 1st rotation of frame of reference during relative transformation
θ_{wheelf}	additional roll-angle due to un-even vertical displacement of the front wheels
θ_{wheelr}	additional roll-angle due to un-even vertical displacement of the rear wheels
φ	pitch angle; 2nd rotation of frame of reference during relative transformation
ψ	yaw angle; 3rd rotation of frame of reference during relative transformation
ω	angular velocity of the global frame of reference

Chapter 1: Introduction

1.1 Handling, Stability and the Role of the Pneumatic Tyre

Modern ground vehicles are expected to satisfy a large number of requirements that are very often in conflict with each other. For example, a passenger car needs to be powerful and at the same time fuel efficient. It has to achieve high standards of passive, and progressively active safety and protect passengers in case of collision, while being lightweight and providing enough internal space. Handling qualities and stability refer to the directional responsiveness of a vehicle and are related more than any other factor to the original purpose of an automobile, being the safe transportation of passengers and goods to desired destinations by responding smoothly to the driver's commands.

Handling and stability are frequently used as synonyms, without due distinction. Although these two terms have a lot in common and are interrelated in many cases, there are a few differences, which are worth identifying by attempting to provide them with broad definitions.

The stability of a ground vehicle can be described as its performance under manoeuvres, which result in alterations to the state of its motion in a generic, vectorial sense. Performance, in this context, is related to the capability of achieving high values of acceleration in braking, cornering, lane change and other manoeuvres, while the driver maintains control over the vehicle. Stability can also be defined in a more mathematical way. For example, by adopting some necessary simplifications, a vehicle's motion can be described by a linear system of differential equations. General theories that describe the mathematical stability of such systems can then be employed in order to assess the response of a vehicle to certain excitations.

There seems to be a slightly different use of the term *handling* by test/competition drivers and research engineers. The former describe handling as the driver's

perception of the vehicle's stability [1]. It reflects the confidence a driver may or may not feel about the extent of a car's responsiveness to his commands. Usually, this feeling is related to the feedback provided via the steering wheel and the tendency of a car to roll during cornering or dive during braking, but more experienced drivers may also refer to a number of other subjective factors. A vehicle with good handling qualities is almost always good in terms of stability, but the converse of this argument is not necessarily held true. A stable vehicle may be described as poor in terms of handling, if the feedback to the driver is rather hazy, reducing his anticipation of the vehicle's motion [1]. On the other hand, handling is frequently used by researchers (for example in [2-4]) in order to describe stability issues. In this thesis, the term handling is used hereinafter to encompass the handling as well as the stability qualities of a vehicle.

Very often, advances in technology precede the evolution of science and this fact is demonstrated dramatically in the area of ground transportation. It is believed that the wheel was invented in Mesopotamia or Asia sometime around 3500-4000 BC. From the early 19th century the importance of the independent steering of the front wheels of horse-drawn carriages was appreciated and the well-known Ackerman steering principle was soon established [5]. Nevertheless, the first attempts to study a vehicle's motion in a dynamic manner, paying attention to the relation of the forces involved and the resulting path came almost a hundred years later, in the beginning of the 20th century. Still, the importance of the forces generated on the contact patch between the tyres and the road was fully appreciated only after 1930. Today the use of pneumatic tyre has well established its position as the cornerstone in vehicle handling analyses. Apart from its original purpose as a cushion between the vehicle and the rough road, the tyre's role in the generation of all major controlling forces, including longitudinal traction, braking and lateral cornering forces is the factor that determines the handling behaviour of a vehicle. This role is demonstrated more than anywhere else in the area of racing. The choice of tyres hugely influences the overall performance of a competition vehicle and the competition between major tyre suppliers is often more interesting to follow than the rivalry between car manufacturers and drivers.

Arguably, the pneumatic tyre is one of the most successful human inventions and one of the most difficult to study. For more than 50 years it has received enormous

attention by many researchers (see for example the collection of research achievements published in [6]) who have achieved insight into several aspects of tyre behaviour and their effects on the handling qualities of vehicles. The present research continues this evolutionary trend, mainly dealing with the steady-state and transient responses of the pneumatic tyre and their relation with the handling performance of ground vehicles.

It should be noted that throughout the present thesis, for the sake of brevity, the word "Vehicle" is used in place of the most appropriate term: "Ground Vehicle".

1.2 Brief Experimental and Theoretical Background

Both the nature of, and the importance of handling investigations have been addressed in relation to the role of the pneumatic tyre in the mechanism of force generation. In order to clarify the matter, handling and tyre dynamics are discussed further in the following paragraphs.

In general, handling investigations are conducted experimentally, analytically or numerically. Experimental testing usually involves driving a vehicle on a test track and measuring several kinematic outputs such as lateral acceleration, yaw velocity, roll angle and braking distance. Experimental investigations are most representative of reality and when conducted by professional test drivers provide a spherical perception of the vehicle's handling performance. The drawbacks include high costs, the fact that tests are carried out on the manufactured product and, for some tests, the possibility that the results might be affected by the drivers' subjective judgement. On the other hand, analytical approaches and computer simulations allow engineers to investigate the handling performance far ahead of the production phase, in a way that even the first prototypes can be more or less optimised. Apart from that, it is possible to investigate dangerous driving scenarios and precisely determine the effect of certain parameters. Finally, simulations are most valuable in designing control strategies for the improvement of the handling performance of ground vehicles.

Irrespective of whether handling tests are carried out on a test track or on a computer in an office, they can be further divided into two categories, namely Steady-State or

Transient handling investigations. In general, the former category involves cornering at a constant radius with constant forward velocity. Given the magnitude of forward velocity, the required steer-angle for negotiating a corner of known radius of curvature is an important measure of the handling behaviour of a vehicle. As opposed to Steady-State, transient handling refers to rapidly changing driving commands, such as step-changes in the steer-angle, severe braking, hard acceleration, lane-change or a combination of these.

For Steady-State predictions, relatively simple vehicle models, incorporating two or three degrees of freedom can be used as a starting point for analytical or numerical solutions. For instance, in analytical steady-state approaches, it is common practice [2] to reduce the degrees of freedom of the full vehicle and concentrate on the lateral and yaw velocities, assuming constant forward speed and steer-angle. For transient analyses the approach is mostly numerical, and the models usually take into account all the six possible motions of the vehicle in space. Depending on the level of detail required, a more realistic representation of the suspension system may be included, resulting in an increase in the number of degrees of freedom for the vehicle model.

In line with this philosophy of vehicle handling analyses, tyre behaviour may be investigated experimentally, analytically or numerically and, as already implied, the distinction between Steady-State and Transient conditions applies in the case of features of tyre behaviour as well. Broadly, Steady-State tyre analysis refers to the generation of conditions similar to the ones observed in the neighbourhood of a wheel of a vehicle operating under Steady-State conditions, whereas Transient tyre analysis refers to the generation of conditions that characterise the neighbourhood of a wheel of a vehicle operating under Transient manoeuvres. The most common exception to this rough rule is related to braking. Although steady-state braking is an essential ingredient in tyre behavioural analyses, when referring to the handling characteristics of a vehicle as a whole, braking manoeuvres are mostly related to transient operating conditions.

Steady State and Transient conditions alike may be generated experimentally with the aid of specially designed tyre test rigs, consisting of rotating drums or flat belts, which

represent the road surface and the necessary mechanisms, which support and move the tyre-rim system.

Depending on the type of application, tyre data may be used in handling simulations directly as obtained by experiments or it may be generated within the simulation procedure, using tyre models of varying detail. In general, tyre models can be divided into two main categories, namely empirical or physical. Empirical models use analytical formulae, which are based on successful fitting of experimental measurements in the form of empirical relations, while physical models attempt a physical description of the tyre structure and the mechanics of its interaction with the road surface in a fundamental manner, based on established physics rather than pure observations or measurements.

1.3 Problem Definition

Prior to the broad expansion of powerful computer systems, handling studies were carried out using simple linear differential equations in order to describe the vehicle's motion. This approach is demonstrated in research papers [2] and text books [6], [7] and [8]. In this procedure the tyre behaviour is assumed to be linear, which is a valid simplification for a vehicle operating under low acceleration levels. In recent years, the evolution in the computer technology has enabled a more complex, non-linear modelling of the vehicle and tyre. A presentation of modern simulation methodologies is given in [9]. Lagrangian dynamics provide a well-defined, consistent method for modelling the entire vehicle in what has become known as a multi-body dynamics approach [10], [11]. Several components, such as the suspension links, can be modelled separately resulting in a non-linear system, incorporating hundreds of degrees of freedom and, of course, including the corresponding kinematic constraints. The Newton-Euler approach is less generic, as it lacks the ability to include the effect of holonomic constraints [11] in the equations of motion. Nevertheless, it can provide complex non-linear equations for the motion of the vehicle model. Regardless of the modelling approach, the differential-algebraic system of equations can be solved numerically on a modern computer with very high degree of accuracy. In terms of modelling, the weakest link in this procedure remains the pneumatic tyre. Unlike the vehicle itself, which is governed by the laws of rigid body motion in space, the tyre

demonstrates an extremely complex behaviour which spreads into the areas of contact mechanics, viscous friction, elasticity, vibration of structures, thermodynamics and hydrodynamics, requiring a multi-physics approach to deal with its complex behaviour.

Typically, tyre force generation is studied either under steady-state operating conditions, or under transient manoeuvres. Even in steady state investigations, the influence of a number of factors such as the normal pressure distribution along the contact patch, the compliance of the tyre tread, belt and carcass and the friction between the tyre tread and the road is not yet fully understood. Although some very successful tyre models have been proposed (see for example [6]) and are widely used, it seems that no tyre model describes fully the aforementioned features, their interactions, and other relevant factors.

Most importantly, the steady state analysis and the role of the aforementioned factors need to be expanded on in order to account for the various transient operating conditions. Again, significant progress has been achieved and the transience related to the complex deformation of the tyre under rapidly changing conditions have been investigated with the aid of a variety of elaborate tyre models such as those presented in [12-20]. In the majority of these approaches the models are primarily concerned with the transient response of the structure of the tyre, with less emphasis on frictional issues. On the other hand, the models discussed in [21-25], aim in a more accurate estimation of the friction forces. Finally, experimental studies [26-28] show the dependency of friction on the operating conditions and suggest the existence of phenomena such as stick-slip. In any case, the issue of fiction should be looked at more closely with an emphasis on transient behaviour.

Consequently, there is a need for additional investigations towards attaining a better understanding of tyre force generation under both steady-state and transient operating conditions. A critical approach should be adopted, the inherent physical limitations of proposed tyre models need to be assessed and the role of friction force generation should be taken into account in a fundamental manner.

1.4 Aim and Objectives

The aim and objectives of the present research follow directly from the problems stated in the preceding section. A theoretical investigation of tyre Steady-State dynamics serves as a starting point. The influence of certain parameters such as the normal pressure distribution and the frictional properties of the contact between the tread and the road will be investigated in parallel with the development of a new brush-type tyre model, appropriate for Steady-State studies. The inclusion of the aforementioned factors in the physical characteristics of the tyre model is of fundamental importance and requires extensive analysis. An increasingly complex treatment to the problem will be followed, based on the fundamentals of theory of contact mechanics. Through this procedure, the inherent limitations of the proposed brush-type models will be identified and assessed.

Based on the knowledge gained from the steady-state model, an expansion of the theory in the area of transient tyre dynamics will be attempted. The key issue here is the interaction between the mechanism of friction force generation within the contact patch and the dynamics of the flexible structure of the tyre.

The influence of tyre dynamics on the handling behaviour of vehicles will be evaluated by incorporating the models thus developed in a series of full vehicle handling simulations. The results will be compared with those obtained by well established and regarded empirical tyre models such as the widely used "Magic Formula".

Towards the achievement of the aims stated thus far, a set of well defined tasks have been performed and are given below in the form of bullet points:

- Development of a new, yet simple Steady-State brush model of the tyre, incorporating anisotropic bristles represented by viscoelastic Kelvin elements. The normal pressure distribution is assumed to be parabolic.

- Enhancement of the tyre model in order to facilitate the on-line calculation of the normal pressure distribution depending on running conditions

- Modification of the initial Steady-State model for the simulation of transient conditions and the investigation of the role of the mechanism of friction generation

- Development of a new transient tyre model with flexible belt and carcass, incorporating a separate tread for the simulation of the friction generation mechanism

- Development of a vehicle model for the evaluation of the influence of tyre dynamics in vehicle handling

1.5 Structure of the Thesis

The work is organised in six chapters. A brief description of the issues discussed in each chapter is given below, in order to provide with an overall view of the approach followed in the thesis.

Chapter 1 – Introduction: The role of the pneumatic tyre in the handling behaviour of vehicles is addressed. Some fundamental ideas are presented and the areas of interest are highlighted. As a result, the aim and objectives of the investigations are defined and a brief description of the frame of work is given.

Chapter 2 – Review of Literature: The fields of tyre and vehicle dynamics have received the attention of numerous researchers. This chapter attempts to provide a critical review of the major findings. In particular, the areas of steady-state and transient tyre and vehicle handling dynamics are covered with extensive references to experimental, analytical and simulation techniques. Also, an extensive reference is made to work carried out in the area of friction mechanics, since friction represents the main limiting factor in the tyre-force generating procedure.

Chapter 3 – Steady-State Tyre Analysis: A physical description of the structure of the pneumatic tyre is provided and some important modelling considerations are discussed. These include the definition of coordinate systems and the representation of tyre forces, possible ways of modelling various parts of the tyre as well as modelling of viscoelasticity and friction. A separate section is dedicated to the "Magic Formula"

tyre model, which serves as a benchmark throughout the work reported in this thesis. The chapter closes with the step-by-step development of a simple and a more elaborate steady-state brush model. The behaviour of the models is investigated and the influence of several factors is analysed.

Chapter 4 – Transient Tyre Analysis: The necessity for the development of transient tyre models is discussed. Special reference is made to the modelling of viscoelastic friction between the tread and the road surface and the influence of some parameters such as sliding speed is investigated. The initial steady state tyre model undergoes two successive modifications, which result in two versions of a transient model, one with independent and one with interconnected bristles. Simulation results provide some insight into the qualities of the models. The rest of the chapter is dedicated to the development of the final, most elaborate transient model with flexible belt and carcass and a separate tread for the simulation of friction.

Chapter 5 – Tyre models in handling analysis: A relatively complex vehicle model is developed for the study of vehicle handling behaviour. Some fundamental considerations about coordinate systems, rigid body motions in space and the implementation in vehicle dynamics are presented. The Newton-Euler approach is chosen for the formulation of the differential system of equations and the numerical procedure is also discussed. The tyre models developed in the previous chapters work in combination with the vehicle model in a series of simulations.

Chapter 6 – Conclusion and Suggestions for Future Work: This chapter summarises the major findings of the research. The advantages as well as the shortcomings of the approach are pointed out and some suggestions for further improvement are given. Possible expansion of the theory in other areas is discussed and a set of experimental guidelines is proposed in order to investigate aspects of the theoretical predictions.

Chapter 2: Review of Literature

2.1 Introduction

This chapter is dedicated to the achievements previously accomplished in the fields of tyre and vehicle dynamics by other research workers. In particular, the issues of steady-state and transient tyre force and moment generation, vehicle modelling and handling performance are reviewed. A separate section is dedicated to the mechanics of friction. This section follows the discussion of tyre modelling which points out the special characteristics of tyre friction and the important issues that should be taken into account. All publications retrieved, are included in the list of references, at the end of the thesis. In the following pages the most representative approaches are critically analysed, while a significant amount of supporting literature concerning, for instance, the modelling of friction, the viscoelastic behaviour of rubber or numerical methods for use in vehicle dynamics may be referred to later in the thesis, when dealing with these relevant issues.

The literature is divided into the following areas, according to the specific topics discussed:

1) Steady-state tyre analysis
2) Transient tyre analysis
3) Mechanics of friction
4) Vehicle modelling
5) Vehicle handling analysis

2.2 Steady-State Tyre Analysis

The investigation of tyre force and moment generation is based on a significant amount of experimental measurements. Ultimately, the goal is to describe the procedure of force generation mathematically, with the development of tyre models of

varying complexity. There are a large number of different aspects of tyre behaviour, which should be taken into account and this has resulted in the development of tyre models from different perspectives. As already mentioned, a first classification separates steady-state from transient tyre models. Pacejka [6] suggests another very convenient distinction between *in-plane* and *out-of-plane* models. In-plane tyre models are concerned with force vectors, which ideally lie within the centre plane of the wheel such as the braking force, rolling resistance and normal force, while out-of-plane models deal with forces that lie outside this centre plane, such as lateral forces and the resulting moments. Out-of-plane models are mainly related with the handling dynamics of a vehicle, since tyre lateral forces are primarily responsible for the change in the direction of a vehicle's motion. Nevertheless, lateral forces depend largely, not only on the vertical load of the tyre, but also on the possible application of a simultaneous braking or traction force. Therefore, out-of-plane models always incorporate a number of in-plane characteristics in order to account for the aforementioned effects.

Traditionally, steady-state models, appropriate for handling applications, refer to out-of-plane models able to calculate the tyre lateral force, the resulting self-aligning moment and the longitudinal force (a conventionally in-plane characteristic) as functions of a time-invariant lateral slip angle, camber angle and longitudinal slip. Any analytical or numerical results are compared with experimental data obtained from specially designed experimental rigs. A large number of variations of a basic experimental concept can be found in literature. The following paragraph briefly presents this concept together with a number of common variations and some typical results.

2.2.1. Experimental Measurements and Results

Prior to discussing some of the most important steady-state modelling approaches, an experimental background is given. The principle is similar for both steady-state and transient measurements and will be covered only in this section.

Tyre testing rigs are described in text books [6], [29] and research papers [30-37]. Moore [29] divides tyre-testing equipment into two main categories, namely

laboratory-based machines and field machines. The former consists of a wheel-hub assembly pressed against a rolling drum or a flat rolling belt, as a means of simulating the motion of a vertically loaded tyre rolling on the road surface. Joy et al [32] describe a tyre test-rig, based on a rotating steel drum with a maximum circumferential speed of 125 mph. The vertical load is imposed hydraulically on the wheel supporting mechanism, which presses the tyre against the external circumference of the drum. The design of the mechanism allows a range of slip angles between 0 and 12 degrees, while the camber angle can vary in the range ± 5 degrees. A set of two dynamometers, which can operate alternatively as motors, is used for the simulation of traction and braking. Dunlop Ltd [29] has used a drum testing machine, where instead of the external, the internal drum surface is used. This arrangement permits the formation of a water film for the evaluation of tyre performance in wet conditions. Drum testing machines are favoured for their simplicity, low cost and the potential of using different road surface samples, mounted on the drum. The major drawback is the contact curvature imposed by the finite drum radius. This factor alters the normal pressure distribution along the contact patch and as shown by Pottinger et al [38], affects the cornering behaviour of tyres. To overcome this problem, researchers have used rotating flat-belt machines. The Calspan Corporation's machine described in [30], [35], consists of a wide stainless steel belt supported by two 0.7 m diameter drums. The belt is covered by a grit surface and is supported by an air-bearing pad under the footprint of the tyre. Slip angle, camber angle and normal load can be set automatically through a computer. Lagner [31] and Cabrera et al [37] follow a similar approach, replacing the air-bearing with hydrodynamic water-bearings.

The need for measuring forces generated by tyres rolling on virtually any type of road has resulted in the development of field-testing equipment. Essentially, these machines consist of the upper half (wheel supporting and moving mechanism) of the laboratory machines, mounted on or pulled by dedicated vehicles. The drum or belt is replaced by the real road and data is collected by on-board acquisition systems. Gohring et al [36] use a mobile tyre testing apparatus and compare the results with those obtained in the laboratory, using a drum-type machine. It is reported that the results differ up to 40% in the measurement of cornering stiffness and this is due to

the interaction of two factors, namely the curvature of the drum and the difference in the frictional characteristics between the drum surface and the real road surface.

In Steady-State measurements, side-slip angle, camber angle, longitudinal slip and vertical load are kept constant. In addition, air pressure and temperature are monitored through sliding electrical and pneumatic connections [29], [34]. Typically, graphs are produced showing the lateral tyre force as a function of steady-state slip angle for a given camber angle, longitudinal slip and normal load. The self-aligning moment, as a result of the interaction between lateral force and pneumatic trail [6], is plotted against the slip angle for the same conditions. Longitudinal forces are plotted against longitudinal slip, for a predefined vertical load, side-slip and camber angles. Finally, lateral force is also presented as a function of the longitudinal force for pre-specified side-slip angles. Figures 2.1-2.4 illustrate some typical experimental results from reference [36]. Figure 2.1 shows the non-linear increase in lateral force with the increase in side-slip angle for four different load cases of a commercial vehicle tyre. At high slip angles, towards the right end of the graph, if tyre friction was subjected to the laws of friction as stated by Amontons and Coulomb [39-40], the maximum force should be governed only by the normal load and the coefficient of sliding friction at a given speed. In particular, the maximum values of the lateral forces should be proportional to the normal load. However, it is clear that this is not the case, since, for example, the maximum lateral force at a vertical load of 40 kN is only approximately 2.4 times higher than the maximum force at 10 kN. This behaviour influences greatly the handling properties of vehicles and will be discussed thoroughly later. Figure 2.2 shows the variation of braking force with longitudinal slip for four different load cases, while figure 2.3 plots the braking forces corresponding to six combinations of simultaneous side-slip under the same vertical load. Apparently, not only the maximum braking force is reduced with the increase of slip angle, but the shape of the curve is altered as well. Figure 2.4 illustrates how the lateral force, corresponding to a specific slip angle, varies with the increase in the braking force. By varying the side slip angle, a parametric plot is obtained. The black line defined by the outer limits of the plots constitutes the traction limit of the tyre under combined braking and cornering manoeuvres for a specific vertical load. Finally, figure 2.5 illustrates an example of self-aligning moment plotted against slip-angle for varying vertical loads, as measured and fitted by Bakker et al [41].

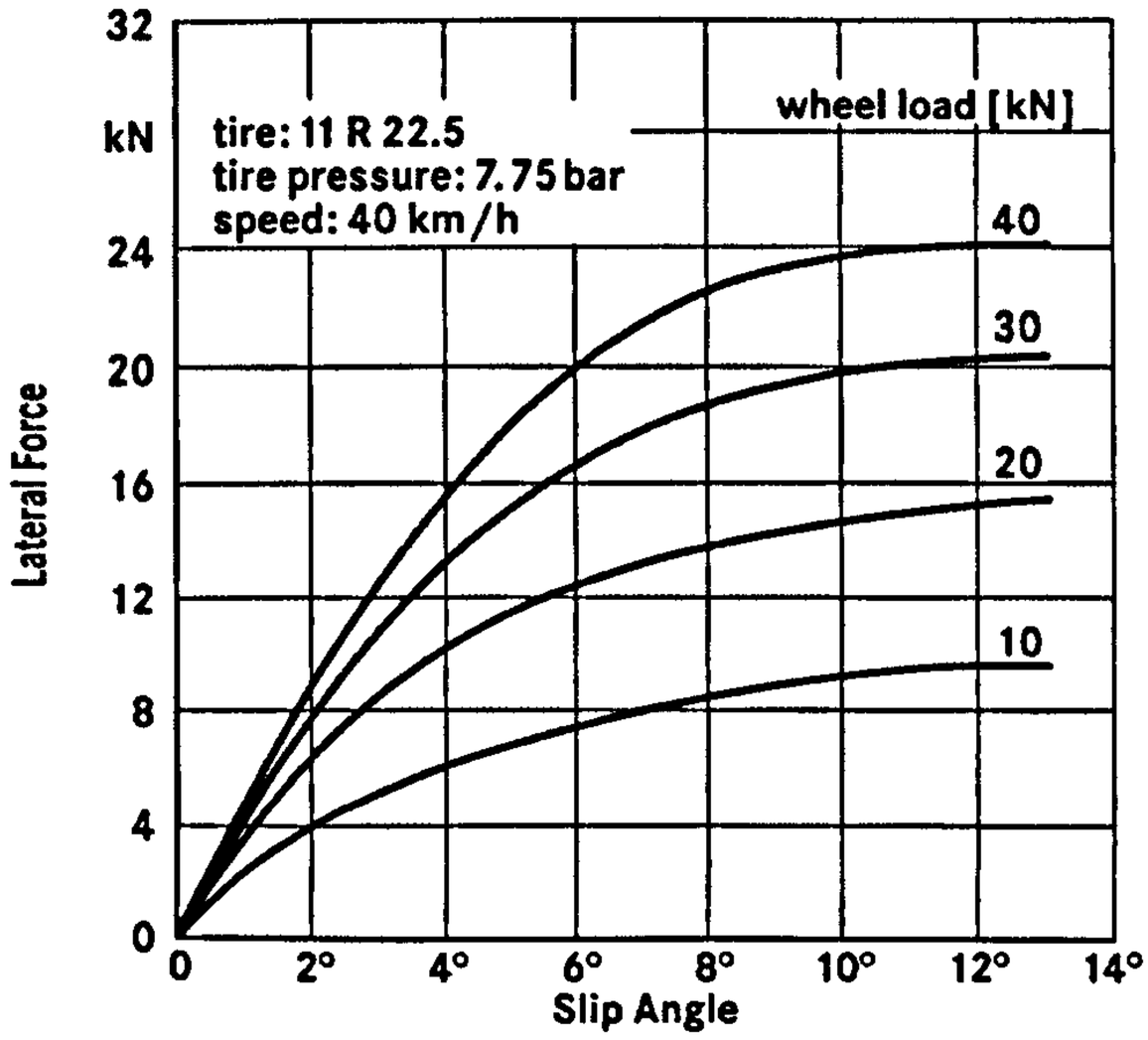

Figure 2. 1 Lateral force vs slip angle for different vertical loads (after [36])

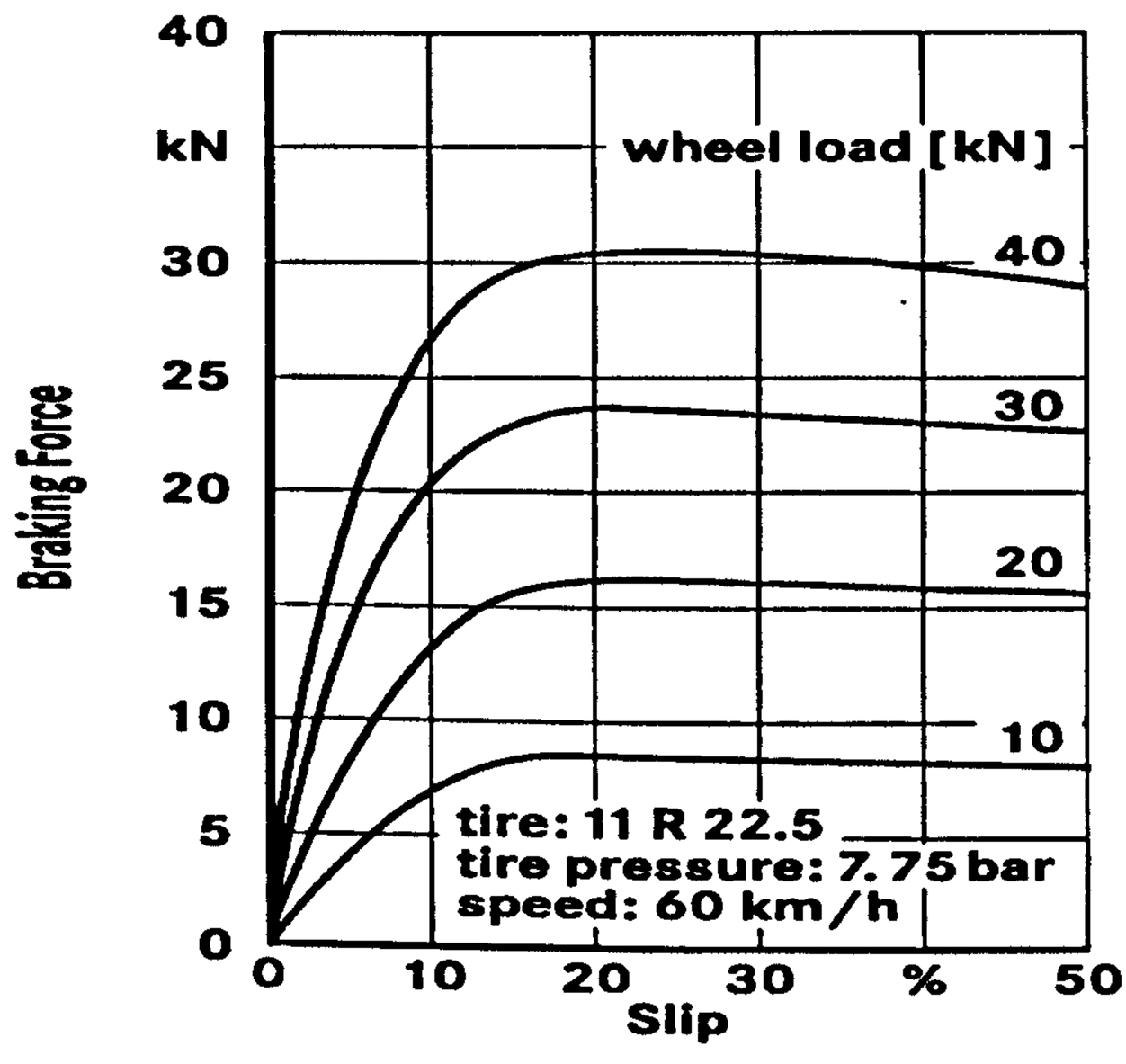

Figure 2. 2 Brake force vs longitudinal slip for different vertical loads (after [36])

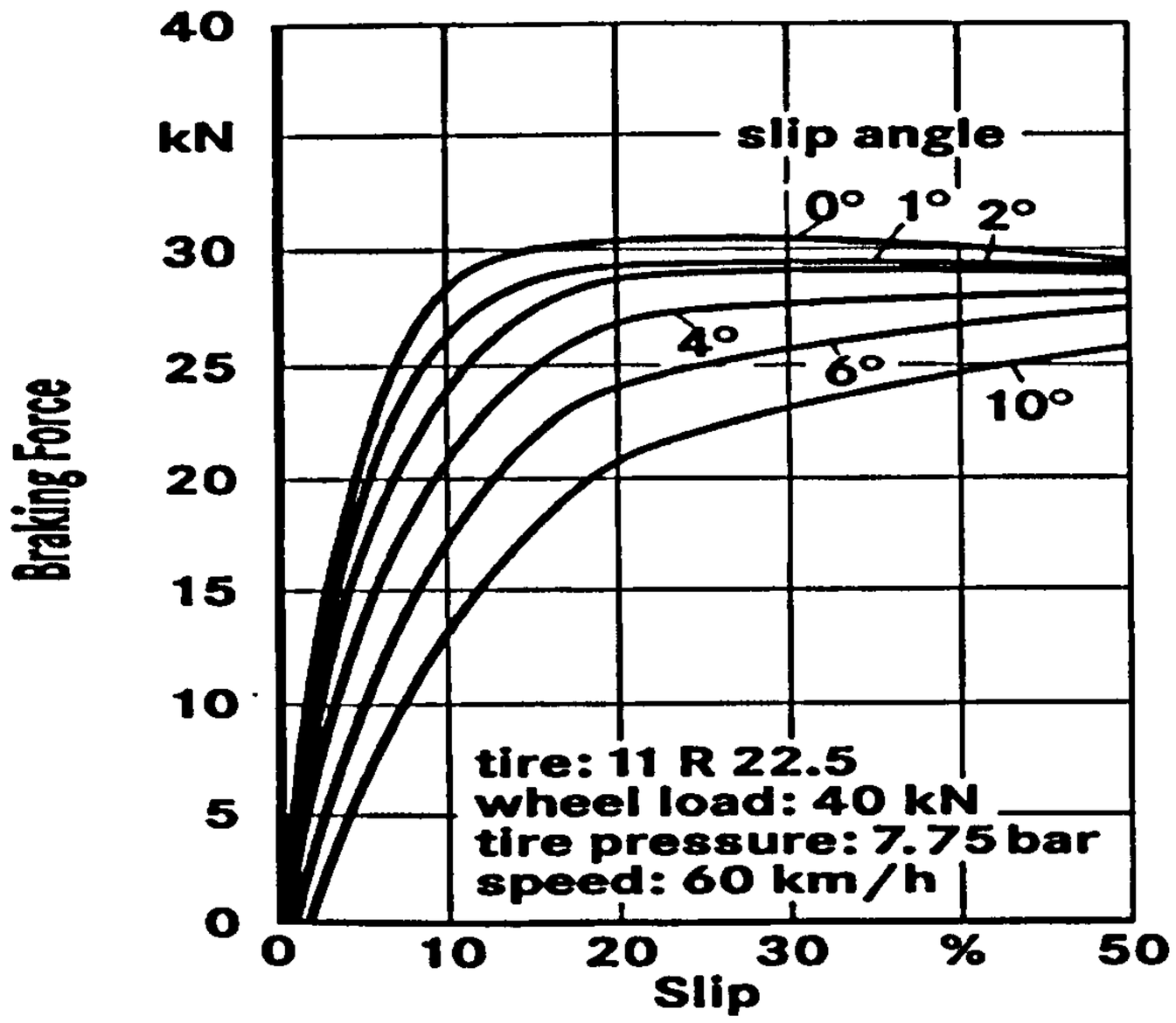

Figure 2. 3 Effect of lateral slip on the generation of brake force (after [36])

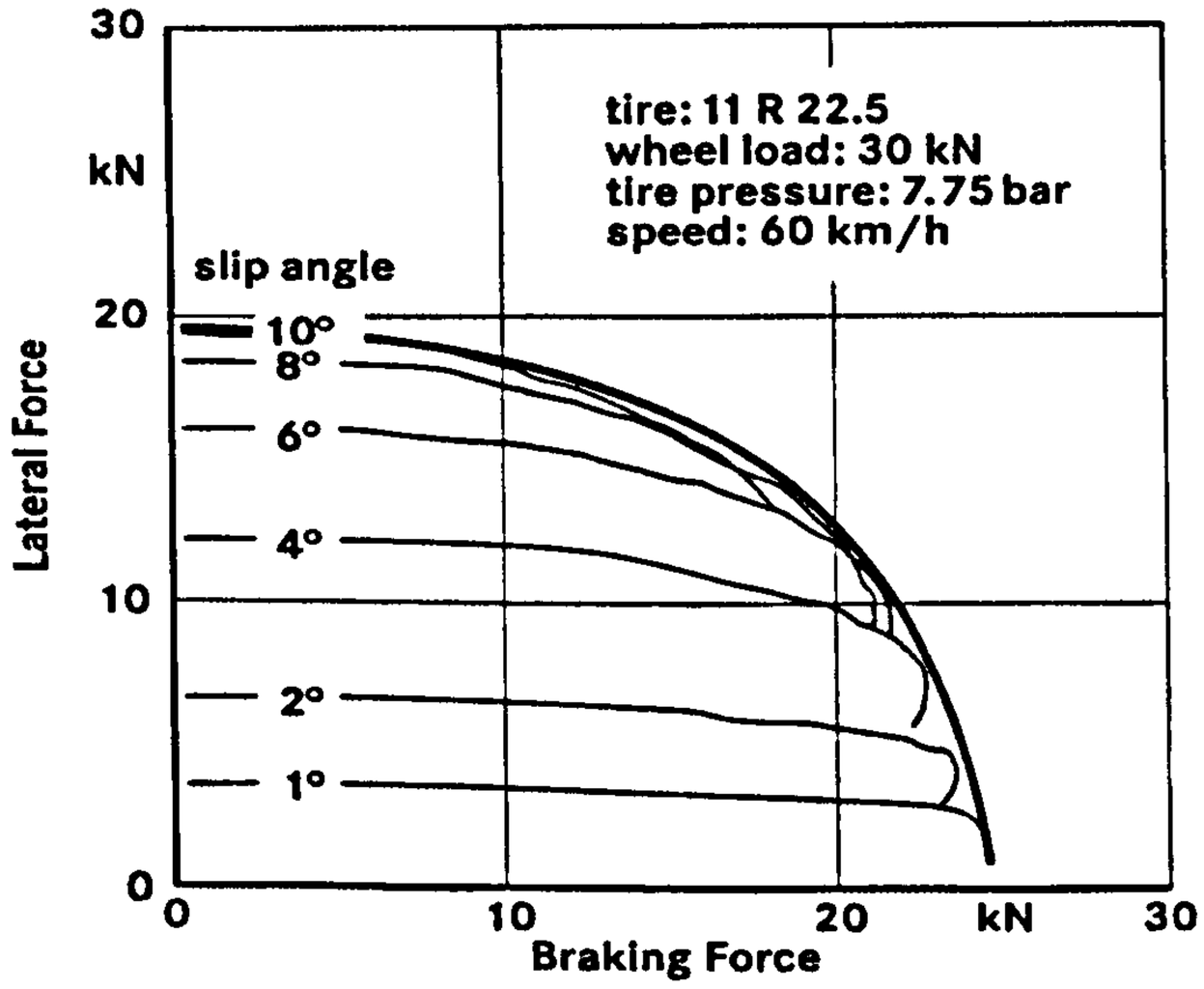

Figure 2. 4 Combined braking - cornering. The 1st quadrant of the friction ellipse (after [36])

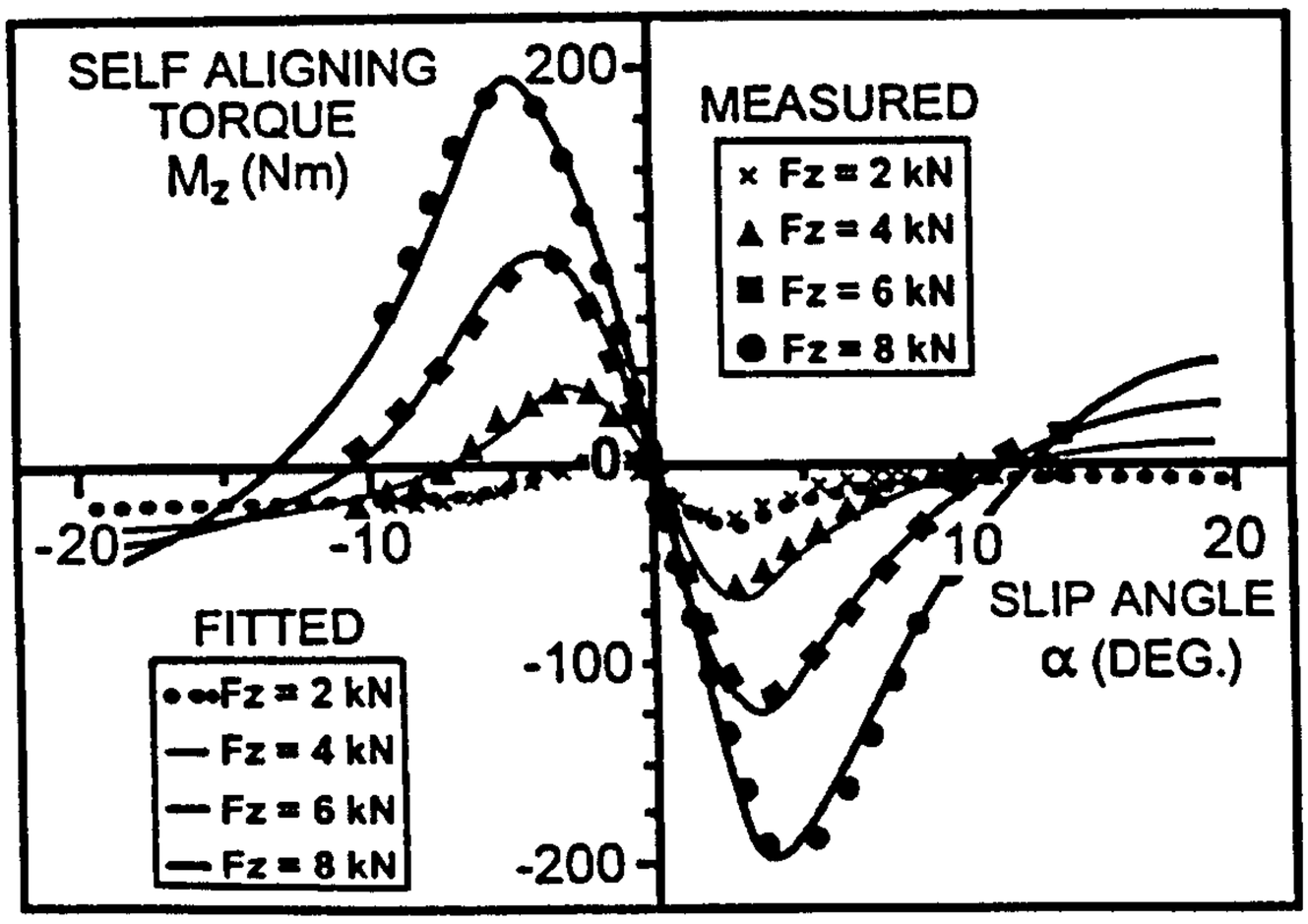

Figure 2. 5 Self aligning torque vs slip angle for different vertical loads (after [41])

2.2.2 Modelling Approaches

Pacejka and Sharp [42] have conducted a comprehensive review of modelling aspects in relation to the steady-state tyre force and moment generation. They distinguish two main categories of models, namely *physical* and *empirical* tyre models. Physical models are based on the mathematical representation of the most important physical properties of the tyre and can vary in complexity. The simplest among the physical models can be solved analytically, while the most complex models, incorporating detailed representations of the tyre structure, are solved numerically and can be computationally very time and memory intensive. Empirical models are based on the use of formulae that fit successfully a wide range of experimental results, such as the ones presented in the previous section. While providing little insight into the physics of tyre behaviour, empirical models have become very accurate and are also computationally very effective. Another important observation mentioned in [42] is the fact that all physical models require experimental identification of one or more parameters. This can be considered as inevitable proof of the complexity of the mechanics of the pneumatic tyre.

2.2.2.1 Physical Models with Analytical Solutions

Temple and von Schlippe [43], [44], [45] propose a simple physical representation of the tyre for the calculation of the steady-state lateral force. This model is based on the assumption that the tread of the tyre is equivalent to a stretched string, restrained by lateral springs which represent the sidewall, as shown in figure 2.6. The free ends of the springs are connected to the wheel rim, which is travelling at a constant slip angle. As a result, the string deforms laterally, while the circumferential distribution of the lateral component of the force due to string tension is proportional to the second derivative of the lateral displacement with respect to the circumference. Over the part of the tyre not in contact with the ground, the distribution of lateral string force is balanced by the distribution of lateral forces generated by the springs. By solving the appropriate second order differential equation, the shape of the lateral deformation is calculated as a hyperbolic function of the free circumference. This function can be simplified to a pair of exponential functions, which describe the deformation of the string in front and behind the contact patch area. The lateral force and the self-aligning moment can be found easily by assuming a linear lateral displacement of the string along the length of the contact patch and applying integration techniques. The results are expressed as functions of the slope of the lateral displacement along the contact patch. For small slip-angles this slope can be assumed equal to the slip-angle, in which case both the lateral force and the self-aligning moment are proportional to the slip angle. Clearly, the model assumes that the combination of vertical load and lateral slip-angle is such that the tyre operates always in the linear range and does not include any provisions for a sliding region within the contact patch.

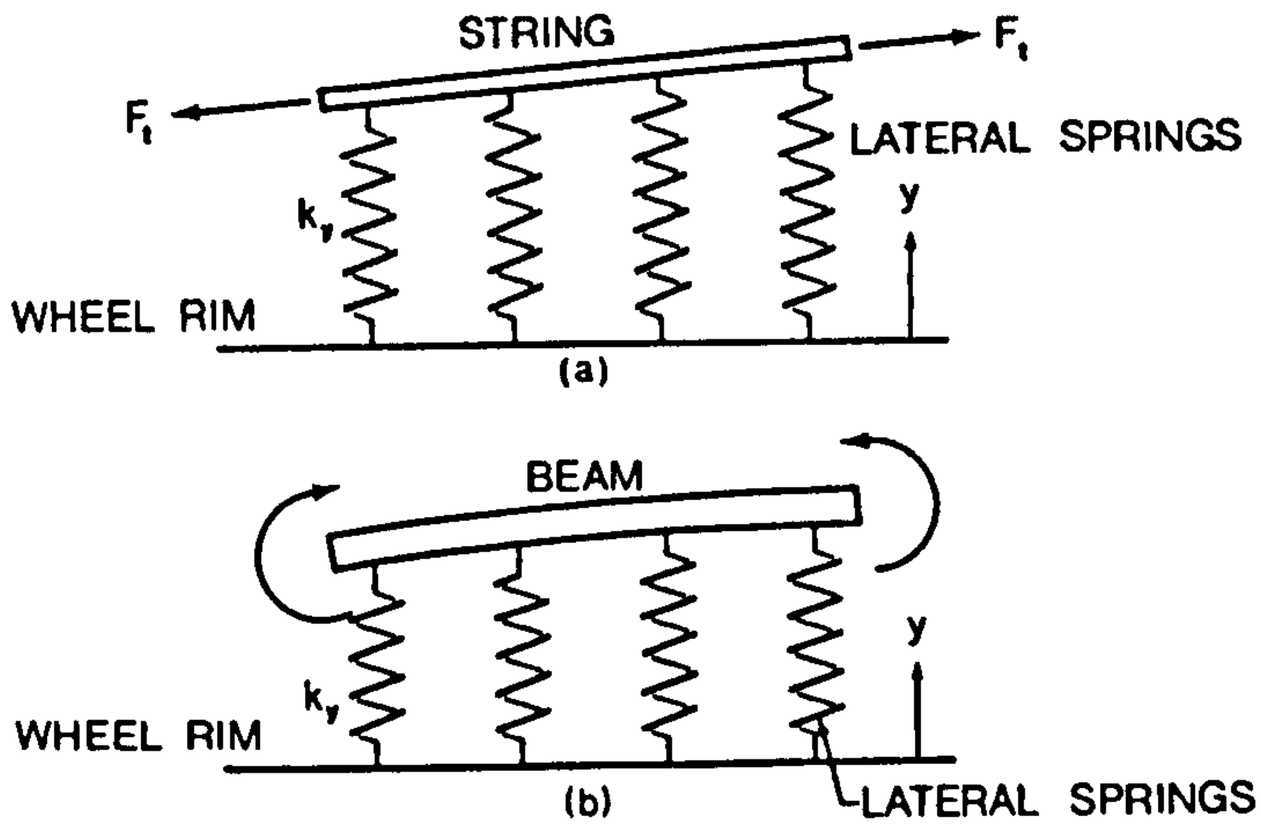

Figure 2. 6 Representation of the tyre as a stretched string (a) or bending beam (b) (after [44])

The cases of traction and braking are treated conceptually in a similar manner, by Julien [43] and by Wong [44]. The tyre tread is represented by an elastic band, the contact patch is assumed rectangular and the normal pressure distribution is considered uniform along the length of the contact patch. In this model there is provision for an adhesive, as well as a sliding zone within the contact patch. The longitudinal force is calculated by integrating the corresponding longitudinal force distribution along the length of the contact patch. The critical length after which the tread starts sliding is calculated as the length up to the point where the longitudinal force distribution becomes equal to the normal force distribution multiplied by the peak value of the coefficient of friction. The total force is equal to the sum of the elastic force developed in the leading adhesive region and the friction force developed in the trailing sliding region. The combination of a sliding and adhesive zone results in a non-linear model, able to depict the behaviour of the tyre at high slip ratios. A fundamental observation is that the adaptation of a uniform pressure distribution allows the entire contact area to be an adhesive region, when the slip ratio is low. Therefore, the initial part of a traction or braking curve should always be linear. In reality, the shape of the pressure distribution can vary from parabolic to trapezoidal and always allows for a small sliding region towards the trailing end of the contact patch. As a result, tyre force generation is, by definition, a non-linear problem.

Fiala [45] proposes a more elaborate physical model, which is still in use and is offered as a standard model in multi-body software packages such as *ADAMS*. The

tyre is modelled as a flexible ring connected to a rigid disc through circumferentially distributed springs. When subjected to a lateral force, the ring deflects according to Eulerian beam theory in pure bending. The lateral force is considered as a point force, acting in the middle of the contact patch. By applying the corresponding boundary conditions, the lateral deformation of the ring is calculated and approximated by a quadratic polynomial through use of Taylor expansion. The contact area is assumed rectangular and the normal pressure is taken to be uniform in the lateral direction and quadratic along the length of the contact patch. The contact patch demonstrates an adhesive zone, where the tread deforms linearly and the lateral forces are dictated by the relative deformation of the tread with respect to the elastic beam, followed by a sliding zone, where the forces depend on the local normal pressure distribution and the coefficient of sliding friction. Consequently, the calculation of the total lateral force is performed by separate integration of the lateral force distribution along the adhering and sliding regions and superimposing them. This approach allows the model to extend its operation in the non-linear range, as opposed to the string model described in [43]. In addition, the assumption of a quadratic pressure distribution permits the existence of a sliding region even at low slip angles.

Sakai [46-49], in a series of four papers, presents an in-depth study of the steady-state behaviour of tyres. He investigates the influence of several factors such as the shape of the normal pressure distribution and the variations of rubber friction due to changes in temperature, vertical force and sliding velocity. As a base model for his study he uses an enhanced version of Fiala's model. For the calculation of the lateral force and self-aligning moment, he uses successive approximation and this results in an extra term in the expression for the self-aligning moment, which is omitted by Fiala. It appears that the inclusion of this term yields better agreement between experimental and theoretical results for the self-aligning moment. Sakai [46] extends the capabilities of Fiala's model by assuming that the tread is characterised by a single spring constant, which affects both lateral and longitudinal directions. By using simple geometrical relations he expresses the lateral and longitudinal force distributions as functions of the slip angle and slip ratio and finally he considers the vectorial sum of both lateral and longitudinal forces when calculating the transition point from adhesion to sliding. Since, under combined cornering and braking/traction, the

direction of the friction force for the part of the tread within the sliding zone is not known, an approximate geometrical relation is used for its determination.

Sakai [46] uses the enhanced model to illuminate some of the problems in the theory of steady-state tyre modelling, as proposed by Fiala. He reports that the shape of the contact patch is not rectangular, the normal pressure distribution is in reality more trapezoidal than parabolic and that it is also affected by the existence of camber angle. Furthermore, friction between the tread and the road should not be based on the Coulomb's law, as it depends on the vertical load, temperature, sliding velocity and additionally, stick-slip may develop within the contact area. In order to investigate the influence of these parameters, Sakai conducts a series of experimental studies in [47]. Based on the measurements, he derives empirical relations for the normal stiffness, the shape of the contact patch, the normal pressure distribution and some important structural mechanical properties such as the stiffness of various parts of the tyre and in various directions of deformation. Special attention is paid to the differences between rubber friction and friction between hard surfaces, as described by Amontons and Coulomb. It is observed that rubber friction consists of two separate terms, namely adhesion and deformation friction. The former corresponds to the same frictional mechanism observed between hard contacts, quantified by Coulomb's law of friction. The latter is due to hysteresis phenomena, attributed to the viscoelastic nature of rubber. It is mentioned that the highly deformable nature of rubber results in a non-proportional relation between vertical load and contact surface and this affects the adhesion term in a way that the coefficient of friction decreases, when the vertical load increases. Moore [29] explains this effect in some detail by pointing out that both terms of rubber friction are affected by viscoelasticity. The viscoelastic properties of rubber are discussed thoroughly by Ward [50] and Findley et al [51]. The linear viscoelastic constitutive equations are presented and the modelling of rubber, using combinations of linear springs and dampers is discussed. The most commonly used Maxwell, Kelvin and Burgers models are described and their agreement with simple creep and recovery tests is assessed. It is found that the generic Burgers model yields the best results in terms of agreement with the actual behaviour of rubber, while the Maxwell and Kelvin models pose certain limitations. The modelling of the rubber viscoelasticity is discussed in more detail in chapter 3.

Gim and Nikravesh [52-54] present a step-by-step analysis of tyre force and moment generation using a simple model and compare the results with experimental measurements. Initially, the force generation procedure is described for pure longitudinal slip, pure side-slip and pure camber conditions [52]. The model assumes parabolic normal pressure distribution and the friction coefficient is taken to be velocity dependent. The analysis is then extended to combined slip and camber situations in [53]. Finally, longitudinal and lateral forces show very good agreement with experimental results [54] under pure slip and combined slip conditions, while the self-aligning moment shows significant deviations from experimental measurements. It is suspected that the deviations in the self-aligning moment result from the assumption of a parabolic pressure distribution. Although the lateral and longitudinal forces depend mainly on the total normal force and the sliding conditions, the pneumatic trail changes significantly with any change in the normal pressure distribution and this affects the generation of self-aligning moment.

Bernard et al [55] use a model with trapezoidal normal pressure distribution and assume anisotropic stiffness and friction in the longitudinal and lateral directions. Furthermore, the friction coefficient is speed dependent and the lateral stiffness depends on the slip angle, in an attempt to achieve better agreement with experimental results.

Pacejka and Sharp [42], in their review of steady-state modelling aspects, provide an analytical description of a large family of physical models, based on the brush concept. The simplest brush models can be solved analytically and the authors have followed a step-by-step procedure starting from some fundamental definitions and building gradually on the complexity of the brush models until they reach the limits of analytic solutions. The generic brush model consists of a series of elastic bristles, radially distributed to a circular belt, which deforms in the radial direction under the application of a vertical load. As a result, a finite contact length arises and the bristles are assumed undeformed in the absence of friction. If the wheel deviates from the free rolling state under the presence of friction, the bristles deform within the horizontal plane of contact. Figure 2.7 depicts an arbitrary position of the rolling brush model, together with the possible situations of pure side-slip, pure longitudinal slip and the combination of the two. The deformation of the bristles apparently depends on their

elastic properties, the kinematic conditions imposed by the relative motion of the tyre with respect to the ground, the coefficient of friction and the normal pressure distribution. Under steady-state operating conditions the state of all the bristles at any instant of time can be obtained by following the motion of one representative bristle along the contact patch from the moment it enters until the moment it exits the contact patch. The concept of the bristle aids primarily the visualisation of the situation along the contact patch and is not important as a structural element of the tread. It is interesting to note that Pacejka and Sharp [42] include the model proposed by Bernard et al [55] in the section of their review dedicated to brush models. However, in the original manuscript there is no reference to a brush model consisting of bristles or elastic cones. Instead, Bernard et al [55] follow the motion of a *point* or *segment* of the tread and derive the equations for the deformation of the tread in a similar way as Pacejka and Sharp in [42] and Pacejka in [6]. Still, the brush concept is superior as an approach for explicitly introducing the relative displacement between the base and the tip of each bristle.

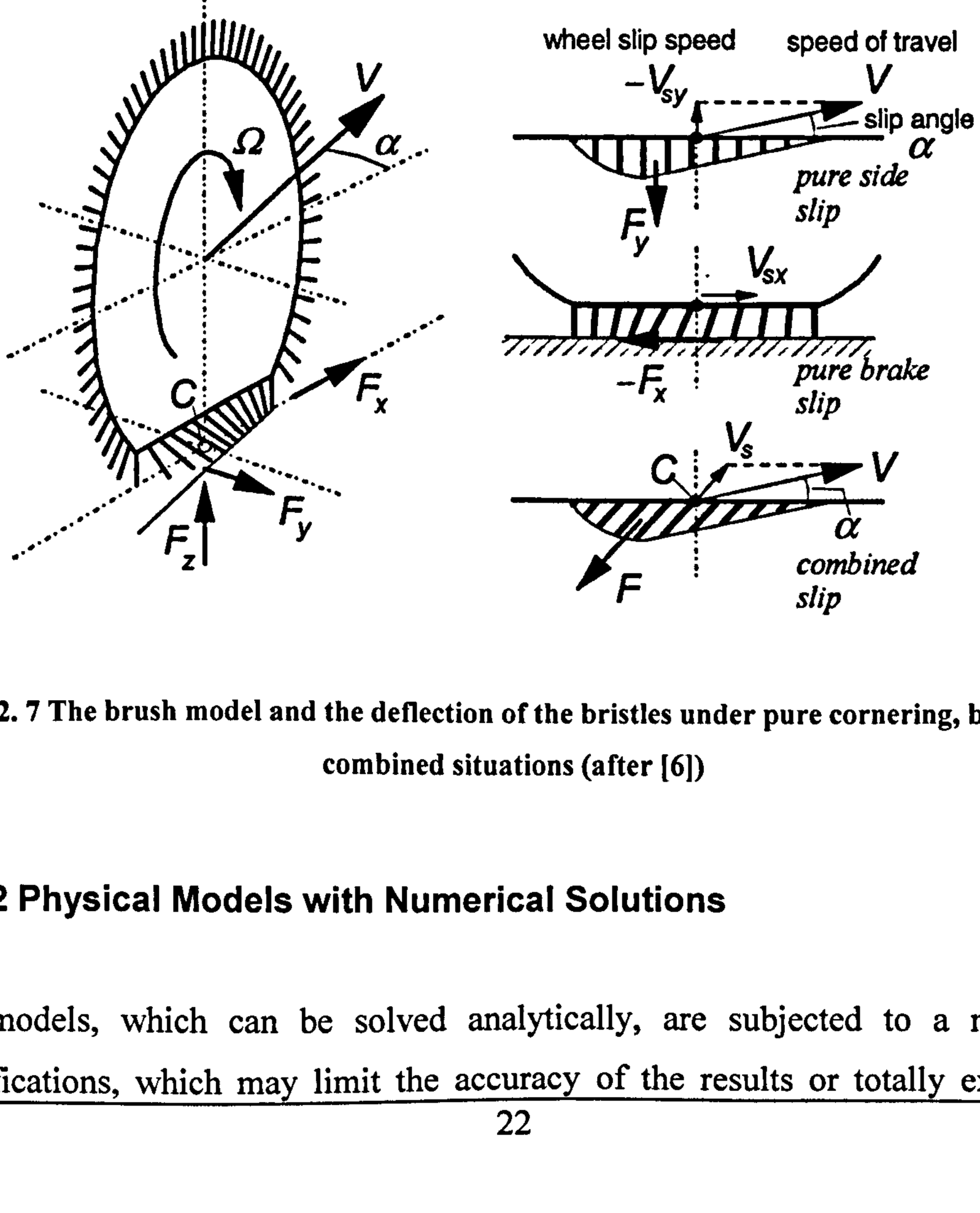

Figure 2. 7 The brush model and the deflection of the bristles under pure cornering, braking and combined situations (after [6])

2.2.2.2 Physical Models with Numerical Solutions

Tyre models, which can be solved analytically, are subjected to a number of simplifications, which may limit the accuracy of the results or totally exclude the

possibility of investigating the influence of certain parameters. It is stated in [42] that analytical brush models are unable to represent accurately the situation within the sliding region. This is because the velocity vector of a tread segment (bristle) at the onset of sliding cannot be determined. In fact, the bristles move through a transition region within the sliding part of the contact patch, until the velocity of their tip relative to the road reaches the resultant slip velocity of the tyre (due to both side-slip and longitudinal slip). Another limitation may be related to the choice of normal pressure distribution. Apparently, it is possible to find the transition point from adhesion to sliding only when the normal pressure distribution is expressed by simple functions as demonstrated, for example, by Fiala [45], Sakai [46], Bernard et al [55] and Julien [43]. However, it is not possible to apply an experimentally measured pressure distribution or to calculate the pressure distribution on-line, taking into account the specific load conditions along the length of the contact area. These and other shortcomings have led to the development of physical models with a numerical formulation, which can be solved with the aid of a computer. It is important to mention that computer algorithms have been used for the automated calculation of forces based on models with analytical solutions, as demonstrated by Gim et al [52-53]. This fact does not immediately justify such models as "numerical". In general, numerical solutions refer to models, which are at least based on some kind of iterative procedure for the solution of algebraic or differential equations.

Sakai [48] describes the motion of a tread block using a differential equation which initially takes into consideration elastic, damping, inertia and friction forces. The equation is simplified by neglecting the damping and inertial terms, and the rate of change of the displacement of the tread block is written finally as a function of the normal load, tread block deformation and friction. The equation is solved numerically along the length of the contact patch using the Runge-Kutta method. The omission of damping and inertial terms has led to a situation where the rate of change of deformation of the tread block cannot be calculated explicitly. Instead, at every time-step, the four intermediate slopes (rates of change) calculated as Runge-Kutta coefficients are checked against a velocity threshold in order to determine whether the tread at the specific point of the contact patch is operating under low or high speed sliding conditions.

Sharp et al [56] propose a computer based tyre model for the calculation of shear forces and the self-aligning moment. The model consists of a series of radial spokes, interconnected through the wheel hub and distributed uniformly in order to cover a full circle (360°). The spokes are characterised by radial, longitudinal (circumferential) and lateral tip flexibilities, as well as a small amount of radial damping for the inclusion of hysteresis associated with rolling resistance. Under steady-state conditions, the motion of one spoke is representative of all spokes, as it moves from the leading to the trailing edge of the contact patch. In the general case, the vector of radial, tangential and lateral deflections can be determined by employing two constraint equations, the first one imposing the condition of constancy of vertical deflection, and the second one that the position of the spoke tip remains unchanged (no-sliding condition). The vector of deflections is then used to calculate the total shear and normal forces and compare the former with the latter, multiplied by the corresponding coefficient of friction. If the shear force is lower than the maximum friction force, then the assumption of no-sliding is deemed satisfied, the deflections are stored and the spoke proceeds to its next position. If the shear forces exceed the maximum friction force, then the deflections are reduced iteratively until equality is reached within a pre-specified tolerance. Because the coefficient of friction is a function of the sliding velocity, which in turn cannot be determined explicitly during the iterative procedure, a mean value for the velocity is used, equal to the corresponding shear deflection divided by the time-step. It is interesting to note that the model implies that the shear forces generated by the spoke are always equal to the friction force, which is a fundamentally unjustified assumption if one takes into account the viscoelastic and inertial properties of the tread. Also, similarly to Sakai's model [48], an approximation of the sliding velocity is used in order to calculate the coefficient of friction. Again, this is a result of the omission of damping and inertial contributions. Apart from these assumptions the model seems to be capable of achieving good qualitative and quantitative agreement with steady-state experimental results. Furthermore, it is unique in that it allows for on-line calculation of the normal pressure distribution based on the resultant vertical deflection of the spokes and a non-linear radial stiffness, which accounts for the effect of air-pressure inside the tyre. Finally, the spoke deflections are calculated in a generic way so as to accommodate immediately the inclusion of camber angle and spin.

Levin [57] proposes a steady-state brush model, appropriate for tyres operating at high rolling velocities. One representative bristle incorporates radial, tangential and lateral stiffness and damping, while the mass is distributed along the tyre periphery, and is taken into account by attaching a point mass at the end of each bristle. A separate vertical Kelvin element is used for the connection between the point mass and the ground. The motion of the bristle is described by three differential equations for the normal, longitudinal and lateral degrees of freedom of the mass respectively. Under steady-state conditions, the rotational velocity of the wheel is constant and this enables the description of the problem as invariant in a temporal sense (omission of time), so that the equations of motion are written with respect to the angular position of the bristle as it travels along the contact patch. The deformation of the vertical Kelvin element yields the normal pressure distribution, while the lateral and longitudinal motions of the bristle determine the shear forces in relation to localised friction. Levin [57] finds that the sudden change in momentum, which takes place in the leading edge of the contact patch is due to an impact with the road. Thus, the proposed model predicts an extremely high peak for the normal pressure distribution at the leading edge, which may be observed experimentally only in studded tyres. On the contrary, normal tyres exhibit a much more subtle peak. As discussed later in the thesis, in reality the change in momentum takes place within the belt of the tyre, which deforms continuously under the application of vertical force and rolling motion.

2.2.2.3 Empirical and Semi-Empirical Tyre Models

All physical models presented in the preceding section are subjected to limitations resulting from the inherent difficulties in precisely modelling all the structural properties of the tyre and incorporating their influence in force and moment generation. Furthermore, models with numerical solution, which in general may be able to describe the tyre with greater accuracy, may increase significantly the computational burden, when used in conjunction with a handling simulation algorithm.

An alternative to using a physical tyre model is the implementation of a direct or in-direct representation of experimental tyre data. Bakker et al [28] distinguish three possible ways of representing tyre data, namely by tables, graphs or formulae. The

first two possibilities of direct representation involve a great deal of measurements in order to cover all combinations of lateral and longitudinal slips under varying normal load and camber angle, possibly on terrains with different coefficients of friction. To minimise experimental effort, researchers have attempted to represent experimental data indirectly by developing mathematical functions, which successfully fit experimental results. In general, a wide range of functions have been used such as exponential, arctangent, polynomial, hyperbolic tangent and Fourier series. When the coefficients involved in the functions do not show any direct connection with the typifying parameters of a tyre (such as the cornering stiffness or the peak coefficient of friction), formulae are usually referred to as empirical. Ideally, the coefficients should have a physical meaning and their manipulation should allow for investigating the properties of hypothetical tyres [58]. In addition, if the formulae contain structures that find their origin in physical models, the approach may be referred to as semi-empirical [6].

In general, the representation of experimental data by series and polynomials is followed by problems such as waviness of the generated curves and unrealistic results, when extrapolating beyond the fitted range [58]. Schieschke [59], [42] uses a simple second order polynomial designed to change slope at the value of slip, where the maximum force is observed. Although the use of a low order polynomial improves waviness, it is required to use a second version of the same polynomial with adjusted coefficients for values of slip beyond the value, which corresponds to the maximum force. Alternatively, Sitchin [60] divides the data into five regions and uses different polynomials to fit data within each region. Rimondi et al [61] propose an interpolative tyre model for use under pure slip conditions. The lateral force is represented by an exponential function, which is designed to converge to the maximum friction force, which is calculated as the product of the normal force and the coefficient of friction. The cornering stiffness appears explicitly as a coefficient and the shape of the curve is optimised using an extra shape-factor. The use of an exponential function implies that the lateral force characteristic does not show a local peak before the saturated area of operation. The longitudinal force is expressed as a sum of exponential functions designed to provide, with the necessary local peak, which is almost always evident in longitudinal force characteristic curves. The self-aligning torque is calculated by multiplying the lateral force with the pneumatic trail, which in turn is given as a

function of slip angle and normal load. A desirable characteristic of the model is the fact that for both lateral and longitudinal forces, the stiffness coefficients, shape factors and coefficients of friction depend on the vertical load. Finally, the formulae proposed show good correspondence with the experimental results.

The most successful formula for the representation of steady-state forces and moments is the well-known *Magic Formula*, initially conceived by Bakker et al [58]. The formula is the result of a joint project between Volvo and Delft University and, since its first release in 1987, has undergone a series of improvements [41], [62]. The formula is based on the recognition of the fundamental trends observed in a large number of experimental results. In particular, the equations for the lateral and longitudinal forces should be able to generate a peak force at a controllable slip angle/ratio and converge asymptotically to the saturated values at high slip angle/ratio. In addition, the slope at zero slip should represent the cornering or longitudinal stiffness of the tyre, while the overall curvature should be controlled separately with the aid of shape factors. The equation for the self-aligning moment should incorporate the aforementioned characteristics and, in addition, should be able to change polarity at high slip angles. It was found that these requirements are fulfilled exceptionally well with the use of a composite sinusoidal-arctangent function which retains the same form for the two forces (lateral and longitudinal) and the self- aligning moment. The differences between the three characteristic curves are handled by implementing different coefficients in the basic formula, while the effects of camber angle and rolling resistance are introduced by a horizontal and vertical shift of the initial curves. One of the major advantages of the formula is the fact that the stiffness at zero slip, the peak force and the slip value at which it occurs and the saturated values can be controlled independently. The coefficients involved in the formulae are computed as functions of the normal load and camber angle. In [58], [41], [62] the problem of combined slip conditions is solved by multiplying the pure slip curves by weighting functions, which are based on a physical representation of the force distribution in the contact patch at combined slip, initially for isotropic and later for anisotropic tyres. In this procedure the definition of a normalised theoretical slip is necessary, in order to account for the anisotropies in lateral and longitudinal directions. Especially for the case of self-aligning moment, carcass compliance, camber angle and static off-set cause a shift of the lines of action of lateral and longitudinal forces and the final

expression results from the addition of extra terms, which follow from the multiplication of the forces with the corresponding shifts. Bayle et al [63] propose a purely empirical method for dealing with combined slip conditions, based on composite cos-arctangent weighting functions. The use of a cosine function in conjunction with a peak coefficient larger than one, allows for the slight increase in lateral force with the introduction of a small brake-slip. The several coefficients contained in the formulae can be estimated from experimental results using regression techniques, as demonstrated by Oosten et al [64].

It is observed that characteristic curves generated by the same tyre show a similar shape when the tyre operates, for instance, under different normal loads or on tracks with varying coefficients of friction. If the characteristic curves are obtained experimentally at a reference condition, it is possible to estimate their shape under a much wider range of conditions, by employing the *similarity* concept. Radt et al [65] demonstrate a procedure for non-dimensionalising tyre data. As a basis for their analysis they use the analytical tyre model presented by Sakai [46]. The non-dimensional parameters are defined with the aid of the analytical equations for the forces and self-aligning moment. By applying the proposed non-dimensionalisation to experimental results, it is shown that characteristic curves obtained under different conditions approximately coincide with each other, when plotted in a non-dimensional form. This experimental finding suggests that similarity indeed exists between tyre characteristic curves. The *similarity* concept proves extremely useful for the extension of the range of operation of empirical and semi-empirical tyre models. Irrespective of the type of formula, the generated curves can be multiplied with specially selected coefficients in order to account for the effect of the change of various factors on the shape of the original curve (i.e. the one obtained under reference conditions). This use of the *similarity* concept is demonstrated in [6] for the case of a varying normal load and its influence in cornering stiffness, peak value and camber stiffness.

2.3 Transient Tyre Analysis

While steady-state tyre models provide a satisfactory description of force and moment generation for use in steady-state vehicle handling studies, a large variety of transient phenomena are related to the operation of tyres under time-varying conditions. The

coupling of in-plane and out-of-plane characteristics, as well as the compliance and the inertia of the tyre structure result in transient responses, which cannot be generated simply by applying a time-varying input to a steady-state tyre model. In general, transient studies are focused on the force and self-aligning moment responses to time-varying lateral and longitudinal slip, while the response of the self-aligning moment to time-varying yaw rotation around the wheel steering axis is also of high interest. To complicate things further, a time-varying camber angle or normal load may also be introduced. Tyre responses are usually investigated for step changes in the aforementioned input quantities, while the frequency response to sinusoidal excitations is also considered. In transient tyre models, attention is moved from the contact patch to the flexible belt and carcass of the tyre. Depending on the complexity required and the overall aim of the analysis, the following types of models can be found in literature, together with hybrids that incorporate more than one approach:

- String based models
- Single point contact models
- Multi-spoke – brush based models
- Rigid ring models
- Models based on discretisation of the tyre (finite element models, discretised belt models)

Similar to the steady-state analyses, transient models can be solved either analytically or numerically. In the steady-state case, the existence of a large number of effective and easy to employ analytical or numerical non-linear models has limited the use of the simple linear model. In transient investigations the linear theory is very often preferred for its relative simplicity and its ability to generate realistic results for a range of practically interesting operating conditions.

Due to the high complexity of transient tyre models and the combination of non-linear with linear, kinematic with dynamic and transient with steady-state approaches (hybrid models), the idea of dividing transient models into discrete groups was abandoned. Instead, the most important approaches are presented below in a single section.

2.3.1 Transient Tyre Models

Pacejka [13] has developed a theory for the prediction of the frequency response of a tyre, subjected to lateral wheel plane vibrations and swivelling motion around the steering axis. The tyre is modelled as a series of parallel flexible strings, which are kept under pretension by a uniform radial force distribution. The circular strings are elastically supported by the wheel rim, but are prevented from moving in the circumferential direction. In order to account for the longitudinal deformations which occur asymmetrically when the wheel is swivelled round the vertical axis, the strings are provided with elastic tread elements, which are flexible in the circumferential direction only. Initially the strings are assumed to be mass-less and the spatial differential equation for the lateral deformation of a string with respect to circumferential position is kept linear by assuming that no sliding occurs in the contact patch. The differential equation is solved for the free length of the string (an identical approach to that of von Schlippe [43]) to obtain the slopes at the leading and trailing edges of the contact patch. A fundamental observation is the fact that at the leading edge the slope should be continuous and this aids the formulation of the differential equation that describes the rate of change of lateral deformation at the front edge of the contact patch with respect to time. By combining the equations for the deformation of the string with the kinematic equation, which results from the rolling without sliding condition, the lateral displacement of the string can be obtained with respect to time and position on the contact patch. Lateral force and self-aligning moment are calculated by integrating the corresponding elastic forces and moments along the contact patch and are expressed in the frequency domain. Finally, an extra term is added to the self- aligning moment as a result of the effect of longitudinal stiffness of the tread when the wheel is swivelled about the vertical axis. Force and moment response to the variations of the non-dimensional frequency of lateral and yaw vibrations is provided via Nyquist and Bode diagrams. The gyroscopic moment is also taken into account in order to improve the accuracy of the moment response. Comparisons with experimental results show good qualitative and quantitative agreement at low frequencies, whereas at higher frequencies the effect of inertia is thought to play a more significant role. To account for this, a constant mass density along the circumference of the strings is introduced. The new differential equations are obtained using Laplace formulation and the resulting Nyquist diagrams for

hypothetical tyres show qualitative agreement with experimental results. Pacejka's analytical methodology [13] provides invaluable insight into the transient behaviour of tyres and can be used in a wide variety of transient phenomena such as the wheel shimmy phenomenon [66], [6], which is described as the self-excited oscillatory motion of a wheel about the vertical steering axis.

The relaxation length is a quantity often encountered in transient tyre models and appears with various different definitions. In the case of the string model [13], the relaxation length is defined as the square root of the ratio of the total effective tension of the string and the lateral stiffness of the carcass per unit length of the tyre circumference. It appears that this is equivalent to a geometrical definition, which describes the relaxation length as the longitudinal distance calculated by dividing the lateral deflection at the leading edge by the tangent of the slip angle, for low lateral slips. The definition of the relaxation length might change slightly depending on the tyre model and might also vary depending on running conditions. In any case, it represents a structural property of the tyre and is directly connected to the kinematic transience in tyre behaviour. Various definitions of the relaxation length can be found in [67-68]. A definition, which illuminates the physical meaning of the relaxation length describes it as the distance travelled by a point on the tyre circumference until the tyre reaches a certain percent (c.a. 1-1/e or 63%) of the steady-state equilibrium deflection, after a step-change of the input. The physical significance and the derivation of this definition will become more apparent in chapter 4, where the relaxation length concept is discussed in more detail.

The so-called single contact point transient tyre models are based on the representation of the tyre carcass as a single spring able to deform in lateral and longitudinal directions. In this case the relaxation length can be defined as the ratio between tyre cornering stiffness and carcass lateral stiffness [68]. The rate of change of slip angle is then described with the aid of a linear differential equation. Such models can be used for low frequency handling simulations, where the representation of tyre transience, based on the kinematic approach is sufficient. Clover and Bernard [69] use a single contact point transient model in order to investigate transient braking manoeuvres. For this purpose the authors provide an equivalent definition of the longitudinal relaxation length. The differential equation for the transient longitudinal

slip is combined with a steady-state representation of the braking force versus slip ratio, which is locally linearised. By introducing the wheel spin differential equation, a linear differential system is created with respect to the rotational wheel velocity and longitudinal slip ratio. The linearised equations can be used in vehicle simulations with the local linearization of the braking force being valid across one time step. In this way, the time-step of the handling simulation can be kept large and is not affected by the reduced time-step needed to simulate wheel-spin. Also, the authors find that at low vehicle speeds the corresponding algebraic system (after Laplace transformation) may be characterised by complex roots, a fact which implies the existence of oscillatory response under such conditions.

Zdobyskaw [70] has established a theory for the determination of the necessary conditions for the occurrence of self-excited shimmy vibrations. The author assumes that self-excited vibrations might occur only when energy is transferred to the tyre from the external environment through the generalised force vector. This principle is applied to a series of different models such as the kinematic version of the Pacejka's model [13], Von Schlippe' s model [43], a single-point contact model and the dynamic version of the Pacejka's model [13]. It is pointed out that the single point model cannot generate shimmy vibrations, while Pacejka' s dynamic model is stable at low velocities and shows oscillations at higher velocities, which disappear only when increasing the exciting frequency.

Maurice et al [14] have proposed an analytical methodology for the investigation of short wavelength side-slip variations. The approach follows from the recognition that the self-aligning moment cannot be calculated simply by using a single point, relaxation length based transient model. The general differential equations for the deformation of a rolling and slipping body are applied on a simple brush model and the frequency response functions for the force and self-aligning moment with respect to deviations of the steady-state slip angle are obtained. Bode plots show clearly that the lateral force transfer function can be approximated by a first order system, while the self-aligning moment demonstrates a less straight-forward behaviour. The first order transfer function for the lateral force is easily identified. The relaxation length, which represents the delay parameter of the system is found to be an order of magnitude lower than the values indicated by experimental measurements. This

problem is resolved by connecting a lateral spring in series with the brush tread model in order to incorporate the effect of lateral carcass flexibility. The transfer function is modified accordingly and it is easily shown that the addition of the spring does not affect the steady-state characteristics. The self-aligning moment is treated by considering the frequency response function of the pneumatic trail with respect to side-slip variations. It is found that this function can be written approximately as a product of a first order function and the transfer function of a phase leading network. A procedure for the identification of the transfer function parameters is given and finally all equations are written in the time domain, where the transfer functions take the form of differential equations and are combined with the steady-state brush model or the Magic-Formula tyre model for use in vehicle handling simulations.

Zhou et al [15] use a modified version of the steady-state numerical multi-spoke model presented in [56] for the simulation of transient tyre behaviour. The model includes three planes of spokes, as opposed to the single-plane steady-state model. The planes are equally spaced along the width of the tyre in order to account for anisotropies in the lateral direction and to improve the simulation of camber effect. Under transient conditions, the motion of one bristle is no longer representative of the motion of all bristles, thus, the state of each individual bristle at time t+dt is calculated by the state of the same bristle at time t. Also, the model incorporates a rigid mass-less spoke base with lateral and longitudinal degrees of freedom, which is elastically connected to the wheel hub. The exact positions of the spoke tips and the rigid base are calculated iteratively so that the corresponding elastic forces are in equilibrium, while the sliding condition is checked in the same manner as in [56]. The normal pressure distribution is calculated on-line as in [56] and there are no restrictions in the possible motions of the wheel. These qualities are rare to find in transient tyre models. Nevertheless, inertial effects are not taken into account and this limits the application of the model to relatively low-frequency excitations. It is likely that this problem could be resolved by using a spoke base with inertia, although this would complicate the numerical procedure by adding the essential integration scheme for the spoke base.

Zanten et al [16] conduct a combined experimental – numerical investigation on the transient behaviour of tyres. They use a complete instrumented vehicle equipped with a rotating wheel dynamometer for the measurement of wheel forces and moments

under braking, cornering and combined manoeuvres. In their numerical approach they use a rigid ring connected to the rim via lateral and circumferential springs and dampers in order to capture the transients involved in the motion of the tyre belt. The contact forces are obtained by a separate tread model, which is based on the brush concept. The bristles are mass-less and un-damped and their deflections are calculated by taking into account the transient kinematic conditions of the belt. Results are provided as graphs showing the adhesion coefficient plotted against slip ratio, slip angle or time. Plots obtained numerically show good agreement with experimental measurements. However, the selected way of presenting the results does not give any information about the frequency response of the tyre model.

Mastinu et al [17] present tyre models appropriate for transient simulations. In [17] membrane theory is applied to obtain the normal pressure distribution and lateral stiffness of the carcass. The belt is discretised using finite elements for the determination of bending modal behaviour. Along the contact patch the belt is divided into an adequate number of elements, while the part of the belt outside the contact is modelled as a single bending element. The belt is connected to the rim by springs with a lateral stiffness that varies depending on the local radial deflection of the tyre. The tread is modelled as a one-dimensional series of mass-less undamped bristles with anisotropic stiffness in lateral and longitudinal directions. Lateral force and self-aligning moment depend on the relative deflections of the belt and tread elements, while longitudinal forces depend only on the deflections of the tread. In other words, the belt does not possess circumferential degrees of freedom. The tyre model operates under steady-state conditions with the motion of one tread element being representative of the motion of all elements, while the simulation of transient conditions is achieved by updating the states of all elements independently. An enhanced version of the model presented in [17], is given by Mastinu et al in [18]. While in [17] the normal pressure distribution is considered uniform in lateral direction, in [18] the effects of camber and lateral slip are taken into account and the pressure distribution varies both in the longitudinal and lateral directions. The contact area is divided laterally into parallel strips and the shear forces are calculated within each strip depending on the corresponding "slice" of normal pressure distribution. The transient version of the model is improved by introducing the gyroscopic, turn-slip (for a definition see [6]), and damping effects. Simulation results show good

agreement with measurements especially in the calculation of the size of the contact patch. Transient results show good agreement in terms of magnitude and phase angle for low frequency variations in the slip angle. Results are not provided for the frequency response of the longitudinal force, however a larger deviation between simulation and experiment would be expected due to the absence of a circumferential degree of freedom for the belt, which would result in an increase in the longitudinal relaxation length of the model.

Ftire [19] is a commercially available tyre model, optimised for use in multi-body dynamics simulation environments. The main structure of the model is a tyre belt which consists of a number of discrete segments. The belt segments are elastically founded on the rim by distributed stiffness in the lateral, circumferential and radial directions. Adjacent segments are coupled by translational and bending springs and each segment can perform in-plane and out of plane motions. The radial stiffness is defined by a spring connected in parallel with a spring-damper series, in order to provide dynamic hardening as rolling velocity increases. For the simulation of the contact, each segment is associated to a number of mass-less tread bristles with non-linear radial, tangential and lateral stiffness and damping properties. The model is developed primarily for ride and comfort analyses and works in conjunction with a predefined road profile. The stiffness and damping parameters of the model are identified by a pre-processing procedure which uses experimentally measured in-plane and out-of-plane vibration modes of the tyre.

A similar philosophy is followed in the tyre-model system RMOD-K [20] which is also used in multi-body simulation codes such as ADAMS. The model focuses mainly on ride and comfort studies and is characterised by the switching between individual tyre models depending on the operating conditions (hence its characterisation as a tyre-model system). For example, when the wheel negotiates a surface irregularity perpendicular to the direction of travel, a model incorporating a discretised two-dimensional belt is used, which neglects the effects of the width of the belt. On the other hand, when the irregularity is met by the tyre at an angle, a more complex three-dimensional tyre model is implemented, taking into account the effect of the cords of the carcass.

2.4 The Mechanics of Friction

The importance of the study of friction in tyre mechanics has already been highlighted. In section 2.2.1 the fact that tyre friction forces are not proportional to the normal load is demonstrated through experimental results [36], while in section 2.2.2.1, some details of rubber friction are discussed, triggered by the research conducted by Sakai [48]. In the present section, a brief history of the evolution of friction science is given. Initially, the classical theory of dry friction between hard surfaces is discussed. The role of surface asperities and the mechanics behind friction force generation are presented. The range of the validity of the classical laws of friction is also discussed and the necessity of the separate study of elastomeric – in particular rubber – friction is pointed out. A brief description of the theory of rubber friction is presented and finally, a number of frequently used mathematical models for the simulation of friction force generation are discussed.

2.4.1 Fundamentals of Friction – the Laws of Dry Friction

The work of some of the pioneers in the study of friction is presented in the books by Dowson [39] and by Bowden and Tabor [40]. It is stated in [40] that the ancient Egyptians, Greeks and Romans were fully aware of the use of lubricants. Much later, in the middle of the fifteenth century, Leonardo da Vinci showed that the friction force is proportional to the vertical load. This early observation was reconsidered 200 years later in what is probably the first scientific study of friction, by the French scientist: Guillaume Amontons. Amontons carried out friction measurements using an apparatus consisting of a spring, which provided the normal loading and a spring balance for the measurement of the force required to initiate sliding between two specimens [39]. Amontons presented his major findings together with an interpretation of his measurements in a classical paper in 1699 [39]. He reported that the resistive force (friction) is proportional to the normal load but independent of the size of the areas in contact. This observation summarises the first and second laws of dry friction. He also found that the friction between various surfaces is always equal to one third of the vertical load, provided that the surfaces are covered with pork fat. It is interesting to note that while Amontons' laws are usually referred to as laws of "dry" friction, the actual experiments were carried out with a thin film of pork fat

between the rubbing surfaces. The most interesting part of Amontons' work is probably the physical explanation of the mechanism of friction force generation in relation to his laws. Amontons attributed friction to the surface irregularities of the specimens in contact. He noted that these irregularities should be partly convex and partly concave and that during contact the former enter upon the latter. This interlocking of the irregularities should produce a certain resistance when one attempts to move them. In order for the interlocking to brake, the load, which presses the irregularities against each other needs to be increased and this is equivalent to raising a load along an inclining plane. It follows from this observation that the greater the load, the greater the resistive force. Amontons observed that when the contact area increases, the number of interacting asperities increases proportionally, but the vertical load on each interlocking of pair of asperities reduces so that the total load required to be raised for the initiation of sliding between the surfaces remains constant. This explains why friction is proportional to the load, but independent of the size of the rubbing surfaces. Amontons went further by recognising that these laws are valid for both "rigid" and "elastic" asperities. He supported this argument by using springs for the representation of elastic asperities. He pointed out that the force required to deflect the spring (elastic asperity) is in no way different from that required to raise a weight to comparable height equal to the strength of the spring.

The next major contribution to the science of friction was provided by Charles Augustin Coulomb [39,40]. Coulomb reported his work on friction in a lengthy memoir, in 1785. He conducted detailed experiments to determine the frictional properties of various materials, including dry and lubricated oak, elm, iron and yellow copper. Similarly to Amontons, he observed that the friction force is *almost* proportional to the vertical load and independent of the size of the contact area. He considered the concept of cohesion, first introduced by Desagulier [39] as an additional friction-generating mechanism, which acts together with the interlocking of the asperities introduced by Amontons. Coulomb was the first to express the friction as an addition of two terms, the first term being associated with the effect of cohesion, and the second one resulting from the relative motion of the asperities. Coulomb also distinguished static from kinetic friction and found that, in general, kinetic friction is lower than static friction. An important observation was that kinetic friction is independent of the sliding velocity and this statement formed the third of the classical

laws of dry friction. Coulomb used the concept of interlocking asperities to explain the difference between static and kinetic friction. He argued that the meshing of the asperities is responsible for the higher values of static friction. Under the application of a tangential force the asperities deform until sliding begins. Once sliding is initiated, the asperities fold over, filling up the voids previously occupied by the opposing surfaces and thus reduce their slopes. This explains why the friction force generated during sliding is lower than static friction.

The laws of Amontons and Coulomb have passed the test of time and still hold true for a wide range of conditions. Nevertheless, the next major step towards the better understanding of friction required the use of elaborate methodologies of the 20^{th} century. A comprehensive analysis of the modern theories of friction is provided by Bowden and Tabor in [71]. Instruments such as the electron microscope and methodologies such as optical interference have allowed scientists to determine the exact shape and size of the asperities of assumedly flat surfaces. The modern view of friction pays much attention to the area of *real* or *intimate* contact, versus the area of apparent contact, as perceived by the early investigators. It is reported in [71] that even well polished surfaces consist of microscopic hills and valleys. As a result, when two surfaces come into contact, they will touch only on the summits of the hills and the area of intimate contact will be very small compared to the area of apparent contact. For example, for steel plates of a total area of 20 square centimetres, the real area of contact is approximately $1/200^{th}$ of the apparent area for a vertical load of one ton, whereas the area of intimate contact drops to $1/100000^{th}$ of the apparent area for a load of 2 kg (see [71]). This observation leads to some very interesting results, briefly summarised here. The case of rubbing metals is discussed in detail in [71] and it is noted that because the area of real contact is very small, the resulting pressure around the contact points (summits of the hills) exceeds in most practical applications the elastic limit of the materials involved. The materials flow plastically and any further increase in the normal load does not cause any increase in pressure. Consequently, the extra load is handled by an almost proportional increase in the area of real contact. This leads to the observation that the area of real contact is equal to the ratio of the normal load and the mean yield pressure of the materials [71]. In order to initiate sliding between the bodies in contact, the mean tangential strength of the plastic junctions needs to be reached. Therefore, the total force required is equal to the

product of the mean tangential strength (stress) and the total area of intimate contact. Finally, assuming that the tangential strength of the junctions is constant and because of the fact that the area of intimate contact is proportional to the normal load, the tangential force (friction) required, is also proportional to the normal load. Clearly, the result of this analysis agrees with the observations of Amontons. Nevertheless, it should be emphasised that Amontons' laws hold true only when the area of intimate contact increases proportionally with the applied load. It is noted in [71] that if, by some artificial device, the area of contact is prevented from increasing proportionally with the normal load, Amontons' laws would no longer be valid. The above analysis is carried out considering idealised asperities of spherical, conical and pyramidal shapes and applying the Hertzian contact theory [71], [72] for the determination of the pressure around the contact points. It should also be noted that the explanation of friction between metals given thus far, is based on the shearing of the metallic junctions formed at the points of contact of the surface asperities. In the case of hard metal surfaces rubbing against softer ones, for example steel rubbing against lead, the effect of ploughing action may become significant. The hills of the asperities of the harder material sink into the softer material and the total friction force is increased by the force required to displace the softer material from the front of the asperities of the harder one.

While this theory makes use of the advanced concept of the area of real contact, it assumes that the contact conditions between the asperities are such that plastic flow is always the case and that the only way of increasing the load carrying potential is by increasing the area of real contact. However, the conditions upon which such an assumption is valid are not always very clear and one may expect partially plastic flow and partially elastic deformation or even pure elastic deformation within a contact. Archard [73] notes that when materials of similar hardness rub together repetitively, a protuberance may be plastically deformed at its first encounter with the other surface, but its relaxation would be elastic. At its subsequent encounters it would bear the same load by elastic deformation [73]. The obvious question that rises from this observation is how could the laws of Amontons' be still valid for elastic contacts, when it is known from the Hertzian theory [72] that for a single elastic contact the area increases proportionally to the 2/3 power of the load. Archard [73] starts from a perfectly polished sphere in contact with an ideal flat plane and, as expected, he

calculates that the area of contact is proportional o the 2/3 power of the load. Next, he assumes that the surface of the sphere is not completely flat. Instead, it is characterised by a surface finish represented by spherical protuberances of a radius much smaller than the radius of the sphere, evenly distributed over the surface of the sphere. By applying the Hertzian theory on the contacts between the small spheres and the flat surface, he calculates an overall area of real contact, which is proportional to the 8/9 power of the load. By assuming even smaller protuberances on the small protuberances, he states a law, which indicates that the area of real contact is proportional to the 26/27 power of the load. By further assuming tiny protuberances on the smaller protuberances he finds that the area of real contact becomes almost proportional to the normal load. He also notes that the number of individual contacts between the sphere and the flat surface also become proportional to the load, as the number of scales of protuberances increase on the surface. Apparently, for a polished sphere, the number of contacts is constant and equal to one, while the area is proportional to the 2/3 power of the load. For a single series of protuberances the area is proportional to the 8/9 power of the load and the number of contacts proportional to the 2/3 power of the load and for a second series of protuberances, the number of contacts is proportional to the 8/9 power of the load, with the area being proportional to the 26/27 power of the load. Archard's analytical predictions are supported by experimental results [73], which show that under light loads, the coefficient of friction between abraded Perspex specimens remains constant for elastic contacts. This is attributed to the effect of the small protuberances. However, at higher loads the smaller protuberances deform flat and the contact conditions resemble those between perfectly polished surfaces, resulting in the reduction of the coefficient of friction.

It is now clear that, for a constant shear strength of the junctions formed between rubbing surfaces, the main factor that influences the coefficient of friction is the total area of the formed junctions, or, in other words, the area of real contact. The approximate proportionality between the real contact surface and the normal load has been highlighted for plastic and elastic contacts. Greenwood and Williamson [74] focus on the features of a somewhat more realistic surface than the one used by Archard [73]. The authors consider the case of a rough surface in contact with a completely flat plane. The contact conditions are determined primarily by the distance between the flat plane and a reference plane in rough surfaces. Assuming a certain

distribution of the heights of the asperities, the probability of an asperity being deformed by the flat plane can be found as the area under the probability density function for asperities higher (with respect to the reference plane) than the distance between the reference plane and the flat plane [74]. Assuming a known number of asperities per unit area and also that all asperities have spherical summits with the same radius, Greenwood and Williamson derive equations for the total number of contact spots, the total conductance, the real contact area and the load, as functions of the separation between the flat plane and the reference plane, for a given distribution of the heights of asperities. The equations are applied initially for an exponential distribution, to find that the area of real contact, the conductance and the number of contact points are all exactly proportional to the normal load. Approximate proportionality is found for a Gaussian distribution, which is a better approximation of reality. Greenwood and Williamson extend their analysis further by using the distribution of heights of the asperities in order to determine the proportion of contacts operating under plastic flow, for a specific separation of the surfaces. The result is the definition of the plasticity index, which may be used for the prediction of the type of contact between surfaces. Low values of this index indicate elastic contacts, while large values indicate plastic contacts. The topography of real surfaces is studied experimentally, using a stylus profilometer connected to a data acquisition system. It is found that the distribution of heights, the distribution of peaks and the distribution of peak curvatures are approximately Gaussian. What is worth noting about this experimental technique is that a peak is defined as a point higher than its two adjacent points, with its curvature being calculated by three-point curve-fitting.

In the field of surface modelling, Whitehouse and Archard [75] point out that the assumption of a single radius of curvature by Greenwood and Williamson is a major simplification. They propose an alternative surface representation, based on a random signal with an exponentially decaying autocorrelation function. It turns out that this choice results in a power spectral density, which is constant at lower frequencies (larger wavelengths of asperities) and cuts-off at 6 db per octave at higher frequencies (smaller wavelengths of asperities). Consequently, similarly to the idealised model introduced by Archard in [73], this model predicts the existence of asperities of large wavelengths with significant amplitude and asperities of short wavelengths with small amplitudes (the concept of protuberances on protuberances on protuberances). A local

peak is now defined as the product of the probabilities of three successive heights being shorter, higher and shorter respectively. In recognition that the shape of the autocorrelation function would affect the independence of these probabilities, the authors express the probability density of an ordinate being a peak, as a function of both the height of the ordinate and the correlation value. Finally, by using the concept of three-point curve fitting, they calculate the radius of the peaks and express the distribution of this radius with the value of correlation as a parameter. Archard's point of view that surface roughness consists of protuberances on protuberances on protuberances is strengthened by the late work of Greenwood and Wu [76]. The authors examine the similarities of Archard's theory with the fractal theory and report that the spectral density of a fractal curve is close to the spectral density of the surface model of Whitehouse and Archard [75]. The analysis is supported by measurements that show clearly the reduction of the curvature of the asperities as their wavelength increases.

The previous analysis highlights the difficulties associated with the study of friction. The simple laws of friction by Amontons and Coulomb apply conditionally, the main requirement being that the area of real contact increases in proportion with the normal load. Whether this is the case, is determined mainly by the statistics of the surfaces in contact [73-75].

2.4.2 The Friction of Elastomers

The term "elastomer" refers to a group of polymers characterised by high elasticity, viscous flow and a glass transition temperature [77] far below normal room temperature [78]. Rubber represents a sub-category of this group, but the words "elastomer" and "rubber" are interchangeable to such an extent that they are most often used as synonyms [78].

The reader may find an extensive analysis of a wide range of physical properties of rubber in relation to the structure of its molecules in [77]. From the point of view of the mechanical engineer, the most important among these properties are rubber's low elastic modulus, its large deformability with almost complete recoverability and its high internal damping – also known as internal friction. Internal damping results in the

generation of stresses, which depend highly on the rate of deformation applied on a rubber specimen. In general, internal damping is responsible for the time-dependent relationship between stress and strain for rubber [50]. The exact analogy between internal damping and viscous flow of a Newtonian liquid is demonstrated by Ward [50]. The combination of the elastic and viscous behaviour of rubber is commonly referred to as "viscoelasticity" [77], [50]. Details on the modelling of viscoelasticity and the response of rubber to certain stress and strain situations are given in chapter 3. Here, the unique frictional characteristics of rubber are discussed, in relation to its viscoelastic properties.

Rubber friction has been studied by Grosch [79], Schallamach [80], Persson [81] and others. Grosch [79] reports the results of an extensive experimental investigation of rubber friction. The coefficient of friction is measured for a number of rubber compounds sliding against a glass plate (representing an ideally polished surface), silicon carbide paper (representing a rough surface) and silicon carbide paper covered with a thin layer of magnesia powder (representing a lubricated rough surface). The measurements are carried out in a controlled environment with the temperature ranging from -50°C to 100°C and the sliding speed varying from 0-3 cm/s, in order to eliminate frictional heating. The results are given as plots of the coefficient of friction versus the sliding velocity, in a logarithmic scale. It is reported that the variation with temperature of the coefficient of friction between a specific rubber and a specific substrate follows exactly the variation of the rubber's stress-strain frequency response function with temperature. The stress-strain frequency response of polymers is discussed thoroughly in [50] and it is shown that under different temperatures, rubber exhibits a frequency response function, which is displaced horizontally on the frequency axis. In particular, higher temperatures lead to a displacement of the frequency response function to the right, i.e. to higher frequency values. The quantification of this displacement is achieved with the Williams, Landel and Ferry Equation (W.L.F.) [77], [50], which provides the horizontal displacement (in a logarithmic form) as a function of the current temperature and a reference temperature. Grosch [79] found that by applying the W.L.F. equation to friction measurements performed at different temperatures, it is possible to combine all experimental curves to a single "master" curve, corresponding to a reference temperature (usually 20°C). The results show that in all cases, the master curves

exhibit a distinct maximum [79]. As the sliding velocity approaches the value to which the maximum friction corresponds, steady friction changes to stick-slip friction. This phenomenon is attributed to the negative slope of the coefficient of friction, immediately after the peak value. Grosch also observes that the stick-slip phenomenon always starts at the same value of the frictional force (for a certain combination of materials) and does not depend on the sliding velocity or temperature. This can be seen as a direct proof that stick-slip follows the W.L.F. transform [79]. Grosch distinguishes two different behaviours in rubber friction, the first one occurring during sliding over smooth surfaces, the second one characterising sliding on rough surfaces. In the first case, the coefficient of friction exhibits a peak at relatively low velocities of a few cm/s at room temperature [79]. Grosch determined experimentally the frequency at which rubber's loss modulus (for a definition refer to chapter 3 and also to references [50], [51]) demonstrates a peak at the same temperature. By dividing the sliding velocity with this frequency for several rubber compounds he observed that the resulting wavelength ($6X10^{-7}$ cm) is of molecular dimensions. This leads to the conclusion that rubber friction on smooth surfaces is a result of a dynamic excitation of molecular scale. In particular, the rubber molecules form adhesive bonds with the hard surface. Under the application of an external force the molecules stretch, the bonds with the surface brake and the molecules jump a distance approximately equal to the calculated wavelength, before a new bond is formed. When a rough surface is involved in the contact, the peak coefficient is observed at much higher sliding velocities of several thousands m/s. Grosch found that if one divides the velocity at which friction is maximum with the frequency at which the dynamic loss factor (for a definition refer to chapter 3 and also to references [50], [51]) reaches a maximum, the resulting wavelength is equal to the spacing between the particles of the abrasive paper. This observation indicates that rubber friction at high velocities is also a dynamic phenomenon, related to the large scale asperities of the rough surface. As a conclusion, rubber friction consists of two separate terms, the adhesion term and the deformation term (the latter referring to large scale deformation). Both terms depend on the bulk viscoelastic properties of rubber.

Schallamach [80] provides a different view of rubber friction. He observes that when soft rubber compounds slide over hard surfaces, "waves of detachment" propagate along the contact, at velocities much higher than the imposed sliding velocity. The

waves appear as narrow bands, perpendicular to the direction of motion and the stereoscopic microscope reveals that the contact between the specimens is lost along the hills of the waves. Schallamach [80] attributes these waves (also known as Schallamach waves) to elastic instabilities due to the buckling of rubber in the front part of the contact area. He observes that the rubber involved in the leading part of the contact undergoes compression, while the rear part undergoes tension. This behaviour is confirmed by a mathematical model, which describes the deformation of the rubber surface by means of a differential equation. By assuming a parabolic normal pressure distribution along the contact between the rubber and the hard surface, Schallamach [80] calculates the strain distribution along the contact. The analytical results show qualitative agreement with experimental results, provided mainly as photographs of a deformed square grid drawn on transparent rubber compounds. Schallamach suggests that the macroscopic sliding of a rubber specimen on a hard surface (or a hard specimen on a rubber track) corresponds to the propagation of the waves from the front to the rear end of the contact patch. The energy loss associated with the propagation of the waves from the front to the rear manifests itself as friction. Schallamach recognises that the waves of detachment are not always the case and that the possibility of true frictional sliding should also be considered. He concludes that the actual frictional mechanism is the one that offers less resistance to motion and he observes that highly hysteretic rubbers require more energy for the maintenance of the waves of detachment; therefore such rubbers should promote true frictional sliding.

Persson [81] supports the views of Grosch [79] and expresses the friction between rubber and a hard substrate directly as a function of the rubber's viscoelastic properties. Persson [81], like Grosch, distinguishes the friction related to the long-wavelength asperities of the hard substrate (deformation term), from the friction due to adhesive forces (adhesion term). The approach to adhesive friction is most interesting and illuminates issues such as the static friction of rubber. Persson calculates the conditions upon which a rubber with low elastic modulus would deform enough in order to completely fill in the asperities of a highly polished surface such as glass polished with alumina powder. He suggests that a complete filling of a single cavity would occur only when the adhesion energy throughout the cavity is just enough to sufficiently deform the solid, in order to occupy the cavity. Based on this condition, Persson calculates the frictional stress generated at low sliding velocities,

corresponding to a frequency range from 0.1-10^6 s^{-1} (frequency is always given as the ratio between the sliding velocity and the wavelength of the asperities). It appears that this stress can be expressed as a function of the viscoelastic properties of rubber. Through this procedure, it is shown that significant frictional stresses might occur at very low sliding velocities, even below 10^{-8} m/s for a wavelength of asperities below 1000 $\mathring{A}$. As a conclusion, it is shown that even the so-called static friction of rubber is strongly related to the bulk viscoelastic properties of the material.

Finally, an interesting observation by both Persson [81] and Grosch [79], is that the coefficient of friction between rubber and hard surfaces remained approximately unaffected by the normal load for lightly to moderately loaded specimens. This can be explained by considering the theories of Archard [73], [75] and Greenwood and Williamson [74], [76]. Under light loads, rubber forms elastic contacts with a real area significantly smaller than the area of apparent contact. An increase in the vertical load would result in an almost proportional increase in the area of real contact, leaving the coefficient of friction unaffected. Nevertheless, due to its low elastic modulus, rubber deforms easily and if the normal load is high enough, a situation is reached where the area of real contact is almost equal to the area of apparent contact, i.e. the rubber fills in all the cavities. Any further increase in the normal load is not handled by a proportional increase in the area of contact and the coefficient of friction reduces.

From a more practical point of view, Browne, Ludema and Clark [82] distinguish four separate terms in rubber friction. The first two, namely adhesion and deformation friction, are the same terms investigated by Grosch and Persson. Nevertheless, it is stated in [82] that the definition of adhesion friction is not very clear in the literature (a different approach to the adhesion component is evident by comparing the work of Grosch [79] and Persson [81]). To complicate things further, the deformation friction in [82] is studied for sliding on surfaces with a size of asperities that gives a possible peak of the deformation friction at sliding velocities where normally the adhesion peak is observed, according to Grosch [79]. The two extra friction terms dealt with in [82] are the viscous and tear terms. The former is due to very thin layers of lubricants (most frequently water) inevitably trapped within the contact between the rubber and the hard surface. The existence of such a film would reduce adhesional bonding between rubber molecules and the hard surface and consequently eliminate the

adhesion term of friction. Finally, the tear term accounts for the fact that some solid surfaces tear particles from the rubber. These particles do not remain attached to the hard surface and this mechanism can occur on contaminated surfaces where the coefficient of friction is low.

Persson et al [83] examine the nature of static friction, kinetic friction and creep, with some reference to rubber friction. The authors focus on boundary lubrication and calculate the friction force as a function of sliding velocity using a numerical model of the molecular dynamics of the lubricant trapped within contact. Some interesting results are obtained regarding the transition between slip and stick. It is observed that in the case of a rigid body, the kinetic energy stored in its mass while sliding, needs to be converted into elastic energy in the lubrication film. From this requirement, a critical velocity is calculated for the transition between slip and stick, of the order of 10 μm/s. If, instead of a rigid body, a flexible one is considered, the authors note that for the transition from slip to stick, a full deceleration of the lump mass of the body is not required. Instead, the lower layer of the body sticks first, transmitting a wave along the height of the body. In this way, the kinetic energy is transformed into energy carried by the wave. Therefore, the stick slip phenomenon is not necessarily governed by the inertia of the sliding bodies. Finally, it is observed that due to the dependency of rubber friction to the relaxation time of the rubber, it is difficult to draw a fine line between static and kinetic friction. For a range of very low velocities (say 10^{-4} to 10^{-8} m/s) rubber might or might not exhibit a peak coefficient of friction, so that static friction, as perceived macroscopically, depends on the initial dwell time and the rate of starting [83].

2.4.3 Friction Modelling

It has now become clear that a spherical study of friction requires the contribution from various fields such as contact mechanics, surface statistics, molecular dynamics, viscoelasticity and others. In practical applications it is almost impossible to achieve such a complete representation, especially if one considers the dependency of friction on environmental conditions such as temperature, liquid or solid state lubrication (contamination of rubbing surfaces) and the co-existence of low and high sliding velocities. As a result, simple friction models are used for the representation of

friction in mechanical systems. The complexity of these models may vary from a constant coefficient of friction as dictated by the laws of Amontons and Coulomb, to more elaborate representations of friction, depending on the nature of the application and the level of accuracy required. The models discussed here are chosen based on their applicability in tyre friction. All such models originate mainly from investigations on the modelling of friction for use in control simulations [23], [84], [85]. The philosophy of these models is pretty much standard. The aim is to simulate the friction force as a function of the relative velocity and displacement of the rubbing bodies. For this purpose, simple differential representations are used [21], [23] which can be employed in real time simulations.

A typical friction model, which conforms to the standards stated above and a good starting point for the discussion of such models is the model proposed by Dahl [22]. Dahl derived his model observing the behaviour of the friction force with respect to the relative displacement of the rubbing bodies. He noticed that as long as the relative velocity is positive, the friction force monotonically approaches a maximum value. When the direction of motion is reversed, i.e. the relative velocity becomes negative the friction force reduces till it approaches its minimum, i.e. the negative maximum. However, the friction slope always remains positive, irrespective of the sign of the sliding velocity. In this way, a hysteretic loop is formed [22] with an area equal to the work of the friction force. Dahl found that this behaviour can be represented by a differential equation that describes the slope of the friction with respect to displacement, as a function of the friction force itself and the sign of the sliding velocity [22]. The main characteristic of the Dahl model is that it does not account for a peak friction force, as the maximum friction (positive or negative) is reached asymptotically. A comparison between the Dahl model and simple Coulomb friction reveals the advantages of the former representation. In Coulomb friction, the friction force always opposes the motion and does not depend on the displacement. Thus, the maximum friction, either positive or negative in direction, is reached immediately. The main disadvantage is the ambiguity in the determination of the friction force at zero sliding velocity. This is an unwanted characteristic, especially for the simulation of dynamic systems involved in control investigations.

A similar approach is followed by Bliman [21]. Bliman provides the equations for his single-point-contact friction model and then extends the model for application in tyre force estimation. For this purpose, he assumes a rectangular contact patch with a uniform normal pressure distribution and derives the friction force equation in the form of a partial differential equation with respect to time and distance along the contact patch. The case of longitudinal tyre-force generation is compared with results obtained by the Magic Formula and good agreement is found.

A similar approach is followed by Deur [24], and by Canudas de Wit et al [25]. In both cases the so-called LuGre friction model [23] is used for the calculation of tyre forces. The LuGre fiction model can be seen as an evolution of the Dahl model. Its main advantage over the Dahl model is its ability to generate a frictional peak at a pre-specified sliding velocity. This is achieved by incorporating the Stribeck effect [84] in the differential equation describing the friction model. The necessary modifications for the use of the LuGre friction model in tyre modelling are discussed with reference to the work carried out in [25]. The authors first present the lumped LuGre model, which is applicable for single point contacts, or completely rigid contacts (where the relative displacement is common for all points of the surfaces in contact). The distributed LuGre model is then derived for the case of a braking tyre, taking into account various normal pressure distributions, such as uniform and exponentially decreasing. The derivation is similar to that proposed by Bliman [21], where a partial differential equation is employed, describing the friction along the contact patch and with respect to time. The distributed LuGre model is used for the estimation of the steady-state friction under braking and traction situations. It is recognised that the distributed LuGre model theoretically incorporates an infinite number of states and therefore cannot be introduced in transient simulations. Hence, the distributed model is simplified to an average lumped LuGre model using the concept of a representative average displacement along the contact patch. This model is used for the generation of the transient braking force and the results are compared with experiments. The experiments involve hard braking from a given forward velocity, without the activation of an ABS system. There seems to be a good agreement between analytical and experimental results, yet some important observations can be made. The authors plot the experimental results in the form of friction coefficient versus time. In the beginning of the paper it is stated that a simple quarter car model including rotational

wheel dynamics can be used for the testing of the friction model. However, nowhere in the experimental section, is it stated explicitly that a complete parallel simulation is run for the generation of the friction force by the LuGre model. Instead, it seems that the authors have used various velocities obtained by the measurements in order to generate the necessary velocity and longitudinal slip information required by the LuGre model. This is confirmed by closely observing the comparison between the experimental findings and the simulation results in the time domain. Just before braking is applied, the experimentally measured coefficient of friction is relatively smooth and very close to zero (no friction force is yet generated). On the contrary, the numerically calculated coefficient shows significant fluctuations. It can be safely assumed that if the numerical results were obtained through a full simulation based on the simple system (vehicle – wheel – friction) proposed in the beginning of the paper, the coefficient of friction would appear as a perfectly straight line, crossing the zero point. The fluctuations of the friction coefficient (i.e. the friction force) may be attributed to the influence, on the LuGre model, of small fluctuations in the experimentally measured velocities. To resume, the friction coefficient is calculated using the LuGre model and experimentally measured velocities. In these calculations, the forward velocity of the vehicle is used, together with the rotational velocity of the wheel, as measured by the ABS sensor. These velocities generate the "macroscopic" longitudinal slip and not the actual slip conditions in the neighbourhood of the contact patch. This is somewhat equivalent to the treatments based on the relaxation length concept, where the required kinematic quantities, based on the motions of the vehicle and the wheel, are fed at each time-step into the differential equation which yields the transient slip ratio or slip angle [6] (i.e. the slip quantities in the neighbourhood of the contact patch). In the case of the LuGre model, a transient slip ratio is not defined, but the macroscopic kinematic quantities are passed to the appropriate differential equation for the estimation of the instantaneous friction force. Therefore, it may be argued that, provided the kinematic quantities, a relaxation-length based tyre model would yield similar results. As a conclusion, the usefulness of the LuGre model would be better emphasized by comparison of the numerical results with the results obtained using a relaxation-length based model. Finally, the LuGre model does not incorporate any carcass-belt dynamics. It is shown experimentally and numerically by Zegelaar and Pacejka [86] that under brake torque variations the tyre responds with an overshoot followed by decaying oscillations which coincide with certain vibratory

modes of the tyre structure. The LuGre model certainly does not incorporate such capabilities and its usefulness in the investigation of ABS systems where such vibrations are highly likely to be excited is expected to be limited.

2.5 Vehicle Modelling

In order to investigate a vehicle's dynamic behaviour either analytically, or with the aid of computer simulation, it is essential to define a vehicle model, which takes into account all the important parameters that affect the qualities under investigation. At the outset, the model should not be overcomplicated, as this would make it difficult to interpret the results, and decide which parameters are responsible for the outcome. Once these parameters are clearly identified, it is usually required to proceed with more elaborate models, in order to take into account the non-linearities, or to investigate the effect of under-estimated parameters and employed simplifications. This procedure has been followed by most researchers.

Furthermore, the modelling approach differs according to the purpose of the study. Blundell [87-90] and Hegazy and Rahnejat [91] use a multi-body dynamics approach in order to compose highly complex, non-linear vehicle models, for the assessment of vehicle handling, using computer simulation. On the other hand, when the aim is to develop techniques for chassis control, researchers usually prefer less complicated models. This requirement follows directly from the advantage in expressing the transfer functions of controlled systems in an analytical form.

2.5.1 Linear Models

It should be noted from the very beginning that a vehicle's dynamic behaviour is highly non-linear. Therefore, one should always be aware of the limitations of the studies, which are carried out with linear models. Nevertheless, the linear theory provides accurate results for low lateral acceleration (up to 0.3-0.4 g), where the behaviour of most components resides still in the linear region. Furthermore, the linear theory is most effective in describing the fundamental laws, which govern a vehicle's motion.

The most popular example of linear model is the "bicycle model" with lateral and yaw degrees of freedom. Forward speed is assumed to be constant and is considered as a parameter, rather than a degree of freedom. The bicycle model is used in text books, such as that by Dixon [5], Ellis [7] and Wong [44]. Also, Pacejka [2] has conducted a comprehensive study on handling, which reveals the basic trends of vehicle behaviour, starting with a simple four-wheel linear model that is reduced to an equivalent bicycle model for the purpose of the analysis.

When using a linear model, certain purpose-specific assumptions are made, which allow the implementation of linear relations, but also restrict the validity of the analysis to low lateral accelerations. For the case of the bicycle model the most important among these assumptions are:

- The tyre behaviour is linear
- There are no pitch and roll degrees of freedom and the load transfer during cornering is not taken into account
- Neglecting the load transfer, the tyre forces are assumed to be independent of the normal forces on each wheel
- Forward speed of the vehicle is constant
- Steering angles are relatively small
- No longitudinal forces are applied

Considering the simplifications mentioned above, it is obvious that such a model cannot be used for accurate studies on the effects of braking and traction, while it is also inappropriate for simulating transient manoeuvres.

2.5.2 Non-linear Models

Non-linear models include one or more sources of non-linearity and are appropriate for use in studies, which involve high lateral accelerations -- sometimes extended to the vehicle's limiting behaviour. These models provide the same results as the linear models at low lateral accelerations, a fact which validates the latter for use in such studies. The most common sources of non-linearity in vehicle dynamics include:

- Tyre forces and moments
- Bump and rebound stop forces
- Suspension kinematics
- Steering characteristics
- Suspension and Steering compliance due to bushings
- Non-linear Spring and Anti-roll bar stiffness
- Non-linear Damper characteristics

The disadvantage in using non-linear models is the difficulty in obtaining analytical expressions for the results. Instead, researchers have to rely on data obtained via computer simulation, which – in many cases – is difficult to interpret effectively.

In order to include - in an effective manner – all the sources of non-linearity mentioned above, a multi-body dynamic methodology is most appropriate. Blundell, in a series of four papers [87-90] provides a detailed description of the application of this methodology. In the first paper [87] he gives the background of multi-body dynamics, while in the second paper [88] he uses this methodology for modelling a vehicle's suspensions, including suspension and steering geometry and bushings. The third paper [89] is dedicated to tyre modelling aspects and describes the most frequently used non-linear tyre models, while in the last paper [90] he presents the results of the previous analysis by implementing a highly non-linear, multi-degree of freedom vehicle model in the ADAMS program (Automatic Dynamic Analysis of Mechanical Systems).

The superiority of the multi-body dynamics approach lays mainly on the ability of including suspension geometry and kinematic constraints. Nevertheless, other researchers such as Pacejka and Allen have used much simpler models, which incorporate non-linear tyre behaviour and weight transfers, but do not pay much attention to the non-linearities that result from the suspension geometry and assembly constraints. Pacejka [2-4] published a series of papers on the investigation of Vehicle Handling, where he uses models of increasing complexity. Starting with the aforementioned bicycle model, he adds non-linear tyre characteristics. Then, he uses the concept of *effective slip angle* of the front and rear axles and subsequently defines the *effective cornering stiffness* of the axles. Finally, he takes into account the weight

transfer, roll angle and steer compliance by introducing coefficients, which at the end appear in the equation for the calculation of the effective cornering stiffness. Allen et al [92], in the first part of their study, use a similar approach (i.e. they introduce coefficients in order to include the roll and compliance effects in his analysis), without increasing the degrees of freedom of his bicycle model.

It is interesting to note that both Pacejka and Allen have tried to include the effects of roll motion, without implementing this degree of freedom in the differential equations.

2.6 Vehicle Handling Analysis

2.6.1 Steady-State Handling

Steady state analysis is concerned with a vehicle's directional behaviour under time invariant conditions. In particular, the vehicle is supposed to be negotiating a corner with constant radius, while maintaining a constant forward speed. Thus, there is an equilibrium state in which the tyres have developed appropriate slip angles and subsequently sufficient lateral force to compensate for the centrifugal force acting on the vehicle's centre of mass. Mathematically, this is not a time invariant condition, as circular motion is by definition a dynamic situation (see Rahnejat [93]). Nevertheless, the absolute values of velocities and forces remain constant, a fact which transforms the differential equations into simple algebraic equations, that can be easily solved in order to reveal the basic trends of handling behaviour. It is worth noting that the steady state analysis is almost always conducted with the use of the bicycle model possessing two degrees of freedom (i.e. yaw and lateral motions).

This procedure is followed in text-books such as Wong [44] and Dixon [5], while it is also used by researchers like Pacejka [2-4], [94]. All these studies outline the relationship between the front and rear slip angles, as the most important factor that determines a vehicle's handling behaviour. Omission of the time derivatives in the 2X2 system of differential equations for the yaw and lateral degrees of freedom yields the conditions for a steady turn. Assuming that the tyre behaviour is linear and after the consideration of the force and moment equilibrium, the following relation is obtained, which expresses the difference between front and rear slip angles $\alpha_f - \alpha_r$,

as a function of the vehicle's forward speed, mass distribution between front and rear axles, cornering stiffness of the front and rear tyres and turning radius:

$$\alpha_f - \alpha_r = \left(\frac{W_f}{C_{af}} - \frac{W_r}{C_{ar}}\right)\frac{U^2}{gR} \tag{2.1}$$

Where α_f, α_r denote the slip angles of front and rear tyres, W_f, W_r are the front and rear vehicle weights, C_{af} and C_{ar} are the coefficients of cornering stiffness of the front and rear tyres respectively, U is the forward velocity and R is the turning radius.

By simple geometrical considerations, Pacejka [2] derives for the case of the bicycle model a simple, yet very important relation:

$$\delta_f = \frac{l}{R} + \alpha_f - \alpha_r \tag{2.2}$$

This relation indicates that the front steering angle δ_f depends – at any instant – on the turning radius R, the wheelbase l and the difference between front and rear slip angles $\alpha_f - \alpha_r$.

By combining equations 2.1 and 2.2, the following relation is obtained:

$$\delta_f = \frac{l}{R} + \left(\frac{W_f}{C_{af}} - \frac{W_r}{C_{ar}}\right)\frac{U^2}{gR} \tag{2.3}$$

The term $\left(\frac{W_f}{C_{af}} - \frac{W_r}{C_{ar}}\right)$ can be replaced by the *Under Steer Coefficient* K_{us}, so that:

$$\delta_f = \frac{l}{R} + K_{us}\frac{U^2}{gR} \tag{2.4}$$

This final relationship clarifies the situation: It indicates that the front wheel steering angle, required in order to negotiate a given corner, depends on the turning radius, the vehicle's wheelbase, the forward (tangential) speed and the vehicle's under-steer coefficient, which is a function of the weight and cornering stiffness distribution between the front and rear part of the vehicle.

In case of a linear vehicle model, the under-steer coefficient, K_{us} is used in order to classify vehicles, based on their cornering behaviour. According to this classification, a vehicle's handling behaviour is considered as under-steering when $K_{us} > 0$, neutral-steering when $K_{us} = 0$ and over-steering when $K_{us} < 0$. For the under-steering vehicle it is essential to increase the steering angle when the forward speed increases and vice versa, in order to follow a curve of constant radius. On the contrary, the over-steering vehicle requires the decrease of the steering angle as forward speed increases. Finally, the neutral-steering vehicle is capable of maintaining its path without adjusting the steering angle, regardless of the changes in forward speed. As it will be discussed later, the value of K_{us} is insufficient for assessing the steady-state handling behaviour of a vehicle, when the non-linear behaviour of tyres is taken into account.

Pacejka [2] used the bicycle model in order to obtain a simple transfer function for the steering angle δ_f with respect to the path curvature $1/R$ for steady state conditions. He then plotted the value of the transfer function versus the forward speed squared (U^2), for the cases of under, over and neutral steering vehicles. With the aid of geometrical equation (2.2), he modified this plot in a way that it represents the difference of slip angles $\alpha_f - \alpha_r$ with respect to the non-dimensionalised lateral acceleration (U^2/Rg). Finally, by rotating the plot, Pacejka [2] introduces the *Handling Diagram,* which represents the non-dimensionalised lateral acceleration of the vehicle versus the difference between rear and front slip angles $\alpha_r - \alpha_f$. When

both the vehicle and tyre operate in the linear range, the Handling Diagram consists of straight lines starting from the origin (0,0). The slope of these lines differs according to the handling behaviour: Under-steering vehicles give negative slope, neutral-steering vehicles are described by a vertical line, and over-steering vehicles attain a positive slope.

The advantage of the Handling Diagram is that it can be extended for the assessment of vehicles and tyres with non-linear characteristics, as demonstrated by Pacejka in [2-4], [94] and [95]. In this case, the plots are no longer linear and the behaviour of a given vehicle may change from under to over-steering in high lateral accelerations. Since the tyre cornering stiffness depends on the slip angles, the under-steer coefficient K_{us} cannot be defined and the assessment of the vehicle's behaviour relies on the sign of the slope of the Handling Curve. A similar analysis is carried out by Lukowski et al [96], who have used a four wheel – two degree of freedom model and linear tyre characteristics to obtain the same handling diagrams as that of Pacejka.

Allen et al, in the first part of the work described in [92], use a steady-state methodology for the assessment of vehicle handling behaviour under combined cornering and braking manoeuvres. The authors use a fairly accurate steady-state tyre model able to deal with combined longitudinal and lateral slip situations. The steady-state dynamics of the vehicle are dealt with in a simple manner: It is assumed that a steady-state solution is reached when the longitudinal tyre forces are sufficient to give the required braking or traction acceleration, while the lateral forces at each axle balance the resulting (due to cornering) centrifugal force. A computer program is developed, which cycles through the full braking-in-a-turn manoeuvring range. This procedure outlines the fact that the application of braking torque during cornering causes a shift of the vehicle's behaviour towards over-steer and can ultimately lead to spin-out of the vehicle. Pacejka [3] points out the inherent instability of over-steering vehicles by solving the characteristic equation of the 2X2 system of differential equations of the perturbed steady-state motion of the bicycle model. He finds that an under-steering vehicle is always stable, while the perturbed motion of an over-steering vehicle is always aperiodic i.e. diverts exponentially. Although the perturbed motion of a vehicle is by definition a transient situation, the author is not interested in the full transient response of the vehicle (for example the response to a step-steer input).

Instead, his aim is to investigate the stability of the steady-state motion, hence this study refers to steady-state operating conditions.

Abe [97] conducted a theoretical analysis on vehicle cornering behaviour in acceleration and in braking for forward, rear and four wheel drive vehicles. By plotting the turning radius versus speed for different values of longitudinal acceleration and deceleration, he showed that for a forward drive vehicle, the application of driving torque on the front wheels and the weight transfer to the back of the vehicle result in the early saturation of the lateral forces of the front tyres, a fact which increases the turning radius (i.e. the vehicle exhibits an under-steering behaviour). The same behaviour, but less intense is observed in the case of the four wheel drive vehicles. On the contrary, for rear wheel drive vehicles, tyre force saturation first takes place at the back tyres, thus the turning radius decreases with speed and the vehicle becomes over-steering. Finally, regardless of the type of transmission, braking results in an over-steering behaviour, which is again expressed by the decrease of the turning radius with speed. This is caused by the combined effect of braking forces on the rear tyres and the weight transfer to the front of the vehicle.

2.6.2 Transient Handling

According to the definition given by SAE [98], a vehicle operates in transient state when either the vehicle's responses, the external forces relative to the vehicle, or the control positions are changing with time. This definition does not require that the vehicle has entered the non-linear region of operation. Nevertheless, the study of transient handling behaviour usually takes into account the most important sources of non-linearities. In reality, most of the transient handling studies involve high lateral accelerations, which result from relatively steep control inputs. Because the vehicle usually operates in the non-linear range, analytical expressions such as the ones derived for steady state handling are impossible, thus results are obtained either experimentally, or by simulation.

Undoubtedly, the transient part of the handling response of a vehicle determines the driver's perception of its overall handling qualities. Under a pre-specified transient manoeuvre, the transient response time may be defined as the time needed by the

vehicle in order to reach a specific percentage of its final steady-state response. There is no universal agreement on the exact percentage that characterises better the transient response of a vehicle and various researchers have used different values. For example, Whitcomb and Milliken [99] assume this percentage to be 63%, while Bickerstaff [100] has chosen a value of 50%.

Perhaps the most common transient manoeuvre involves a step increase in the steer-angle. Lee et al [101] use, among other, a transient step-steer manoeuvre for the assessment of the contribution of certain suspension parameters to the handling performance of a vehicle. Antoun et al [102] have developed a vehicle model which is subjected to an approximately step-steer command at a forward velocity of 96 Km/h, resulting in a lateral acceleration as high as 0.7 g. The vehicle model is based on a detailed multi-body approach using the ADAMS multi-body software and the simulated responses show generally very good agreement with experimental results. Nevertheless, the simulated response times seem to be shorter than the response times measured experimentally. This difference is attributed to the use of a steady-state tyre model which neglects the relaxation properties of the tyres. Hackert et al [103] have developed a multi-body model of a light truck for the investigation of transient responses, including the study of cross wind stability issues. Naude et al [104] use a double lane-change manoeuvre for the assessment of the transient behaviour of the vehicle. The model used in their investigation is an enhanced non-linear vehicle model appropriate for transient simulations, combined with a driver model which steers the vehicle using closed-loop control. Hegazy [105] has also developed a complex multi-body model which is tested under a double lane-change manoeuvre and a step-steer input. The adoption of a multi-body methodology allows the changes in suspension geometry to be monitored together with the yaw rate response and lateral acceleration response.

In contrast with the aforementioned time domain studies, Allen et al [92] use a frequency domain methodology to analyse the steady-state behaviour of a vehicle. In his study he takes into account the effects of combined cornering and braking forces. Allen outlines the fact that the application of braking torque during cornering causes a shift of the vehicle's behaviour towards over-steer. Furthermore, he points out the inherent instability of over-steering vehicles by showing that the bandwidth of the

transfer function of yaw rate with respect to steering angle is proportional to the equivalent rear axle cornering coefficient. When the rear axle side-forces saturate under high g manoeuvres, the bandwidth approaches zero.

2.7 Some Concluding Remarks on the State of the Art in Tyre Modelling

A significant amount of modelling work has been discussed, both in the fields of steady-state and transient modelling. Also, the importance of tyre force generation in vehicle handling simulations has been highlighted. In this section, the main trends and the status of tyre modelling for vehicle handling studies are summarised.

In steady-state studies, the Magic Formula [6], [58], [41], [62] seems to be the model of choice. Although a semi-empirical model with little physical significance, the Magic Formula possesses the distinctive and highly desired advantage of being easily adopted to experimental results. The formula is characterised by a very flexible, well defined mathematical structure which accounts in a straightforward way for almost all experimentally observed tendencies in steady-state tyre force generation. On the other hand, physical models ([46-49], [52-54], [56]), both analytical and numerical, are still struggling to compete in terms of accuracy and ease of use. In many cases good agreement is achieved between experimental and simulation results ([52-54], [56]), but there is a lack of confidence whether a physical model would be able to handle a very wide range of operating conditions. At this point, it should be emphasized that a tyre model can be judged from at least two different points of view. First, it can be evaluated in terms of being an all-around performer i.e. being able to deliver sensible results when used in simulations in a wide range of operating conditions. Second, it can be judged in terms of enabling the study and assessment of certain parameters that influence tyre force generation. Such parameters may be related to the friction law governing the contact, the shape of the normal pressure distribution, or other relevant issues. Probably the main strength of the current physical models lies in their potential to reveal the influence of such parameters. To this end, some purpose-specific models exist. For example, the model proposed in [106] aims to the investigation of the rolling conditions in terms of normal pressure distribution and rolling resistance. In some cases, a single physical model combines successfully the requirements for all-around performance together with a modelling approach that

reveals the influence of certain parameters, as demonstrated by the model proposed by Sharp and El-Nashar [56].

In the area of transient tyre modelling, it is recognised by the majority of researchers that the transient response of the tyre is mainly related to the dynamic properties of its structure, i.e. the carcass and the belt. In many cases, the contact conditions are treated in a simple manner and the main focus is on the response of the structure. This approach is followed for example in the development of the string-type model by Pacejka in [13]. In its simplest form, transient force generation is treated using the relaxation length concept [6], [67-69]. Again, the relaxation length is a measure of the influence of the structure of the tyre and needs to be combined with a steady-state model for the description of the situation in the contact patch. This view is also supported by the findings of Maurice et al [14] who show that the transient properties of a tyre may be successfully represented by a flexible carcass, while the behaviour within the contact may be represented using a brush-type model. It is clearly stated in [14] that the brush model is closely related to the tread behaviour, while the transient behaviour depends primarily on the modelling of the carcass.

With the latest advances in computer technology, numerical transient tyre models have emerged [15], [17], [18], [19] where the tread deformation along the contact patch depends on the belt-carcass deformation and the tread forces are updated in a transient manner. These models are assumed to simulate, or at least have the potential to simulate transient force generation in a more realistic way.

In the section dedicated to friction, a number of tyre models were presented [21], [22], [25], based on friction models previously developed for control studies. In [25], the LuGre model is used for the "dynamic" simulation of braking and traction. It seems that in this approach, the traditional connection between transient or "dynamic" behaviour and carcass dynamics is not emphasized. Most of the parameters of the LuGre friction model are identified through steady-state simulations and only one parameter is identified from transient simulations. The final model does not show any direct physical connection with the structural properties of the tyre, as for example is the case with the relaxation length concept. However, this category of models points

towards a very interesting direction, that is, the use of advanced friction models in tyre dynamics.

There is a chance that the aforementioned or other friction models (possibly based on the observations stated in the section about friction) might yield more useful and realistic results if restricted to the area of contact. The overall behaviour would then be dictated by the interaction of the "frictionally advanced" tread and a flexible belt and carcass.

Chapter 3: Steady-State Tyre Analysis

3.1 Introduction

Traditionally steady-state tyre analysis serves as the starting point for the investigation of tyre handling dynamics. Not only does it form the background for transient approaches, but it also deals with several aspects of tyre mechanics, which are very often overlooked in transient analyses due to the difficulties involved. Some very effective steady-state models have been referred to in the previous chapter. However, there is still room for improvements, both in the understanding of tyre mechanics as well as the implications of various modelling approaches. Such investigations might lead to the development of new, more successful models or even improve the accuracy of the existing models by revealing the influence of certain parameters.

3.2 General Considerations

3.2.1 Construction of the Tyre

Prior to discussing any modelling approach, it is beneficial to describe the physical structure of the pneumatic tyre and identify the structural parameters that influence its behaviour.

The pneumatic tyre is a toroidal flexible tube, filled with compressed air. The pressure inside the tyre varies from 120 to 200 KPa for cars and up to a much higher 300 – 600 KPa for trucks. In general, the toroidal tube is a composite structure, consisting of cords of high modulus of elasticity, enclosed in a much softer rubber matrix. Referring to figure 3.1, the most important structural elements of the tyre are the carcass, the belt and the tread.

The carcass forms the hollow tube and is mainly responsible for the toroidal shape of the tyre. It consists of a number of layers of flexible cords extending from the inner

side of the rim to the outer side, along the rim circumference. The material of the cords was initially cotton (up to 1945), then rayon and finally nylon, polyester, steel, aramid and glass. The carcass is fitted on the rim with the aid of the beads. The beads are circular high tensile strength steel wires extending along the circumference of the rim. The cord layers composing the carcass are tied on the beads and thus may transfer forces from the carcass to the rim. The cord layers are enclosed in rubber compounds of various properties, depending on the type of application. In general, carcass rubber is soft in order to achieve good fatigue properties. In tubeless tyres the air pressure acts directly on the inside walls of the carcass and for this reason the inside surface is covered by a thin layer of rubber with high impermeability to air. In tubed tyres, a separate rubber tube is inflated with air and the carcass cords are tensioned through the contact of the inner inflated tube with the inside surface of the carcass. Tubeless tyres have become dominant for being more economical and demonstrating better puncture resistance compared to the tubed tyres.

The alignment of the cords of the carcass influences largely the dynamic behaviour of the tyre. The direction of the cords is defined by the crown angle, which is described as the angle between the cords and the circumferential line of the tyre, as shown in figure 3.1. Experience shows that when the cords are laid in small angles, the tyre shows better handling behaviour, but poor ride characteristics. On the other hand, when the cords are positioned radially at a right angle with respect to the circumferential line, ride characteristics improve but the handling behaviour deteriorates.

Based on the alignment of the tread cords, two main types of tyres can be found. As shown in figure 3.1(a). The bias-ply tyre is characterised by cord layers (plies) positioned in intermediate crown angles of approximately 40^{o}, in an attempt to combine good ride and handling characteristics. The number of plies in a bias-ply tyre varies from a minimum of two for light loading conditions, up to twenty for heavy vehicles. Bias-ply tyres show high rolling resistance and wear, as a result of the relative displacement of the cord layers during rolling. They are mainly used in cycles, motorcycles and agricultural vehicles.

Radial tyres have dominated the world of passenger, racing and recently heavy-duty vehicles. The carcass of a radial tyre consists of one or more layers of cords, positioned at right angles with respect to the tyre centre-line (crown angle of 90°), as shown in figure 3.1(b). Between the carcass and the tread, along the circumference of the tyre, lies a separate belt consisting of several cord layers of high modulus of elasticity, positioned at a low crown angle of approximately 20°. The belt constrains the radial layers of the carcass, thus, preventing buckling, but also increases the lateral stiffness of the tyre, a fact which influences cornering behaviour. The construction of the radial ply tyre reduces the relative deformation of the layers of cords during rolling and this results in the reduction of energy dissipation, compared to bias-ply tyres.

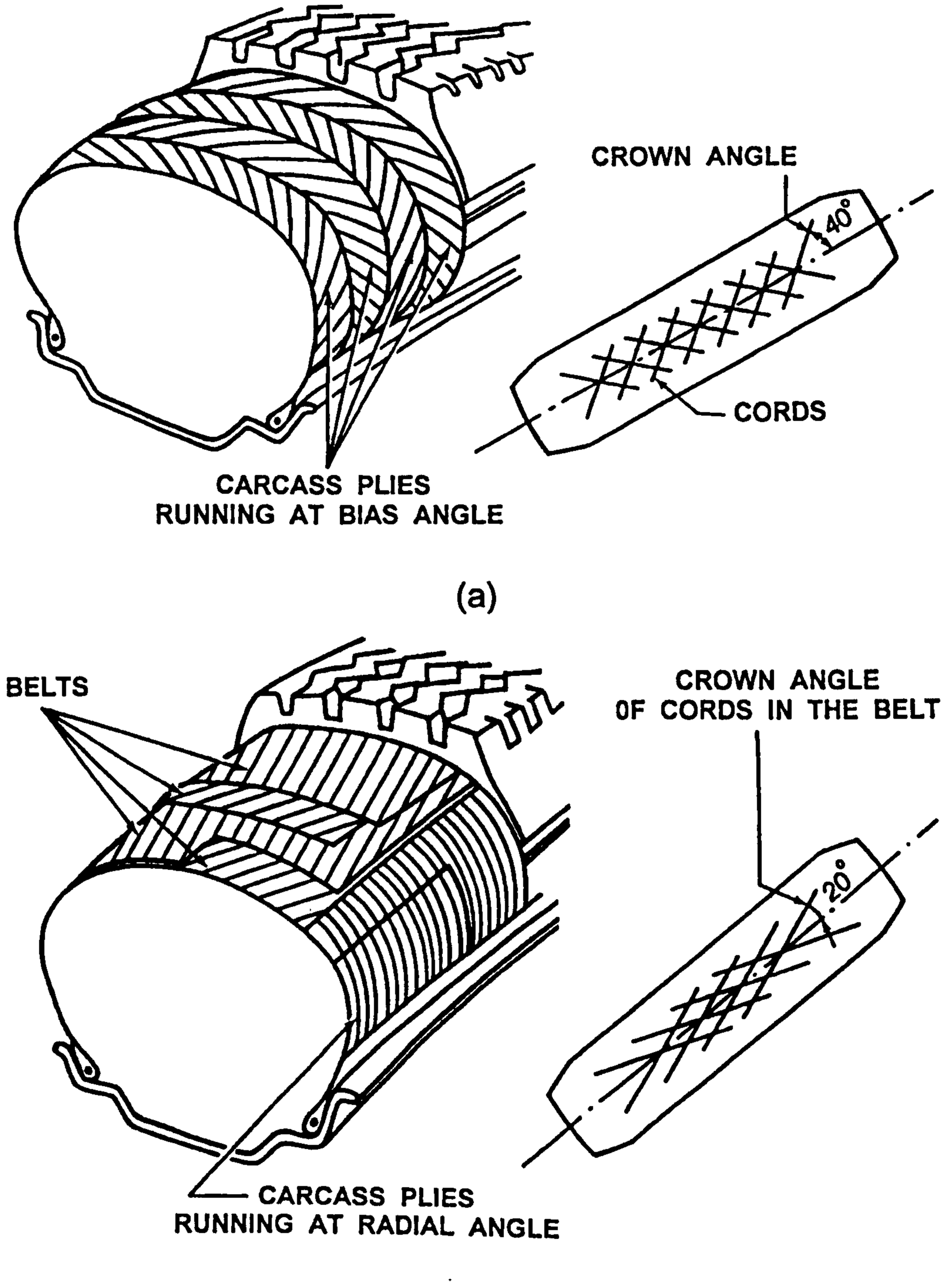

Figure 3. 1 The construction of the tyre (after [44])

A less common type of tyre is the bias-belted tyre, which can be described as a bias-ply tyre with a separate belt. The belt constrains the carcass layers in a similar way, as in the case of radial ply tyres and reduces energy losses and tread wear compared to bias-ply tyres.

The tread extends along the outer circumference of the tyre and serves as the contact interface between the tyre and the road. The tread is made of rubber and its shape depends largely on the type of application. At lower lateral accelerations (below 0.3g) the tread operates mainly in the adhesion region and the deformations of the carcass and belt affect mostly the behaviour of the tyre. At higher accelerations the friction limits of the tyre-ground interface are approached or even exceeded and the contribution of the tread in tyre behaviour becomes significant. The frictional potential between the tread and the road surface depends largely on the material and shape of the tread, the running conditions and the type of road surface. On high quality dry tarmac, such as that found on racing tracks, maximum friction is achieved by using tyres with un-patterned flat tread (slick tyres) made of soft rubber compounds. The tread behaves literally like gum and sticks on the ground with extremely high wear rates. Much harder rubber compounds are used for the tread of passenger car tyres in order to reduce wear, with a consequent reduction in friction levels. In addition, the tread of passenger and truck tyres is usually patterned with grooves and slots as shown in figure 3.1, in order to enable water drainage and eliminate the tendency to hydroplane.

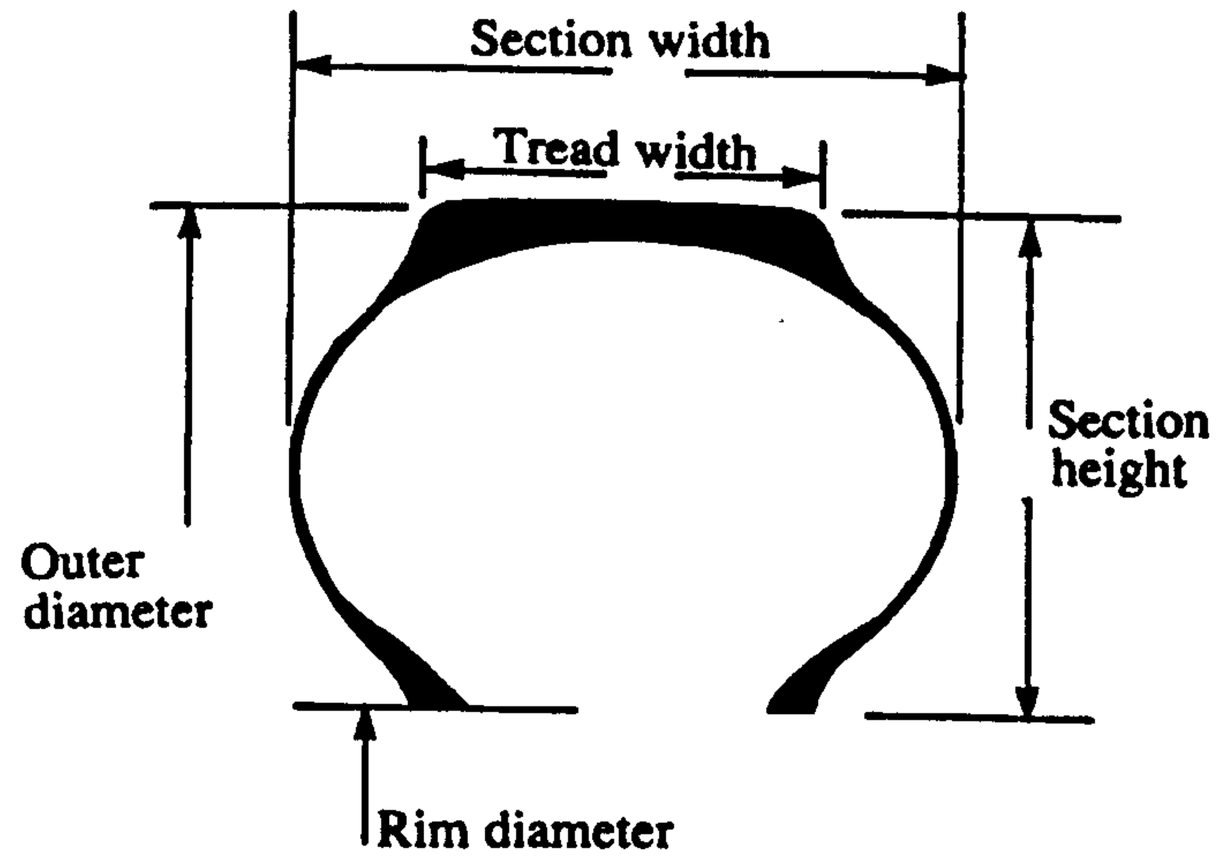

Figure 3. 2 Principal dimensions of the tyre (after [5])

Figure 3.2 shows the most important dimensions of a tyre. The principal dimension is the rim diameter, usually given in inches. The rest of the dimensions may vary – for the same rim – within certain limits dictated by the type of the rim, the space available and the operating conditions. The section width is normally given in millimeters, while the section height is given as a percentage of the section width. The dimensions of a tyre are usually printed on the side of the carcass according to a generally adopted convention. For example, a tyre with dimensions "175/60 R13" is a tyre, which fits on a 13 inch diameter rim, has a section width of 175 mm and the section height is 0.6 times that of the nominal section width.

3.2.2 Modelling Representations of the Structure of the Tyre

In the preceding section three main tyre structures were underlined, namely the carcass, the belt and the tread, while in chapter 2 the most representative modelling approaches were presented. In this section, an attempt is made to relate the structural elements of the tyre and various modelling representations.

Under the application of lateral (cornering) and longitudinal (traction and braking) forces, the carcass deforms laterally as well as circumferentially. The nature of such deformations depends on the structure of the carcass, in other words the number and orientation of the plies, the rigidity of the ply cords and the properties of the rubber matrix within which they are enclosed. Additionally, the pre-tensioning of the carcass due to inflation pressure alters its mechanical properties. A detailed description of the composite structure of the carcass requires the combined modelling – possibly using finite element methodology – of the assumedly elastic cords and the much softer viscoelastic rubber matrix. For the purpose of vehicle dynamic analyses this approach is not favoured due to its complexity and its numerical intensiveness. Instead, as discussed in chapter 2, most researchers use simplified representations of the carcass, consisting mainly of lateral and circumferential (longitudinal) elastic elements with properties that are representative of the carcass as a whole. Furthermore, investigations are usually restricted within the area near the contact patch. Hence, the circumferential properties of the carcass are often referred to as longitudinal properties. In most steady-state approaches the lateral and longitudinal elements of the carcass lack damping and inertia, while their stiffness may vary with internal pressure

and normal load. The radial deformation of the carcass is of great importance for the estimation of rolling resistance and vertical deformation under the application of a normal load. Typically, radial elements are used for the modelling of the radial deflection of the carcass in the neighbourhood of the contact patch. If the main interest is the calculation of the normal pressure distribution, simple elastic elements may be used for a rough estimation. On the other hand, the calculation of rolling resistance requires the modelling of hysteresis losses and therefore radial elements with damping need to be introduced. The effect of inflation pressure on the radial stiffness of the tyre should also be taken into consideration. Well within the contact patch, the contact pressure is balanced by the inflation pressure, and this produces a more or less constant contact pressure, as opposed to the parabolic pressure distribution predicted by the classical Hertzian contact theory. Therefore, the shape of the contact pressure distribution becomes trapezoidal in the longitudinal direction. To account for this phenomenon, the radial stiffness of the carcass should vary with deflection in a non-linear manner, resulting in a radial force that converges asymptotically to a maximum value dictated by the inflation pressure.

The tyre belt may be represented as a circumferential beam, subjected to lateral bending. In this case, the radial, lateral and circumferential carcass elements are evenly distributed along the length of the beam. Alternatively, the belt may be realised by connecting elastically adjacent carcass elements. In the steady-state investigations the beam is assumed to be mass-less, and its main purpose is to laterally offset the point of application of the longitudinal force under combined cornering and braking/traction.

Although the belt is a typical structural feature of radial tyres, it can be used as a modelling element in any tyre, in order to account for the continuity of the deformation along the circumference of the tyre. In the event that the same tyre model is to be used for both bias-ply and radial tyres, the stiffness of the belt should be adjusted in conjunction with that of the carcass in order to yield realistic results for both types of tyres.

The tread is modelled as a series of elastic or viscoelastic elements connected to the belt. Usually tread elements are considered as mass-less and their deformation is

mainly used to determine the frictional conditions between the road and the tread. Tread elements are able to deform laterally and longitudinally, but in some cases, an additional radial deflection might be introduced.

Instead of using separate elements for the carcass, belt and tread, it is common to use a single series of flexible elements for the representation of the combined lateral and longitudinal deformations. In this case, the properties of the elements are carefully selected in order to represent the combined properties of the aforementioned structures. The size of the contact patch and the shape of the pressure distribution are assumed to be known *apriori*, or may be calculated using radial deflection elements.

Finally, the rolling resistance predicted by a tyre model can be adjusted by changing the damping factor of the radial elements of the tyre carcass or tread. Again, it is shown that it is possible to predict the different behaviours of radial and bias-ply tyres by adjusting the value of a single parameter. In reality, the mechanism of intensive relative motion of the cord layers observed in bias-ply tyres during rolling is much more complicated to analyse.

3.2.3 Some Aspects of Rubber Modelling

Rubber represents approximately one third of the weight of a modern passenger tyre. With its incompressible nature (Poisson ratio near 0.5) and its viscoelastic behaviour, it influences the mechanical behaviour of the tyre, affecting the levels of energy dissipation, the shape of the contact pressure distribution and, last but not least, friction between the tread and the road.

3.2.3.1 Viscoelasticity

In general, viscoelastic materials demonstrate a time varying strain response under the application of a constant stress and vice versa. These phenomena are summarised below:

- Instantaneous elasticity
- Creep under constant stress

- Instantaneous recovery
- Delayed recovery
- Permanent set
- Stress relaxation under constant strain

The first four phenomena are related to the strain response of a viscoelastic material when a constant stress is applied for a certain period of time and then is removed from the specimen. This test is referred to as a creep and recovery test [50], [51], [107]. The stress relaxation refers to the decay in stress, when a viscoelastic material is subjected to a constant strain [50], [51]. In this section, the nature of viscoelasticity and possible ways of modelling viscoelastic behaviour are demonstrated through the creep/recovery test. The reader may refer to the literature [50], [51] for a study of the relaxation phenomenon.

The linear theory of viscoelasticity yields simple linear constitutive equations that describe the relation between stress, strain and time [50], [51]. These equations are based on a number of viscoelastic models of varying complexity. The basic elements of such models are the linear spring and linear damper.

The Burger's model is the simplest model capable of reproducing the full range of phenomena observed in a creep/recovery test. It consists of two springs and two dampers connected as shown in figure 3.3 (a). The constitutive equation of the Burger's model reads [51]:

$$\sigma+\left(\frac{\eta_1}{R_1}+\frac{\eta_1}{R_2}+\frac{\eta_2}{R_2}\right)\cdot\dot{\sigma}+\frac{\eta_1\cdot\eta_2}{R_1\cdot R_2}\cdot\ddot{\sigma}=\eta_1\cdot\dot{\varepsilon}+\frac{\eta_1\cdot\eta_2}{R_2}\cdot\ddot{\varepsilon} \tag{3.1}$$

Where:

σ	is the stress
ε	is the strain
$\eta_{1,2}$	are the damping coefficients
$R_{1,2}$	are the stiffness coefficients

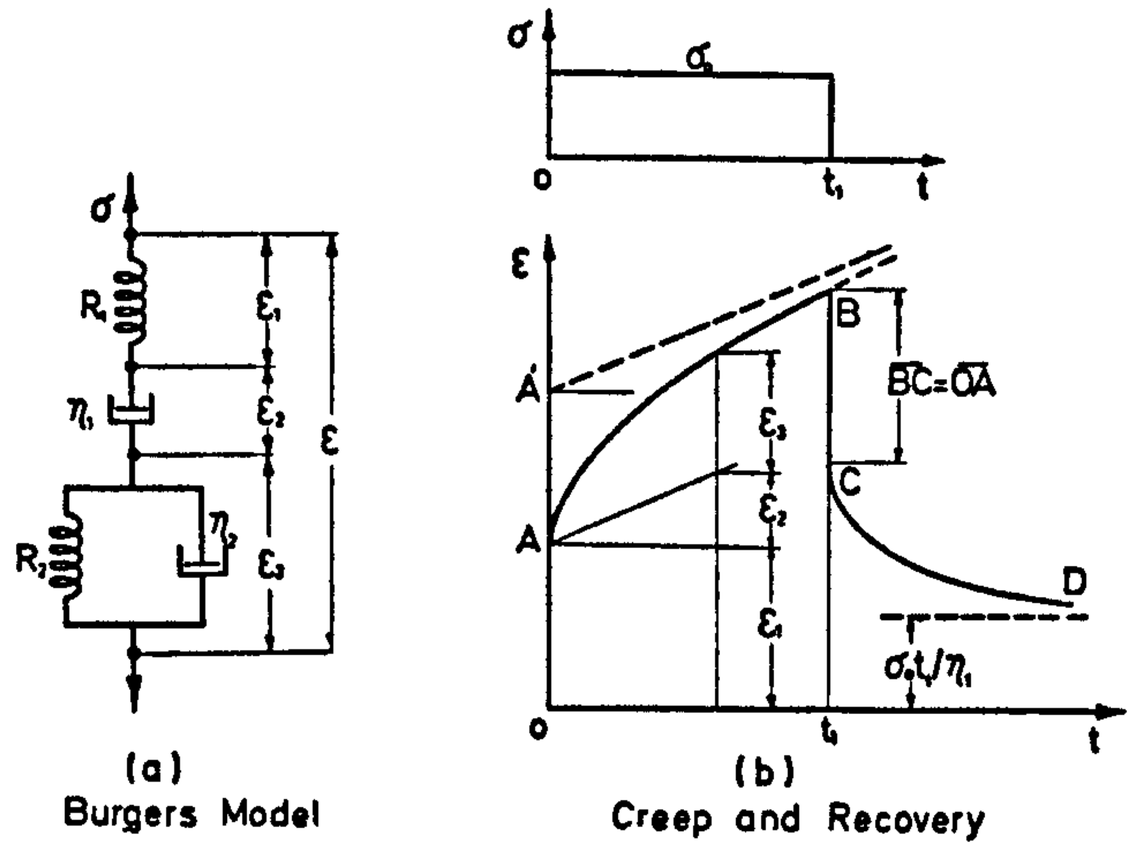

Figure 3. 3 Creep and recovery of Burger's model (after [51])

Solving the constitutive equation for creep and recovery involves finding the strain rate $\varepsilon(t)$ when a specimen is subjected to a constant stress σ_o which ceases suddenly at time t_1. The solution of equation (3.1) reads [51]:

$$\varepsilon(t)=\frac{\sigma_0}{R_1}+\frac{\sigma_0}{\eta_1}t+\frac{\sigma_0}{R_2}\left(1-e^{-R_2t/\eta_2}\right), \qquad \text{for } t\le t_1 \tag{3.2}$$

and:

$$\varepsilon(t)=\frac{\sigma_0}{\eta_1}t_1+\frac{\sigma_0}{R_2}\left(e^{R_2t_1/\eta_2}-1\right)e^{-R_2t_1/\eta_2}, \qquad \text{for } t>t_1 \tag{3.3}$$

Figure 3.3 (b) shows the creep and recovery behaviour of a viscoelastic material as predicted by the Burger's model. The theoretical prediction is in close agreement with the behaviour of rubber as observed experimentally [51]. The strain reaches the initial value instantaneously (instantaneous elasticity) and increases under the combined effect of viscous flow (second right hand side term of equation (3.2)) and delayed elasticity (third right hand side term of equation (3.2)). When the application of stress ceases, the Burger's model shows instantaneous recovery, which is followed by a delayed recovery which converges to the remaining permanent set.

The Burgers model can serve as a fairly accurate representation of a rubber element. Nevertheless, the constitutive equation may prove over-complicated for use in a tyre

model. Instead, it is common practice [108] to use a Kelvin-Voigt model for the representation of tyre rubber elements. The Kelvin model consists of a spring and a damper connected in parallel, as shown in figure 3.4 (a). The constitutive equation of the Kelvin model reads [51]:

$$\dot{\varepsilon} + \frac{R}{\eta}\varepsilon = \frac{\sigma}{\eta} \tag{3.4}$$

Where:

σ	is the stress
ε	is the strain
η	is the damping coefficient
R	is the stiffness coefficient

Solving equation (3.4) for creep and recovery yields:

$$\varepsilon(t) = \frac{\sigma_0}{R}\left(1 - e^{-Rt/\eta}\right), \qquad \text{for } t \le t_1 \tag{3.5}$$

and

$$\varepsilon(t) = \frac{\sigma_0}{R} e^{-Rt/\eta}\left(e^{Rt_1/\eta} - 1\right), \qquad \text{for } t > t_1 \tag{3.6}$$

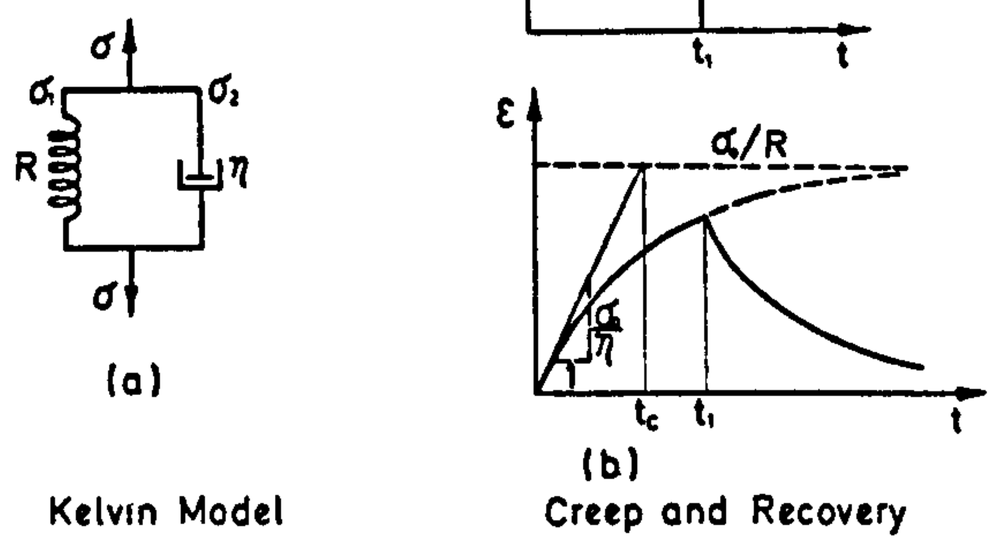

Figure 3. 4 Creep and recovery of the Kelvin model (after [51])

It is evident from equations (3.5) and (3.6) and figure 3.4 (b) that the Kelvin model is not capable of reproducing the effects of instantaneous elasticity, viscous flow and instantaneous recovery.

When choosing a viscoelastic model, its frequency response to a periodic strain is often more important than that due to creep and relaxation behaviour. The generic form of periodic strain may be written as follows:

$$\varepsilon(t) = \varepsilon_0 e^{i\omega t} \tag{3.7}$$

Where: ε_0 is the amplitude of the strain and ω is the frequency of the excitation.

In this case, the stress response of a linear viscoelastic model obtains the form:

$$\sigma(t) = \sigma_0 e^{i(\omega t+\varphi)} \tag{3.8}$$

Where: σ_0 is the amplitude of the stress and φ is the phase angle of the strain response.

The complex relaxation modulus is defined as:

$$E^* = \frac{\sigma_0}{\varepsilon_0} e^{i\varphi} = E_c + iE_L \tag{3.9}$$

Obviously:

$$E_c = \frac{\sigma_0}{\varepsilon_0}\cos\varphi \text{ and } E_L = \frac{\sigma_0}{\varepsilon_0}\sin\varphi \tag{3.10}$$

E_c is designated the *storage modulus* and is in phase with the strain, whilst E_L is the *loss modulus* and represents the imaginary part of the complex relaxation modulus. Finally, the *tangent modulus* (often referred to as the *loss* tangent) is defined as:

$$\tan\varphi = \frac{E_L}{E_c} \tag{3.11}$$

The tangent modulus, or alternatively the phase angle, is a measure of the relative effect of internal damping on the stress build-up by the viscoelastic material and depends on the exciting frequency ω and the material properties. An example of the frequency dependence of E_L, E_c and $\tan\varphi$ is given in figure 3.5. At low frequencies, the behaviour is governed by the storage modulus and there is no significant viscous flow (Rubbery behaviour). At intermediate frequencies the loss modulus and consequently the loss tangent rise, as a result of the effect of internal viscous damping (Viscoelastic behaviour). At this stage the storage modulus rises as well. Finally, at higher frequencies the material demonstrates a glassy behaviour. The loss and tangent moduli drop again and the response is governed by the significantly increased storage modulus.

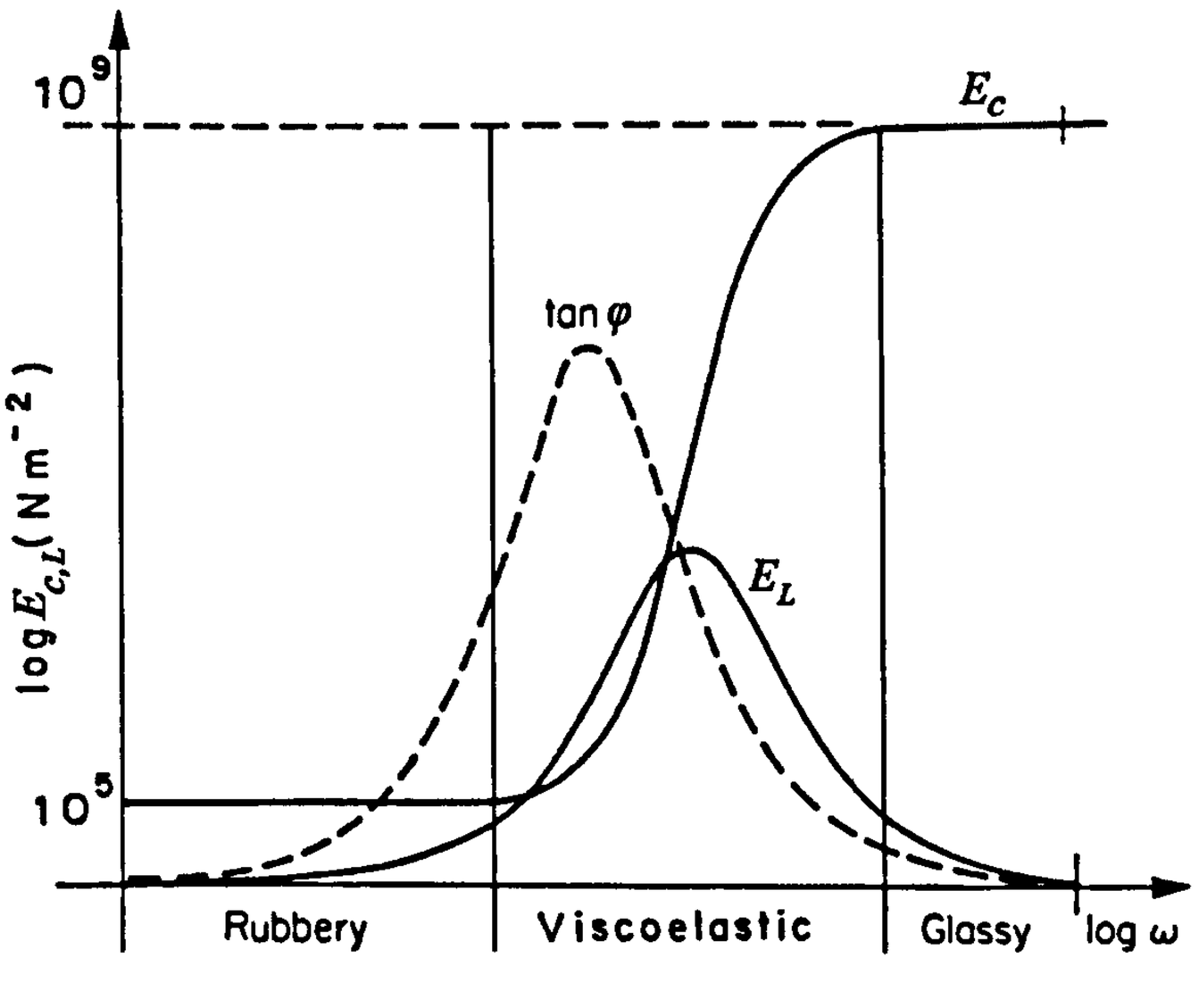

Figure 3. 5 The frequency dependence of the loss modulus, storage modulus and loss tangent for a typical polymer (after [50])

By applying a periodic strain on any linear viscoelastic model, it is possible to obtain the complex modulus and tangent modulus as functions of frequency and damping and stiffness coefficients of the elements of the model.

By applying this methodology it is shown that the Burger's model yields a rather good representation of viscoelastic behaviour throughout the frequency range. The behaviour of the Kelvin model is governed by the spring constant for very low frequencies, while a rapid increase in the complex modulus and the phase angle is predicted as the frequency increases. Still, for a frequency range between zero and a couple of hundreds of cycles per second (depending of course on the properties of the material as well), the behaviour predicted by the Kelvin model is in satisfactory agreement with that of viscoelastic materials such as rubber. It is noted in [107] that for most viscoelastic materials operating above the glass transition temperature [77], the response is relatively flat from about five to several hundred Hz. As an example, rubber compounds used in the tread exhibit a tangent modulus ranging from 0.1 to 0.2 for low amplitude vibrations in room temperature [107].

The behaviour of a viscoelastic material subjected to a periodic strain has been discussed in terms of the stress response, with the complex relaxation modulus E^* representing the connecting parameter (eq. (3.9)). Due to the effect of internal damping, each strain cycle involves a certain amount of energy loss. If one plots the stress as a function of the strain – say between two strain values – it becomes obvious that the area under the curve is a measure of the work lost. It is shown that for a sinusoidal strain, an ellipse is formed in the strain-stress plane. As expected, the area of the ellipse is a measure of the energy lost per strain cycle. Because the ellipse corresponds to a full strain cycle, it is often referred to as a hysteresis loop. A typical hysteresis loop for a rubber-like material is shown in figure 3.6., where the relation between the dimensions of the elliptical loop and E_c, E_L and φ is also provided. Energy dissipation depends only on the internal damping and therefore the area of the ellipse is a function of the loss modulus E_L and the maximum strain ε_0. The total energy dissipated per cycle shows the same dependency on frequency as E_L, while it is apparent from figure 3.6 that the overall shape of the ellipse is also frequency dependent. At high excitation frequencies where E_c dominates and E_L vanishes (see figure 3.5), the hysteresis loop is reduced to a straight line, i.e. there is no energy dissipation. It should be noted that this behaviour is valid for linear viscoelastic materials [107]. It is known that the response of tread rubber to periodic strains is also amplitude dependent [107] and this gives rise to non linear behaviour.

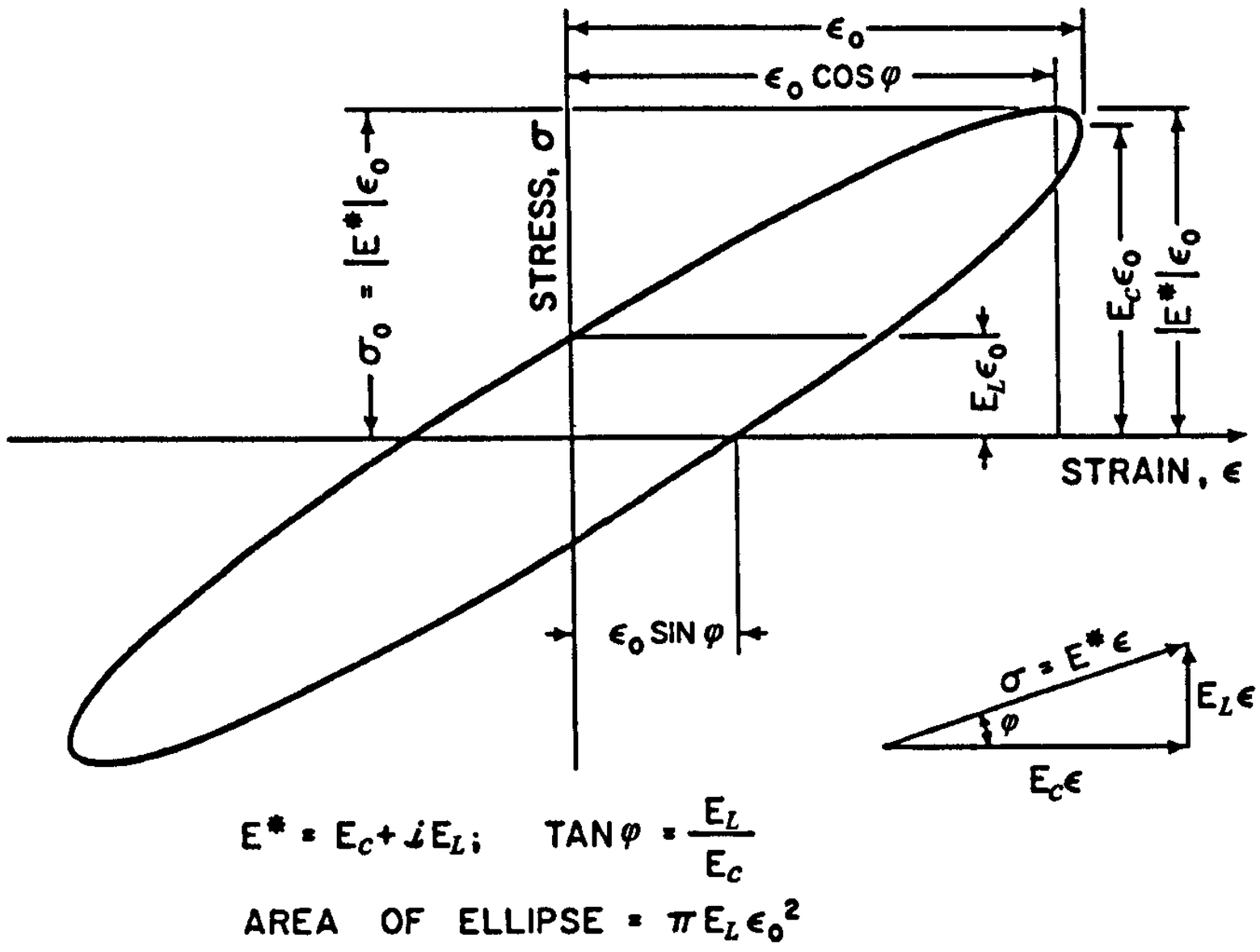

Figure 3. 6 A typical hysteresis loop corresponding to a sinusoidal strain excitation (after [107])

3.2.3.2 Rubber Friction

The principles of linear viscoelasticity as presented briefly in the previous section not only aid the modelling of rubber hysteresis, but also prove extremely useful in the investigation of rubber friction.

As discussed thoroughly in chapter 2, friction between a large number of hard materials can be described satisfactorily by the classical laws of friction (due to Amontons and Coulomb), which are summarised below:

- Friction force is proportional to normal load
- Friction coefficient is independent of the contact area
- Friction coefficient is independent of sliding velocity

Experience shows that the validity of the classical laws deteriorates, when viscoelastic materials such as rubber are involved in the contact. The somewhat awkward frictional behaviour of rubber is discussed to some extent in the section dedicated to friction, in chapter 2. It is widely accepted (see section 2.4.2) that rubber friction may

be explained by the recognition of the two different mechanisms of shear resistance generation. In general, the shear resistance is the result of adhesion and hysteresis phenomena within the contact.

If a vertically loaded elastomer, resting on a hard rough surface is pulled tangentially, the frictional force developed consists of two components, namely adhesion and hysteresis or deformation friction, as indicated by the following relation:

$$F_{friction} = F_{adhesion} + F_{hysteresis} \tag{3.12}$$

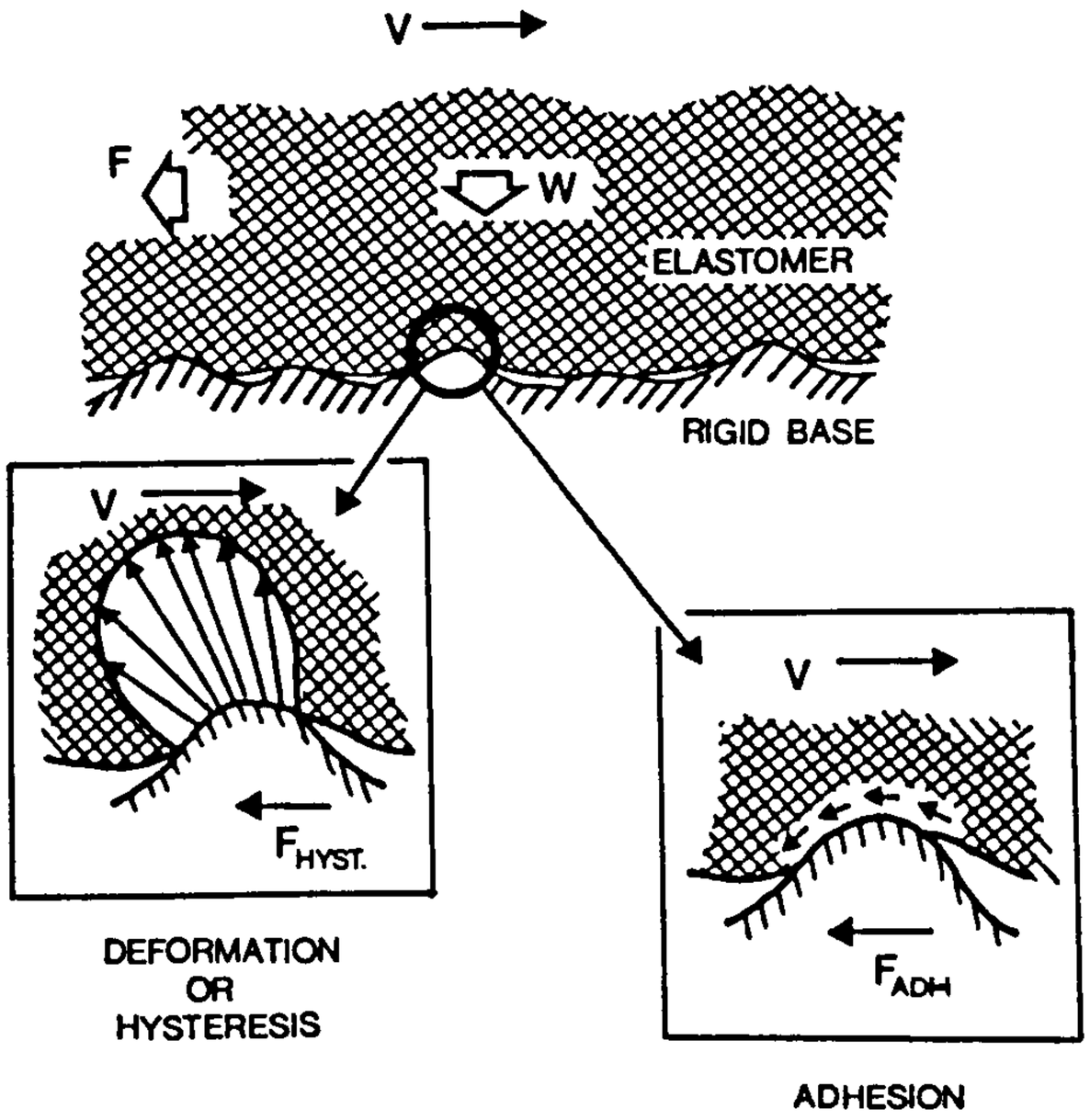

Figure 3. 7 The mechanism of viscoelastic friction (after [29])

These two terms are discussed in the work of Grosh [79] and Persson [81], while Browne, Ludema and Clark [82] suggest the existence of two more terms, namely *tear* and *viscous* friction (see section 2.4.2). The present analysis is restricted to the explanation and quantification of the two terms in equation (3.12).

The origin of the two friction components may be realised by referring to figure 3.7. Under the application of a vertical load W, a draping of the elastomer about the surface asperities of the rigid base is observed, resulting in an interlocking of the surfaces. Adhesion friction is the term that is not affected by this kind of interlocking. It is equivalent to the friction mechanism observed between hard materials and occurs

within the sliding interface as a result of molecular-kinetics, micro stick-slip thermally activated mechanism. The flexible molecular chains of an elastomer attempt to link with the molecules of the adjacent hard surface and form weak local bonds. Under the action of sliding, the bonds stretch, break and the flexible molecular chains recover before a new bond with the hard molecules is achieved. Thus, a stick-slip action is observed in microscopic level. Since the mechanism involves an alternate loading and recovery of flexible elastomer molecules, it is expected that the viscoelastic nature of rubber affect the mechanism of adhesion as will be shown later.

The hysteresis (deformation) component of friction is generated macroscopically, as a result of the non-symmetrical pressure distribution in the local contacts between the hard surface asperities and the elastomer during sliding. As shown in figure 3.7, the contact pressure is shifted in an opposite sense to the direction of sliding. A portion of the generated pressure distribution is due to internal damping and, therefore, should depend on the sliding velocity. This portion is never regained and represents the hysteresis losses, which are sensed as the hysteresis component of friction.

The coefficient of friction for the contact between a hard and a viscoelastic material may be obtained by dividing equation (3.12) by the normal load W:

$$\mu = \mu_{adhesion} + \mu_{hysteresis} \tag{3.13}$$

According to the previous analysis, it is expected that both the terms would be related to the viscoelastic nature of rubber. Using the quantities defined in section 3.2.3.1, the corresponding adhesion and hysteresis terms are given by the following relations [29]:

$$\mu_{adhesion} = K_1 s \frac{E_c}{p^r} \tan\varphi \qquad r < 1 \tag{3.14}$$

$$\mu_{hysteresis} = K_2 \left(\frac{p}{E_c} \right)^n \tan\varphi \qquad n \geq 1 \tag{3.15}$$

Where p is the normal pressure, s is the effective shear strength of the sliding interface, r is an exponent approximately equal to 0.2, n is an index greater or equal to unity and K_1, K_2 are constants.

Substituting the expressions for the coefficients of friction (equations (3.14) and (3.15)) into equation (3.13) yields:

$$\mu = K_1\left(s\frac{E_c}{p^r} + \frac{K_2}{K_1}\left(\frac{p}{E_c}\right)^n \right)\tan\varphi \tag{3.16}$$

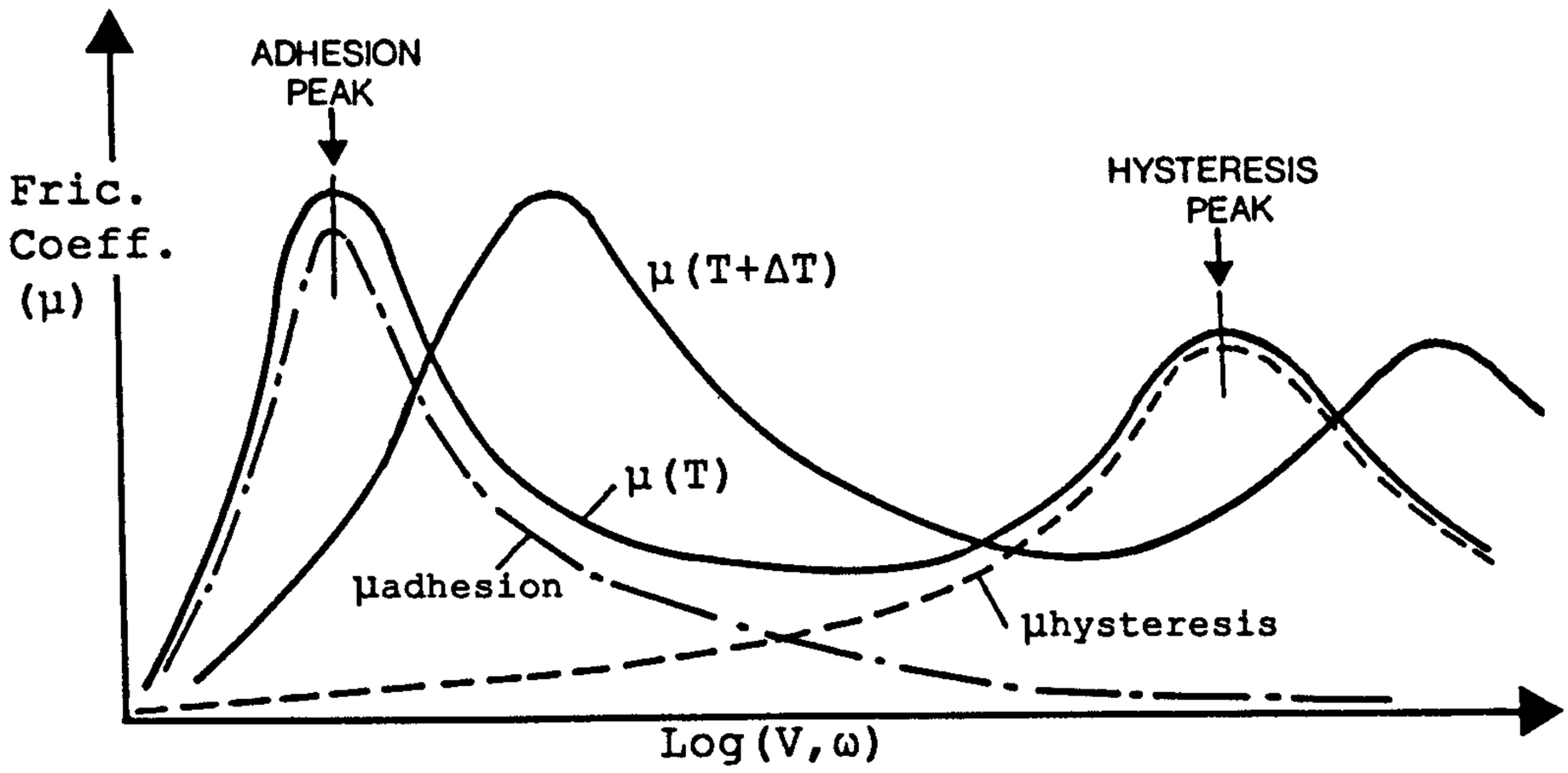

Figure 3. 8 Velocity and temperature dependency of rubber friction (after [29])

As discussed in section 3.2.3.1, both E_c and $\tan\varphi$ vary with excitation frequency ω, which, in the case of friction, is directly related to the sliding velocity. In addition, rubber properties and consequently E_c and $\tan\varphi$ also vary with temperature. Figure 3.8 shows a qualitative picture of the coefficient of friction and its components as given by equations (3.16), (3.15) and (3.14) plotted against frequency or, alternatively, sliding velocity. The equivalence between sliding velocity V and frequency ω can be easily understood if one considers a rubber specimen sliding with velocity V on a hard surface with large-scale asperities of wave-length ξ. In this case the periodic excitation of the tread rubber has a frequency $\omega = 2\pi(V/\xi)$. Figure 3.8 shows that the total coefficient of friction exhibits an adhesion peak at low velocities, followed by a hysteresis peak at higher velocities.

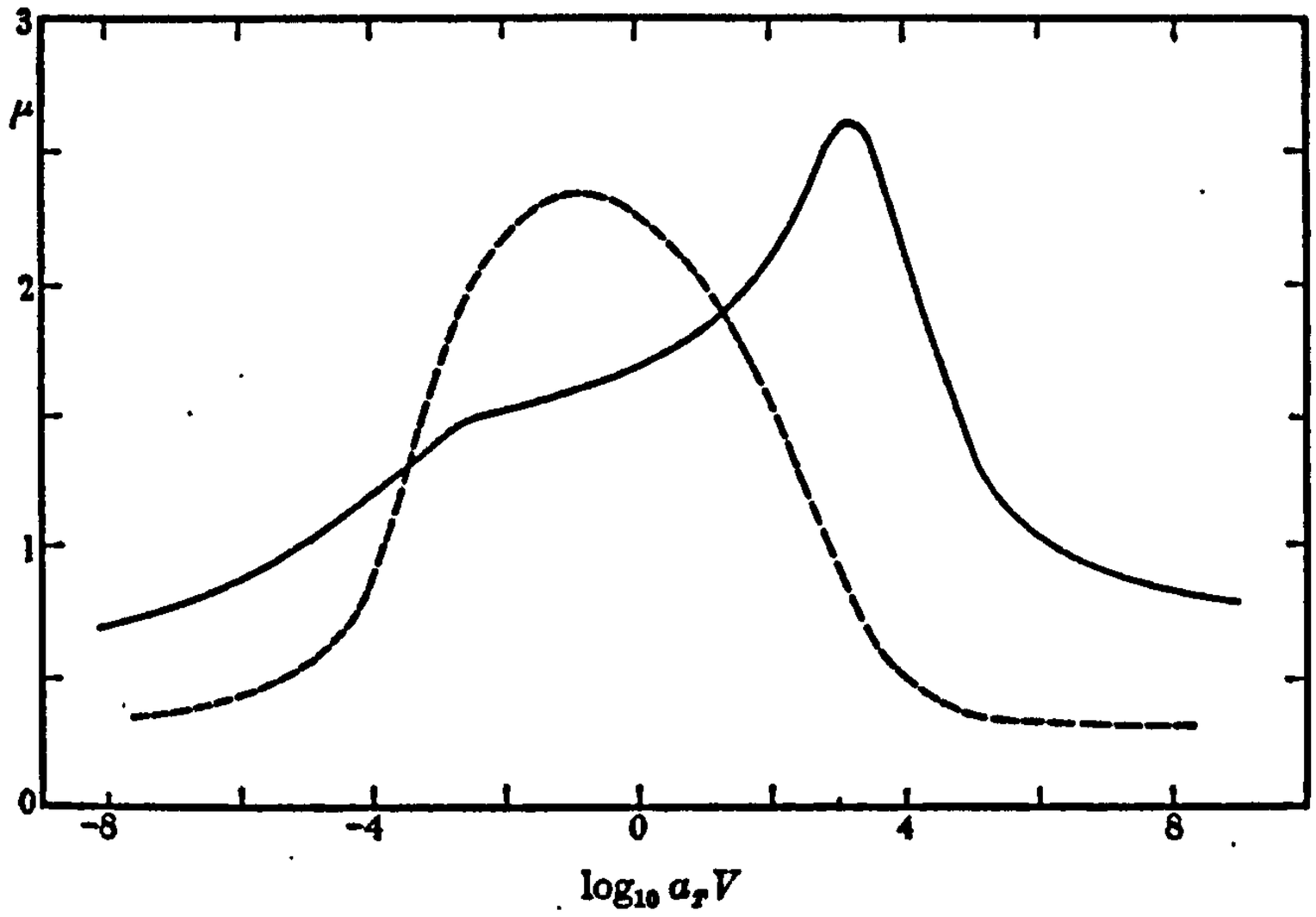

Figure 3. 9 Coefficient of friction between acrylonitrile-butadiene rubber sliding on glass (broken line) and silicon carbide paper (solid line) at a temperature of 20°C. V is given in m/s (after [79])

Figure 3.9 shows experimental measurements (see [79]) of the coefficient of friction between rubber and two hard surfaces. The coefficient of friction is plotted as a function of the sliding velocity V in logarithmic scale, where a_T represents a horizontal shift parameter, which is discussed in the following paragraph. The dashed line shows the coefficient of friction between rubber and a polished glass surface. The peak coefficient of friction is observed at relatively low sliding velocities (below 1m/s). Since glass doesn't show any large-scale asperities, the dashed line corresponds to the adhesion component of friction as calculated by equation (3.14) and shown in figure 3.8. On the other hand, the solid line represents the friction coefficient between rubber and a rough silicon carbide paper with a mean particle size of approximately 0.01 cm. The peak friction is observed at high sliding velocities and corresponds to the hysteresis peak on the right-hand side of figure 3.8.

It has been found experimentally [79] that the friction coefficient of rubber shows the same dependency on temperature, as rubber's viscoelastic properties. Starting from the latter, figure 3.5 shows the main viscoelastic parameters (E_c, E_L, $\tan\varphi$) of a typical viscoelastic material, as functions of the excitation frequency ω at a specific test temperature. If the frequency response test is carried out at a different temperature, the same curves are obtained, only this time they are shifted horizontally

along the frequency axis. In particular, if the temperature increases, all curves will be shifted to the right hand side, i.e. towards higher frequencies, whereas if the test temperature is reduced, the curves will be shifted to the left, towards lower frequencies. The amount of the required horizontal displacement is given by the WLF (Williams-Landel-Ferry) [50], [77] transformation, as indicated by equation (3.17). This equation states that if, for example, the peak tangent modulus at a reference temperature T_0 occurs at a frequency ω, then at temperature T, the peak will occur at a frequency equal to $a_T\omega$, or in logarithmic scale, the curve will be shifted horizontally for a distance equal to $\log a_T$. As stated earlier, rubber friction demonstrates the same temperature dependency, as the friction is governed mainly by rubber's viscoelastic properties. Since, for the case of sliding, the frequency ω is directly related to the sliding velocity through the wavelength of the asperities, the shift factor can be applied for moving the friction curves along the velocity axis. This principle is shown qualitatively in figure 3.8, where the coefficient of friction as a function of the sliding speed has been shifted to the right for a higher temperature. In figure 3.9, a large number of measurements of the coefficient of friction at various temperatures and for low sliding velocities were combined using the WLF transformation to generate a couple of "master" curves covering a wide velocity range at a temperature of 20^{o} C.

$$\log a_T = \frac{-8.86(T - T_0)}{101.5 + T - T_0} \tag{3.17}$$

Where: a_T is the horizontal shift, T is the operating temperature and T_0 is a reference temperature.

The analysis carried out thus far explains the dependence of the coefficient of friction on sliding velocity and operating temperature. Furthermore, equations (3.14) and (3.15) can be used to explain why the friction force is not proportional to the normal load. By increasing the load, the apparent contact pressure increases proportionally, yet this pressure appears in the expressions for both the adhesive and hysteresis components of friction in a non-linear manner. In the case of pneumatic tyres the excitation frequency (calculated as the sliding velocity divided by the mean

wavelength of the macro texture of the road surface) rarely reaches the levels, where the hysteresis peak can be observed. Therefore, for tyres operating on dry roads, the adhesion component given by equation (3.14) dominates friction and causes a reduction in the overall coefficient of friction with the increase of normal load.

Finally, by increasing the contact area while maintaining a constant load, contact pressure reduces and equation (3.14) predicts an increase in the adhesion term of the coefficient of friction.

It has now become apparent that rubber friction depends in a rather complex and not yet fully understood way on a number of different factors such as temperature, sliding velocity, contact area, normal load and surface asperities. Additionally, some general ideas are presented on how the influence of these factors may be quantified.

3.3 Steady-State Tyre Modelling

Thus far, a general background is given, including a brief description of the construction of the tyre. The principal structures were outlined and connected to the most frequently used modelling representations. Special attention was paid to the viscoelastic behaviour of rubber and the mechanism by which it affects rubber friction. In the following sections a mathematical modelling of tyre force generation is presented. Since tyre forces are directly related to the motion and position of the tyre with respect to the road, it is essential that any modelling approach should commence with the definition of the kinematic quantities that serve as primary inputs to the tyre system.

3.3.1 Tyre Kinematics

The frame of reference proposed by SAE is widely used for the description of the position and motion of a tyre. Referring to figure 3.10, the origin of the SAE system is defined as the intersection of two lines. The first line results from the intersection of the wheel plane and the road plane, while the second line is the projection of the wheel spin axis on the road plane. The x-axis coincides with the intersection of the wheel plane and road plane and points forward, while the z- axis is perpendicular to

the road plane and points downwards. The y- axis is directed to the right so as to achieve a right-handed Cartesian co-ordinate set, in which the cross product of unit vectors $\hat{x}$ and $\hat{y}$ yields the unit vector $\hat{z}$. In the same figure camber (inclination) angle γ is defined as the angle between the wheel plane and the plane, which contains the x- axis and is perpendicular to the road plane. According to the definition given by SAE, camber angle is positive when the wheel leans outward from the vehicle centreline, but the sign of camber angle might also be considered positive when it results as a right hand rotation around the x- axis. Finally, the slip angle a is defined as the angle between the x- axis and the projection of the velocity of the wheel centre on the road plane.

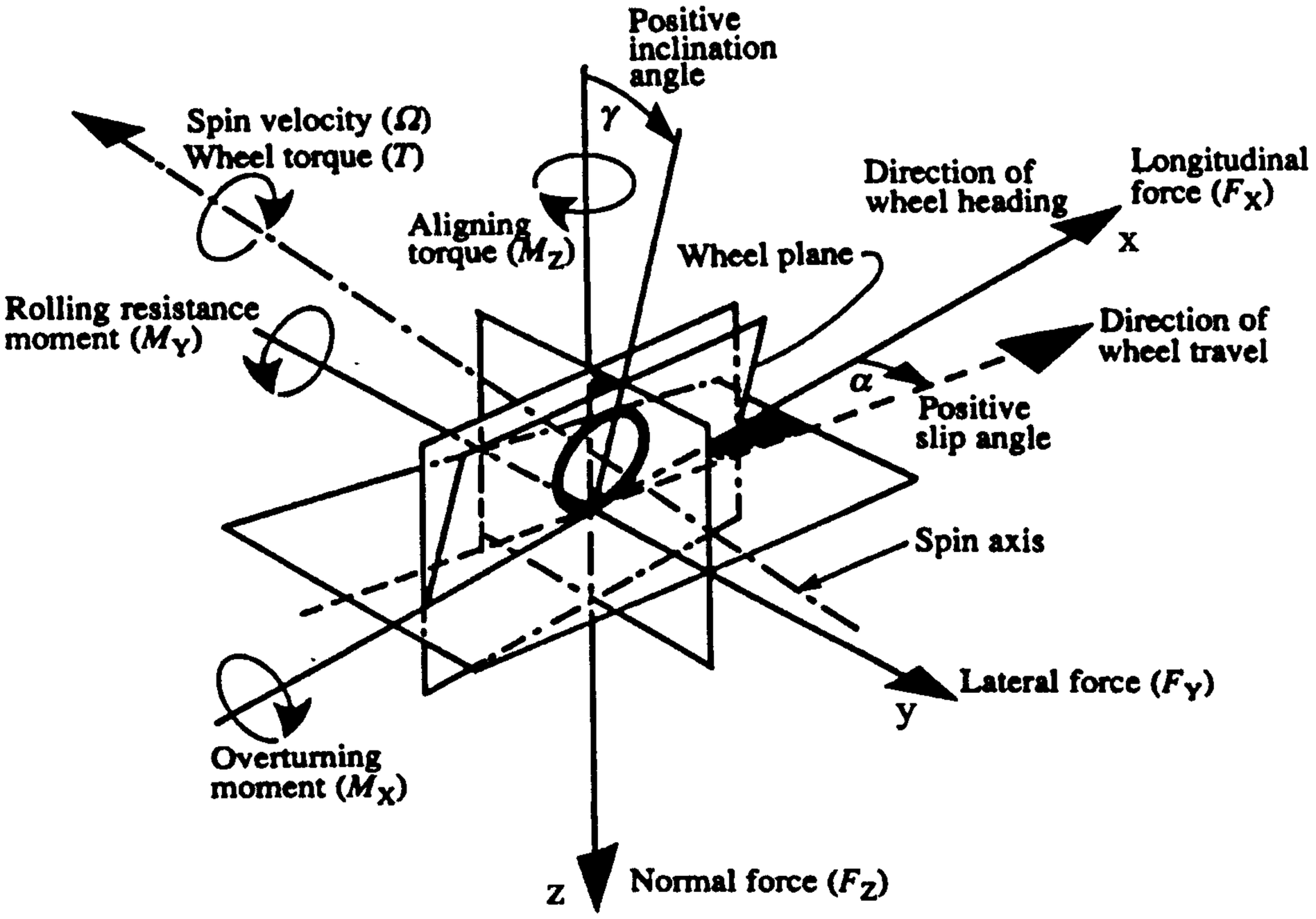

Figure 3. 10 The SAE frame of reference used in tyre kinematics and dynamics (after [5])

The motion of the tyre can be determined, using the moving SAE axis system in conjunction with a global frame of reference attached to the ground. In figure 3.11, XYZ is the global frame of reference, while the SAE frame is denoted as xyz. The position vector of the origin B of the moving frame of reference with respect to the global frame of reference is given by the vectorial sum:

$$\vec{R}_B = \vec{R}_O + \vec{R}_{OB} \tag{3.18}$$

Assuming that points O and B do not move relative to each other in the local frame of reference, velocity of point B with respect to the global frame reads as:

$$\vec{V}_B = \frac{d\vec{R}_O}{dt} + \vec{\omega} \times \vec{R}_{OB} \tag{3.19}$$

Where $\vec{\omega}$ is the vector of rotational velocity of the wheel as composed by the three rotations indicated below:

$$\vec{\omega} = \dot{\psi}\hat{z} + \dot{\gamma}\hat{x} + \dot{\phi}\vec{U}_{sp} \tag{3.20}$$

Where: $\dot{\psi}$ is the yaw rate of the wheel, $\dot{\gamma}$ is the camber rate and $\dot{\phi} = \Omega$ is the rotational velocity of the wheel about its axis.

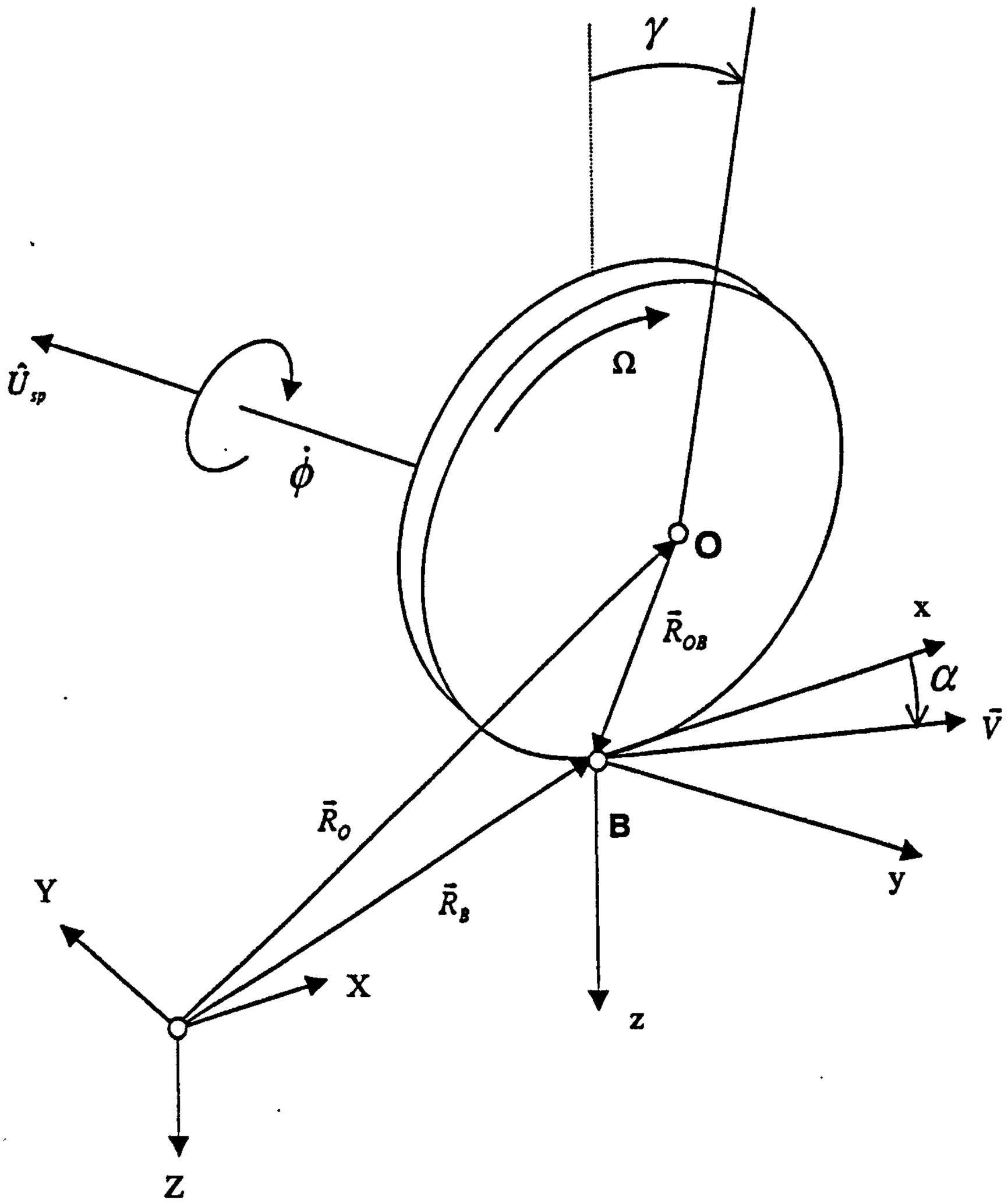

Figure 3. 11 The general motion of the tyre (after [105])

For a free rolling tyre with $\dot{\gamma} = 0$ and $\dot{\psi} = 0$, $\vec{\omega}$ becomes:

$$\vec{\omega} = \Omega \vec{U}_{sp} \tag{3.21}$$

and velocity of point B then becomes:

$$\vec{V}_B = \frac{d\vec{R}_O}{dt} + \Omega \vec{U}_{sp} \times \vec{R}_{OB} \tag{3.22}$$

The effective rolling radius is then defined as the radius R_e that yields zero velocity for point B in the global frame of reference. For free rolling with $\dot{\psi} = 0$:

$$\vec{V}_B = \vec{0} = \frac{d\vec{R}_O}{dt} + \Omega \vec{U}_{sp} \times R_e \hat{n} \tag{3.23}$$

Where $\hat{n}$ is the unit vector in the direction of $\vec{R}_{OB}$.

For a free rolling un-cambered wheel, the linear speed of rolling is defined as:

$$V_r = \left(\vec{\omega} \cdot \vec{U}_{sp}\right) R_e = \Omega R_e \tag{3.24}$$

Note that according to equation (3.24), V_r is positive for a wheel rolling forward, as it is expressed as a product of R_e and a positive dot-product.

In the case of a wheel rolling at a constant camber angle γ, V_r becomes:

$$V_r = \left(\dot{\psi} \cos\left(\frac{\pi}{2} - \gamma\right) + \Omega\right) R_e \tag{3.25}$$

or

$$V_r = \left(\dot{\psi} \sin(\gamma) + \Omega\right) R_e \tag{3.26}$$

where in the above relations camber angle is considered positive when it results from a right hand rotation about $\hat{x}$.

For a free rolling tyre with $\dot{\psi} = 0$, equation (3.23) yields for the absolute velocity of the wheel centre O:

$$\vec{V}_O = \frac{d\vec{R}_O}{dt} = -\Omega \vec{U}_{sp} \times R_e \hat{n} \tag{3.27}$$

Apparently, $\vec{V}_O$ is parallel to $\hat{x}$, representing the longitudinal velocity of the wheel centre:

$$V_x = \Omega R_e \tag{3.28}$$

In the event of braking or driving, the longitudinal velocity of the centre of the wheel is no longer equal to the product ΩR_e. The slip speed is then defined as:

$$V_{sx} = V_x - \Omega R_e \tag{3.29}$$

The generic longitudinal slip ratio is then defined as:

$$k = -\frac{V_{sx}}{V_r} = -\frac{V_x - \Omega R_e}{V_r} = -\frac{V_x - \Omega R_e}{(\dot{\psi}\sin(\gamma) + \Omega)R_e} \tag{3.30}$$

In the absence of camber angle or yaw rate, this relation reduces to:

$$k = -\frac{V_x - \Omega R_e}{\Omega R_e} \tag{3.31}$$

Finally, in the existence of a lateral component V_{sy} in the velocity of the wheel centre $\vec{V}_O$, the generic slip angle a is defined:

$$\tan a = \frac{V_{sy}}{V_r} \tag{3.32}$$

The generic definitions of slip ratio and slip angle given by relations (3.30) and (3.32) can be used as inputs to various tyre models in a wide range of analyses. However, in full vehicle handling studies it is common to use simplified practical definitions of the aforementioned slip quantities. Longitudinal slip can then be defined with respect to forward velocity as follows:

$$k = -\frac{V_x - \Omega R_e}{V_x} \tag{3.33}$$

Similarly, the lateral slip reads:

$$\tan a = \frac{V_{sy}}{V_x} \tag{3.34}$$

The slip ratio and slip angle (or alternatively the tangent of the slip angle) defined by relations (3.33) and (3.34) shall be used throughout the thesis when plotting tyre forces and moments, unless otherwise noted.

Finally, the spin slip Φ is defined as the ratio between the component of $\vec{\omega}$ in the direction of z axis of the SAE frame (see figure 3.11) and the forward velocity of the wheel, as indicated in equation (3.35):

$$\Phi = \frac{\vec{\omega} \cdot \hat{z}}{V_x} \tag{3.35}$$

In the case of a cambered rolling wheel, the spin slip is written as:

$$\Phi = \frac{\dot{\psi} - \Omega \sin \gamma}{V_x} \tag{3.36}$$

The right-hand side of equation (3.36) can be split into two components, namely the turn-slip Φ_T and camber slip Φ_C, given in relations (3.37) and (3.38) respectively.

$$\Phi_T = \frac{\dot{\psi}}{V_x} \tag{3.37}$$

$$\Phi_C = -\frac{\Omega \sin \gamma}{V_x} \tag{3.38}$$

The turn slip corresponds to the instantaneous path curvature of a steered wheel travelling with a forward velocity V_x, while the camber slip corresponds to the equivalent path curvature induced by the rotation of a cambered wheel about its axis. This is demonstrated by relations (3.39) and (3.40):

$$\Phi_T = \frac{\dot{\psi}}{V_x} = \frac{1}{R_C} \tag{3.39}$$

$$\Phi_C = -\frac{\Omega \sin\gamma}{V_x} = -\frac{1}{R_e}\sin\gamma \tag{3.40}$$

where R_C denotes the instantaneous radius of the path of the wheel and R_e is the wheel effective radius.

Both turn slip and camber slip are kinematic inputs, which, like the slip angle and longitudinal slip generate tyre forces and moments. The influence of turn slip is insignificant compared to the influence of the slip angle and therefore it may be overlooked in most applications [6]. However the influence of the camber angle is more important and is usually accounted for, as will be discussed in the following sections.

3.3.2 Tyre Forces and Moments

The position and motion of the tyre relative to the ground lead to the generation of a force-moment system, which essentially governs the motion of the vehicle. This system is the result of the combined effect of vertical deflection of the tyre under the application of normal load and shear deformation due to frictional forces generated within the contact patch. In addition, the hysteresis phenomenon contributes to the force-moment system, if one considers the rate of the aforementioned deflections. As expected, tyre forces are distributed throughout the contact area, yet one might also adopt the concept of force generation along the circumference of the tyre, as a result of the global deformation of the carcass. Still, it is convenient to consider the net

result of such a force distribution. The major tyre forces and moments with respect to the SAE frame of reference are depicted in figures 3.10, 3.12 and listed in table 3.1.

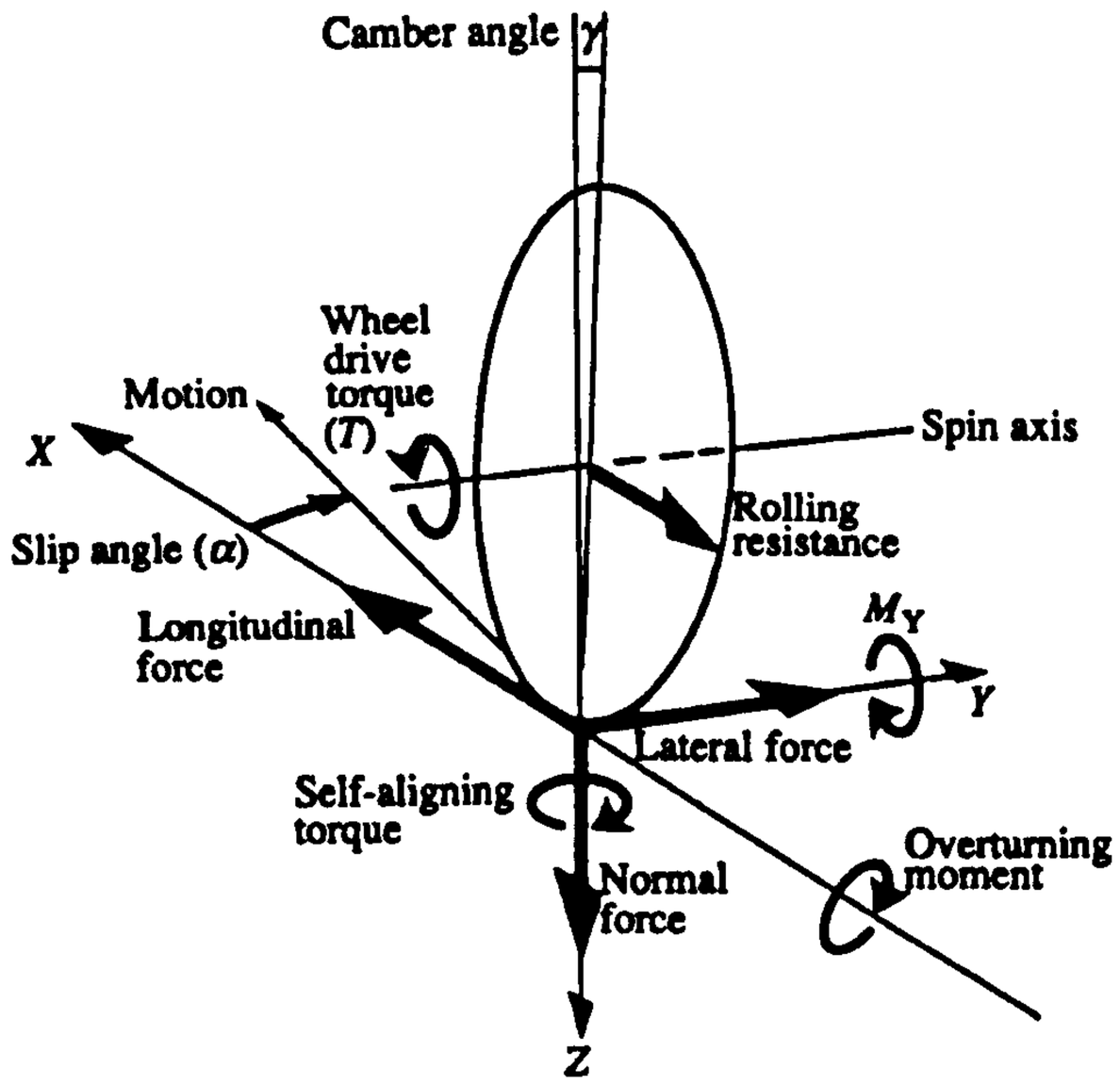

Figure 3. 12 Principal tyre forces and moments (after [5])

3.3.2.1 Forces and Moments Involved in Handling Dynamics

The lateral and longitudinal forces together with the self aligning moment are of great importance in the analysis of the handling behaviour of a vehicle. For steady-state conditions and a given coefficient of friction between the tread and the road surface, these forces depend on the normal load and a set of kinematic conditions, as summarised by the following relations:

$$F_x \equiv f_x(k, a, \gamma, F_z) \tag{3.41}$$

$$F_y \equiv f_y(k, a, \gamma, F_z) \tag{3.42}$$

$$M_z \equiv m_z(k, a, \gamma, F_z) \tag{3.43}$$

where, k, a and γ are the longitudinal ratio, slip angle and camber angle, as defined in section 3.3.1.

Figure 3.13 shows a top view of a tyre travelling at a slip angle a. Lateral slip results in the lateral deformation of the tyre and the consequent generation of a lateral force F_y. The lateral force distribution is such that the resultant force does not fall exactly on the y- axis. The offset t is the so-called pneumatic trail and gives rise to the self-aligning moment M_z. If the lateral force and the self- aligning moment are measured at the same instant of time, the pneumatic trail can be defined as:

$$t = \frac{M_z}{F_y} \tag{3.44}$$

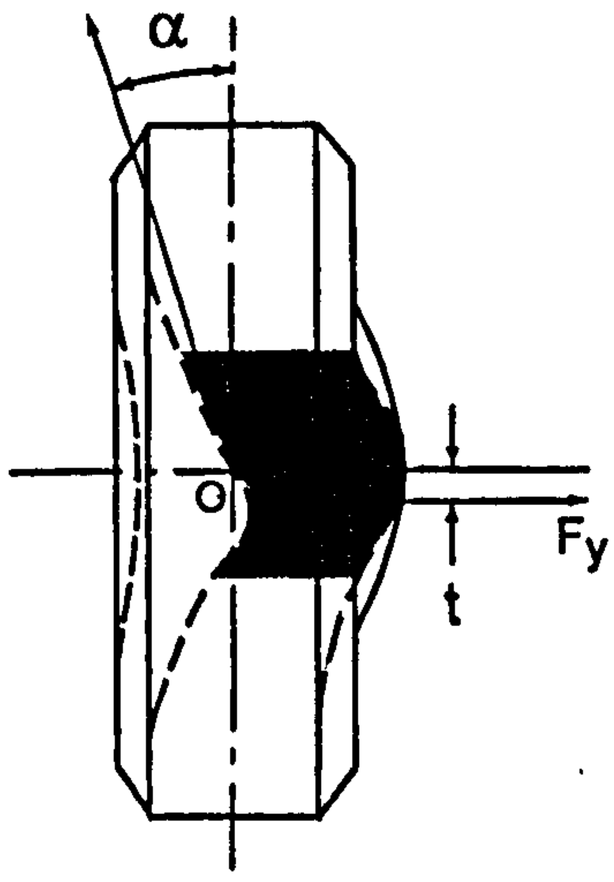

Figure 3. 13 The generation of slip angle and the pneumatic trail (after [44])

Similarly, a longitudinal force is generated in the presence of longitudinal slip k, in other words, when the longitudinal velocity of the wheel centre is not equal to the product of the rotational velocity of the wheel and the effective tyre radius (see equations (3.30) and (3.31)). This condition causes the tread to deform longitudinally in the neighbourhood of the contact patch and gives rise to a braking (k negative) or traction (k positive) force.

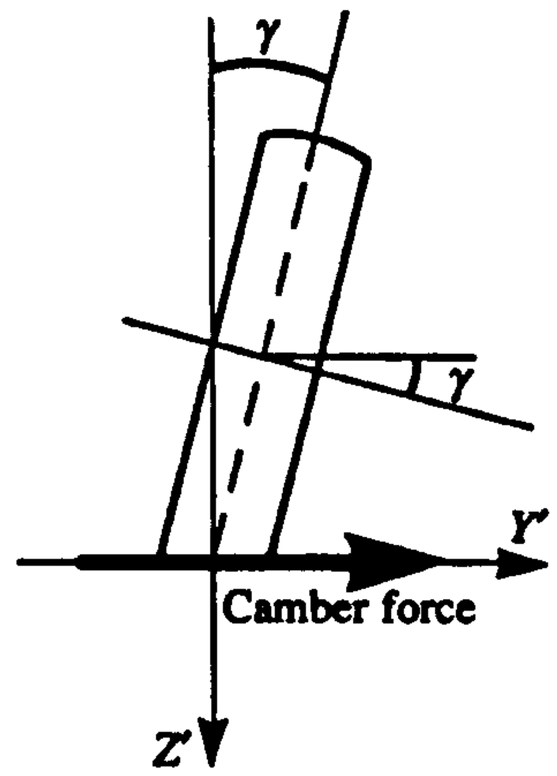

Figure 3. 14 Lateral force as a result of camber angle (after [5])

Figure 3.14 demonstrates the generation of lateral force in the presence of camber angle γ. When the tyre is loaded at an inclination angle other than zero the local asymmetrical deformation in the neighbourhood of the contact patch results in a lateral force pointing in the direction of inclination.

All shear forces and the resulting moments are inter-related, mainly through the limited frictional potential of the contact area. Given the surface characteristics of the road and tread, the frictional potential of the contact area is dictated by the normal force distribution, or, to simplify the situation, by the net normal load. Hence, it is expected that the combined effect of slip angle a, longitudinal slip ratio k and camber angle determines the value of each of the forces and moments, as implied by the relations (3.41)-(3.43).

The generic force and moment functions, as given by relations (3.41-3.43) are highly non-linear. Although a dependency on the net normal load F_z is assumed, in reality the actual normal force distribution throughout the contact patch plays an important role, especially in the calculation of the self-aligning torque. Also, in section 3.2.3.2 the dependency of the friction coefficient of rubber on normal load and sliding velocity was pointed out. Immediately, it becomes obvious that, depending on the complexity of the approach, relations (3.41)-(3.43) might contain the sliding velocity as an extra variable or parameter, while the variation of the coefficient of friction with normal load may also be considered.

Table 3.1

Tyre Forces and Moments

Force/Moment	Mechanism of force generation
Normal Force, F_z	Integration of normal pressure throughout the area of contact. Depends on the vertical deflection of the tyre (Δz) and rolling velocity (Ω).
Longitudinal Force, F_x	Integration of the longitudinal shear pressure distribution throughout the area of contact. Depends on normal force (F_z), longitudinal slip ratio (k), slip angle (a) and camber angle (γ).
Lateral Force, F_y	Integration of the lateral shear pressure distribution throughout the area of contact. Depends on normal force (F_z), longitudinal slip ratio (k), slip angle (a) and camber angle (γ).
Self Aligning Torque, M_z	Moment generated about Z axis as a result of the offset of the point of application of F_y on x-axis. Depends on normal force (F_z), longitudinal slip ratio (k), slip angle (a) and camber angle (γ).
Overturning Couple, M_x	Moment generated about an axis parallel to x-axis passing from the centre of the wheel O, as a result of lateral force F_y. Depends on normal force (F_z), longitudinal slip ratio (k), slip angle (a) and camber angle (γ).
Rolling Resistance moment, M_y	Moment resisting the rotation of the

	wheel, as a result of the forward offset on x-axis of the reaction to the net normal force F_z. Depends on the vertical deflection of the tyre (Δz) and rolling velocity (Ω).
Rolling Resistance Force, F_r	Longitudinal force applied on the contact patch. The resulting moment about the wheel spin axis cancels the rolling resistance moment.

3.3.2.2 Rolling Resistance Force and Moment

Rolling resistance represents a less important shear force, developed within the contact patch. The rolling resistance opposes the motion of a rolling body, such that energy needs to be transferred to the system in order to maintain rolling. In general, the influence of rolling resistance in the overall capability of a tyre to generate lateral and longitudinal forces is limited. Nevertheless, at high travelling velocities, rolling resistance is one of the main contributors to the total power loss, thus increasing fuel consumption and limiting the maximum speed of the vehicle.

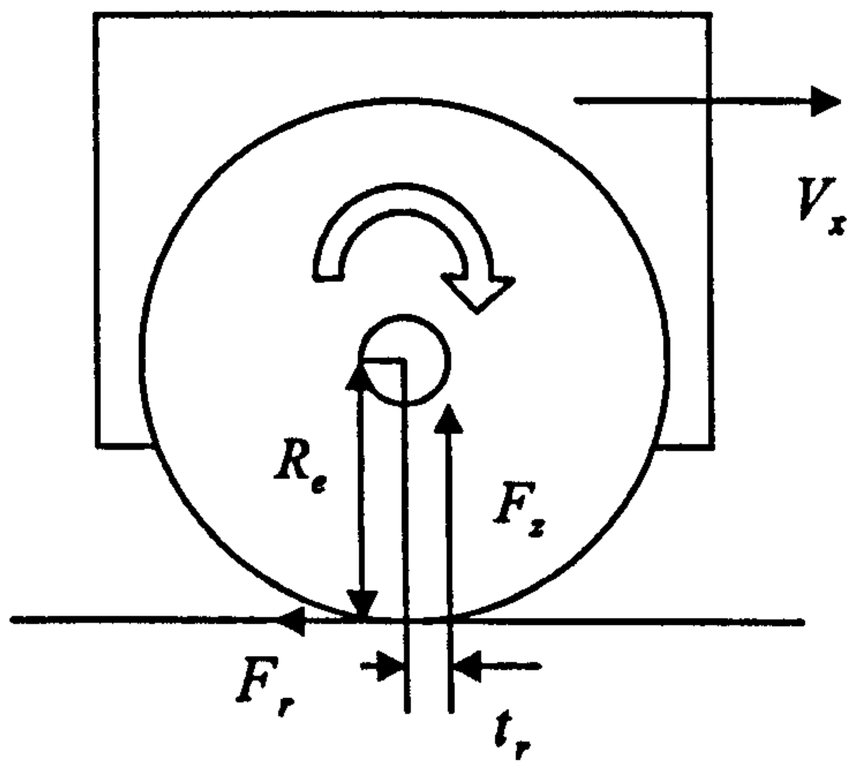

Figure 3. 15 Rolling resistance generation

Clark [109] distinguishes five separate mechanisms which have been proposed in order to explain the need for energy supply to a wheel, in order to maintain steady rolling. These mechanisms are summarised below:

a. The increase in the potential energy level when a wheel surmounts an asperity of a flat surface
b. Energy loss due to slip between a wheel and a surface
c. Aerodynamic losses due to the wheel moving through the atmosphere
d. Material hysteresis of the wheel material
e. Material hysteresis of the surface upon which the wheel rolls

The first mechanism is of limited applicability, as it is shown that rolling even over the smoothest of surfaces might generate significant amounts of rolling resistance. Slip between the rolling wheel and the surface occurs under various operation conditions, but this mechanism of resistance generation seems to be weak compared to the remaining three [109]. Aerodynamic losses represent an important factor, nevertheless, the required tyre standards for enhanced safety and control of a vehicle do not allow much experimentation with tyre size and surface geometry. It appears that the mechanisms related to material hysteresis are the primary rolling resistance contributors [109]. In the area of tyre mechanics, rolling resistance is mostly related to the hysteresis of the tyre rubber, as in most cases the road may be considered as a perfectly hard surface. On the other hand, the hysteresis of the road material plays an important role when studying the mechanics of a wheel rolling on soft soil.

Figure 3.15 depicts a tyre, rolling freely under the action of a vertical load. As the wheel rolls on the assumedly flat road, the part of the tread within the first half of the contact patch undergoes compression. Due to the viscoelastic nature of rubber and the relative displacement of the carcass plies, part of the compression work is dissipated in the form of heat. As the tread moves towards the rear half of the contact patch, only a portion of the elastic energy stored in the carcass-tread returns to the tyre, as a result of the delayed recovery of rubber (known in contact mechanics terms as relaxation time). This effect causes a horizontal shift t_r of the net reaction $(-F_z)$ towards the front of the contact patch. The longitudinally displaced point of action of the reaction to the normal load generates the rolling resistance moment about the spin axis, which

tends to decelerate the wheel's rotational motion. Under steady-state rolling conditions, a rolling resistance force F_r is generated in the contact patch, opposing the forward motion of the wheel. F_r gives rise to a moment about the spin axis, which balances the rolling resistance moment. Apparently, for the maintenance of steady-state rolling, a force with a magnitude equal to $|F_r|$ is needed to be applied on the wheel centre, in the direction of motion. Then, both the sum of moments about the spin axis and the sum of longitudinal forces are equal to zero.

The rolling resistance has been explained in terms of force and moment balance, based on figure 3.15. In this simple approach, the horizontal shift of the point of application of the net vertical reaction is a measure of the rolling resistance, given the radius and the normal load. Alternatively, the problem can be treated in terms of the energy dissipated while rolling, as demonstrated in [110]. Referring to figure 3.16, as the wheel rolls towards the right, the front part of the contact undergoes compression. The resulting moment due to forward compression is:

$$M_f = \int_0^a p_v \cdot b \cdot x \cdot dx \tag{3.45}$$

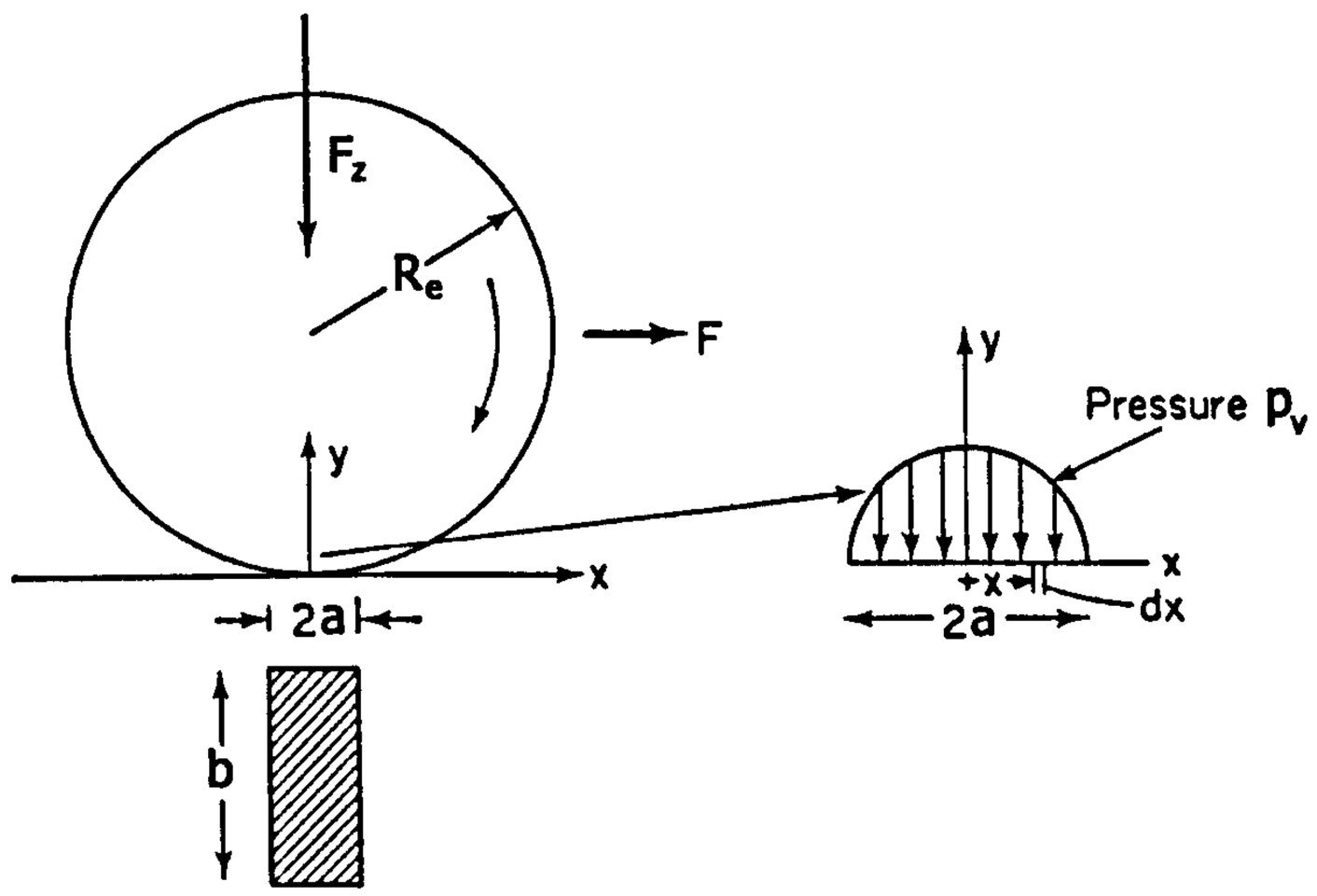

Figure 3. 16 Relation between rolling resistance and normal pressure distribution (after [110])

If the wheel rolls a distance S corresponding to an angle ϑ_r, the compression work will be equal to:

$$W_f = M_f \cdot \vartheta_r \tag{3.46}$$

As the wheel continues to roll, most of this work is recovered at the rear part of the contact, but a small amount, say W_L, is lost due to internal damping which gives rise to hysteresis phenomena. Since the procedure involves the periodic loading and unloading of the tread, the amount of energy lost can be directly related to the area of a hysteresis loop similar to the one shown in figure 3.6. The moment generated at the rear part of the contact opposes the moment generated at the front and is given by the following equation:

$$M_r = \int_a^0 p_v \cdot b \cdot x \cdot dx \tag{3.47}$$

The work returned back to the wheel during the recovery of the rear half of the contact as the rolling wheel covers an angle equal to ϑ_r is calculated as follows:

$$W_r = M_r \cdot \vartheta_r \tag{3.48}$$

The work lost due to hysteresis is then given by the following equation:

$$W_L = W_f + W_r \tag{3.49}$$

Note that in equation (3.49) W_r is negative, as dictated by the integral in eq. (3.47) for positive p_v and b.

Finally, by combining equations (3.45)-(3.48) equation (3.49) can be written as follows:

$$W_L = \left(\int_0^a p_v \cdot b \cdot x \cdot dx + \int_a^0 p_v \cdot b \cdot x \cdot dx \right) \cdot \vartheta_r \tag{3.50}$$

Equation (3.50) shows that hysteresis losses during rolling can be expressed directly as a function of the normal pressure p_v along the contact. In the event of a completely symmetrical pressure distribution with respect to the centre of the wheel, the work done against losses (W_L) is equal to zero. In general, rolling resistance generation is associated with a non-symmetrical pressure distribution showing higher pressure in the front part of the contact and lower in the rear. In terms of rolling resistance force, the following relations apply:

$$F_r \cdot S = W_L \Leftrightarrow F_r = \frac{W_L}{S} \Leftrightarrow F_r = \frac{W_L}{R_e \cdot \vartheta_r} \Leftrightarrow F_r = \frac{M_f + M_r}{R_e} \Leftrightarrow F_r = \frac{-F_z \cdot t_r}{R_e} \qquad (3.51)$$

Relations (3.50) and (3.51) summarise the connections between rolling resistance force, hysteresis losses and normal pressure distribution along the contact.

Rolling resistance depends largely on the normal load, the rolling velocity of the wheel and factors that influence the overall damping of the tyre structure. The most prominent among these factors is the inflation pressure. Variations in inflation pressure alter the size of the contact patch and the manner of deformation of the carcass during rolling, directly affecting the overall damping of the tyre. In particular, lower inflation pressures promote hysteresis phenomena and lead to a significant rise in rolling resistance. The dependency of rolling resistance on the rolling speed can be directly related to the dependence of the area of a typical hysteresis loop on the frequency of excitation, as described in section 3.2.3.1.

Figure 3.17 shows the pressure distribution along the contact patch of a passenger tyre, while figure 3.18 shows the rolling resistance expressed as units of rolling resistance per 1000 units of normal load, as a function of rolling speed for various operating temperatures. A general definition of the coefficient of rolling resistance is given in equation (3.52).

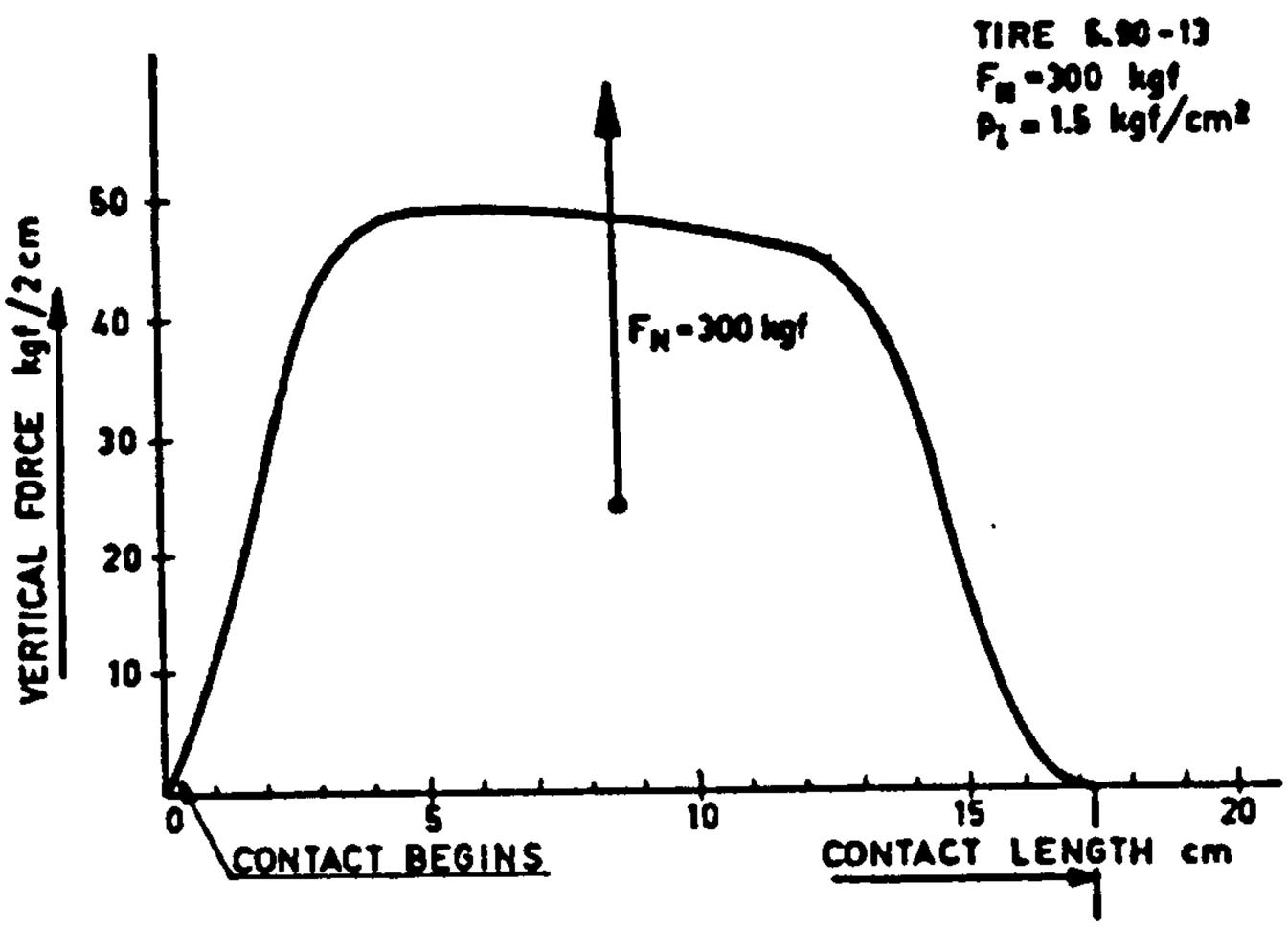

Figure 3. 17 A typical normal pressure distribution along the contact patch of a passenger tyre (after [111])

$$c_r = \frac{F_r}{F_z} \tag{3.52}$$

In figure 3.17 the normal pressure distribution is non-symmetrical, with higher pressure intensity towards the front part of the contact. This shape gives rise to a rolling resistance moment about the wheel spin axis.

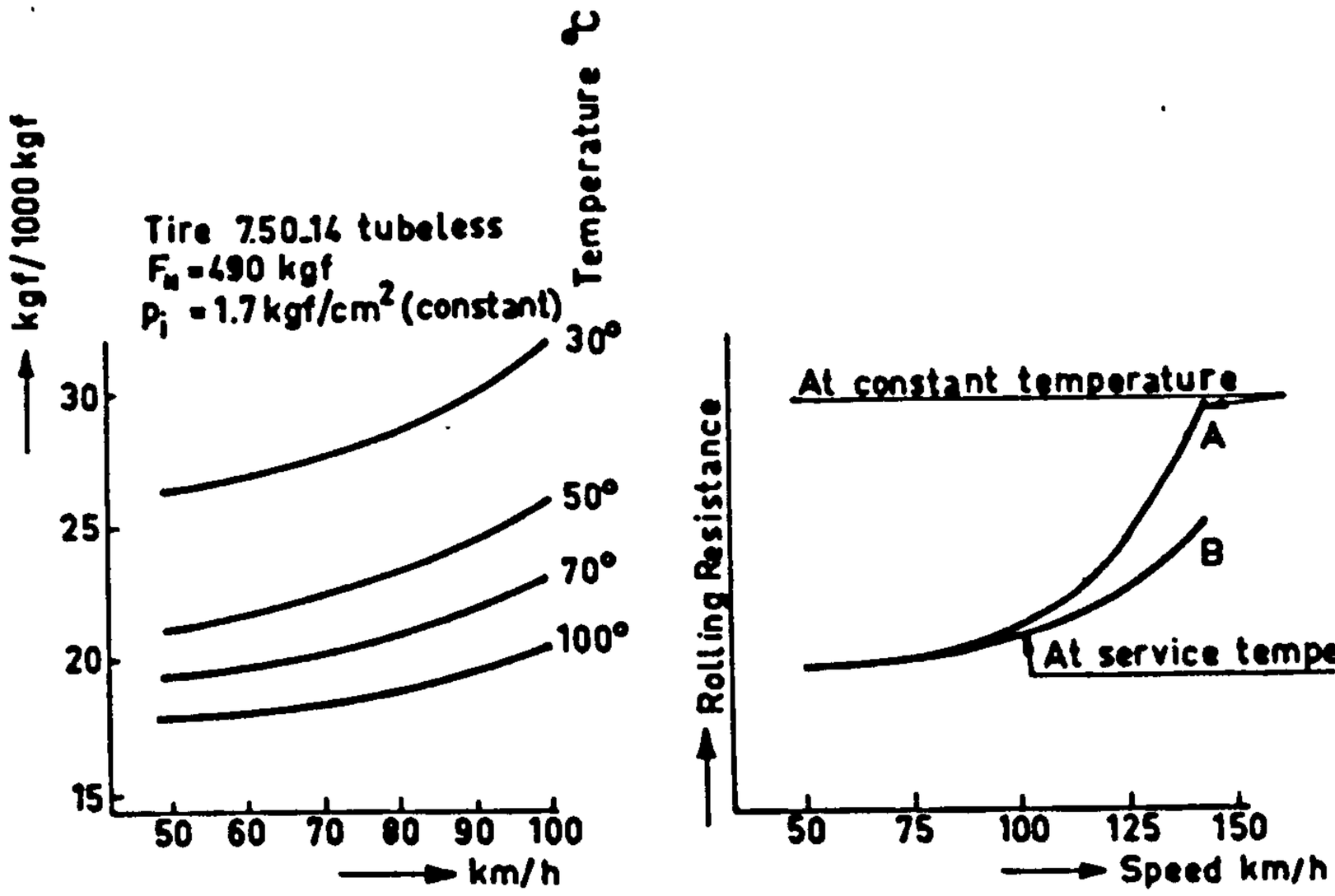

Figure 3. 18 Variation of the coefficient of rolling resistance with speed and temperature (after [111])

In figure 3.18, the rolling resistance shows variation both with rolling speed and operating temperature. The graph of the left shows the same tyre operating at different temperatures. The inflation pressure is kept constant, so the variations due to temperature are not related to the expansion of the air inside the tyre. Instead, the increased rolling resistance observed at lower temperatures may be related to the dependency of the frequency response of a viscoelastic material on temperature (see sections 3.2.3.1 and 3.2.3.2). At low temperatures, the frequency at which maximum hysteresis is observed is shifted closer to the frequency of the periodic loading of the tyre tread, while at higher temperatures the reverse effect reduces the rolling resistance. It should be noted that both the increase in inflation pressure and the reduction in rubber hysteresis tend to reduce the rolling resistance as the tyre heats up during operation. This fortunate effect is shown in the second graph of figure 3.18 where the rolling resistance of a tyre at service temperature is plotted together with the rolling resistance of the same tyre at a constant temperature.

While rolling resistance is not of great importance in handling studies, its calculation appears as a common sub-product of the calculation of the normal force distribution along the contact patch, which, in turn, influences the generation of shear forces and the self-aligning moment.

3.3.3 The Magic Formula Tyre Model

3.3.3.1 Introduction

The physical mechanism of steady-state tyre force and moment generation is discussed later in this chapter, with the step-by-step presentation of two newly developed physical models. In this section, the shape and basic qualities of the force and moment characteristic curves are discussed with the aid of the Magic Formula tyre model. This model is chosen as a substitute for experimental measurements for its high accuracy and its ability to depict the variations observed experimentally, when a tyre operates in a wide range of different conditions.

3.3.3.2 Description of the Model

As already discussed in chapter 2, section 2.2.2.3, the Magic Formula tyre model describes the steady-state behaviour of tyres under pure side-slip, longitudinal slip and combined slip operating conditions. It is able to accurately regenerate characteristic curves, measured experimentally such as those presented in figures 2.1-2.3 and 2.5. The model consists of a set of continuous mathematical functions falling in the general category of relations (3.41)-(3.43), with the slip angle and longitudinal slip ratio, being the primary input variables. In terms of result representation, the lateral force and the self-aligning moment are usually plotted against slip angle, while the braking/traction force is plotted against longitudinal slip ratio.

3.3.3.2.1 Pure Slip Operating Conditions

The model is described initially for the case of pure side-slip or pure longitudinal slip conditions. For a given vertical load and camber angle, the general form of the Magic Formula reads:

$$y = D\sin\left[C\arctan\left\{Bx - E\left(Bx - \arctan Bx\right)\right\}\right] \tag{3.53}$$

$$Y(X) = y(x) + S_V \tag{3.54}$$

$$x = X + S_H \tag{3.55}$$

Where X represents the primary input variable (in the form of $\tan a$ or k) and Y represents the primary output variable (in the form of F_x, F_y or M_z)

Equations (3.53)-(3.55) are used for the calculation of both forces (lateral and longitudinal) and the self-aligning moment. The distinction between these three cases is based on the values of several factors involved. These factors are related to the shape of the characteristic curves in a straightforward manner and their influence is, to some extent, revealed by their names, as indicated in table 3.2.

Table 3.2	
Magic Formula Parameters	
Factor	Name
B	Stiffness Factor
C	Shape Factor
D	Peak Value
E	Curvature Factor
S_H	Horizontal Shift
S_V	Vertical Shift

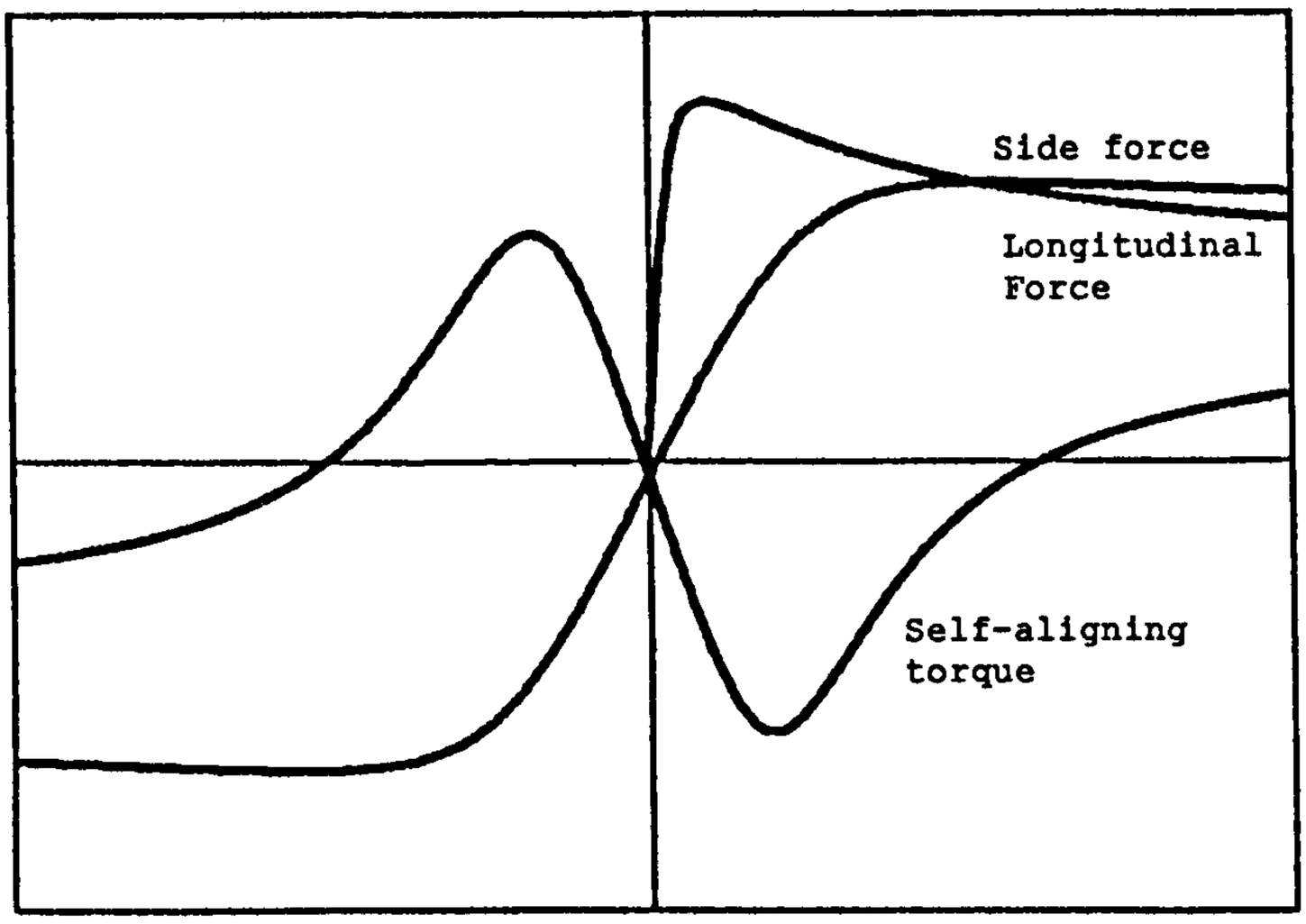

Figure 3. 19 Typical appearance of steady-state tyre characteristics (after [58])

Figure 3.19 shows the typical appearance of the steady-state side (lateral) force, self-aligning torque and brake force characteristics, while figure 3.20 provides a geometrical interpretation of some of the important factors. The implications in relations (3.53)-(3.55) are analysed, considering the case of a tyre operating under pure lateral slip. It is observed, experimentally, that as the slip angle a increases in a sequence of steady-state values, the lateral force F_y also increases, initially in an approximately linear manner. With a further increase in slip angle, the lateral force gradually converges to a maximum value, or alternatively, the force exhibits a peak, after which it drops slightly and converges to a value lower than the peak value of the

curve. For an un-cambered tyre, the lateral force characteristics pass through the origin (0,0) of the co-ordinate system. The sinusoidal function in equation (3.53) ensures a smooth, continuous increase of the force, until it reaches its maximum, dictated by the peak value, D. For a further increase in slip angle, the arctangent function within the sinusoidal function ensures that the force calculated by the relation (3.53) converges to:

$$y_a = D\sin\left[\pm C\frac{\pi}{2}\right] \tag{3.56}$$

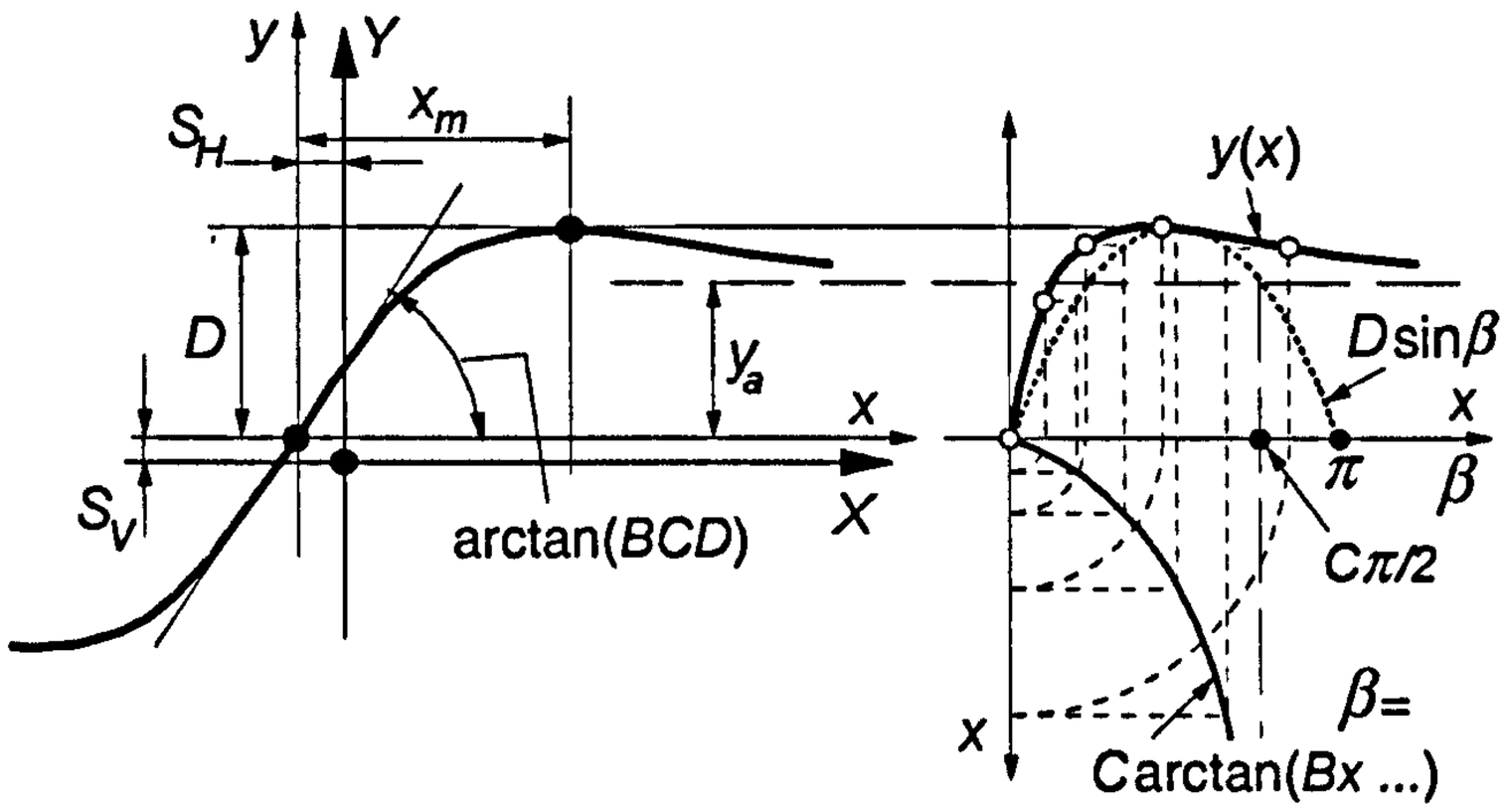

Figure 3. 20 Geometrical interpretation of the magic formula coefficients (after [6])

If the peak value D and the height of the horizontal asymptote y_a are measured experimentally, the value of the shape factor C can be calculated by solving equation (3.56).

$$C = \pm\frac{2}{\pi}\arcsin\left(\frac{y_a}{D}\right) \tag{3.57}$$

While it is obvious that the peak value (D) determines the maximum force, the shape factor (C) is used to control the shape of the curve and makes it look more like a cornering force, brake force or the self aligning moment characteristic.

It is observed through experimentation that the lateral force does not usually exhibit a pronounced peak. Initially, the force increases in a relatively steep manner, but the

slope of the curve reduces gradually as the slip angle increases. Apparently, for a value of the shape factor $C<1$, the force does not even reach the peak value D, whereas for $C=1$, the force asymptotically tends to the maximum value $D=y_a$. Not very often, the lateral force exhibits a peak after which it drops slightly to a value $y_a<D$, leading to a shape factor C slightly greater than unity. On the contrary, the brake force characteristics exhibit a well-defined peak in the great majority of the cases. Thus, the value of the shape factor C is always greater than unity. Finally, the self-aligning torque usually exhibits a change in sign at high values of slip angle ($y_a<0$). Equation (3.56) then requires a shape factor $C>2$ for the successful representation of the self-aligning moment characteristics.

By differentiating relation (3.53), the slope of the characteristic curve at the origin is calculated as:

$$\frac{\partial Y}{\partial X}=BCD \tag{3.58}$$

Therefore, the stiffness factor B is left to control the slope of the characteristic curves.

For the cases where $C>1$, the characteristic curve shows a maximum at slip value x_m as shown in figure 3.20. Based on the position of the peak, the value of the curvature factor E can be calculated as:

$$E=\frac{Bx_m-\tan\{\pi/(2C)\}}{Bx_m-\arctan(Bx_m)} \tag{3.59}$$

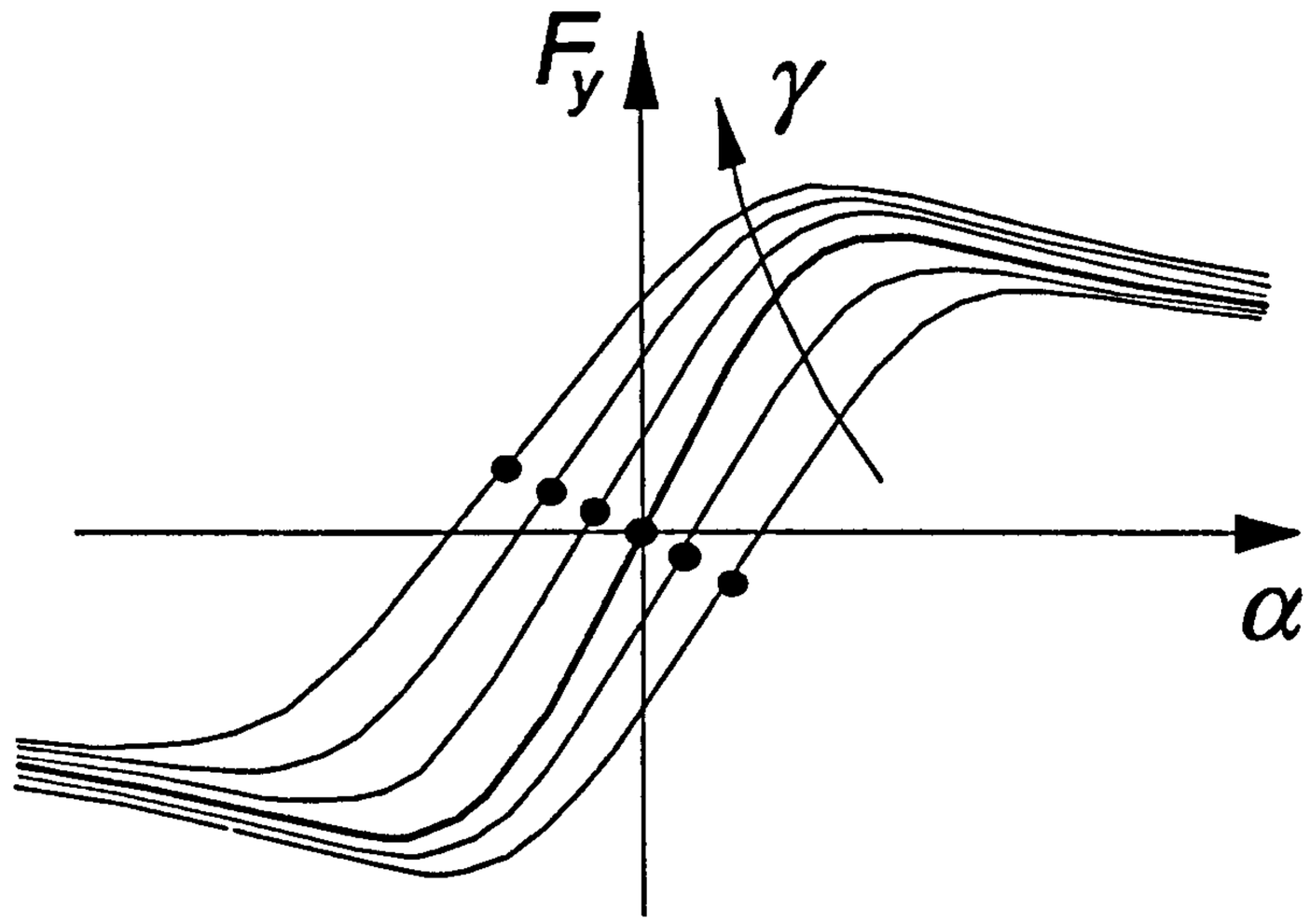

Figure 3. 21 The effect of camber angle on cornering stiffness (after [6])

The existence of a conicity in the lateral tyre profile, ply steer, camber angle and rolling resistance lead to a horizontal (S_H) and vertical (S_V) shifts of the characteristic curves with respect to the origin (0,0). In particular, camber angle might result in a significant horizontal offset of the side force. This observation is accompanied by two repercussions, namely the deterioration of the symmetric shape of the curve with respect to the origin and a drop in the cornering stiffness $\frac{\partial F_y}{\partial a}$ as $|\gamma|$ increases. This behaviour is shown graphically in figure 3.21.

The effect of camber angle in the asymmetry of the curve is handled by modifying the value of the curvature factor E as follows:

$$E = E_0 + \Delta E \cdot sign(x) \tag{3.60}$$

According to this relationship, a small quantity ΔE is added to the curvature factor E_0 for positive slip values, resulting in a more pronounced peak as shown in figure 3.21. For negative slip, the same quantity ΔE is subtracted from the curvature factor, leading to the deterioration of the existing peak. In addition, by using the relation

(3.60) the asymmetries observed between driving and braking curves can be dealt with.

The drop in the cornering stiffness can be taken into account by expressing the product $BCD_y = \frac{\partial F_y}{\partial a}$ as a function of camber angle γ, as demonstrated below:

$$BCD_y = p_1 \sin[2\arctan(F_z / p_2)] \cdot (1 - p_3 \gamma^2) \tag{3.61}$$

Where, p_1, represents the peak cornering stiffness, which occurs at $F_z = p_2$, and p_3 is a parameter.

Although relation (3.53) can be used successfully for the calculation of the self-aligning moment, an alternative approach makes use of the lateral force F_y, the pneumatic trail t and the relatively small residual torque M_{zr}, as follows:

$$M_z = -t \cdot F_y + M_{zr} \tag{3.62}$$

The pneumatic trail t decreases as the slip angle increases. This behaviour can be described by the cosine version of the Magic Formula, as shown below:

$$t(a_t) = D_t \cos[C_t \arctan\{B_t a_t - E_t(B_t a_t - \arctan(B_t a_t))\}] \tag{3.63}$$

Where

$$a_t = \tan a + S_{Ht} \tag{3.64}$$

S_{Ht}, being the horizontal shift of the pneumatic trail t with respect to the origin (0,0).

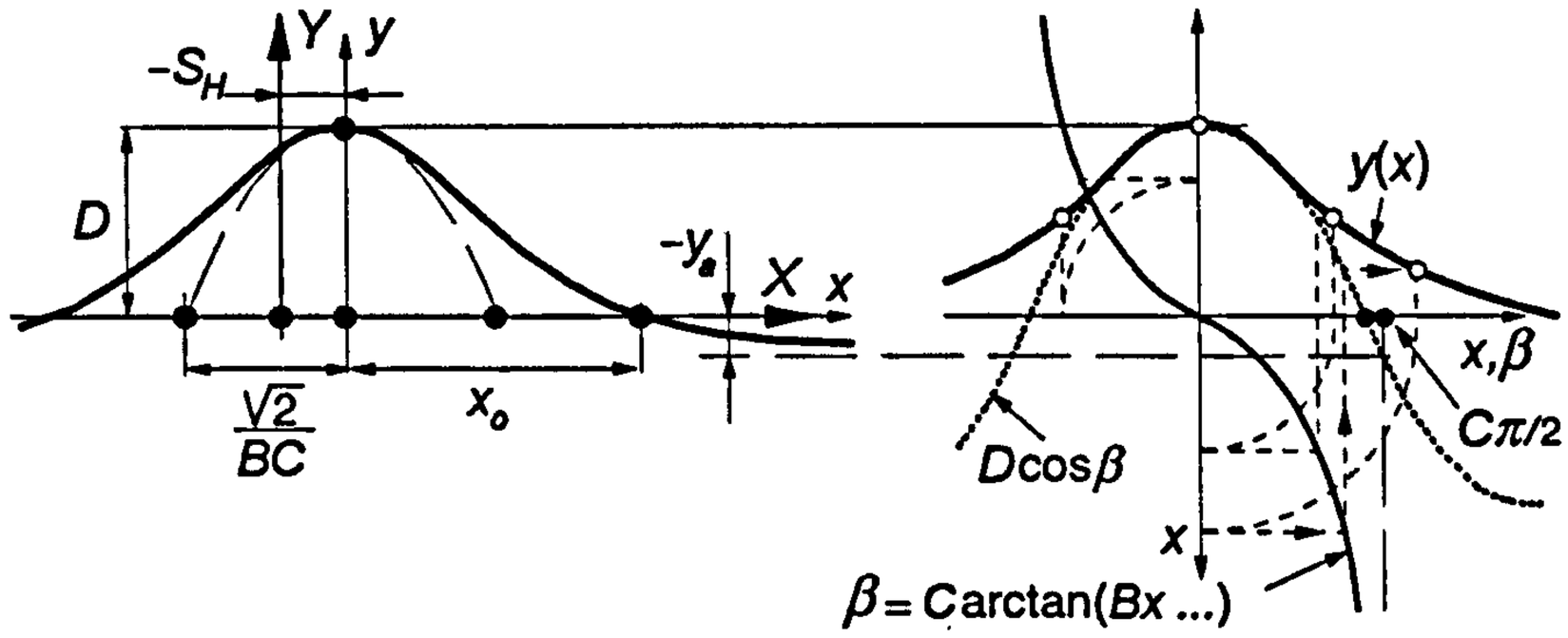

Figure 3. 22 Geometrical explanation of the cosine version of the magic formula (after [6])

Equation (3.63) generates a hill shaped curve as shown in figure 3.22. Factor D_t represents the peak value, C_t is a shape factor governing the height of the horizontal asymptote y_a, B_t determines the sharpness of the hill and E_t governs the point of intersection x_0 between the curve and the horizontal axis.

The residual torque M_{zr} can also be described by the cosine version of the Magic Formula:

$$M_{zr}(a_r) = D_r \cos[\arctan(B_r a_r)] \tag{3.65}$$

Where

$$a_r = \tan a + S_{Hf} \tag{3.66}$$

S_{Hf}, being the horizontal shift of the residual torque with respect to the origin (0,0).

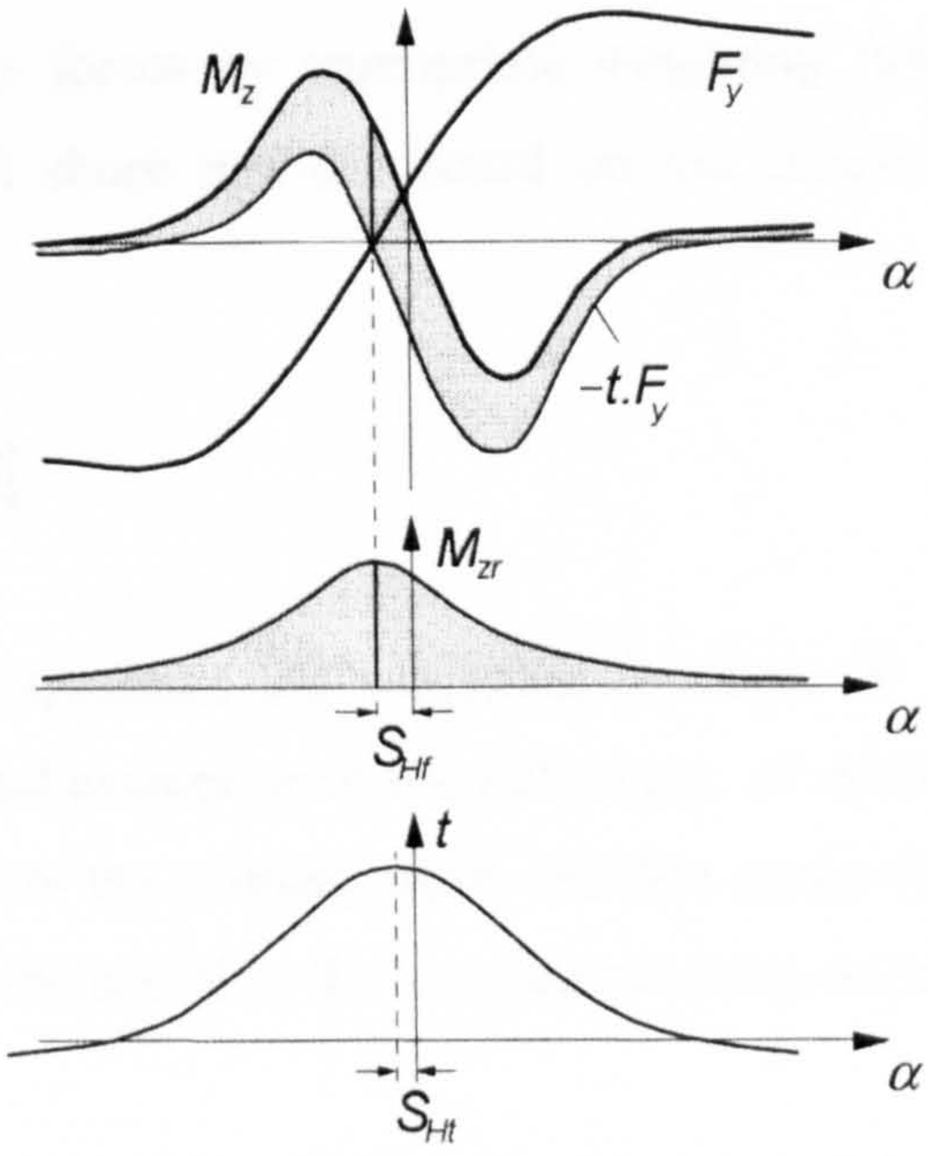

Figure 3. 23 Self-aligning torque as a result of the lateral force and the pneumatic trail (after [6])

Figure 3.23 demonstrates, graphically, the construction of the self-aligning torque characteristics, M_z, resulting from the addition of the residual torque M_{zr} to the product of the lateral force F_y and the pneumatic trail t. The second and third graphs show the hill shape of the cosine version of the Magic Formula, as predicted by relations (3.65) and (3.63) respectively.

3.3.3.2.2 Combined Slip Operating Conditions

It is expected that the simultaneous existence of a slip angle a, and longitudinal slip k reduces the forces predicted by equation (3.53) for pure slip conditions. The situation can be handled by taking into account some basic principles, describing the relative magnitude of the contact forces for an anisotropic tyre, operating under combined lateral and longitudinal sliding. This somewhat complex approach is undertaken in [58], [41] and [62] and involves the definition of additional slip values and the non-dimensionalisation of the characteristic curves for pure longitudinal and pure lateral slip. The details of this procedure can be found in literature ([58], [41], [62] and [6]). Here, the purely empirical approach adopted in [63] is briefly described.

The effect of k on F_y and a on F_x is taken into account by multiplying the corresponding pure slip forces by appropriate weighting functions. The weighting functions exhibit a hill shape and are based on the cosine version of the Magic Formula shown below:

$$G = D\cos[C\arctan(Bx)] \tag{3.67}$$

In relation (3.67) G represents the weighting function, D is the peak value, C determines the horizontal asymptote of the hill's base, B determines the sharpness of the hill and x represents the primary input variable in the form of k or a for the weighting functions of the lateral or the longitudinal force respectively.

For example, in the event that a brake slip k is introduced to a cornering tyre, operating at a slip angle a, the side-force F_{y0}, predicted by equation (3.53) for pure side-slip is multiplied by the weighting factor, G expressed as a function of the slip ratio k. It is observed, experimentally, that for low values of longitudinal slip, the lateral force shows a slight increase in magnitude compared to pure side-slip operating conditions. This phenomenon can be taken into account, using a peak value $D > 1$, in conjunction with an additional horizontal shift of the weighting function. In this manner the weighting function can be made equal to unity for zero longitudinal slip, increase above unity for low values of k, and drop again as k further increases.

3.3.3.3 Full Set of Equations

A revised set of equations, including improvements and extensions of the model together with the definition of a large number of additional parameters and scaling factors may be found in [6]. In this section, the equations proposed in [41] for pure slip conditions are considered. This second version of the Magic Formula model serves as a good compromise between simplicity, accuracy and physical substance of the parameters used.

3.3.3.3.1 Lateral Force

$$F_y(a) = y(x) + S_V \tag{3.68}$$

$$y(x) = D\sin[C\arctan\{Bx - E(Bx - \arctan Bx)\}] \tag{3.69}$$

$$x = a + S_H \tag{3.70}$$

Factors:

$$C = \mathrm{a}_0 \tag{3.71}$$

$$D = \mu_{ym} F_z \tag{3.72}$$

$$\mu_{ym} = \mathrm{a}_1 F_z + \mathrm{a}_2 \tag{3.73}$$

Where:

μ_{ym} is the lateral coefficient of friction

a_1 is the load dependency of lateral friction

a_2 is the lateral friction level

$$BCD = \mathrm{a}_3 \sin(2\arctan(F_z/\mathrm{a}_4)) \cdot (1 - \mathrm{a}_5|\gamma|) \tag{3.74}$$

Where:

a_3 is the maximum cornering stiffness at $\gamma = 0$

a_4 is the load at maximum cornering stiffness

a_5 is the camber sensitivity of cornering stiffness

$$E = \mathrm{a}_6 F_z + \mathrm{a}_7 \tag{3.75}$$

$$B = BCD/CD \tag{3.76}$$

$$S_H = a_8\gamma + a_9 F_z + a_{10} \tag{3.77}$$

$$S_V = a_{11} F_z \gamma + a_{12} F_z + a_{13} \tag{3.78}$$

3.3.3.3.2 Longitudinal Force

$$F_x(k) = y(x) + S_V \tag{3.79}$$

$$y(x) = D\sin[C\arctan\{Bx - E(Bx - \arctan Bx)\}] \tag{3.80}$$

$$x = k + S_H \tag{3.81}$$

Factors:

$$C = b_0 \tag{3.82}$$

$$D = \mu_{xm} F_z \tag{3.83}$$

$$\mu_{xm} = b_1 F_z + b_2 \tag{3.84}$$

Where:

μ_{xm} is the longitudinal coefficient of friction

b_1 is the load dependency of longitudinal friction

b_2 is the longitudinal friction level

$$BCD = \left(b_3 {F_z}^2 + b_4 F_z\right)\cdot \exp(-b_5 F_z) \tag{3.85}$$

$$E = b_6 {F_z}^2 + b_7 F_z + b_8 \tag{3.86}$$

$$B = BCD/CD \tag{3.87}$$

$$S_H = b_9 F_z + b_{10} \tag{3.88}$$

$$S_V = 0 \tag{3.89}$$

3.3.3.3.3 Self-Aligning Torque

$$M_y(a) = y(x) + S_V \tag{3.90}$$

$$y(x) = D\sin[C\arctan\{Bx - E(Bx - \arctan Bx)\}] \tag{3.91}$$

$$x = a + S_H \tag{3.92}$$

Factors:

$$C = c_0 \tag{3.93}$$

$$D = c_1 F_z^{\,2} + c_2 F_z \tag{3.94}$$

$$BCD = \left(c_3 F_z^{\,2} + c_4 F_z\right)\cdot\left(1 - c_6|\gamma|\right)\cdot\exp\left(-c_5 F_z\right) \tag{3.95}$$

Where:

c_6 is the camber sensitivity of aligning stiffness

$$E = \left(c_7 F_z^2 + c_8 F_z + c_9\right)\cdot\left(1 - c_{10}|\gamma|\right) \tag{3.96}$$

$$B = BCD/CD \tag{3.97}$$

$$S_H = c_{11}\gamma + c_{12} F_z + c_{13} \tag{3.98}$$

$$S_V = \left(c_{14}F_z^2 + c_{15}F_z\right)\gamma + c_{16}F_z + c_{17} \tag{3.99}$$

3.3.4 Development of a Simple Physical Tyre Model

Some fundamental trends for the steady-state behaviour of tyres have been described with the aid of the Magic Formula tyre model. In this section the actual mechanism of tyre force and moment generation is discussed with the description of two new physical models. The first relatively simple model forms the basis for the analysis and serves as a platform for the development of the second, more elaborate model.

3.3.4.1 Description of the Model

The first step in all such investigations is to determine the contact conditions, in conformance with established theories of contact mechanics, and with the necessary assumptions that make the modelling of the problem tractable. For the case of tyre-road interactions the road surface may be considered as flat in the first instance and with surface height irregularities (roughness) much smaller than the local deformation of the tyre. The surface waviness of the road is assumed to possess wavelengths in excess of the contact dimensions [72].

The behaviour of the tyre can be ascertained by discretisation of the continuous contact domain, as is the case for all contact mechanical treatments. The modelling of the generation of shear forces is based on the brush concept. The tyre tread is modelled as a one-dimensional series of bristles, distributed around the tyre periphery. The bristles incorporate anisotropic stiffness and damping in the lateral and longitudinal directions, forming viscoelastic Kelvin elements. In this case, the combined effects of the carcass, the belt and the tread are integrated into the bristles. The distributed tread mass on the tyre periphery is also taken into account by attaching a small (infinitesimal) mass to the free end of each bristle. Initially, for the sake of simplicity, the length of the contact patch is assumed to be constant for a given normal load and the vertical pressure distribution is regarded as parabolic. The assumption of a parabolic distribution is held valid for an elastic solid of revolution against a semi-infinite surface (such as the road) as a first approximation. Since the contacting profile

of the tyre has a finite width, one would need to accept the uniformity of the lateral distribution of pressure for the one-dimensional model. This assumption is generally accepted as the starting point for the evaluation of contact mechanic behaviour of tyre-road interaction [6], [46], [52].

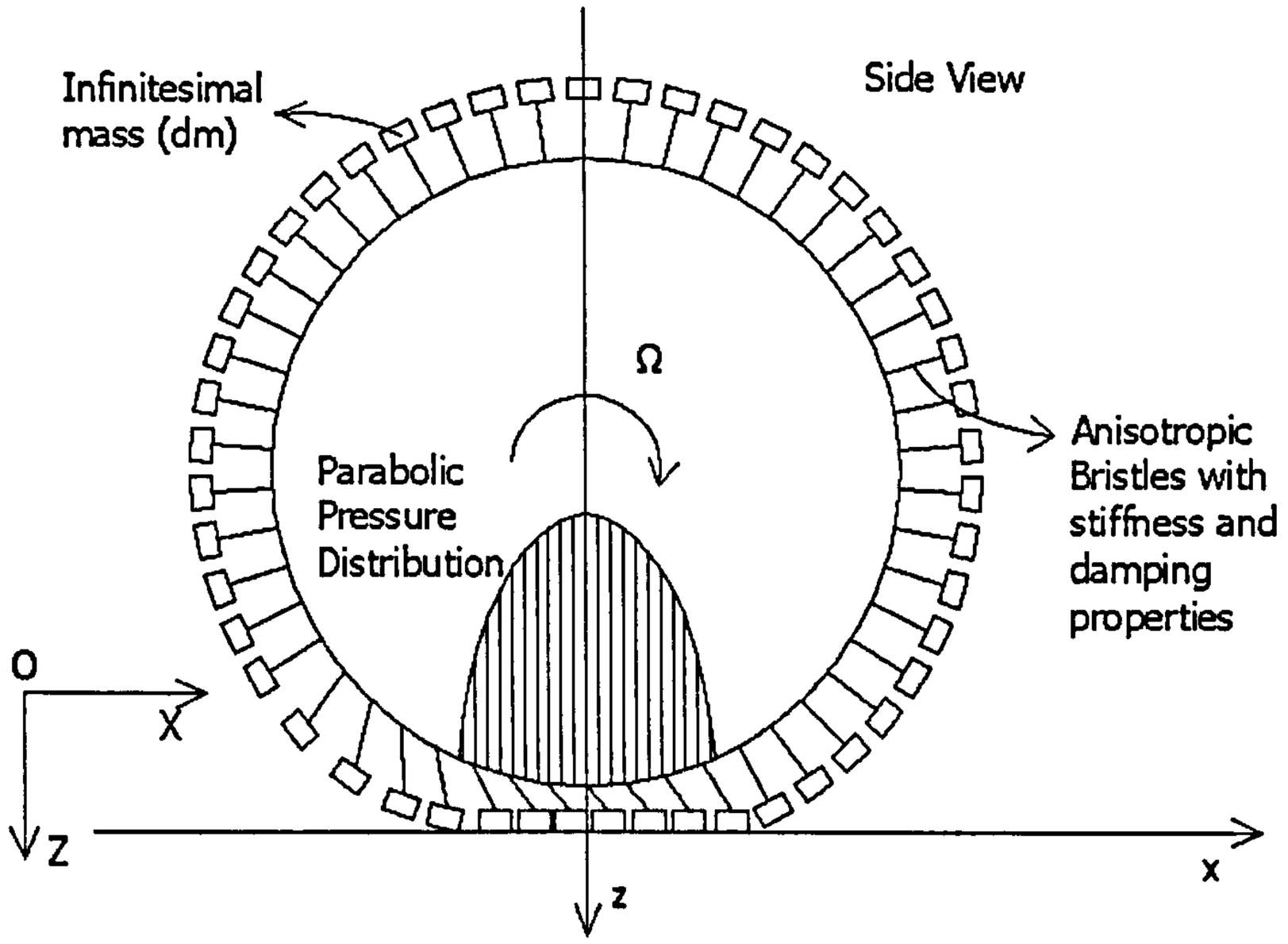

Figure 3. 24 A side view of the simple tyre model including the contact pressure distribution

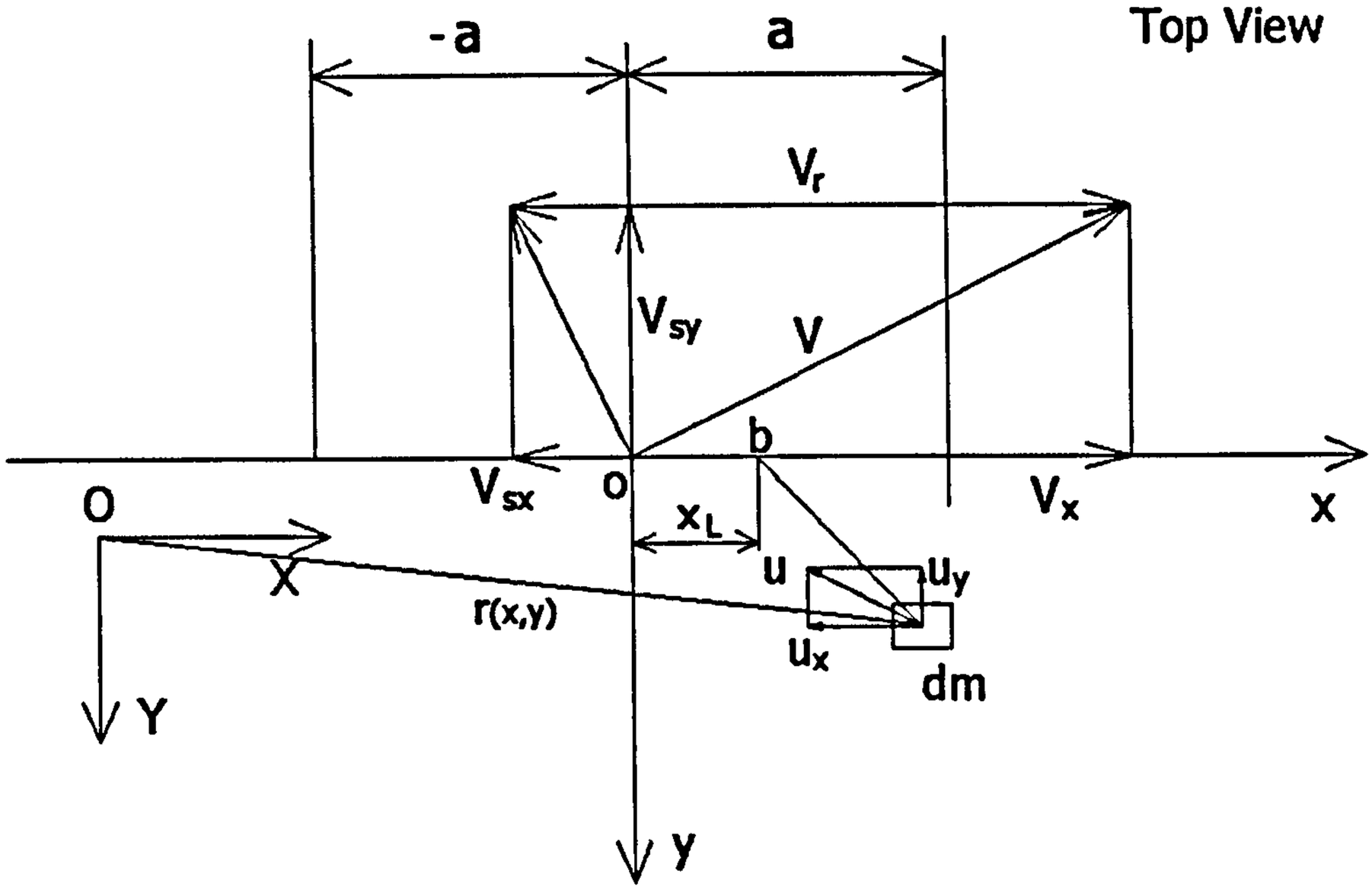

Figure 3. 25 Top view of a tyre segment at a random position of operation

Figure 3.24 shows a side view of the tyre model including the normal pressure distribution, while figure 3.25 shows a top view of the model, depicting an arbitrary position of the mass, dm, which corresponds to a segment of length dx of the tyre tread. A bristle connecting the mass to the wheel periphery, is deformed laterally as well as longitudinally and, the mass may or may not be sliding on the ground, depending on the forces applied by the bristle (viscoelastic element), the vertical force at the specific position and the local coefficient of friction.

In agreement with section 3.3.1, the SAE moving frame of reference (o,x,y,z) and the global frame of reference (O,X,Y,Z), attached to the ground, are used for the determination of the motion of the tyre and its components. Both frames are shown in figures 3.24 and 3.25.

For the purpose of the analysis, the motion of the infinitesimal mass is traced throughout the length of the contact patch. The analysis, therefore, considers the physics of motion of a single infinitesimal mass (segment) through the contact to be representative of all such discrete elements. Thus, the proposed model represents steady-state contact conditions.

As already mentioned, the length $l = 2 \cdot \mathrm{a}$ of the contact patch is kept constant. Point b, where the bristle is connected to the tyre periphery (i.e. the bristle base, see figure 3.25) enters the contact patch at coordinates $(x, y, z) = (\mathrm{a},0,0)$ in the moving frame of reference and travels throughout the contact patch with velocity $-|V_r| = -|(\dot{\psi}\sin(\gamma) + \Omega)R_e|$. The longitudinal component of the velocity of the bristle base relative to the ground (i.e. the global frame of reference) is V_{sx}, the lateral component being V_{sy}. When the vertical force, at the point under consideration results in the generation of a high enough frictional force, the mass dm tends to stick to the ground. In any other case, the mass moves with respect to the ground with sliding velocity, $u = d\mathbf{r}(x, y)/dt$, consisting of u_x and u_y in the longitudinal and lateral directions respectively.

In general, the origin of the global frame of reference can be positioned anywhere in space, as shown in figure 3.25. Nevertheless, the derivation of the equations is simplified if the origin of the global frame of reference is made to coincide with point $(\mathrm{a},0,0)$ of the SAE frame where the representative tyre segment enters the contact patch. In this way, the position vector $\mathbf{r}(x, y)$ of the small mass in the global frame of reference is equal to zero until sliding begins.

Since the distribution of bristles is one-dimensional and the lateral distribution of the normal tyre force is assumed uniform, all the forces, including the vertical tyre forces, are stated per unit length of the tread. Consequently, elastic and damping properties are also given per unit length of the tread.

The mass distribution along the tyre tread is $C = dm/dx$, the stiffness coefficients per unit tread length are $K_x = \left(\frac{dF}{dx}\right)\Big/dx$, $K_y = \left(\frac{dF}{dy}\right)\Big/dx$ for the longitudinal and lateral deformations of the bristles respectively, and the coefficients of damping are $D_x = \left(\frac{dF}{d(V_{sx} - u_x)}\right)\Big/dx$, $D_y = \left(\frac{dF}{d(V_{sy} - u_y)}\right)\Big/dx$.

The equation of the parabola, yielding the vertical force distribution per tyre tread length can be easily derived, given the length of the contact patch $l = 2 \cdot \mathrm{a}$ and taking into account the fact that the integral of the force along the contact patch balances the normal load applied on the wheel hub by the suspension. In accordance with these simple considerations, the vertical force distribution per tread length becomes:

$$F_{vertical} = \frac{3 \cdot F_z}{4 \cdot \mathrm{a}} \cdot \left(1 - \left(\frac{x_L}{\mathrm{a}}\right)^2\right) \tag{3.100}$$

where F_z denotes the total vertical force applied on the wheel hub and x_L is the position of the segment along the contact patch.

3.3.4.2 A Note on the Length of the Contact Patch

The length of the contact patch $l = 2 \cdot \mathrm{a}$ has been assumed to remain constant. Certainly, the simple formulation of the contact-mechanical aspect of the tyre model does not allow a dynamic update of the size of the contact patch, based on the rolling velocity. Furthermore, the middle of the contact is always assumed to coincide with the projection of the wheel centre on the road. Nonetheless, it is necessary to relate the total length of the contact, given the width of the tyre, to the net vertical load applied on the wheel hub. This can be done in a simple analytical way, as demonstrated by Gim and Nikravesh [52]. According to this approach, it is assumed that under the application of a vertical load, the tyre penetrates the road and the total length of the contact is equal to the chord of the resulting arc, as demonstrated in figure 3.26. Simple geometry yields:

$$\mathrm{a} = \sqrt{R^2 - (R - \delta)^2} \tag{3.101}$$

and because $\delta << R$, the above relation reduces to:

$$\mathrm{a} \approx \sqrt{2R\delta} \tag{3.102}$$

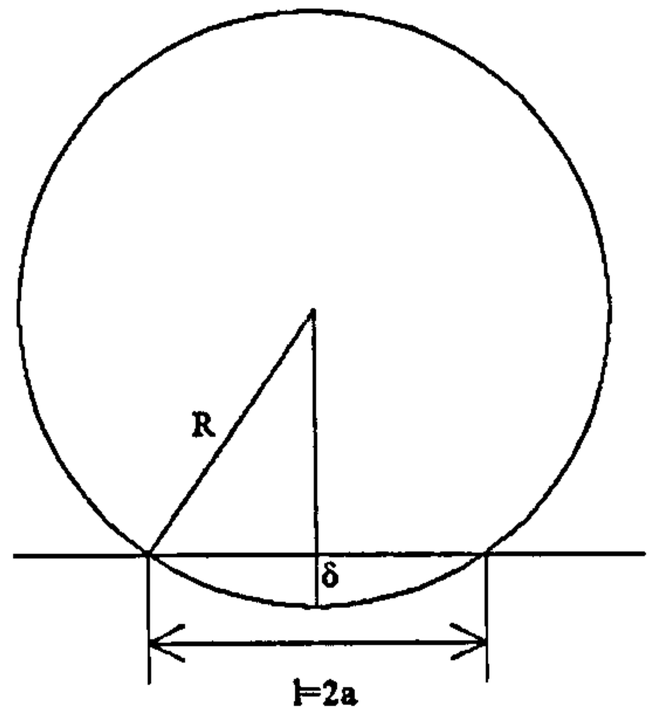

Figure 3. 26 The principle for the calculation of the length of the contact patch

Given the radius R of the tyre, length $l = 2a$ can be calculated by relation (3.102) if penetration or alternatively vertical deflection δ is known. Assuming a linear relationship between normal load and the resulting vertical displacement, δ is given by the following equation:

$$\delta = \frac{F_z}{C_z} \tag{3.103}$$

where, C_z denotes the static vertical stiffness of the tyre in $[N/m]$. Note that this relation assumes an infinite line contact condition (into the depth of the tyre contact with the ground, i.e. laterally) for which a deflection exponent of unity can be assumed, as an approximation to the actual value of 1.1 [72].

This simple static approach is adopted in order to vary the length of the contact patch depending on the normal load.

3.3.4.3 Modelling of Friction

Although rubber exhibits a rather complex frictional behaviour, it is possible to simplify the situation by considering the fact that the hysteresis peak is rarely observed under normal tyre operation. As stated in section 3.2.3.2, excitation frequencies within the contact patch rarely reach the levels, where the hysteresis term of friction becomes dominant. Under these circumstances, the adhesion peak can be

substituted by a simple stick-slip friction law, appropriate for hard materials that are in accord with Coulomb's classical laws of friction. In general, for dry contacts between hard materials, stick-slip friction can be modelled as a transition between two different states. This type of behaviour is described by considering a hard elastic body sliding on a hard surface. When the velocity of the specimen reduces to zero, friction force may attain any value between zero and maximum static friction, F_{max}. At this stage, the friction force balances all the external forces. In the event that the sum of external forces exceeds F_{max}, sliding between the specimen and the surface occurs. Then, it is assumed that the friction force drops instantaneously from F_{max} to a lower value, F_{kin}, known as kinetic friction. From this point onwards friction might show a dependency on sliding velocity, usually expressed as a slight decrease in the coefficient of kinetic friction, as velocity increases further. This behaviour can be summarised in the following relations:

$$f = -F_{external} \text{ for } u = 0 \text{ AND } \left|F_{external}\right| \leq F_{\max} = \mu_s \cdot F_{vertical} \tag{3.104}$$

$$f = \mu_k \cdot F_{vertical} \text{ for } \left|u\right| > 0 \text{ OR } \left|F_{external}\right| > \mu_s \cdot F_{vertical} \tag{3.105}$$

where f denotes the friction force opposing the motion of the specimen, u is the sliding velocity, $F_{external}$ is the resultant external force applied on the specimen, μ_s is the coefficient of static friction, $F_{vertical}$ is the vertical force applied on the specimen and μ_k is the coefficient of kinetic friction with $\mu_k < \mu_s$.

In the case of rubber, μ_s corresponds to the adhesion peak, observed at low sliding velocities, while μ_k represents an average value for the coefficient of friction, succeeding the adhesion peak. The significance of coefficients μ_s and μ_k is better understood by referring to figures 3.8 and 3.9. The value of μ_k would need to take into account sliding velocities of a maximum of up to 50-100 m/s, a range more than enough for the simulation of tyre friction. Finally, it should be noted that contamination films reduce the effect of adhesion [82] and the peak adhesion coefficient of friction should is expected to be lower than the value shown in figure 3.9.

Karnopp [112] proposes a simple algorithm for the implementation of relations (3.104) and (3.105) in a computer simulation environment. The numerical feasibility of the stick-slip friction law requires that the velocity conditions, appearing in relations (3.88) and (3.89) are replaced by the following relations:

$$|u| \leq threshold \tag{3.106}$$

$$|u| > threshold \tag{3.107}$$

where, *threshold* is a relatively small velocity value in the range between 0.005 and 0.05 m/s.

3.3.4.4 Equations of Motion for the Infinitesimal Mass

The motion of an infinitesimally small segment of length dx is considered. According to the aforementioned definitions, the mass, stiffness and damping properties of this specific part of the tread can be written as follows:

$$dm = C \cdot dx \tag{3.108}$$

$$dK_x = K_x \cdot dx \tag{3.109}$$

$$dK_y = K_y \cdot dx \tag{3.110}$$

$$dD_x = D_x \cdot dx \tag{3.111}$$

$$dD_y = D_y \cdot dx \tag{3.112}$$

Before entering the contact patch, the infinitesimal mass is assumed to be in an equilibrium condition and no forces are applied by the corresponding bristle. The

motion of the mass is followed from the moment it enters the contact patch, until it reaches the trailing edge of the contact.

In accordance with figure 3.25 the differential equations describing the motion of the mass in the longitudinal and lateral directions become:

$$\dot{u}_x \cdot C \cdot dx = (x_s - x) \cdot K_x \cdot dx + (V_{sx} - u_x) \cdot D_x \cdot dx - f_x \cdot dx \tag{3.113}$$

$$\dot{u}_y \cdot C \cdot dx = (y_s - y) \cdot K_y \cdot dx + (V_{sy} - u_y) \cdot D_y \cdot dx - f_y \cdot dx \tag{3.114}$$

$$\dot{x}_s = V_{sx} \text{ so that } x_s = \int_0^{travel} V_{sx} dt \tag{3.115}$$

$$\dot{y}_s = V_{sy} \text{ so that } y_s = \int_0^{travel} V_{sy} dt \tag{3.116}$$

$$\dot{x} = u_x \text{ so that } x = \int_0^{travel} u_x dt \tag{3.117}$$

$$\dot{y} = u_y \text{ so that } y = \int_0^{travel} u_y dt \tag{3.118}$$

where, f_x, f_y denote the friction forces per unit length in the longitudinal and lateral directions respectively and $t_{travel} = 2 \cdot a / V_r$ is the duration of travel of the bristle base throughout the contact patch.

Irrespective of whether the tyre is sliding or not, the velocity of travel of point b along the length of the contact patch is $-V_r$. Obviously, this is also the velocity throughout the normal force distribution. Thus, the vertical force on point b varies according to the following relations:

$$F_{vertical} = \frac{3 \cdot F_z}{4 \cdot a} \cdot \left(1 - \left(\frac{x_L}{a}\right)^2\right) \tag{3.119}$$

$$\dot{x}_L = -V_r \text{ so that } x_L = \mathrm{a} + \int_0^{travel} -V_r dt \tag{3.120}$$

The value of friction $\vec{f} = \vec{f}_x + \vec{f}_y$ is determined by relations (3.104) and (3.105). If the sticking condition is satisfied, the magnitude of the friction force equals the magnitude of the forces applied by the bristle. When the mass is sliding on the road surface the magnitude of the friction force becomes:

$$\left|\vec{f}\right| = \mu_k \cdot \frac{3 \cdot F_z}{4 \cdot \mathrm{a}} \cdot \left(1 - \left(\frac{x_L}{\mathrm{a}}\right)^2\right) \tag{3.121}$$

The components of $\vec{f}$ in the longitudinal and lateral directions become:

$$f_x = \frac{u_x}{\sqrt{u_x^{\,2} + u_y^{\,2}}} \cdot \mu_k \cdot \frac{3 \cdot F_z}{4 \cdot \mathrm{a}} \cdot \left(1 - \left(\frac{x_L}{\mathrm{a}}\right)^2\right) \tag{3.122}$$

and

$$f_y = \frac{u_y}{\sqrt{u_x^{\,2} + u_y^{\,2}}} \cdot \mu_k \cdot \frac{3 \cdot F_z}{4 \cdot \mathrm{a}} \cdot \left(1 - \left(\frac{x_L}{\mathrm{a}}\right)^2\right) \tag{3.123}$$

3.3.4.5 Some Improvements in the Friction Law

Equations (3.104), (3.105), (3.122) and (3.123) assume isotropic friction in the lateral and longitudinal directions. Experimental evidence shows that this is rarely the case (see for example the 1st quadrant of the friction ellipse in figure 2.4). On the contrary, the maximum friction force, calculated as the vectorial addition of the lateral and longitudinal components, usually defines an ellipse, as demonstrated graphically in figure 3.27.

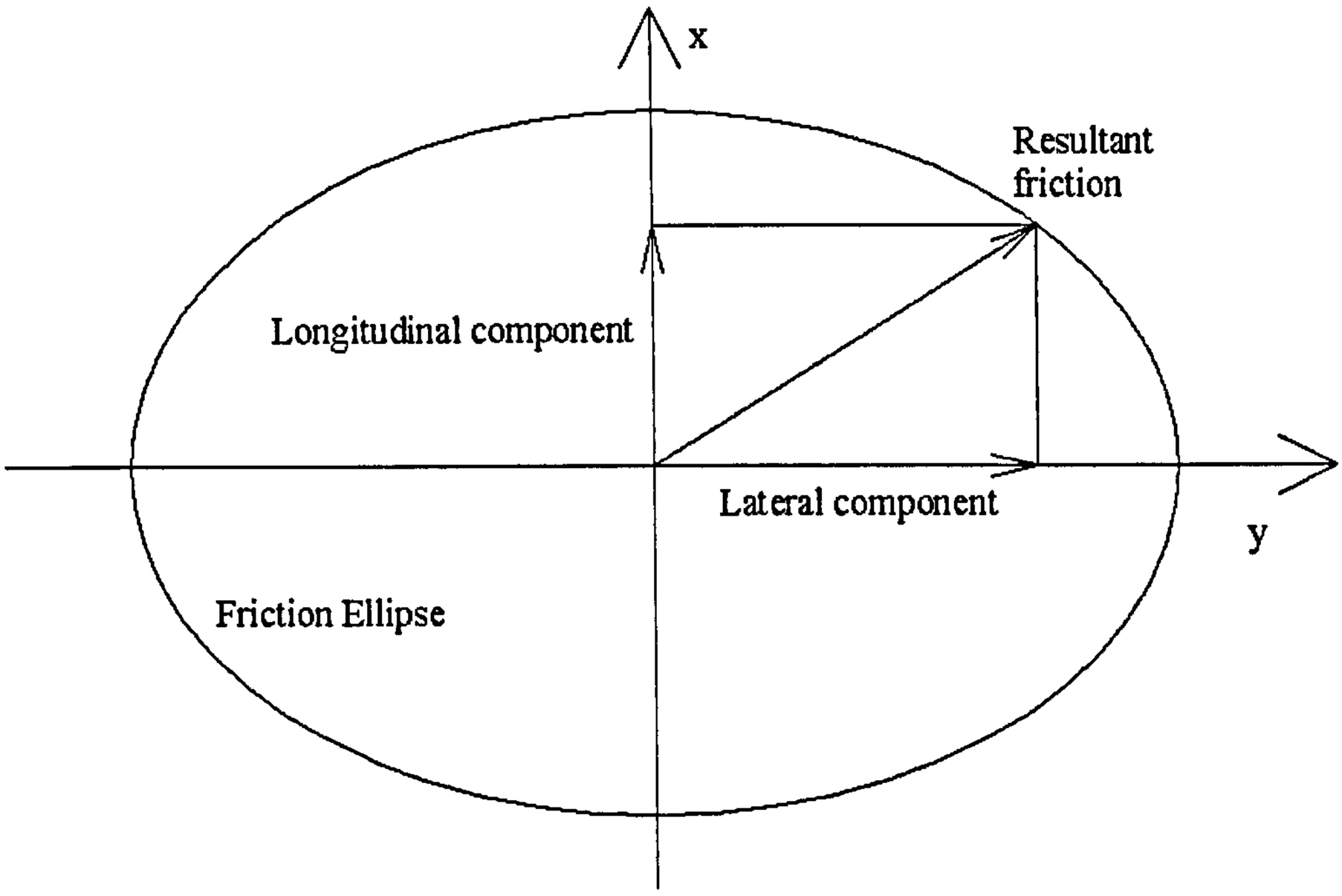

Figure 3. 27 The friction ellipse concept

In order to take into account the anisotropy of friction in the lateral and longitudinal directions it is essential to modify the generic stick-slip friction law defined by relations 3.104 and 3.105. The force threshold now is expressed as:

$$\left(\frac{F_x}{\mu_{sx}}\right)^2+\left(\frac{F_y}{\mu_{sy}}\right)^2 \le F_{vertical}^2 \tag{3.124}$$

where, F_x and F_y denote the decoupled longitudinal and lateral components of the bristle force acting on the infinitesimal mass, and μ_{sx}, μ_{sy} are unequal coefficients of static friction in the longitudinal and lateral directions respectively.

Equation (3.124) defines an ellipse with its semi-minor and semi-major widths being $\left|2\mu_{sx}F_{vertical}\right|$ and $\left|2\mu_{sy}F_{vertical}\right|$ respectively. When both equations (3.106) and (3.124) are satisfied, the infinitesimal mass sticks to the ground and the friction force opposes the net force applied by the bristle. In any other case, the sliding condition is satisfied, and the friction forces are calculated by the following relationships, which take into consideration the anisotropic nature of kinetic friction:

$$f_x = \frac{u_x}{\sqrt{(u_x/\mu_{kx})^2 + (u_y/\mu_{ky})^2}} \cdot F_{vertical} \tag{3.125}$$

$$f_y = \frac{u_y}{\sqrt{(u_x/\mu_{kx})^2 + (u_y/\mu_{ky})^2}} \cdot F_{vertical} \tag{3.126}$$

where μ_{kx}, μ_{ky} denote the coefficients of kinetic friction in the longitudinal and lateral directions respectively.

In an attempt to further improve upon the accuracy of the calculations, coefficients μ_{kx} and μ_{ky} can be made velocity dependent. In order to avoid the estimation of the parameters involved in relation (3.16), the part of the friction coefficient curve, succeeding the adhesion peak (see figure 3.8) can be approximated by an exponential function as demonstrated below:

$$\mu_{kx} = \mu_{sx} + \mu_{xred}\left(e^{-qx|u_x|} - 1\right) \tag{3.127}$$

$$\mu_{ky} = \mu_{sy} + \mu_{yred}\left(e^{-qy|u_y|} - 1\right) \tag{3.128}$$

where, μ_{xred}, μ_{yred}, qx, qy are coefficients.

Relations (3.127) and (3.128) indicate that the coefficients of kinetic friction reduce in an exponential manner, starting from the peak values of static friction (adhesion peak). It is surmised that the total reduction is dictated by the value of parameters μ_{xred} and μ_{yred}, while the coefficients qx and qy regulate the rate of reduction in the corresponding directions. Although all parameters can be estimated by using graphs similar to the one shown in figure 3.9, it is often more convenient to use experimentally measured tyre data or even curves generated by the Magic Formula model. This approach will be shown later in section 3.3.6.

3.3.4.6 The Inclusion of Spin-Slip

So far, the lateral and longitudinal deformations of a representative bristle within the contact patch have been explained using the lateral and longitudinal sliding velocities V_{sy} and V_{sx} as kinematic inputs to the bristle base. As the bristle travels along the contact patch with velocity $-V_r$, the kinematic inputs V_{sy} and V_{sx} remain constant, provided that the tyre operates under steady-state conditions.

If one considers a cambered rolling wheel with an additional yaw rate, for example due to a steering action, the resulting yaw-rate parallel to the z axis of the SAE frame of reference can be easily calculated, based on the analysis in section 3.3.1.:

$$\vec{\omega} \cdot \hat{z} = \dot{\psi} - \Omega \cdot \sin\gamma \tag{3.129}$$

In the simple case of a single-plane tyre model with a contact patch extending from –a to a, the resulting yaw rate calculated in equation (3.129) generates an additional lateral velocity which is a function of the position along the contact patch. Throughout the contact, the lateral velocity at the base-points of the bristles is given as:

$$V_{syc}(x_L) = (\dot{\psi} - \Omega \cdot \sin\gamma) \cdot (x_L) \text{ with } x_L \in (-\mathrm{a}, \mathrm{a}) \tag{3.130}$$

The resulting lateral displacement along the contact can be found by integrating the velocity with respect to time. To achieve this, the position x_L along the contact needs to be written as a function of time:

$$x_L = \mathrm{a} - V_r \cdot t \tag{3.131}$$

For steady-state operating conditions V_r remains constant and the time required to reach a position x_L along the contact, i.e. to move from a to x_L, is equal to $(\mathrm{a} - x_L)/V_r$. Hence, by combining equations (3.130) and (3.131), the lateral displacement of the bristle-base points can be found by the following integral:

$$y_{sc}(x_L) = \int_0^{(a-x_L)/V_r} (a - V_r \cdot t) \cdot (\dot{\psi} - \Omega \cdot \sin\gamma) dt \tag{3.132}$$

Simple calculations yield:

$$y_{sc}(x_L) = \frac{(\dot{\psi} - \Omega \cdot \sin\gamma)}{V_r} \cdot \left(\frac{a^2}{2} - \frac{x_L^2}{2} \right) \tag{3.133}$$

If no longitudinal sliding exists, then $V_r = V_x$ and equation (3.133) can be written as follows:

$$y_{sc}(x_L) = \frac{(\dot{\psi} - \Omega \cdot \sin\gamma)}{V_x} \cdot \left(\frac{a^2}{2} - \frac{x_L^2}{2} \right) = \Phi \cdot \left(\frac{a^2}{2} - \frac{x_L^2}{2} \right) \tag{3.134}$$

The above equation reveals the significance of spin-slip Φ as a kinematic input for the calculation of the deformation along the contact patch. If one assumes that the slip angle is equal to zero and that there is no sliding throughout the contact, i.e. the friction force is enough to keep the free ends of the bristles stuck to the ground, then, the lateral displacement of the bristle-base points $y_{sc}(x_L)$ due to spin-slip is equal to the deformation of the bristles along the contact. Under these conditions a parabolic lateral deformation occurs, which is symmetrical with respect to the centre of the contact patch. The result obtained here is identical to the result obtained in [6] for the calculation of the lateral deformation along the contact in the case of a simple brush model with a known contact length equal to 2a, for which the non-sliding condition applies.

It should be noted that due to the symmetry of the lateral deformation, the spin-slip does not generate a self-aligning moment when a single plane tyre model is considered. However, if one takes into account the width of the tyre, it becomes obvious that the resulting yaw rate $\vec{\omega} \cdot \hat{z}$ introduces anti-symmetrical longitudinal velocities along the width of the contact. Following exactly the same procedure, the longitudinal deformations along the width can be calculated and the resulting self-aligning moment is then easily obtained.

Based on the previous analysis, the inclusion of the effect of spin-slip (camber and turn-slip) in the modelling approach is achieved by substituting V_{sy} in equations (3.113)-(3.118) with the resulting V_{syr} due to the addition of spin-slip. Equations (3.113)-(3.118) are modified as follows:

$$\dot{u}_x \cdot C \cdot dx = (x_s - x) \cdot K_x \cdot dx + (V_{sx} - u_x) \cdot D_x \cdot dx - f_x \cdot dx \tag{3.135}$$

$$\dot{u}_y \cdot C \cdot dx = (y_s - y) \cdot K_y \cdot dx + (V_{syr} - u_y) \cdot D_y \cdot dx - f_y \cdot dx \tag{3.136}$$

$$\dot{x}_s = V_{sx} \text{ so that } x_s = \int_0^{travel} V_{sx} dt \tag{3.137}$$

$$\dot{y}_s = V_{syr} \text{ so that } y_s = \int_0^{travel} V_{syr} dt \tag{3.138}$$

$$\dot{x} = u_x \text{ so that } x = \int_0^{travel} u_x dt \tag{3.139}$$

$$\dot{y} = u_y \text{ so that } y = \int_0^{travel} u_y dt \tag{3.140}$$

with:

$$V_{syr} = V_{sy} + (\dot{\psi} - \Omega \cdot \sin\gamma) \cdot x_L \tag{3.141}$$

and

$$\dot{x}_L = -V_r \text{ so that } x_L = \mathrm{a} + \int_0^{travel} -V_r dt \tag{3.142}$$

In analytical tyre models based on the brush concept, the consideration of sliding regions within the contact patch and the general case of the co-existence of spin-slip and lateral slip, introduce certain complications in the calculation of the deformations and the resulting forces and moments [6]. The methodology presented above uses only the additional velocities at the bristle-base points, resulting from spin-slip. Thus, a separate treatment of combined side-slip and spin-slip is not required, nor is the

method restricted by any assumptions regarding the adhesion and sliding regions within the contact.

3.3.4.7 Numerical Solution of the Differential Equations

Equations (3.135)-(3.142) are solved numerically, using a 4^{th} order, fixed time-step size Runge Kutta method [113], [114]. At every time-step, the conditions (3.106) and (3.124) are checked and the friction is determined accordingly, by considering equations (3.125) and (3.126). The forces transferred to the wheel are the reactions applied by the bristles on their respective base points. The analysis is carried out initially for steady state conditions (i.e. velocity V_r is kept constant). Therefore, if the duration of the time-step is h, the distance travelled along the contact patch during each integration step is essentially $Dx = V_r \cdot h$. The assumption for uniform nature of motion is justified due to the infinitesimal time step size. Following the positions of the infinitesimal mass dm from the moment it enters the contact patch, until it reaches the trailing edge, (e.g. after n integration steps) is analogous to assuming n number of infinitesimal masses in a row, at the same instant of time. Multiplying the force generated by each mass (analogously at each time-step) with the distance Dx and adding all the products, the total forces applied on the wheel can be calculated. The self-aligning moment can be derived easily by multiplying the individual forces with the distance from axis oz at each time step, prior to the summation process.

3.3.5 Extension of the Simple Tyre Model

The assumption of a parabolic pressure distribution is certainly not valid for all possible operating conditions [46]. This simplification neglects the effects of rolling velocity on the shape of the normal pressure distribution along the contact patch. Rolling at high velocities promotes hysteresis losses and causes a shift of the pressure distribution towards the leading edge. In section 3.3.2.2 the direct link between the hysteresis losses and the shift in the normal pressure distribution is discussed thoroughly. As a result, rolling resistance increases and the frictional potential becomes unevenly distributed. Then the leading part of the contact area would exhibit higher frictional capabilities as compared to its trailing part. Still, the most important deviations from the parabolic shape are attributed to the effect of air pressure acting

on the inside surface of the tyre carcass. The effect is prominent, especially under high vertical loads, when the pressure distribution becomes more trapezoidal than parabolic. These phenomena are completely overlooked by the simple tyre model. A modified model is required with provision for on-line calculation of the normal pressure distribution, based on the overall normal force applied on the wheel hub and the rolling velocity of the tyre.

3.3.5.1 Physical-Mathematical Description of the Improved Tyre Model

A mechanism needs to be incorporated in order to simulate the build-up of the normal component of pressure along the tyre contact patch. For this purpose, a number of modifications are made to the simple tyre model. Firstly, radial and tangential Kelvin elements are introduced. Secondly, a vertical Kelvin element is used for the connection between the infinitesimal mass and the ground. The vertical Kelvin element mainly represents the properties of the tread in the vertical direction, while the combined effect of tangential and radial compliance replaces the longitudinal stiffness and damping of the bristles. The modified tyre model is shown in figure 3.28.

It is noted that x_r, x_t and z denote the deformations of the radial, tangential and vertical Kelvin elements respectively, with respect to their un-deformed state, i.e. prior entering the contact patch. All three deformations are considered positive when the corresponding elements are compressed and negative when the elements are stretched.

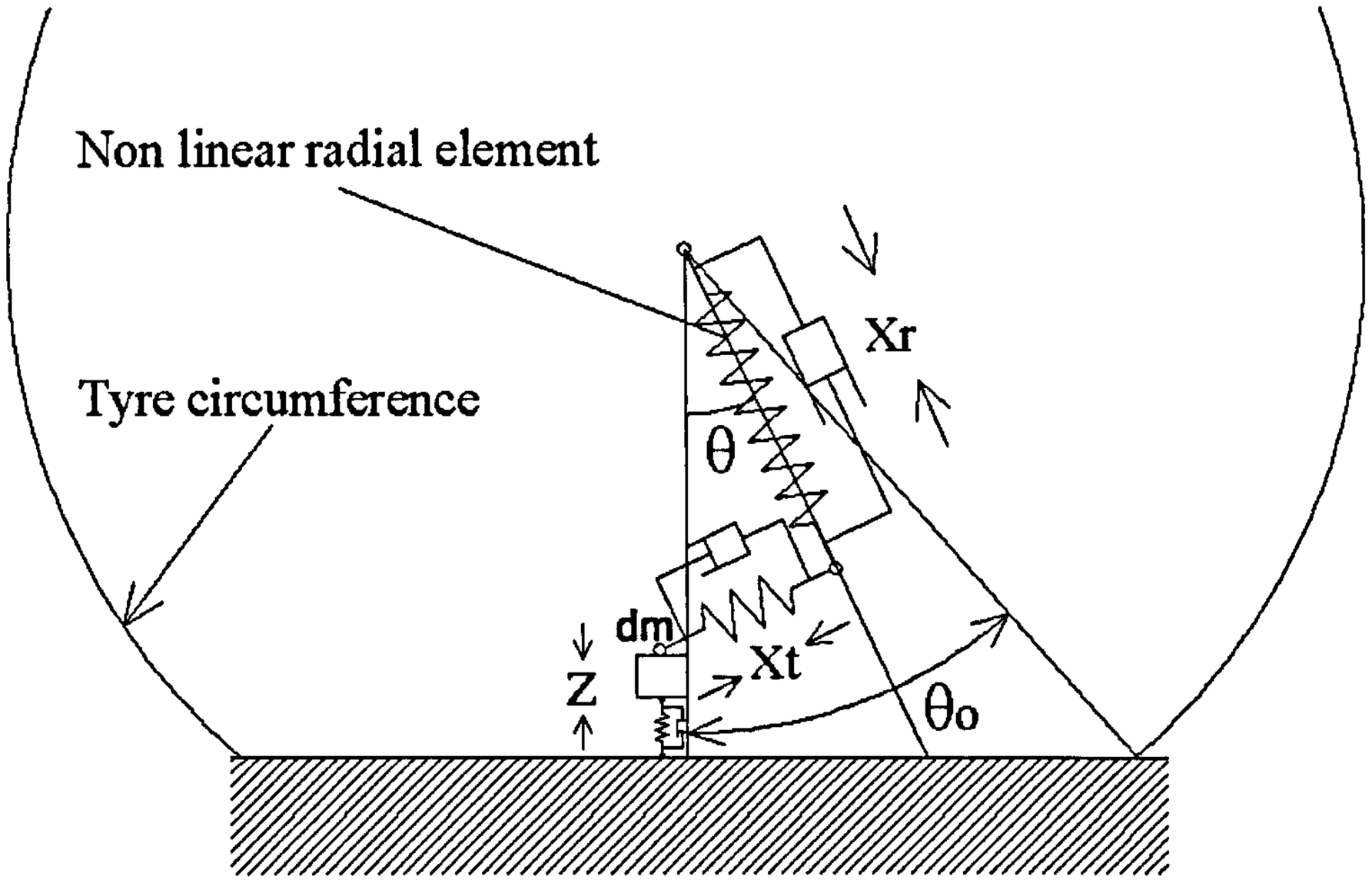

Figure 3. 28 The advanced tyre model with radial, tangential and vertical degrees of freedom

The motion of one representative discrete segment of mass *dm* is followed throughout the contact patch. It is assumed that prior to entering the contact patch, no radial, tangential or vertical compression exists. As the infinitesimal mass travels along the contact, the overall vertical compression of the tyre is undertaken by the radial, tangential and normal Kelvin elements. If one considers a segment of the tread, lying well within the contact patch, and a normal force large enough to generate a significant radial deflection, it becomes apparent that the contact pressure generated at the specific point between the tread and the road should be balanced by the air pressure inside the tyre. If, moreover, the air pressure is considered constant and independent of the normal deflection of the tyre, any increase in normal force should be undertaken by a subsequent increase in the overall contact area. As a consequence, the pressure generated within the inner part of the contact area remains approximately constant, resulting in a smoothened trapezoidal shape of the pressure distribution along the contact patch. This behaviour is handled by implementing a radial elastic force, which saturates as the radial deflection of the tyre increases.

Referring to figure 3.28, equations (3.135)-(3.140) can be re-written as follows, taking into consideration the convention that x_r, x_t and z are positive when they denote compression of the corresponding Kelvin elements and that the positive directions are as indicated by the SAE frame of reference (see fig. 3.10):

$$\dot{u}_x \cdot C \cdot dx = radforce(x_r) \cdot \sin\vartheta \cdot dx - K_t \cdot x_t \cdot \cos\vartheta \cdot dx + D_r \cdot \dot{x}_r \cdot \sin\vartheta \cdot dx - D_t \cdot \dot{x}_t \cdot \cos\vartheta \cdot dx - f_x \tag{3.143}$$

$$\dot{u}_y \cdot C \cdot dx = (y_s - y) \cdot K_y \cdot dx + (V_{syr} - u_y) \cdot D_y \cdot dx - f_y \tag{3.144}$$

$$\dot{u}_z \cdot C \cdot dx = C \cdot g \cdot dx + radforce(x_r) \cdot \cos\vartheta \cdot dx + K_t \cdot x_t \cdot \sin\vartheta \cdot dx + D_r \cdot \dot{x}_r \cdot \cos\vartheta \cdot dx + D_t \cdot \dot{x}_t \cdot \sin\vartheta \cdot dx - K_z \cdot z \cdot dx - D_z \cdot u_z \cdot dx \tag{3.145}$$

$$\dot{x} = u_x \text{ so that } x = \int_0^{travel} u_x dt \tag{3.146}$$

$$\dot{y} = u_y \text{ so that } y = \int_0^{travel} u_y dt \tag{3.147}$$

$$\dot{z} = u_z \text{ so that } z = \int_0^{travel} u_z dt \tag{3.148}$$

$$\dot{y}_s = V_{syr} \text{ so that } y_s = \int_0^{travel} V_{syr} dt \tag{3.149}$$

where:

Function $f(x_r) = radforce(x_r)$ is responsible for the saturation of the radial force as the contact deflection increases and is defined as follows:

$$radforce(x_r) = pb\left(1 - e^{-wx_r}\right),\ w = \lambda(K_r / pb) \tag{3.150}$$

where, p denotes the pressure in $\lfloor N/m^2 \rfloor$, b is the width of the tyre in $[m]$, K_r is the radial stiffness per unit length of the Kelvin element in $\lfloor N/m^2 \rfloor$ and λ is an adjustable parameter given in $\lfloor m^{-1} \rfloor$, responsible for the rate of saturation of the radial force. By differentiating the force function *radforce* with respect to x_r, the radial stiffness function is obtained in $\lfloor N/m^2 \rfloor$. Apparently, λK_r is the radial stiffness per unit length at zero radial compression of the carcass.

Note that in equations (3.146)-(3.149), the duration of travel along the contact t_{travel} is not known *apriori* as is the case in the simple model. Instead, t_{travel} needs to be calculated on-line. Thus, starting from t=0, t_{travel} is the moment when the force generated by the normal Kelvin element reduces to zero, i.e. when contact between the tyre segment and the road surface is lost.

If the state variables of the dynamic system are chosen as $x, y, z, u_x, u_y, u_z, y_s, x_r, x_t$, it becomes clear that the set of differential equations is insufficient to arrive at an analytic solution. Furthermore, the absence of variable x_s adversely affects the definition of longitudinal slip.

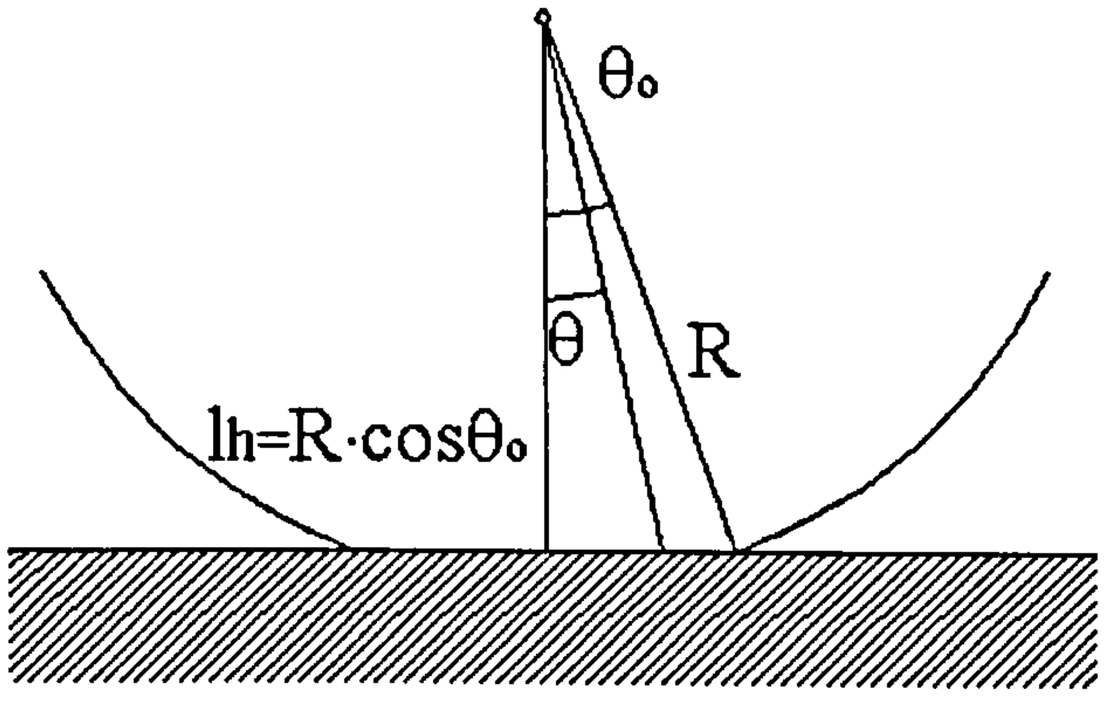

Figure 3. 29 Geometrical constraints for the advanced model

This problem is resolved by introducing a set of kinematic constraints. Referring to figure 3.29, the radius of the tyre prior to entering the contact patch of the vertically loaded rolling tyre is assumed to be R, which is considered to remain constant in the area outside the contact patch and equal to the radius of the unloaded tyre. The angle between R and the vertical line, connecting the tyre centre to the ground is ϑ_o. Given R, the height of the tyre centre above the ground is $l_h = R \cdot \cos\vartheta_o$. This height is assumed to be equal to the radius of the vertically loaded tyre under pure rolling conditions, R_e. Centrifugal effects are neglected, thus when the mass enters the

contact patch, no deflections of the tangential, radial and Kelvin elements are deemed to exist. At an arbitrary position of the mass inside the contact patch, the total deflection ΔR is given by the following scalar constraint function:

$$\Delta R = R - R \cdot \frac{\cos \vartheta_o}{\cos \vartheta} \tag{3.151}$$

The vertical projection of the total deflection ΔR is:

$$\Delta R_{vertical} = \Delta R \cdot \cos \vartheta = R \cdot (\cos \vartheta - \cos \vartheta_o) \tag{3.152}$$

At any instant of time, $\Delta R_{vertical}$ is equal to the vertical deflection of the Kelvin element (i.e. the "local" deflection) added to the vertical components of the deflections of the radial and tangential elements (i.e. the "global" deformation of the continuum), as described in the following equation (see figures 3.28, 3.29):

$$x_r \cdot \cos \vartheta + x_t \cdot \sin \vartheta + x_z = R \cdot (\cos \vartheta - \cos \vartheta_o) \tag{3.153}$$

Analogously, the horizontal components of the deflections of the radial and tangential elements are equal to $x_s - x$, which represent the distances between the base and the tip of the bristles, as defined previously for the simple tyre model. Consequently, the following constraint function also holds true:

$$x_r \cdot \sin \vartheta - x_t \cdot \cos \vartheta = x_s - x \tag{3.154}$$

Equations (3.153), (3.154), provide a way of expressing x_r, x_t with respect to x, x_s and ϑ, while their derivatives provide two more relations, which include velocities $\dot{x}_r, \dot{x}_t, \dot{\vartheta} = \Omega$, as follows:

$$\dot{x}_r \cdot \cos \vartheta - x_r \cdot \Omega \cdot \sin \vartheta + \dot{x}_t \cdot \sin \vartheta + x_t \cdot \Omega \cdot \cos \vartheta + u_z = -R \cdot \Omega \cdot \sin \vartheta \tag{3.155}$$

$$\dot{x}_r \cdot \sin \vartheta + x_r \cdot \Omega \cdot \cos \vartheta - \dot{x}_t \cdot \cos \vartheta + x_t \cdot \Omega \cdot \sin \vartheta = V_{sx} - u_x \tag{3.156}$$

Relations (3.153)-(3.156) result in the omission of variables $x_r, x_t, \dot{x}_r, \dot{x}_t$ and enable the formulation of the system of differential equations in a way that x_s is retained as a state variable, thus providing a means for the definition of longitudinal slip.

The rate of change of angle ϑ can be obtained by solving the equation of motion of the wheel for the rotational degree of freedom, while height l_h, or alternatively angle ϑ_o (for a given radius R) can be obtained by solving the equation of motion of the wheel for the vertical degree of freedom. For an unsuspended quarter-car model as shown in figure 3.30, the equations of motion can be summarised as follows:

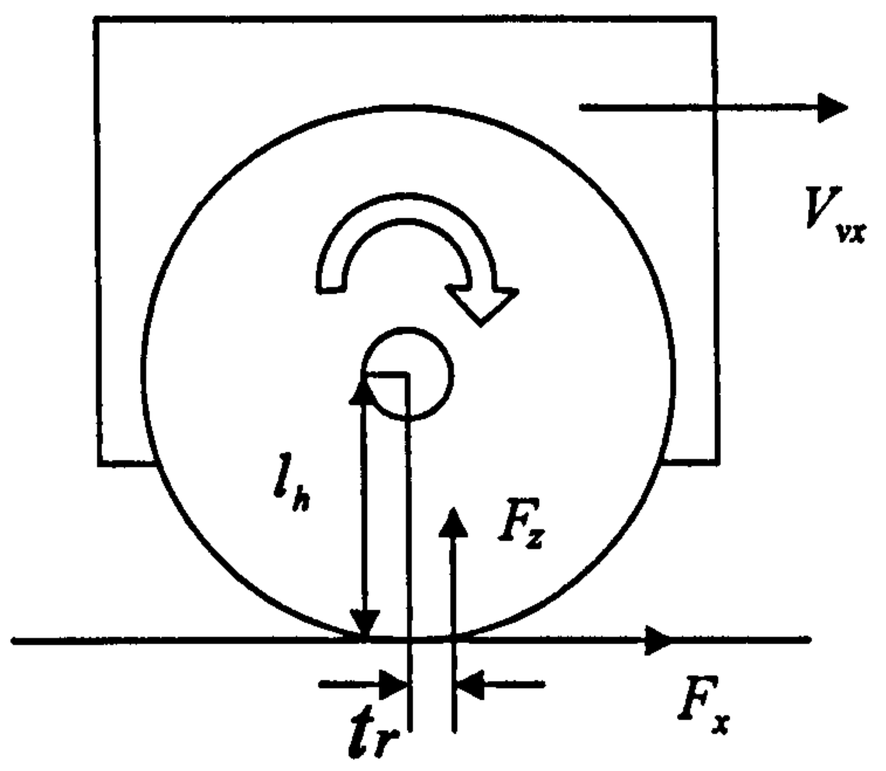

Figure 3. 30 Integration of wheel-tyre dynamics

$$\dot{u}_x \cdot C \cdot dx = radforce(x_r) \cdot \sin\vartheta \cdot dx - K_t \cdot x_t \cdot \cos\vartheta \cdot dx + D_r \cdot \dot{x}_r \cdot \sin\vartheta \cdot dx - D_t \cdot \dot{x}_t \cdot \cos\vartheta \cdot dx - f_x \quad (3.157)$$

$$\dot{u}_y \cdot C \cdot dx = (y_s - y) \cdot K_y \cdot dx + (V_{syr} - u_y) \cdot D_y \cdot dx - f_y \quad (3.158)$$

$$\dot{u}_z \cdot C \cdot dx = C \cdot g \cdot dx + radforce(x_r) \cdot \cos\vartheta \cdot dx + K_t \cdot x_t \cdot \sin\vartheta \cdot dx + D_r \cdot \dot{x}_r \cdot \cos\vartheta \cdot dx + D_t \cdot \dot{x}_t \cdot \sin\vartheta \cdot dx - K_z \cdot z \cdot dx - D_z \cdot u_z \cdot dx \quad (3.159)$$

$$\dot{x} = u_x \text{ so that } x = \int_0^{travel} u_x dt \quad (3.160)$$

$$\dot{y} = u_y \text{ so that } y = \int_0^{travel} u_y dt \tag{3.161}$$

$$\dot{z} = u_z \text{ so that } z = \int_0^{travel} u_z dt \tag{3.162}$$

$$\dot{x}_s = V_{sx} \text{ so that } x_s = \int_0^{travel} V_{sx} dt \tag{3.163}$$

$$\dot{y}_s = V_{syr} \text{ so that } y_s = \int_0^{travel} V_{syr} dt \tag{3.164}$$

$$V_{syr} = V_{sy} + \left(\dot{\psi} - \Omega \cdot \sin\gamma\right) \cdot x_L \tag{3.165}$$

$$\dot{x}_L = -V_r \text{ so that } x_L = \mathrm{a} + \int_0^{travel} -V_r dt \tag{3.166}$$

$$x_r \cdot \cos\vartheta + x_t \cdot \sin\vartheta + x_z = R \cdot \left(\cos\vartheta - \cos\vartheta_o\right) \tag{3.167}$$

$$x_r \cdot \sin\vartheta - x_t \cdot \cos\vartheta = x_s - x \tag{3.168}$$

$$\dot{x}_r \cdot \sin\vartheta + x_r \cdot \Omega \cdot \cos\vartheta - \dot{x}_t \cdot \cos\vartheta + x_t \cdot \Omega \cdot \sin\vartheta = V_{sx} - u_x \tag{3.169}$$

$$\dot{x}_r \cdot \cos\vartheta - x_r \cdot \Omega \cdot \sin\vartheta + \dot{x}_t \cdot \sin\vartheta + x_t \cdot \Omega \cdot \cos\vartheta + u_z = -R \cdot \Omega \cdot \sin\vartheta \tag{3.170}$$

$$I \cdot \dot{\Omega} = T_{d,b} - F_z \cdot t_r - F_x \cdot l_h \tag{3.171}$$

$$\dot{\vartheta} = \Omega \tag{3.172}$$

$$M \cdot \frac{d^2(l_h)}{dt^2} = M \cdot g - F_z \tag{3.173}$$

$$M \cdot \dot{V}_{vx} = F_x \tag{3.174}$$

$$V_{sx} = V_{vx} - \Omega \cdot R_e \tag{3.175}$$

where, I denotes the polar moment of inertia of the wheel, M the quarter car mass, g the acceleration of free fall, V_{vx} the forward velocity of the vehicle, F_x the longitudinal force generated by the tyre, $T_{d,b}$ the driving or braking torque, F_z the resultant normal force and t_r the length of the lever between the normal force and the tyre centre.

The block diagram in figure 3.31 shows the interactions between contact mechanics of tyre-road pair and the inertial rigid body dynamics of the vehicle-wheel sub-system.

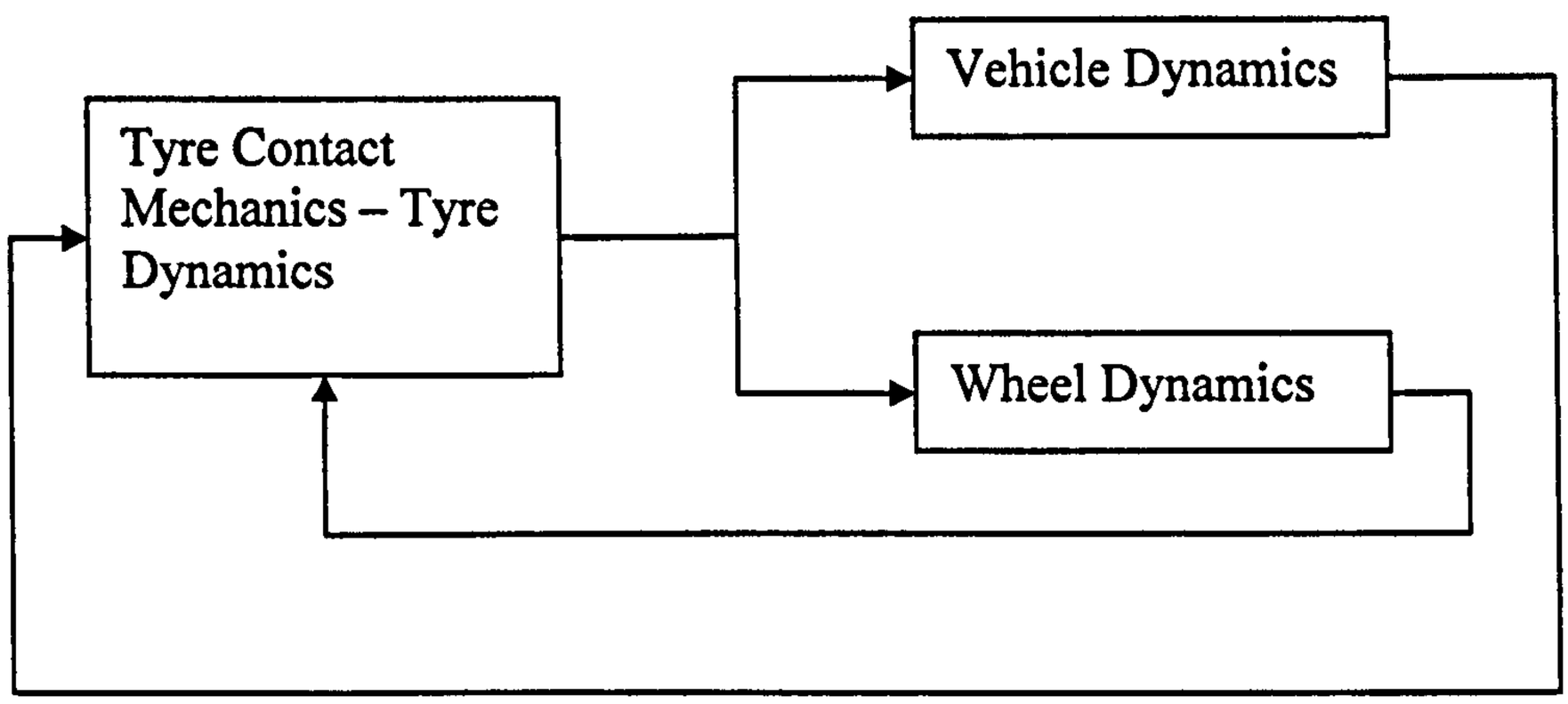

Figure 3. 31 A block diagram showing the vehicle-wheel-tyre interaction

Very often, in vehicle handling analyses the vertical degree of freedom of the wheel is not included in the description of the vehicle-wheel-tyre system. Alternatively, the force applied by the suspension to the wheel hub is used as an estimation of the normal load undertaken by the tyre. Hence, it is assumed that at any instant of time the contact pressure along the contact patch balances the vertical component of the suspension force. For a given tyre, the normal pressure distribution predicted by the modified version of the tyre model depends on the contact angle ϑ_0 and the linear velocity of rolling V_r. In the event that the tyre model is required to operate with the normal load as an input, a surface plot is needed, providing angle ϑ_0 as a function of

the normal load F_z and velocity V_r. For this purpose, the tyre model can run for a combination of velocities and contact angles. For each combination, the generated normal force is recorded, and finally the results are plotted in a way that contact angle ϑ_0 appears as a function of the normal load F_z and velocity V_r, as shown in figure 3.32. This pre-processing procedure is carried out only once for each individual tyre. The results are stored and the data is used for estimating contact angle ϑ_0 through linear, 2-dimensional interpolation.

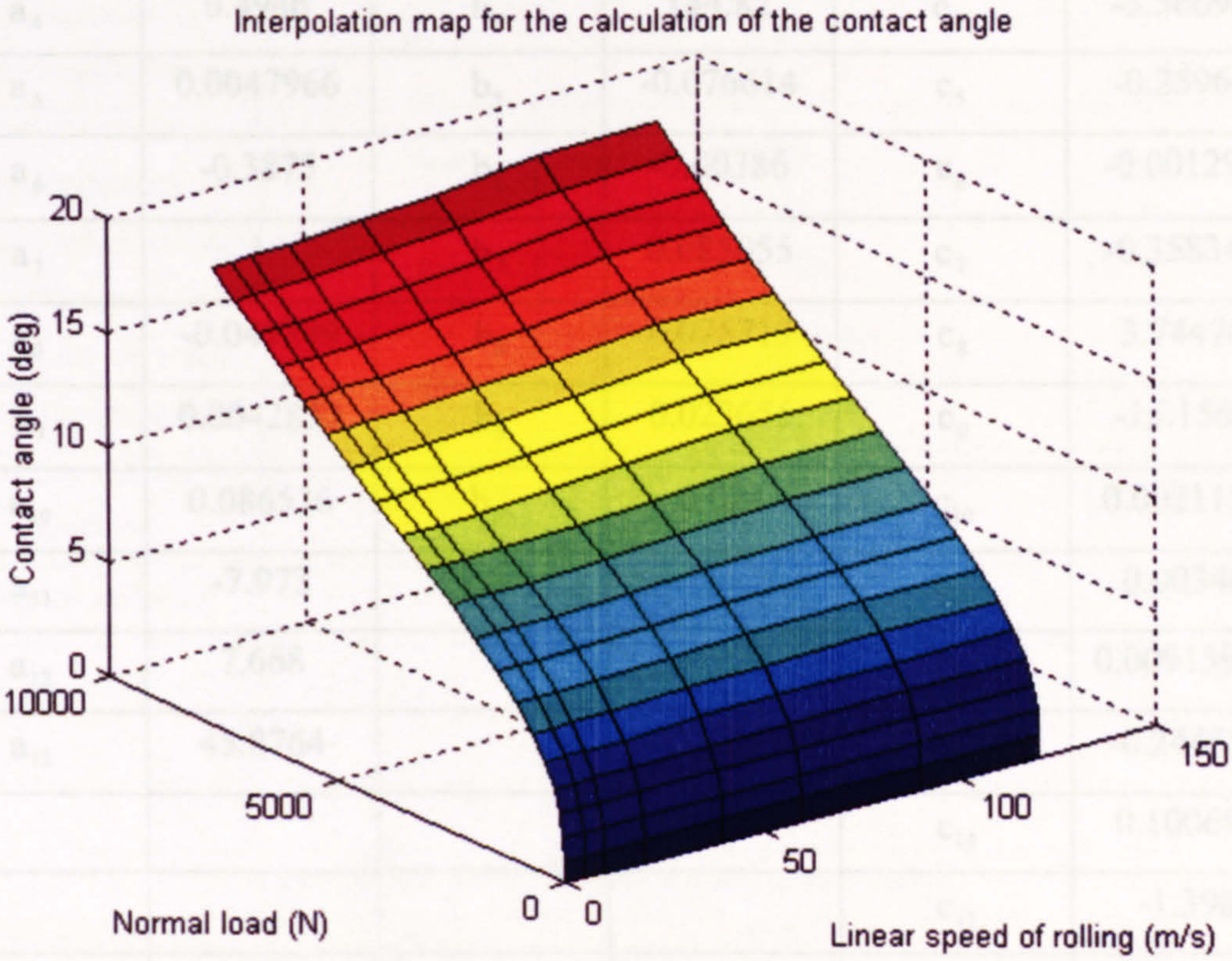

Figure 3. 32 Surface plot of the contact angle vs load and velocity

3.3.6 Simulation Results

Both the simple and modified models are solved numerically following the procedure described in section 3.3.4.7. In addition, both models use the modified friction law incorporating anisotropy in the lateral and longitudinal directions, as well as velocity dependent coefficients of kinetic friction (see relations (3.124)-(3.128)).

Table 3.3

Magic formula coefficients (after [105])

Lateral force		Brake force		Self aligning moment	
a_0	1.6929	b_0	1.65	c_0	2.2264
a_1	-55.2084	b_1	-7.6118	c_1	-3.0428
a_2	1271.28	b_2	1122.6	c_2	-9.2284
a_3	1601.8	b_3	-0.00736	c_3	0.5
a_4	6.4946	b_4	144.82	c_4	-5.56696
a_5	0.0047966	b_5	-0.076614	c_5	-0.25964
a_6	-0.3875	b_6	-0.00386	c_6	-0.001297
a_7	1	b_7	0.085055	c_7	-0.358348
a_8	-0.045399	b_8	0.075719	c_8	3.74476
a_9	0.0042832	b_9	0.023655	c_9	-15.1566
a_{10}	0.086536	b_{10}	0.024	c_{10}	0.0021156
a_{11}	-7.973			c_{11}	0.00346
a_{12}	7.668			c_{12}	0.00913952
a_{13}	45.8764			c_{13}	-0.244556
				c_{14}	0.100695
				c_{15}	-1.398
				c_{16}	0.44441
				c_{17}	-0.998344

Table 3.4

Parameters for the simple tyre model

Parameter Description	Symbol	Value	Units
Tyre Radius	R	0.29	$[m]$
Contact patch width	b	0.185	$[m]$

Longitudinal damping	D_x	8e2	$[Ns/m^2]$
Lateral damping	D_y	8e2	$[Ns/m^2]$
Longitudinal stiffness	K_x	1.2e7	$[N/m^2]$
Lateral stiffness	K_y	1.17e7	$[N/m^2]$
Mass per unit length	C	2	$[Kg/m]$
Long. coeff. of static fr.	μ_{sx}	1.3	-
Lat. coeff. of static fr.	μ_{sy}	1.3	-
Friction reduction factor (longitudinal)	μ_{xred}	0.65	-
Friction reduction factor (lateral)	μ_{yred}	0.65	-
Friction reduction rate factor (longitudinal)	qx	0.07	$[s/m]$
Friction reduction rate factor (longitudinal)	qy	0.07	$[s/m]$
Friction velocity threshold	$threshold$	0.012	$[m/s]$
Normal stiffness	Cz	2.89e5	$[N/m]$

Table 3.5

Parameters for the advanced tyre model

Parameter Description	Symbol	Value	Units
Tyre Radius	R	0.29	$[m]$
Contact patch width	b	0.185	$[m]$
Tangential damping	D_t	8e2	$[Ns/m^2]$
Lateral damping	D_y	8e2	$[Ns/m^2]$
Radial damping	D_r	1.6e3	$[Ns/m^2]$
Vertical damping	D_z	1e4	$[Ns/m^2]$
Tangential stiffness	K_t	1.2e7	$[N/m^2]$
Lateral stiffness	K_y	1.17e7	$[N/m^2]$

Radial stiffness	K_r	4.8e6	$[N/m^2]$
Vertical stiffness	K_z	4e7	$[N/m^2]$
Mass per unit length	C	2	$[Kg/m]$
Long. coeff. of static fr.	μ_{sx}	1.3	-
Lat. coeff. of static fr.	μ_{sy}	1.3	-
Friction reduction factor (longitudinal)	μ_{xred}	0.65	-
Friction reduction factor (lateral)	μ_{yred}	0.65	-
Friction reduction rate factor (longitudinal)	qx	0.07	$[s/m]$
Friction reduction rate factor (longitudinal)	qy	0.07	$[s/m]$
Friction velocity threshold	$threshold$	0.012	$[m/s]$
Air pressure	p	2.3e5	$[N/m^2]$
Rate of pressure saturation	λ	4	$[m^{-1}]$

Simulation results are compared with results obtained using the version of the Magic Formula model described in section 3.3.3.3. The Magic Formula coefficients are taken from reference [105], and are included in table 3.3. The parameters of the models are identified, using the lateral force characteristics under pure cornering conditions and the brake force characteristics under pure braking conditions, as generated by the Magic Formula model for a reference normal load of 4 KN. Based on these graphs, the optimum values of the coefficients involved in the calculation of friction and the stiffness of the tyre in the lateral and longitudinal directions can be easily estimated. The parameter identification procedure is performed separately for the cornering and braking forces, using the MATLAB function *fmins* [115]. The parameter vector $\mathbb{P}$ is given below for the cases of cornering and braking, both for the simple and advanced models:

a. Cornering

- Simple model:

$$\mathbb{P} = \begin{bmatrix} K_y & \mu_{ys} & \mu_{yred} & q_y \end{bmatrix}^T \tag{3.176}$$

- Advanced model:

$$\mathbb{P} = \begin{bmatrix} K_y & \mu_{ys} & \mu_{yred} & q_y \end{bmatrix}^T \tag{3.177}$$

b. Braking

- Simple model:

$$\mathbb{P} = \begin{bmatrix} K_x & \mu_{xs} & \mu_{xred} & q_x \end{bmatrix}^T \tag{3.178}$$

- Advanced model:

$$\mathbb{P} = \begin{bmatrix} K_t & \mu_{xs} & \mu_{xred} & q_x \end{bmatrix}^T \tag{3.179}$$

It can be seen that while both models use the same parameters for cornering, in the case of braking, parameter K_x of the simple model is replaced by K_t of the advanced model.

It follows from the analysis in section 3.3.3, that the magic formula generates velocity independent results. Since the friction law in both models is velocity dependent and predicts different friction for the same slip angle at various operating velocities, the objective function for the case of cornering uses values from two runs, one at 30 m/s and one at 60 m/s. The run at 30 m/s is used for determining mainly the value of K_y and considers low side-slip angles, say from 0 up to 2.5 deg. The run at 60 m/s affects mainly the remaining optimisation parameters of vector $\mathbb{P}$ and uses high side-slip angles, say from 8 to 15 deg. The objective function for the cornering case is shown below, using 3 force values from the low-slip range and 3 force values from the high-slip range, at 30 and 60 m/s respectively:

Objective function for the case of cornering:

$$Ob_c(\mathbb{P}) = \sum_{i=1}^{3}\left(F_{y(Magic)}(a_i) - F_{y(Model)}(a_i)\right)^2_{(30m/s)} + \sum_{j=1}^{3}\left(F_{y(Magic)}(a_j) - F_{y(Model)}(a_j)\right)^2_{(60m/s)} \tag{3.180}$$

where $a_i \in (0^o, 2.5^o)$ and $a_j \in (8^o, 15^o)$

In the case of braking, a single run at 30 m/s is used for the identification of the parameters in vector $\mathbb{P}$. Since braking characteristics extend almost until wheel lock, a higher forward velocity, for example 60 m/s, would generate extremely high sliding velocities which initially are thought to be unreasonable for the estimation of the friction parameters. Of course, if experimental results exist for such high velocities then they can be used for the estimation of the parameters. The objective function for the case of braking reads:

Objective function in the case of braking:

$$Ob_b(\mathbb{P}) = \sum_{i=1}^{10}\left(F_{x(Magic)}(k_i) - F_{x(Model)}(k_i)\right)^2_{(30m/s)} \tag{3.181}$$

where $k_i \in (0, 0.9)$

It should be pointed out that details on the values of the structural parameters of the tyre for which the Magic Formula coefficients were obtained were not available separately. Therefore, the comparison procedure and the subsequent analysis of the results are limited to some general observations. For example, while it has been possible to accurately estimate the lateral stiffness of the tyre by demanding the condition of coincidence of the linear parts of the cornering curves, it is impossible to estimate the parameters, such as the radial stiffness and damping factors, using the Magic Formula results. Similarly, there is no way of incorporating the effect of changes in air-pressure into the Magic Formula model; hence no comparisons can be

made with the predictions by the advanced model, which does offer these opportunities. The parameters for the simple and advanced models are given in tables 3.4 and 3.5 respectively. A wide range of test conditions were simulated and the results are critically assessed. The behaviours of the tyre models are explained based on their inherent characteristics and the resulting modelling limitations.

To aid the interpretation of the simulation results, a key to the colours used in the graphs is given in table 3.6.

Table 3.6

Key to colours and line-types used in the graphs

1. Force and torque characteristic curves		
	Line type	Colour
Magic formula	Solid	Blue
Simple model	Solid	Green
Advanced model	Solid	Red
2. Distributions along the contact		
	Line type	Colour
Longitudinal force	Solid	Green
Lateral force	Solid	Red
Total shear force	Solid	Blue
Normal force	Solid	Black
Longitudinal velocity	Dash-dotted	Magenta
Lateral velocity	Solid	Magenta
Note: In cases where only lateral or longitudinal shear forces occur, the solid blue line of the total shear force obscures the relevant red or green lines.		

3.3.6.1 Pure Cornering Manoeuvres

Simulations are carried out initially for the case of pure cornering under steady-state conditions. The curves generated by the two models are compared with the Magic Formula results for a combination of vertical loads and rolling velocities. Figure 3.33 shows the lateral force as predicted by the Magic Formula and the two physical models for a reference load of 4 KN, and a relatively low velocity of 5 m/s. The first

observation is a significant reduction in cornering force predicted by the Magic Formula for large values of side-slip. This is the result of an exceptionally large shape factor (see table 3.3 and equation (3.71)), which is rarely the case in cornering force characteristic curves. The behaviour of the two physical models is determined by the sideways sliding velocity, which is kept low in order to maintain equivalent slip angles, taking into account the low value of forward velocity. This means that equation (3.128) does not predict a significant reduction in the coefficient of kinetic friction and, therefore, the side force cannot exhibit a similar reduction as the one predicted by the Magic Formula. Any attempt to further increase μ_{yred} or qy in order to improve agreement between the curves would result in bad quality curves for higher running velocities. In particular, higher values of qy might lead to abrupt changes in the slope of the cornering curve, especially at higher velocities.

The self-aligning torque characteristics, generated by the three models, are plotted in figure 3.34. It is important to emphasise the fact that none of the parameters of the physical models are manipulated in order to improve coincidence of the moment curves, as the parameter identification procedure relies only on the cornering characteristics. Besides a generally acceptable agreement of the results, it is noteworthy that both physical models predict a self-aligning moment converging to zero for large values of side-slip. Taking into consideration the completely symmetrical parabolic pressure distribution used in the simple physical model, this prediction is completely justified. On the other hand, low rolling velocity reduces hysteresis phenomena and results in an almost symmetrical trapezoidal pressure distribution, as predicted by the advanced model. Consequently, when sliding occurs throughout the length of the contact patch, the more or less symmetrical distribution of the lateral force leads to a diminished self- aligning moment.

Figures 3.35 and 3.36 illustrate the force distributions along the contact patch, as predicted by the advanced physical model. It is shown that for such a low rolling velocity, the normal pressure distribution is approximately symmetrical with respect to the projection of the centre of the wheel onto the road surface. Figure 3.35 corresponds to a small slip angle, showing the linear build-up of the lateral force as a result of lateral deformation, starting from the leading edge of the contact patch, on the right-hand side of the graph. When the adhesion limit is reached, the deformation

of the tyre segment (or the infinitesimal mass) is governed mainly by the interaction between elastic forces and kinetic friction. The contribution of damping remains insignificant, considering the low rolling velocity of the tyre. Figure 3.36 depicts tyre sliding throughout the length of the contact patch. The previous triangular, non-symmetrical lateral force has now turned into a symmetrical smoothened trapezoidal shape. Again, because of a relatively low sliding velocity, the coefficient of kinetic friction attains a value near the coefficient of static friction, the latter being greater than unity. Thus, the trapezoidal lateral force contains the normal force distribution throughout the contact patch.

Figures 3.37 and 3.38 show the cornering force and the self-aligning moment characteristics for a practically more interesting forward velocity of 30 m/s. By observing figure 3.37, it becomes evident that the exponentially decreasing coefficient of friction has now come into play. Still, the physical models do not seem to be capable of producing such a prominent peak as the one predicted by the Magic Formula. In figure 3.38, the simple model has generated a self-aligning moment characteristic similar to the one shown in figure 3.34. Obviously, the increase in rolling velocity does not alter the symmetry of the normal pressure distribution, which in turn affects the self-aligning moment. On the contrary, the absolute value of the peak moment, generated by the advanced model, shows a significant reduction, whilst at large values of side-slip the moment changes sign, showing much better agreement with the moment predicted by the Magic Formula.

The force distribution along the contact patch of the advanced tyre model is shown in figure 3.39 for a low value of side-slip. The increase in rolling velocity promotes hysteresis and has led to the generation of a peak in the normal pressure distribution towards the leading edge of the contact patch. At low slip angles the triangular shape of the lateral force distribution is maintained and results in the generation of a negative self-aligning torque. At this point an interesting observation can be made. Referring to figure 3.32, a slight increase in the contact angle ϑ_o is predicted for a given vertical load, as the linear velocity of rolling increases. In addition, a comparison between figures 3.35 and 3.39 shows a slight reduction in the total length of the contact patch with an increase in the rolling velocity. Essentially, combination of the two leads to a shift of the contact patch towards the front of the tyre. The

triangular lateral force distribution corresponds to relatively small slip angles. This is responsible for the disposition of the peak self-aligning torque towards the leading edge of the contact, and thus its torque generating potential is reduced. The normal pressure distribution as predicted by the advanced model directly influences the generation of self-aligning torque, and explains the physical mechanism behind the reduction of the peak aligning torque observed in figure 3.38. A further comparison between figures 3.35 and 3.39 reveals the influence of the radial and tangential damping elements. In figure 3.35 the longitudinal force intensity at the very beginning of the contact is practically equal to zero, while figure 3.39 and some subsequent figures demonstrate a non-zero longitudinal force. This is attributed to the non-zero rates of deflection in the radial and tangential direction as soon as a representative tread element enters the contact. The effect is intensified as the rolling velocity increases, hence the difference between figure 3.35 and 3.39. Figure 3.40 depicts the force distribution along the contact patch for a tyre running at a large slip angle. The shape of the lateral force distribution agrees with the shape of the normal pressure distribution. Because of sliding at a higher velocity, the coefficient of kinetic friction has reduced enough so that the lateral force distribution is contained within the normal force. Figures 3.41 and 3.42 show the equivalent force distributions, predicted by the simple physical model for low and high slip angles. The parabola representing the normal force distribution remains completely symmetrical throughout the velocity range, resulting in an almost velocity independent self-aligning torque.

Figures 3.43 and 3.44 show results obtained at an even higher rolling velocity of 60 m/s. In figure 3.43, the tendency of the lateral force to reduce even further at larger slip angles determines the downward slope of the cornering curves at the saturated region of tyre operation. Similarly, in figure 3.44, the absolute value of the maximum self-aligning moment, predicted by the advanced model, shows a further decrease, while at large slip angles the self-aligning moment obtains a slightly higher value than that predicted by the Magic Formula.

In figures 3.45 and 3.46 the trapezoidal shape of the normal pressure distribution has deteriorated completely due to intensive hysteresis phenomena. The length of the contact patch has reduced further, and moved towards the front of the tyre. This, in combination with the pronounced peak of the normal force near the leading edge,

explains the aforementioned alterations observed in the self-aligning torque characteristics predicted by the advanced model.

Pure cornering tests continue with an investigation of the effect of different normal loads at a reference forward velocity of 30 m/s. Figures 3.47 and 3.48 show the force and moment results for a vertical load of 2KN. The peak lateral force predicted by both physical models has reduced significantly compared to the peak generated by the Magic Formula. This behaviour can be explained by taking into consideration the fact that the peak coefficient of friction is not load dependent for the two physical models. On the contrary, as indicated by the relation (3.73), the peak coefficient of friction used in the Magic Formula reduces as normal load increases. A simple solution would be to use the relation (3.73) for the calculation of the peak coefficient of friction for the physical models. Alternatively, the parameters involved in the relation (3.16) could be obtained by appropriate experiments.

The force distribution along the contact patch, as predicted by the advanced model for a normal load of 2 KN, is given in figures 3.49 and 3.50 for low and high values of side-slip respectively. It is shown that under the application of a reduced normal load, the radial deformation near the centre of the contact is not sufficient in order to generate a trapezoidal pressure distribution. For this specific combination of normal load and rolling velocity, a trapezoidal distribution is just about to form, yet the shape of the distribution still resembles more to a slightly shifted parabola.

The lack of a load-dependent coefficient of friction is also evident in figure 3.51, showing the lateral force characteristics for an increased normal load of 6 KN. The forces generated by the physical models seem to have increased almost proportionally to the normal load, exceeding significantly the forces predicted by the Magic Formula. In figure 3.52, it is shown that under heavily loaded conditions, the parabolic pressure distribution leads to large deviations in the calculation of self-aligning torque, especially with large slip angles, where the Magic Formula and advanced physical model predict a rise of the torque well above zero, as opposed to the zero torque calculated by the simple model. Figures 3.53 and 3.54 deal with the force distribution under the application of a high vertical load, and show clearly the effect of the non-linear radial stiffness in the predictions of the advanced physical model.

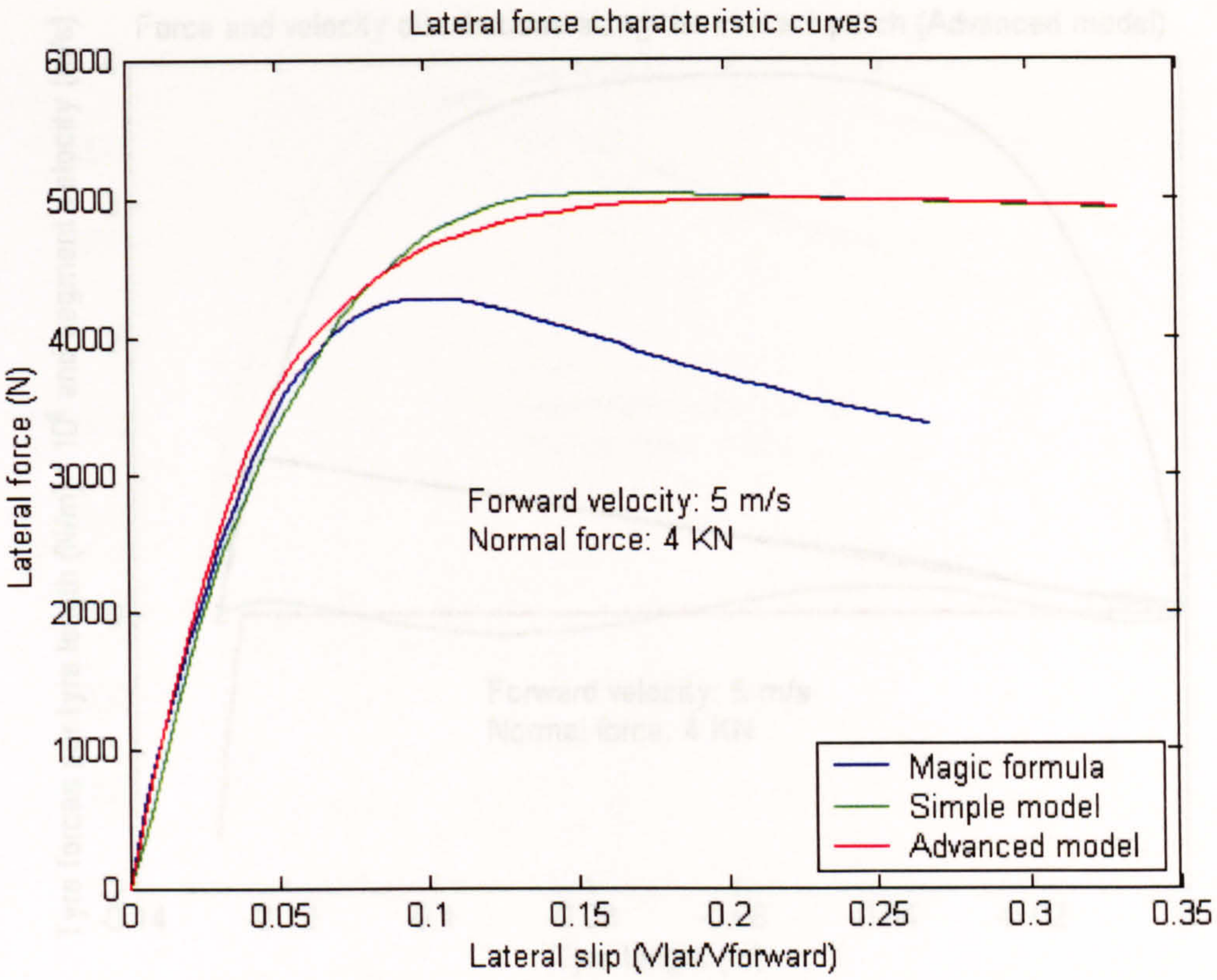

Figure 3. 33 Cornering force for 4KN load and 5 m/s forward velocity

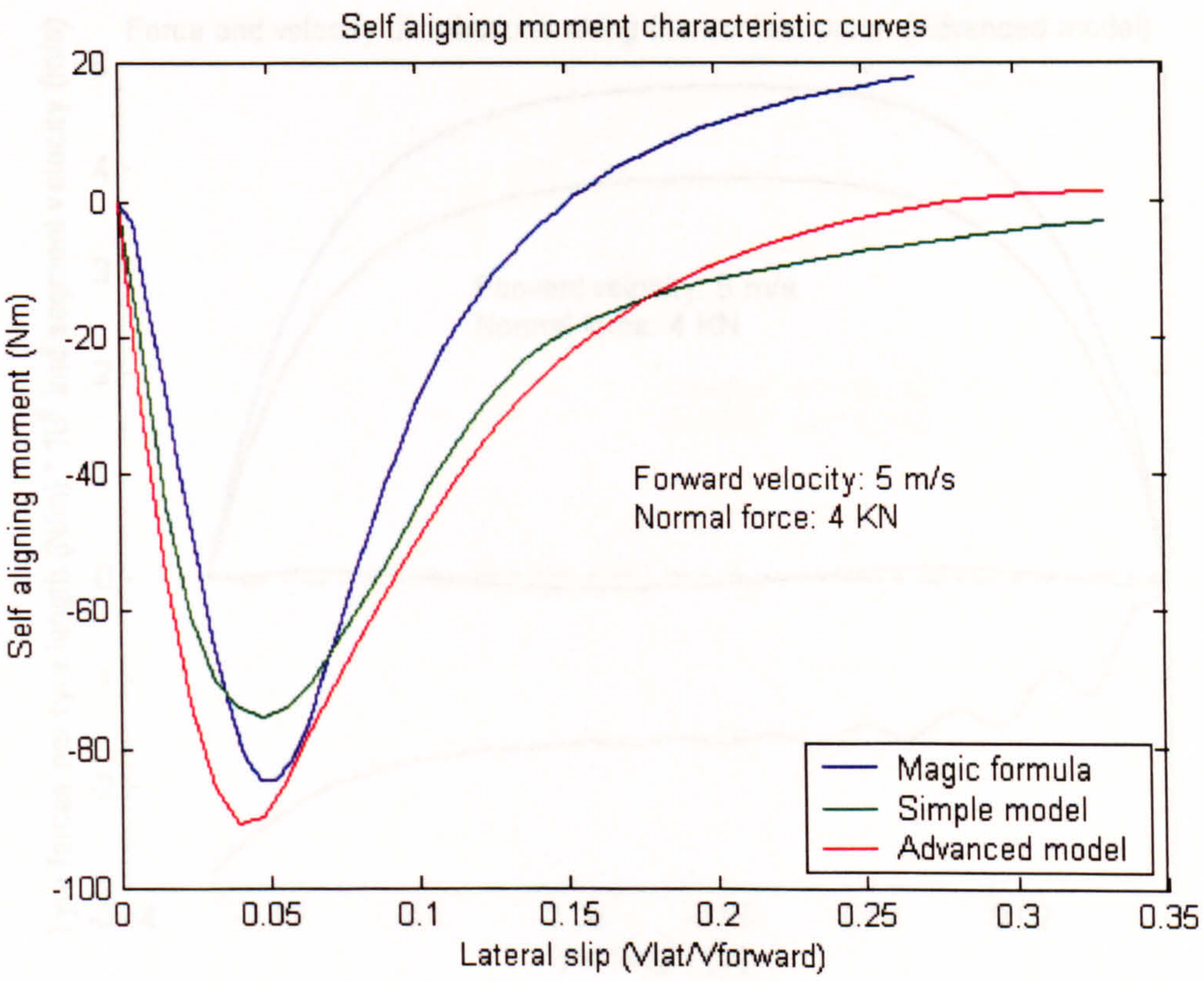

Figure 3. 34 Self-aligning moment for 4KN load and 5 m/s forward velocity

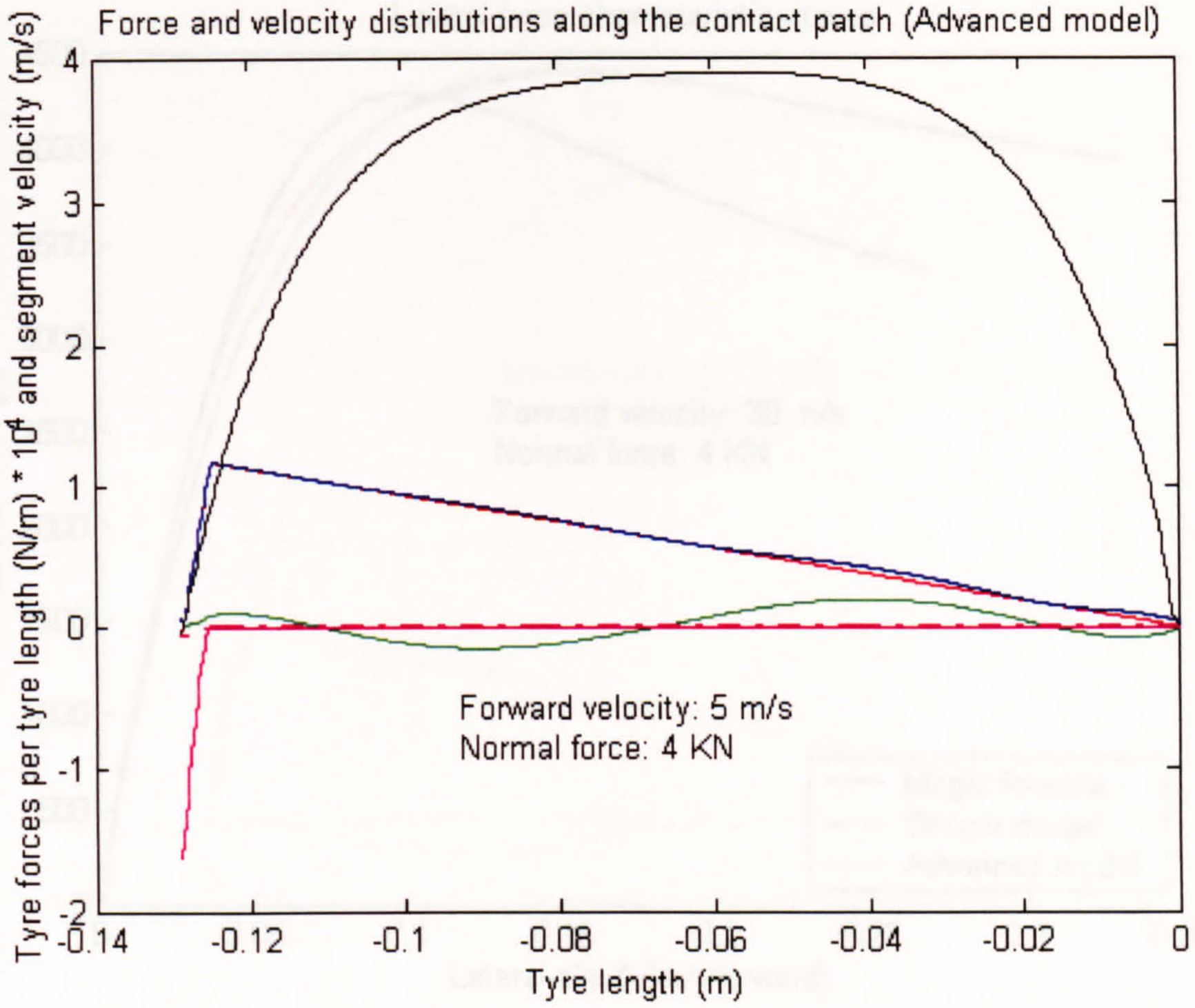

Figure 3. 35 Force distribution along the contact patch at 0.46° slip angle

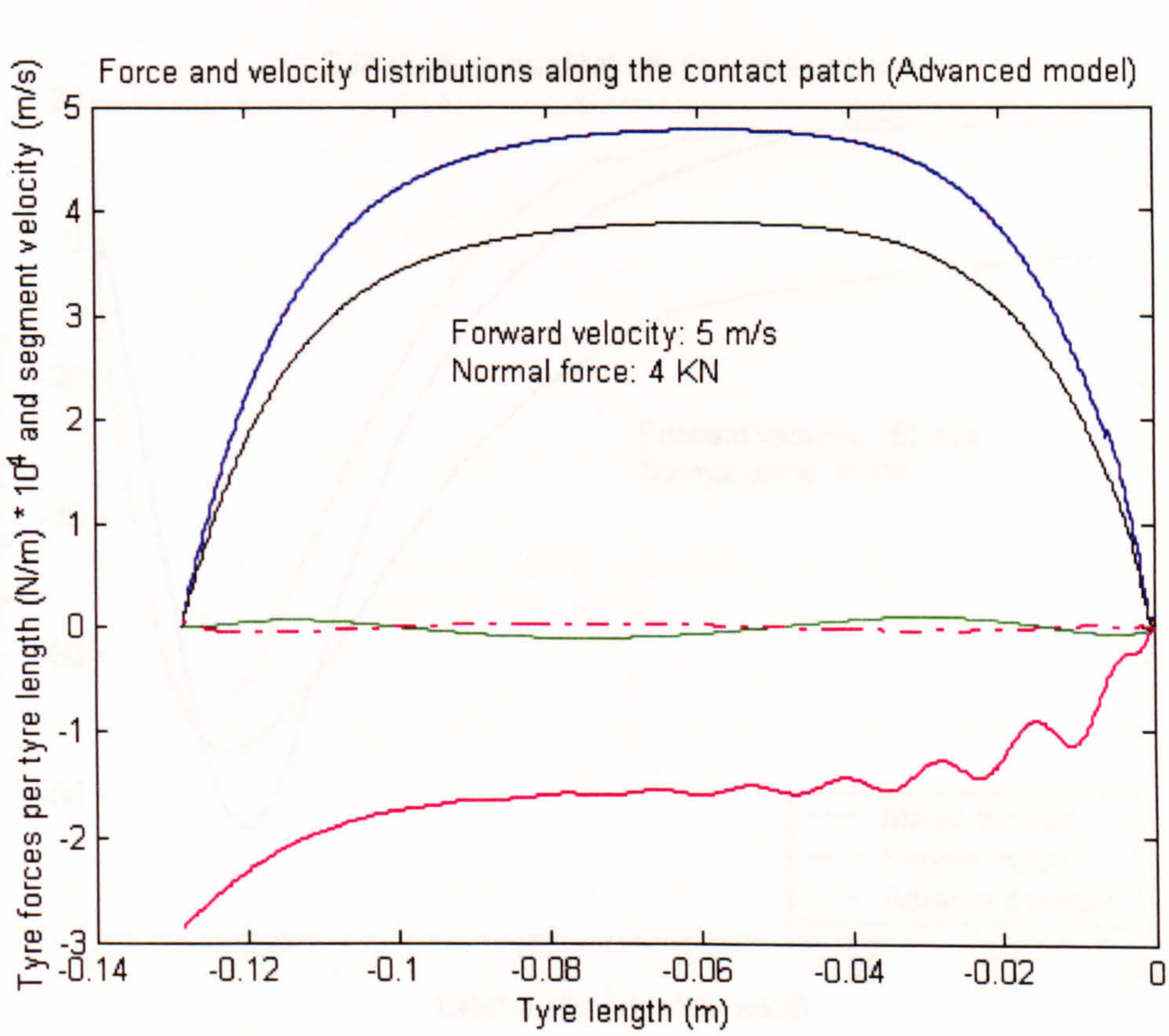

Figure 3. 36 Force distribution along the contact patch at 17.75° slip angle (saturated area of operation)

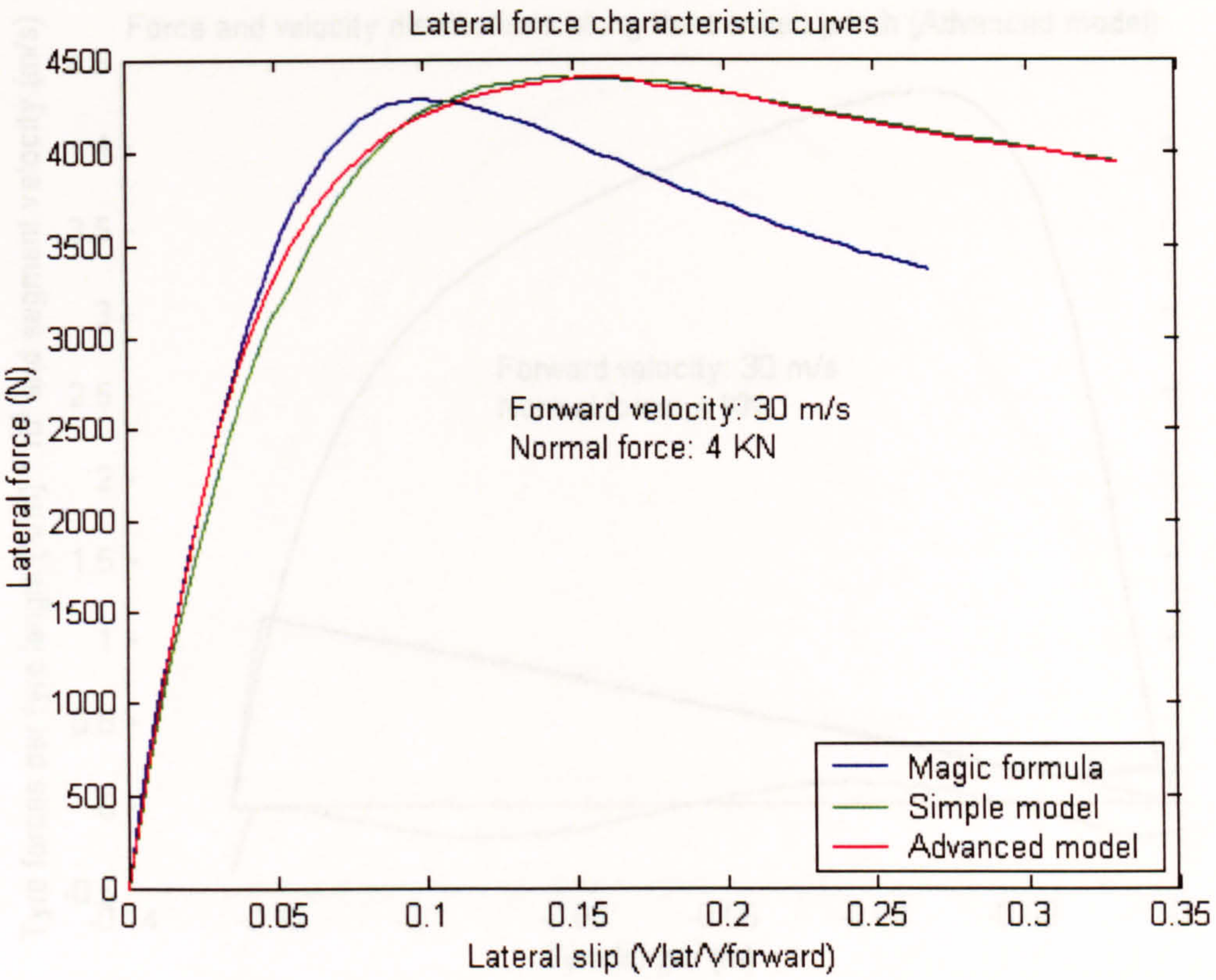

Figure 3. 37 Cornering force for 4KN load and 30 m/s forward velocity

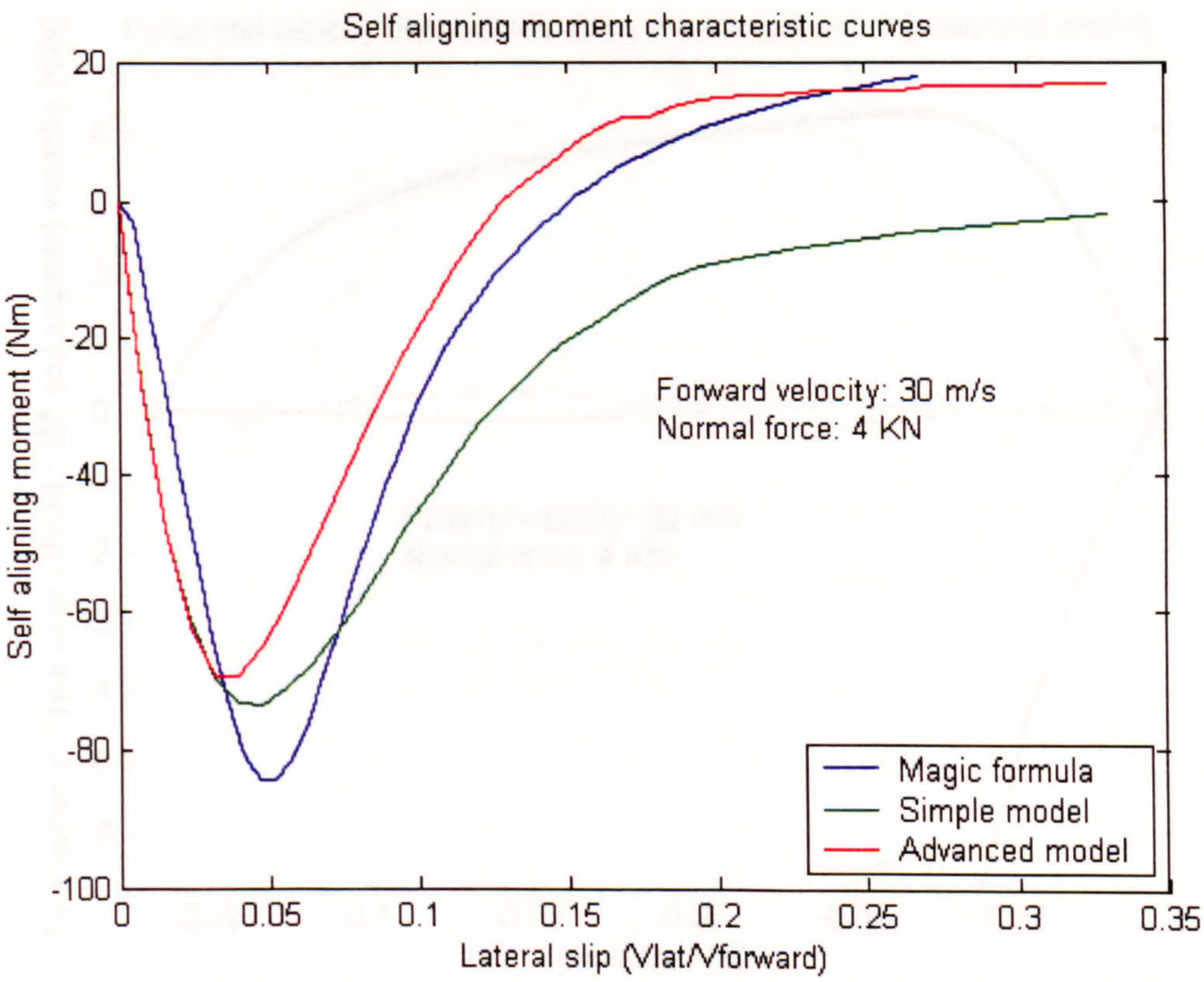

Figure 3. 38 Self-aligning moment for 4KN load and 30 m/s forward velocity

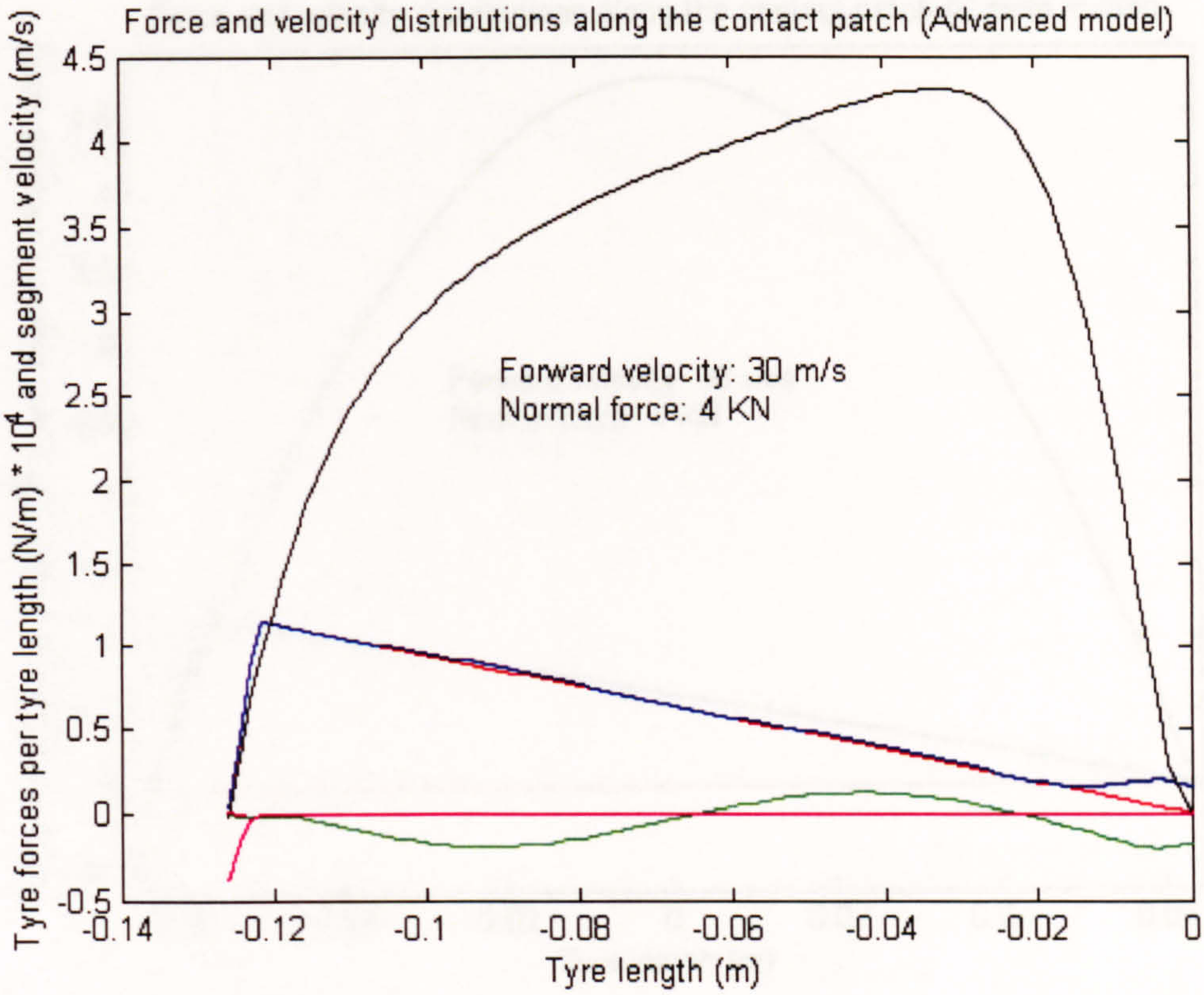

Figure 3. 39 Force distribution along the contact patch at 0.46° slip angle

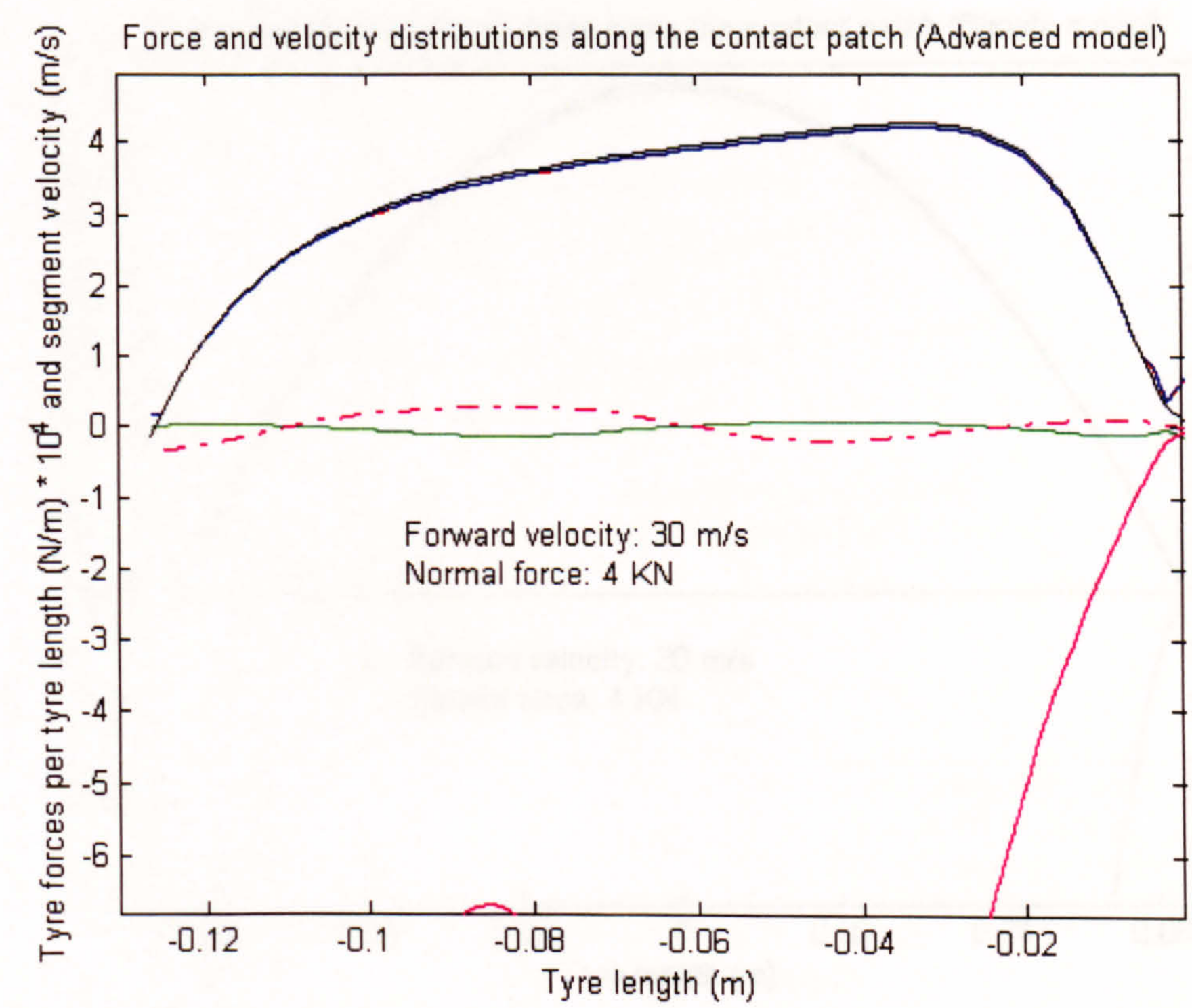

Figure 3. 40 Force distribution along the contact patch at 17.75° slip angle (saturated area of operation) (see the same results in appendix B, where different scaling is used)

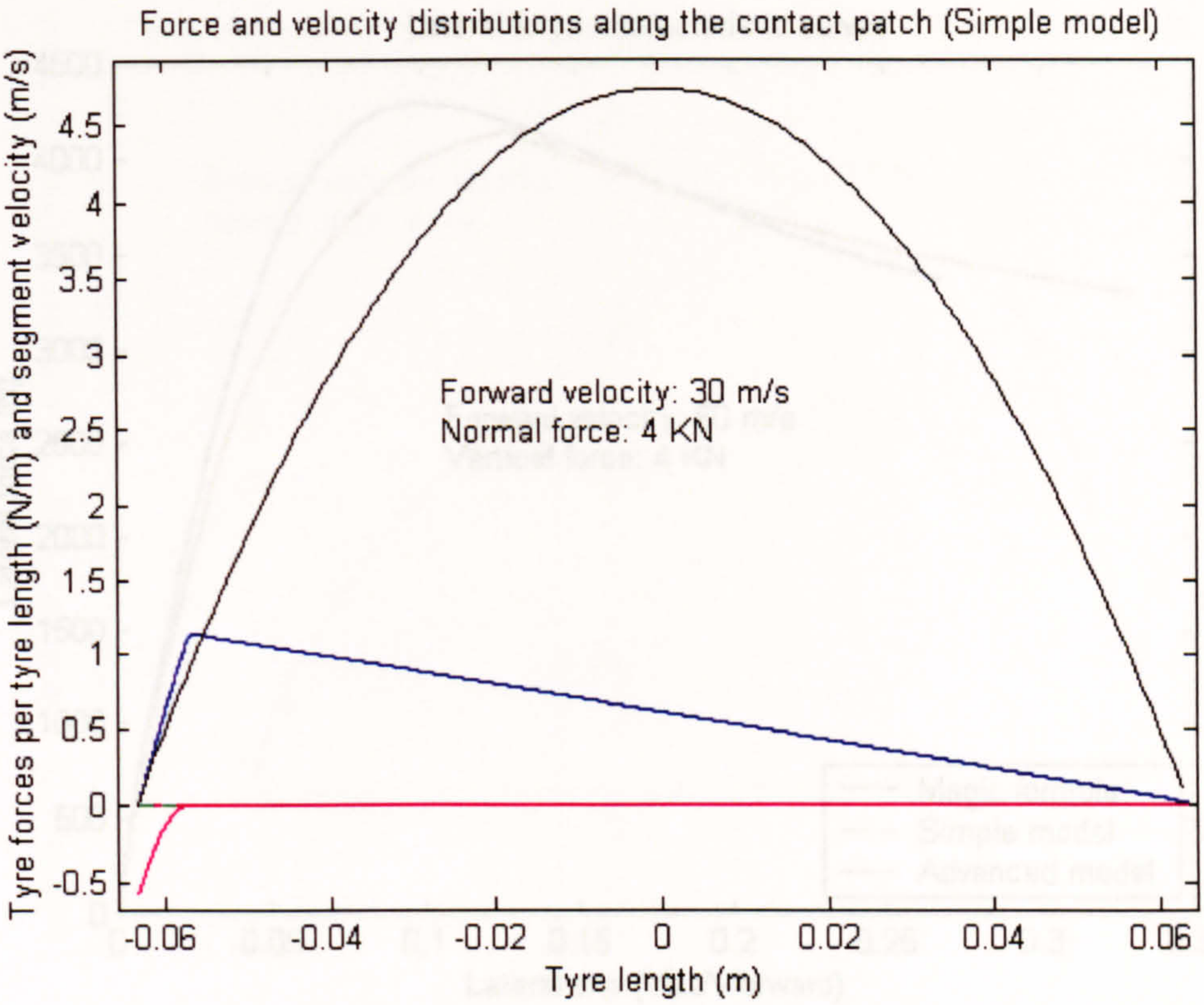

Figure 3. 41 Simple model: Force distribution along the contact patch at 0.46° slip angle

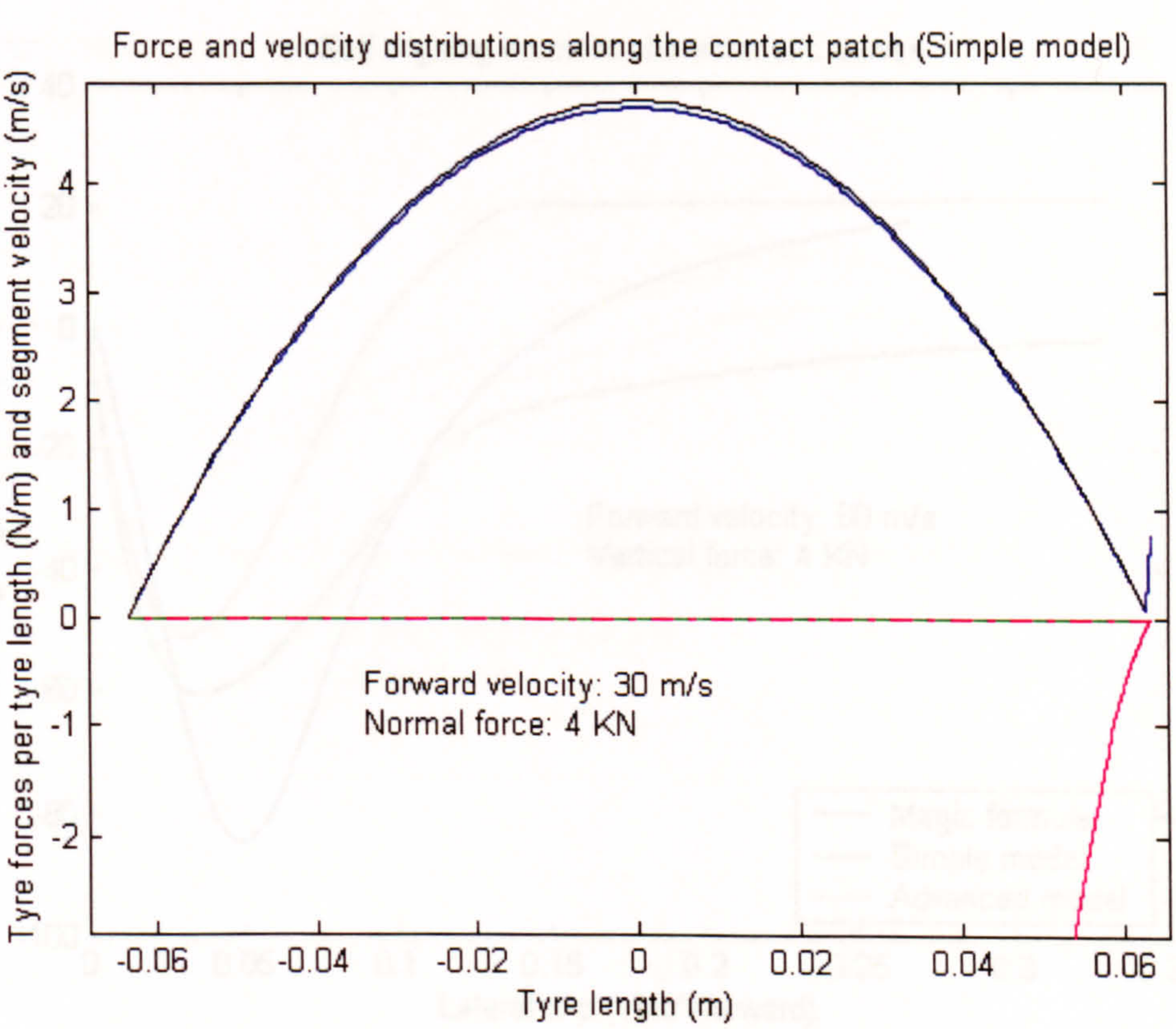

Figure 3. 42 Simple model: Force distribution along the contact patch at 17.75° slip angle (see the same results in appendix B, where different scaling is used)

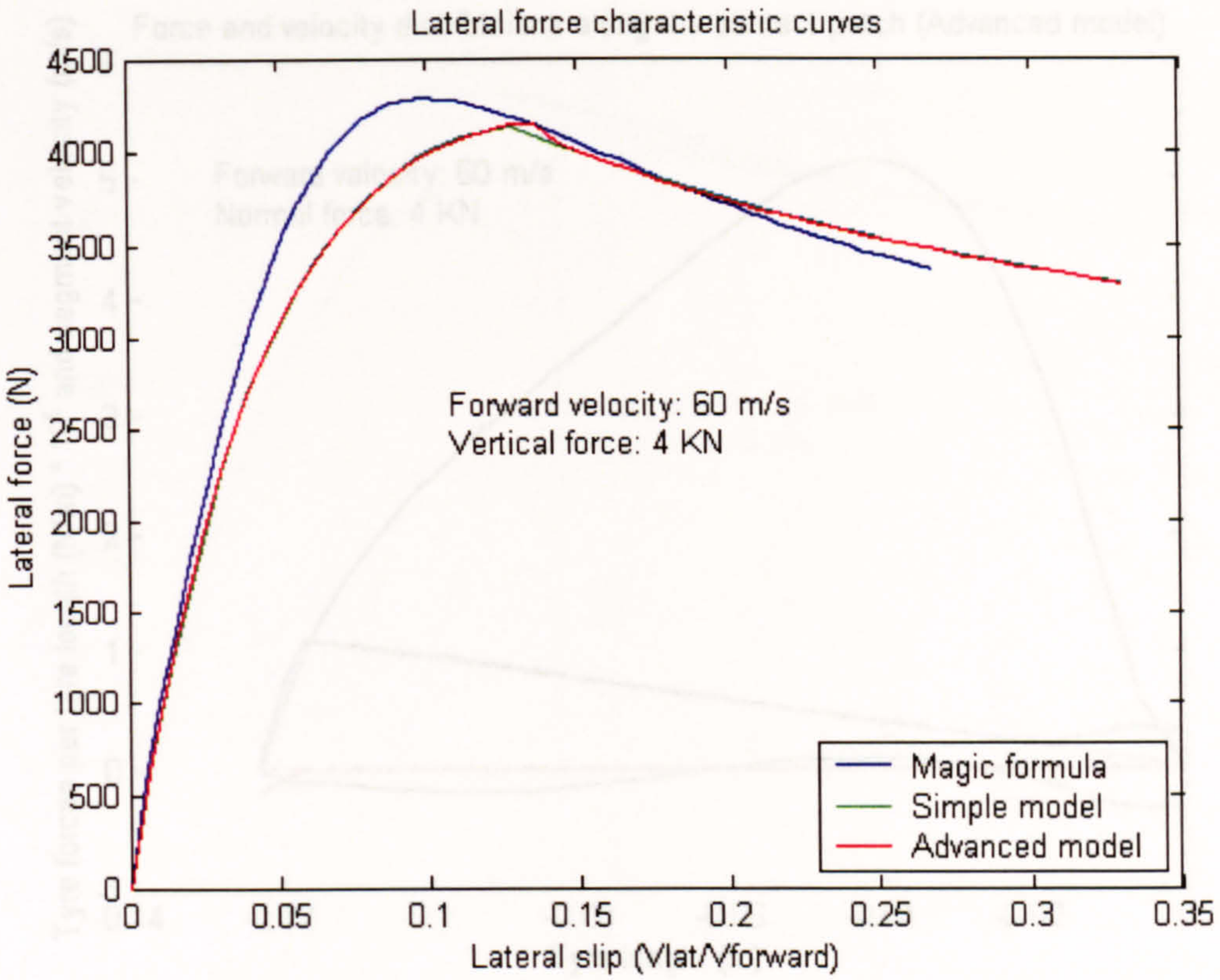

Figure 3. 43 Cornering force for 4KN load and 60 m/s forward velocity

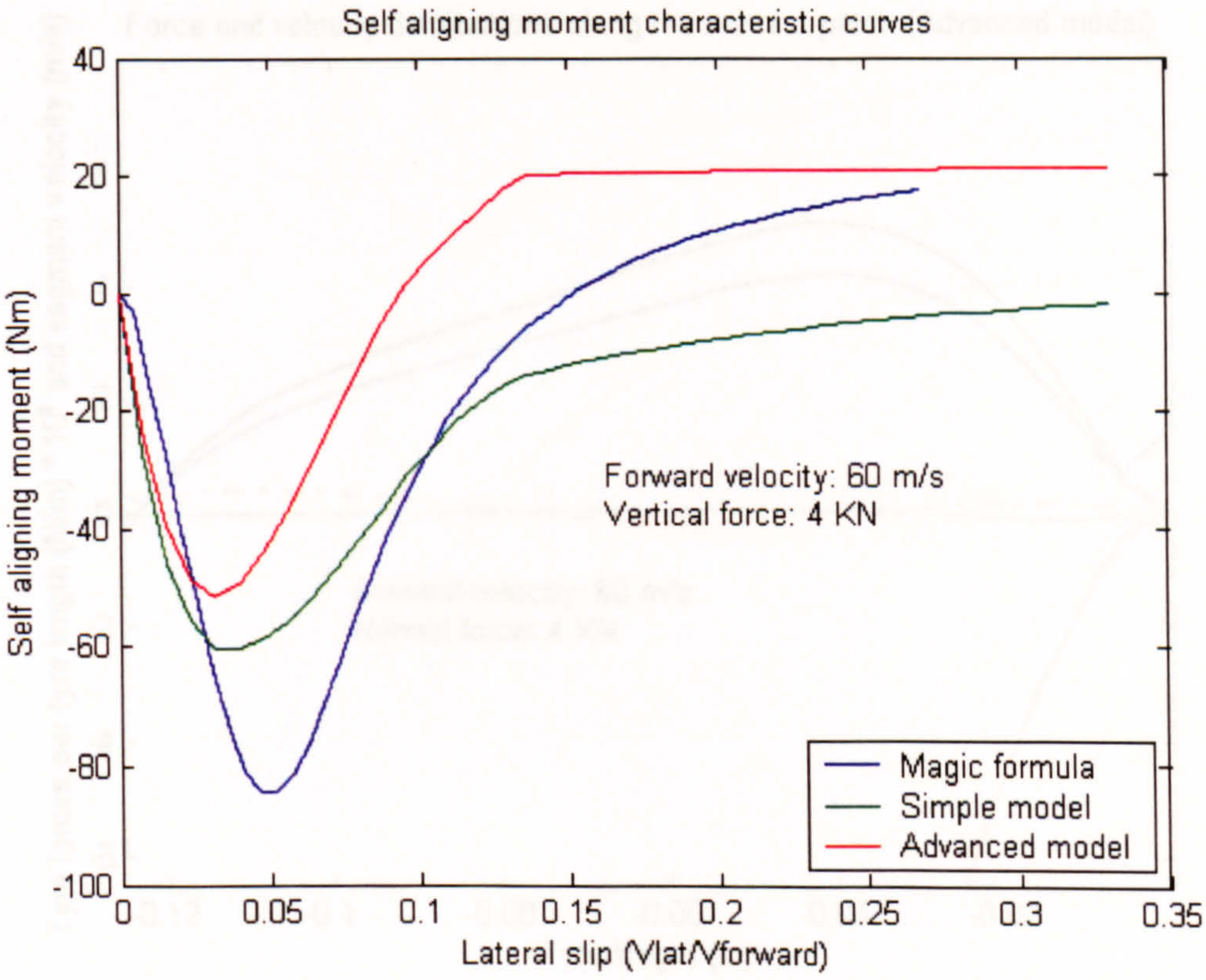

Figure 3. 44 Self-aligning moment for 4KN load and 60 m/s forward velocity

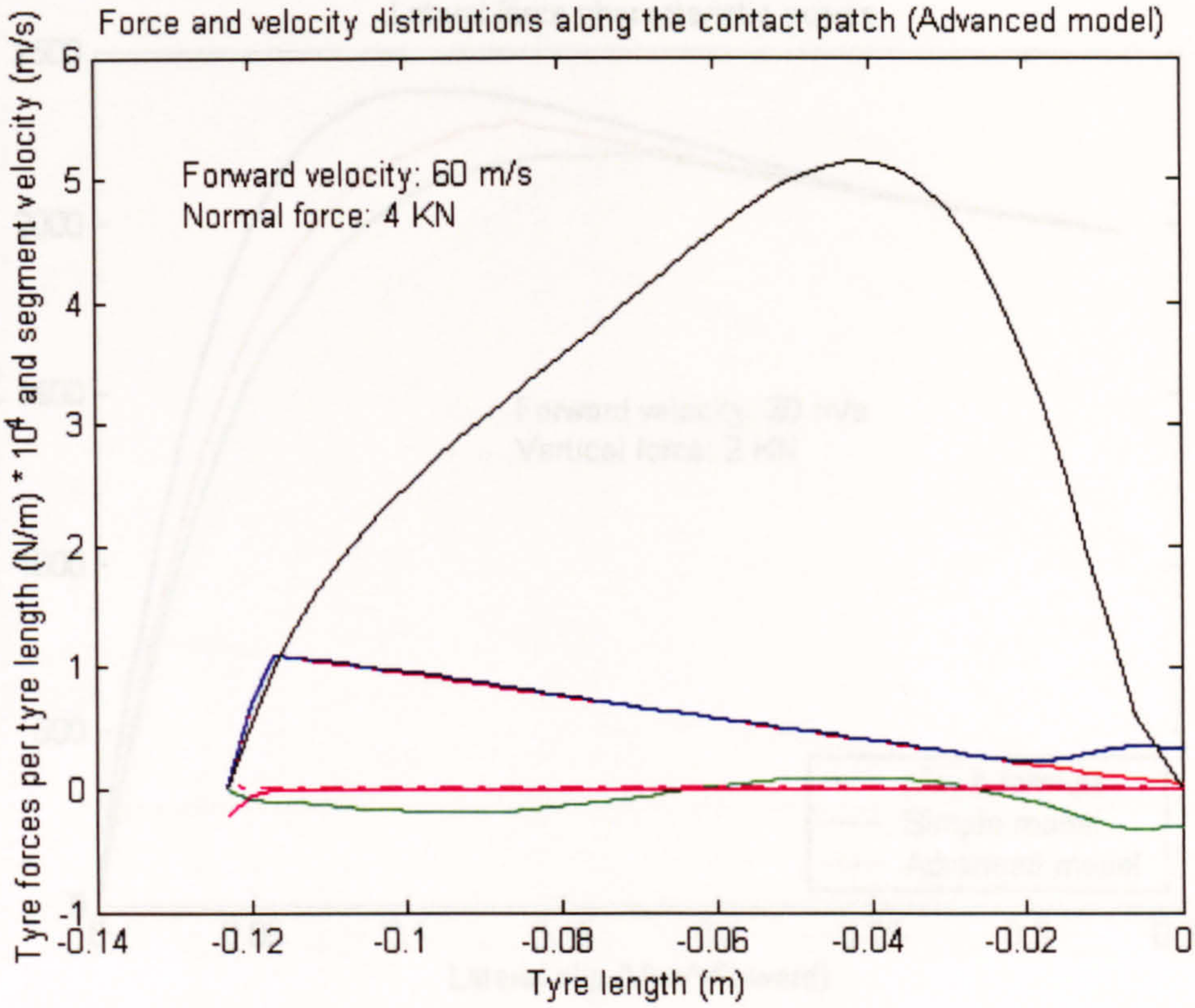

Figure 3. 45 Force distribution along the contact patch at 0.46° slip angle

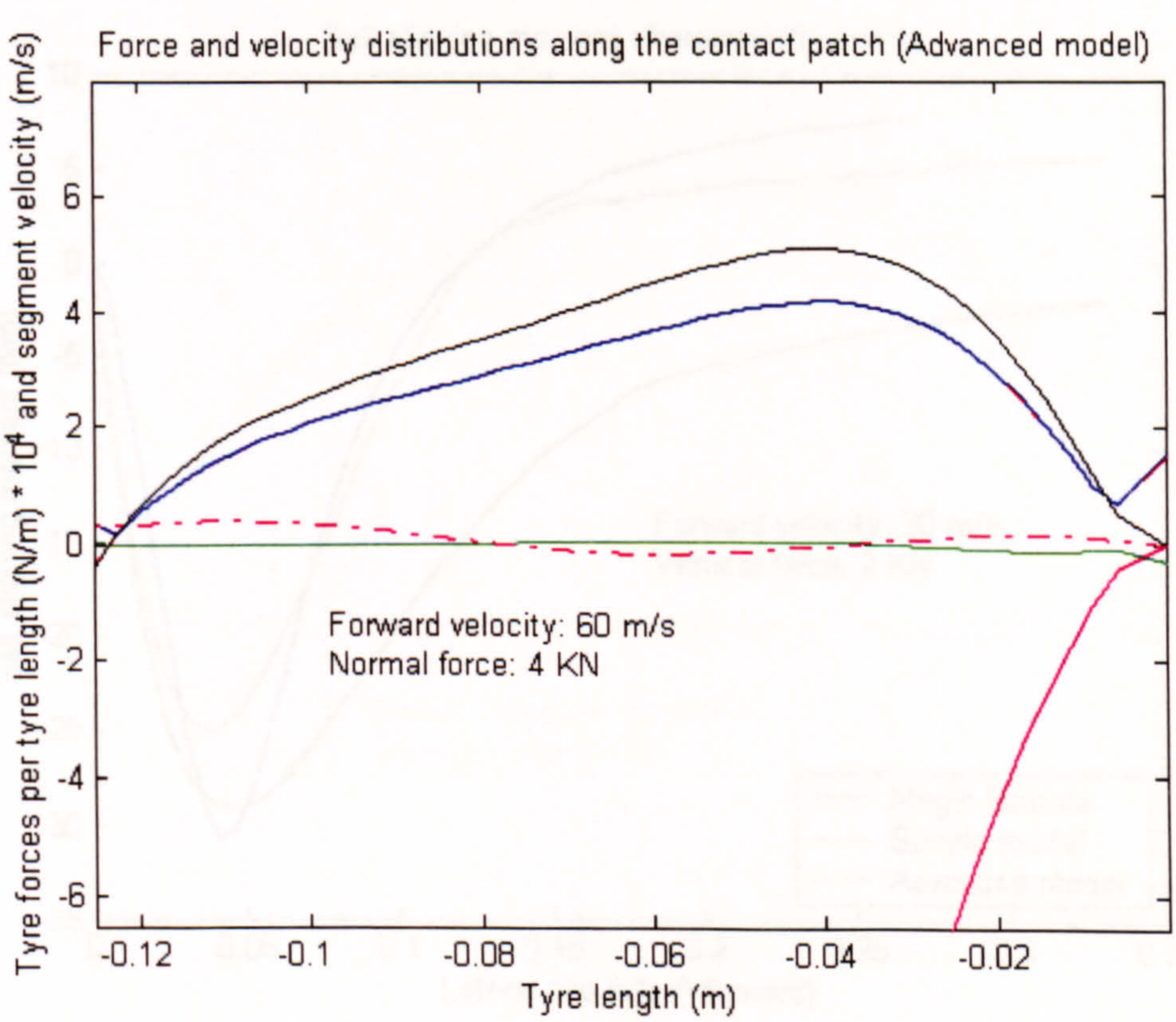

Figure 3. 46 Force distribution along the contact patch at 17.75° slip angle (saturated area of operation) (see the same results in appendix B, where different scaling is used)

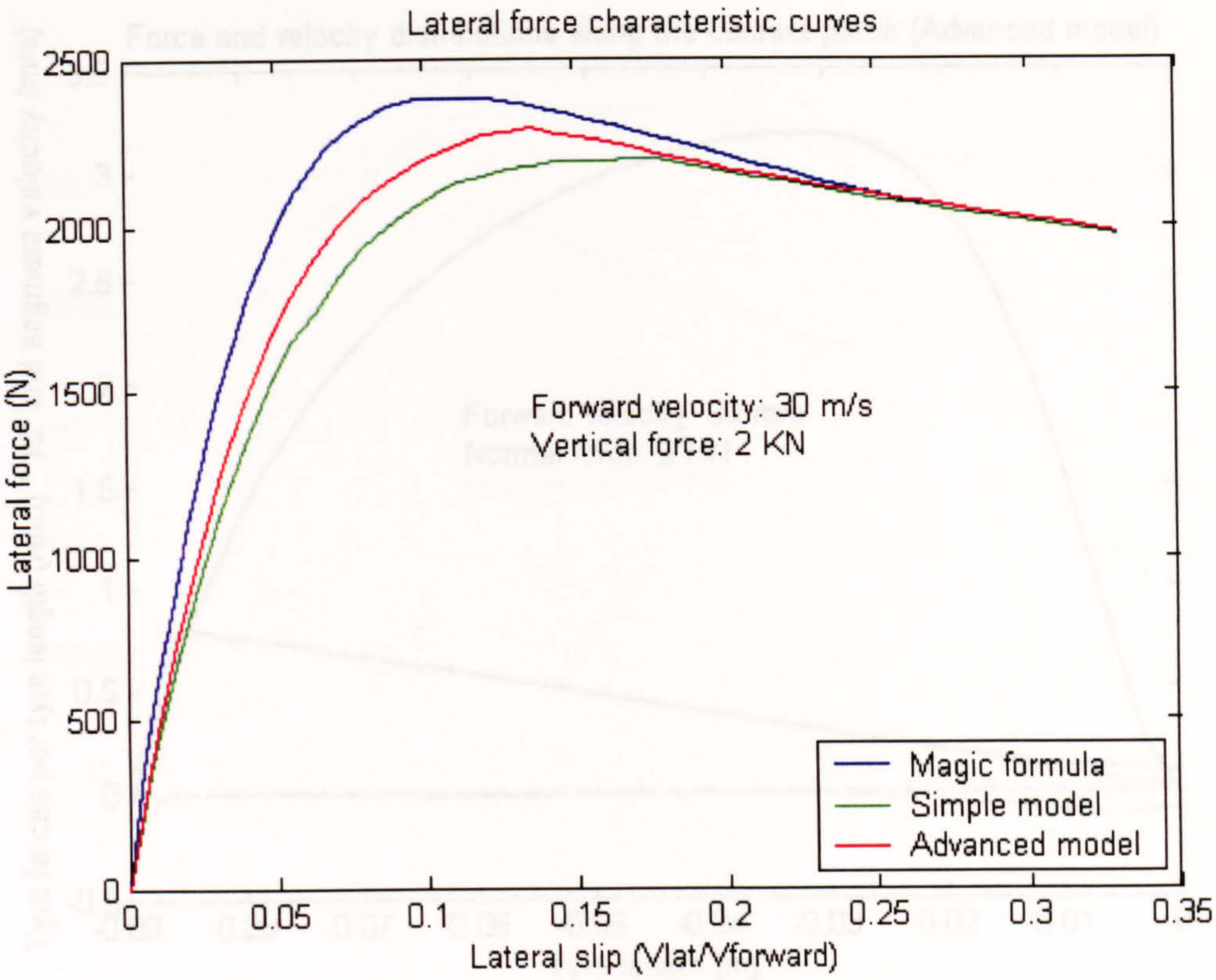

Figure 3. 47 Cornering force for 2KN load and 30 m/s forward velocity

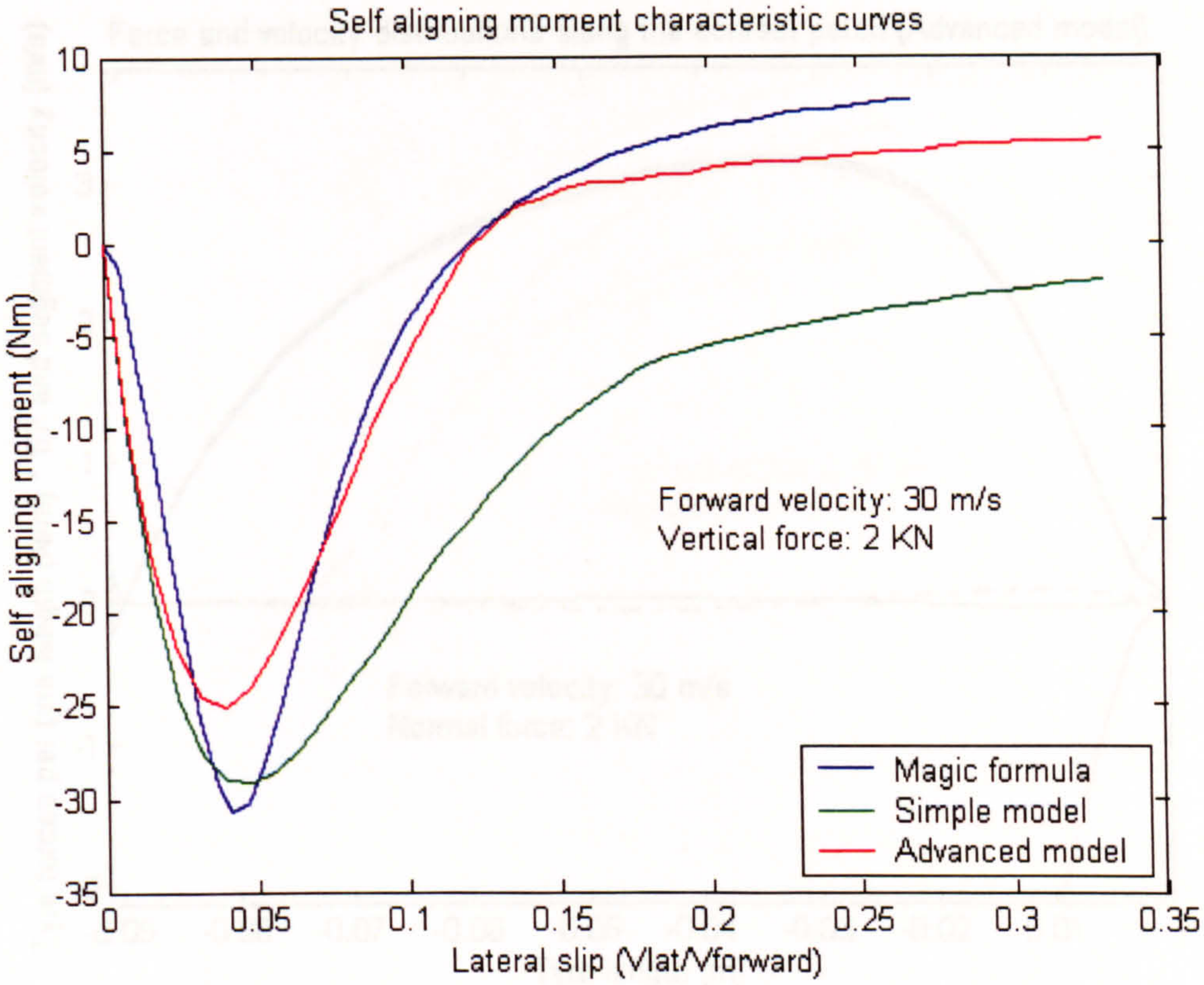

Figure 3. 48 Self-aligning moment for 2KN load and 30 m/s forward velocity

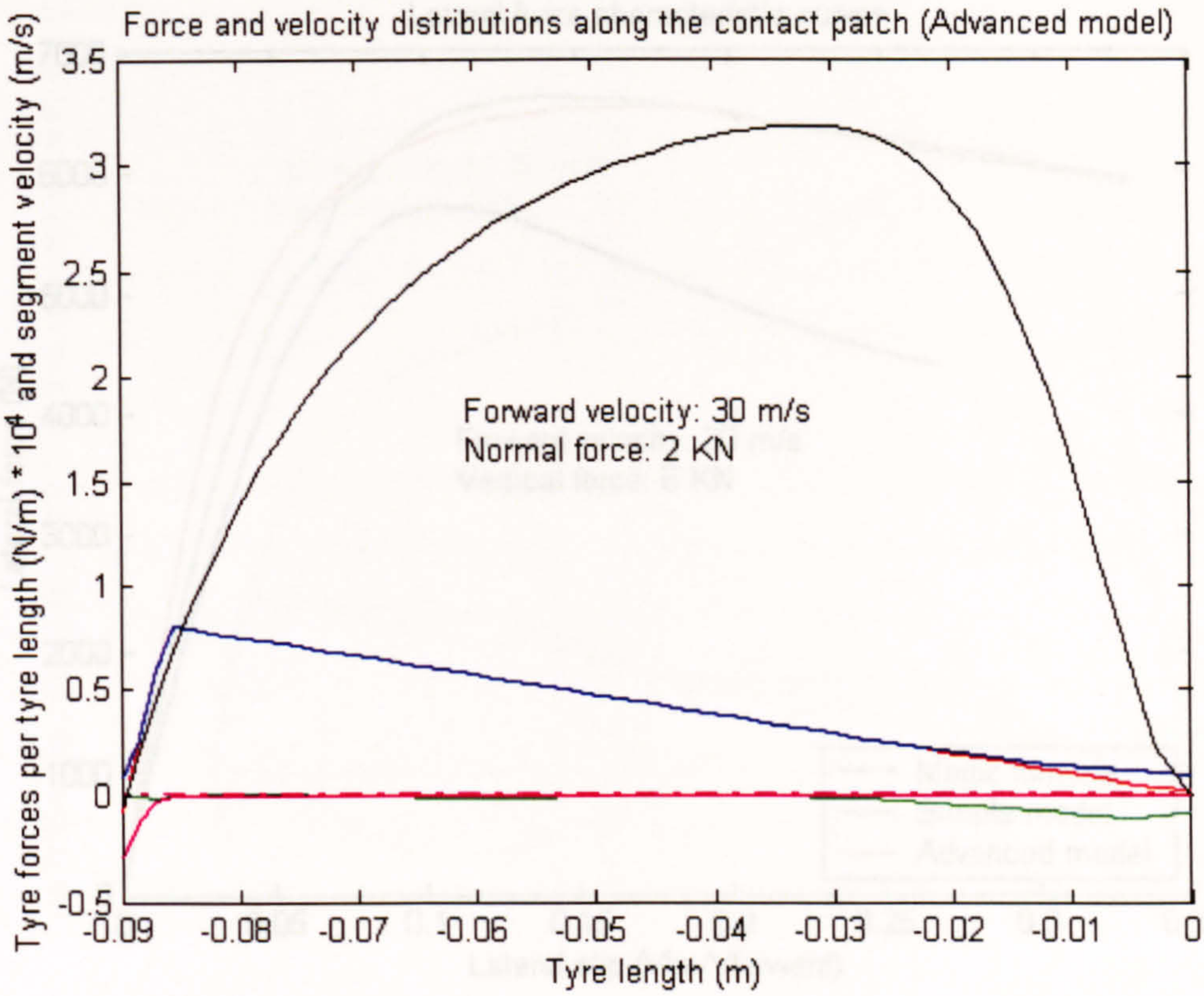

Figure 3. 49 Force distribution along the contact patch at 0.46° slip angle

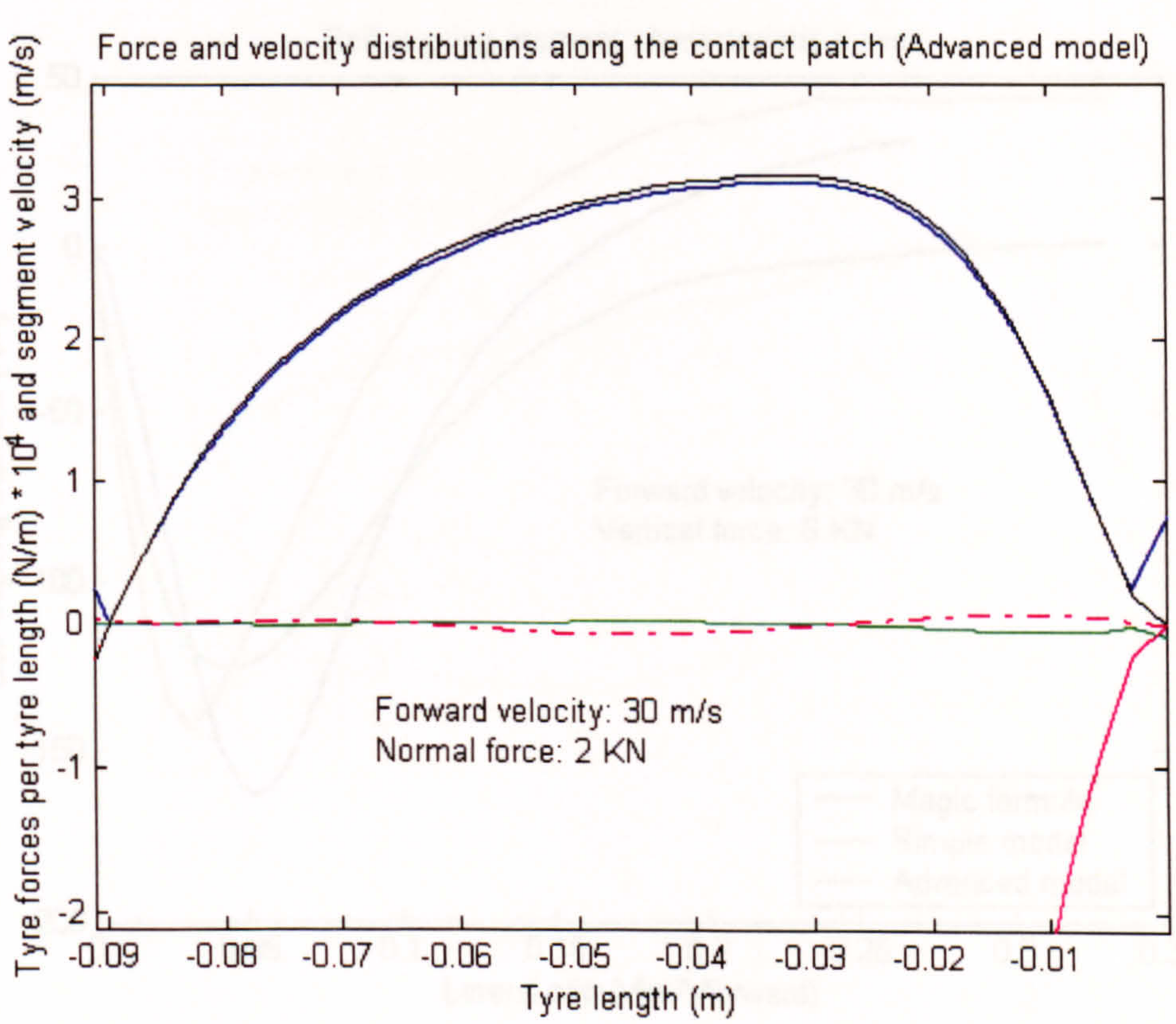

Figure 3. 50 Force distribution along the contact patch at 17.75° slip angle (saturated area of operation) (see the same results in appendix B, where different scaling is used)

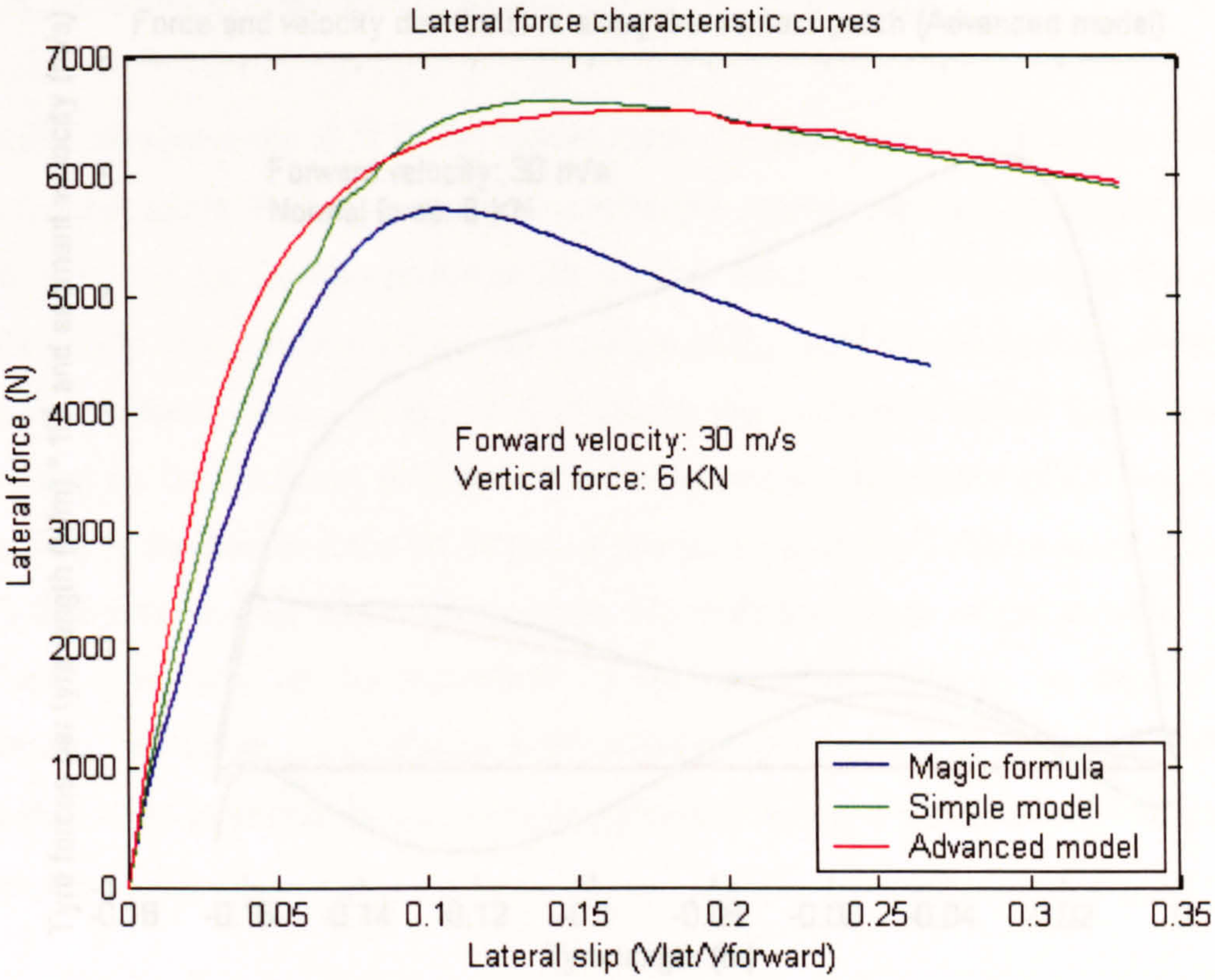

Figure 3. 51 Cornering force for 6KN load and 30 m/s forward velocity

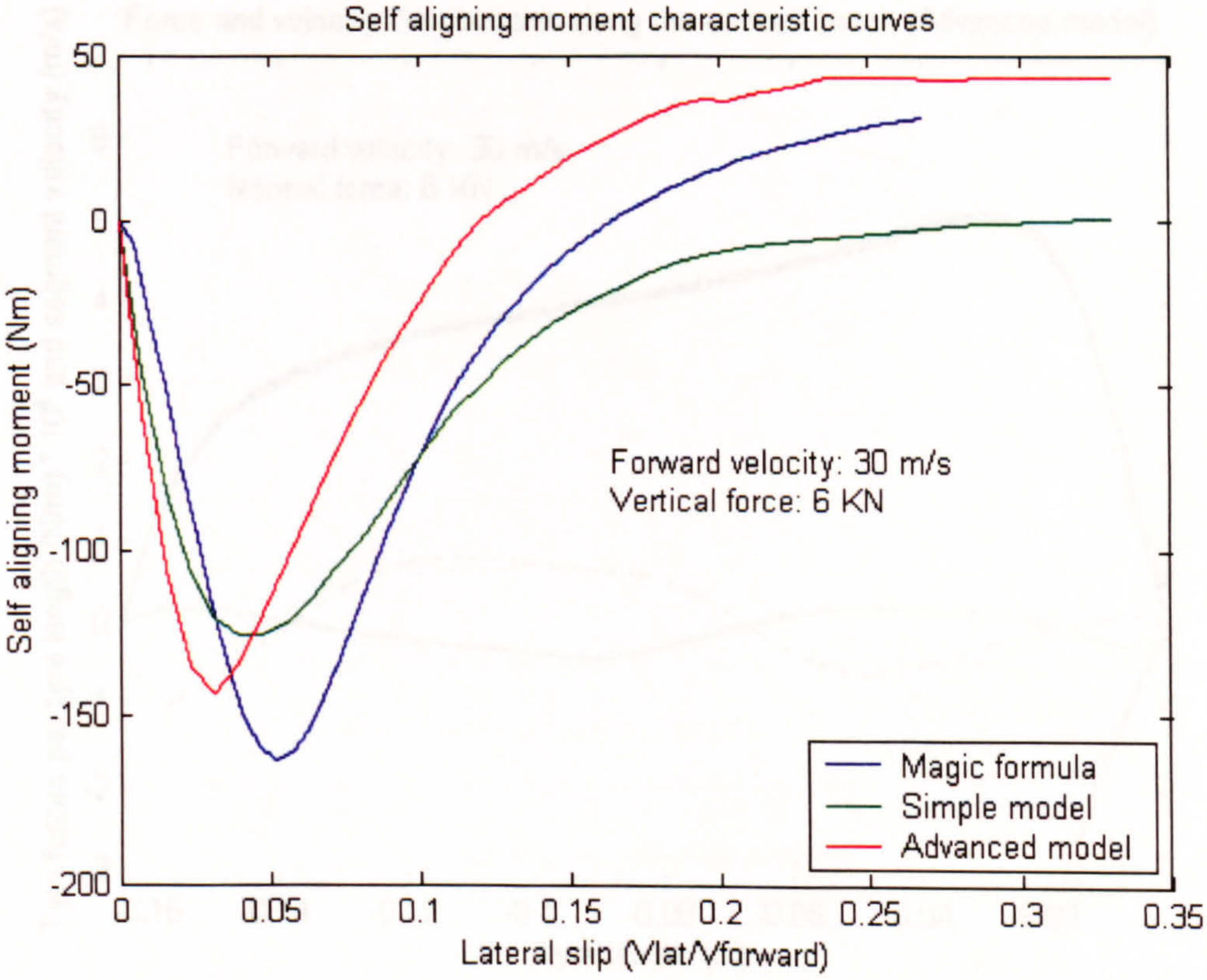

Figure 3. 52 Self-aligning moment for 6KN load and 30 m/s forward velocity

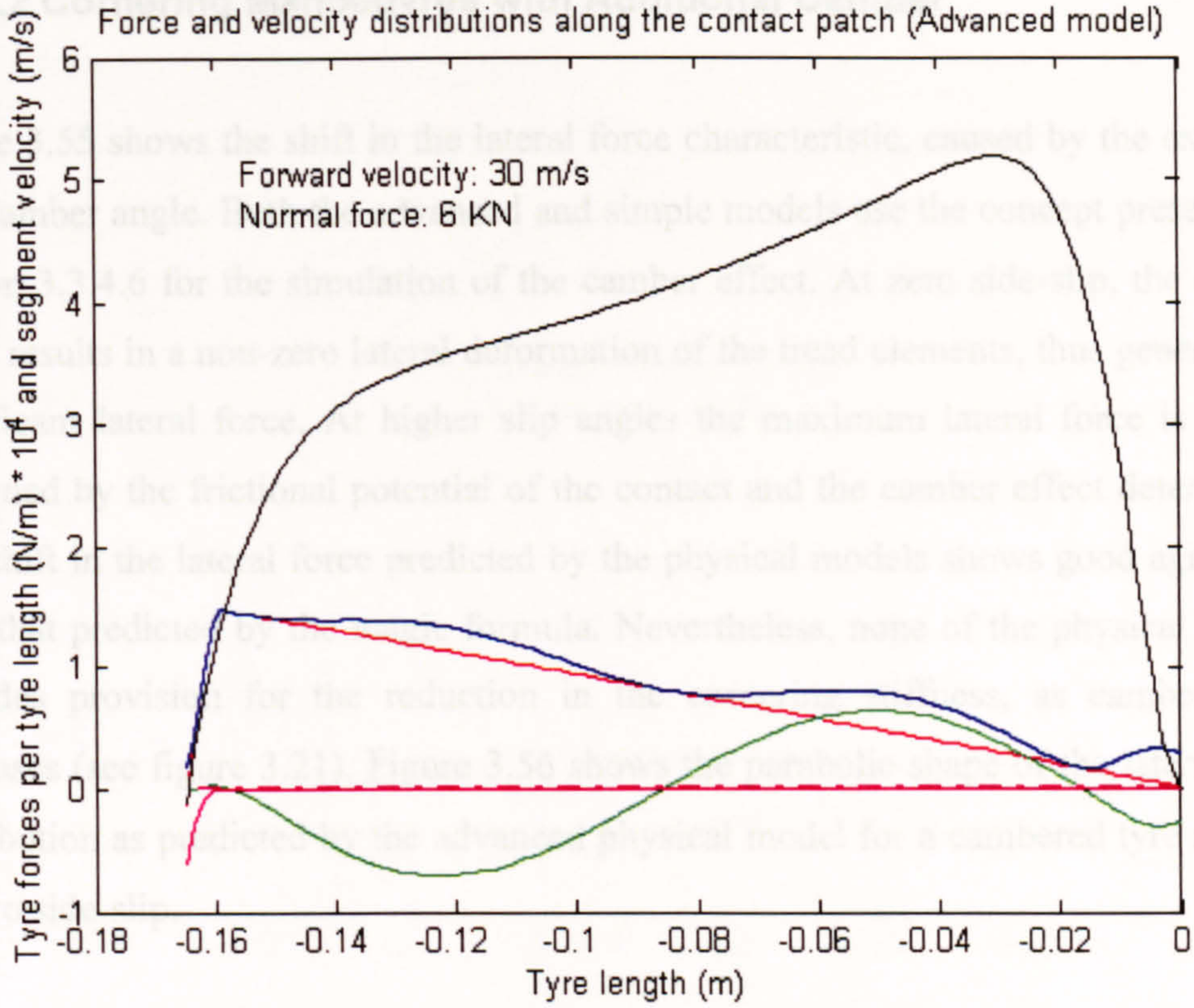

Figure 3. 53 Force distribution along the contact patch at 0.46° slip angle

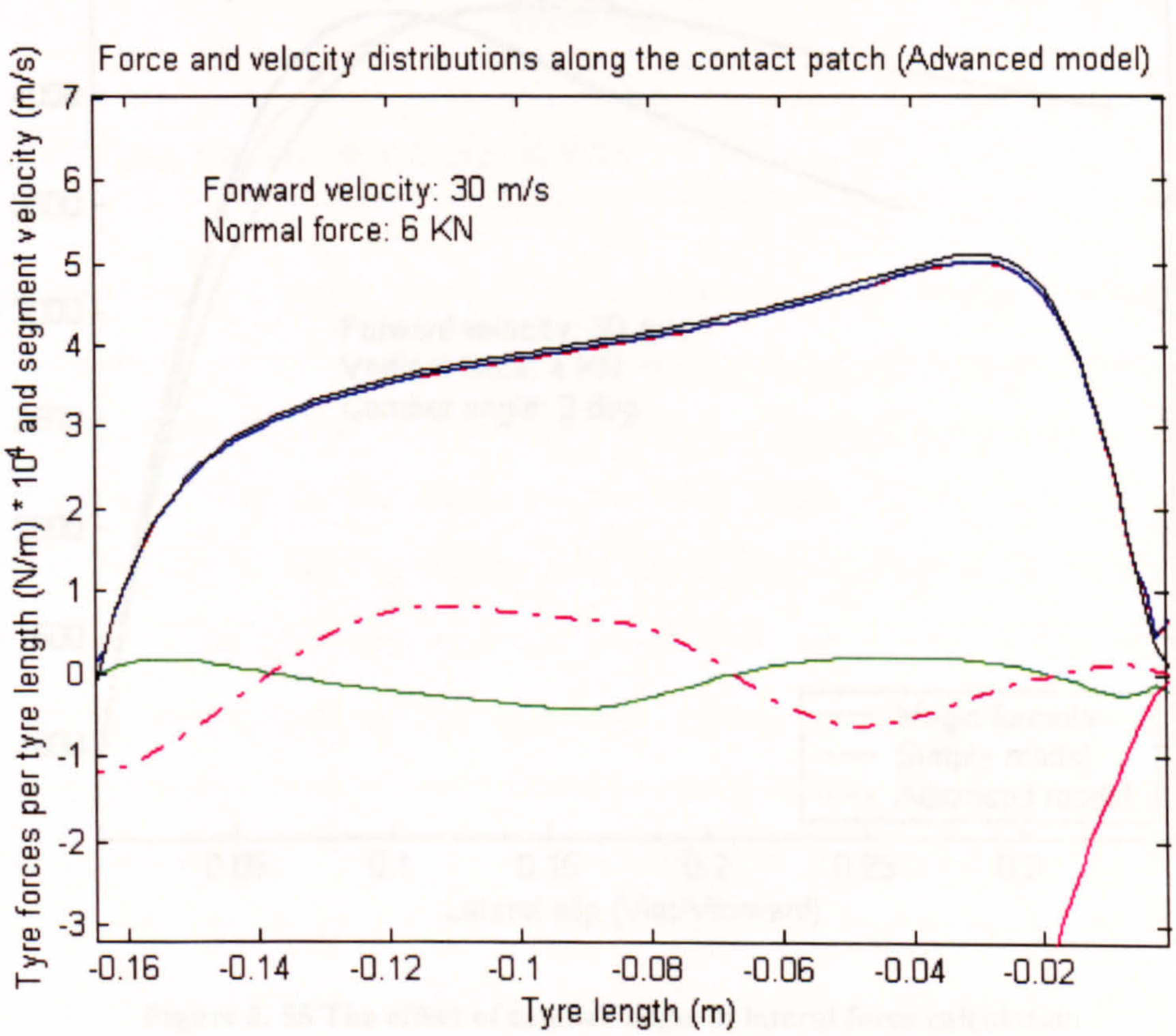

Figure 3. 54 Force distribution along the contact patch at 17.75° slip angle (saturated area of operation) (see the same results in appendix B, where different scaling is used)

3.3.6.2 Cornering Manoeuvres with Additional Camber

Figure 3.55 shows the shift in the lateral force characteristic, caused by the existence of a camber angle. Both the advanced and simple models use the concept presented in section 3.3.4.6 for the simulation of the camber effect. At zero side-slip, the camber angle results in a non-zero lateral deformation of the tread elements, thus generating a significant lateral force. At higher slip angles the maximum lateral force is mainly governed by the frictional potential of the contact and the camber effect deteriorates. The shift in the lateral force predicted by the physical models shows good agreement with that predicted by the magic formula. Nevertheless, none of the physical models includes provision for the reduction in the cornering stiffness, as camber angle increases (see figure 3.21). Figure 3.56 shows the parabolic shape of the lateral force distribution as predicted by the advanced physical model for a cambered tyre running at zero side-slip.

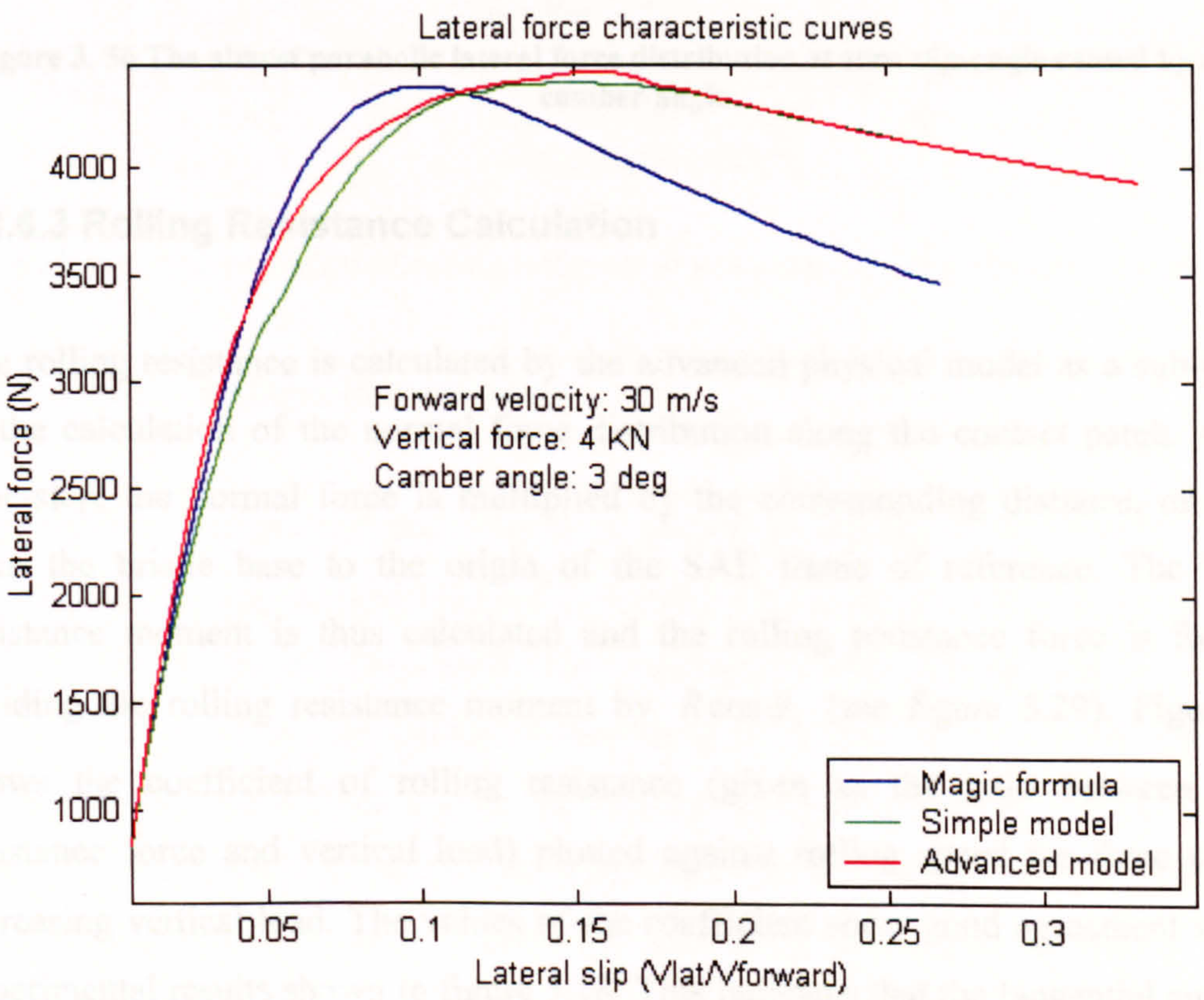

Figure 3. 55 The effect of camber angle in lateral force calculation

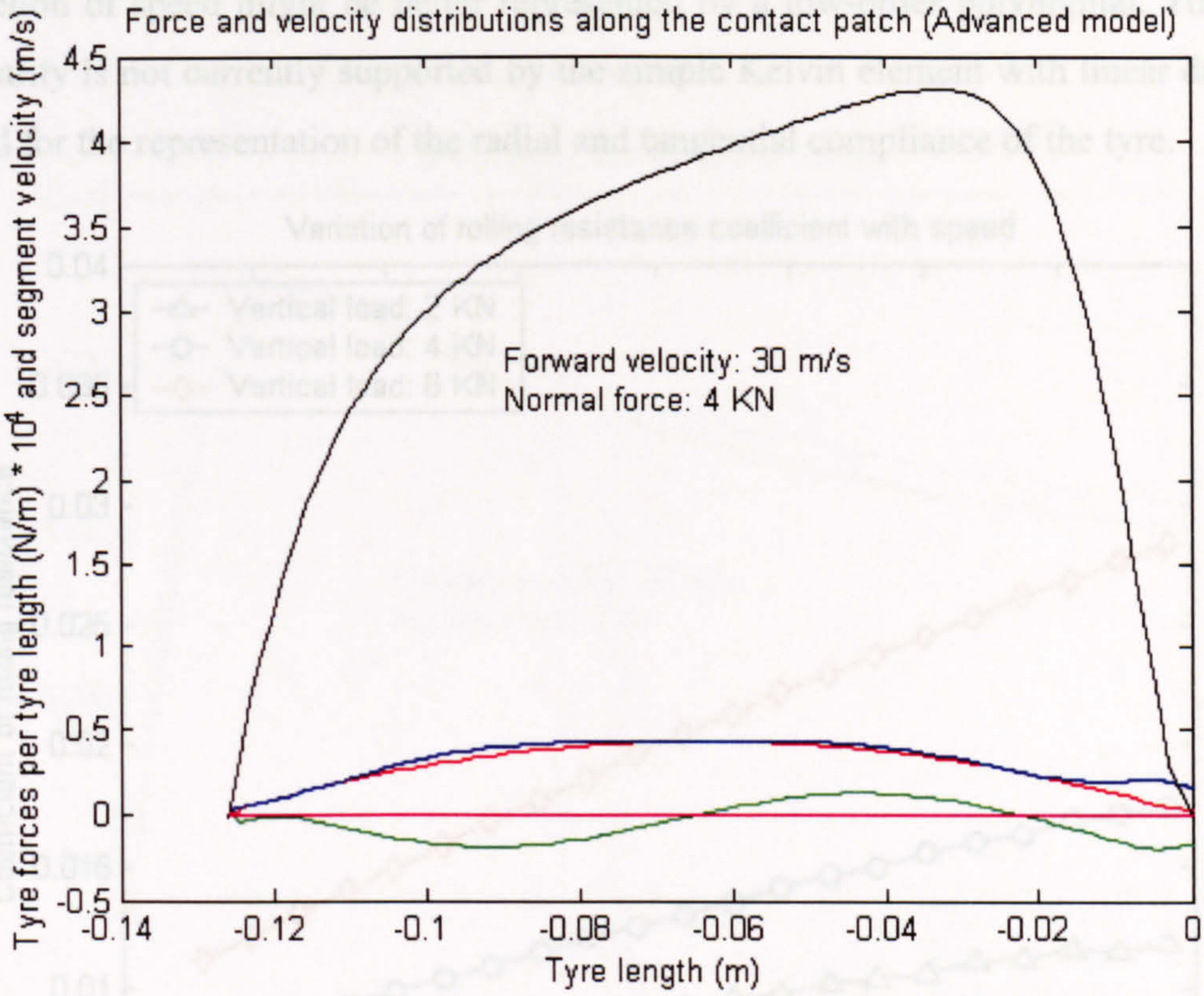

Figure 3. 56 The almost parabolic lateral force distribution at zero slip-angle caused by a 3 deg camber angle

3.3.6.3 Rolling Resistance Calculation

The rolling resistance is calculated by the advanced physical model as a sub-product of the calculation of the normal force distribution along the contact patch. At each time-step, the normal force is multiplied by the corresponding distance, on x-axis, from the bristle base to the origin of the SAE frame of reference. The Rolling resistance moment is thus calculated and the rolling resistance force is found by dividing the rolling resistance moment by $R\cos\vartheta_o$ (see figure 3.29). Figure 3.57 shows the coefficient of rolling resistance (given as the ratio between rolling resistance force and vertical load) plotted against rolling speed for three cases of increasing vertical load. The values of the coefficient show good agreement with the experimental results shown in figure 3.18. This indicates that the tangential and radial Kelvin elements are capable of simulating the hysteresis losses and the resulting shift of the normal pressure distribution towards the front of the contact patch. Nevertheless, all three curves shown in figure 3.57 are approximately linear, whereas experimental results as seen in figure 3.18 indicate that the rolling resistance as a

function of speed might be better represented by a low-order polynomial. This non-linearity is not currently supported by the simple Kelvin element with linear damping used for the representation of the radial and tangential compliance of the tyre.

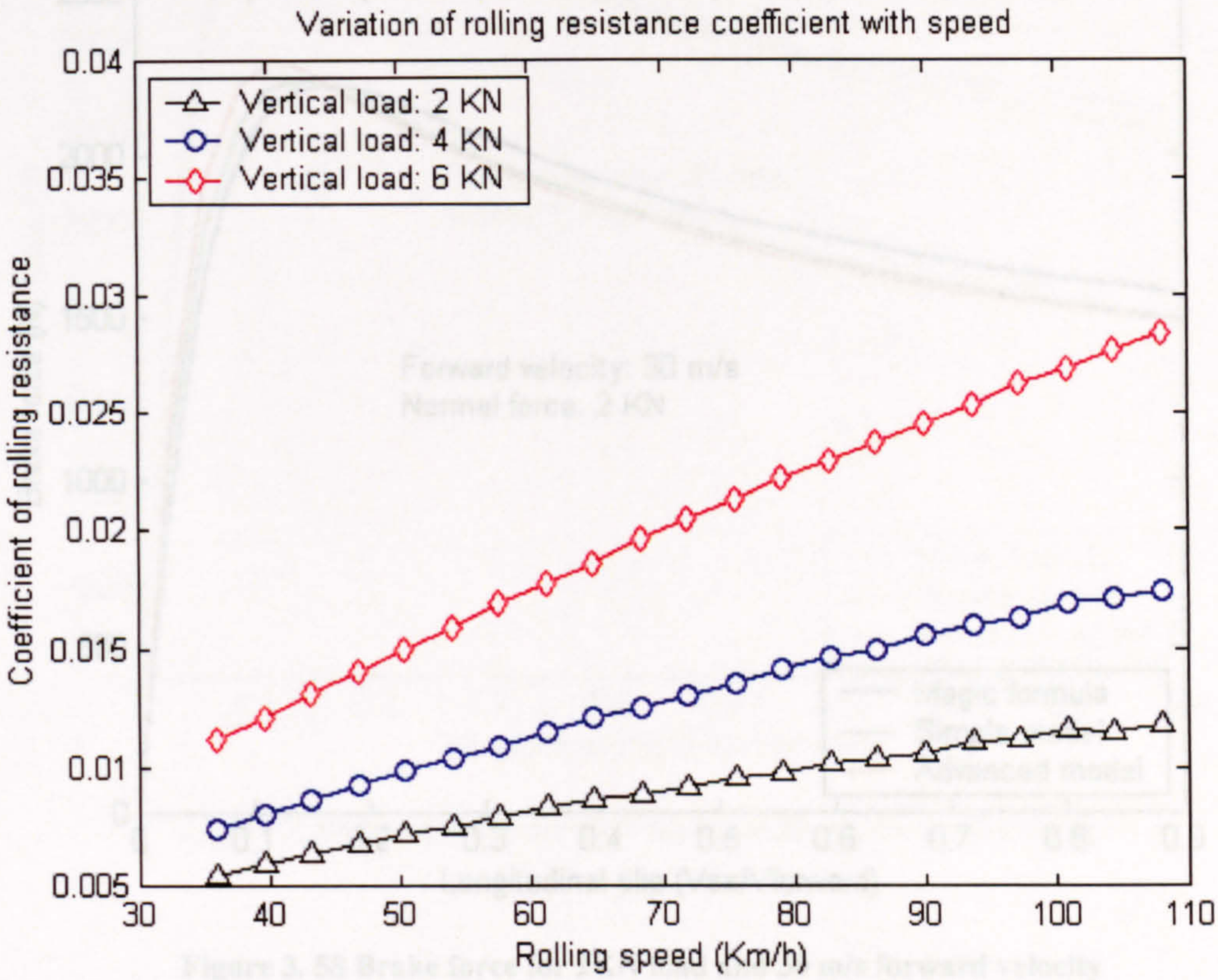

Figure 3. 57 The coefficient of rolling resistance as calculated by the advanced physical model

3.3.6.4 Pure Braking Manoeuvres

The braking response of the models is shown in figures 3.58 through 3.60 for gradually increasing vertical loads of 2, 4 and 6 KN. In all cases the forward velocity maintains the value of 30 m/s, while the rotational velocity reduces so as to generate a resulting longitudinal slip gradually increasing from zero up to a maximum of 0.9 (absolute value). All three graphs show good agreement between the two physical models and the Magic Formula. The brake force characteristics serve as a benchmark for the assumption of an exponentially decreasing coefficient of kinetic friction. Unlike the cornering curves, the braking curves extend to higher sliding velocities, which, in this case reach the value of 27 m/s at 0.9 longitudinal slip. The smoothness of the curves throughout the slip range and the good coincidence with the forces predicted by the Magic Formula indicate that the velocity dependent coefficient of

kinetic friction as described by equations 3.127 and 3.128 can be employed successfully in the tyre force generation mechanism.

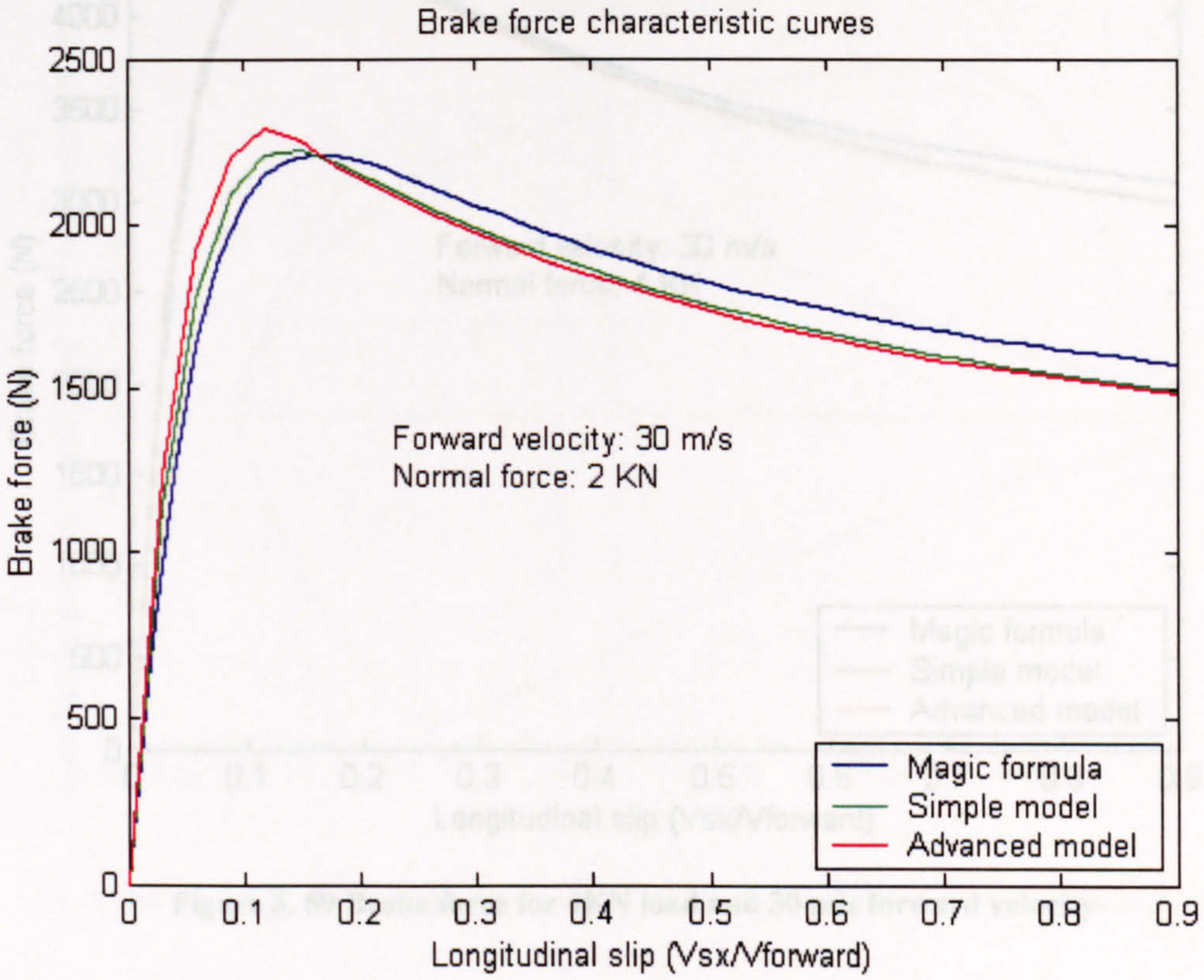

Figure 3. 58 Brake force for 2KN load and 30 m/s forward velocity

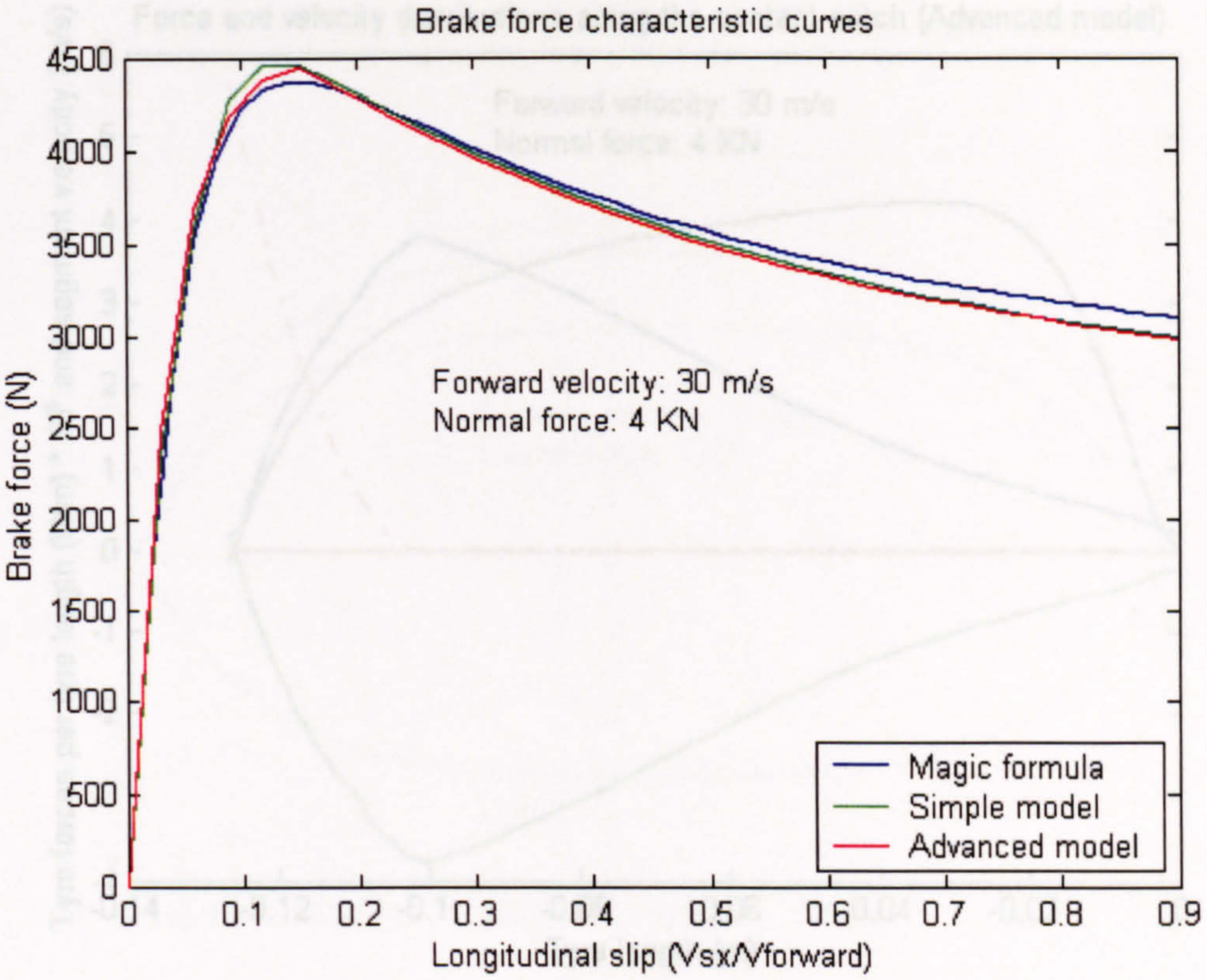

Figure 3. 59 Brake force for 4KN load and 30 m/s forward velocity

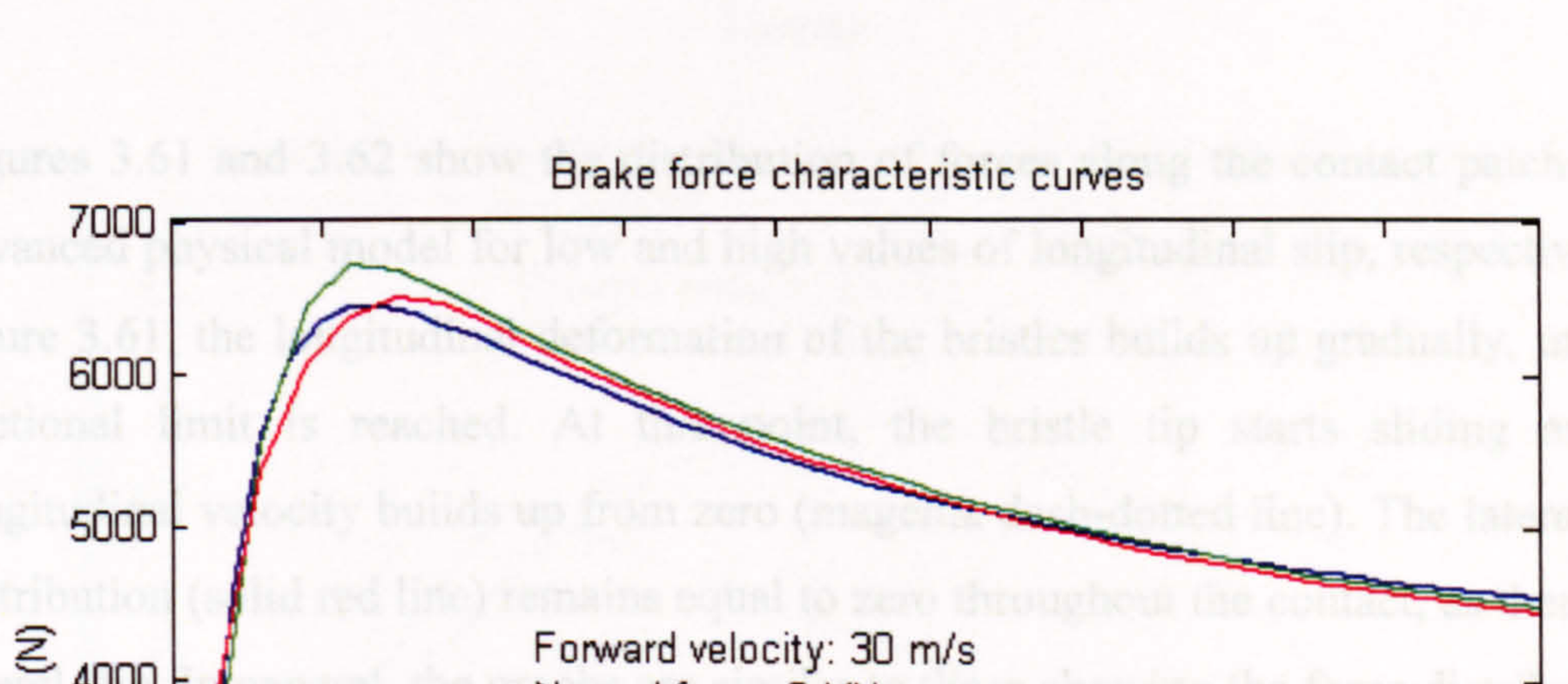

Figure 3. 60 Brake force for 6KN load and 30 m/s forward velocity

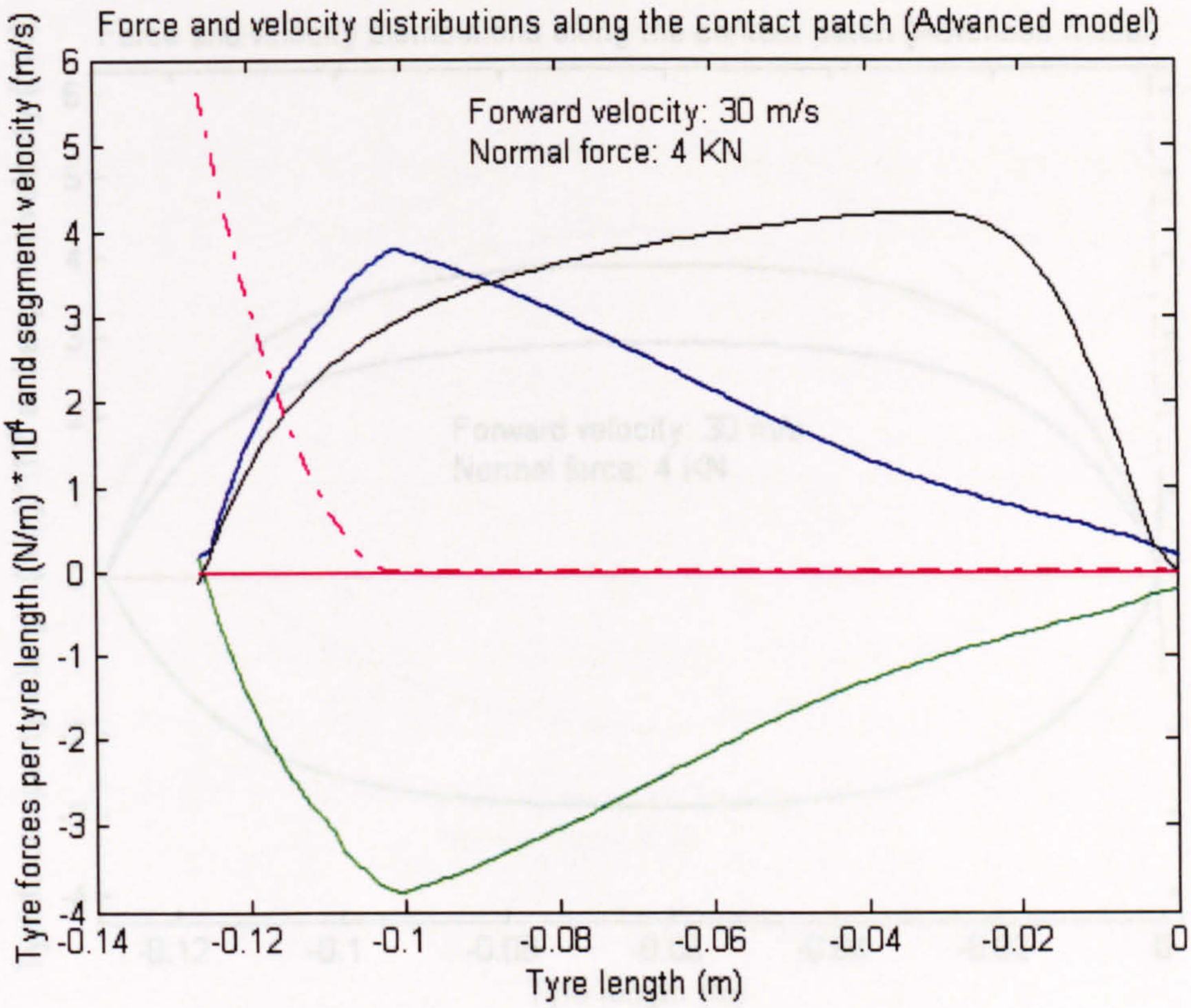

Figure 3. 61 Force distribution along the contact patch at 3% longitudinal slip

Figures 3.61 and 3.62 show the distribution of forces along the contact patch of the advanced physical model for low and high values of longitudinal slip, respectively. In figure 3.61, the longitudinal deformation of the bristles builds up gradually, until the frictional limit is reached. At this point, the bristle tip starts sliding and the longitudinal velocity builds up from zero (magenta dash-dotted line). The lateral force distribution (solid red line) remains equal to zero throughout the contact, as there is no lateral slip. In general, the graphs are similar to those showing the force distribution in the case of cornering. Probably the main difference lies on the fact that during braking, for a constant forward velocity, the rolling velocity of the tyre reduces significantly. As a result, at high slip ratios, the normal pressure distribution becomes more or less symmetrical, as demonstrated in figure 3.62. Apparently, due to the mechanism of brake force generation, the change in the shape of the normal pressure distribution should not affect the values of braking force, as it affects for example the levels of self-aligning torque. The equivalent force distributions for the simple tyre model are given in figures 3.63 and 3.64, for low and high slip ratios respectively.

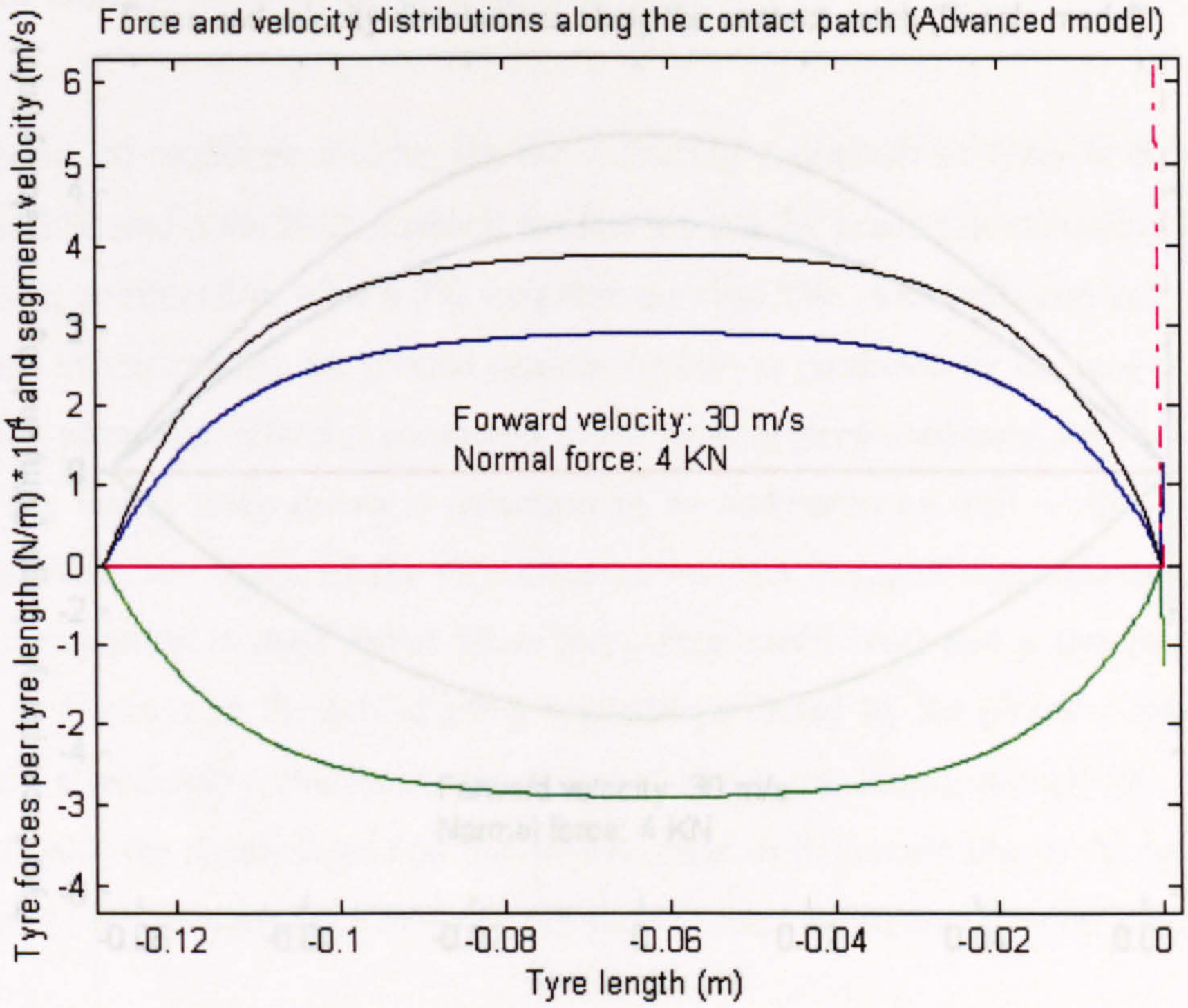

Figure 3. 62 Force distribution along the contact patch at 90% longitudinal slip (saturated area of operation)

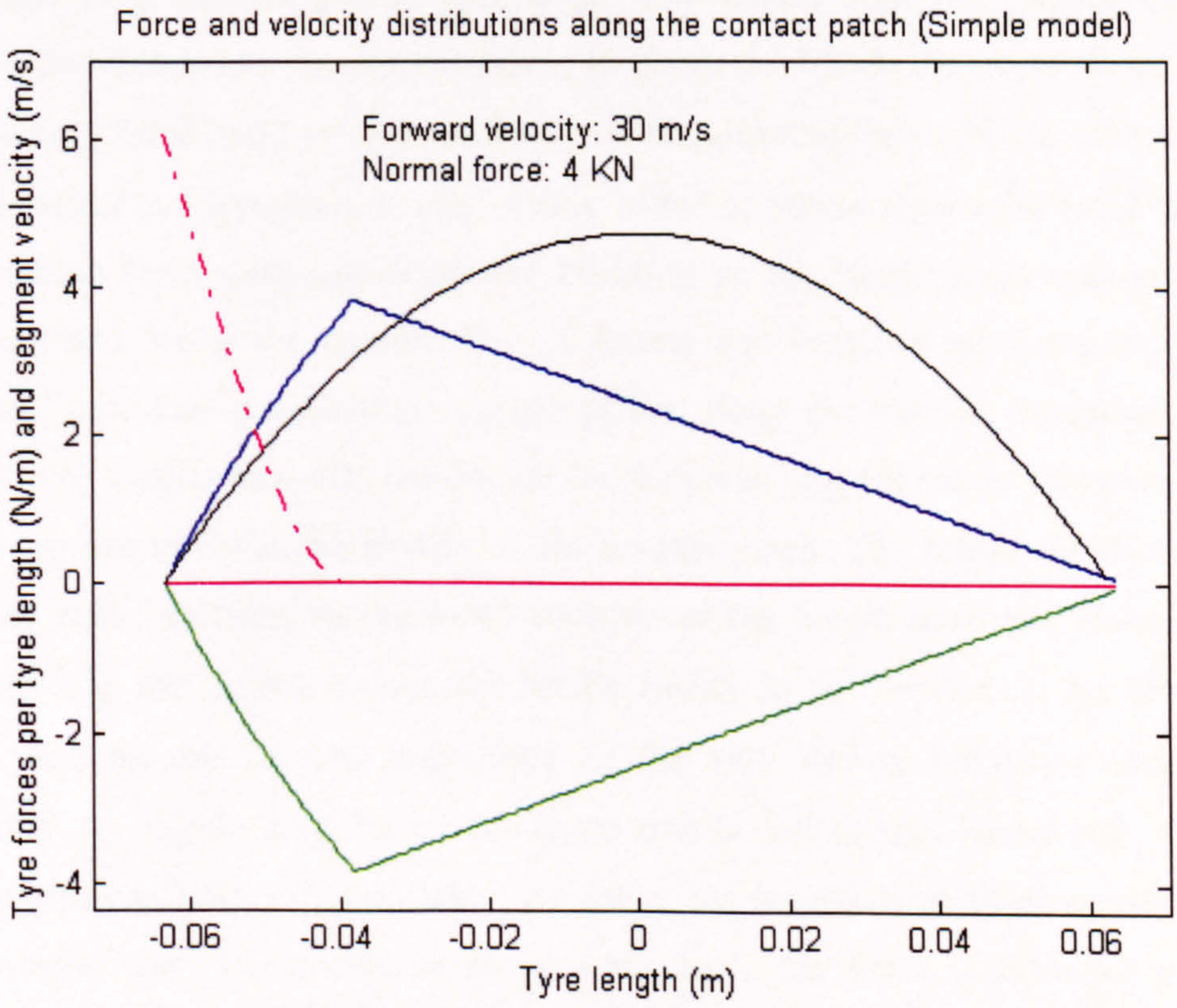

Figure 3. 63 Force distribution along the contact patch at 3% longitudinal slip

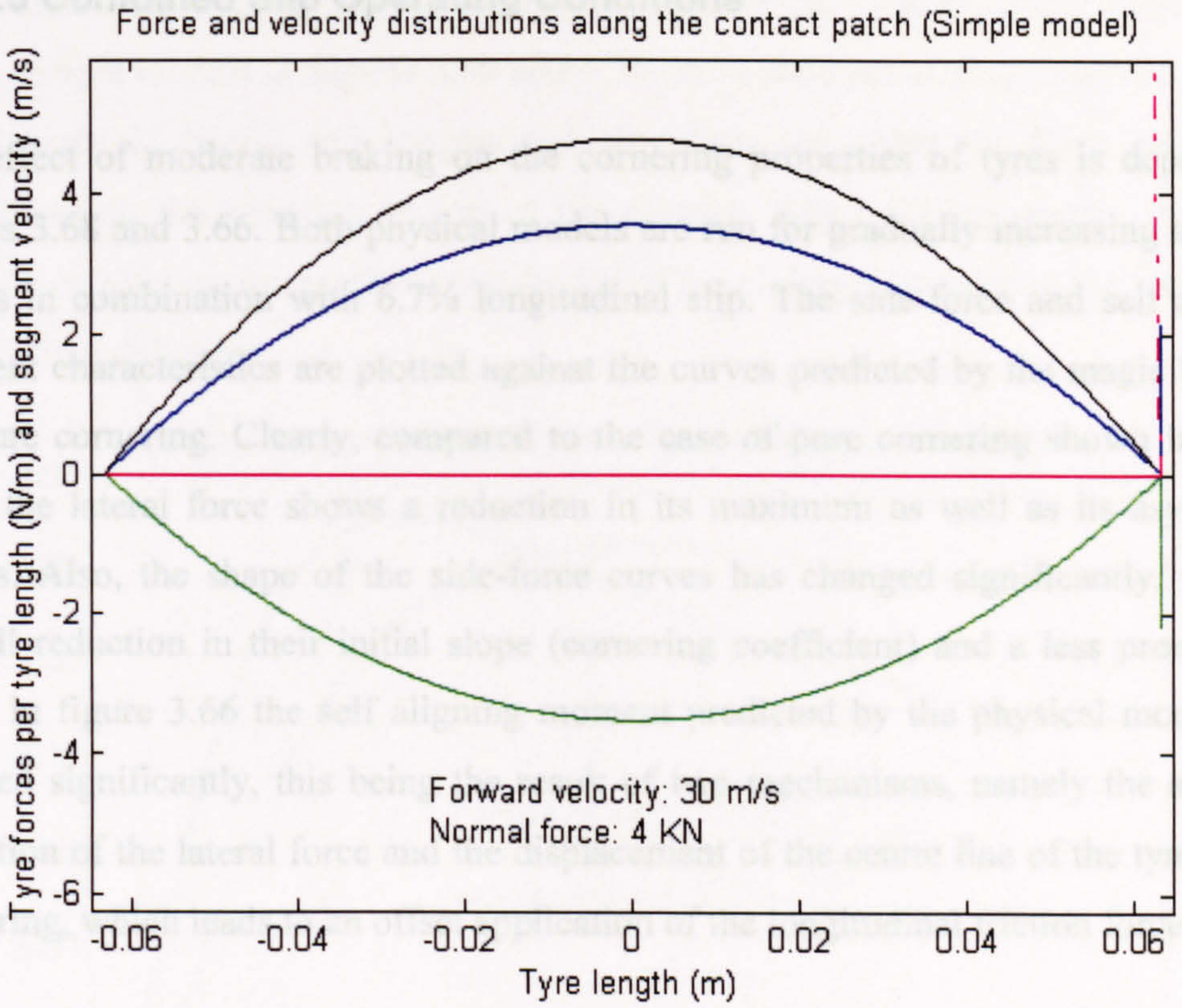

Figure 3. 64 Force distribution along the contact patch at 90% longitudinal slip (saturated area of operation)

3.3.6.5 Combined Slip Operating Conditions

The effect of moderate braking on the cornering properties of tyres is depicted in figures 3.68 and 3.66. Both physical models are run for gradually increasing side-slip values in combination with 6.7% longitudinal slip. The side-force and self aligning moment characteristics are plotted against the curves predicted by the magic formula for pure cornering. Clearly, compared to the case of pure cornering shown in figure 3.37, the lateral force shows a reduction in its maximum as well as its asymptotic values. Also, the shape of the side-force curves has changed significantly, with an overall reduction in their initial slope (cornering coefficient) and a less pronounced peak. In figure 3.66 the self aligning moment predicted by the physical models has reduced significantly, this being the result of two mechanisms, namely the apparent reduction of the lateral force and the displacement of the centre line of the tyre due to cornering, which leads to an offset application of the longitudinal friction forces.

The shapes of the force distributions along the contact patch for the advanced and simple models under combined cornering-braking are given in figures 3.67 – 3.70. As expected, both models predict that under low lateral slip, the longitudinal force distribution dominates the contact patch. In figure 3.67 both the lateral force and the longitudinal force build up independently in the adhesion region of the contact, based on the lateral and longitudinal slip values. In the adhesion region the build-up of the longitudinal force does not affect the build-up of the lateral force and vice-versa. Sliding starts when the combination of lateral and longitudinal force exceeds the friction limit. This point always occurs earlier along the contact, compared to pure side-slip or longitudinal-slip conditions for the same slip values. In this case, sliding starts approximately at the middle of the contact patch. The bristle tip slides with a velocity resulting from the vectorial addition of the longitudinal and lateral sliding velocities. In the sliding region, the bristle forces do not depend on the slip values alone, but on the relative magnitude of the two sliding velocities (lateral and longitudinal). Figure 3.68 depicts the force distribution at high lateral slip. Although the longitudinal slip value remains the same, the longitudinal force (green line) is much lower than that shown in figure 3.67. Now, the force distribution is mainly governed by the resultant sliding velocity. Because the lateral velocity contributes much more than the longitudinal, the longitudinal force corresponds to a small portion

of the total friction force. Similar comments apply on the force distributions generated by the simple models in figures 3.69 and 3.70. As a conclusion, it is observed that the co-existence of lateral and longitudinal slip does not affect the force generating mechanism in the adhesion region of the contact. When sliding occurs, the effect depends entirely on the relative magnitudes of the sliding velocities in the lateral and longitudinal directions.

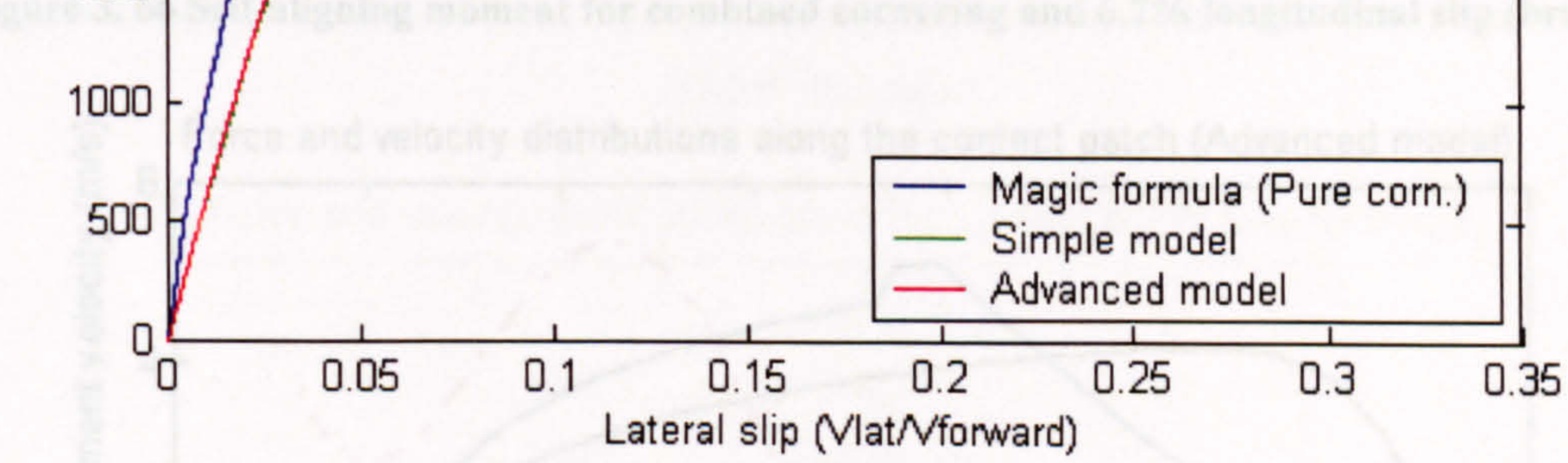

Figure 3. 65 Lateral force for combined cornering and 6.7% longitudinal slip (braking)

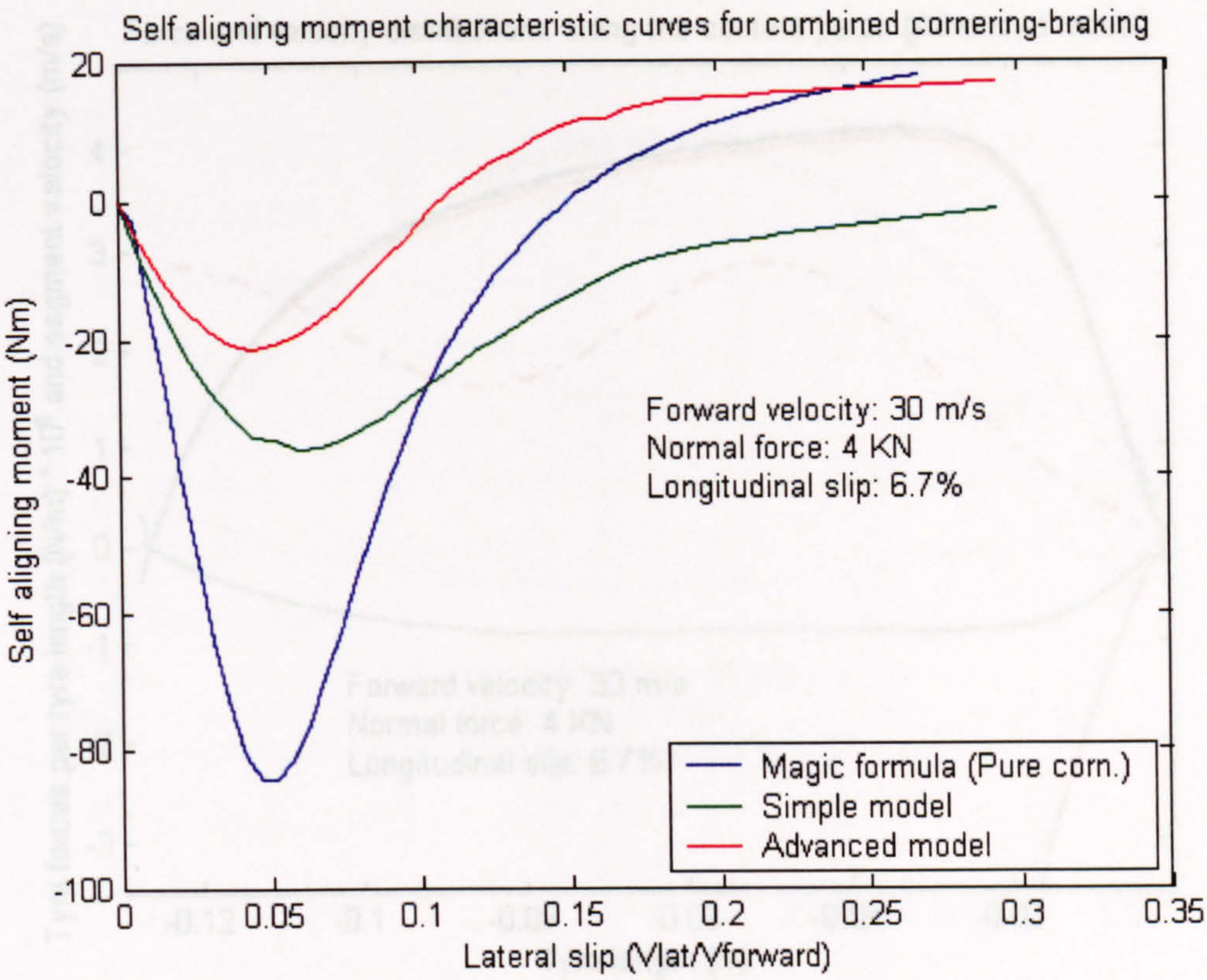

Figure 3. 66 Self-aligning moment for combined cornering and 6.7% longitudinal slip (braking)

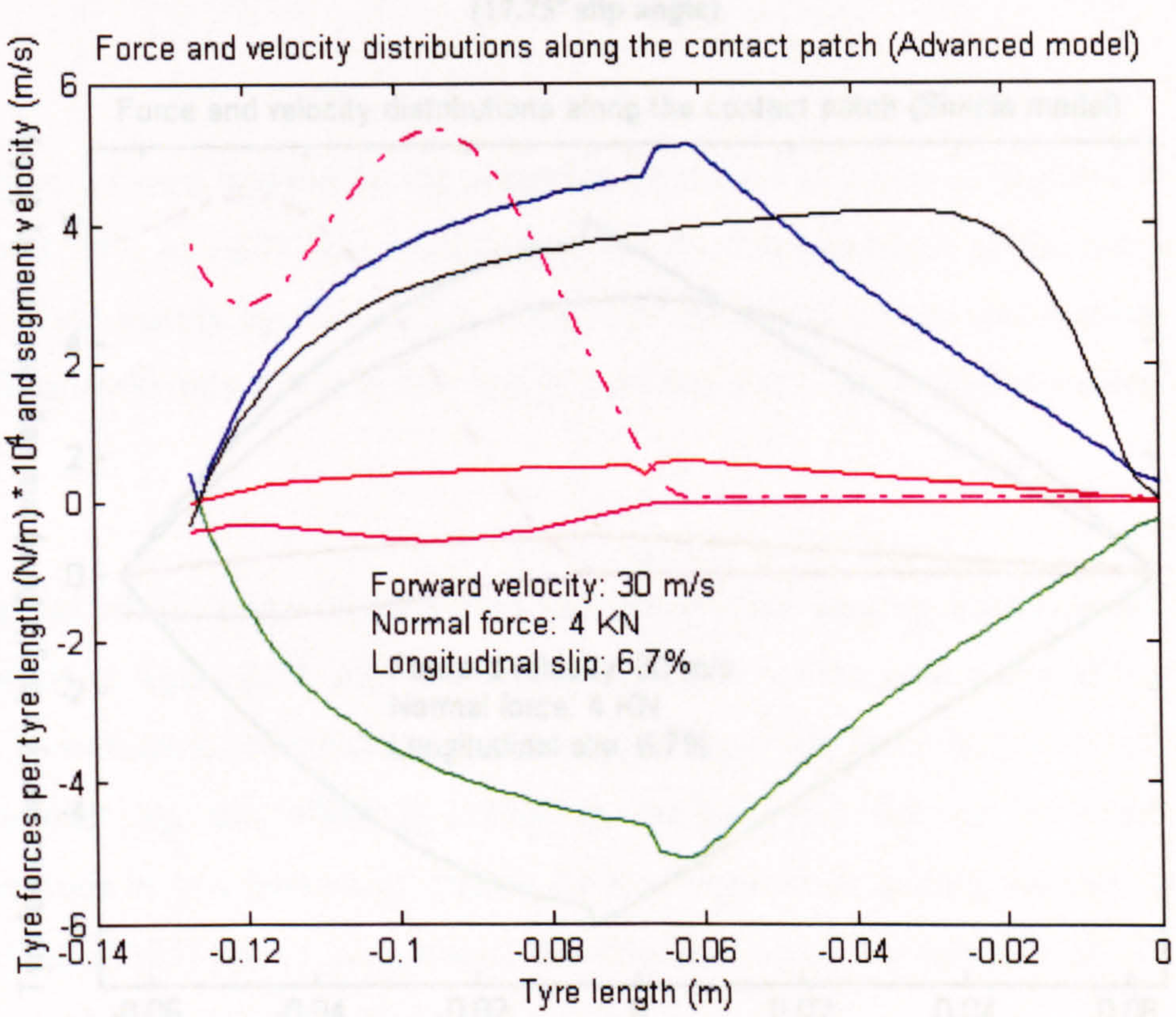

Figure 3. 67 Force distribution along the contact patch for combined lateral - longitudinal slip (0.46^{o} slip angle)

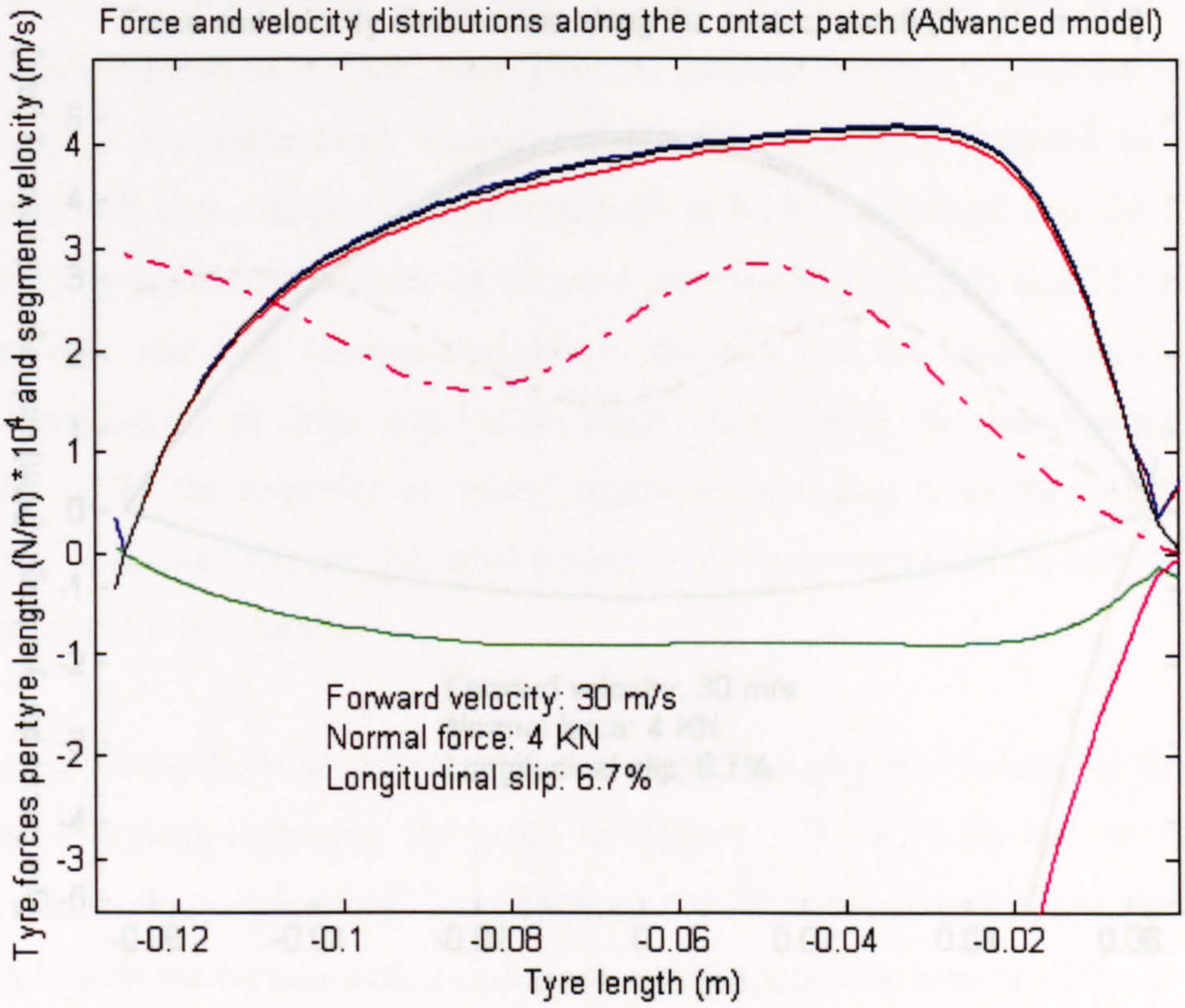

Figure 3. 68 Force distribution along the contact patch for combined lateral - longitudinal slip (17.75^{o} slip angle)

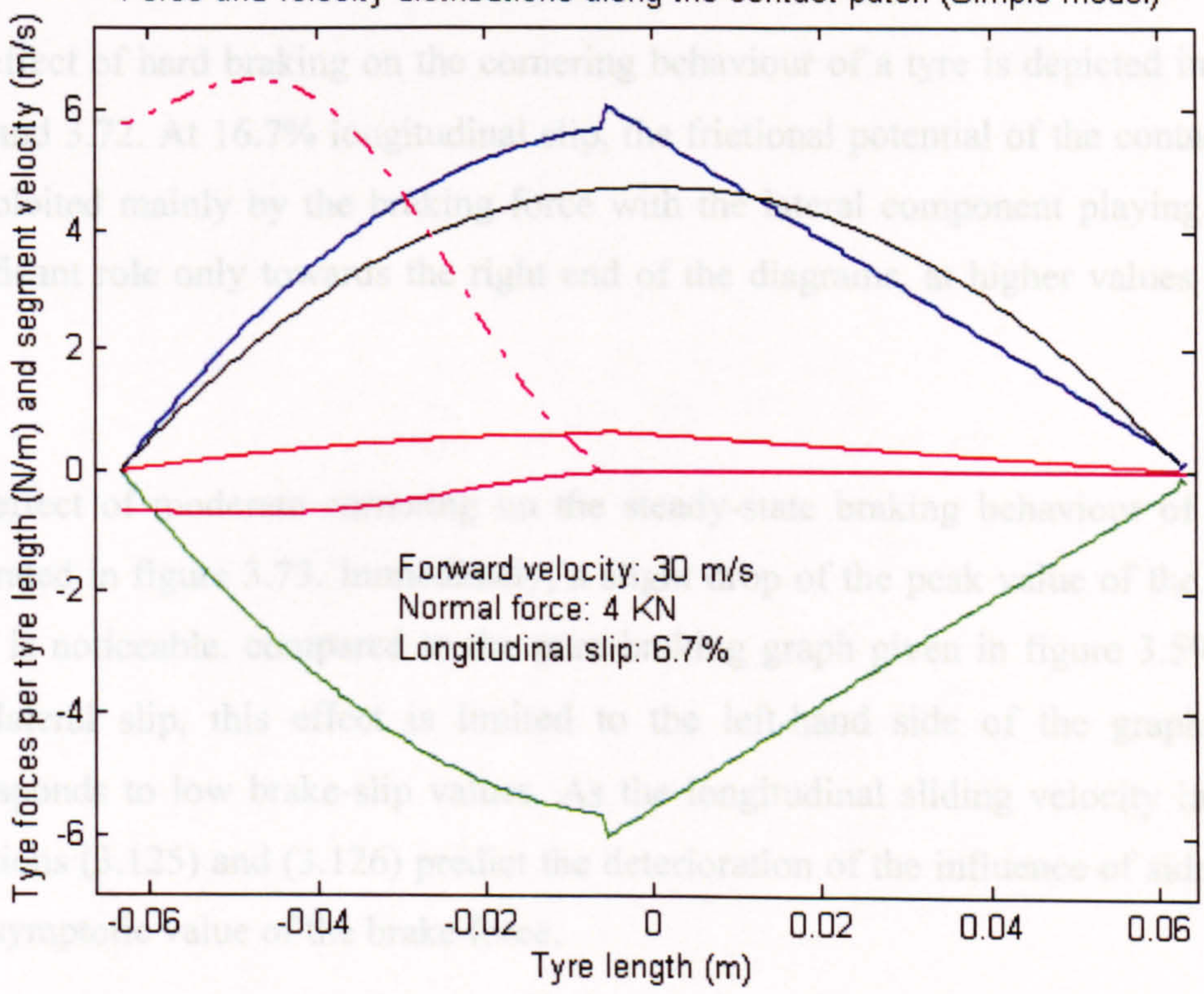

Figure 3. 69 Force distribution along the contact patch for combined lateral - longitudinal slip (0.46^{o} slip angle)

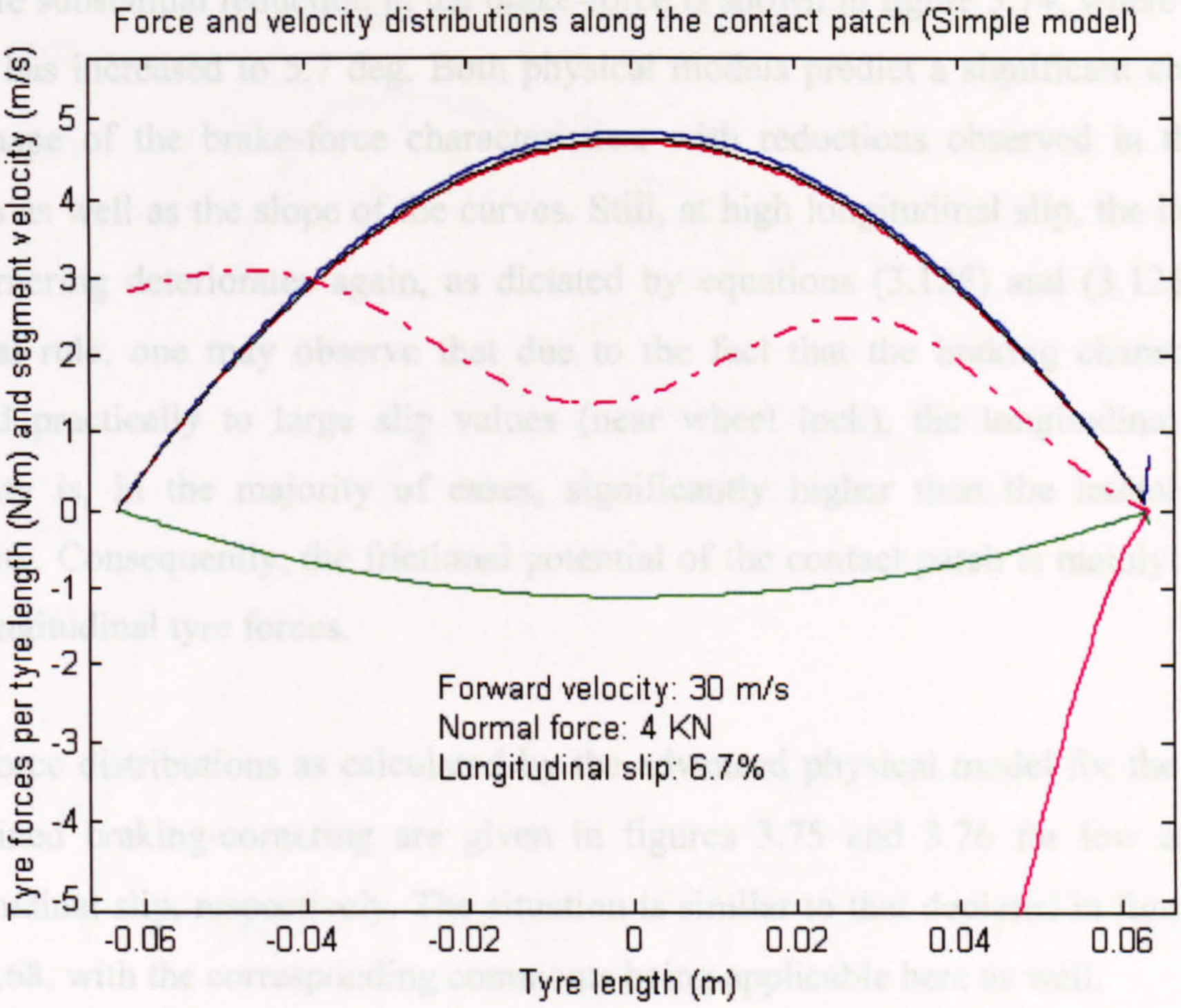

Figure 3. 70 Force distribution along the contact patch for combined lateral - longitudinal slip (17.75^{o} slip angle)

The effect of hard braking on the cornering behaviour of a tyre is depicted in figures 3.71 and 3.72. At 16.7% longitudinal slip, the frictional potential of the contact patch is exploited mainly by the braking force with the lateral component playing a more significant role only towards the right end of the diagrams, at higher values of side-slip.

The effect of moderate cornering on the steady-state braking behaviour of tyres is illustrated in figure 3.73. Immediately, a slight drop of the peak value of the braking force is noticeable, compared to the pure braking graph given in figure 3.59. Under low lateral slip, this effect is limited to the left-hand side of the graph, which corresponds to low brake-slip values. As the longitudinal sliding velocity increases, equations (3.125) and (3.126) predict the deterioration of the influence of side-slip on the asymptotic value of the brake force.

A more substantial reduction in the brake-force is shown in figure 3.74, where the slip angle has increased to 5.7 deg. Both physical models predict a significant change in the shape of the brake-force characteristics, with reductions observed in the peak values as well as the slope of the curves. Still, at high longitudinal slip, the influence of cornering deteriorates again, as dictated by equations (3.125) and (3.126). As a general rule, one may observe that due to the fact that the braking characteristics extend practically to large slip values (near wheel lock), the longitudinal sliding velocity is, in the majority of cases, significantly higher than the lateral sliding velocity. Consequently, the frictional potential of the contact patch is mainly used by the longitudinal tyre forces.

The force distributions as calculated by the advanced physical model for the case of combined braking-cornering are given in figures 3.75 and 3.76 for low and high longitudinal slip, respectively. The situation is similar to that depicted in figures 3.67 and 3.68, with the corresponding comments being applicable here as well.

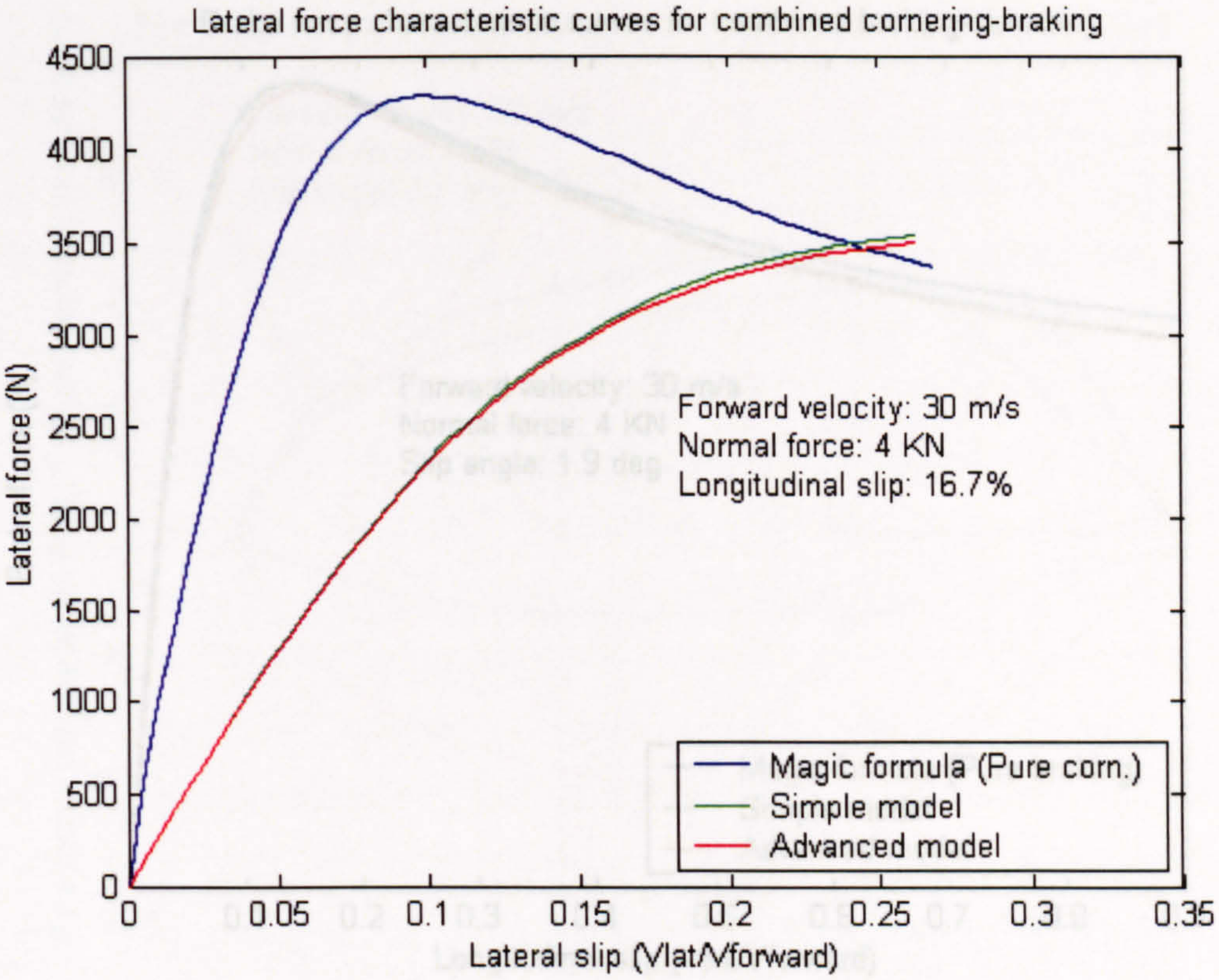

Figure 3. 71 Lateral force for combined cornering and 16.7% longitudinal slip (braking)

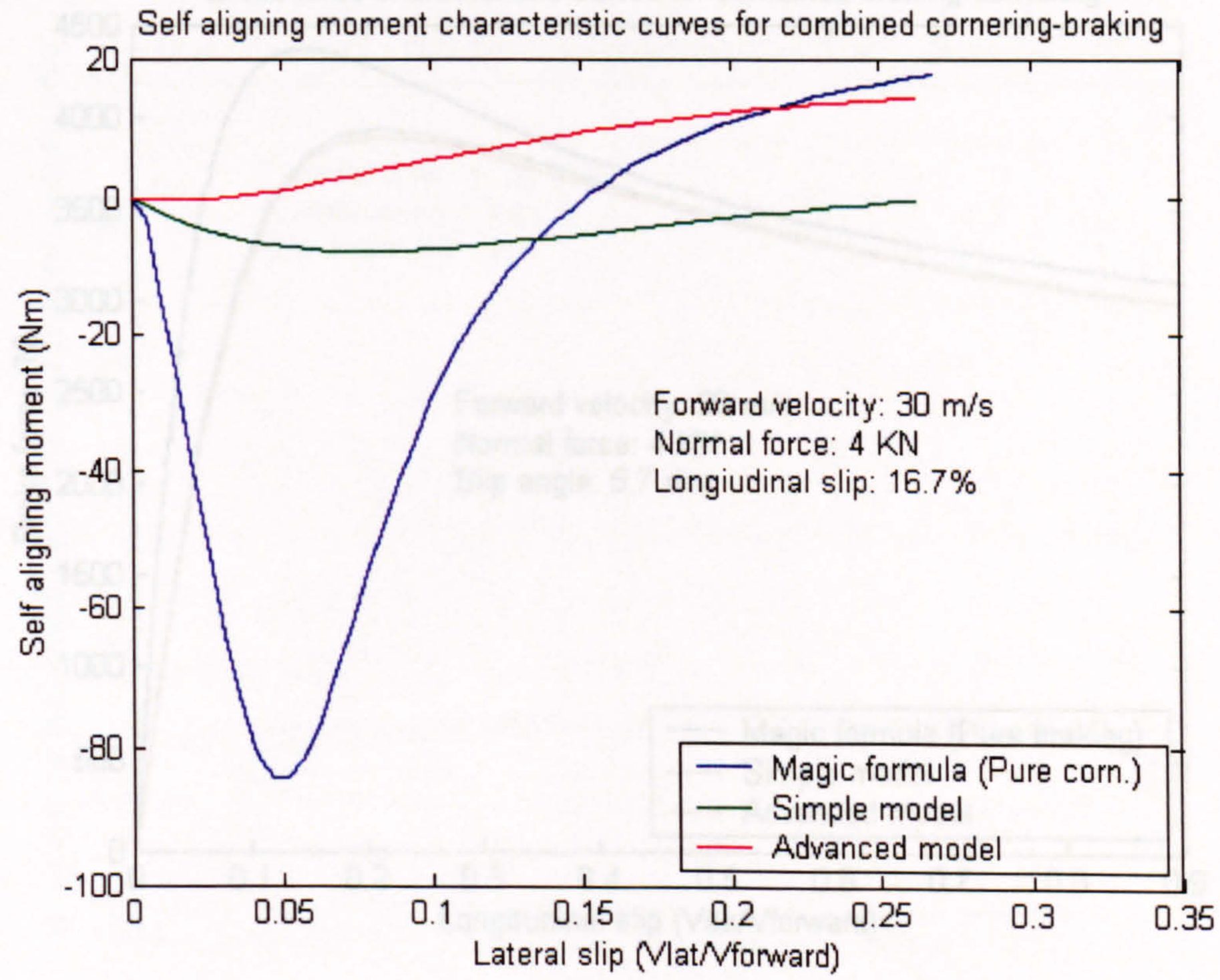

Figure 3. 72 Self-aligning moment for combined cornering and 16.7% longitudinal slip (braking)

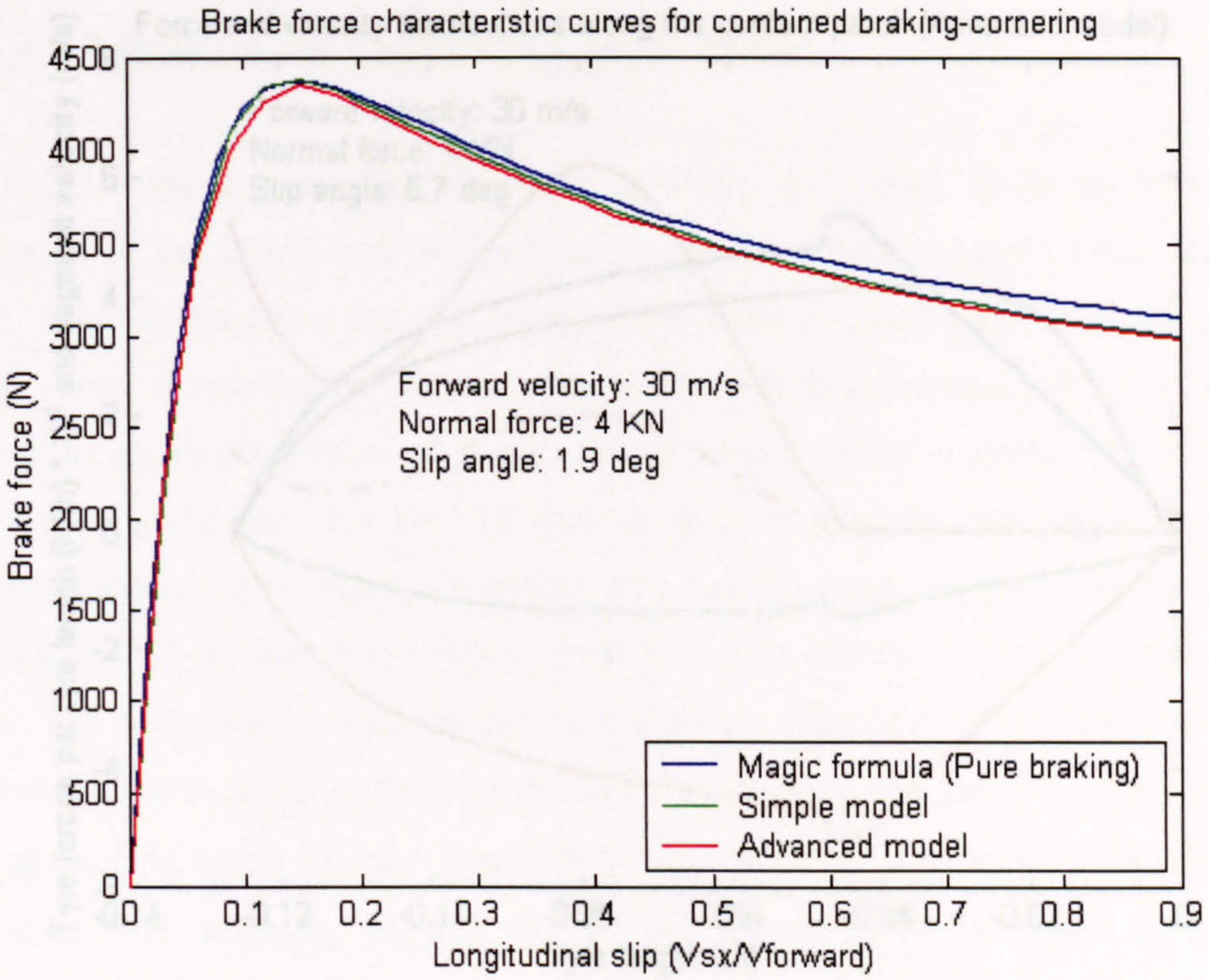

Figure 3. 73 Longitudinal force for combined braking and 1.9 deg lateral slip

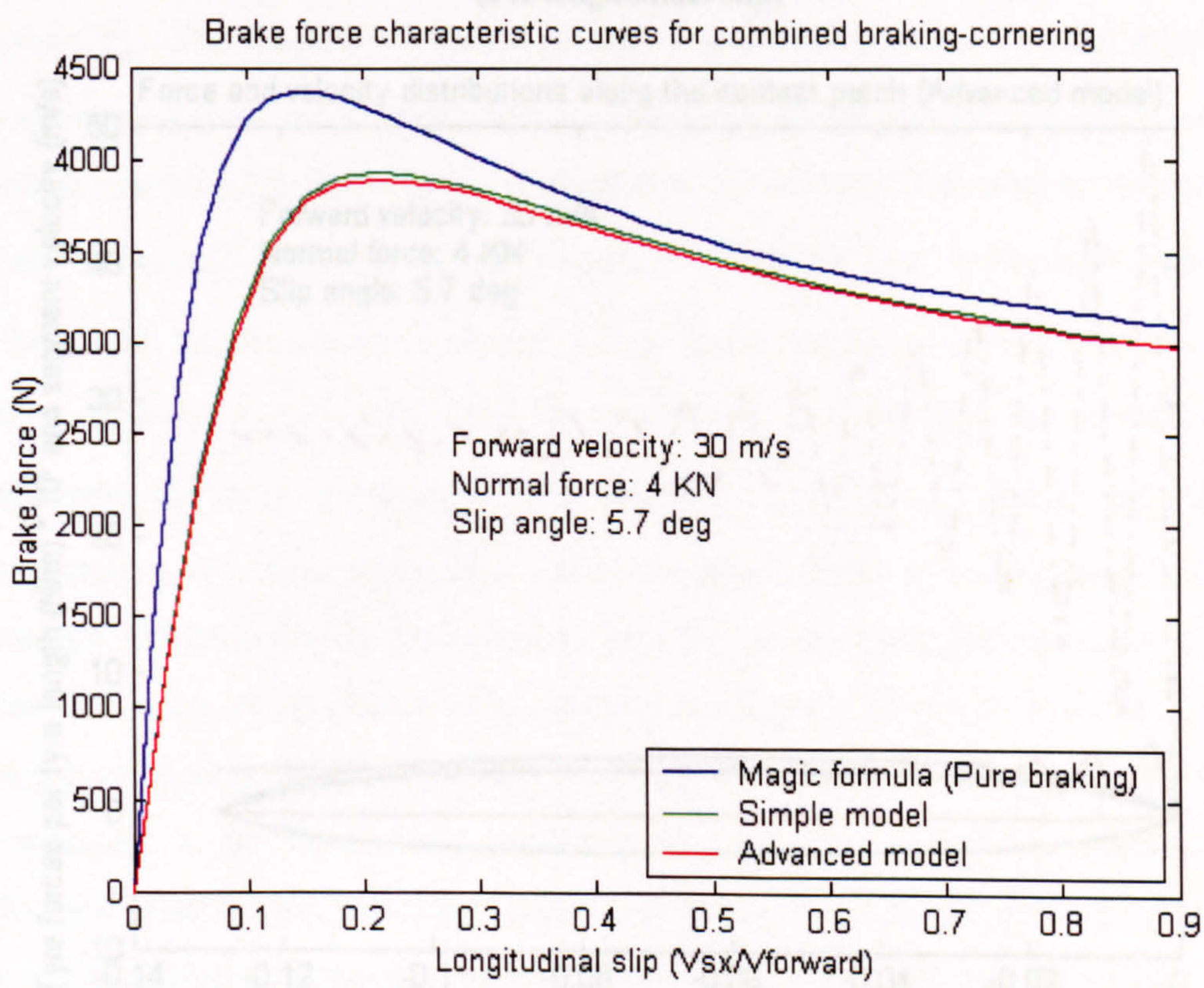

Figure 3. 74 Longitudinal force for combined braking and 5.7 deg lateral slip

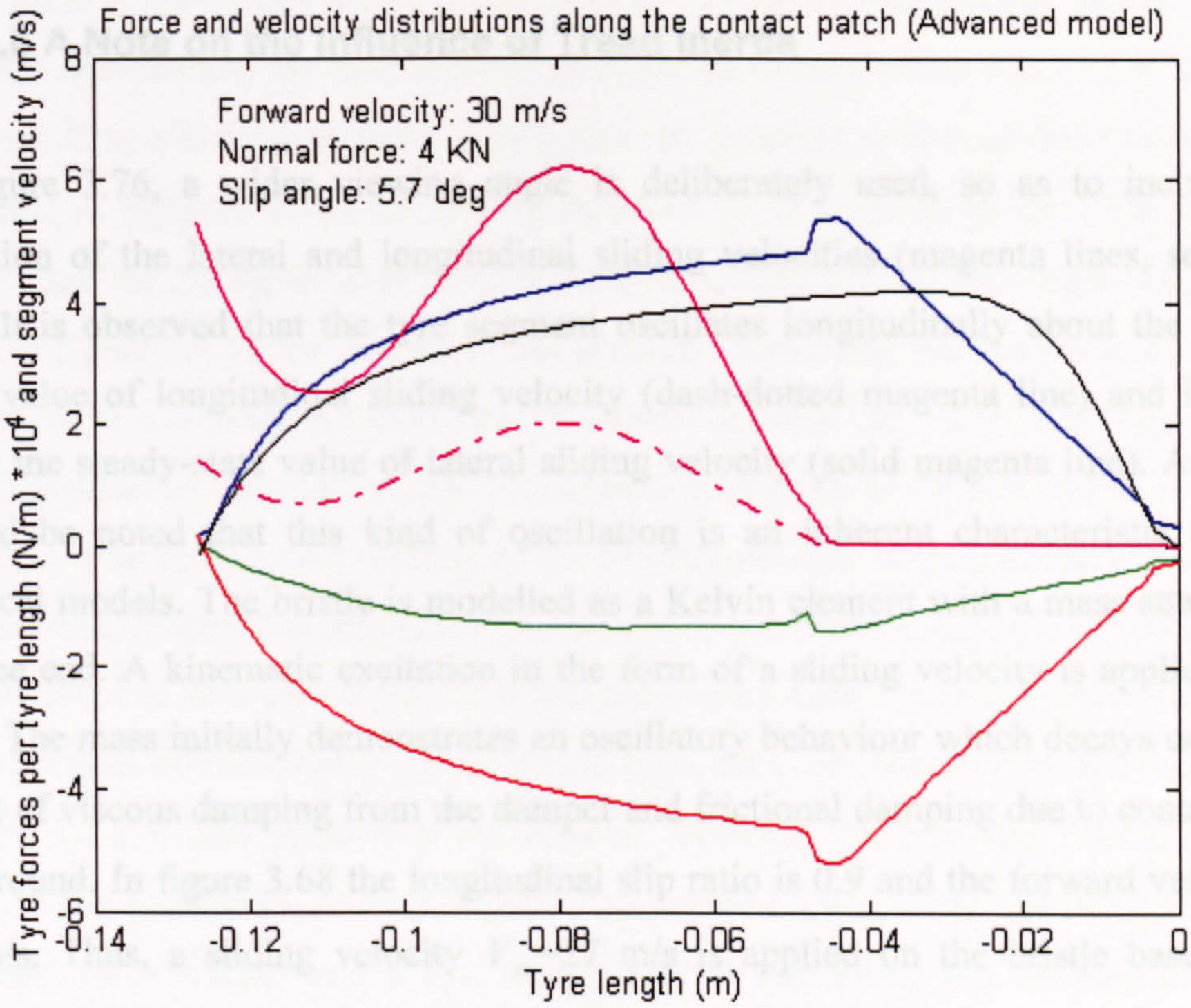

Figure 3. 75 Force distribution along the contact patch for combined longitudinal - lateral slip (3% longitudinal-slip)

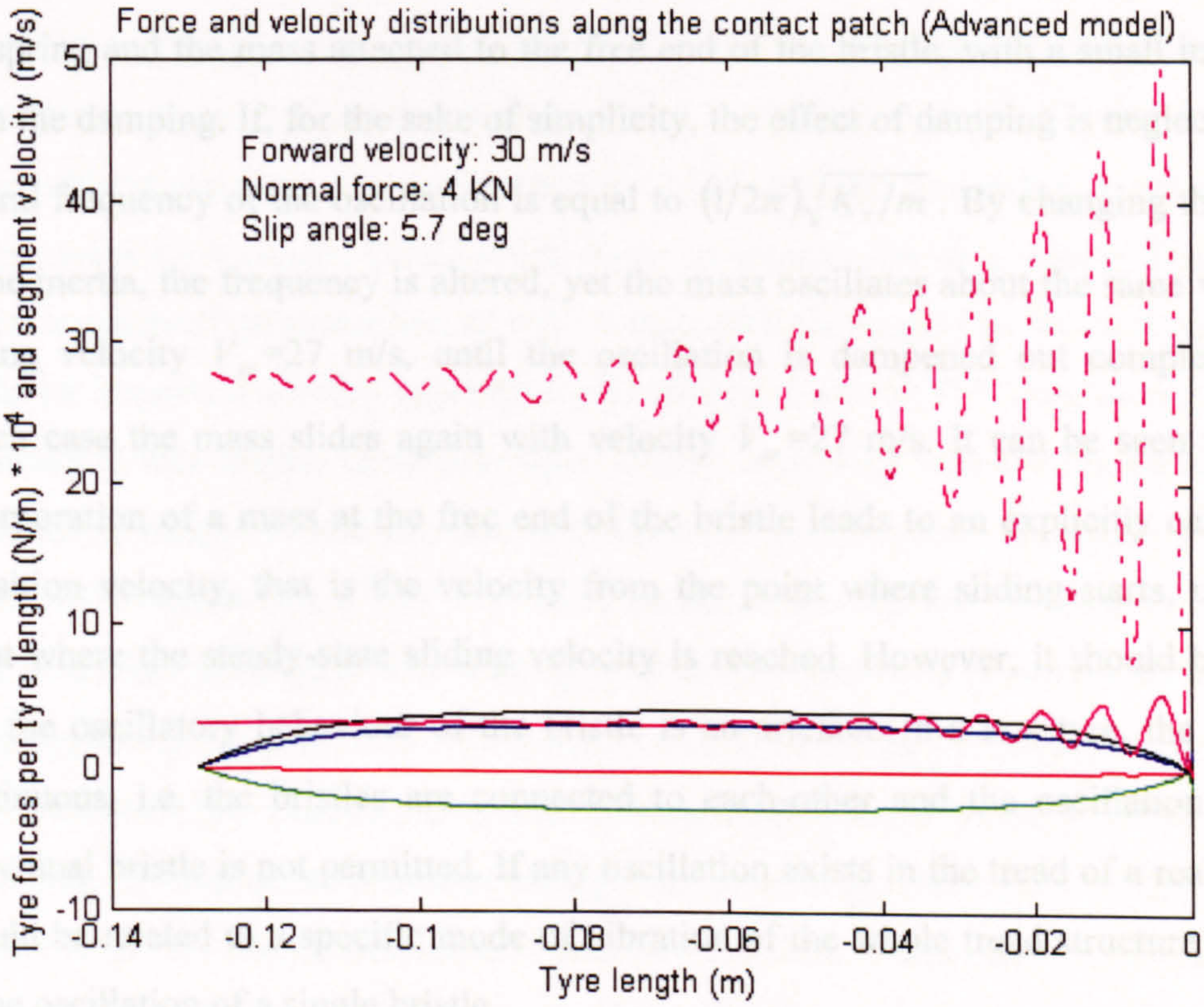

Figure 3. 76 Force distribution along the contact patch for combined longitudinal - lateral slip (90% longitudinal-slip)

3.3.6.6 A Note on the Influence of Tread Inertia

In figure 3.76, a wider viewing angle is deliberately used, so as to include the variation of the lateral and longitudinal sliding velocities (magenta lines, see table 3.6). It is observed that the tyre segment oscillates longitudinally about the steady-state value of longitudinal sliding velocity (dash-dotted magenta line) and laterally about the steady-state value of lateral sliding velocity (solid magenta line). At first it should be noted that this kind of oscillation is an inherent characteristic of both physical models. The bristle is modelled as a Kelvin element with a mass attached to its free end. A kinematic excitation in the form of a sliding velocity is applied to its base. The mass initially demonstrates an oscillatory behaviour which decays under the effect of viscous damping from the damper and frictional damping due to contact with the ground. In figure 3.68 the longitudinal slip ratio is 0.9 and the forward velocity is 30 m/s. Thus, a sliding velocity V_{sx}=27 m/s is applied on the bristle base in the longitudinal direction. It is clear from figure 3.68 that the longitudinal velocity of the mass at the free end of the bristle oscillates about the steady-state value of the sliding velocity V_{sx}. The frequency of the oscillation is mainly governed by the stiffness of the spring and the mass attached to the free end of the bristle, with a small influence from the damping. If, for the sake of simplicity, the effect of damping is neglected, the natural frequency of the oscillation is equal to $(1/2\pi)\sqrt{K_x/m}$. By changing the value of the inertia, the frequency is altered, yet the mass oscillates about the same value of sliding velocity V_{sx}=27 m/s, until the oscillation is dampened out completely, in which case the mass slides again with velocity V_{sx}=27 m/s. It can be seen that the incorporation of a mass at the free end of the bristle leads to an explicitly calculated transition velocity, that is the velocity from the point where sliding starts, until the point where the steady-state sliding velocity is reached. However, it should be noted that the oscillatory behaviour of the bristle is an artefact. In a real tyre, the tread is continuous, i.e. the bristles are connected to each-other and the oscillation of one individual bristle is not permitted. If any oscillation exists in the tread of a real tyre, it should be related to a specific mode of vibration of the whole tread structure and not to the oscillation of a single bristle.

If the mass at the end of the bristle reduces to zero, a sole Kelvin element remains to describe the contact. By considering equation (3.4) in section 3.2.3.1., it becomes apparent that a Kelvin element is adequate to generate a rate of deformation. For example, in figure 3.4 the solution of equation (3.4) is given in the form of strain versus time for the application of a constant stress (creep test). The slope of the strain curve in figure 3.4 yields the rate of deformation. Assuming that the constant stress is equivalent to a constant friction force, the slope of the strain curve represents the rate of deformation of a sliding bristle. The transition velocity at the free end of the bristle would then be equal to the velocity of the bristle base (excitation), added to the rate of deformation (slope of strain). Clearly, for a constant friction, the rate of deformation quickly reaches zero (see figure 3.4) and the sliding velocity of the bristle tip at this point is equal to the velocity of the bristle base. Also, it follows from the analysis in section 3.2.3.1. that mass-less viscoelastic elements such as the Kelvin element describe the response of rubber to step and periodic excitations relatively well. The argument is now clear: probably the best way of simulating the situation along the contact is a mass-less Kelvin element. In this case, a first order differential equation needs to be solved along the contact patch (as opposed to the second order differential equation in the case of an element with inertia). The transition velocity can still be calculated explicitly and it is expected to be close to the actual behaviour of rubber. Nevertheless, there is a fundamental drawback in this approach: A Kelvin element is not capable of generating stick-slip friction. As soon as the tip reaches its steady-state sliding velocity, it cannot decelerate in order to re-enter the stick phase. This hardly affects a steady-state model but, as will be discussed thoroughly in the next chapter, it might be important for the generation of transient friction. The steady-state models presented in this chapter were developed almost in parallel with the transient models presented in chapter 4 and the inertia of the tread was retained. In reality, the exact value of the inertia is not very important, as the bristle tip will oscillate in all cases until it reaches the steady-state sliding velocity. At this point a comment should be made regarding the numerical steady-state models presented by Sakai [48] and Sharp and El-Nashar [56]. These models neglect both the effects of damping and inertia and the bristle deflection is calculated taking into account the bristle's stiffness and the friction force. As already discussed in section 2.2.2.2. the transition velocity cannot be determined explicitly and some approximate techniques are implemented for its estimation. In both cases, it turns out that the steady-state sliding velocity is reached

quickly in a way that resembles more or less the behaviour of a mass-less Kelvin element. Therefore, it may be concluded that the transition velocity predicted by these models is not far from reality. Also, the fact that the tread inertia is neglected is justified if one considers that even at high excitation frequencies where inertia would typically play an important role, a simple mass-less viscoelastic element is capable of generating the response of rubber.

3.4 General Conclusions

The steady state behaviour of the pneumatic tyre under a variety of operating conditions has been discussed thoroughly. The important aspects of rubber viscoelasticity and friction have been incorporated in the study to some extent. The main contribution of the chapter has been the development of two physical tyre models which require numerical solution. Based on these models, the tyre force generating mechanism has been discussed and the influence of certain parameters is assessed.

The first, simple physical model assumes a parabolic pressure distribution along the contact patch. It was found that while this simplification hardly affects the generation of tyre forces, it largely influences the generation of the self-aligning torque. The completely symmetrical normal pressure distribution dictates an equally symmetrical shape for the lateral force distribution along the contact patch at large slip-angles i.e. when the lateral force is governed only by the sliding friction which in turn depends on the normal pressure. Under these conditions, the torque about the z axis of the SAE frame of reference is equal to zero. As a result, the self-aligning moment predicted by the simple tyre model always converges to zero at high slip angles. This does not constitute an experimental fact, as demonstrated for example in [41]. It was shown that the advanced version of the physical model predicted a more realistic self-aligning moment by employing a new method for the on-line calculation of the normal pressure distribution along the contact. The method is based on a combination of radial, tangential and vertical viscoelastic Kelvin elements for the estimation of the deformation and rate of deformation of the tyre along the contact. The stiffness of the radial Kelvin element was made non-linear, so as to saturate under large deflections and thus simulate the effect of air-pressure inside the tyre. It was demonstrated that

this modelling approach is capable of generating the approximately trapezoidal normal pressure distribution observed experimentally. In addition, the normal pressure was shown to shift towards the front part of the contact with increasing rolling velocity. The direct relation between the amount of energy dissipated during rolling and the shift in the normal pressure distribution was established and related to the generation of rolling resistance force and moment. The advanced physical model was used for the estimation of the rolling resistance as a function of rolling velocity and the results were in good agreement with experimental measurements in terms of the values of the rolling resistance force and the general trend of the curves. Nevertheless, the shape of the experimental curves indicates that the use of a non-linear damper in the radial Kelvin element would yield more realistic results. While the rolling resistance itself is not a primary output from the advanced model, its successful estimation indicates that the shape of the normal pressure distribution and its influence on the self aligning moment are both predicted successfully.

The velocity dependent anisotropic friction law implemented in both physical models seems to yield reasonable results. The anisotropy in both the static and kinetic friction and the anisotropic stiffness of the bristles in the lateral and longitudinal directions form a solid foundation for the simulation of combined slip situations, without the need for use of weighing functions and normalisations, as is the case with some other models [6], [41], [58]. Also, camber and turn-slip are accounted for in a simple yet fundamental manner and the simulation results show good agreement with the results by the Magic Formula. However, there is no provision in the models for the prediction of the drop in the cornering stiffness, caused by the existence of a camber angle. Also, the fact that both models lack the effect of tyre width results in a zero self-aligning moment when camber and/or turn-slip are present.

Finally, following the extensive discussion in section 3.3.6.6, it appears that the inertia of the tread is not a crucial characteristic of the tyre models. The behaviour of a viscoelastic bristle with and without inertia was discussed and the influence of the two alternatives in the transition velocity was determined. Based on this analysis it may be concluded that any reasonable transition velocity may be used and that, in general, the omission of the damping and inertia terms is justified in steady-state models.

Chapter 4: Transient Tyre Analysis

4.1 Introduction

Steady-state handling manoeuvres can only provide a limited perception of the overall handling qualities of a vehicle. When a vehicle is subjected to rapidly changing driving commands, the interactions of vehicle inertia with the stiffness and damping properties of the suspension cause phase delays in the handling responses. These delays are of similar, if not of more importance to the steady-state handling responses of the vehicle, influencing driver confidence about the levels of active safety provided by the vehicle. For example, when a vehicle is cornering under steady state conditions, not many things can be said about its behaviour. The driver may only sense the total lateral acceleration and to a certain extent assess whether the vehicle is operating near the limit of the force generating capabilities of the tyres. Still, it is not known how smoothly the vehicle would respond to an abrupt steering manoeuvre or an emergency braking. The pneumatic tyre plays a major role in these situations. From the outset one would be correct to surmise that its dynamic properties such as stiffness, damping and inertia would influence the transient response of the tyre, and in turn alter the dynamic response of the vehicle as a whole. What is not immediately evident is the effect of rolling velocity on tyre transient dynamics. What distinguishes the pneumatic tyre from a large number of dynamic structures is the existence of a periodically rotating viscoelastic contact of significant inertia. This fact fundamentally alters the formulation of the differential equations that describe the deformation of the tyre in space and time and introduces unique – to tyre mechanics – concepts, such as the relaxation length. Following from the analysis and discussion in the previous chapter, steady-state models prove inadequate for the description of such situations. A more generic approach is required, which would take into account the findings from the steady-state analysis, and additionally employ new concepts and methods for the successful representation of transient tyre behaviour.

4.2 General Considerations

4.2.1 The Relaxation Length Concept

An introduction to the transient behaviour of tyres is attempted by presenting the well-known relaxation length concept. The relaxation length serves as a first order, kinematic approach for the calculation of the delayed response of the tyre subjected to relatively low-frequency excitations. Initially this concept was employed for the prediction of side-force response to a transient increase in the slip angle. Later it was realized that the same principle may be used for the description of brake force response to transient longitudinal slip. Although simple, the relaxation length approach gives invaluable insight into the transient behaviour of tyres. More importantly, it is connected to some basic physical properties of the tyre, providing a simple measure of the quality of its transient response. Complex tyre models, suitable for use in a higher frequency range, may benefit from these connections, employing similar or more elaborate definitions of the relaxation length, as a measure of tyre transient characteristics.

4.2.1.1 Lateral Relaxation Length

Figure 4.1 depicts the neighbourhood of the contact patch of a free-rolling tyre under the application of a lateral force. A hypothetical point, Po, is assumed to lie on the longitudinal centre of the contact patch. The position of point Po with respect to the centre-plane of the wheel is laterally displaced as a result of lateral slip. Another point, P, lies on the wheel centre-plane at a longitudinal distance, σ_y, in front of point Po. The position of the hypothetical point P is assumed to remain unaltered in the SAE frame of reference. Furthermore, it is assumed that point Po satisfies the non-sliding condition, thus remains connected firmly to the ground. Because point P is attached to the SAE moving frame of reference, its velocity with respect to Po is u and v in the longitudinal and lateral directions respectively. Referring to figure 4.1, the lateral displacement of point Po leads to the following geometrical relation:

$$\tan a' = \frac{\eta}{\sigma_y} \tag{4.1}$$

Differentiation of relation (4.1) with respect to time yields:

$$\frac{d}{dt}\tan a' = \frac{v\sigma_y - u\eta}{\sigma^2{}_y} \tag{4.2}$$

Rearranging equation (4.2) yields:

$$\frac{d}{dt}\tan a' + \frac{u}{\sigma_y}\tan a' = \frac{v}{\sigma_y} \tag{4.3}$$

In order for equation (4.3) to be applicable both for positive and negative values of u, the following formulation may be used:

$$\frac{d}{dt}\tan a' + \frac{|u|}{\sigma_y}\tan a' = \frac{v}{\sigma_y} \tag{4.4}$$

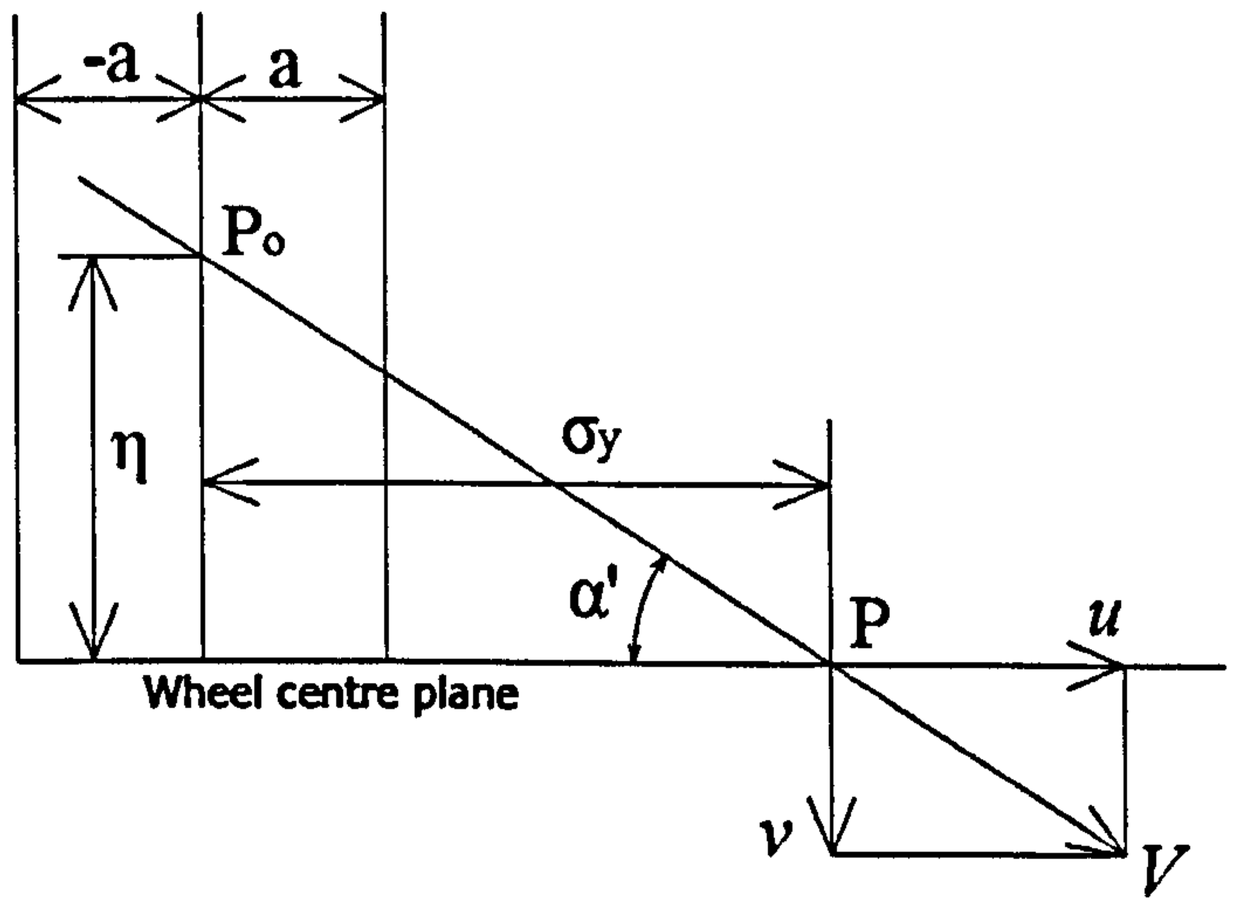

Figure 4. 1 The lateral relaxation length concept

Length σ_y represents the relaxation length of the tyre and a' is the transient slip angle. Equation (4.4) calculates the slip angle a' as a function of time, based on the

value of the relaxation length σ_y and the lateral and longitudinal velocities $u(t)$, $v(t)$. As expected, the steady-state solution of equation (4.4) reduces to:

$$\tan a' = \frac{v}{|u|} \tag{4.5}$$

The lateral tyre stiffness can be defined as:

$$C_y = \frac{|F_y|}{|\eta|} \tag{4.6}$$

Similarly, the cornering stiffness can be defined for small slip angles as:

$$C_a = \frac{|F_y|}{|a'|} \tag{4.7}$$

In addition, for small slip angles and as long as point Po satisfies the non-sliding condition, the following relation applies:

$$\tan a' \approx a' = \frac{\eta}{\sigma_y} \tag{4.8}$$

Combination of relations (4.6)-(4.8) yields:

$$\sigma_y = \frac{C_a}{C_y} \tag{4.9}$$

The significance of relation (4.4) and the influence of the relaxation length on the transient behaviour of tyres can be realised by a simple example. Assuming constant forward velocity u and a step change in the lateral velocity v, equation (4.4) yields the slip angle as:

$$\tan a' = \frac{v}{|u|}\left(1 - e^{-\frac{u}{\sigma_y}t}\right) \tag{4.10}$$

The transient slip angle generated by relation (4.10) can be used as an input to any physical or empirical steady-state tyre model for the calculation of the lateral force generated under the aforementioned step change in the wheel's lateral velocity. Equation (4.10) enables a definition for the relaxation length with physical significance. At time $t = \frac{\sigma_y}{u}$ after the application of the step input, the slip angle will have achieved approximately 63% of its steady-state value. Thus, the relaxation length can be defined as the length covered by a hypothetical point on the tyre circumference, in order to achieve 63% of the maximum lateral displacement under the application of a step rise in the lateral velocity of the wheel. For a given longitudinal velocity, a large relaxation length leads to a slower response, while a reduced relaxation length results in a faster response in terms of lateral force build-up. With the aid of relation (4.9), the transient response of the tyre can be related to some fundamental structural properties. Clearly, increasing lateral stiffness C_y causes a reduction in the relaxation length, thus improving the transient response of the tyre. Nevertheless, cornering stiffness C_a found in the numerator also depends on the lateral stiffness of the tyre. In particular, any increase in the lateral stiffness of the tyre leads to a subsequent increase in cornering stiffness. This kind of dependence does not allow direct predictions, based on relation (4.9), to be made.

4.2.1.2 Longitudinal Relaxation Length

The concept of longitudinal relaxation length is presented, based on the approach followed by Clover et al [40]. Referring to figure 4.2, point, Qo, is assumed to lie on the longitudinal centre of the contact patch. At distance σ_x, in front of point Qo, lies a hypothetical point Q attached to the SAE moving frame of reference. Point Qo is assumed to satisfy the non-sliding criterion and is considered firmly attached to the ground. Consequently, point Q travels with respect to point Qo with a longitudinal velocity u. Assuming a braking situation, where $u > R\Omega$, point Qo represents a longitudinally displaced point of the tyre circumference. The corresponding point on

the undeformed contact patch lies at a longitudinal distance ξ behind point Q and travels with velocity $R\Omega$ with respect to Q. To aid visualization of the situation, point Qo can be seen as the tip of a longitudinally deformed bristle, while the bristle's base is at distance ξ behind Q. The transient longitudinal slip is defined as:

$$k' = \frac{\sigma_x - \xi}{\sigma_x} \tag{4.11}$$

Differentiation of relation (4.11) with respect to time yields:

$$\frac{d}{dt}k' = \frac{(u - R\Omega)\sigma_x - (\sigma_x - \xi)u}{\sigma_x^2} \tag{4.12}$$

Rearranging equation (4.12) gives:

$$\frac{d}{dt}k' + \frac{u}{\sigma_x}k' = \frac{u - R\Omega}{\sigma_x} \tag{4.13}$$

The steady-state solution of (4.13) reduces to:

$$k' = \frac{u - R\Omega}{u} \tag{4.14}$$

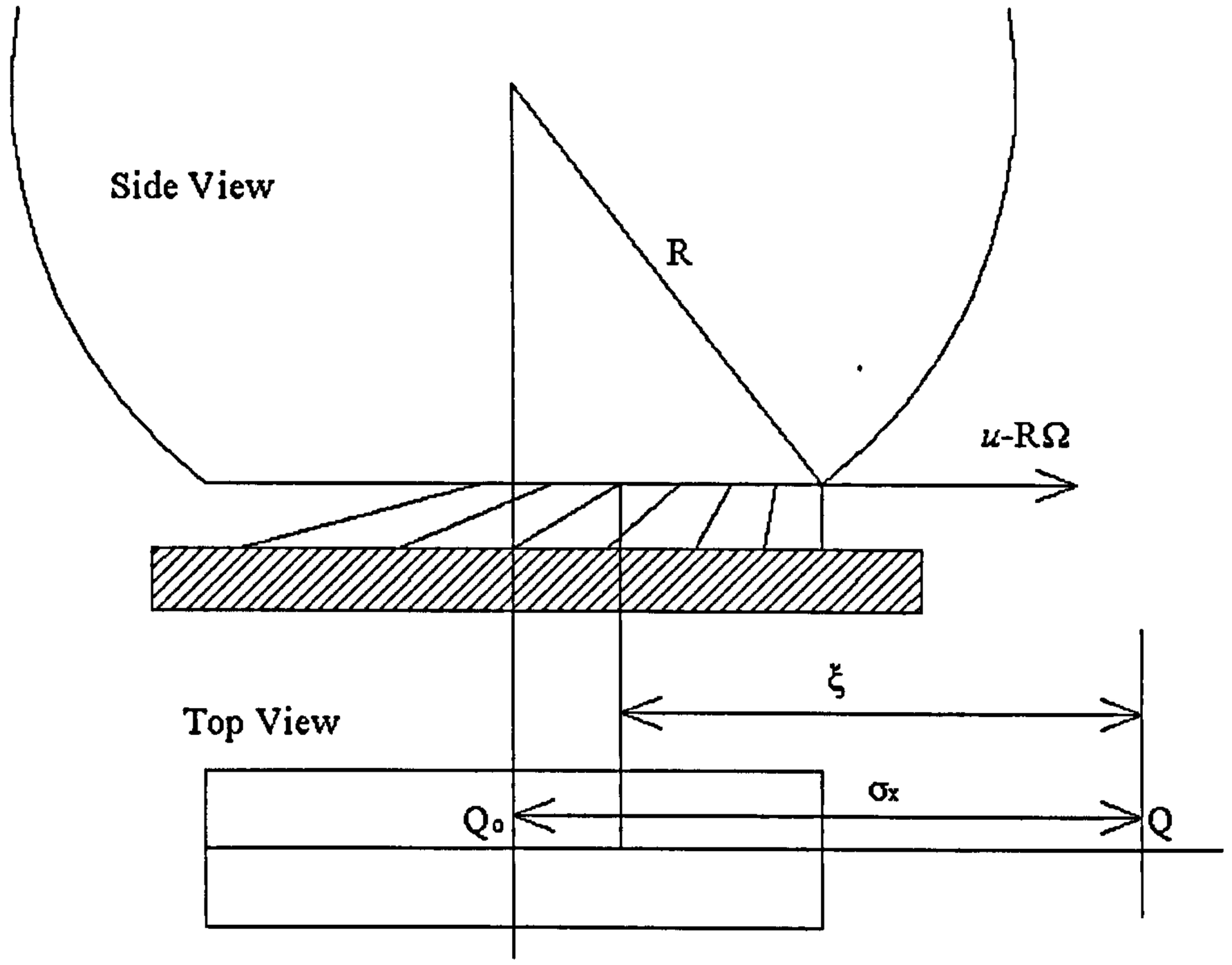

Figure 4. 2 The longitudinal relaxation length concept

In a similar manner to the case of lateral slip, the longitudinal stiffness of the tyre can be defined as follows:

$$C_x = \frac{|F_x|}{|\sigma_x - \xi|} \tag{4.15}$$

Furthermore, for low values of longitudinal slip the braking stiffness of the tyre can be defined as:

$$C_k = \frac{|F_x|}{|k'|} \tag{4.16}$$

The combination of (4.11), (4.15) and (4.16) yields:

$$\sigma_x = \frac{C_k}{C_x} \tag{4.17}$$

Finally, in order for the formulation to handle both positive and negative values of u, the differential equation (4.13) is modified as follows:

$$\frac{d}{dt}k'+\frac{|u|}{\sigma_x}k'=\frac{|u|-R\Omega\,\mathrm{sgn}(u)}{\sigma_x} \tag{4.18}$$

4.3 A Tyre Model for the Investigation of Transient Friction Force Generation

In the previous section the transient response of the pneumatic tyre was approached, using the relaxation length concept. Relaxation length serves as a simple measure of the rate of transient tyre force transfer from the contact patch to the wheel rim. Another phenomenon, which is often neglected, is the mechanism of friction generation within the contact patch under transient handling manoeuvres. Friction force generation, especially when viscoelastic materials are involved in the contact, is a highly dynamic situation. An in-depth approach to the problem of transient tyre dynamics requires some attention to be paid to the aspect of transient friction generation. This type of analysis should then be combined with a tyre model, capable of depicting the transient processes involved in the transfer of contact patch forces to the wheel rim. In the present section a tyre model is developed, based on the simple steady-state physical model described in chapter 3. Some necessary modifications have been carried out in order to facilitate operation of the model in transient mode. In this procedure the realistic simulation of friction force generation is of major importance.

4.3.1 Physical Description of the Transient Friction Model

The transient friction model is developed primarily for the investigation of friction force generation. It has limited application as a generic transient tyre model and is used mainly for the determination of the effect of rapidly changing conditions on the mechanism of friction force generation. The reader may refer to section 3.3.4.1 for a detailed description of the simple steady-state model, which serves as a platform for the development of the transient model. The governing differential equations (3.113-3.118) are shown here for ease of reference:

$$\dot{u}_x \cdot C \cdot dx = (x_s - x) \cdot K_x \cdot dx + (V_{sx} - u_x) \cdot D_x \cdot dx - f_x \cdot dx \tag{4.19}$$

$$\dot{u}_y \cdot C \cdot dx = (y_s - y) \cdot K_y \cdot dx + (V_{sy} - u_y) \cdot D_y \cdot dx - f_y \cdot dx \tag{4.20}$$

$$\dot{x}_s = V_{sx} \text{ so that } x_s = \int_0^{travel} V_{sx} dt \tag{4.21}$$

$$\dot{y}_s = V_{sy} \text{ so that } y_s = \int_0^{travel} V_{sy} dt \tag{4.22}$$

$$\dot{x} = u_x \text{ so that } x = \int_0^{travel} u_x dt \tag{4.23}$$

$$\dot{y} = u_y \text{ so that } y = \int_0^{travel} u_y dt \tag{4.24}$$

In the steady state model, the motion of the infinitesimal mass is followed throughout the contact patch and is representative of the motion of all such elements in contact with the ground. Furthermore, the steady state model is run for pure braking, traction, cornering or combinations of the above, as shown in the general case represented in figure 3.25. The transient model is run for pure cornering conditions, so that V_{sx} vanishes, and equations (4.19), (4.21) and (4.23) yield zero displacements and velocities in the longitudinal direction.

Whilst V_{sy} is constant in the steady state model, it changes at each time step in the transient model. Consequently, the state of all infinitesimal masses in contact with the ground can no longer be obtained by following one representative mass throughout the contact patch. Instead, the state of a mass dm at $t + dt$ results from the state of the same mass at t.

In order to solve the problem, the vectors of the state variables, positions and velocities of all infinitesimal masses (segments), which form the contact patch need to be defined. If the length of the contact patch is $2 \cdot a = n \cdot dx$, n number of infinitesimal masses are involved in the problem. At a random operating point, for

example at time t, each mass is characterised by its velocity and position in the oxy plane. At time $t+dt$, every mass has moved one place backward in the contact patch, travelling a distance of $dx = V_r \cdot dt$. This sequential switching is also reflected in the state vectors, so that the state of the $i+1^{th}$ mass at time $t+dt$ can be calculated by using the state of the i^{th} mass at time t. In order for each mass to take exactly the place of the one adjacent to it, the time-step has to be constant and the number of masses has to be set according to the following relationship:

$$n = \frac{2 \cdot \mathrm{a}}{V_r \cdot dt}, \tag{4.25}$$

with V_r being fixed.

Thus, the total number of small masses (corresponding to small lengths dx) depends on the time-step size and the linear velocity of rolling, V_r. Considering the issues related to numerical stability, the time step-size should be the dominating factor and needs to be set *apriori*. Nevertheless, for a given length $2 \cdot \mathrm{a}$ and velocity V_r, a numerically effective time step can result in the generation of a small number of masses in contact with the ground. For example, if $V_r = 40\,m/\mathrm{sec}$, $2 \cdot \mathrm{a} = 0.16\,m$ and $dt = 0.0001\mathrm{sec}$, then equation (4.25) yields $n = 40$, which means that the contact patch has been divided into 40 discrete parts with mass dm and length dx. Obviously, 200 or 300 segments would give a smoother and more accurate force generation mechanism. The dependence of the number of elements on the rolling velocity and the fact that the latter needs to remain constant are the main disadvantages of the proposed formulation and currently limit the potential use of the model.

The 4^{th} order fixed integration step size Runge-Kutta [113], [114] method is used for advancing the state of each infinitesimal mass from t to $t+dt$. The graphical representation in figure 4.3 shows the integration procedure according to the previous analysis.

n number of small masses on the left are linked to their states at time t. One step of the integration algorithm is applied to every single vector entry, using as initial

conditions the positions and velocities included in the state vector at time t. In this manner, a single step of integration is applied for n different initial conditions, as opposed to the steady state model, where, starting from one set of initial conditions, the integration is applied for n sequential steps, following a single mass dm, from the beginning to the end of the contact area. Meanwhile, every discretised mass element dm moves for a distance of $dx = V_r \cdot dt$, so that the i^{th} entry replaces the $i+1^{th}$ entry and so forth. Thus, the updated states obtained by the integrator are moved one place towards the end of the state vector, in such a way that an empty space is created in the beginning of the vector, whereas at the same time the n^{th} entry is "pushed" out of the vector. The empty space created in the beginning is then occupied by a new mass with the initial conditions $0, V_{sy}$, where V_{sy} is the new value of the lateral sliding velocity, according to an increase in the slip angle in a transient manner. Because this procedure is continuous, the i^{th} entry appears on both sides of the integrator: On the right it appears as a result of the integration of the $i-1^{th}$ state, while on the left it appears as an initial state for the i^{th} entry.

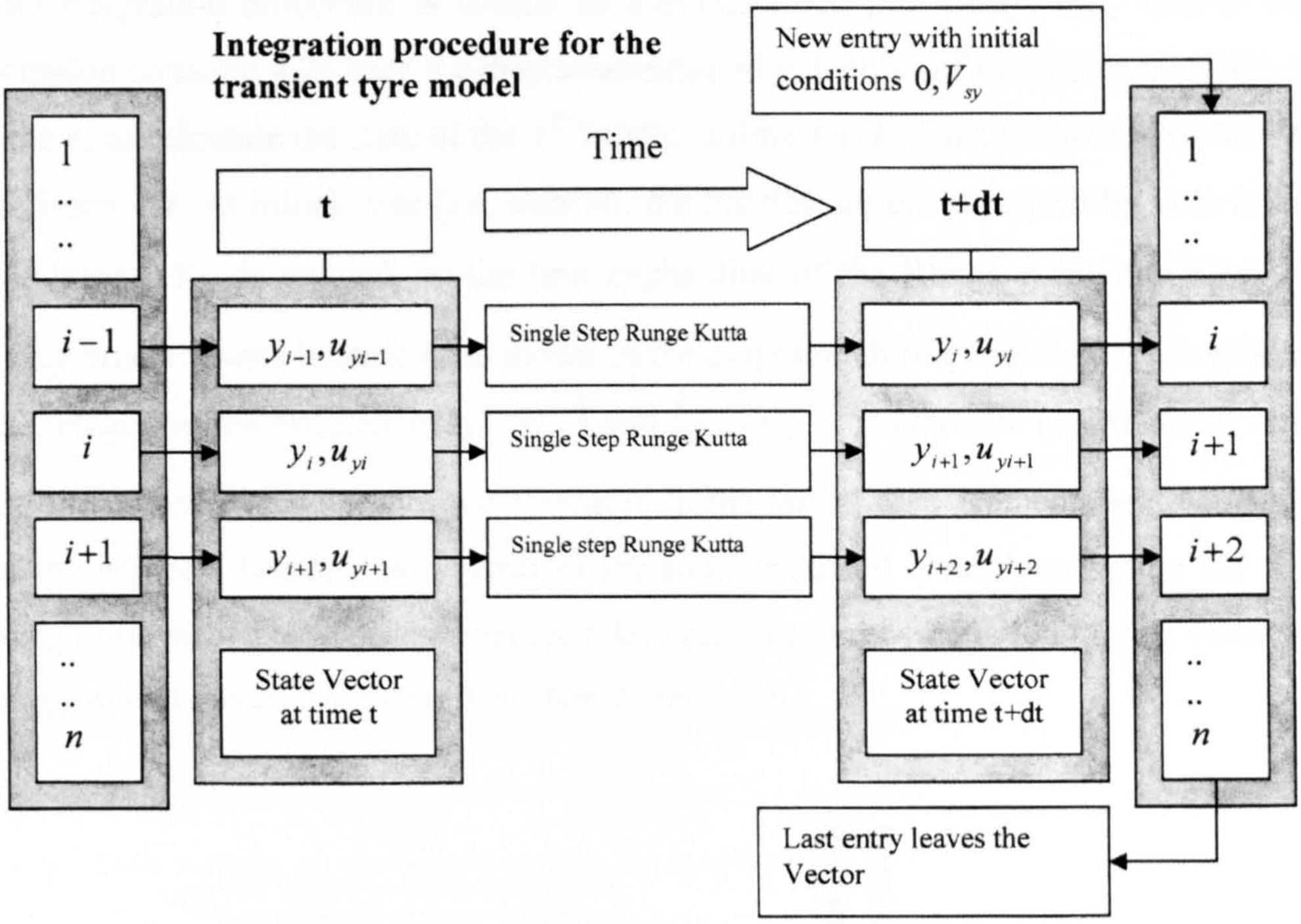

Figure 4. 3 State update scheme for the transient friction model

An unrealistic simplification adopted in most brush models (see for example [6], [42], [52], [55]) is the complete separation of the bristles, representing the tyre tread-carcass. In a steady-state study this representation would not cause any problems. The properties of one representative segment can be set, so that the overall behaviour of the tyre agrees with the experimental steady-state results. On the contrary, under transient operating conditions, where the tread undergoes rapid changes and all tyre segments should be considered simultaneously, it is likely that the physical continuity of the tread could play a more important role. In order to investigate this effect, the bristles of the basic transient model are connected laterally to each other, using viscoelastic Kelvin elements. Equation (4.20) now becomes:

$$\begin{aligned} \dot{u}_y \cdot C \cdot dx = &\left(y_s - y\right)\cdot K_y \cdot dx + \left(V_{sy} - u_y\right)\cdot D_y \cdot dx - \left(y - y_{i-1}\right)\cdot K_{\text{int}\,er} \cdot dx \\ &- \left(y - y_{i+1}\right)\cdot K_{\text{int}\,er} \cdot dx - \left(u_y - u_{yi-1}\right)\cdot D_{\text{int}\,er} \cdot dx - \left(u_y - u_{yi+1}\right)\cdot D_{\text{int}\,er} \cdot dx - f_y \cdot dx \end{aligned} \tag{4.26}$$

where $K_{\text{int}\,er}$ and $D_{\text{int}\,er}$ denote the stiffness and damping properties of the interconnections.

The integration procedure is similar to that described previously, only that in this occasion equation 4.26 uses the displacements and velocities of the adjacent bristles at time t, to calculate the state of the i^{th} bristle at time $t+dt$. This is shown graphically in figure 4.4. At initial state (i.e. state 0), the bristles are characterised by zero initial conditions. V_{sy} is applied, so the first application of the Runge Kutta algorithm on every bristle results in state 1, as shown in the diagram. During this first application of the integrator, the differences $(y-y_{i\pm1})$ and $(u_y-u_{y\pm1})$ in equation (4.26) are all zero. On the contrary, state 1 shows differences in the lateral displacements and velocities of the adjacent bristles, as a result of different frictional conditions during the first integration step. These differences are taken into account by equation (4.26), when the integrator advances from state 1 to state 2 and so on.

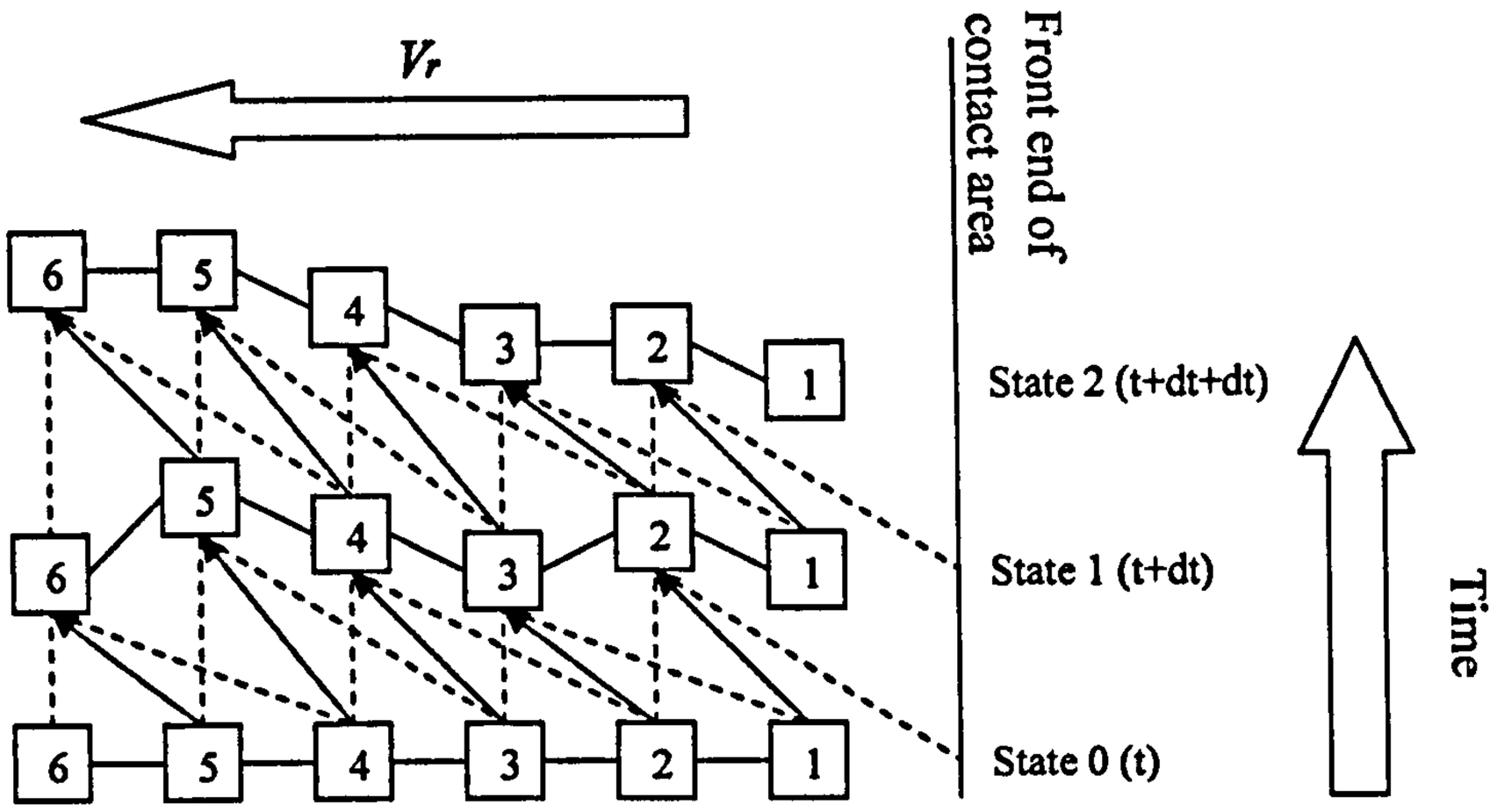

Figure 4. 4 Schematic representation of the motion of interconnected bristles

4.3.2 The Transient Friction Law

A detailed reference to the frictional behaviour of viscoelastic materials was given in section 3.2.3.2. The continuous coefficient of friction variation with slip velocity, shown in figure 3.8, was later approximated by a stick-slip friction law, in combination with an exponentially decreasing coefficient of friction. In addition, anisotropy in the lateral and longitudinal directions of sliding was taken into account. In the steady state case, it is fundamental that the friction law depicts the changes in coefficient of friction with sliding velocity. The transition between stick and slip is

also important as it determines the initiation of the velocity-dependent coefficient of friction, based on the vertical load at a specific point, the coefficient of static friction and of course the forces applied on the segment under consideration. In this procedure, the exact details of the transition between stick and slip are not significant. In the transient case, it is important to depict the frictional behaviour of the surfaces in contact near the transition point between stick and slip. The adoption of a simple stick-slip law alone, such as that described by relations (3.104) and (3.105) does not yield representative results in the case of rubber friction. Such stick-slip laws are developed primarily for hard materials as demonstrated by Karnopp [112]. Nevertheless, if the analysis is restricted – in terms of velocity – to the neighbourhood of the transition point, a stick-slip law appropriate for hard materials might work well, when combined with a viscoelastic Kelvin element. This fact is demonstrated by developing a simple model of a rubber block in contact with a hard surface. Simulation results of the friction forces developed within the contact show good coincidence with results obtained experimentally in [26], by measuring the actual friction force between a block consisting of tyre rubber and a rough surface. The elementary rubber block used in the model is identical to a tyre segment as described in chapter 3. Furthermore, for the purpose of the analysis the simple friction law summarised in relations (3.104) and (3.105) is used. It is shown that, while the transition law is identical to the one used for the steady-state analysis, in transient analysis, factors such as the threshold velocity and the time-step size, play a very important role in the accurate prediction of the frictional behaviour of rubber.

4.3.2.1 Experimental Results

The experiment carried out by Braghin et al [26] is briefly described. The apparatus used can be considered as a flat belt-tyre testing machine in small scale. A small block, consisting of tread rubber is pressed against a rolling belt made of abrasive paper of appropriate surface roughness. The rubber block is kept steady against the moving belt, while the velocity of the belt is monitored accurately. Controllable parameters include vertical load, sliding velocity and bulk temperature of the specimen. The vertical load is so chosen in order to generate contact pressures in the range of 1-2.6 bar, the velocity varies from 0.01 to 1 m/s and the temperature can be set from ambient to 120°. Apart from the measurement of the friction force generated

in the contact patch between the paper and the specimen, the rig is capable of measuring the deformation of the rubber block near the contact with the paper, using laser transducers. This unique feature allows the monitoring of stick-slip motion in the neighbourhood of the contact. Figure 4.5 shows a typical stick-slip response. The graph corresponds to the deformation of the rubber block as measured by the laser transducer. Initially the block sticks to the moving belt. At this point no macroscopic sliding occurs, and the rubber is dragged along by the belt, increasing its deflection. This stage of deflection is represented by the red line in the figure. When the resisting elastic forces exceed a breakthrough value, corresponding to the maximum static friction, sliding between the specimen and the belt occurs. The deflection of the specimen reduces rapidly as shown by the blue line. As expected, a small residual deflection remains before the specimen sticks again to the belt and a new deformation cycle begins. It should be noted that similar stick-slip responses have been measured experimentally by other researchers [27], [28]. Figure 4.6 shows the dependency of stick-slip on vertical load and sliding velocity. It is observed that higher loads promote the generation of stick-slip motion, while stick-slip behaviour vanishes at higher sliding velocities. Figure 4.7 depicts the effect of normal load on the amplitude of the deformation of the rubber block during stick-slip and finally the graph in figure 4.8 predicts an increase in stick-slip frequency with increasing sliding velocity. Also, the same graph indicates that lower vertical loads promote higher frequency stick-slip motion. In general, the frequencies of stick-slip observed, lie within the range of 30-90 Hz.

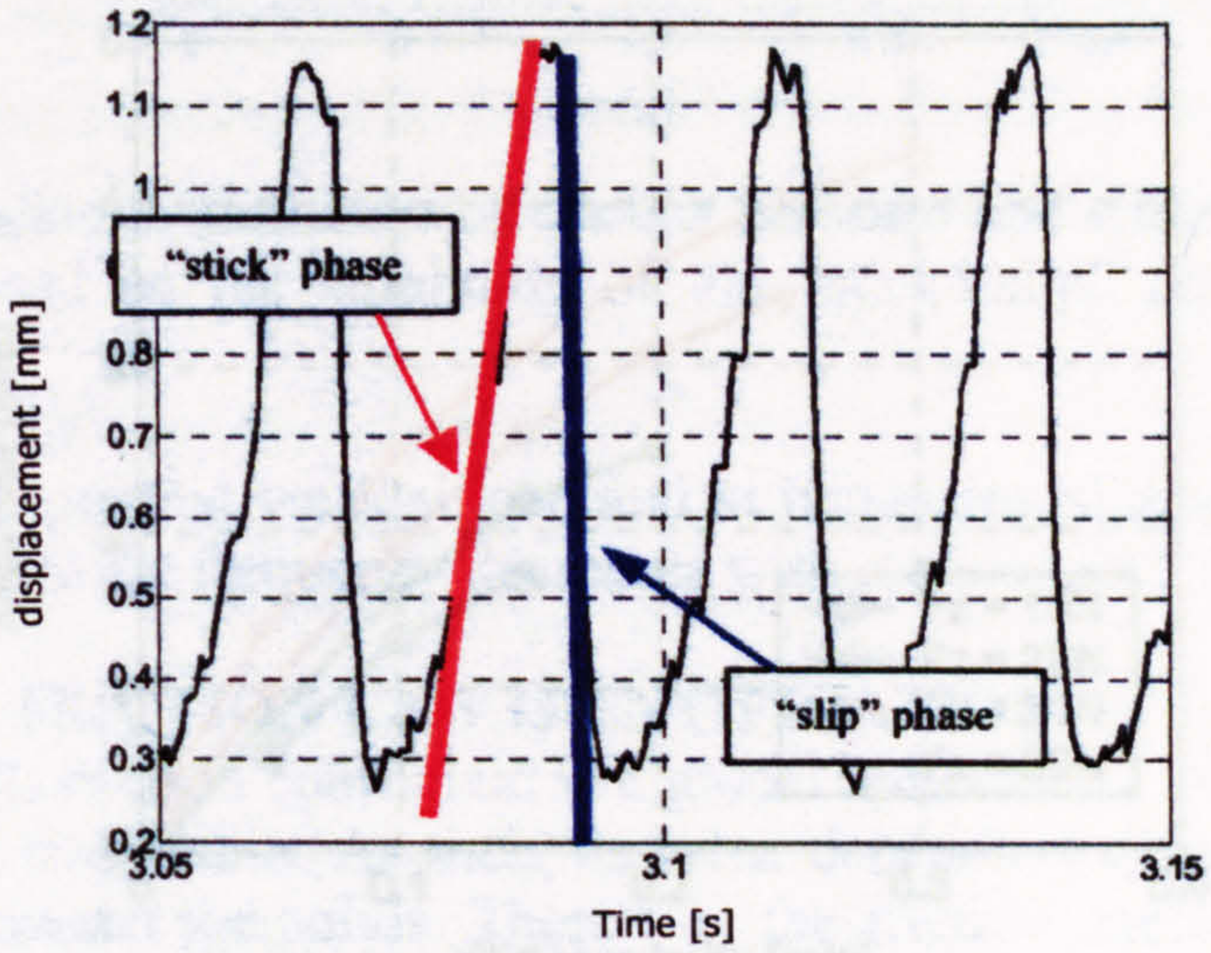

Figure 4. 5 Stick-Slip motion observed on a single rubber specimen (after [26])

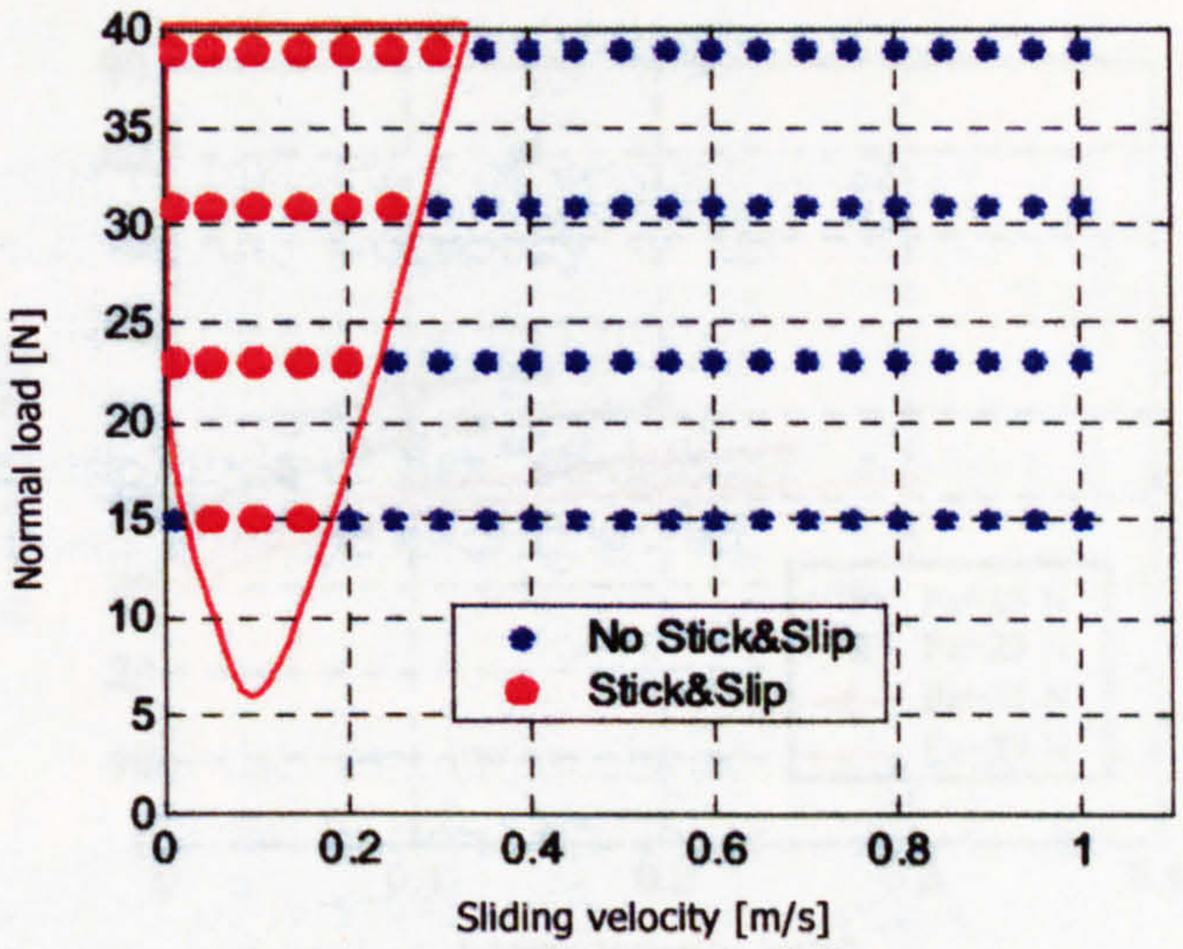

Figure 4. 6 Dependence of the existence of stick-slip on sliding velocity and normal load (after [26])

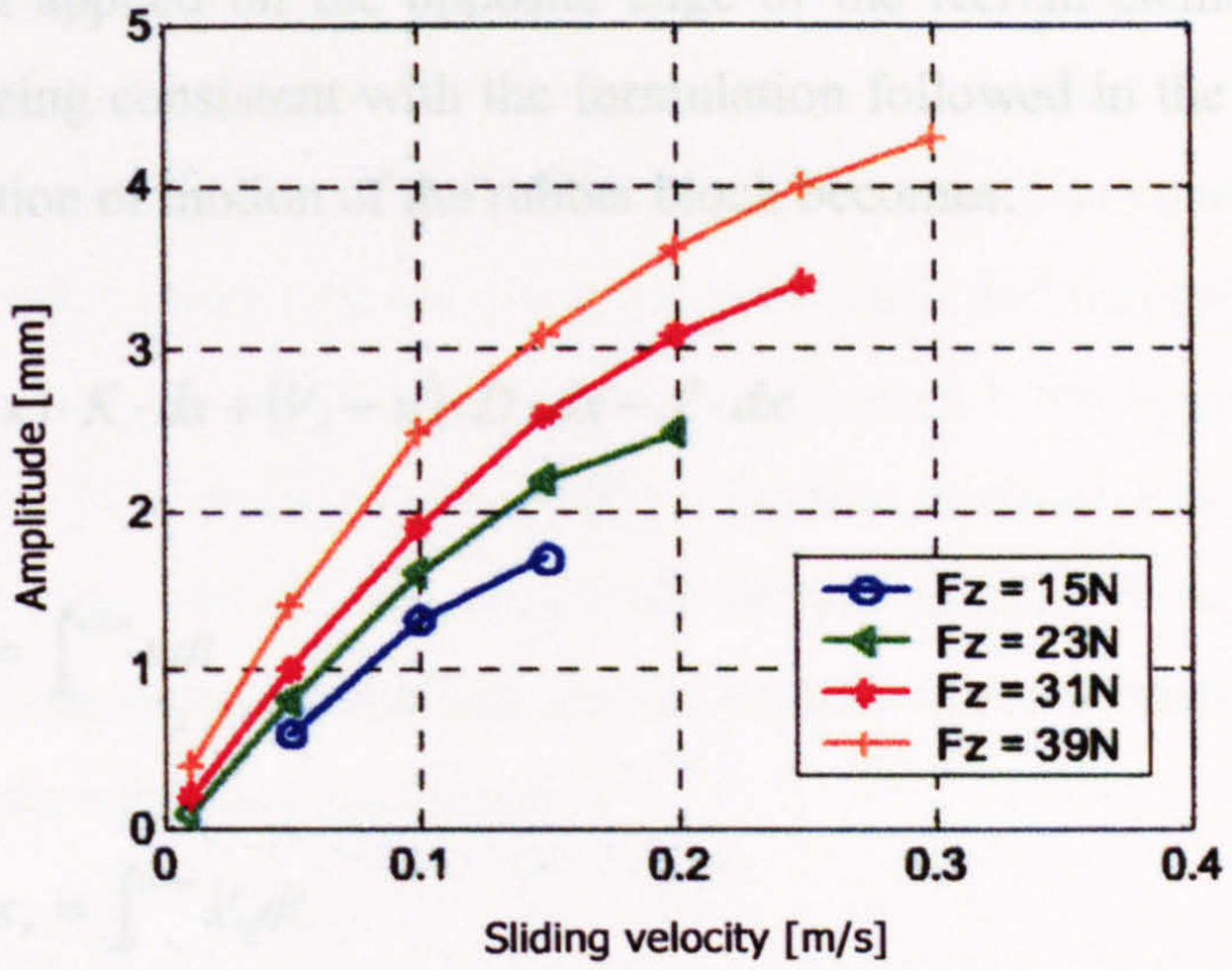

Figure 4. 7 Variation of amplitude of stick-slip deformation with normal load (after [26])

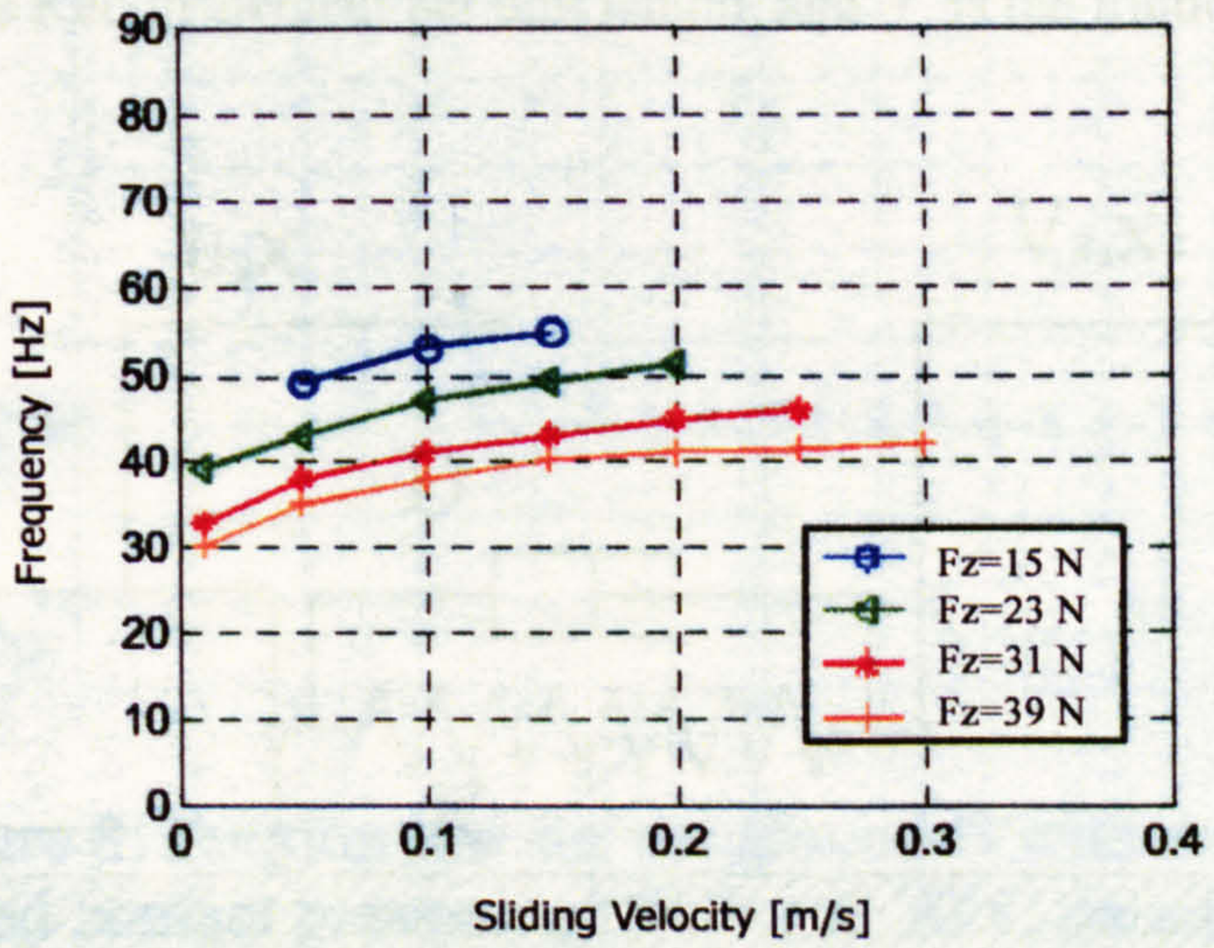

Figure 4. 8 Dependence of stick-slip frequency on sliding velocity for different vertical loads (after [26])

4.3.2.2 Numerical Simulation of Transient Friction

The rubber block used for the measurements described previously is modelled as a viscoelastic Kelvin element attached to a lumped mass. This arrangement is shown graphically in figure 4.9. Unlike the experiment, the virtual rubber block is pulled at a constant velocity against a stationary surface. Depending on the applied forces, the mass may be sticking or sliding on the surface. To achieve results comparable with the deflection graph shown in figure 4.5, the displacement of the mass is subtracted from

the displacement applied on the opposite edge of the Kelvin element. Referring to figure 4.9 and being consistent with the formulation followed in the tyre models, the differential equation of motion of the rubber block becomes:

$$\dot{u} \cdot C \cdot dx = (x_s - x) \cdot K \cdot dx + (V_s - u) \cdot D \cdot dx - f \cdot dx \tag{4.27}$$

$$\dot{x} = u \text{ so that } x = \int_0^{travel} u dt \tag{4.28}$$

$$\dot{x}_s = V_s \text{ so that } x_s = \int_0^{travel} V_s dt \tag{4.29}$$

where C denotes the inertia per unit length, K and D are the stiffness and damping coefficients of the Kelvin element per unit length, and f is the friction force.

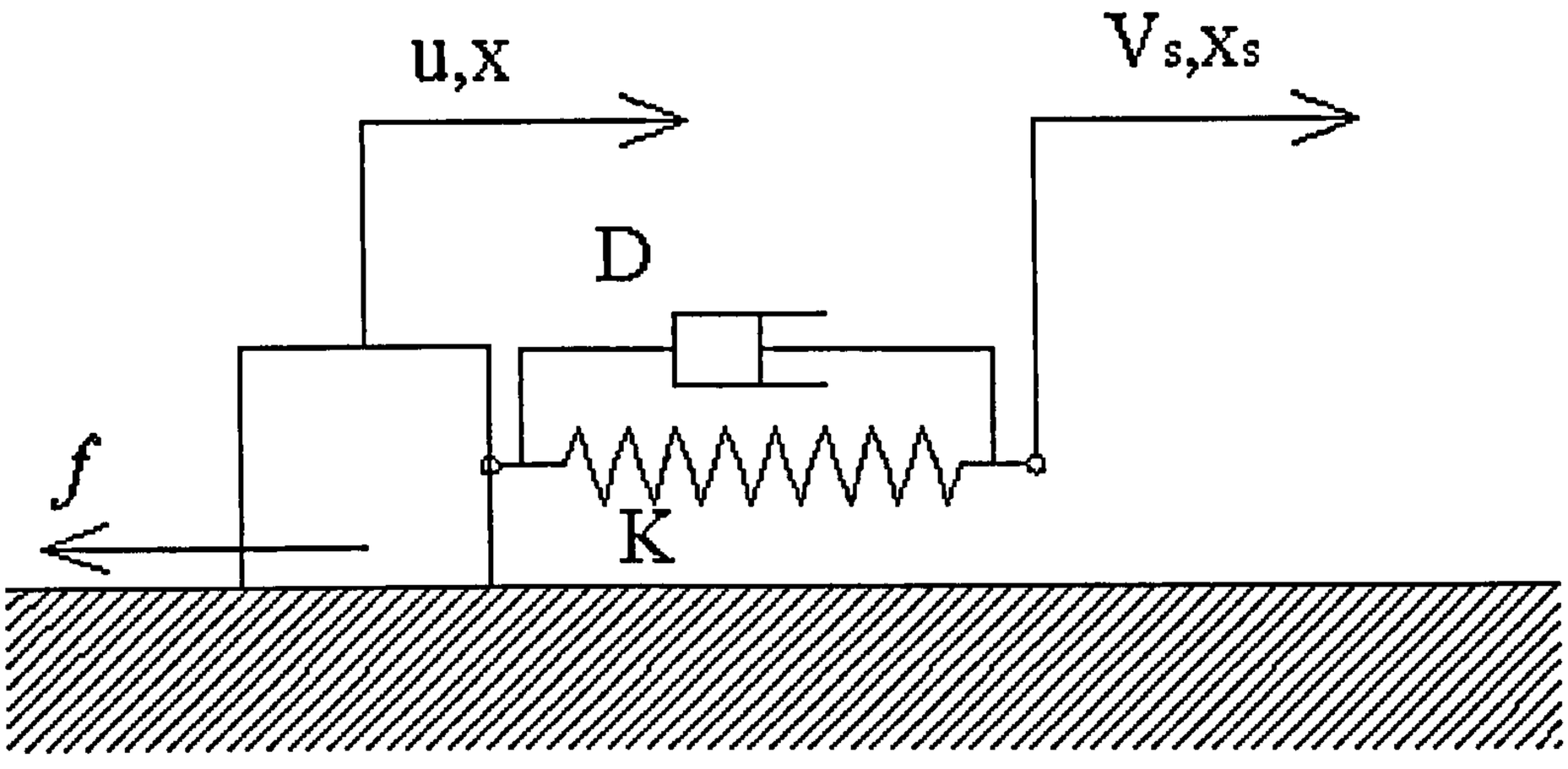

Figure 4. 9 A simple model of the rubber block incorporating viscoelasticity and inertia

The properties of the rubber element are so chosen that, if the same segment were to be used in a tyre model, realistic results would be generated in terms of the cornering force. Furthermore, a set of static and kinetic friction coefficients of friction are assumed for implementation in equations (3.104) and (3.105). Rubber properties and friction coefficients are provided in table 4.1. The apparent contact pressure between the rubber segment and the rough surface is 0.201 MPa, so as to generate identical conditions to those corresponding to the 31 N vertical load case tested in [26], based

on the dimensions of the specimen used (please refer to [26]). In the case of the numerical model, the apparent contact pressure is multiplied by the width of a hypothetical tyre (b =0.18 m), in order to obtain the normal force per unit length. This is done since all other properties are given per unit length and incorporate the effect of the width. At the end, the virtual experiment is equivalent to pulling a stripe of rubber 1 metre long and 0.18 metres wide, with a normal pressure equal to 0.201MPa, parallel to its width. Given the properties of the rubber, simulation results are obtained for various sliding velocities. In this procedure the effects of time-step size and the velocity threshold are addressed.

Table 4.1

Simulation Parameters for the virtual friction test

Normal pressure	K	D	C	μ_k	μ_s
[N/m^2]	[N/m^2]	[Ns/m^2]	[Kg/m]	-	-
2.014e5	9e6	8e2	2	0.9	1.17

Figure 4.10 demonstrates the stick-slip behaviour of the virtual rubber block, sliding at 0.3 m/s. The blue line denotes the displacement of the specimen, while the green line represents the relative velocity of the specimen with respect to the rough surface. In this specific case the time-step is set to 0.1 ms and the velocity threshold for the transition between stick and slip is 12 mm/s. Clearly, the graph shows good qualitative agreement with the corresponding experimental findings shown in figure 4.5. Figures 4.11-4.13 show the dependence of the existence of stick-slip on the time-step size for three progressively increasing transition thresholds. The time-steps considered are dt=1e-4, 3.3e-5 and 1e-5. It is observed that the smallest time-step promotes the generation of stick-slip motion almost throughout the full range of sliding velocities. Of course, this result depends largely on the properties of the rubber and the difference between static and kinetic coefficients of friction. Larger time-steps prohibit the existence of stick-slip at sliding velocities approximately higher than 0.4 m/s. At lower sliding velocities some stick-slip is generated, which may vanish and reappear arbitrarily. It is noted in [26] that in a number of experimental tests, stick-slip appeared suddenly after a period of smooth sliding between the surfaces. In general, the involvement of a large number of parameters poses difficulties in the numerical, as

well as the experimental investigation of the stick-slip phenomenon. For the purpose of tyre friction simulation, the largest time-step is chosen (1e-4 s), in conjunction with a threshold equal to 1.2e-2 m/s. Referring to figure 4.12, this combination yields some stick-slip at velocities up to 0.35 m/s, for a normal pressure of 2.014e5 N/m^2. Having selected the time-step and the velocity threshold, the effect of normal pressure is assessed with the aid of figures 4.14-4.16. Figure 4.14 shows the velocity and displacement of a specimen for a sliding velocity of 0.8 m/s and the usual normal pressure of 2.014e5 N/m^2. It is seen that only one full stick-slip cycle is achieved (the velocity of the lumped mass reduces to zero only once after the initiation of sliding). No further stick-slip is observed and both velocity and displacement converge quickly to the steady-state values. As the normal pressure increases per 20% and 40% in figures 4.15 and 4.16 respectively, the number of full stick-slip cycles increases. This result is in agreement with experimental observations (see figure 4.6) which indicate that higher loads promote stick-slip.

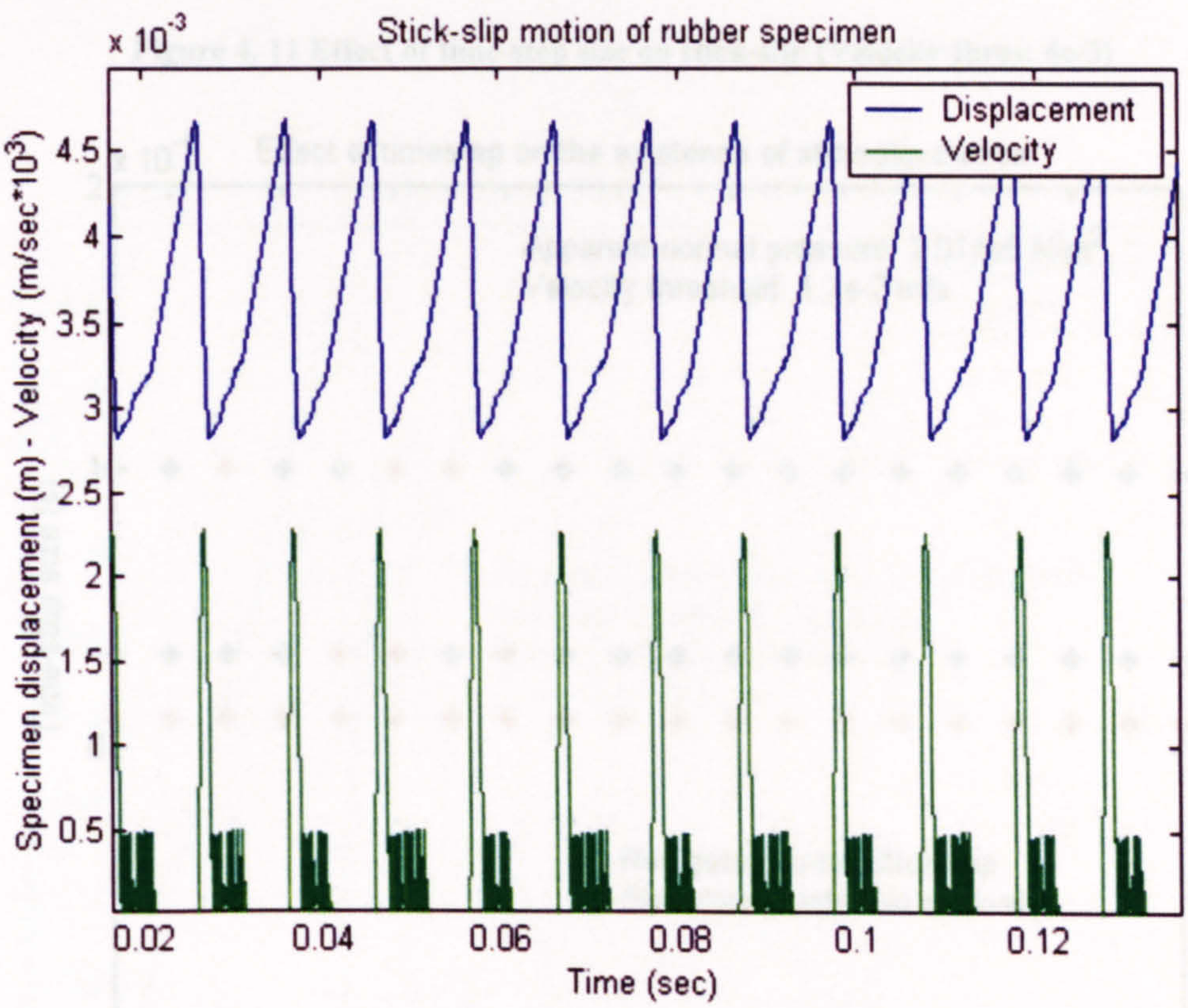

Figure 4. 10 Stick-slip behaviour of the rubber block sliding at 0.3 m/s, subject to 2.014e5 N/m^2 normal pressure

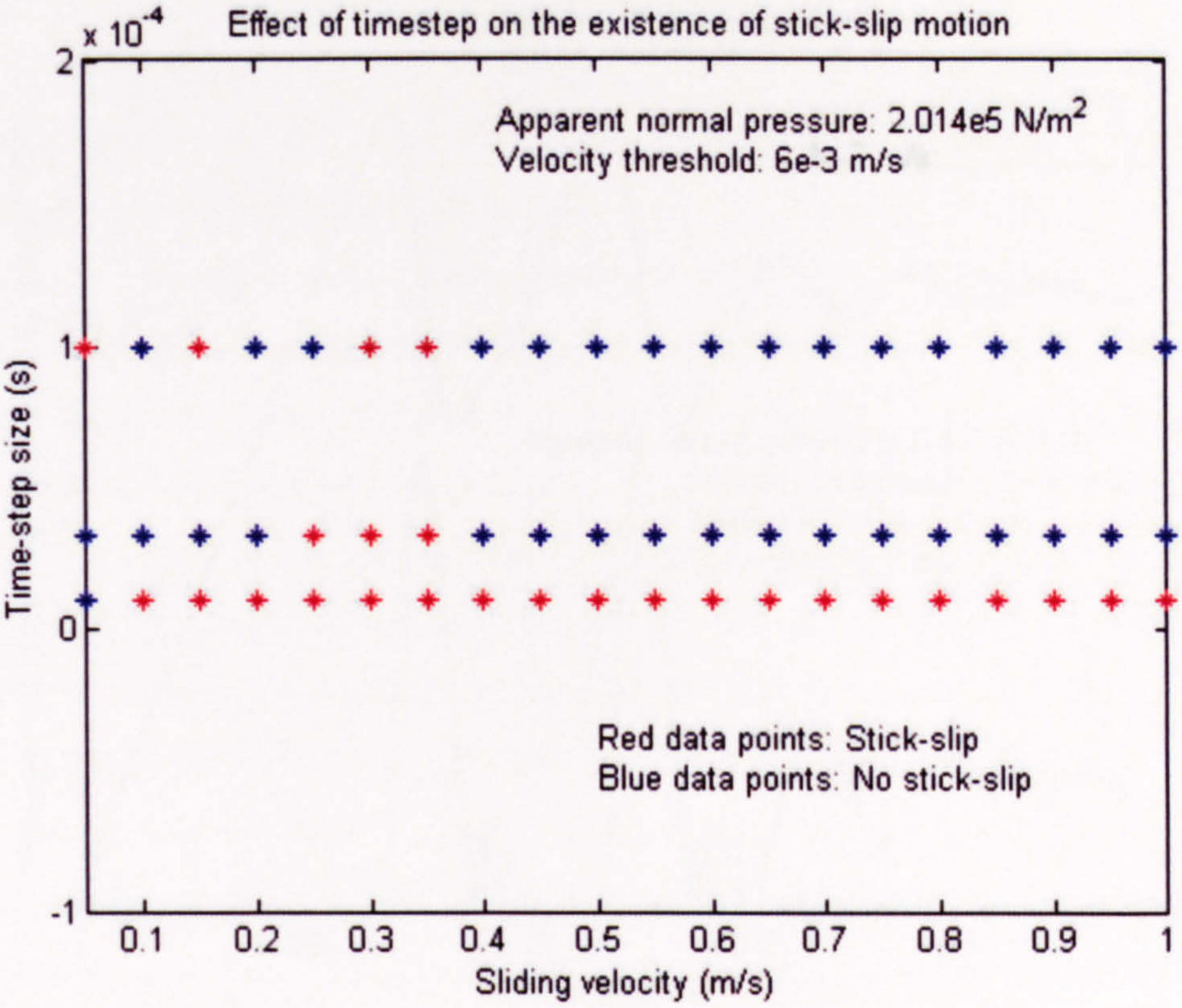

Figure 4. 11 Effect of time-step size on stick-slip (Velocity thres: 6e-3)

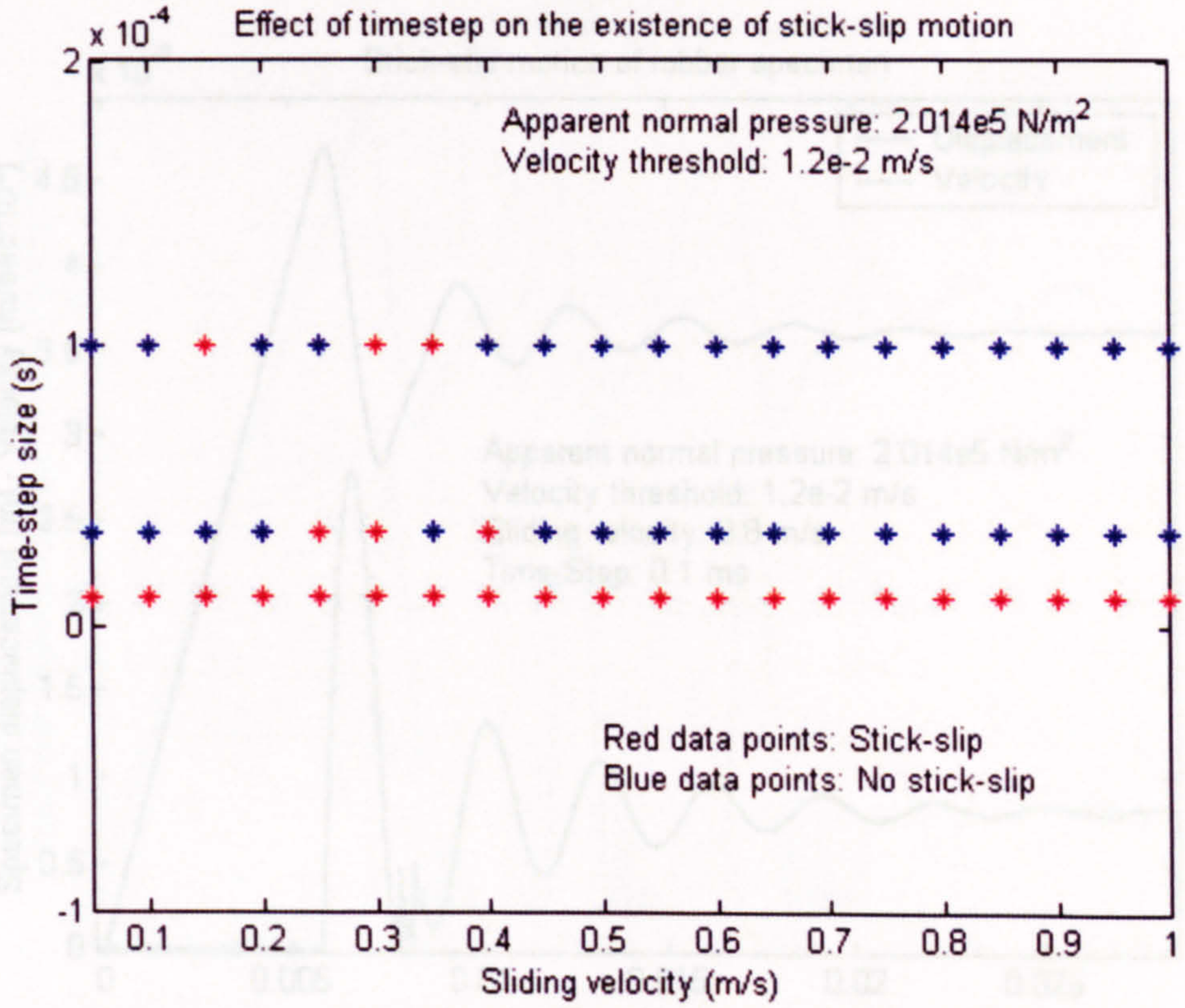

Figure 4. 12 Effect of time-step size on stick-slip (Velocity thres: 1.2e-2)

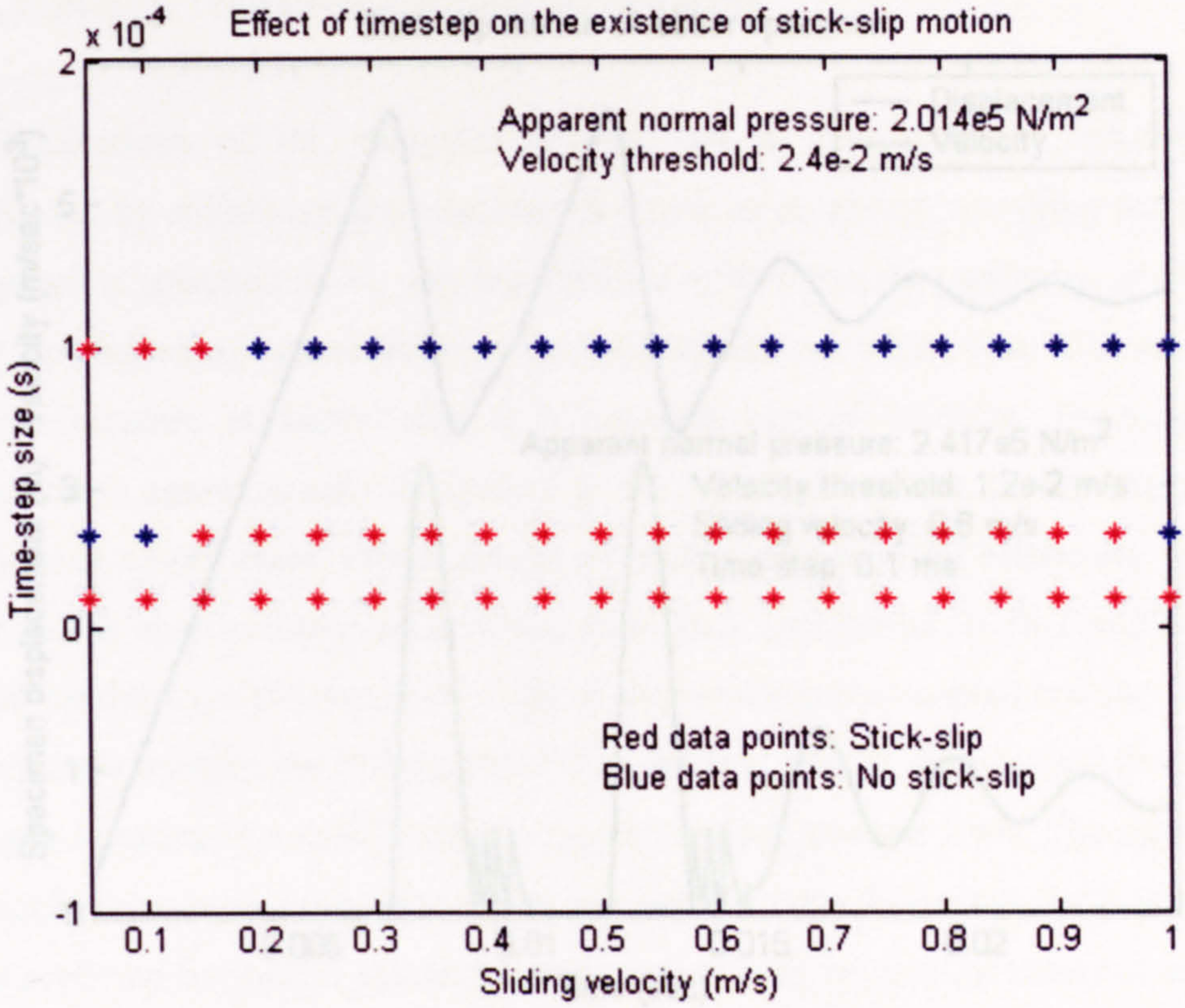

Figure 4. 13 Effect of time-step size on stick-slip (Velocity thres: 2.4e-2)

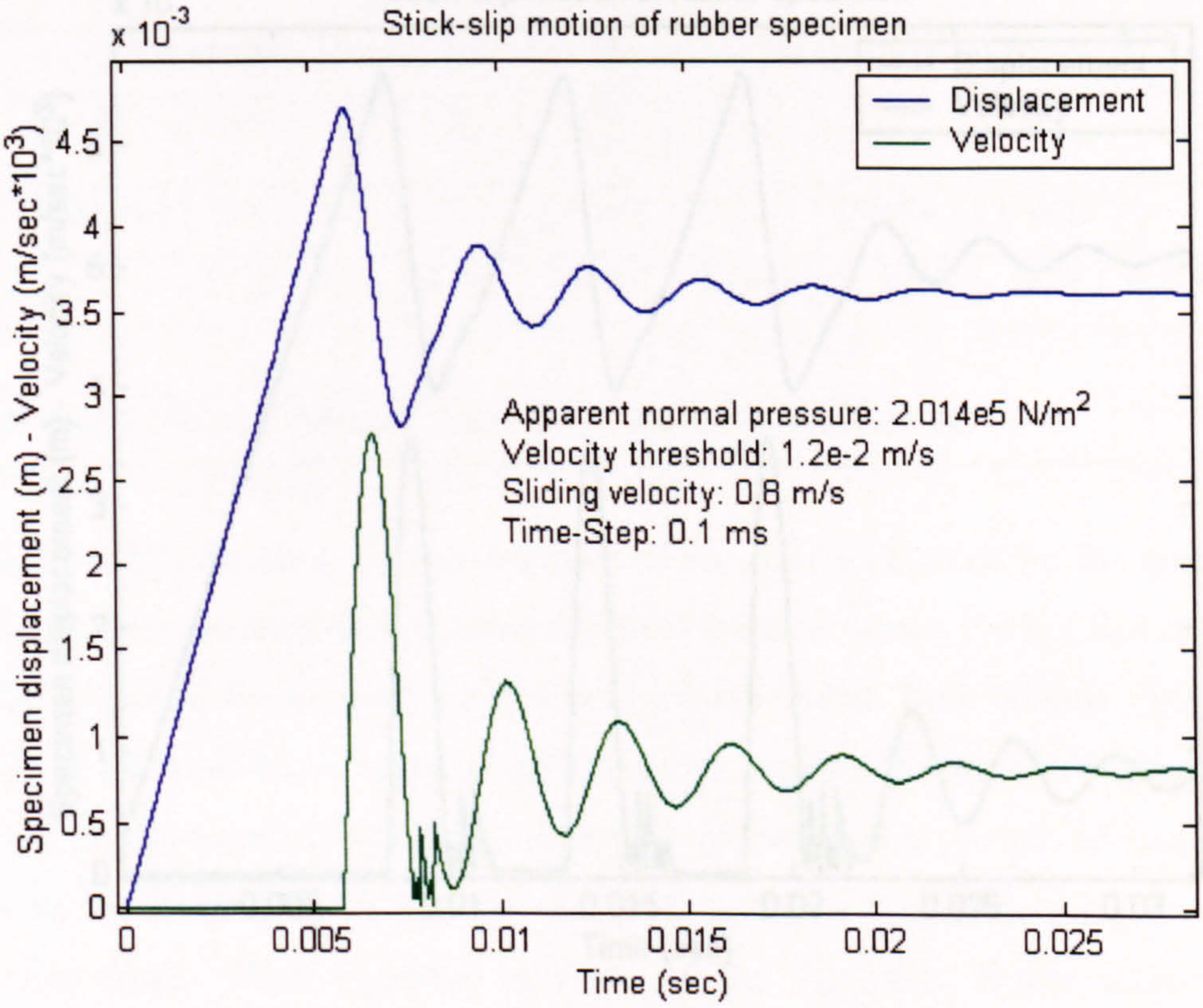

Figure 4. 14 A single stick-slip cycle, as observed at a relatively high sliding velocity

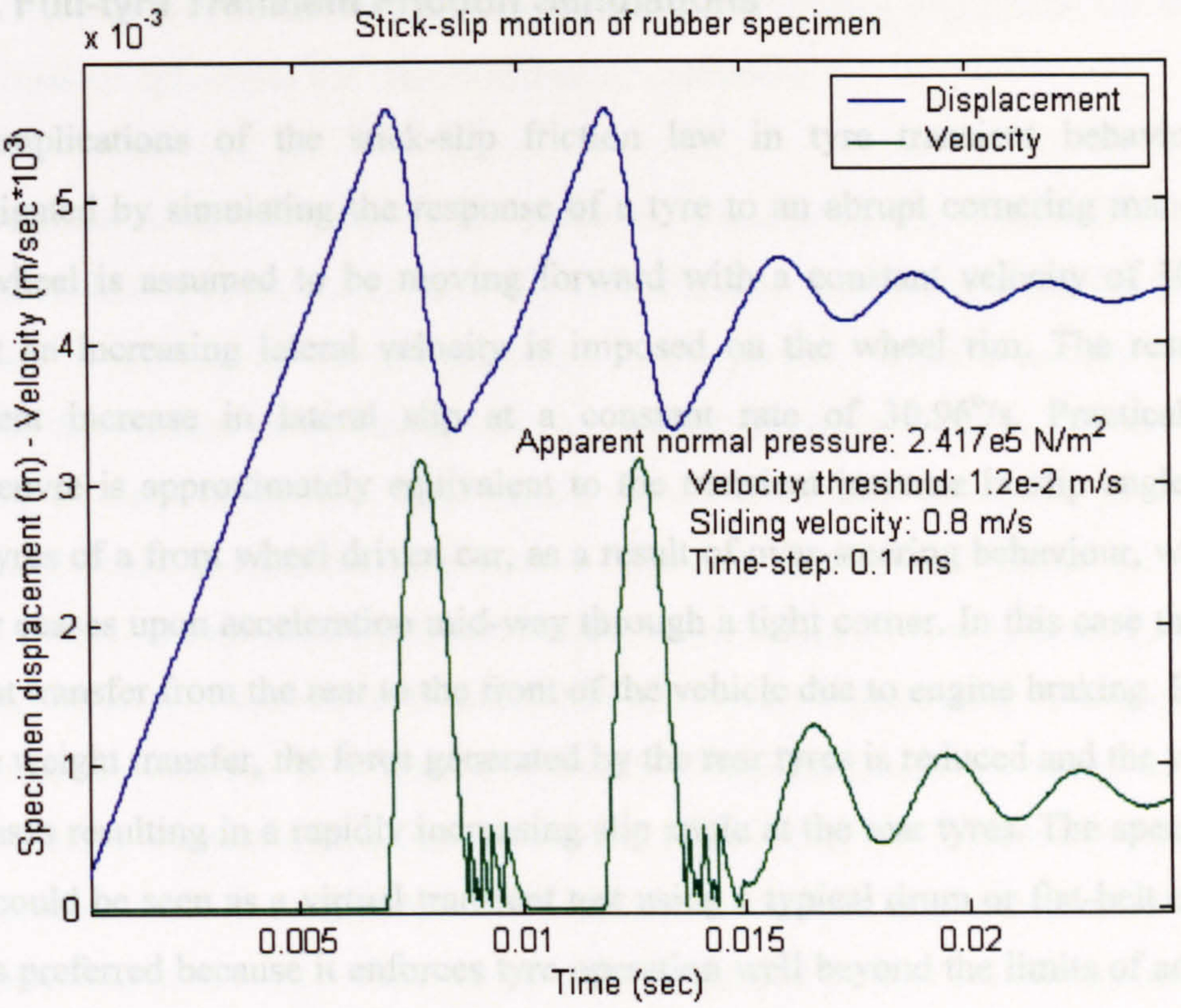

Figure 4. 15 A second stick-slip cycle is observed as the normal pressure increases per 20% compared to figure 4.14

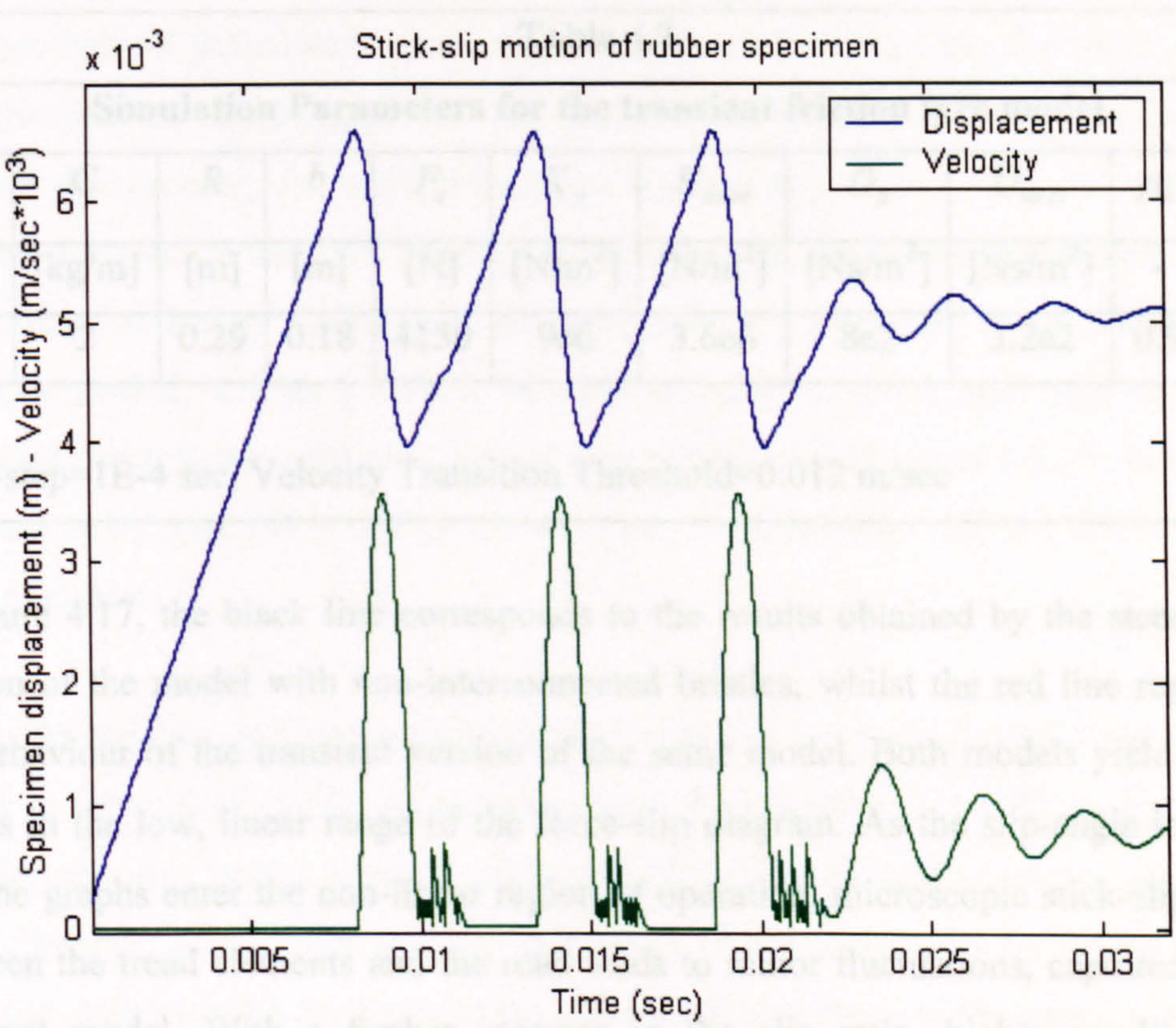

Figure 4. 16 The tendency towards stick-slip increases, as the normal pressure increases up to 40% compared to figure 4.14 (normal pressure=2.82e5 N/m^2, all other parameters remain the same)

4.3.3. Full-tyre Transient Friction Simulations

The implications of the stick-slip friction law in tyre transient behaviour are investigated by simulating the response of a tyre to an abrupt cornering manoeuvre. The wheel is assumed to be moving forward with a constant velocity of 10m/sec, whilst an increasing lateral velocity is imposed on the wheel rim. The result is a transient increase in lateral slip at a constant rate of 30.96°/s. Practically this manoeuvre is approximately equivalent to the transient increase in slip angle of the rear tyres of a front wheel driven car, as a result of over-steering behaviour, when the driver ceases upon acceleration mid-way through a tight corner. In this case there is a weight transfer from the rear to the front of the vehicle due to engine braking. Because of the weight transfer, the force generated by the rear tyres is reduced and the yaw rate increases resulting in a rapidly increasing slip angle at the rear tyres. The specific test case could be seen as a virtual transient test using a typical drum or flat-belt machine and is preferred because it enforces tyre operation well beyond the limits of adhesion. The full set of simulation parameters is given in table 4.2.

Table 4.2

Simulation Parameters for the transient friction tyre model

a	C	R	b	F_z	K_y	K_{inter}	D_y	D_{inter}	μ_k	μ_s
[m]	[kg/m]	[m]	[m]	[N]	[N/m^2]	[N/m^2]	[Ns/m^2]	[Ns/m^2]	-	-
0.065	2	0.29	0.18	4150	9e6	3.6e6	8e2	3.2e2	0.9	1.17

Time-step=1E-4 sec, Velocity Transition Threshold=0.012 m/sec

In figure 4.17, the black line corresponds to the results obtained by the steady-state version of the model with non-interconnected bristles, whilst the red line represents the behaviour of the transient version of the same model. Both models yield similar results in the low, linear range of the force-slip diagram. As the slip-angle increases and the graphs enter the non-linear region of operation, microscopic stick-slip action between the tread elements and the road leads to minor fluctuations, captured by the transient model. With a further increase in the slip ratio, higher amplitudes of oscillation are predicted by the transient model. These oscillations can reach up to 10% of the total lateral force developed by the tyre. As the slip ratio increases further,

the period and amplitude of oscillations decrease continually, and finally the response smoothens completely at the saturated area of operation.

The transient force in figure 4.17 is explained considering the characteristics of the tyre model in use. In particular, the observed behaviour may be related to the stick-slip response of the Kelvin element presented in the previous section and the parabolic pressure distribution along the contact. At low slip angles, the bristle tips stick on the ground, as they operate in areas where bristle deflection generates small forces compared to the maximum static friction. Towards the rear end of the contact, the bristle forces become significant and sliding of the bristles initiates. Once sliding has started, the bristles move continuously towards areas of decreasing normal pressure, due to the assumption of a parabolic pressure distribution. As discussed in section 4.3.2, lower pressures reduce the tendency to stick slip. Even if stick-slip occurs, the overall effect would be limited, as the total force would be determined mainly by the adhesion area in the font of the contact. It is observed in figure 4.17 that significant fluctuations in the lateral force occur at values of $\tan a$ larger than 0.8. At this point, the bristles deform quickly and the maximum static friction is reached somewhere in the front half of the contact patch. Sliding initiates but this time the bristles move towards areas of much higher normal pressure. Due to the parabolic shape of the pressure distribution, the peak pressure is significantly higher than the equivalent uniform distribution that yields an equal normal force. Therefore, the sliding bristles enter areas of higher pressure where stick-slip is promoted. As the lateral slip increases further, a lateral sliding velocity is reached where stick-slip cannot be generated even at the peak pressure of the parabolic distribution. All bristles slide simultaneously and the resulting lateral force is determined by the coefficient of sliding friction.

It is suspected that the three sequential drops in lateral force, predicted by the transient model in figure 4.17, could significantly alter the response of a vehicle. Experience indicates that just before reaching saturation, tyres tend to exhibit macroscopic stick-slip behaviour, sensed indirectly by the driver as a discontinuity in the build-up of yaw-rate, which can be attributed to the aforementioned drops in the lateral force.

Figure 4.18 shows the effect of the interconnections between bristles. Figure 4.19 depicts a window from the lateral force variations shown in figure 4.18. Interconnections clearly reduce the tendency of the bristles to oscillate, especially in the initial part of the time history. Nevertheless, they do not seem to affect the severity of the major fluctuations in the lateral force or the self-aligning moment.

Another interesting observation refers to the fact that the model with interconnected bristles generates a slightly lower lateral force in the region of saturated operation. The overall tyre force is calculated as the force applied by the bristles on the wheel rim and not as a friction force applied by the road to the bristles. This approach was preferred, taking into account the effect of internal damping, which should alter the energy balance between the forces generated along the contact patch and the forces transmitted to the rim. The higher the lateral velocity (saturated region of operation), the more intense is the effect of tyre tread's inertia. Because the bristles are not interconnected, there is no wave propagation and energy dissipation along the tyre tread, and the increased forces generated by the bristles are transferred directly to the rim. On the contrary, interconnections between the bristles enable extra energy dissipation and reduce the overall deflection of the bristles. For the sake of computational cost, the number of interconnected bristles is confined to those just covering the contact patch length. In a full model with bristles distributed all around the tyre's periphery, wave propagation and energy dissipation would continue outside the contact patch and the tendency for generation of an increasing force with increasing lateral velocity would be completely eliminated. Nevertheless, the results show that even though a reduced number of bristles is used, the interconnections between the bristles yield sensible results in a reasonable period of time.

The transient friction model differs from the steady state model described in chapter 3 mainly in the integration procedure, which takes into account the states of all bristles simultaneously. This alteration, in combination with carefully chosen simulation parameters predicts significant fluctuations in the lateral force, as a result of the stick-slip motion of the tyre tread. Nevertheless, the model demonstrates a major drawback that limits its capabilities as a generic transient tyre model. The analysis is restrained within the contact patch of the tyre. Therefore, the global deformation of the tyre carcass, which is surmised to extend outside the contact patch, is neglected. This global deformation and the rate at which it builds up under a transient manoeuvre determines the phase lag between the various excitations and the response of the tyre in terms of force generation. In the discussion concerning the relaxation length concept, it was assumed that point P (see figure 4.1) lies in front of the contact patch so that the relaxation length can obtain values well in excess of the length of the contact patch itself. It is clear that the transient friction model does not include provisions for such deformations. Instead, the maximum possible value of the relaxation length is equal to half the length of the contact patch.

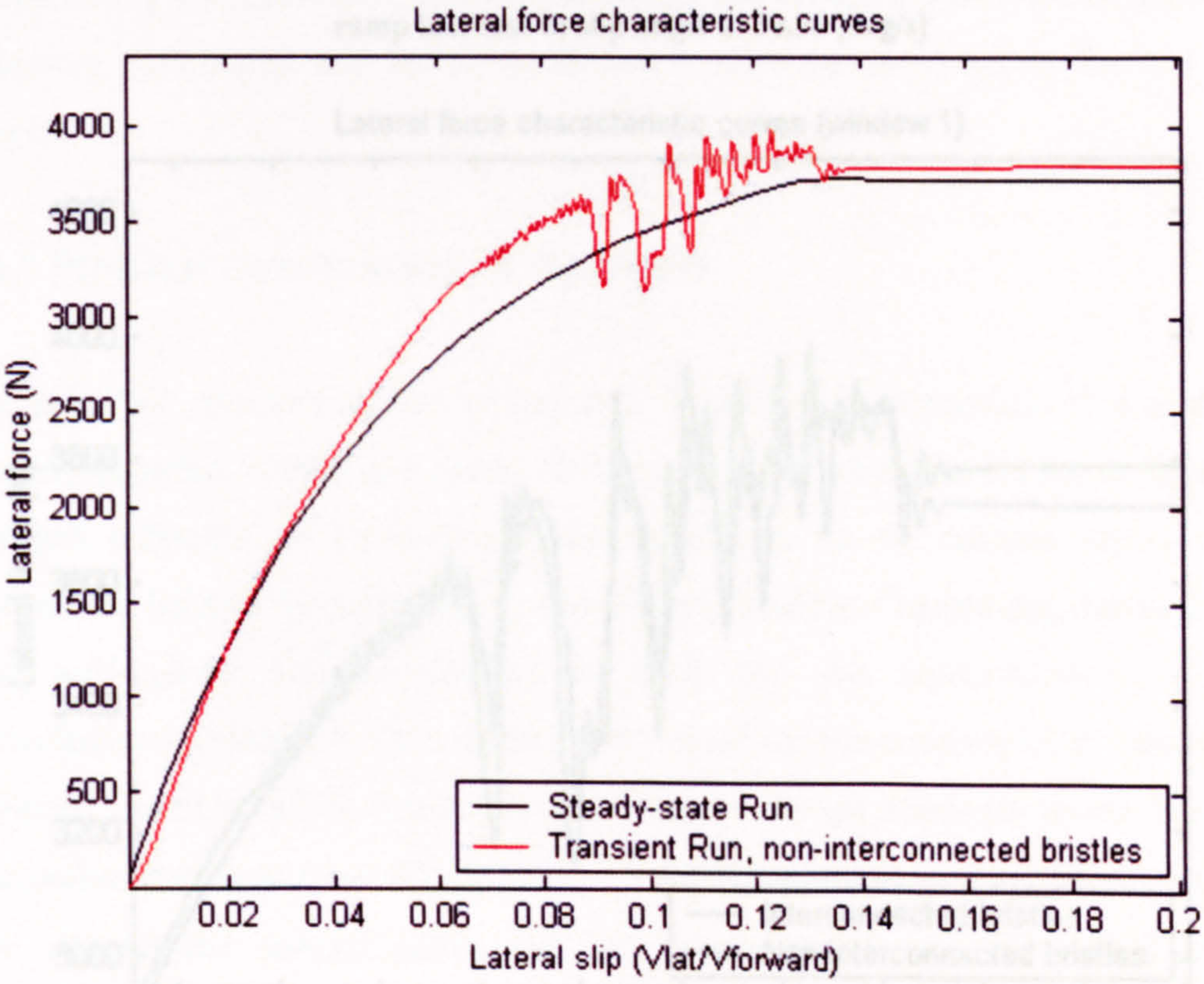

Figure 4. 17 Lateral steady-state and transient response to ramp increase in slip angle at 30.96 [deg/s]

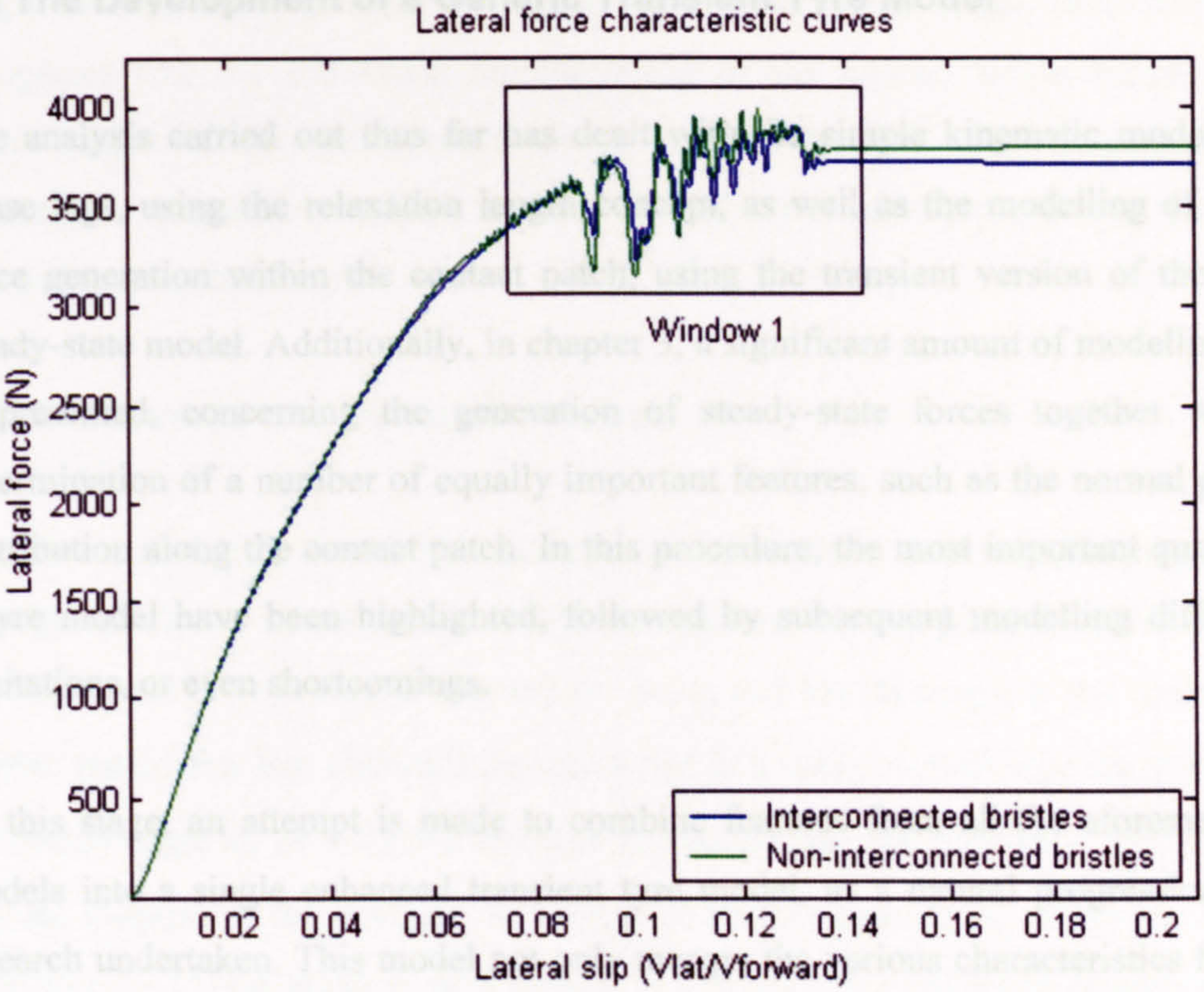

Figure 4. 18 Transient response of models with interconnected and non-interconnected bristles to ramp increase in slip angle at 30.96 [deg/s]

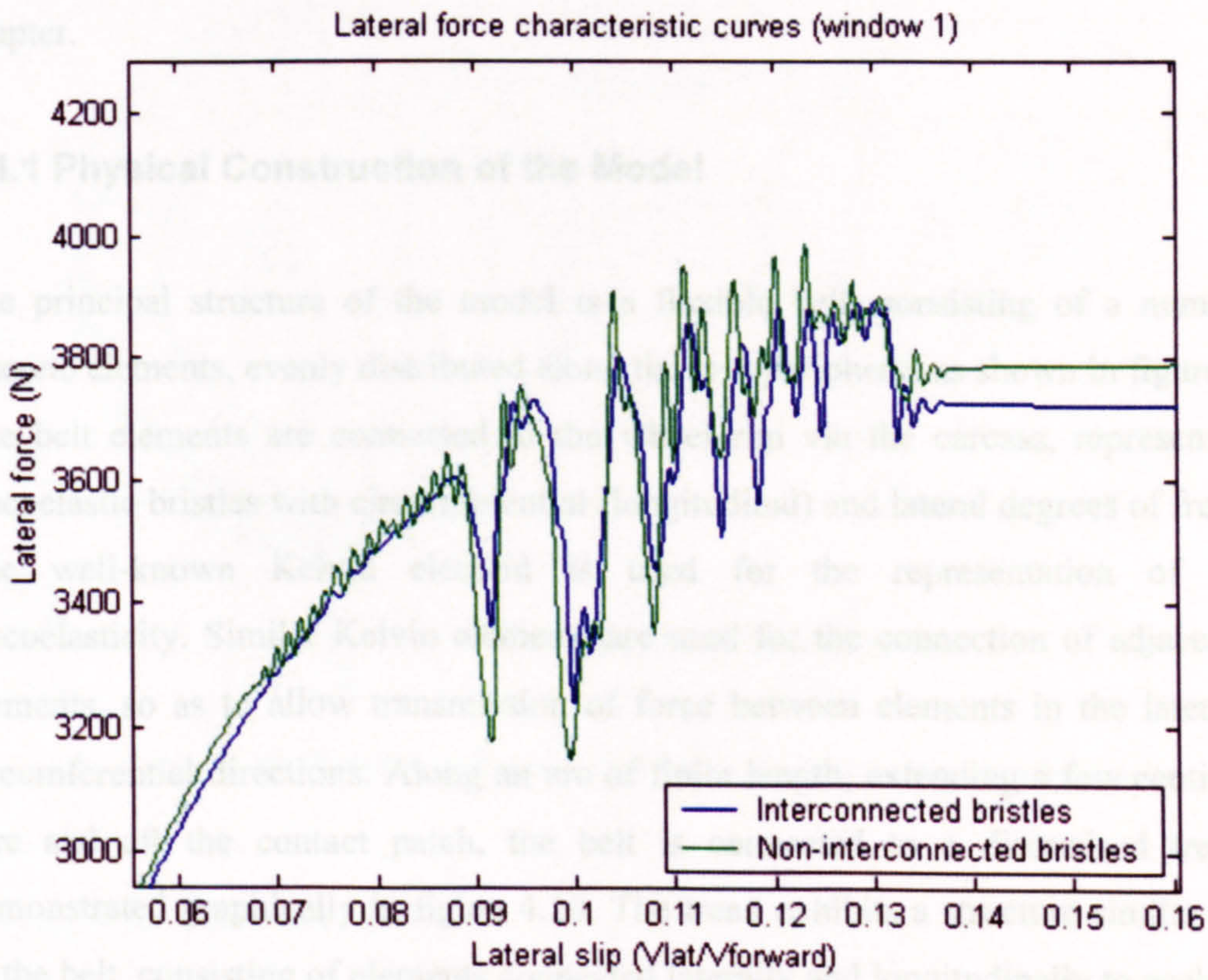

Figure 4. 19 Window 1 from figure 4.18

4.4 The Development of a Generic Transient Tyre Model

The analysis carried out thus far has dealt with the simple kinematic modelling of phase lags, using the relaxation length concept, as well as the modelling of friction force generation within the contact patch, using the transient version of the simple steady-state model. Additionally, in chapter 3, a significant amount of modelling work is presented, concerning the generation of steady-state forces together with the determination of a number of equally important features, such as the normal pressure distribution along the contact patch. In this procedure, the most important qualities of a tyre model have been highlighted, followed by subsequent modelling difficulties, limitations, or even shortcomings.

At this stage, an attempt is made to combine features from all the aforementioned models into a single enhanced transient tyre model, as a natural progression of the research undertaken. This model not only merges the various characteristics from the previous models, it is based on an entirely new representation of the tyre structure, incorporating a flexible belt, carcass and tread. The model is described in detail in the following paragraphs and some simulation results are provided at the end of the chapter.

4.4.1 Physical Construction of the Model

The principal structure of the model is a flexible belt, consisting of a number of discrete elements, evenly distributed along the tyre periphery, as shown in figure 4.20. The belt elements are connected to the wheel rim via the carcass, represented by viscoelastic bristles with circumferential (longitudinal) and lateral degrees of freedom. The well-known Kelvin element is used for the representation of bristle viscoelasticity. Similar Kelvin elements are used for the connection of adjacent belt elements, so as to allow transmission of force between elements in the lateral and circumferential directions. Along an arc of finite length, extending a few centimetres fore and aft the contact patch, the belt is connected to a discretised tread, as demonstrated graphically in figure 4.20. The tread exhibits a structure similar to that of the belt, consisting of elements connected laterally and longitudinally to each other. The tread is used mainly for the simulation of friction within the contact patch. Its

length is kept small in order to reduce the computational effort, especially if one recognises that the successful representation of the contact might require a fine discretisation of the tread, compared to that of the belt. The properties of all viscoelastic connections within the tyre structure are anisotropic in the lateral and circumferential directions.

4.4.2. Kinematic and Dynamic Analysis

The kinematic inputs for the belt elements are determined with the aid of figure 4.21. The global frame of reference $OXYZ$ is attached to the ground, while the SAE moving frame of reference is denoted by $oxyz$, and has its origin at the centre of the contact patch. The belt elements are numbered in a counter-clockwise sense, and their separation angle is: $\vartheta s = 2\pi/n$, where n represents the total number of belt elements. For the purpose of the analysis, an instant of time is considered, when the first belt element ($j = 1$) is at angle θ with respect to line oG. The full set of equations for the kinematic excitation, applied on each individual belt element, reads:

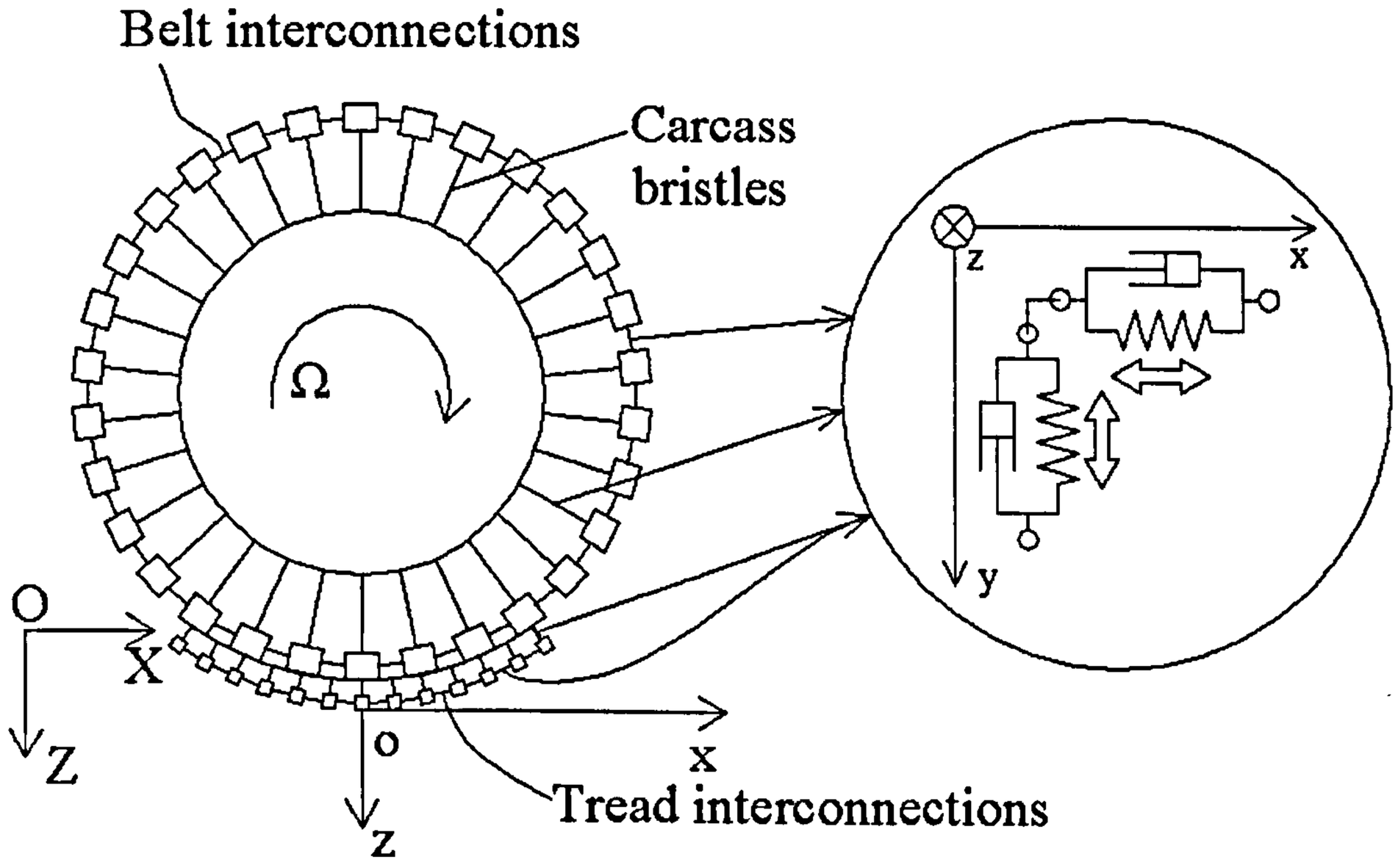

Figure 4. 20 Modelling representation of the physical structure of the tyre

$$Urx_{j=1..n} = (\Omega + \Omega st \cdot \sin\gamma) R_b \tag{4.30}$$

$$Ury_{j=i+1} = Vy + (\Omega st + \Omega \sin\gamma) R_b \sin(\theta + i \cdot \vartheta s) + \dot{\gamma} \cdot R_b \cos(\theta + i \cdot \vartheta s) \tag{4.31}$$

with $i = 0,1,...,n-1$

$$\dot{x}_{rimj} = Urx_j, \ j = 1..n \tag{4.32}$$

$$\dot{y}_{rimj} = Ury_j, \ j = 1..n \tag{4.33}$$

$$\dot{\theta} = \Omega \tag{4.34}$$

where Urx_j and Ury_j denote the circumferential and lateral velocities, imposed on the jth element by the motion of the rim, $\dot{x}_{rimj}$ and $\dot{y}_{rimj}$ are the corresponding displacements, Ω is the rotational velocity of the wheel, Ωst is the rotational velocity of steering, γ is the camber angle, R_b is the radius of the belt and Vy is the lateral component of the velocity of the centre of the wheel.

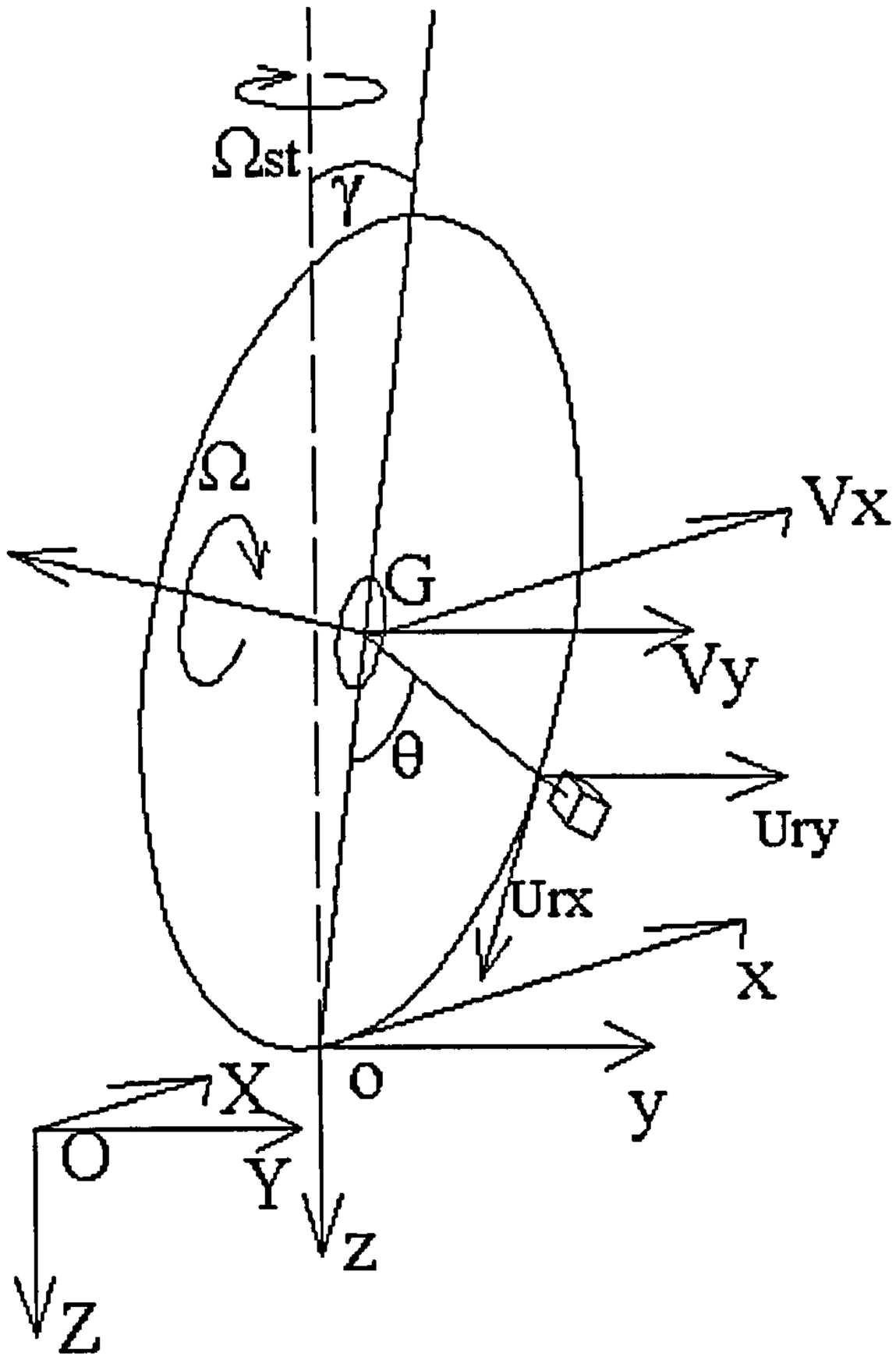

Figure 4. 21 Kinematics of the tyre model

The formulation involves setting up of the equations of motion for the lateral degrees of freedom for the belt and the tread elements respectively. In the general case, the j^{th} belt element is connected to the rim (rigid foundation), two adjacent elements and the corresponding i^{th} tread element, as shown graphically in figure 4.22. The equation of motion for the lateral degree of freedom of an element of unit length becomes:

$$\begin{aligned} &\dot{U}y_j c + Klat\left(y_j - y_{rmj}\right) + Dlat\left(Uy_j - Ury_j\right) + Ktrlat\left(y_j - ytr_i\right) \\ &+ Dtrlat\left(Uy_j - Uytr_i\right) + Ky\left(y_j - y_{j-1}\right) + Ky\left(y_j - y_{j+1}\right) \\ &+ Dy\left(Uy_j - Uy_{j-1}\right) + Dy\left(Uy_j - Uy_{j+1}\right) = 0 \end{aligned} \tag{4.35}$$

where Uy_j denotes the velocity of the element, c is the mass of the belt, $Klat$ is the lateral stiffness of the carcass, $Dlat$ is the lateral damping of the carcass, $Ktrlat$ and $Dtrlat$ are the stiffness and damping coefficients of the lateral connections between the belt and the tread and Ky, Dy denote the stiffness and damping of the lateral

interconnections between adjacent belt elements. All properties are given per unit length (i.e. mass: $[Kg/m]$, stiffness: $[N/m^2]$, damping: $[N \cdot s/m^2]$).

Similarly, the equation of motion for the ith tread element reads:

$$\begin{aligned} &\dot{U}ytr_i c_{tr} + Ktrlat(ytr_i - y_j) + Dtrlat(Uytr_i - Uy_j) + Ktry(ytr_i - ytr_{i-1}) \\ &+ Ktry(ytr_i - ytr_{i+1}) + Dtry(Uytr_i - Uytr_{i-1}) + Dtry(Uytr_i - Uytr_{i+1}) + f_{yi} = 0 \end{aligned} \tag{4.36}$$

where $Uytr_i$ denotes the velocity of the element, c_{tr} is the mass of the tread, $Ktry$, $Dtry$ denote the stiffness and damping of the lateral interconnections of the tread elements and f_{yi} is the friction force between the element and the road, provided that the element under consideration lies within the contact patch.

Equation (4.35) is written in matrix form for n number of belt elements involved, as:

$$\mathbf{A}_y \cdot \dot{\mathbf{I}}_{by} + \mathbf{B}_y \cdot \mathbf{I}_{by} = \mathbf{f}_{bty} + Klat \cdot \mathbf{Y}_{rim} + Dlat \cdot \mathbf{U}_{rim} \tag{4.37}$$

With:

$$\mathbf{A}_y(2n \times 2n) = \begin{bmatrix} c & 0 & \dots & \dots & 0 & Dllat & -Dy & 0 & \dots & -Dy \\ 0 & c & \dots & \dots & \dots & -Dy & Dllat & -Dy & \dots & \dots \\ \dots & \dots & \dots & \dots & \dots & 0 & \dots & \dots & \dots & \dots \\ \dots & \dots & \dots & \dots & \dots & \dots & \dots & \dots & \dots & -Dy \\ \dots & \dots & \dots & \dots\dots\dots & c & -Dy & \dots\dots\dots & 0 & -Dy & Dllat \\ & & & & & 1 & 0 & \dots & \dots & 0 \\ & & & & & 0 & 1 & \dots & \dots & \dots \\ & & 0 & & & \dots & \dots & \dots & \dots & \dots \\ & & & & & \dots & \dots & \dots & \dots & \dots \\ & & & & & \dots & \dots & \dots & \dots\dots\dots & 1 \end{bmatrix} \tag{4.38}$$

$$\mathbf{B}_y(2n \times 2n) = \begin{bmatrix} & & & & & Kllat & -Ky & 0 & \dots & -Ky \\ & & & & & -Ky & Kllat & -Ky & \dots & \dots \\ & & 0 & & & 0 & -Ky & \dots & \dots & \dots \\ & & & & & \dots & \dots & \dots & \dots & -Ky \\ & & & & & -Ky & \dots & \dots & -Ky & Kllat \\ -1 & 0 & \dots & \dots & 0 & & & & & \\ 0 & -1 & \dots & \dots & \dots & & & & & \\ \dots & \dots & \dots & \dots & \dots & & & 0 & & \\ \dots & \dots & \dots & \dots & \dots & & & & & \\ 0 & \dots & \dots & \dots\dots\dots & -1 & & & & & \end{bmatrix} \tag{4.39}$$

$$\mathbf{I}_{by}(2n\times 1)=\begin{bmatrix} Uy_1 \\ Uy_2 \\ \cdots \\ \cdots \\ Uy_n \\ y_1 \\ y_2 \\ \cdots \\ \cdots \\ y_n \end{bmatrix} \tag{4.40}$$

$$\mathbf{Y}_{rim}(2n\times 1)=\begin{bmatrix} y_{rim1} \\ y_{rim2} \\ \cdots \\ \cdots \\ y_{rimn} \\ 0 \\ \cdots \\ \cdots \\ \cdots \\ 0 \end{bmatrix} \tag{4.41}$$

$$\mathbf{U}_{rim}(2n\times 1)=\begin{bmatrix} Ury_1 \\ Ury_2 \\ \cdots \\ \cdots \\ Ury_n \\ 0 \\ \cdots \\ \cdots \\ \cdots \\ 0 \end{bmatrix} \tag{4.42}$$

Where: $DIlat = Dlat + 2Dy$ and $KIlat = Klat + 2Ky$.

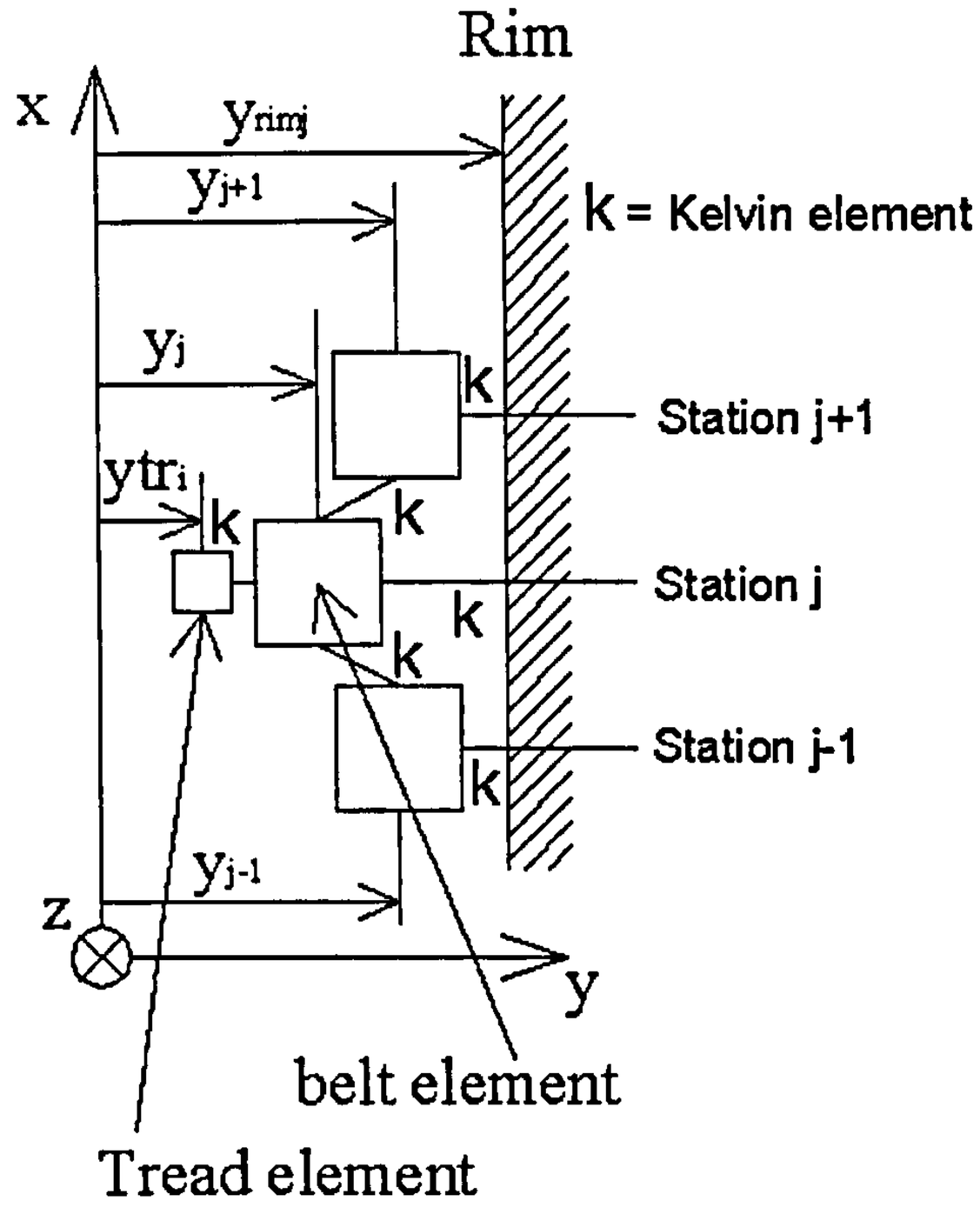

Figure 4. 22 Interaction between belt and tread elements

Vector $\mathbf{f}_{bt}$ represents the forces generated between the belt and the tread, with its entries depending on the instantaneous position and velocity of the belt relative to the tread. The entries: $\mathbf{f}_{bt}$, corresponding to the part of the belt connected to the tread have the form: $-\left[Ktrlat\left(y_j - ytr_i\right) + Dtrlat\left(Uy_j - Uytr_i\right)\right]$, while all the remaining entries are equal to zero. Because the discretisation of the belt does not necessarily coincide with that of the tread, it is not expected that the j^{th} belt element will always coincide with an i^{th} tread element. Thus, tread velocities and displacements found in $\mathbf{f}_{bt}$ represent interpolation values, as shown graphically in figure 4.23. Finally, the entries of vectors $\mathbf{Y}_{rim}$ and $\mathbf{U}_{rim}$ are defined explicitly by equations (4.31)-(4.33).

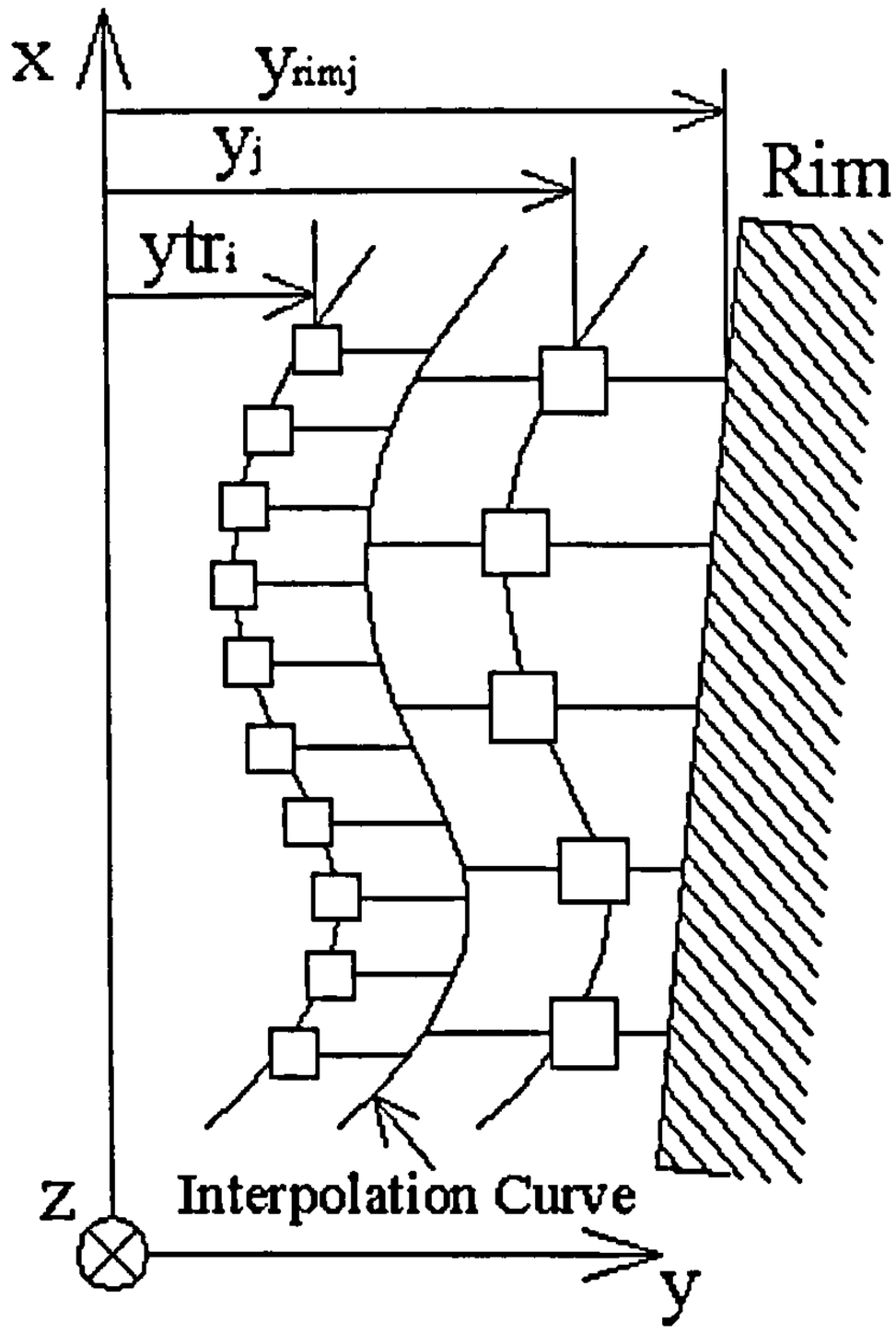

Figure 4. 23 Schematic representation of the connection - through interpolation - of the states of the belt to the states of the tread

Following the same procedure, equation (4.36) is written for n_{tr} number of tread elements in matrix form as:

$$\mathbf{Atr}_y \cdot \dot{\mathbf{I}}_{try} + \mathbf{Btr}_y \cdot \mathbf{I}_{try} = \mathbf{F}_y + Ktrlat \cdot \mathbf{Y}_{belt} + Dtrlat \cdot \mathbf{U}_{belt} \tag{4.43}$$

With:

$$\mathbf{Atr}_y(2n_{tr} \times 2n_{tr}) = \begin{bmatrix} c_{tr} & 0 & \dots & \dots & 0 & DItrlat & -Dtry & 0 & \dots & 0 \\ 0 & c_{tr} & \dots & \dots & \dots & -Dtry & DItrlat & -Dtry & \dots & \dots \\ \dots & \dots & \dots & \dots & \dots & 0 & \dots & \dots & \dots & \dots \\ \dots & \dots & \dots & \dots & \dots & \dots & \dots & \dots & \dots & -Dtry \\ \dots & \dots & \dots & \dots\dots\dots & c_{tr} & 0 & \dots\dots\dots & 0 & -Dtry & DItrlat \\ & & & & & 1 & 0 & \dots & \dots & 0 \\ & & & & & 0 & 1 & \dots & \dots & \dots \\ & & 0 & & & \dots & \dots & \dots & \dots & \dots \\ & & & & & \dots & \dots & \dots & \dots & \dots \\ & & & & & \dots & \dots & \dots & \dots\dots\dots & 1 \end{bmatrix} \tag{4.44}$$

$$\mathbf{Btr}_y(2n_{tr}\times 2n_{tr})=\begin{bmatrix} & & & & & KItrlat & -Ktry & 0 & \dots & 0 \\ & & & & & -Ktry & KItrlat & -Ktry & \dots & \dots \\ & & 0 & & & 0 & -Ktry & \dots & \dots & \dots \\ & & & & & \dots & \dots & \dots & \dots & -Ktry \\ & & & & & 0 & \dots & \dots & -Ktry & KItrlat \\ -1 & 0 & \dots & \dots & 0 & & & & & \\ 0 & -1 & \dots & \dots & \dots & & & & & \\ \dots & \dots & \dots & \dots & \dots & & & 0 & & \\ \dots & \dots & \dots & \dots & \dots & & & & & \\ 0 & \dots & \dots & \dots\dots & -1 & & & & & \end{bmatrix} \tag{4.45}$$

$$\mathbf{I}_{try}(2n_{tr}\times 1)=\begin{bmatrix} Uytr_1 \\ Uytr_2 \\ \dots \\ \dots \\ Uytr_n \\ ytr_1 \\ ytr_2 \\ \dots \\ \dots \\ ytr_{ntr} \end{bmatrix} \tag{4.46}$$

$$\mathbf{Y}_{belt}(2n_{tr}\times 1)=\begin{bmatrix} y_1 \\ y_2 \\ \dots \\ \dots \\ y_{n_{tr}} \\ 0 \\ \dots \\ \dots \\ \dots \\ 0 \end{bmatrix} \tag{4.47}$$

$$\mathbf{U}_{belt}(2n_{tr}\times 1)=\begin{bmatrix} Uy_1 \\ Uy_2 \\ \dots \\ \dots \\ Uy_{n_{tr}} \\ 0 \\ \dots \\ \dots \\ \dots \\ 0 \end{bmatrix} \tag{4.48}$$

where $DItrlat = Dtrlat + 2Dtry$ and $KItrlat = Ktrlat + 2Ktry$.

Vector $\mathbf{F}_y$ contains the lateral friction forces sensed by the tread, depending on the normal force at the specific point, the coefficient of friction and the direction of motion of the tread elements. The length of the contact patch is calculated on-line and covers only a small part of the tread, where friction forces are generated. The

remaining entries are all equal to zero. Again, because of differences in tread and belt discretisation, vectors $\mathbf{Y}_{belt}$ and $\mathbf{U}_{belt}$ contain interpolation values of the states of the belt elements in connection with the tread at the instant under consideration.

An identical procedure is followed for the circumferential degrees of freedom, resulting in two further equations for the belt and the tread. The equations of motion of the belt element in the circumferential direction are given below in the matrix form as:

$$\mathbf{A}_x \cdot \dot{\mathbf{I}}_{bx} + \mathbf{B}_x \cdot \mathbf{I}_{bx} = \mathbf{f}_{btx} + Klong \cdot \mathbf{X}_{rim} + Dlong \cdot \mathbf{V}_{rim} \tag{4.49}$$

With:

$$\mathbf{A}_x(2n \times 2n) = \begin{bmatrix} c & 0 & \dots & \dots & 0 & Dllong & -Dx & 0 & \dots & -Dx \\ 0 & c & \dots & \dots & \dots & -Dx & Dllong & -Dx & \dots & \dots \\ \dots & \dots & \dots & \dots & \dots & 0 & \dots & \dots & \dots & \dots \\ \dots & \dots & \dots & \dots & \dots & \dots & \dots & \dots & \dots & -Dx \\ \dots & \dots & \dots & \dots\dots\dots & c & -Dx & \dots\dots\dots & 0 & -Dx & Dllong \\ & & & & & 1 & 0 & \dots & \dots & 0 \\ & & & & & 0 & 1 & \dots & \dots & \dots \\ & & & 0 & & \dots & \dots & \dots & \dots & \dots \\ & & & & & \dots & \dots & \dots & \dots & \dots \\ & & & & & \dots & \dots & \dots & \dots\dots\dots & 1 \end{bmatrix} \tag{4.50}$$

$$\mathbf{B}_x(2n \times 2n) = \begin{bmatrix} & & & & & KIlong & -Kx & 0 & \dots & -Kx \\ & & & & & -Kx & KIlong & -Kx & \dots & \dots \\ & & 0 & & & 0 & -Kx & \dots & \dots & \dots \\ & & & & & \dots & \dots & \dots & \dots & -Kx \\ & & & & & -Kx & \dots & \dots & -Kx & KIlong \\ -1 & 0 & \dots & \dots & 0 & & & & & \\ 0 & -1 & \dots & \dots & \dots & & & & & \\ \dots & \dots & \dots & \dots & \dots & & & 0 & & \\ \dots & \dots & \dots & \dots & \dots & & & & & \\ 0 & \dots & \dots & \dots\dots\dots & -1 & & & & & \end{bmatrix} \tag{4.51}$$

$$\mathbf{I}_{bx}(2n\times 1)=\begin{bmatrix} Ux_1 \\ Ux_2 \\ \cdots \\ \cdots \\ Ux_n \\ x_1 \\ x_2 \\ \cdots \\ \cdots \\ x_n \end{bmatrix} \tag{4.52}$$

$$\mathbf{X}_{rim}(2n\times 1)=\begin{bmatrix} x_{rim1} \\ x_{rim2} \\ \cdots \\ \cdots \\ x_{rimn} \\ 0 \\ \cdots \\ \cdots \\ \cdots \\ 0 \end{bmatrix} \tag{4.53}$$

$$\mathbf{V}_{rim}(2n\times 1)=\begin{bmatrix} Urx_1 \\ Urx_2 \\ \cdots \\ \cdots \\ Urx_n \\ 0 \\ \cdots \\ \cdots \\ \cdots \\ 0 \end{bmatrix} \tag{4.54}$$

where $DIlong = Dlong + 2Dx$ and $KIlong = Klong + 2Kx$.

Similarly, the equations of motion in matrix form for the longitudinal degree of freedom of the tread elements are:

$$\mathbf{Atr}_x \cdot \dot{\mathbf{I}}_{trx} + \mathbf{Btr}_x \cdot \mathbf{I}_{trx} = \mathbf{F}_x + Ktrlong \cdot \mathbf{X}_{belt} + Dtrlong \cdot \mathbf{V}_{belt} \tag{4.55}$$

With:

$$\mathbf{At}_{\xi}(2n_{tr}\times 2n_{tr})=\begin{bmatrix} c_{tr} & 0 & \dots & \dots & 0 & DItrlong & -Dtrx & 0 & \dots & 0 \\ 0 & c_{tr} & \dots & \dots & \dots & -Dtrx & DItrlong & -Dtrx & \dots & \dots \\ \dots & \dots & \dots & \dots & \dots & 0 & \dots & \dots & \dots & \dots \\ \dots & \dots & \dots & \dots & \dots & \dots & \dots & \dots & \dots & -Dtrx \\ \dots & \dots & \dots & \dots & c_{tr} & 0 & \dots & 0 & -Dtrx & DItrlx \\ & & & & & 1 & 0 & \dots & \dots & 0 \\ & & & & & 0 & 1 & \dots & \dots & \dots \\ & & 0 & & & \dots & \dots & \dots & \dots & \dots \\ & & & & & \dots & \dots & \dots & \dots & \dots \\ & & & & & \dots & \dots & \dots & \dots & 1 \end{bmatrix} \tag{4.56}$$

$$\mathbf{Bt}_{\xi}(2n_{tr}\times 2n_{tr})=\begin{bmatrix} & & & & & KItrlong & -Ktrx & 0 & \dots & 0 \\ & & & & & -Ktrx & KItrlong & -Ktrx & \dots & \dots \\ & & 0 & & & 0 & -Ktrx & \dots & \dots & \dots \\ & & & & & \dots & \dots & \dots & \dots & -Ktrx \\ & & & & & 0 & \dots & \dots & -Ktrx & KItrlong \\ -1 & 0 & \dots & \dots & 0 & & & & & \\ 0 & -1 & \dots & \dots & \dots & & & & & \\ \dots & \dots & \dots & \dots & \dots & & & 0 & & \\ \dots & \dots & \dots & \dots & \dots & & & & & \\ 0 & \dots & \dots & \dots & -1 & & & & & \end{bmatrix} \tag{4.57}$$

$$\mathbf{I}_{trx}(2n_{tr}\times 1)=\begin{bmatrix} Uxtr_1 \\ Uxtr_2 \\ \dots \\ \dots \\ Uxtr_n \\ xtr_1 \\ xtr_2 \\ \dots \\ \dots \\ xtr_{ntr} \end{bmatrix} \tag{4.58}$$

$$\mathbf{X}_{belt}(2n_{tr}\times 1)=\begin{bmatrix} x_1 \\ x_2 \\ \dots \\ \dots \\ x_{n_{tr}} \\ 0 \\ \dots \\ \dots \\ \dots \\ 0 \end{bmatrix} \tag{4.59}$$

$$\mathbf{V}_{belt}(2n_{tr}\times 1)=\begin{bmatrix} Ux_1 \\ Ux_2 \\ \dots \\ \dots \\ Ux_{n_{tr}} \\ 0 \\ \dots \\ \dots \\ \dots \\ 0 \end{bmatrix} \tag{4.60}$$

where $DItrlong = Dtrlong + 2Dtrx$ and $KItrlong = Ktrlong + 2Ktrx$.

4.4.3 Mechanics of Contact

The accurate calculation of the size of the contact patch and normal pressure distribution requires a fine discretisation of the belt and the inclusion of at least a radial degree of freedom per belt element. Alternatively, a separate quasi-static algorithm is used for the calculation of the normal pressure distribution along the contact area. The algorithm is a simplified version of the method employed in the advanced steady-state model presented in chapter 3.

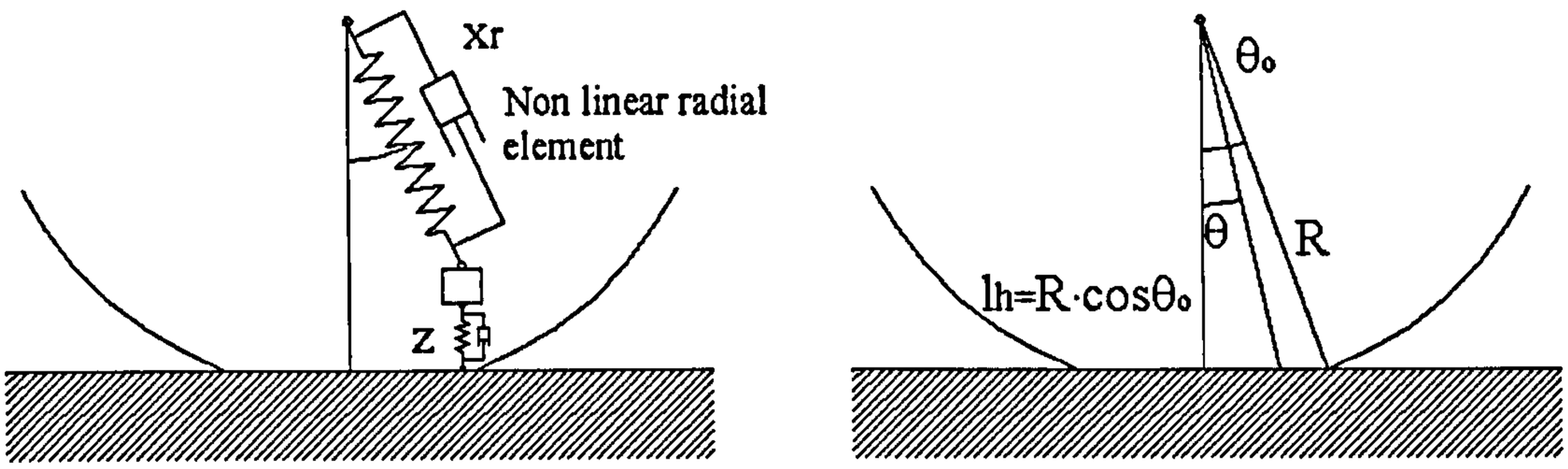

Figure 4. 24 A simple model for the calculation of the normal pressure distribution along the contact

According to this approach, shown graphically in figure 4.24, a single belt element is connected radially to the rim by a Kelvin element, incorporating a non-linear stiffness, in order to account for the effect of air-pressure inside the tyre. The belt element is connected to the ground via a separate vertical Kelvin element. The element enters the leading edge of the contact patch at an angle θ_0, dictated by the height of the centre of the wheel from the ground (l_h) and the radius of the inflated tyre outside the contact patch (R). The element moves along the contact patch in discrete time-steps dt, covering a distance of $\Omega l_h dt$ per time-step. The equation of motion of the belt element in the vertical direction is:

$$\ddot{z}c + D_z\dot{z} + K_z z - radforce(x_r)\cos(\theta) - D_r\dot{x}_r\cos(\theta) = 0 \qquad (4.61)$$

where z denotes the displacement (compression) of the vertical Kelvin element, K_z and D_z are the vertical stiffness and damping coefficients, x_r is the displacement of the radial element and D_r denotes the radial damping. As previously, all coefficients are stated per unit length of the contact patch.

Function $f(x_r) = radforce(x_r)$ represents the elastic force in the radial direction as defined by the relation 3.121. This relation is given below for ease of reference.

$$radforce(x_r) = pb\left(1 - e^{-wx_r}\right),\ w = \lambda(K_r / pb) \tag{4.62}$$

where p denotes the pressure in $\left[N/m^2\right]$, b is the width of the tyre in $[m]$, K_r is the linear component of the radial stiffness of the Kelvin element in $\left[N/m^2\right]$ and λ is an adjustable parameter given in $\left[m^{-1}\right]$, responsible for the rate of saturation of the radial force.

The necessary kinematic constraints for the solution of equation (4.61) are:

$$x_r \cos(\theta) + z = R(\cos(\theta) - \cos(\theta_0)) \tag{4.63}$$

$$\dot{x}_r \cos(\theta) - \Omega \sin(\theta) x_r = -R\Omega \sin(\theta) - \dot{z} - \dot{l}_h \tag{4.64}$$

Equations (4.61), (4.63) and (4.64) are solved at each time-step, until the normal force generated by the vertical Kelvin element diminishes. While the philosophy of the approach is identical to that of the advanced steady-state model, the situation is simplified by eliminating the circumferential degree of freedom of the belt element. Since the tyre model already incorporates a circumferential degree of freedom, the computational effort for the solution of an additional differential equation, together with two more kinematic constraint equations is avoided. In the event that the tyre operates in stand-still i.e. $\Omega = 0$, equations (4.61), (4.63) and (4.64) reduce to a non-linear algebraic system with respect to x_r and z. The normal pressure distribution is then obtained by solving the system at a number of pre-specified positions in the range $\theta \in (-\theta_0, \theta_0)$. Finally, a similar two-dimensional interpolation procedure as the one

described in section 3.3.5 is followed for the immediate calculation of the initial angle θ_0, based on the net normal load and the rolling velocity.

4.4.4 Modelling of Friction

The force and velocity thresholds for the transition between sticking and slipping for a tread segment of the tyre model are:

$$\left(\frac{F_{xi}}{\mu_{sx}}\right)^2 + \left(\frac{F_{y_i}}{\mu_{sy}}\right)^2 \geq F_{zi}^2 \tag{4.65}$$

$$\sqrt{Uxtr^2{}_i + Uytr^2{}_i} \geq threshold \tag{4.66}$$

where μ_{sx}, μ_{sy} denote the coefficients of static friction in longitudinal and lateral directions, F_{xi}, F_{yi} are the forces applied on the tread element by the viscoelastic connections and F_{zi} is the normal force on the tread element.

Like in the previous analyses, the non-sliding condition occurs, when none of relations (4.65), (4.66) are satisfied, in which case friction forces equate to the forces applied on the tread element by the viscoelastic connections. The friction forces in the lateral and longitudinal directions can be calculated, when either one of the relations (4.65) and (4.66) hold true. Thus:

$$f_{xi} = \frac{Uxtr_i}{\sqrt{\left(Uxtr_i/\mu_{kx}\right)^2 + \left(Uytr_i/\mu_{ky}\right)^2}} \cdot F_{zi} \tag{4.67}$$

$$f_{yi} = \frac{Uytr_i}{\sqrt{\left(Uxtr_i/\mu_{kx}\right)^2 + \left(Uytr_i/\mu_{ky}\right)^2}} \cdot F_{zi} \tag{4.68}$$

where $f_{xi,yi}$ denotes the friction force in the respective directions and μ_{kx}, μ_{ky} are the corresponding coefficients of kinetic friction.

Of course, it is possible to assume velocity-dependent coefficients of kinetic friction, as demonstrated in section 3.3.4.5. The coefficient of kinetic friction for each segment then becomes:

$$\mu_{kx} = \mu_{sx} + \mu_{xred}\left(e^{-qx|Uxtr_i|} - 1\right) \tag{4.69}$$

$$\mu_{ky} = \mu_{sy} + \mu_{yred}\left(e^{-qy|Uytr_i|} - 1\right) \tag{4.70}$$

where μ_{xred}, μ_{yred}, qx, qy are coefficients.

It should be noted that, initially, it is beneficial to assume constant coefficients of kinetic friction. This approach allows the assessment of the contribution of the dynamics of the tread, belt and carcass at various sliding and rolling velocities. By keeping friction forces independent of sliding velocity, one can be certain that any variations in tyre forces are not due to different friction levels, but instead can be attributed to the dynamic force transfer from the contact patch to the wheel rim. Later, in a refined version of the tyre model, velocity dependent coefficients of friction would increase the accuracy of the model for a wide range of operating conditions.

4.4.5 Numerical Procedure

Euler and Runge Kutta [113], [114] methods have been employed successfully in the integration scheme for the solution of the equations of motion of the model. The integration algorithms are combined with appropriate numerical schemes for the update of the states of the tread in a way that the rolling motion of the tyre is taken into account. During the integration, the continuous change of the position of the belt relative to the tread is also taken into consideration.

Tyre forces and moments are calculated, taking into account the forces applied on the rim by the carcass elements. Depending on the purpose of the simulation, the inertial forces occurring during the acceleration and deceleration of the belt may also be included, or subtracted from the total force transferred to the wheel rim. Very often, in full vehicle simulations, the inertia of the wheels and tyres is included in the inertia of

the body of the vehicle. If the tyre model is to be used in such an environment, the forces, resulting from the acceleration of the belt should not be included in the output of the model. Similarly, if a transient manoeuvre is conducted, by altering the slip angle of a tyre, rolling over a rotating drum, the tyre model would assume the corresponding lateral velocity applied on the wheel rim. Clearly, inertial effects due to the global acceleration of the tyre belt should be excluded from the results. This should not be misinterpreted as having disregarded the inertia of the belt, as the mass of the belt elements still affects the periodic deformation of the belt, while the wheel is rolling under the application of friction forces.

Figure 4.25 presents graphically the tasks performed parallel to the integration of the equations of motion of the tread and belt. The vector containing the states of the belt plays the role of the reference vector. As the tyre rolls forward, the vector of the states of the tread slides downwards, interacting with different parts of the belt vector. In the event that the tread vector reaches the end of the belt vector, the former is divided into two separate parts. The first part interacts with the bottom part of the belt vector while the second part returns to the top of the belt vector, so as to simulate the continuous rolling motion of the tyre. At the same time, the entries of the tread vector move upwards at a rate dictated by the rolling velocity of the wheel. Finally, the normal pressure distribution is attached to the tread vector, playing a role in the determination of the friction forces applied on the tread elements.

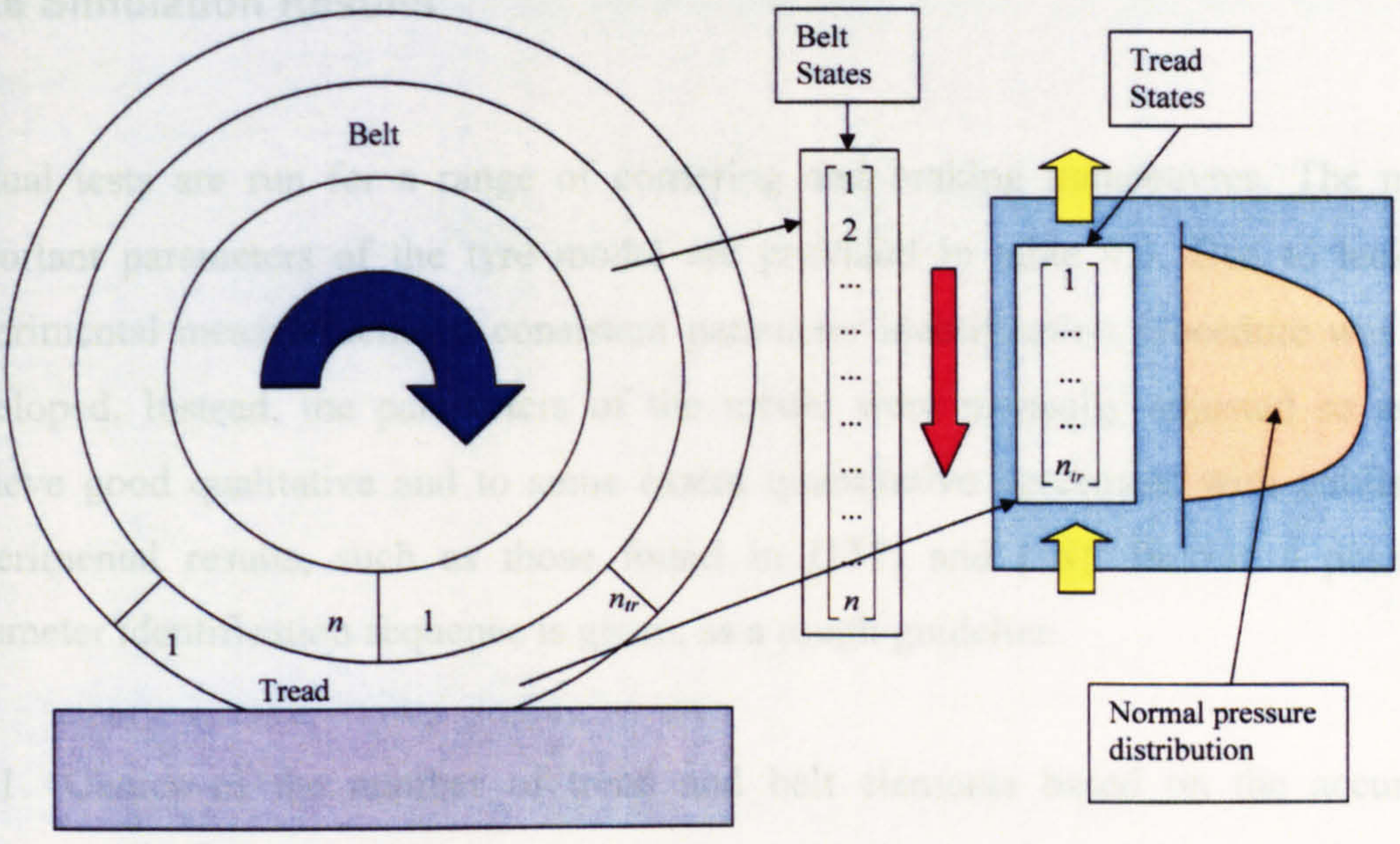

Red Arrow: The states of the tread move with respect to the states of the belt, based on the linear velocity of rolling

Yellow Arrows: The states of the tread move upwards within their own matrix, in order to take into account the linear velocity of rolling

Figure 4. 25 Visualisation of the continuously changing interactions between the belt and tread states

4.4.6 Simulation Results

Virtual tests are run for a range of cornering and braking manoeuvres. The most important parameters of the tyre model are provided in table 4.3. Due to lack of experimental measurements, a consistent parameter identification procedure was not developed. Instead, the parameters of the model were manually adjusted so as to achieve good qualitative and to some extent quantitative agreement with published experimental results, such as those found in [117] and [18]. Below, a possible parameter identification sequence is given, as a rough guideline.

1. Choice of the number of tread and belt elements based on the accuracy required
2. Calculation of *Klong* and *Klat* from the circumferential and lateral deflections under static loads.
3. Calculation of *Kx* and *Ky* from low amplitude transient tests such as the response to step inputs
4. Calculation of belt inertia based on the response to high frequency – low amplitude sinusoidal inputs
5. Calculation of contact parameters (K_r, λ, D_r) based on measurements of the contact patch size and the rolling resistance at pre-specified velocities
6. Calculation of tread stiffness and friction parameters based on steady-state tests
7. Adjustment of various parameters such as tread damping, velocity threshold and tread inertia, in order to achieve acceptable stick-slip friction behaviour (based on the analysis in section 4.3.2)

An iterative procedure between steps 3 and 7 might be required in order to improve agreement between experimental and numerical results.

The sequence stated above is not unique and steps 2-4 can be replaced by a number of modal tests which would facilitate the estimation of both the stiffness and inertia properties of the tyre. For such procedures, a post-processing mode of

operation is required from the model, with the ability to generate the modal behaviour.

Table 4.3

Important tyre parameters

Klong	*Klat*	*Dlong*	*Dlat*	*Kx*	*Ky*	*Dx*	*Dy*	μ_{kx}, μ_{ky}	μ_{sx}, μ_{sy}
[N/m^2]	[N/m^2]	[Ns/m^2]	[Ns/m^2]	[N/m^2]	[N/m^2]	[Ns/m^2]	[Ns/m^2]	-	-
3e5	7e5	8e2	8e2	1.8e8	1.8e8	6.4e3	6.4e3	0.9	1.17
Ktrlong	*Ktrlat*	*Dlong*	*Dtrlat*	*Ktrx*	*Ktry*	*Dtrx*	*Dtry*	*p*	*b*
[N/m^2]	[N/m^2]	[Ns/m^2]	[Ns/m^2]	[N/m^2]	[N/m^2]	[Ns/m^2]	[Ns/m^2]	[N/m^2]	[m]
2e7	0.9e7	1.5e3	8e3	9e7	9e7	3.2e3	3.2e3	2.2e5	0.205
c	c_{tr}	n	n_{tr}	K_r	D_r	K_s	D_s	λ	
[Kg/m]	[Kg/m]			[N/m^2]	[Ns/m^2]	[N/m^2]	[Ns/m^2]	[m^{-1}]	
4	3	250	30	4e6	1.6e3	3.2e7	5e4	6.8	

The normal pressure distributions as calculated by the simplified quasi-static algorithm are shown in figures 4.26 and 4.27 for low and high rolling velocities, respectively. The deviation from the parabolic shape and the expected shift of the peak [111] towards the leading edge are both captured. It should be noted that all tests were carried out using a normal load of 5000 N, unless otherwise noted.

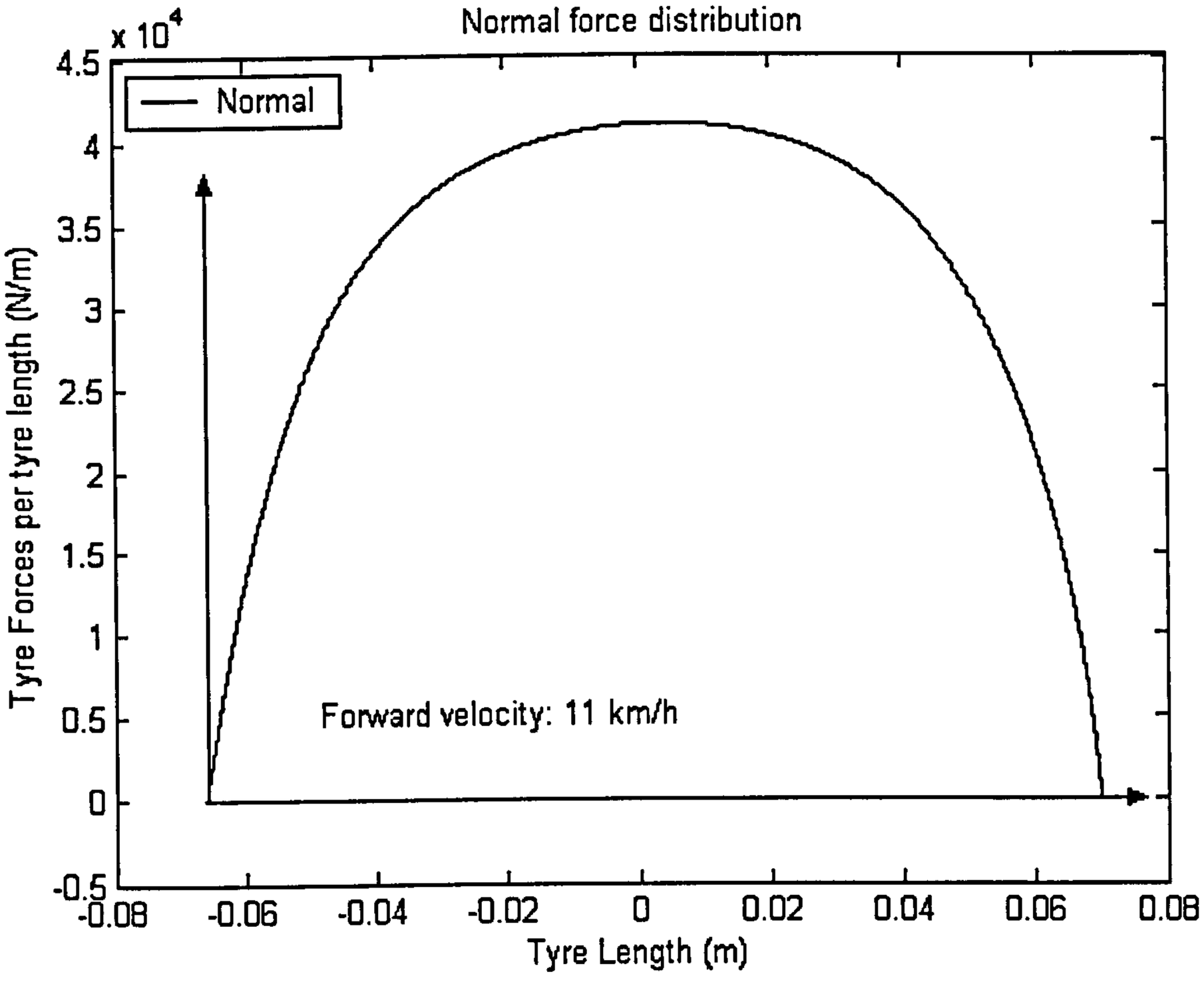

Figure 4. 26 Normal pressure distribution for low rolling velocity

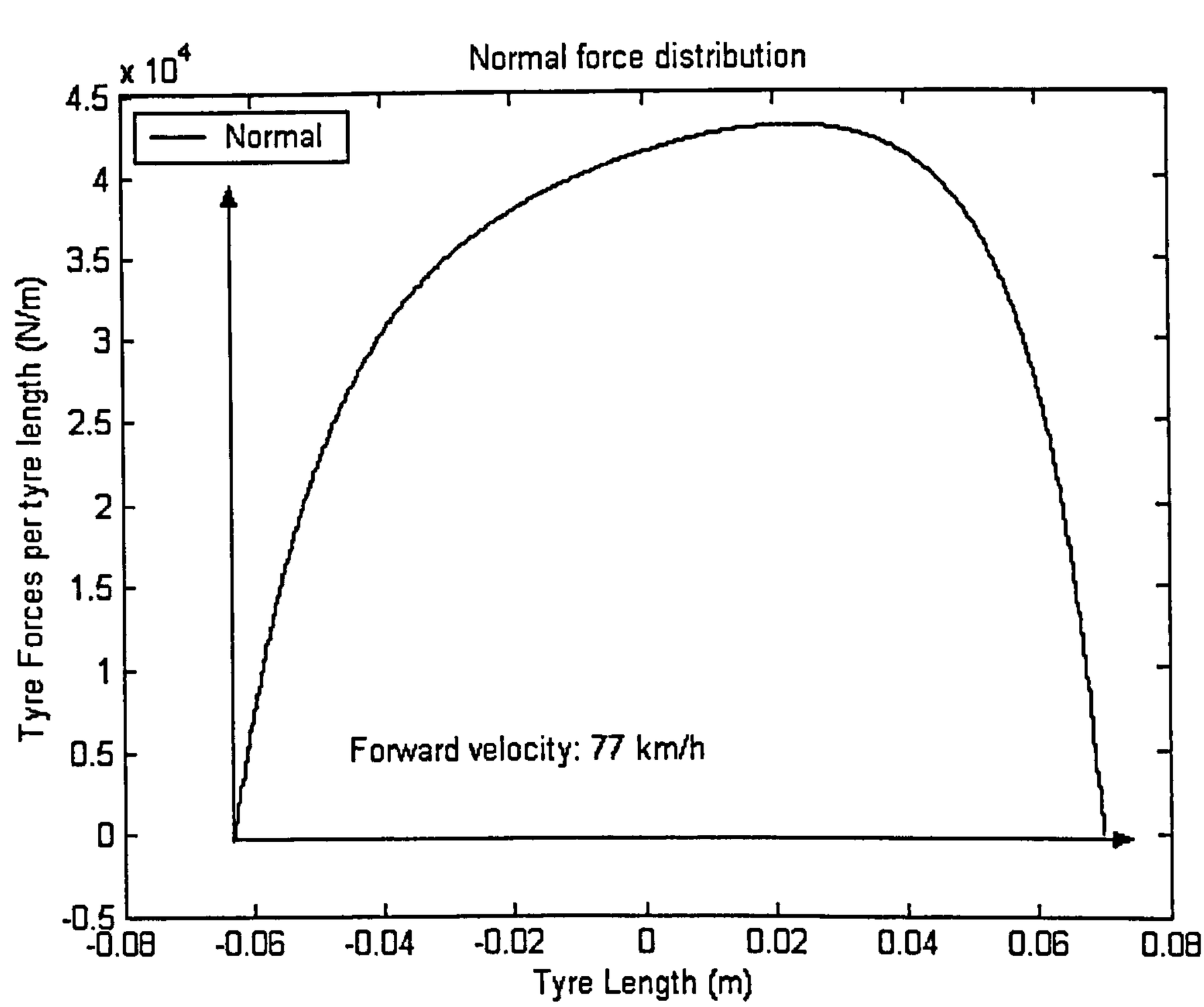

Figure 4. 27 Normal pressure distribution for high rolling velocity

At first, the transient model is subjected to a series of cornering tests. Figure 4.28 captures the lateral deformation of the tyre belt, while figure 4.29 shows the corresponding deformation of the tyre tread. A graphical illustration of the overall deformation of the tyre is given in figure 4.30.

The force response of the tyre to a step change in lateral slip is depicted in figure 4.31 for two different rolling velocities. It is shown clearly that the model predicts the approximately exponential response which is observed experimentally [117] and can be calculated analytically using the relaxation length concept. In addition, the model depicts the effect of rolling velocity in the transient behaviour of tyres, showing a much faster response for the tyre with the higher rolling velocity. The corresponding self-aligning moment is given in figure 4.32. It is observed that as rolling velocity increases, the self-aligning moment response becomes faster. It is interesting to note that at the specific slip angle the steady-state value of the self aligning moment converges to a relatively low level of approximately -5 [Nm]. Still, the transient model predicts a significant overshoot in the self aligning moment which lasts longer at lower rolling velocities. The same trend in the build-up of the self aligning torque is found by Higuchi and Pacejka [117]. This type of torque response is related to the transient response of the pneumatic trail. The discretised model presented here is capable of generating the conditions along the contact patch at each time-step, based on the external kinematic excitations and the interaction between the dynamics of the belt and the frictional characteristics of the tread. Therefore, the effect of the pneumatic trail is already incorporated in the model. In this simple case of a step side-slip input, one may argue that as the lateral force increases, it passes from the stage where maximum self aligning moment is generated. As the side-force increases further, the pneumatic trail reduces and the self-aligning torque converges to its steady-state value.

Figures 4.33 and 4.34 show the force and moment responses to a ramp side-slip input. Again the effect of rolling velocity is depicted, with the curves corresponding to higher velocities being in closer qualitative agreement with steady state characteristics.

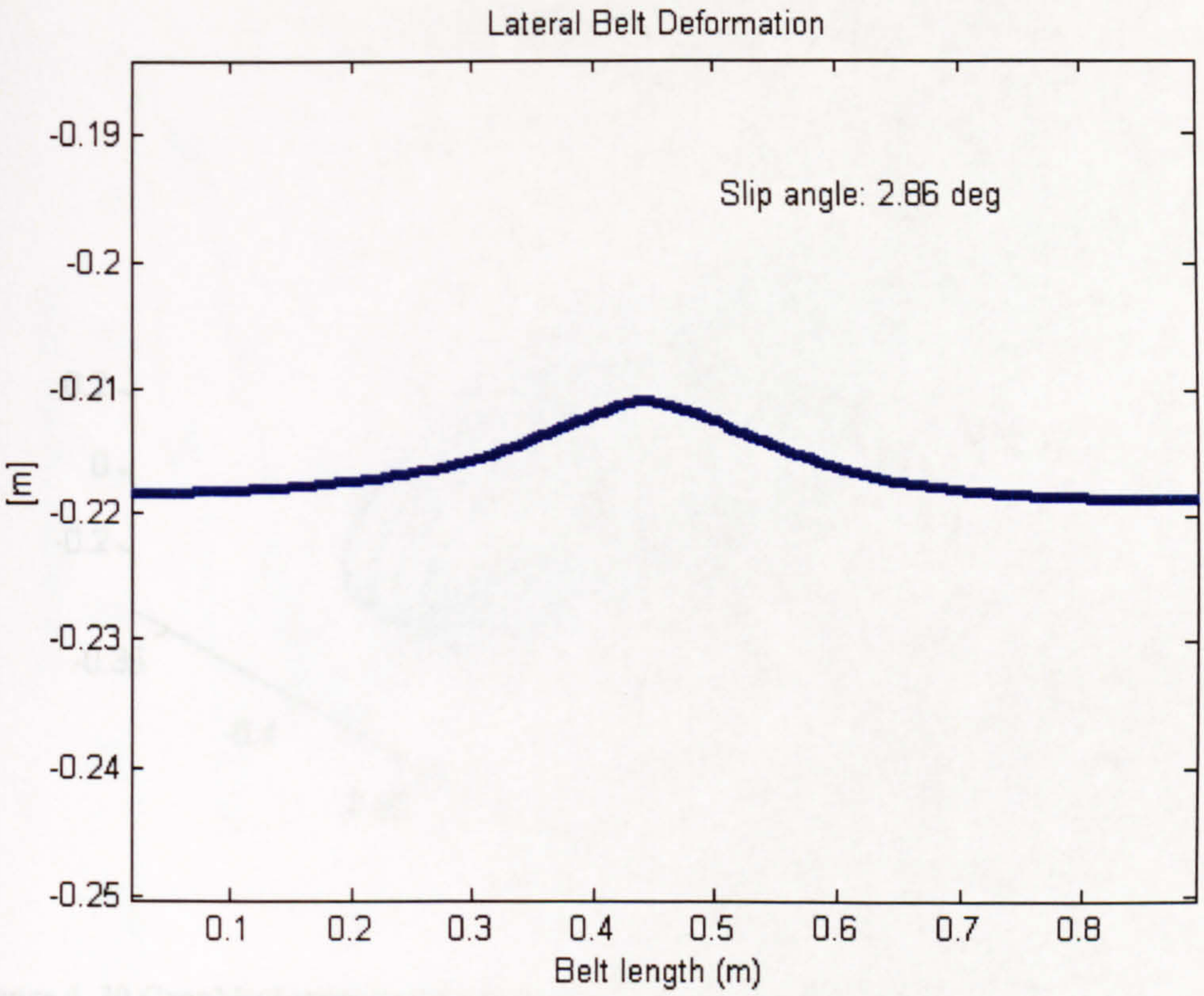

Figure 4. 28 Lateral belt deformation under moderate cornering

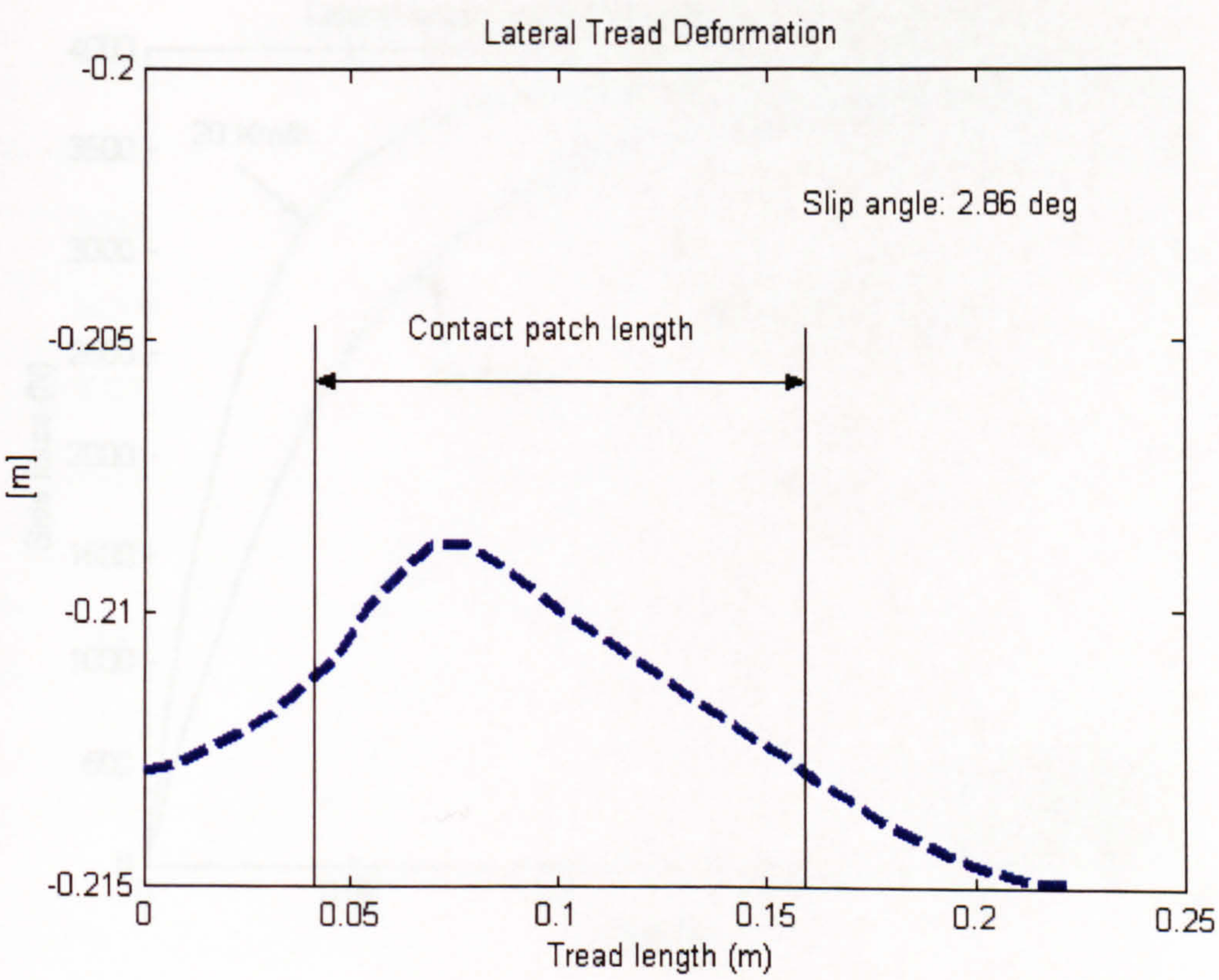

Figure 4. 29 Lateral deformation of the tread under moderate cornering

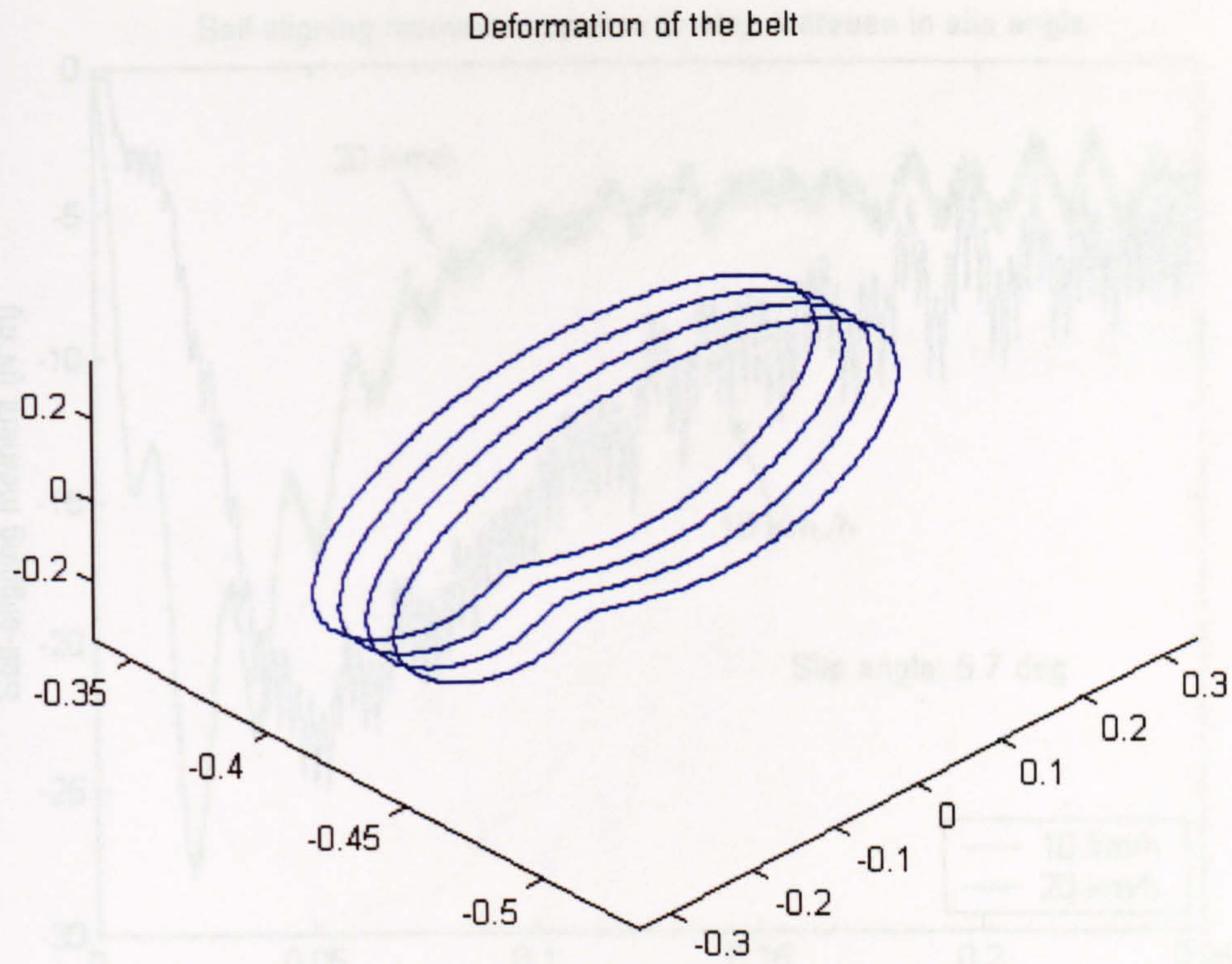

Figure 4. 30 Graphical representation of the lateral deflection of the tyre belt as predicted by the tyre model

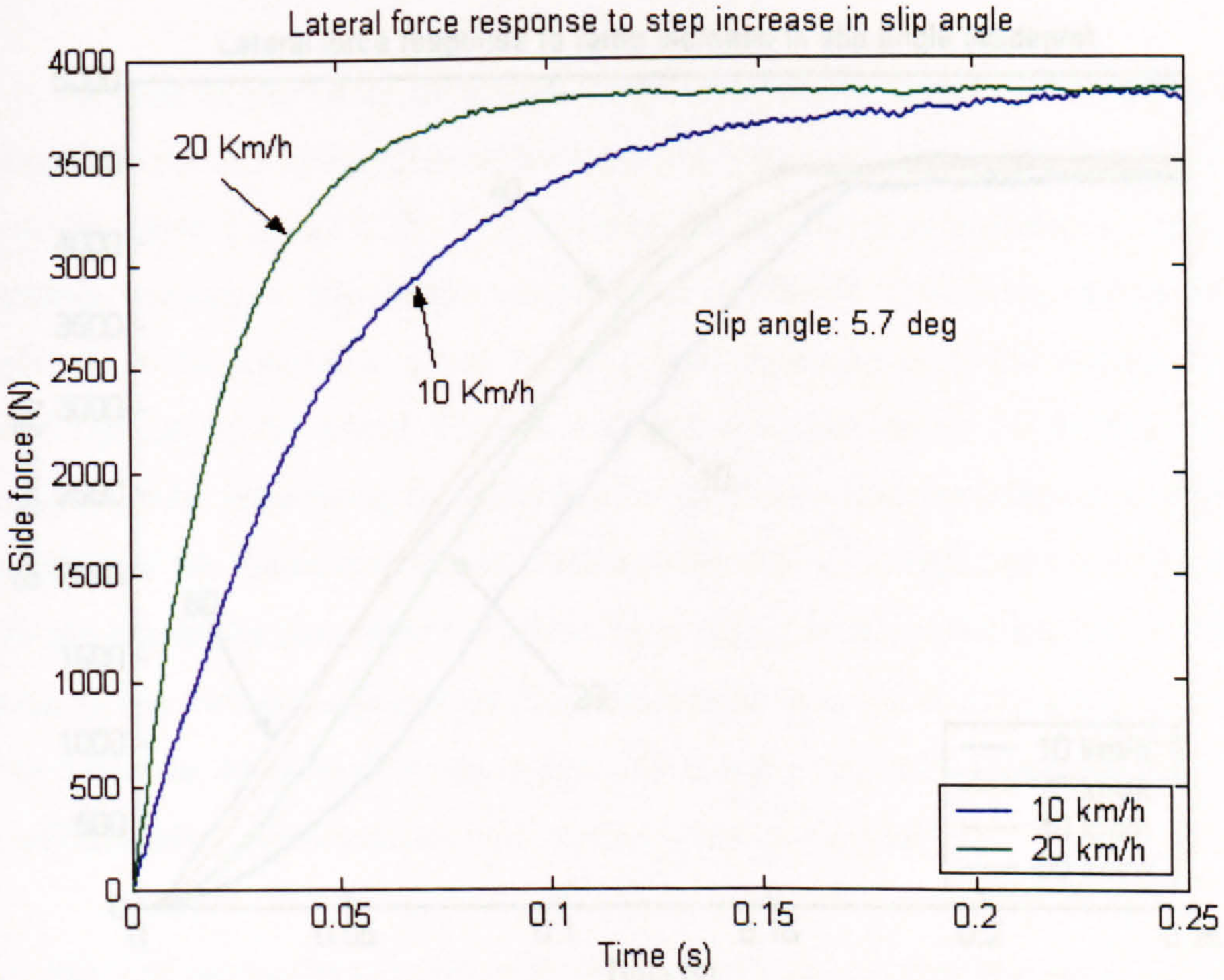

Figure 4. 31 The approximately exponential response of the lateral force to a step change in slip angle

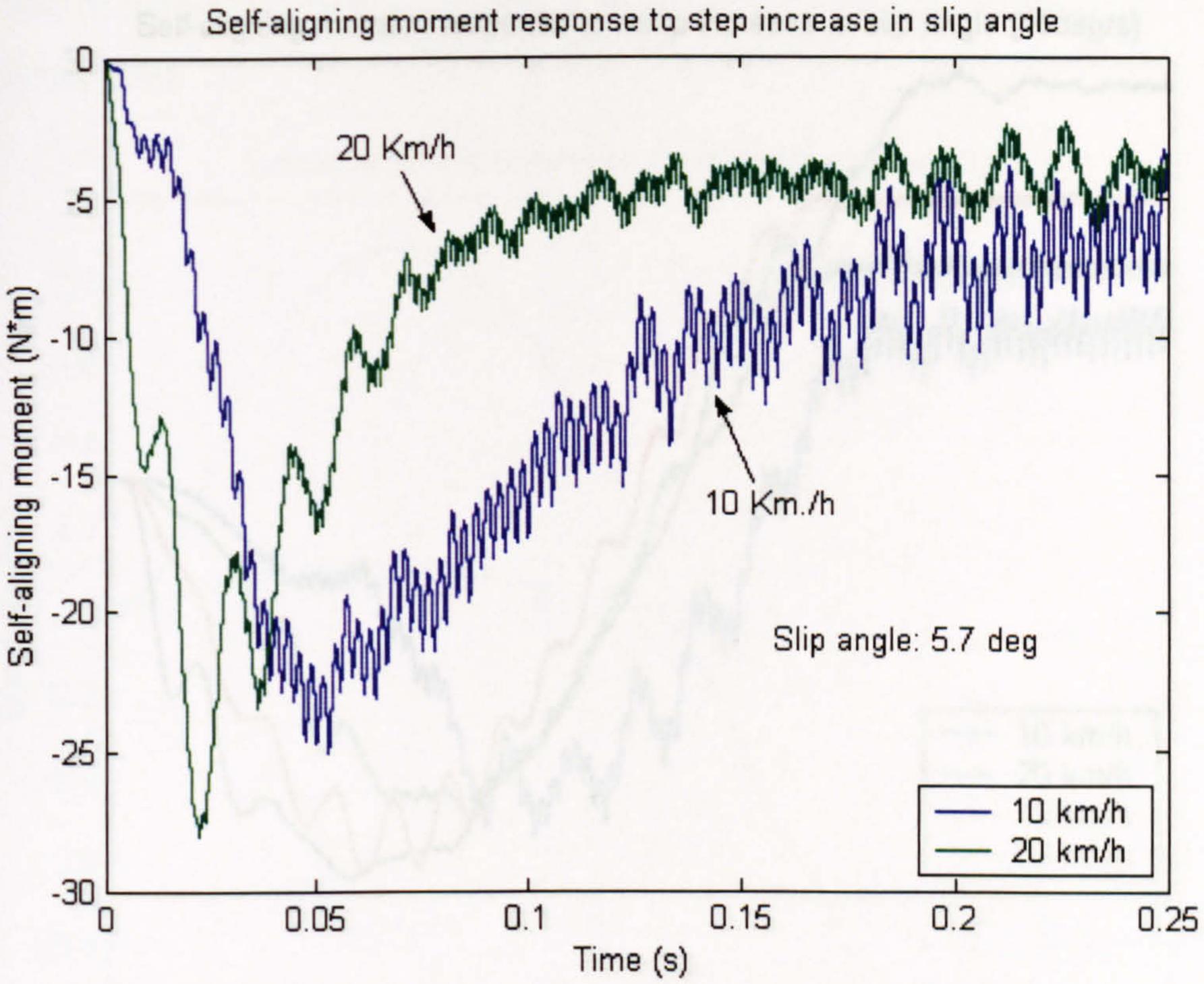

Figure 4. 32 Self-aligning moment response to step change in slip angle

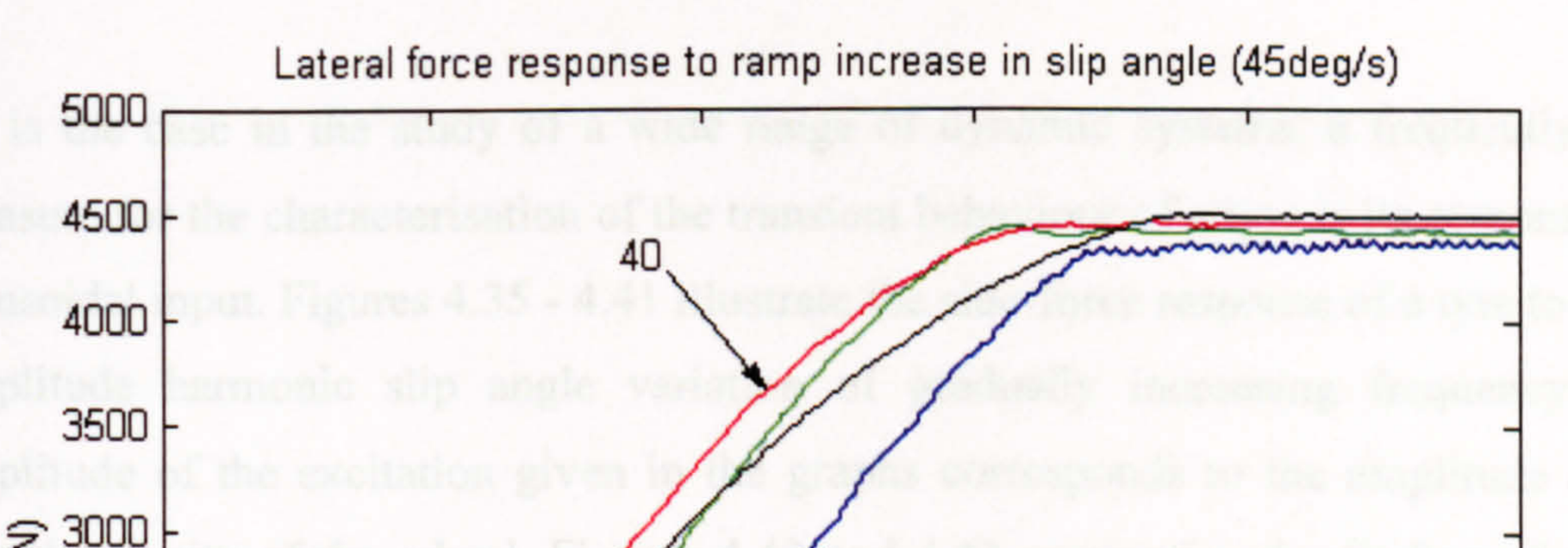

Figure 4. 33 Lateral force response to a linearly increasing slip angle

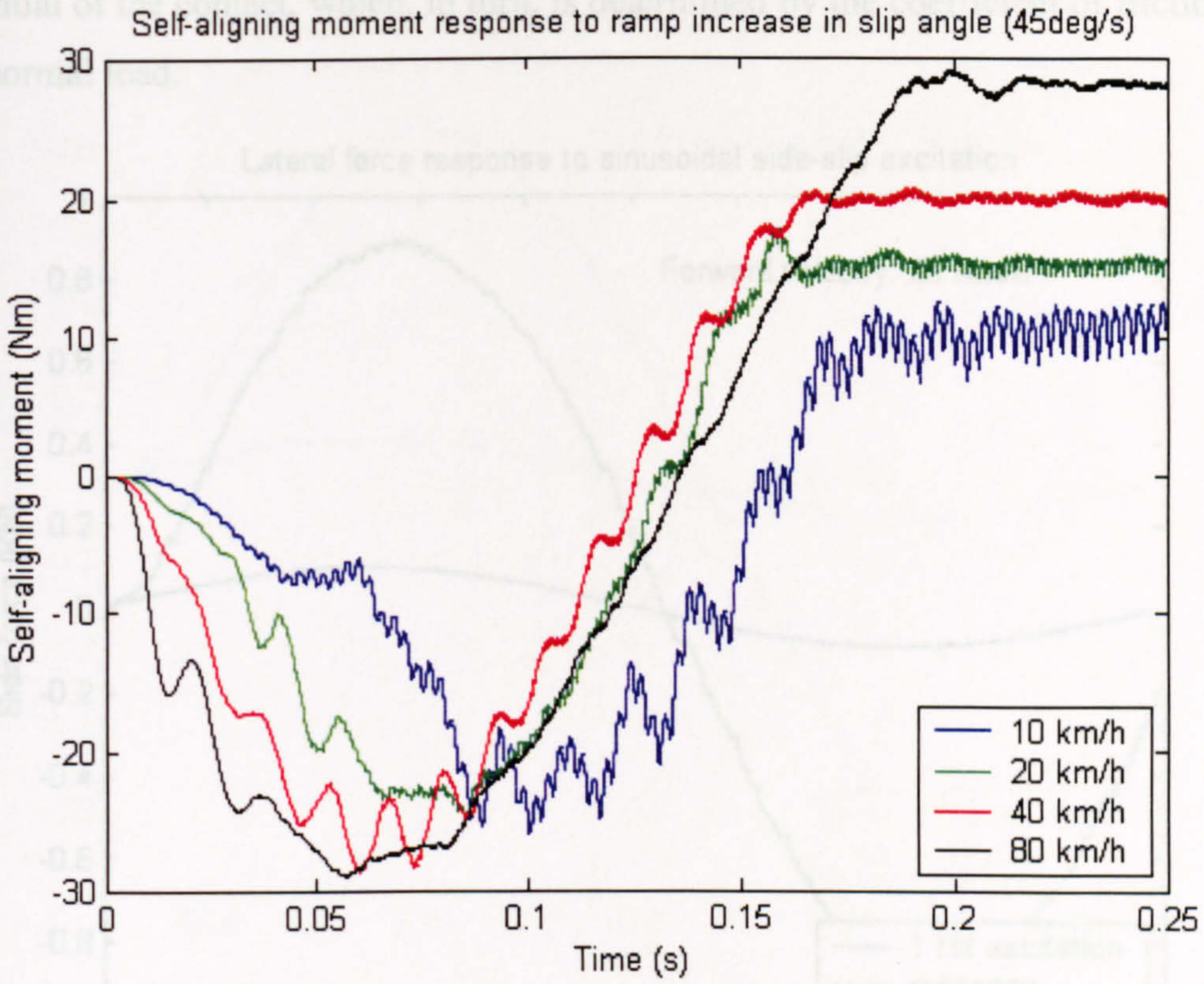

Figure 4. 34 Self-aligning moment response to a linearly increasing slip angle

As is the case in the study of a wide range of dynamic systems, a frequently used measure for the characterisation of the transient behaviour of a tyre is its response to a sinusoidal input. Figures 4.35 - 4.41 illustrate the side-force response of a tyre to a low amplitude harmonic slip angle variation of gradually increasing frequency. The amplitude of the excitation given in the graphs corresponds to the amplitude of the lateral velocity of the wheel. Figures 4.42 and 4.43 summarise the findings from all sinusoidal tests, illustrating the reduction in amplitude and the increase in phase lag, as a result of the increase in the excitation frequency. Similarly, figures 4.44 and 4.45 show the amplitude and phase variations for a higher rolling velocity. It is evident that rolling at low velocities promotes the reduction in amplitude and increases the delay of the response. In general, it can be concluded that a tyre acts a low-pass filter with a cut-off frequency that increases with rolling velocity [6], [18].

The ability of the model to perform in the saturated area of tyre operation is illustrated in figure 4.46. Here, the amplitude of the slip angle excitation is 14 deg and the force response resembles a chopped signal with its maximum limited by the frictional

potential of the contact, which, in turn, is determined by the coefficient of friction and the normal load.

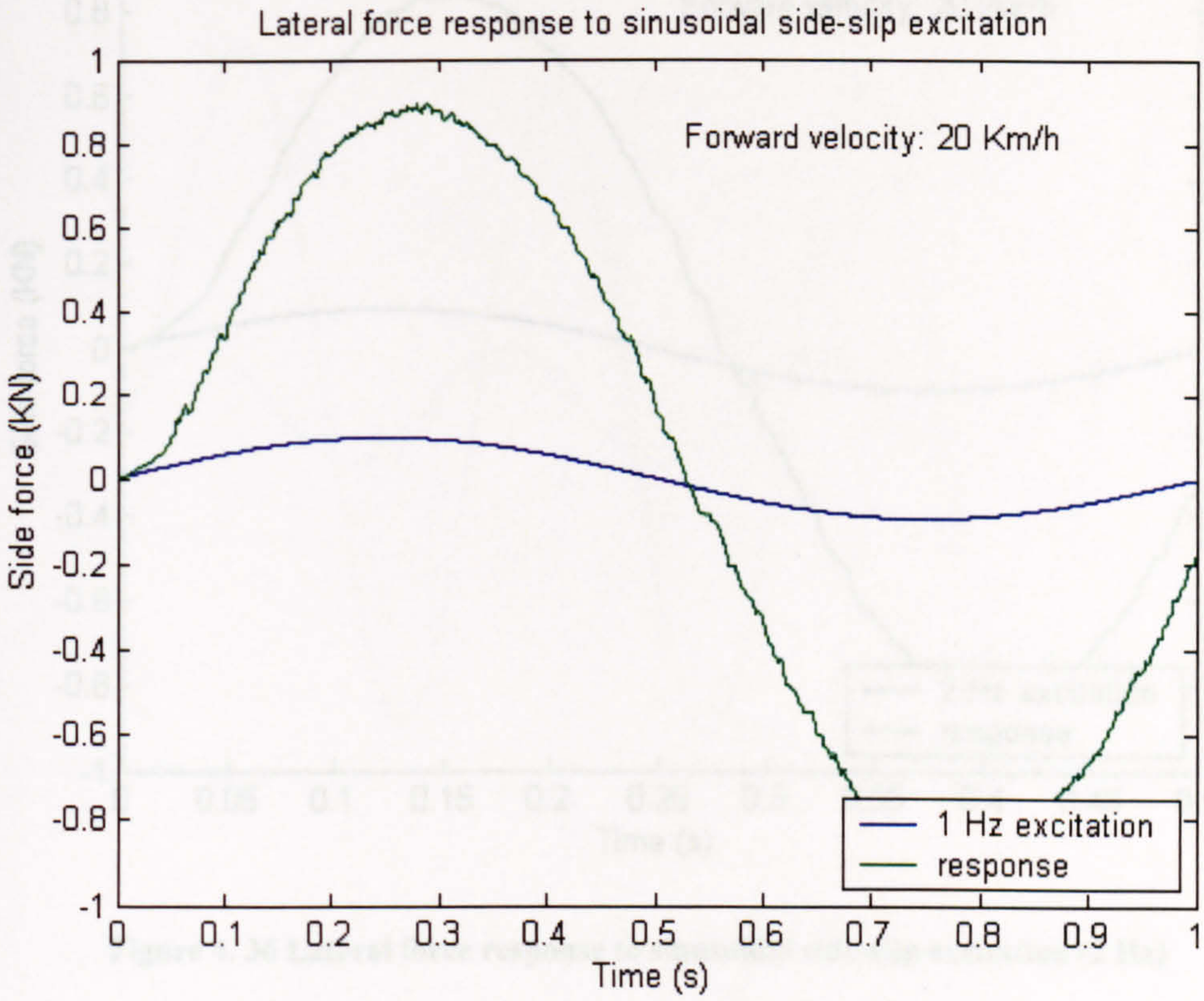

Figure 4. 35 Lateral force response to sinusoidal side-slip excitation (1 Hz)

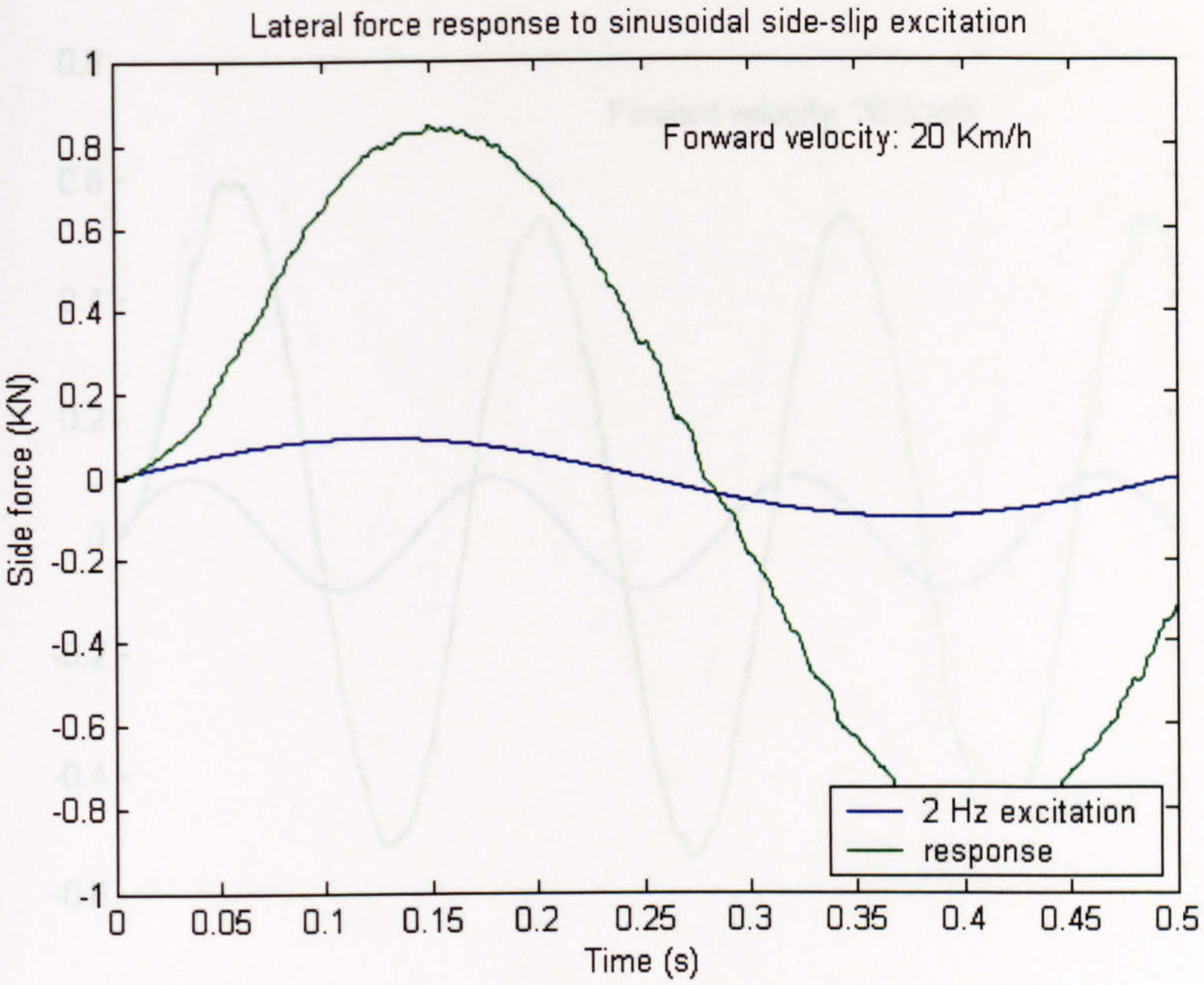

Figure 4. 36 Lateral force response to sinusoidal side-slip excitation (2 Hz)

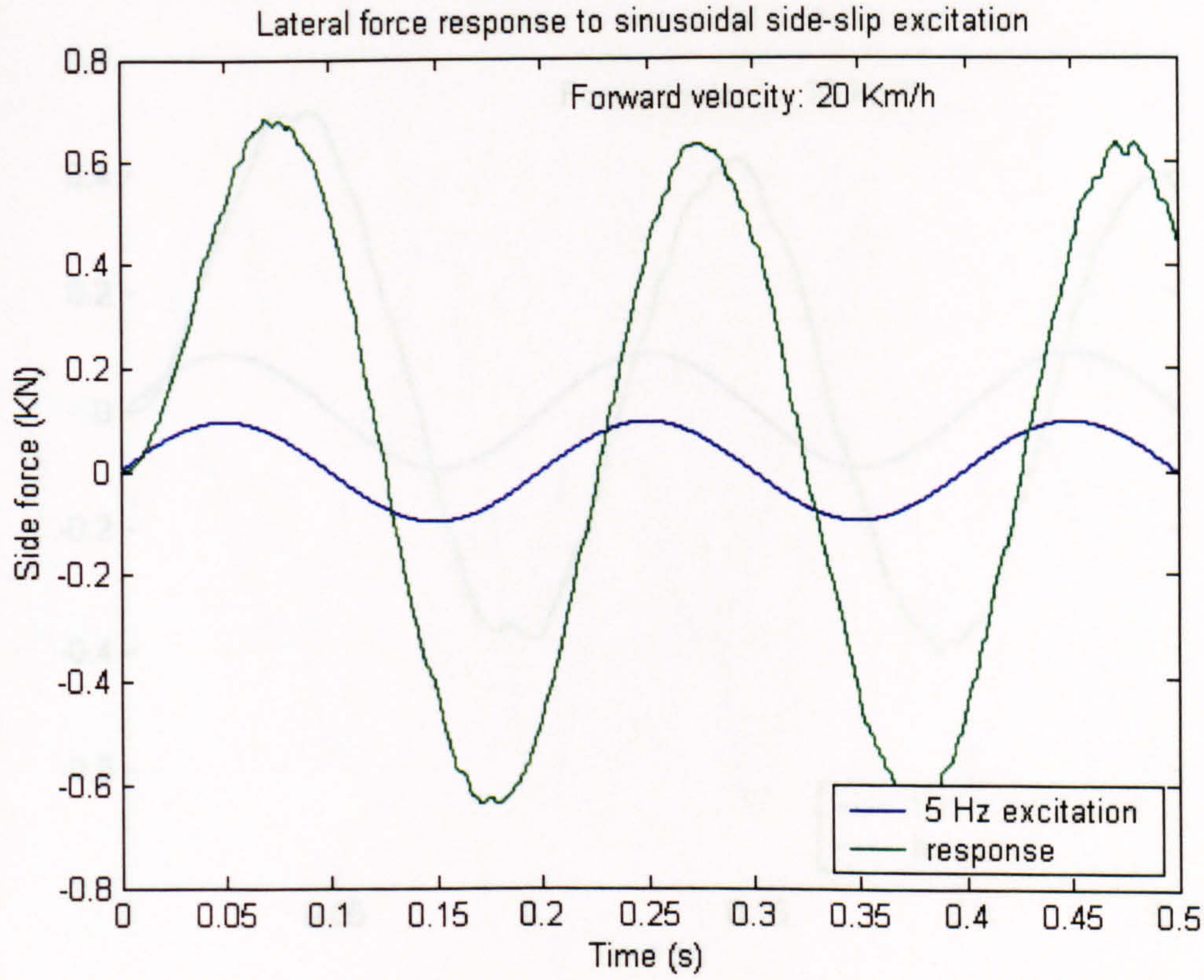

Figure 4. 37 Lateral force response to sinusoidal side-slip excitation (5 Hz)

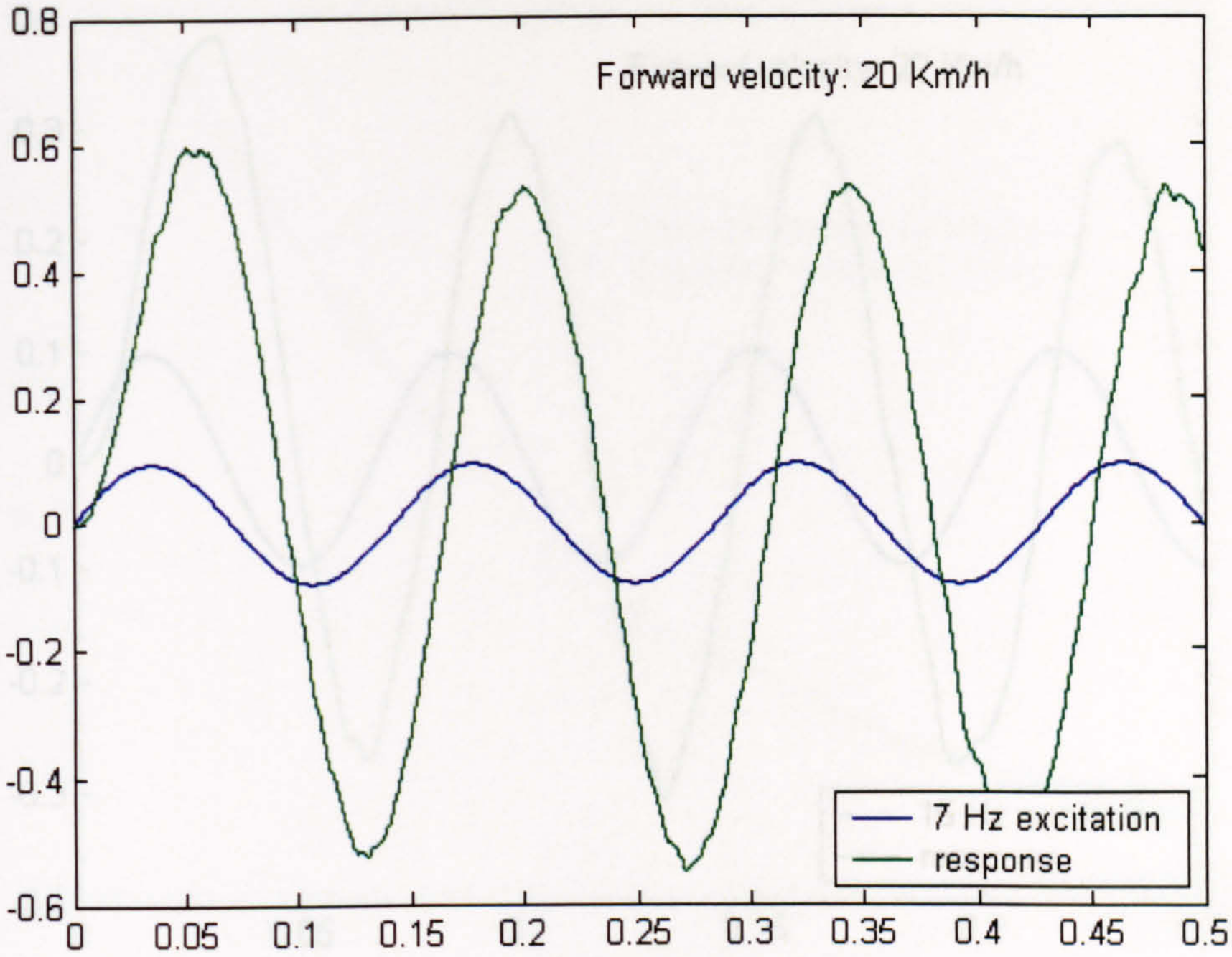

Figure 4. 38 Lateral force response to sinusoidal side-slip excitation (7 Hz)

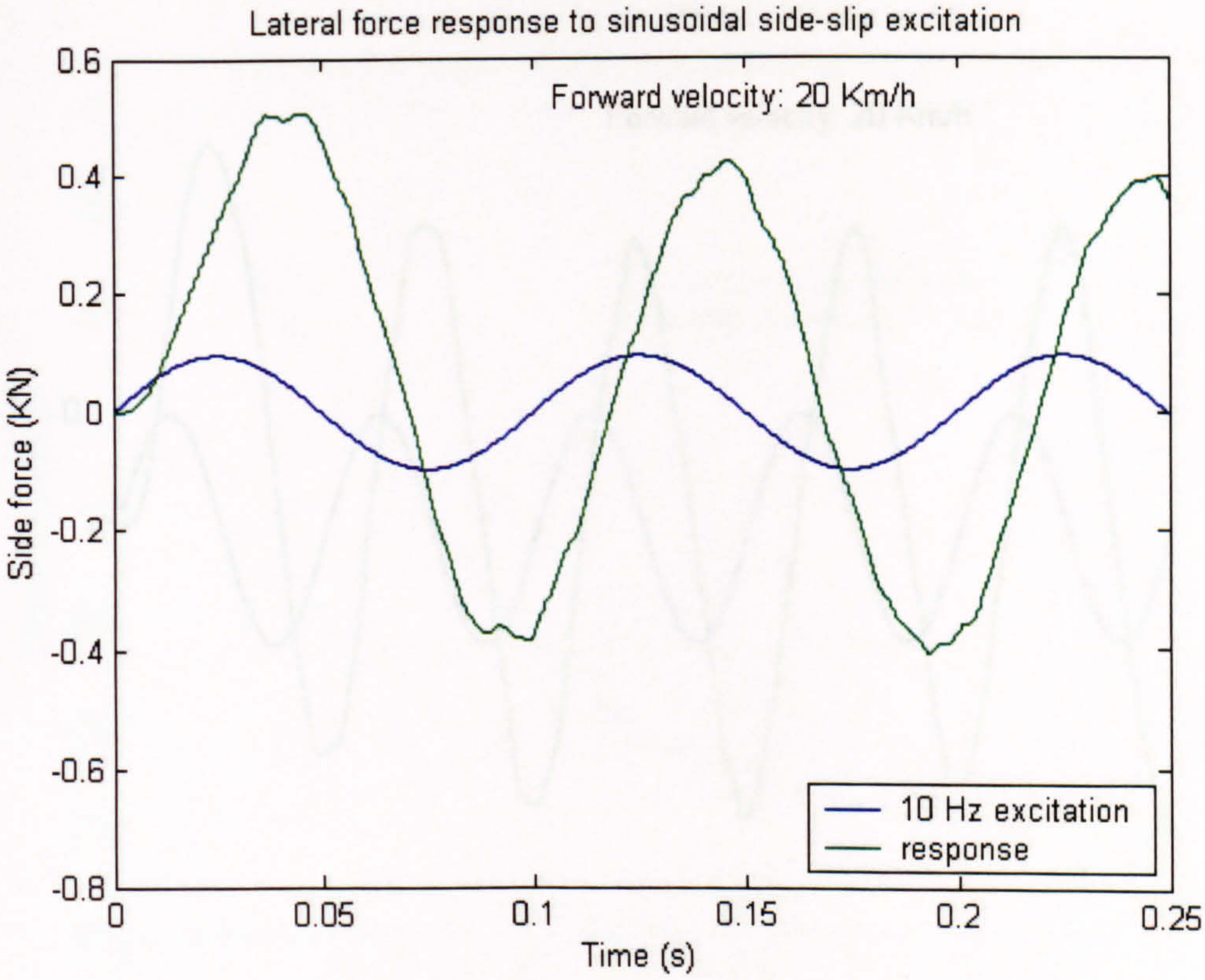

Figure 4. 39 Lateral force response to sinusoidal side-slip excitation (10 Hz)

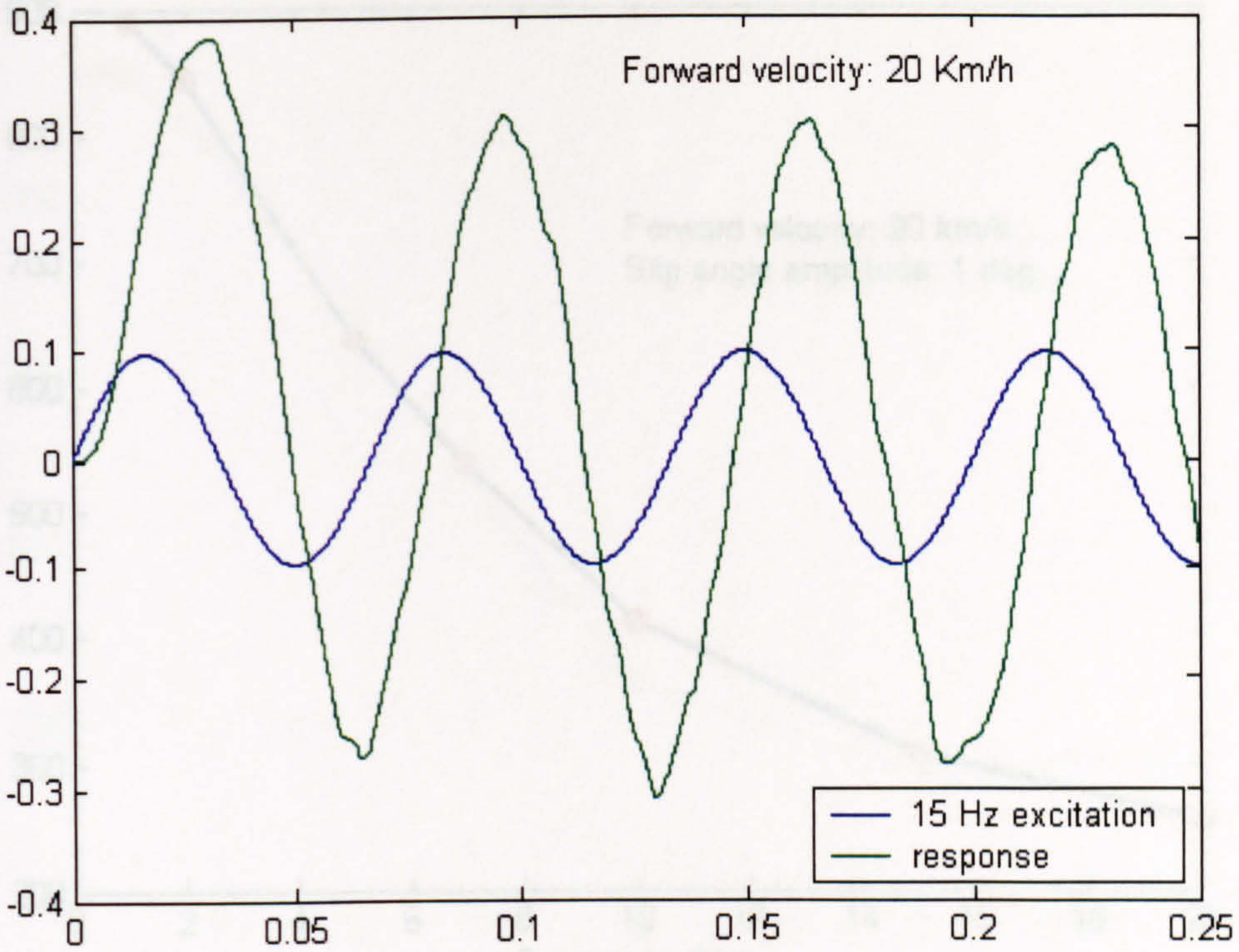

Figure 4. 40 Lateral force response to sinusoidal side-slip excitation (15 Hz)

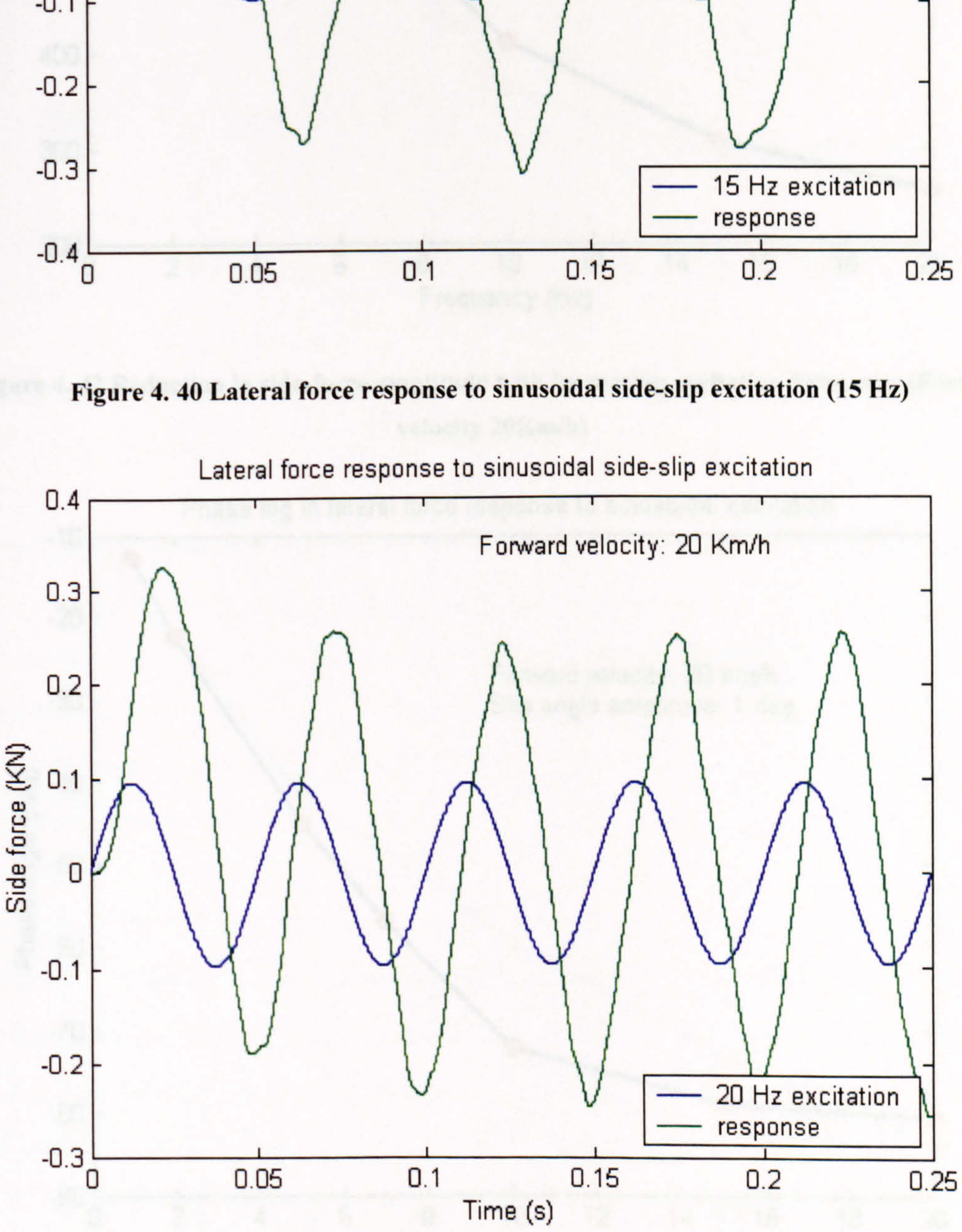

Figure 4. 41 Lateral force response to sinusoidal side-slip excitation (20 Hz)

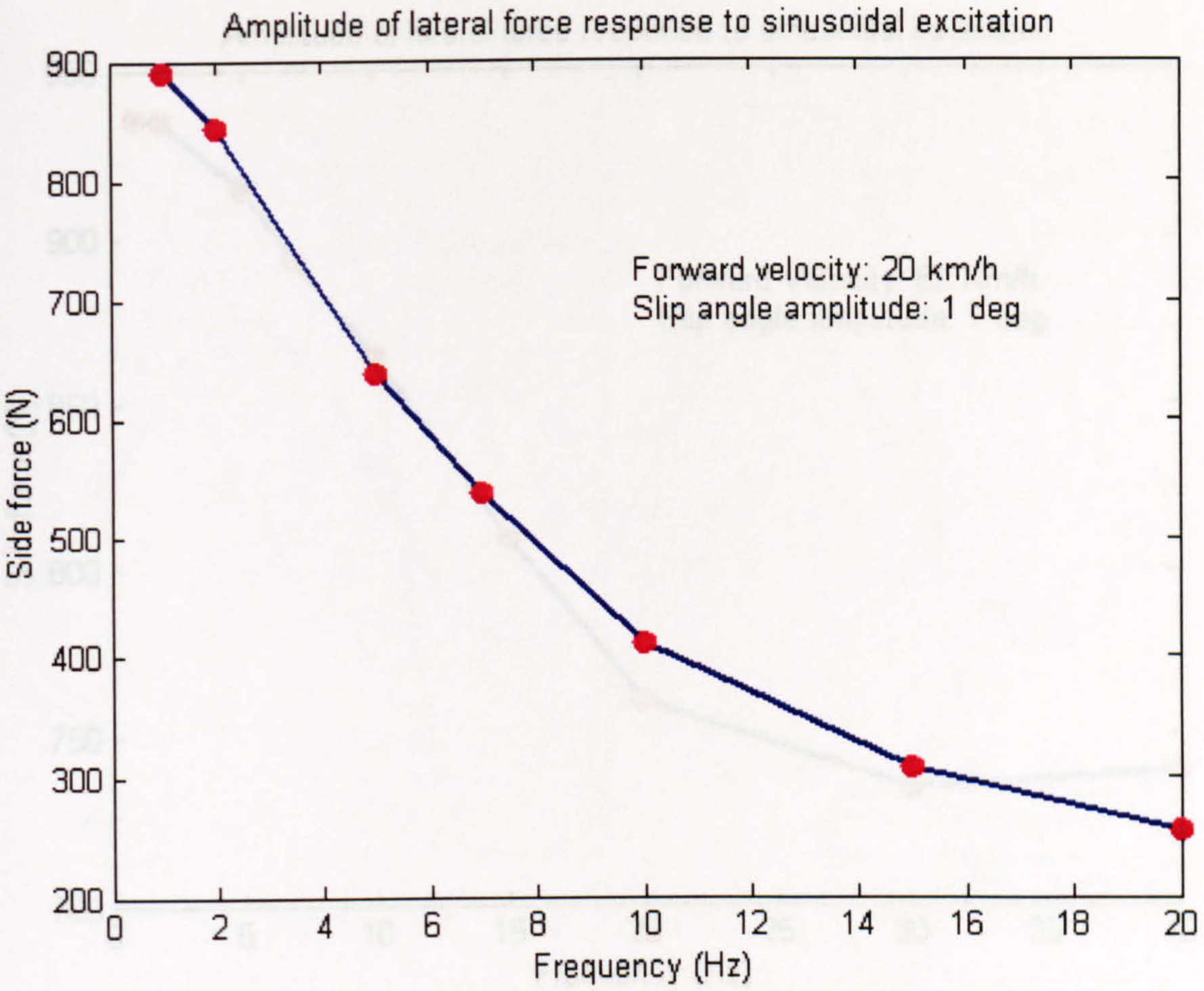

Figure 4. 42 Reduction in side-force amplitude with increasing excitation frequency (Forward velocity 20Km/h)

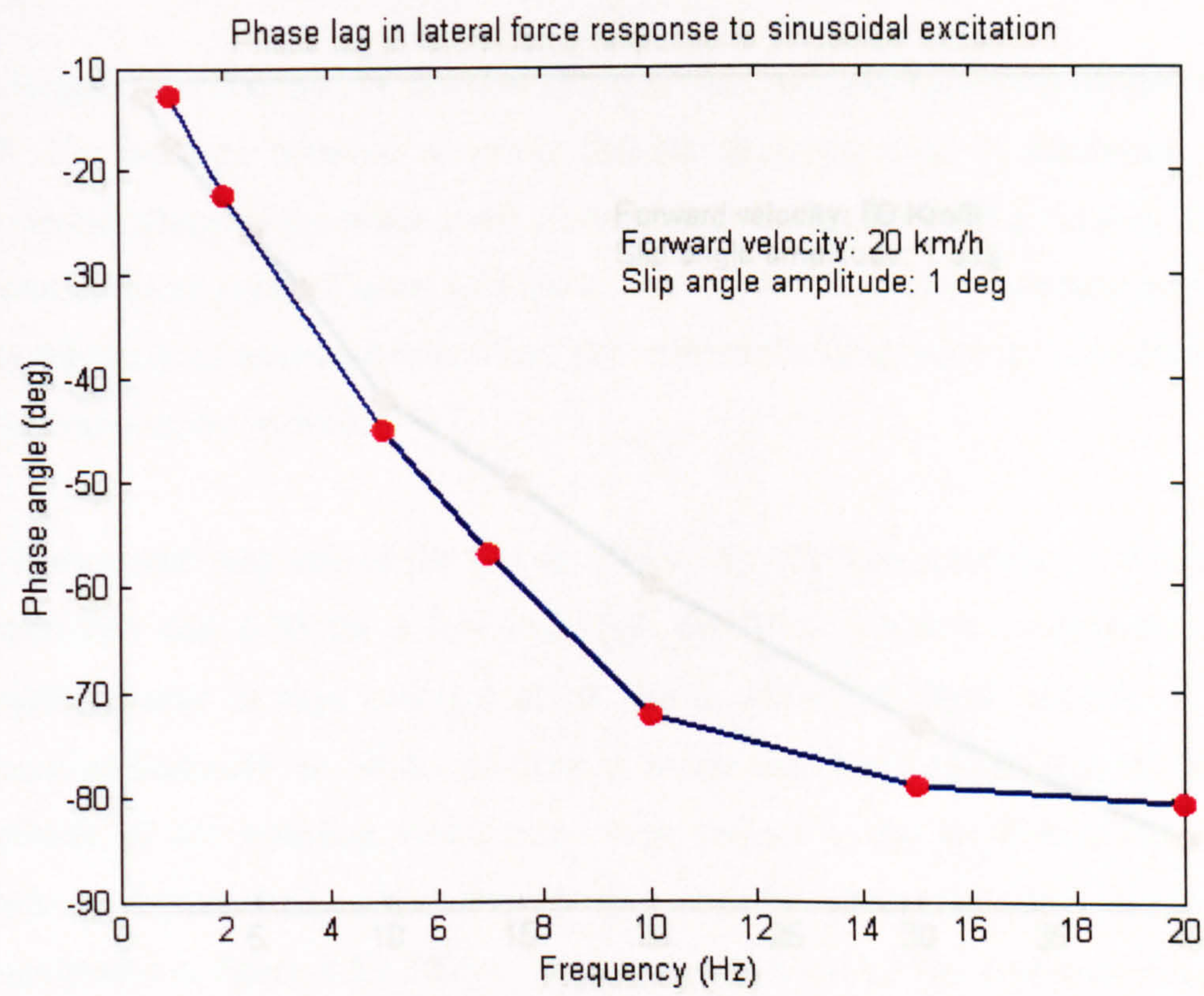

Figure 4. 43 Increase in side-force phase lag with excitation frequency (Forward velocity 20Km/h)

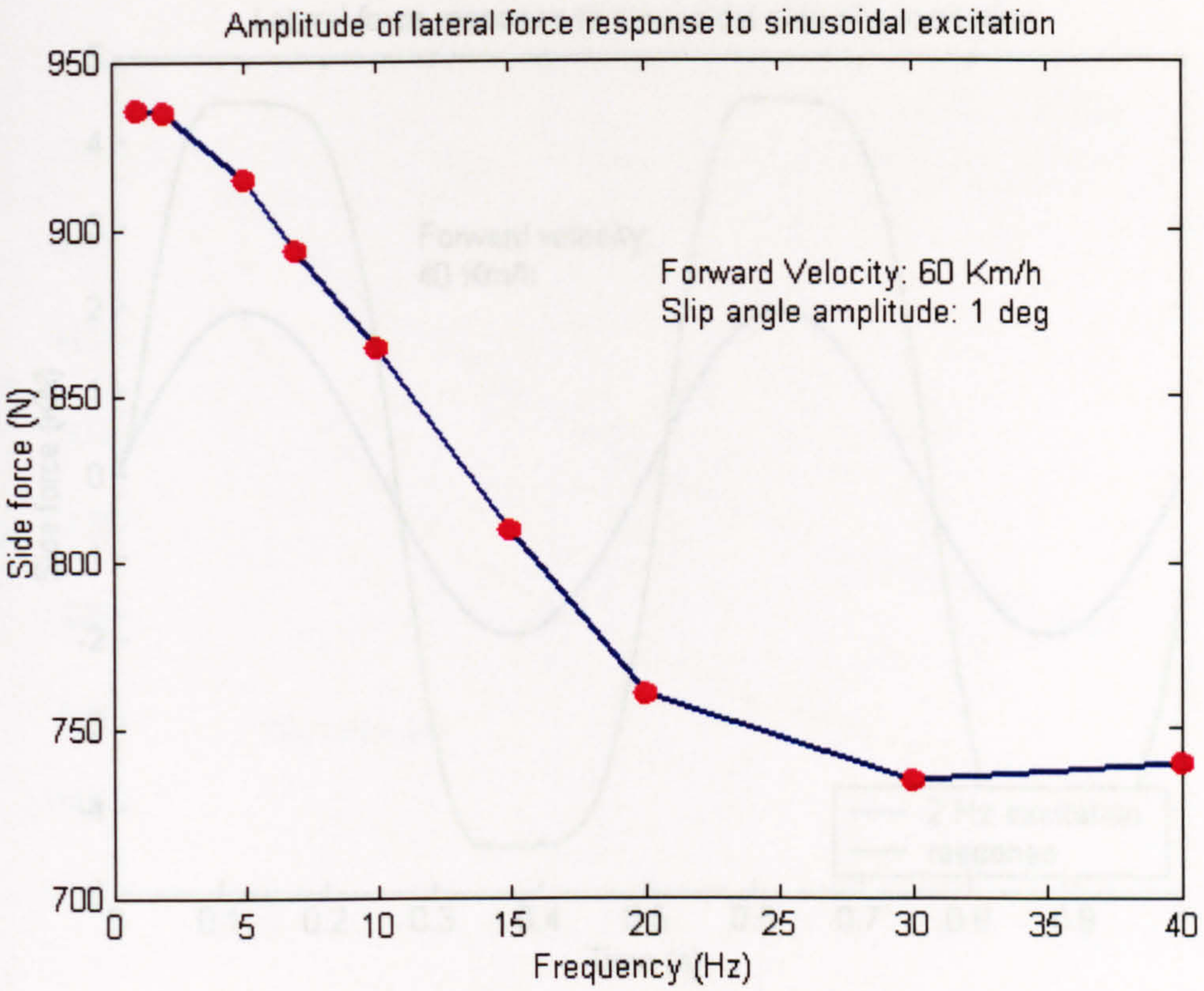

Figure 4. 44 Reduction in side-force amplitude with increasing excitation frequency (Forward velocity 60Km/h)

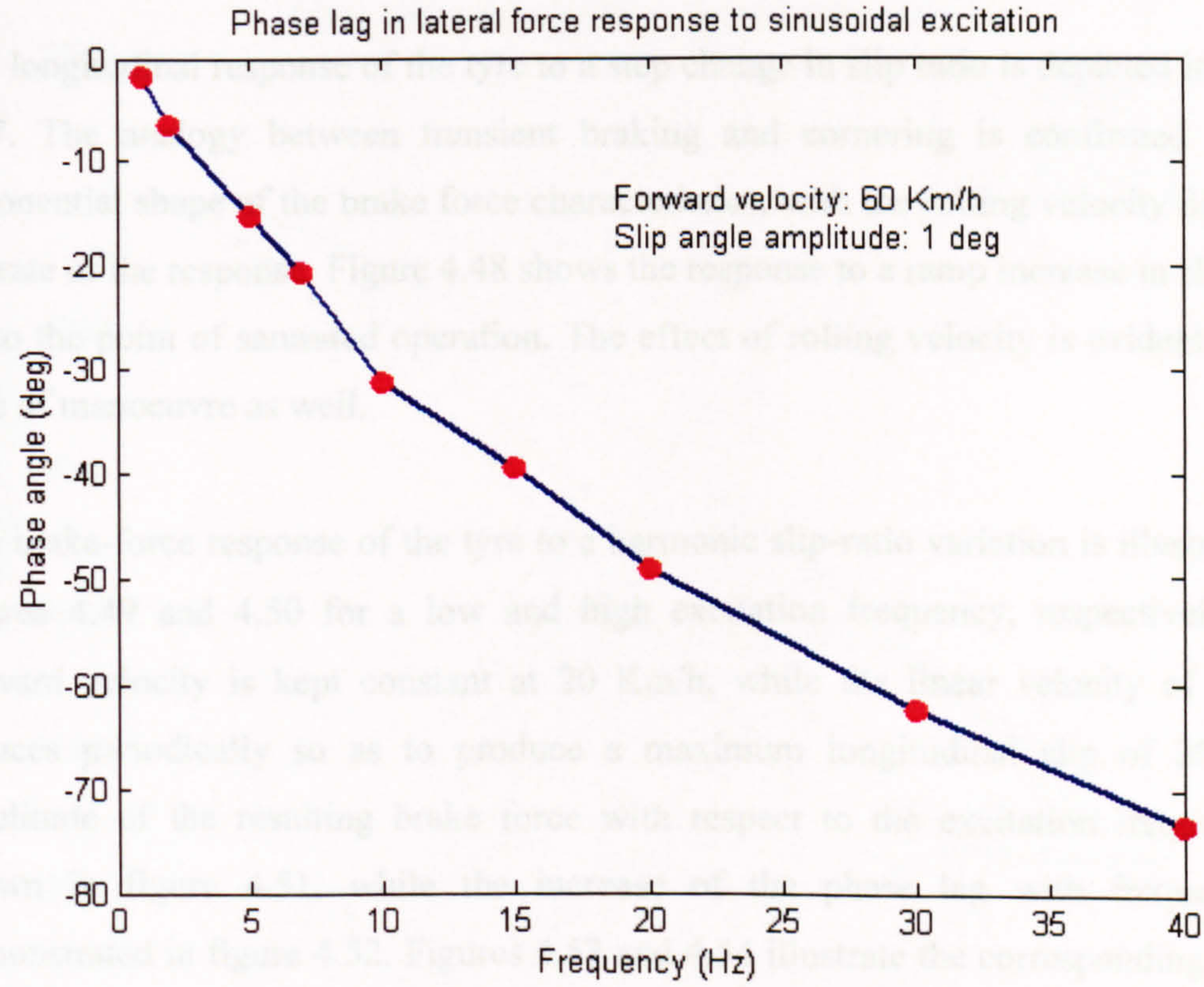

Figure 4. 45 Increase in side-force phase lag with excitation frequency (Forward velocity 60Km/h)

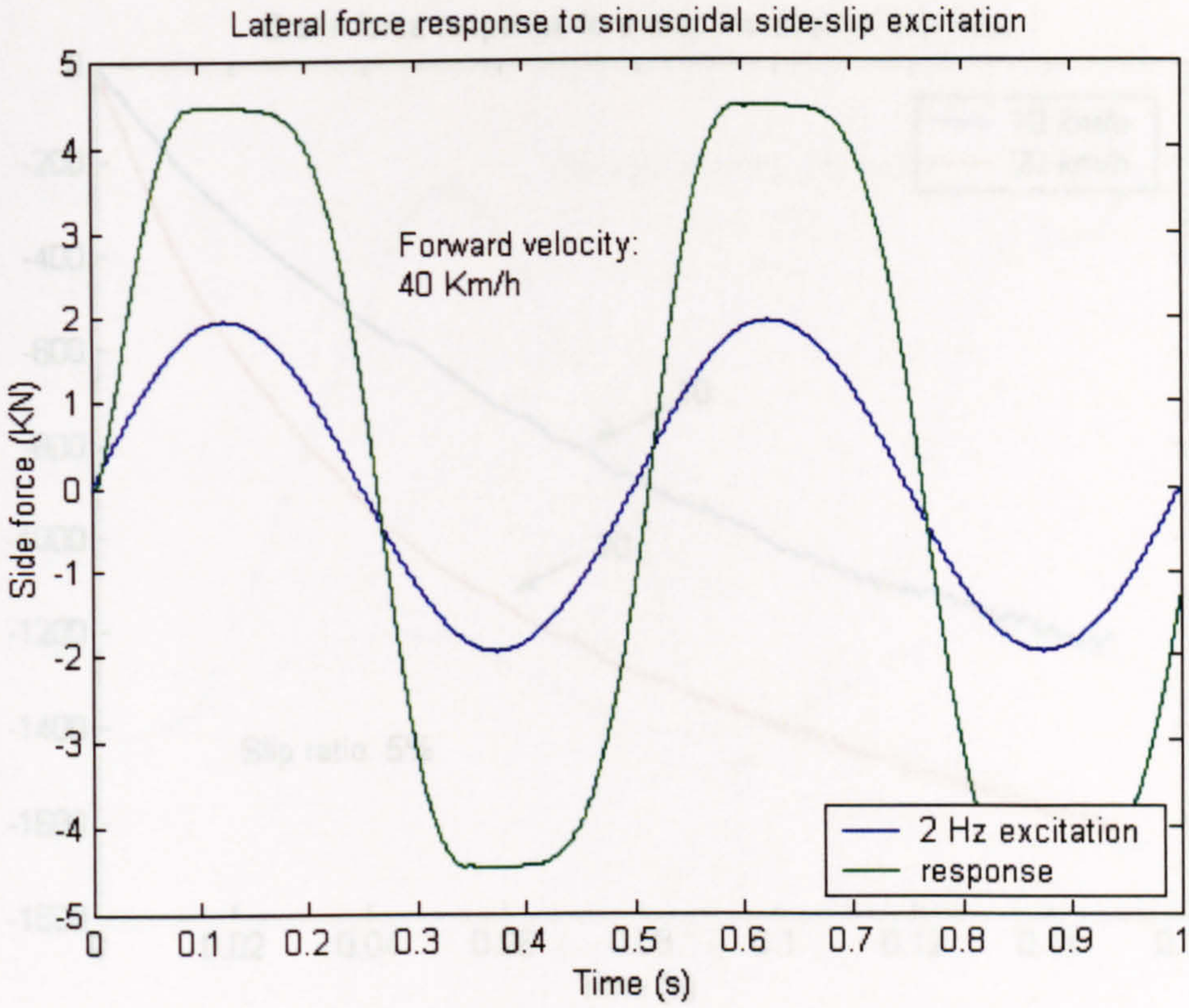

Figure 4. 46 Side force response to high amplitude sinusoidal side-slip excitation (maximum: 14 deg)

The longitudinal response of the tyre to a step change in slip ratio is depicted in figure 4.47. The analogy between transient braking and cornering is confirmed by the exponential shape of the brake force characteristics, with the rolling velocity dictating the rate of the response. Figure 4.48 shows the response to a ramp increase in slip ratio up to the point of saturated operation. The effect of rolling velocity is evident in this type of manoeuvre as well.

The brake-force response of the tyre to a harmonic slip-ratio variation is illustrated in figures 4.49 and 4.50 for a low and high excitation frequency, respectively. The forward velocity is kept constant at 20 Km/h, while the linear velocity of rolling reduces periodically so as to produce a maximum longitudinal slip of 2%. The amplitude of the resulting brake force with respect to the excitation frequency is shown in figure 4.51, while the increase of the phase lag with frequency is demonstrated in figure 4.52. Figures 4.53 and 4.54 illustrate the corresponding results for a higher forward velocity of 60 Km/h.

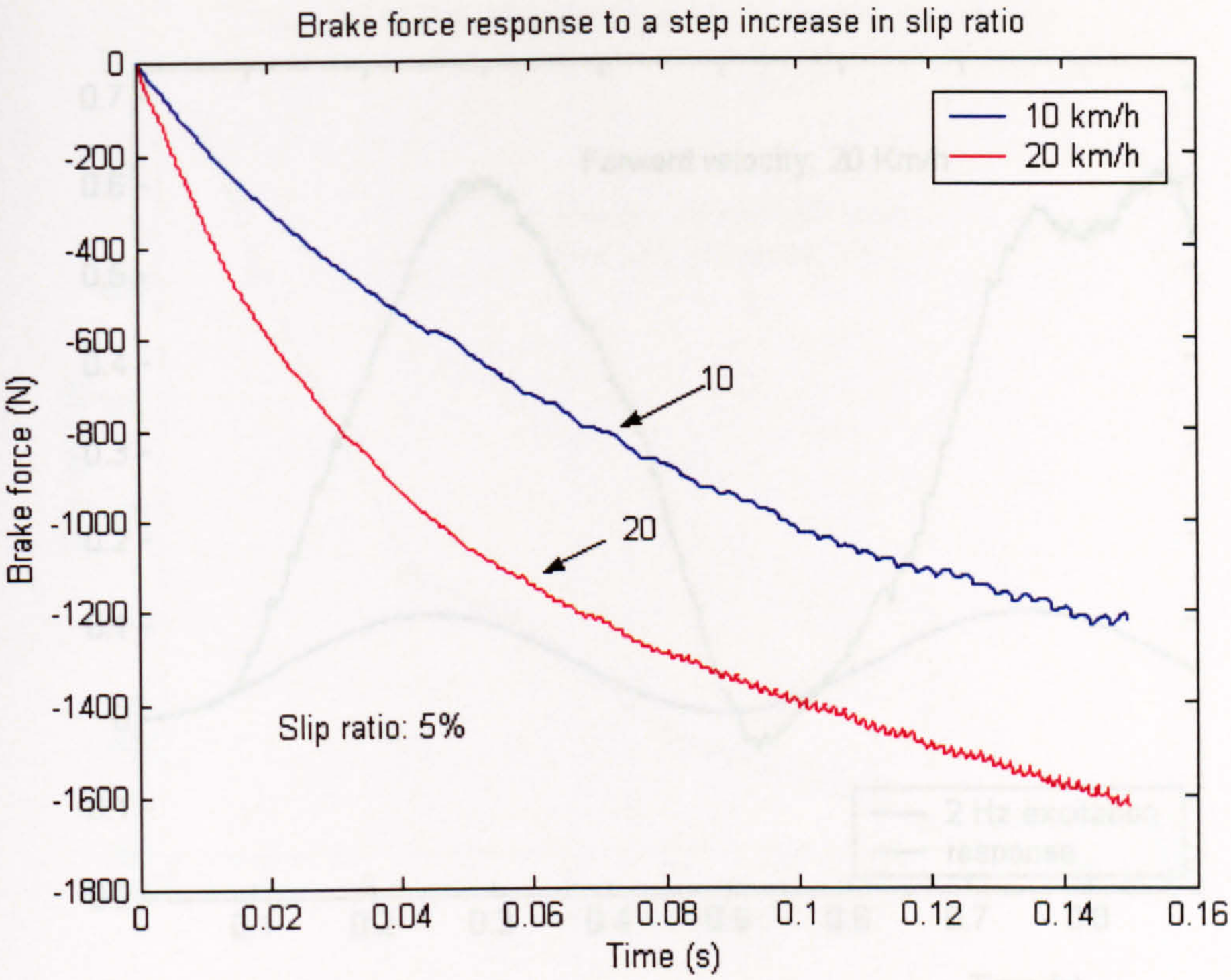

Figure 4. 47 The approximately exponential response of the brake force to a step change in slip ratio

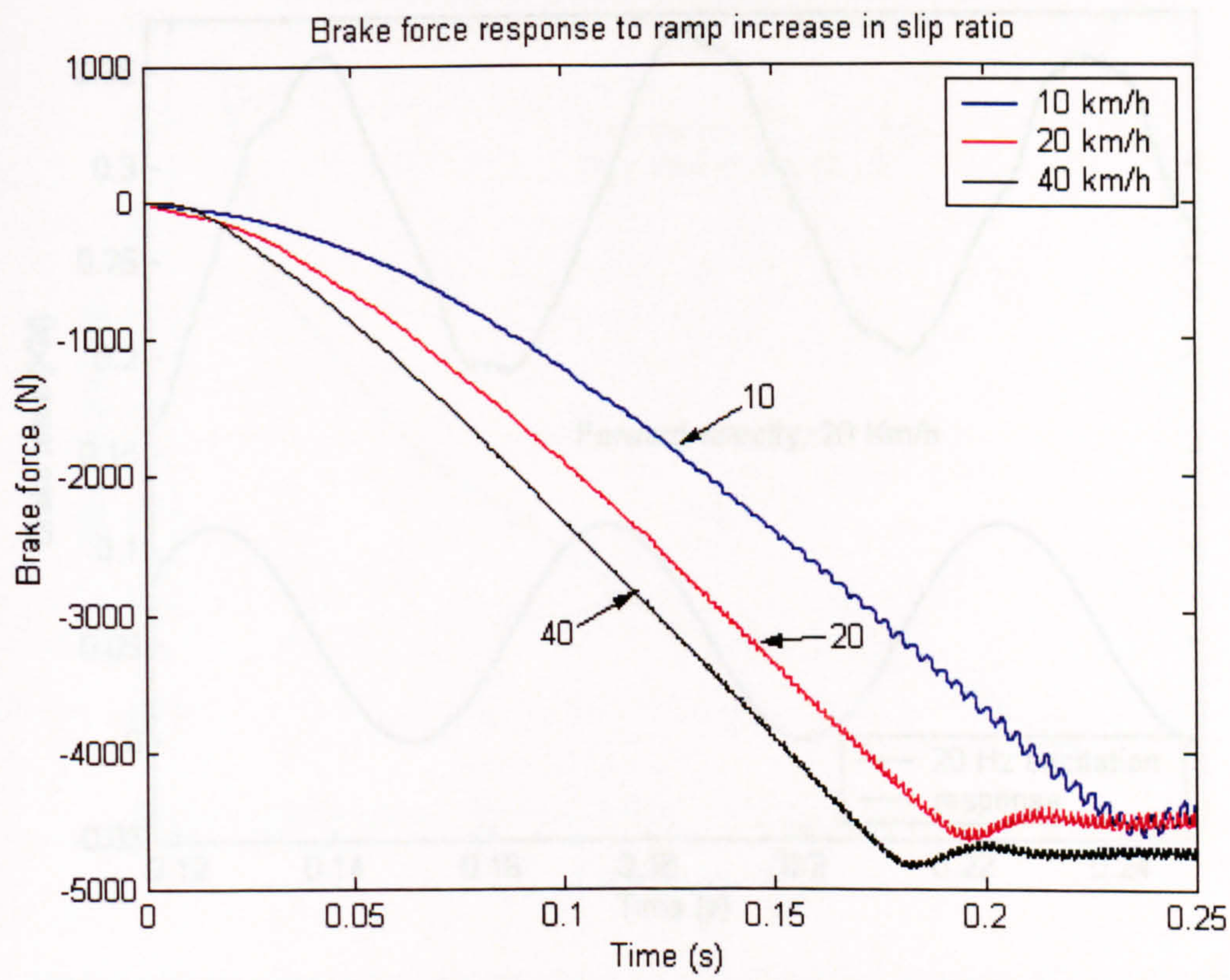

Figure 4. 48 Brake force response to linearly increasing longitudinal slip

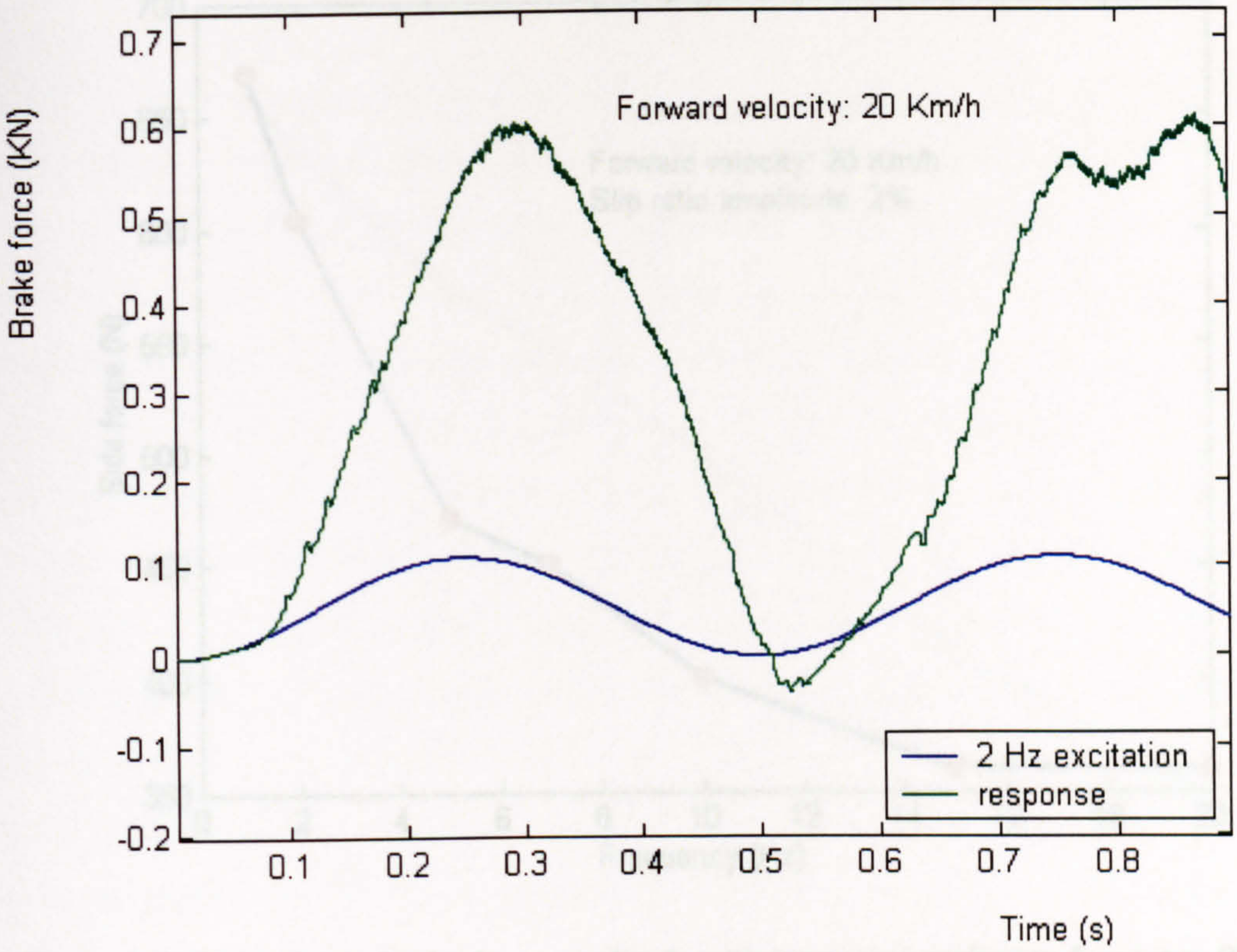

Figure 4. 49 Brake-force response to sinusoidal slip-ratio excitation (2 Hz)

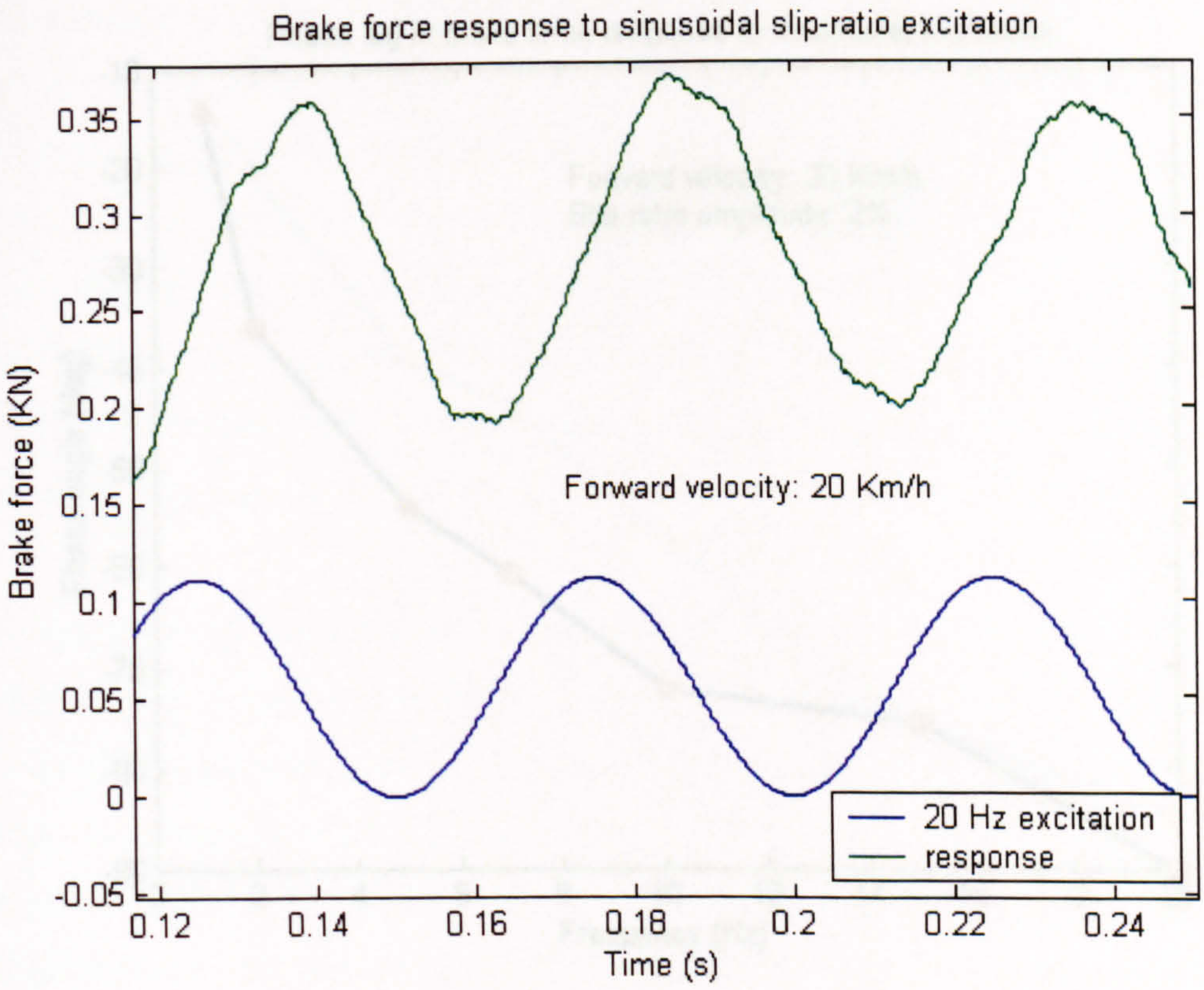

Figure 4. 50 Brake-force response to sinusoidal slip-ratio excitation (20 Hz)

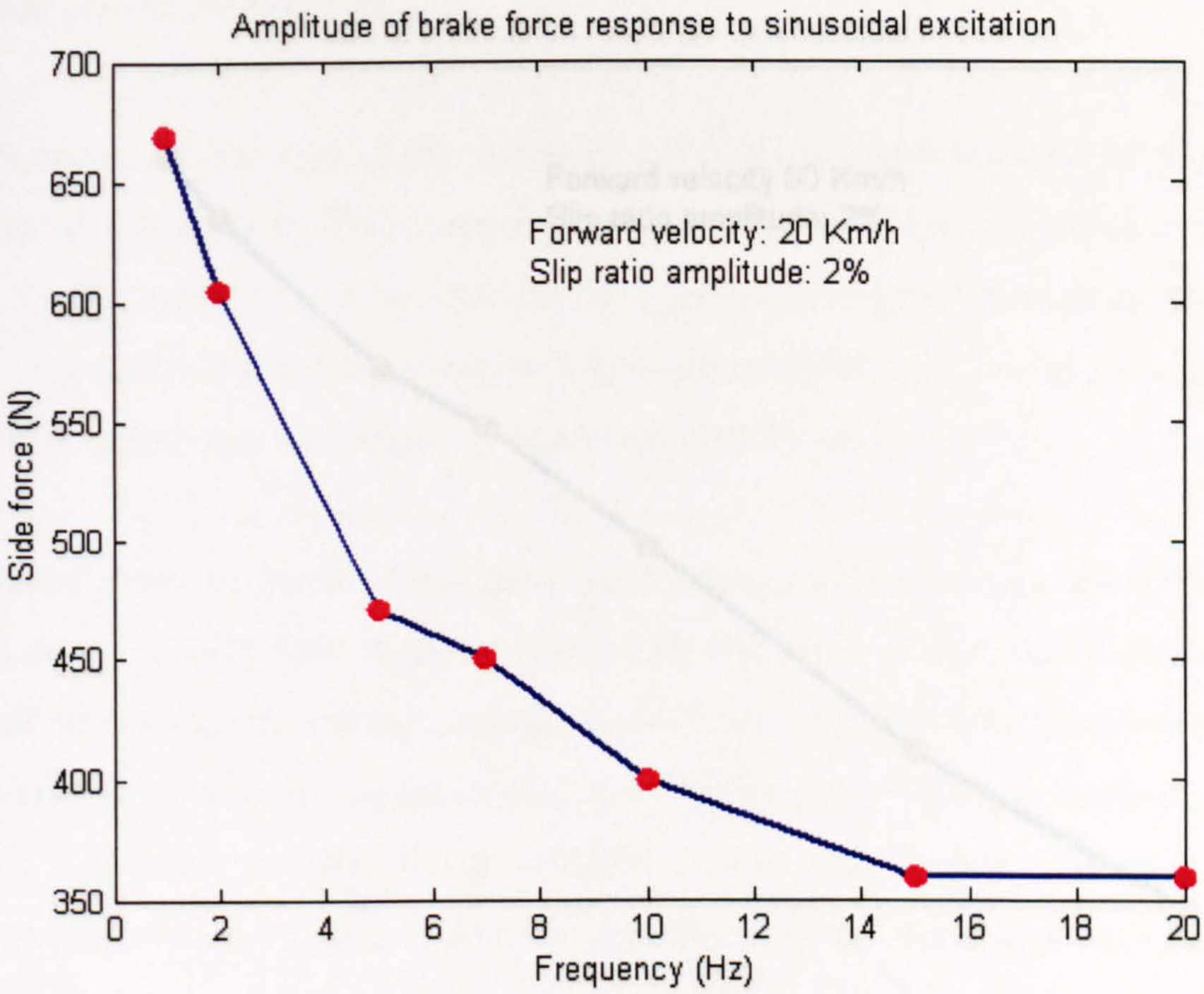

Figure 4. 51 Reduction in brake-force amplitude with increasing excitation frequency (Forward velocity 20Km/h)

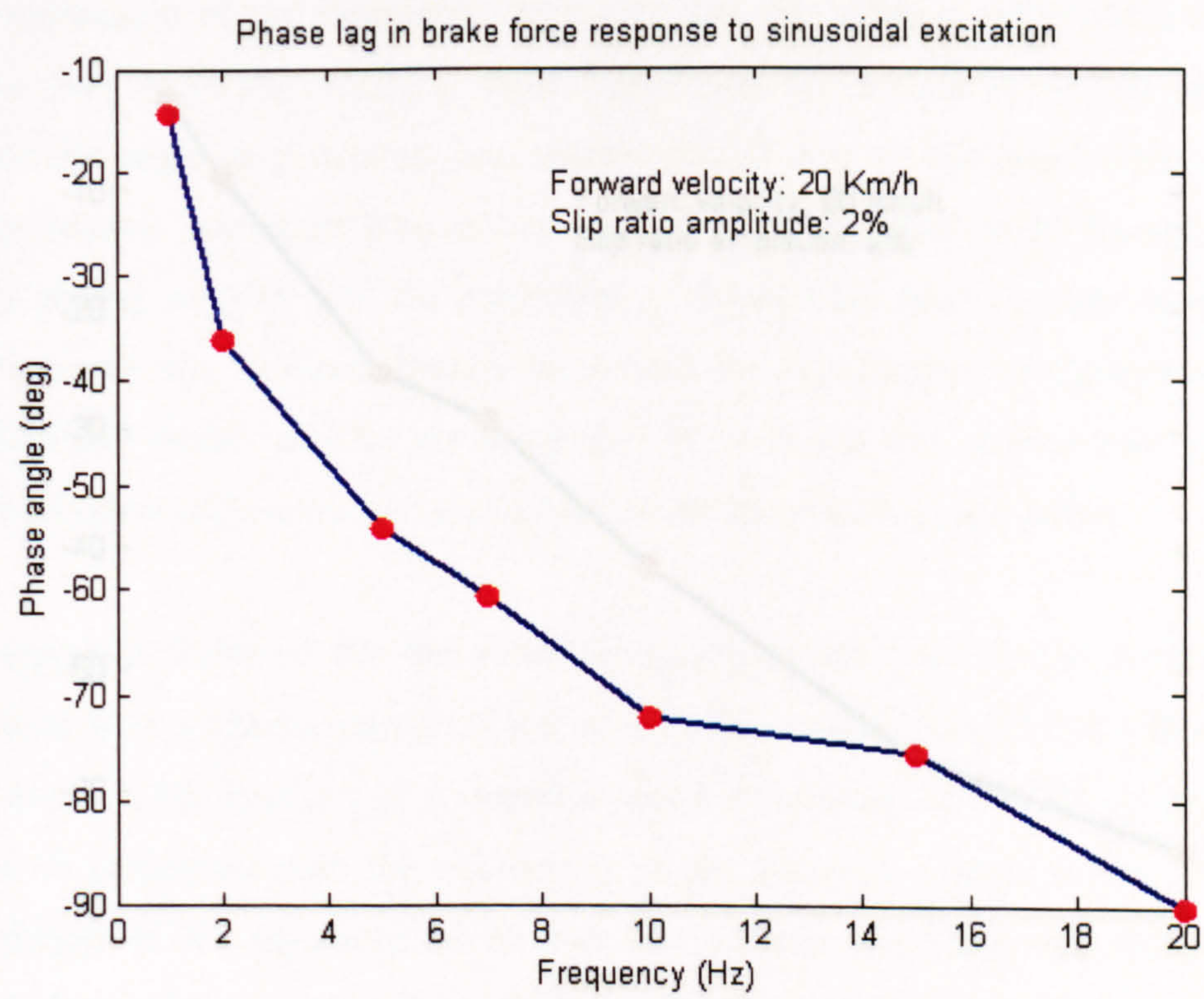

Figure 4. 52 Increase in brake-force phase lag with excitation frequency (Forward velocity 20Km/h)

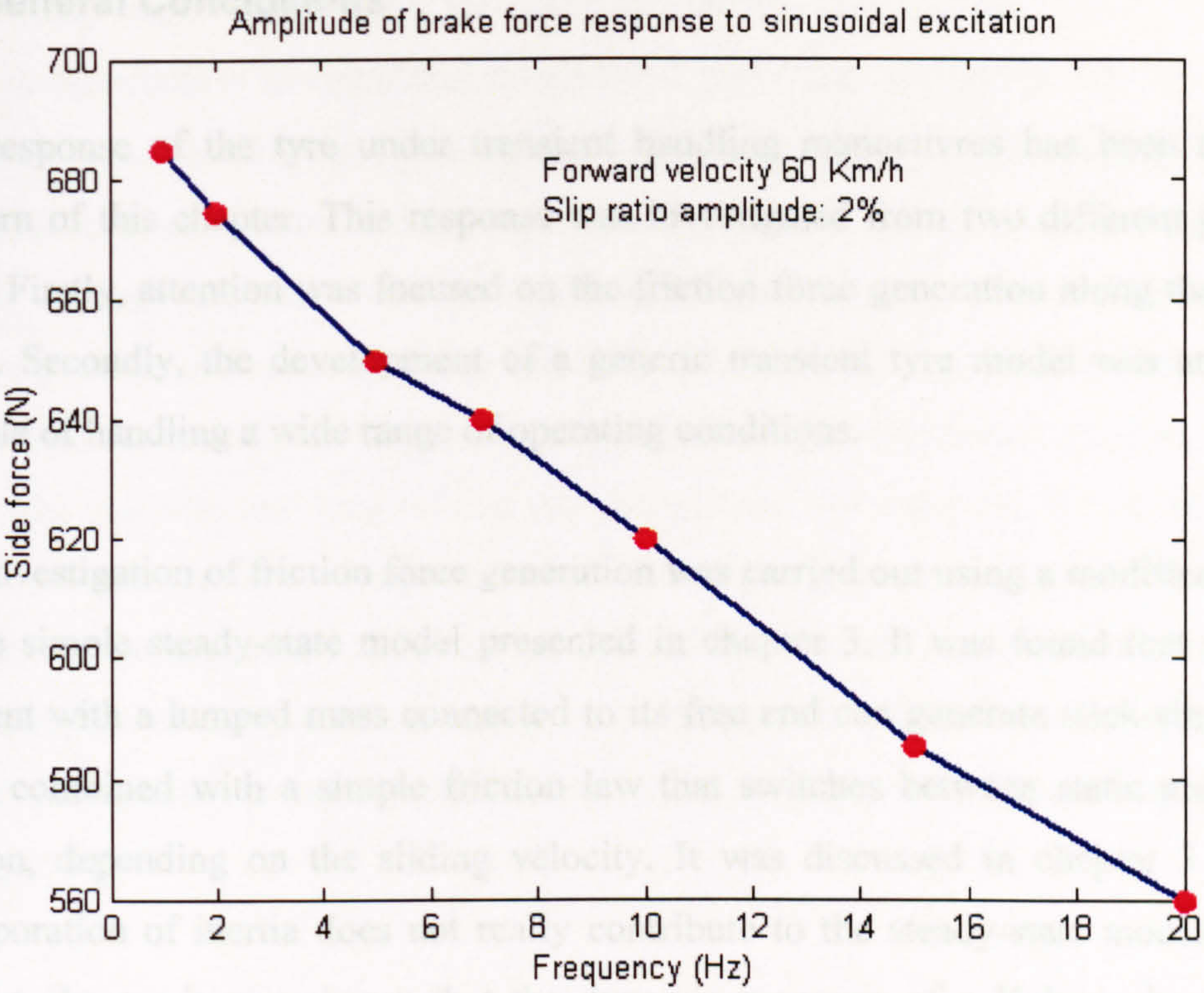

Figure 4. 53 Reduction in brake-force amplitude with increasing excitation frequency (Forward velocity 60Km/h)

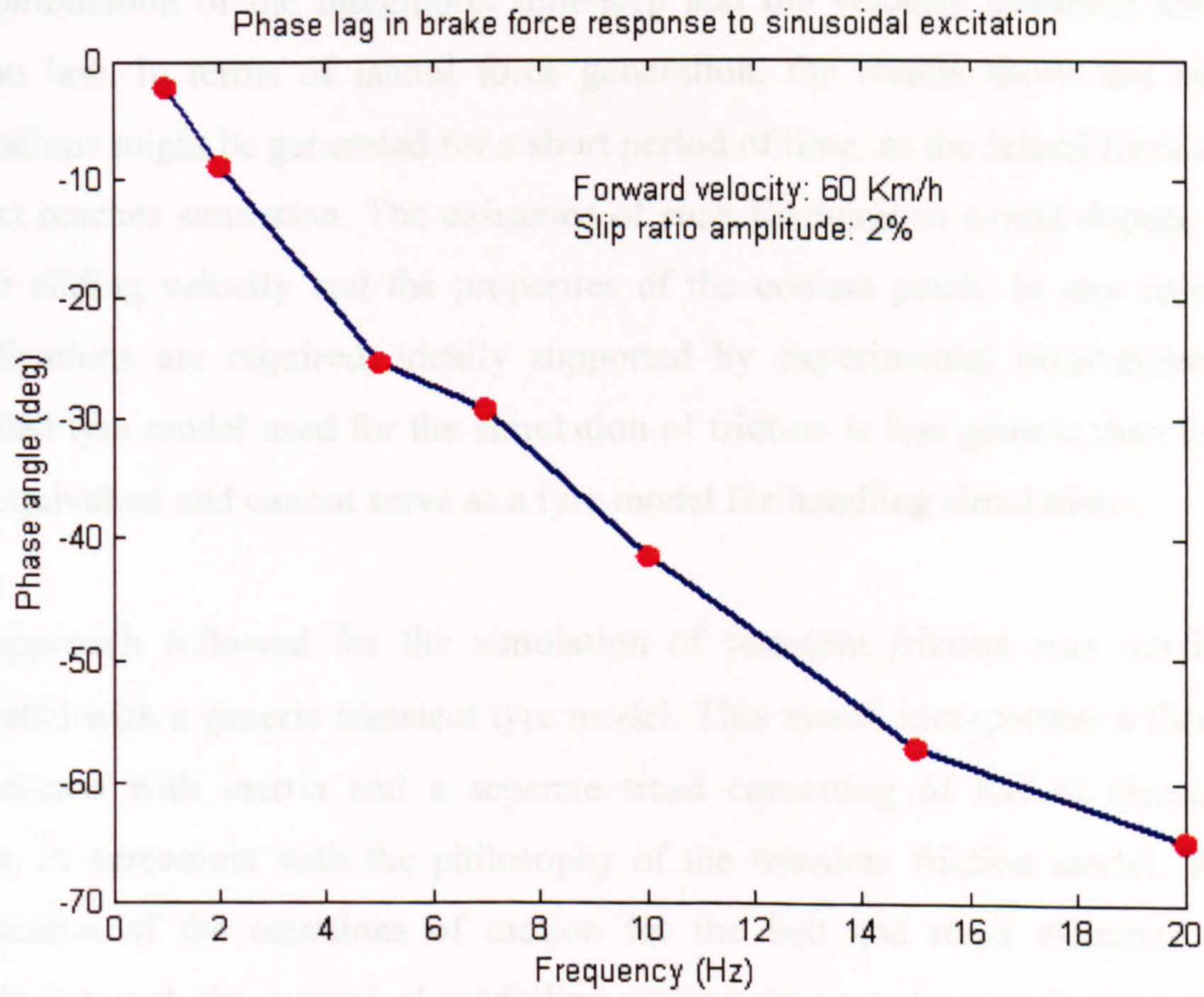

Figure 4. 54 Increase in brake-force phase lag with excitation frequency (Forward velocity 60Km/h)

4.5 General Conclusions

The response of the tyre under transient handling manoeuvres has been the main concern of this chapter. This response was investigated from two different points of view. Firstly, attention was focused on the friction force generation along the contact patch. Secondly, the development of a generic transient tyre model was attempted, capable of handling a wide range of operating conditions.

The investigation of friction force generation was carried out using a modified version of the simple steady-state model presented in chapter 3. It was found that a Kelvin element with a lumped mass connected to its free end can generate stick-slip friction when combined with a simple friction law that switches between static and kinetic friction, depending on the sliding velocity. It was discussed in chapter 3 that the incorporation of inertia does not really contribute to the steady-state models. In the present chapter it was shown that the dynamic response of a Kelvin element with inertia is essential for the generation of stick-slip behaviour. In addition, it was found that, in terms of simulation, the existence of stick-slip behaviour is highly sensitive to the combination of the integration time-step and the velocity threshold used in the friction law. In terms of lateral force generation, the results show that significant fluctuations might be generated for a short period of time, as the lateral force along the contact reaches saturation. The existence of such fluctuations would depend strongly on the sliding velocity and the properties of the contact patch. In any case, further investigations are required, ideally supported by experimental measurements. The modified tyre model used for the simulation of friction is less generic than its steady-state equivalent and cannot serve as a tyre model for handling simulations.

The approach followed for the simulation of transient friction was modified and integrated with a generic transient tyre model. This model incorporates a flexible belt and carcass with inertia and a separate tread consisting of Kelvin elements with inertia, in agreement with the philosophy of the transient friction model. While the formulation of the equations of motion for the belt and tread elements is rather straight-forward, the numerical modelling was set-up so as to restrain the tread in the area of the contact. This choice allows for a finer discretisation of the tread without increasing enormously the computational effort. The generic transient tyre model uses

the velocity dependent friction law from the steady-state models, while the normal pressure distribution is calculated based on a procedure similar to that used by the advanced steady-state model in chapter 3. The model takes into account the possible kinematic excitations due to steering, side-slip, braking and camber inclination in a generic manner and the forces and moments depend at any instant of time on the relative position and velocity of the belt with respect to the tread. It was found that the model behaves rather well under a variety of operating conditions including step and sinusoidal side-slip and longitudinal slip excitations. For example, it was shown that the model predicts the overshoot in the self-aligning torque, as a result of a step increase in the slip angle. This can be thought of as a test that requires a consistent representation of the conditions along the contact patch and it is a case that cannot be treated successfully under all possible conditions with the use of the relaxation length concept [14].

Chapter 5: Tyre Models in Handling Analysis

5.1 Introduction

This chapter focuses on the implementation of various tyre models in vehicle handling simulations. For this purpose, a generic full-vehicle model is developed through a detailed procedure which involves the derivation of the differential equations of motion together with the determination of all external forces and moments. Selected stand-alone tyre models presented in chapters 3 and 4 are modified and interfaced with the vehicle model. It should be pointed out that the main purpose of the present chapter is to demonstrate the feasibility of the implementation of such tyre models in vehicle dynamic analyses and to provide a robust, integrated vehicle-tyre modelling environment for use in further investigations of handling dynamics. Hence, due to time and space limitations, the handling simulations presented here are limited to a few representative cases.

5.2 Physical Description of the Vehicle Model

The vehicle is considered as a rigid body, incorporating 6 degrees of freedom, which include three translations and three rotations in space. According to the SAE J670e [98], these motions are observed relative to the vehicle-fixed local frame of reference, as shown in figure 5.1. Figure 5.2 shows an aerial view of the vehicle model with some of its most important dimensions.

For the purpose of the analysis, no simplifications are made concerning the vehicle's rigid body motions. This implies that the vehicle need not be symmetrical with respect to the planes defined by the local frame of reference, while the origin of the frame does not necessarily coincide with the centre of mass of the vehicle.

The vehicle incorporates four wheels, connected to the body by springs and dampers, as well as front and rear anti-roll bars, which resist vehicle roll during cornering.

The forces and moments that govern the vehicle's motion include:

1) Driving forces developed on the contact patch between the tyres and the road
2) Braking forces developed on the contact patch between the tyres and the road
3) Lateral forces on the tyres, as a result of the development of tyre slip angles
4) Gravitational forces
5) Spring and damper forces
6) Anti-Roll bar moments
7) All moments that result from the aforementioned forces

In order to simulate the handling behaviour of a vehicle, a 6-degree of freedom rigid body model, as the one described above, is fundamental in the sense that it allows the study of all possible combinations of the vehicle's body motion and yields fairly realistic results when used in combination with an accurate tyre model.

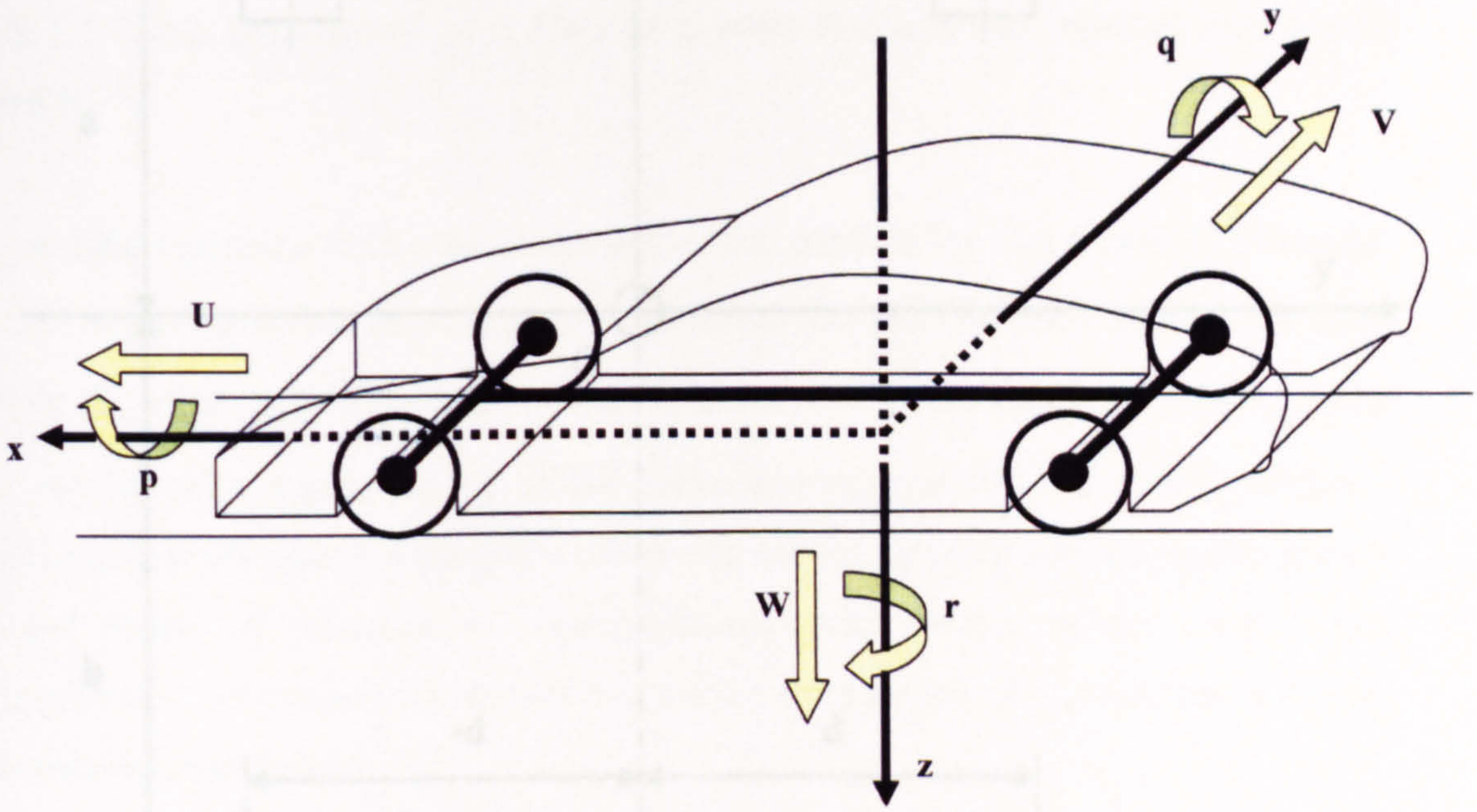

Figure 5. 1 The rigid body motions of the vehicle model

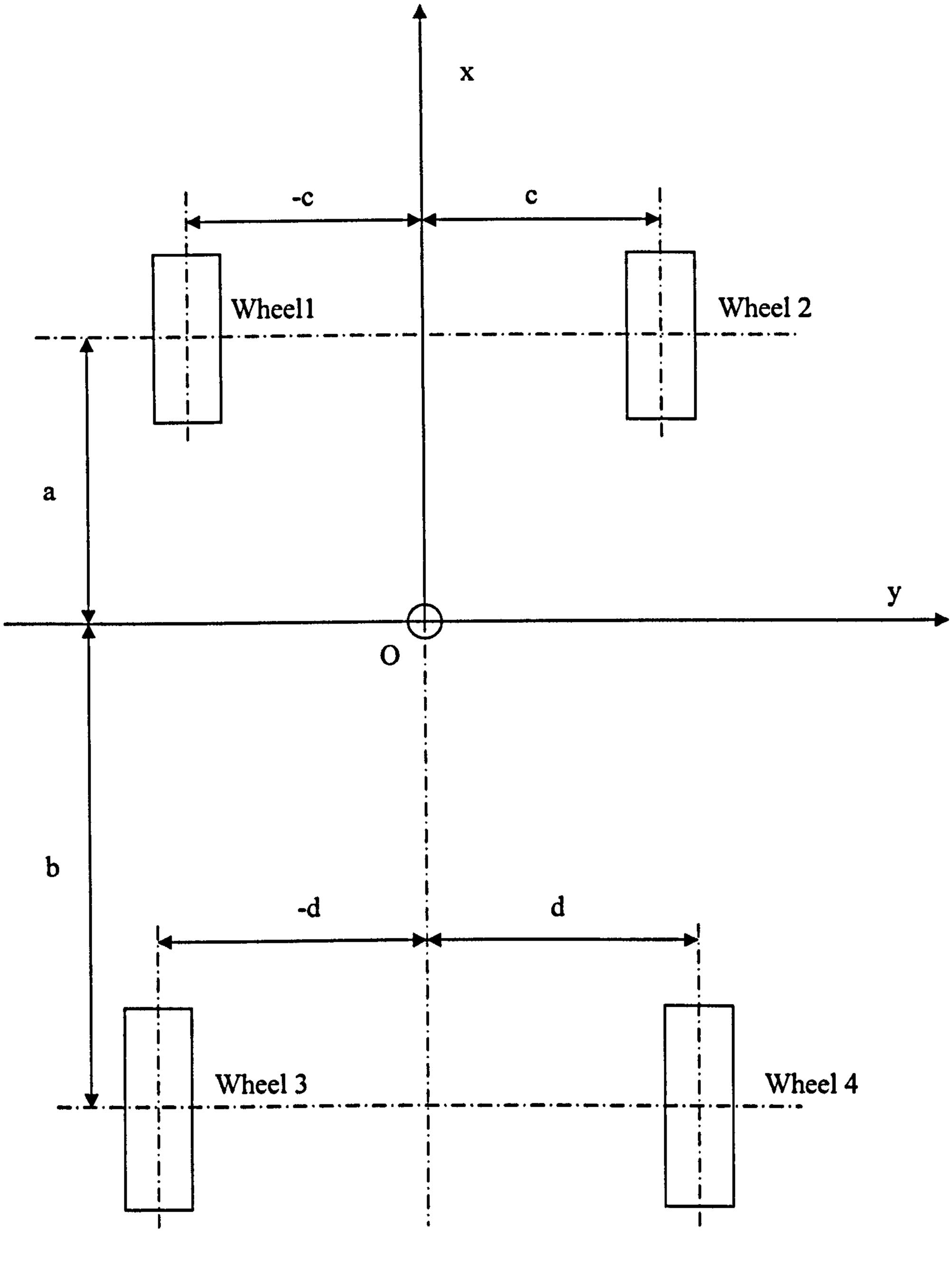

Figure 5. 2 Plan view of the vehicle with the most important dimensions

5.3 Equations of Motion of the Vehicle's Body

The Newton-Euler formulation approach is used to derive the equations of motion of the vehicle body. Firstly, the kinematic equations of a particle with respect to a moving frame of reference are presented. By using the Newton-Euler approach for translational and rotational motion, the effects of the external forces and the masses of all elementary particles that form the rigid body are taken into account, resulting in the differential equations of motion.

5.3.1 General Motion of a Particle

5.3.1.1 Time Derivative of a Vector c with Respect to Inertial Frames R_i and R_j

Kinematic equations for a particle are presented, considering two frames of reference, as shown in figure 5.3. $R_i \equiv O_i x_i y_i z_i$ represents the global/fixed frame of reference, while $R_j \equiv O_j x_j y_j z_j$ is the local frame of reference. The local frame of reference may be moving with respect to the global frame through translational and/or rotational motions. It is obvious that this point of view is not unique: One could consider that the global frame of reference is counter-moving with respect to the local frame. Therefore, it is necessary to declare that during the analysis, the global frame will be considered as stationary.

Assuming that $\mathbf{c}$ represents a vector as measured in the moving/local frame of reference, the time derivative (rate of change of the vector with respect to time) as sensed in the local frame of reference can be expressed as $(d\mathbf{c}/dt)_{R_j}$.

The time derivative of the same vector $\mathbf{c}$, as sensed in the global/fixed frame of reference R_i, is given by the following relation [11]:

$$(d\mathbf{c}/dt)_{R_i} = (d\mathbf{c}/dt)_{R_j} + \boldsymbol{\omega} \times \mathbf{c} \tag{5.1}$$

where $\boldsymbol{\omega} \times \mathbf{c}$ is the cross product of the rotational velocity $\boldsymbol{\omega}$ of the local frame of reference and the vector $\mathbf{c}$. Equation (5.1) is generic and applies to any kind of time varying vector.

In order to distinguish the rate of change of a vector with respect to the global and local frames of reference, the following representations are used:

$D()/Dt = \frac{d()}{dt}_{R_i}$ denotes the time derivative of a vector as sensed in the global frame R_i

while

$d()/dt = \frac{d()}{dt}_{R_j}$ denotes the time derivative of a vector as sensed in the local frame R_j

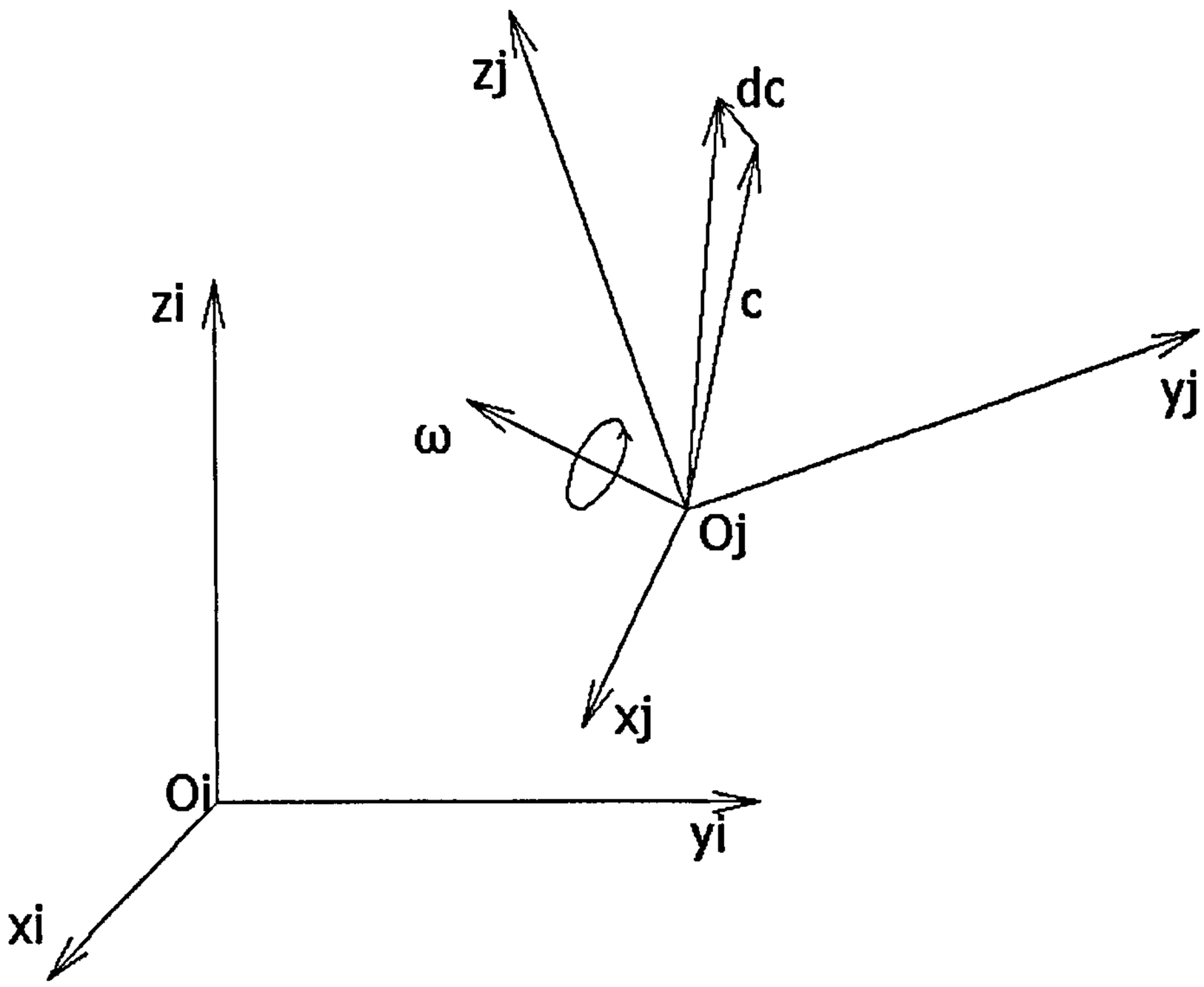

Figure 5. 3 Time derivative of a vector with respect to moving frames of reference

By applying equation (5.1) it is easy to prove that the rotational velocity $\boldsymbol{\omega}$ remains the same for both frames of reference as:

$$\left(d\boldsymbol{\omega}/dt\right)_{Ri} = D\boldsymbol{\omega}/Dt = \left(d\boldsymbol{\omega}/dt\right)_{Rj} = d\boldsymbol{\omega}/dt \tag{5.2}$$

because:

$$\omega \times \omega = 0 \tag{5.3}$$

Equation (5.1) is used to describe the general motion of a particle with respect to the global/fixed frame of reference R_i.

The calculation of the speed of a particle P with respect to the inertial frames R_i and R_j is based on the definition of the following vectors, shown in figure 5.4:

e vector (O_iO_j) (position vector of the origin O_j with respect to the global frame R_i)

$\mathbf{s_i}$ vector (O_iP) (position vector of the particle P with respect to the global frame R_i)

$\mathbf{s_j}$ vector (O_jP) (position vector of the particle P with respect to the local frame R_j)

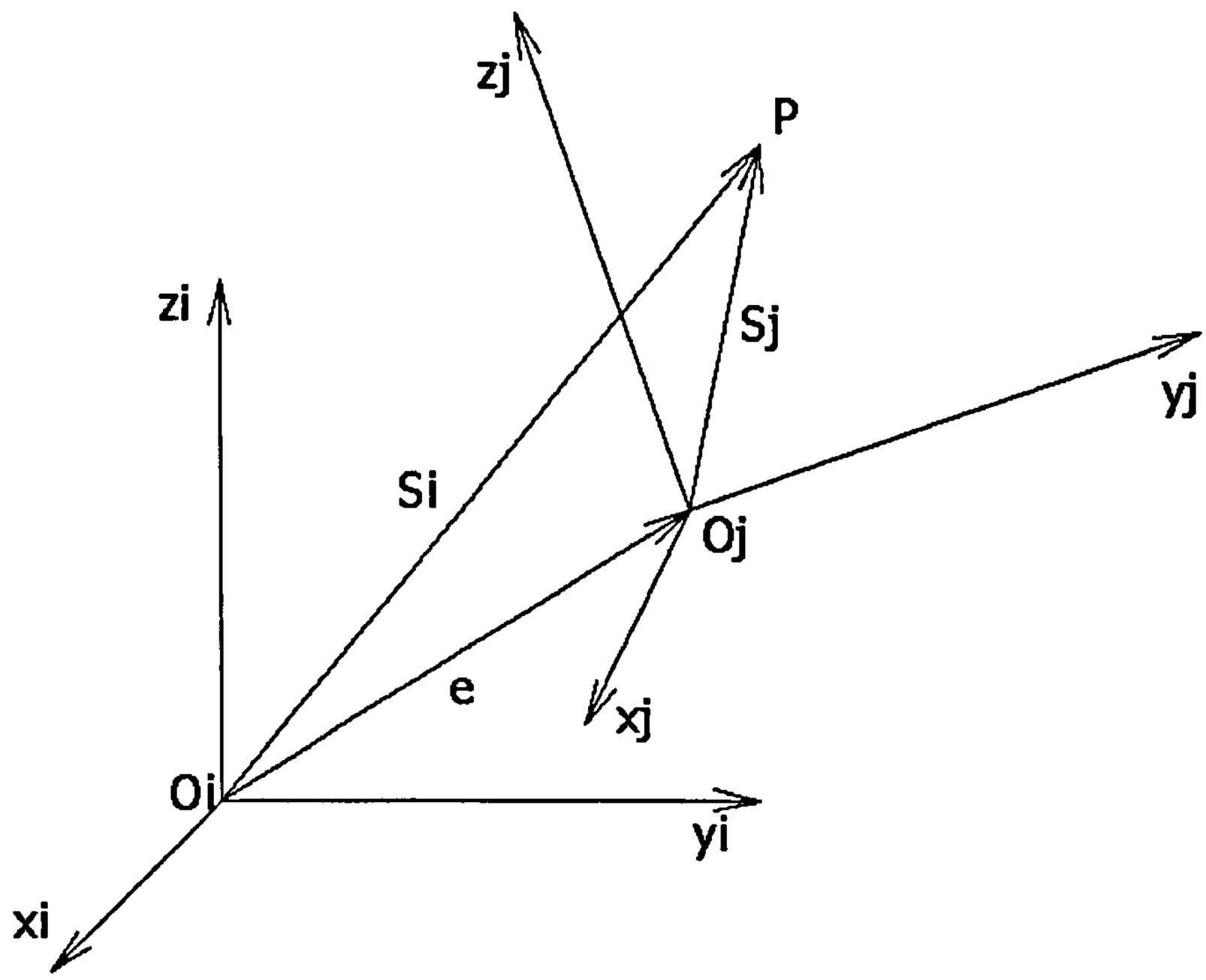

Figure 5. 4 Motion of a point as sensed in the global frame of reference

The velocity of the particle P as sensed in the global frame R_i results from the differentiation of the position vector $\mathbf{s_i}$ with respect to time. Referring again to figure 4, the following relations apply:

$$\mathbf{s}_i = \mathbf{e} + \mathbf{s}_j$$
$$D\mathbf{s}_i/Dt = D\mathbf{e}/Dt + D\mathbf{s}_j/Dt \qquad (5.4)$$
$$D\mathbf{s}_i/Dt = D\mathbf{e}/Dt + d\mathbf{s}_j/dt + \boldsymbol{\omega} \times \mathbf{s}_j$$

Where:

$\mathbf{V}_i(O_j) = D\mathbf{e}/Dt$ is the velocity of O_j at R_i

$\mathbf{V}_i(P) = (d\mathbf{s}_i/dt)_{R_i} = D\mathbf{s}_i/Dt$ is the velocity of P at R_i

$\mathbf{V}_j(P) = (d\mathbf{s}_j/dt)_{R_i} = d\mathbf{s}_j/dt$ is the velocity of P at R_j

$$\mathbf{V}_i(P) = \mathbf{V}_i(O_j) + \mathbf{V}_j(P) + \boldsymbol{\omega} \times \mathbf{s}_j \qquad (5.5)$$

The same procedure is followed for the calculation of acceleration, given that acceleration is the rate of change of the velocity vector with respect to time [11]. Hence, equation (5.1) is applied to the velocity vector $\mathbf{V}_i(P) = (d\mathbf{s}_i/dt)_{R_i} = D\mathbf{s}_i/Dt$, assuming that $\mathbf{V}_i(O_j) = 0$:

$$D^2\mathbf{s}_i/Dt^2 = d[d\mathbf{s}_i/dt]/dt =$$
$$d[d\mathbf{s}_j/dt + \boldsymbol{\omega} \times \mathbf{s}_j]/dt + \boldsymbol{\omega} \times [d\mathbf{s}_j/dt + \boldsymbol{\omega} \times \mathbf{s}_j] =$$
$$d^2\mathbf{s}_j/dt^2 + d(\boldsymbol{\omega} \times \mathbf{s}_j)/dt + \boldsymbol{\omega} \times (d\mathbf{s}_j/dt) + \boldsymbol{\omega} \times \boldsymbol{\omega} \times \mathbf{s}_j \Rightarrow$$

$$D^2\mathbf{s}_i/Dt^2 = d^2\mathbf{s}_j/dt^2 + (d\boldsymbol{\omega}/dt) \times \mathbf{s}_j + \boldsymbol{\omega} \times \boldsymbol{\omega} \times \mathbf{s}_j + 2 \cdot \boldsymbol{\omega} \times (d\mathbf{s}_j/dt) \qquad (5.6)$$

Where:

$d^2\mathbf{s}_j/dt^2$ is the linear acceleration

$(d\boldsymbol{\omega}/dt) \times \mathbf{s}_j$ is the tangential acceleration

$\boldsymbol{\omega} \times \boldsymbol{\omega} \times \mathbf{s}_j$ is the centripetal acceleration

$2 \cdot \boldsymbol{\omega} \times (d\mathbf{s}_j/dt)$ is the coriolis acceleration

The fundamental theory of the general motion of a particle is most useful for describing the motion of rigid bodies, such as the vehicle model.

Firstly, a local frame of reference R_j is assumed to be attached to the rigid body. Hence, the local frame follows the rigid body's motion. The particles that form the rigid body are considered as elementary particles, each of them defined by its position vector in the local frame of reference R_j. The velocity and acceleration of any point of the rigid body can be easily calculated, following the procedure previously described and keeping in mind that the position vector of every elementary particle remains constant in the local frame of reference. This results from the fact that the local frame is firmly attached to the moving body and the relative distance of any pair of particles forming a rigid body does not change. In this procedure, the rotational velocity of the rigid body is also the rotational velocity of the moving frame of reference.

When studying rigid body kinematics, it is often necessary to project velocities on moving frames of reference. For this purpose, in addition to the theory already presented, it is essential to apply relative transforms, as a convenient way to switch between frames of reference.

5.3.2 Relative Transforms in Rigid-Body Kinematics

Rahnejat [11] and Ellis [7] describe the general theory of translational and rotational transformations that are used for expressing vector components in different frames of reference that are moving with respect to each other. For the purpose of the present analysis, the "1-2-3" transformation is used (Referred to as roll pitch and yaw).

Let:

$(x_i\ y_i\ z_i)$ be the coordinates of a point P at $R_i=O_ix_iy_iz_i$

$(x_j\ y_j\ z_j)$ be the coordinates of a point P at $R_j=O_jx_jy_jz_j$

It is possible to move from R_j frame of reference to R_i frame of reference, by three sequential rotations and a linear translation of R_j, until R_j coincides with R_i. It should be noted that in this specific case, each rotation takes place with respect to the previous frame of reference, not the initial frame of reference. The transformation is, therefore, called "relative". The characterisation of the transformation by the sequence of numbers "1-2-3" implies that the first rotation is about x axis, the second about y axis and the third about z axis. It is possible to arrive to the same result by changing

the sequence of rotations, providing that no sequential rotations take place about the same axis. For example, a "3-1-3" rotation could be used, but a "3-3-1" sequence obviously cannot produce a generic transformation between two frames of reference. Summarising, the frame transformation consists of the following steps:

1) Linear translation (–e) resulting coincidence of O_j with O_i
2) 1^{st} rotation (θ) about axis O_jx_j, resulting to the frame: $O_ix_j'y_j'z_j'$
3) 2^{nd} rotation (φ) about axis O_iy_j', resulting to the frame: $O_ix_j''y_j''z_j''$
4) 3^{rd} rotation (ψ) about axis O_iz_j'', resulting coincidence with the frame: $R_i=O_ix_iy_iz_i$

Each rotation results in a new set of axes, which are related to the previous set of axes by a transformation matrix **L** in a way that:

$$[\mathbf{R}_{new}]=[\mathbf{L}][\mathbf{R}_{old}] \tag{5.7}$$

Because three different rotations take place, the initial set of axes is multiplied successively by three different transformation matrices, shown below:

$$L(\theta)=\begin{bmatrix}1 & 0 & 0\\ 0 & \cos\theta & -\sin\theta\\ 0 & \sin\theta & \cos\theta\end{bmatrix} \tag{5.8}$$

$$L(\varphi)=\begin{bmatrix}\cos\varphi & 0 & \sin\varphi\\ 0 & 1 & 0\\ -\sin\varphi & 0 & \cos\varphi\end{bmatrix} \tag{5.9}$$

$$L(\psi)=\begin{bmatrix}\cos\psi & -\sin\psi & 0\\ \sin\psi & \cos\psi & 0\\ 0 & 0 & 1\end{bmatrix} \tag{5.10}$$

$(x_j'y_j'z_j')^T = L(\theta)\cdot(x_j\, y_j\, z_j)^T$ 1^{st} intermediate frame of reference

$(x_j''y_j''z_j'')^T = L(\varphi)L(\theta)\cdot(x_j\, y_j\, z_j)^T$ 2^{nd} intermediate frame of reference

$$(x_i\ y_i\ z_i)^T = L(\psi)L(\varphi)L(\theta)\cdot(x_j\ y_j\ z_j)^T \qquad 3^{rd}\text{ (final) frame of reference}$$

The resulting transformation matrix shown below is obtained by multiplying the three transformation matrices in the following order: $L(\theta,\varphi,\psi) = L(\psi)L(\varphi)L(\theta)$

Thus:

$$L(\theta,\varphi,\psi) = \begin{bmatrix} \cos\psi\cdot\cos\varphi & \cos\psi\cdot\sin\varphi\cdot\sin\theta - \sin\psi\cdot\cos\theta & \sin\psi\cdot\sin\theta + \cos\psi\cdot\sin\varphi\cdot\cos\theta \\ \sin\psi\cdot\cos\varphi & \cos\psi\cdot\cos\theta + \sin\psi\cdot\sin\varphi\cdot\sin\theta & \sin\psi\cdot\sin\varphi\cdot\cos\theta - \cos\psi\cdot\sin\theta \\ -\sin\varphi & \cos\varphi\cdot\sin\theta & \cos\varphi\cdot\cos\theta \end{bmatrix} \quad (5.11)$$

If angles θ,φ,ψ are relatively small, the above matrix can be simplified to the one shown below, since $\cos(\theta,\varphi,\psi)\approx 1$ and $\sin(\theta,\varphi,\psi)\approx\theta,\varphi,\psi$:

$$L(\theta,\varphi,\psi) = \begin{bmatrix} 1 & -\psi & \varphi \\ \psi & 1 & -\theta \\ -\varphi & \theta & 1 \end{bmatrix} \quad (5.12)$$

5.3.3 Application of the Kinematic Equations on the Study of Vehicle Dynamics

For the study of a vehicle's motion, two different sets of axes are used: R_i represents the global/ground fixed frame of reference, while R_j represents the local frame of reference attached to the vehicle. Obviously, R_j is a moving frame of reference. Thus, its position and orientation change constantly with respect to the global frame.

The velocity and acceleration of a point P on the vehicle can be found easily by applying the kinematic equations in a matrix form. Of course, all velocities and accelerations are calculated with respect to the global/ground frame of reference R_i, as velocities and accelerations with respect to the moving set of axes R_j are all equal to zero.

Nevertheless, it is much more convenient to use the projection of these velocities to the moving frame of reference R_j. In this way, one gains a better perception of the situation, as it is very important to know the velocity vectors in certain directions,

specified by the frame of reference attached to the vehicle. For example, when a driver reads 100 miles/hour on the tachometer, he actually reads the forward speed of the vehicle, not the speed with respect to some ground frame of reference. This velocity is the result of the projection of the vehicle's speed, as measured at the ground frame of reference, to the vehicle's longitudinal axis. Figure 5.1 shows the frame of reference attached to the vehicle. The orientation and position of this frame is proposed by SAE and is used in most studies.

Let:

$\mathbf{s}_i = (x_i\ y_i\ z_i)^T$ be the vector of coordinates of a point P of the vehicle with respect to R_i

$\mathbf{s}_j = (x_j\ y_j\ z_j)^T$ be the vector of coordinates of point P of the vehicle with respect to R_j

Equation (5.1) can be rewritten in a matrix form for the study of vehicle motion. In this case $\mathbf{c}$ represents the space vector of a point P of the vehicle with respect to the moving (vehicle attached) frame, i.e. $\mathbf{c} \equiv \mathbf{s}_j$, while $\boldsymbol{\omega}$ represents the space vector of the rotational velocity of the moving frame of reference. Attention should be paid to the fact that while the velocity obtained in equation (5.1) is sensed by an observer, using the ground frame of reference, the actual components are still written for the moving frame of reference R_j. Consequently, equation (5.5) is half written for the ground frame of reference (term $V_i(O_j)$) and half written for the moving frame of reference (term $V_j(P) + \boldsymbol{\omega} \times \mathbf{s}_j$).

Equation (5.5) includes the translational motion of the origin of the moving frame of reference and shall be used for the analysis. In order to write this equation for the ground frame of reference, it is essential to multiply the second term by the transformation matrix **L**, so that the components of the rotational velocities are projected to the ground frame of reference:

$$\mathbf{V}_i(P) = \mathbf{V}_i(O_j) + \mathbf{L}\left(\mathbf{V}_j(P) + \Omega_j \cdot \mathbf{s}_j\right) \tag{5.13}$$

The term $\Omega_j \cdot s_j$ represents the cross product $\omega \times s_j$ in a matrix form. Carrying out the cross product of the vectors, yields the matrix Ω_j so that $\Omega_j \cdot s_j = \omega \times s_j$:

$$\Omega_j = \begin{bmatrix} 0 & -\omega_z & \omega_y \\ \omega_z & 0 & -\omega_x \\ -\omega_y & \omega_x & 0 \end{bmatrix} \tag{5.14}$$

Where $\omega_x, \omega_y, \omega_z$ are the components of the moving frame's rotational velocity, according to the relationship:

$$\omega = \left(d\Theta/dt\right)_{Ri} = \left(\omega_x \; \omega_y \; \omega_z\right)^T{}_{Ri} \tag{5.15}$$

Equation (5.13) represents the velocity of a point P on the vehicle, with respect to the global/ground frame of reference. This velocity should now be projected onto the moving frame of reference. This is achieved by pre-multiplying the velocity by the inverted transformation matrix $\mathbf{L}^{-1}$:

$$\mathbf{V}_j(P) = \mathbf{L}^{-1} \cdot \mathbf{V}_i(P) = \mathbf{L}^{-1}\left[\mathbf{V}_i(O_j) + \mathbf{L}\left(\mathbf{V}_j(P) + \Omega_j \cdot \mathbf{s}_j\right)\right] \Rightarrow$$

$$\mathbf{V}_j(P) = \mathbf{L}^{-1}\mathbf{V}_i(O_j) + \mathbf{L}^{-1}\mathbf{L}\left(\mathbf{V}_j(P) + \Omega_j \cdot \mathbf{s}_j\right) \Rightarrow$$

$$\mathbf{V}_j(P) = \mathbf{L}^{-1}\mathbf{V}_i(O_j) + \left(\mathbf{V}_j(P) + \Omega_j \cdot \mathbf{s}_j\right) \tag{5.16}$$

Equation (5.16) is written in a condensed matrix form. It is easy to obtain the velocity components in all three directions in the moving frame of reference, as follows:

Let $[UVW]^T$ be the projections of the translational velocity to the moving frame of reference, so that $[UVW]^T = \mathbf{L}^{-1}\mathbf{V}_i(O_j)$.

Let $[pqr]^T = [\omega_x \; \omega_y \; \omega_z]^T = \omega$. (5.17)

Then, the components of the velocity in the directions of the moving axes can be written as:

$$\begin{bmatrix} u \\ v \\ w \end{bmatrix} = \begin{bmatrix} U \\ V \\ W \end{bmatrix} + \begin{bmatrix} dx/dt \\ dy/dt \\ dz/dt \end{bmatrix} + \begin{bmatrix} z \cdot q - y \cdot r \\ x \cdot r - z \cdot p \\ y \cdot p - x \cdot q \end{bmatrix} \tag{5.18}$$

Because point P belongs to the vehicle, which is considered as a rigid body, the middle term of the right hand-side of the above equation diminishes. Thus, the velocity of a point P becomes:

$$\begin{bmatrix} u \\ v \\ w \end{bmatrix} = \begin{bmatrix} U \\ V \\ W \end{bmatrix} + \begin{bmatrix} z \cdot q - y \cdot r \\ x \cdot r - z \cdot p \\ y \cdot p - x \cdot q \end{bmatrix} \tag{5.19}$$

In order to calculate the acceleration of point P one can start from equation (5.16):

$$\mathbf{a}_p = d\mathbf{V}_j(P)/dt = d\mathbf{L}^{-1}\mathbf{V}_i(O_j)/dt + d\left(\mathbf{V}_j(P) + \Omega_j \cdot \mathbf{s}_j\right)/dt \text{ or}$$

$$\mathbf{a}_p = d\mathbf{V}_j(P)/dt = d\mathbf{L}^{-1}\mathbf{V}_i(O_j)/dt + d\left(ds_j/dt + \Omega_j \cdot \mathbf{s}_j\right)/dt \Rightarrow$$

$$\mathbf{a}_p = d\mathbf{V}_j(P)/dt = d\mathbf{L}^{-1}\mathbf{V}_i(O_j)/dt + d^2\mathbf{s}_j/dt^2 + \left(d\Omega_j/dt\right)\cdot \mathbf{s}_j$$
$$+ 2 \cdot \Omega_j \cdot \left(ds_j/dt\right) + \Omega_j \cdot \Omega_j \cdot \mathbf{s}_j \Rightarrow$$

$$\mathbf{a}_p = d\mathbf{V}_j(P)/dt = d\mathbf{L}^{-1}\mathbf{V}_i(O_j)/dt + \Omega_j \cdot \mathbf{L}^{-1}\mathbf{V}_i(O_j)$$
$$+ d^2\mathbf{s}_j/dt^2 + \left(d\Omega_j/dt\right)\cdot \mathbf{s}_j + 2 \cdot \Omega_j \cdot \left(ds_j/dt\right) + \Omega_j \cdot \Omega_j \cdot \mathbf{s}_j \tag{5.20}$$

The above equation, after carrying out the matrix calculations, can be written in matrix form:

$$\begin{bmatrix} A_x \\ A_y \\ A_z \end{bmatrix} = \begin{bmatrix} dU/dt \\ dV/dt \\ dW/dt \end{bmatrix} + \begin{bmatrix} -V \cdot r + W \cdot q \\ -W \cdot p + U \cdot r \\ -U \cdot q + V \cdot p \end{bmatrix} + \begin{bmatrix} -x \cdot \left(q^2 + r^2\right) + y \cdot \left(p \cdot q - dr/dt\right) + z \cdot \left(p \cdot r + dq/dt\right) \\ -y \cdot \left(r^2 + p^2\right) + z \cdot \left(q \cdot r - dp/dt\right) + x \cdot \left(p \cdot q + dr/dt\right) \\ -z \cdot \left(p^2 + q^2\right) + x \cdot \left(p \cdot r - dq/dt\right) + y \cdot \left(q \cdot r + dp/dt\right) \end{bmatrix} \tag{5.21}$$

or as separate equations as follows:

$$A_x = Du/Dt = dU/dt - V \cdot r + W \cdot q - x \cdot \left(q^2 + r^2\right) + y \cdot \left(p \cdot q - dr/dt\right) + z \cdot \left(p \cdot r + dq/dt\right) \tag{5.22}$$

$$A_y = Dv/Dt = dV/dt - W \cdot p + U \cdot r - y \cdot (r^2 + p^2) + z \cdot (q \cdot r - dp/dt) + x \cdot (p \cdot q + dr/dt) \quad (5.23)$$

$$A_z = Dw/Dt = dW/dt - U \cdot q + V \cdot p - z \cdot (p^2 + q^2) + x \cdot (p \cdot r - dq/dt) + y \cdot (q \cdot r + dp/dt) \quad (5.24)$$

5.3.4 Dynamic Equations of Motion

Thus far the kinematic equations for the vehicle have been derived. The dynamic equations of motion are obtained by applying the Newton – Euler method.

Newton's law for a single point P of the vehicle is expressed as:

$$\delta F_x = D(\delta m \cdot u)/Dt \quad (5.25)$$

$$\delta F_y = D(\delta m \cdot v)/Dt \quad (5.26)$$

$$\delta F_z = D(\delta m \cdot w)/Dt \quad (5.27)$$

Assuming that the vehicle's mass remains constant, the equations can be rewritten as:

$$\delta F_x = \delta m \cdot (Du/Dt) \quad (5.28)$$

$$\delta F_y = \delta m \cdot (Dv/Dt) \quad (5.29)$$

$$\delta F_z = \delta m \cdot (Dw/Dt) \quad (5.30)$$

The effect of the sum of particles, which form the vehicle, is realised through integration:

$$\int \delta F_x = \int \delta m \cdot (Du/Dt) \quad (5.31)$$

$$\int \delta F_y = \int \delta m \cdot (Dv/Dt) \quad (5.32)$$

$$\int \delta F_z = \int \delta m \cdot (Dw/Dt) \quad (5.33)$$

The following relations also apply:

$$\int \delta m = m \quad (5.34)$$

$$\int \delta m \cdot x = m \cdot x_G \tag{5.35}$$

$$\int \delta m \cdot y = m \cdot y_G \tag{5.36}$$

$$\int \delta m \cdot z = m \cdot z_G \tag{5.37}$$

where (x_G, y_G, z_G) is the vector of coordinates of the position of the centre of mass of the vehicle with respect to the moving frame of reference and m is the total mass of the vehicle.

X,Y and Z denote the sum of all forces along the axes x,y,z respectively, so that:

$X = \Sigma F_x = \int \delta F_x$ is the sum of forces in the direction of axis O_x of frame R_j

$Y = \Sigma F_y = \int \delta F_y$ is the sum of forces in the direction of axis O_y of frame R_j

$Z = \Sigma F_z = \int \delta F_z$ is the sum of forces in the direction of axis O_z of frame R_j

Consequently, the combination of equations (5.22-5.37) yields:

$$\Sigma F_x = m \cdot (dU/dt - V \cdot r + W \cdot q) - m \cdot [x_G \cdot (q^2 + r^2) - y_G \cdot (p \cdot q - dr/dt) - z_G \cdot (p \cdot r + dq/dt)] \tag{5.38}$$

$$\Sigma F_y = m \cdot (dV/dt - W \cdot p + U \cdot r) - m \cdot [y_G \cdot (r^2 + p^2) - z_G \cdot (q \cdot r - dp/dt) - x_G \cdot (p \cdot q + dr/dt)] \tag{5.39}$$

$$\Sigma F_z = m \cdot (dW/dt - U \cdot q + V \cdot p) - m \cdot [z_G \cdot (p^2 + q^2) - x_G \cdot (p \cdot r - dq/dt) - y_G \cdot (q \cdot r + dp/dt)] \tag{5.40}$$

Euler momenta equations for a single point P of the vehicle are expressed as:

$$\delta M_x = y \cdot [D \cdot (\delta m \cdot w)/Dt] - z \cdot [D \cdot (\delta m \cdot v)/Dt] \tag{5.41}$$

$$\delta M_y = z \cdot [D \cdot (\delta m \cdot u)/Dt] - x \cdot [D \cdot (\delta m \cdot w)/Dt] \tag{5.42}$$

$$\delta M_x = x \cdot [D \cdot (\delta m \cdot v)/Dt] - y \cdot [D \cdot (\delta m \cdot u)/Dt] \tag{5.43}$$

By assuming again that the vehicle's mass is constant, the above equations can be written as follows:

$$\delta M_x = \delta m \cdot [y \cdot (Dw/Dt) - z \cdot (Dv/Dt)] \tag{5.44}$$

$$\delta M_y = \delta m \cdot [z \cdot (Du/Dt) - x \cdot (Dw/Dt)] \tag{5.45}$$

$$\delta M_z = \delta m \cdot [x \cdot (Dv/Dt) - y \cdot (Du/Dt)] \tag{5.46}$$

Again, the effect of the sum of particles, which form the vehicle, is realised through integration:

$$\int \delta M_x = \int \delta m \cdot [y \cdot (Dw/Dt) - z \cdot (Dv/Dt)] \tag{5.47}$$

$$\int \delta M_y = \int \delta m \cdot [z \cdot (Du/Dt) - x \cdot (Dw/Dt)] \tag{5.48}$$

$$\int \delta M_z = \int \delta m \cdot [x \cdot (Dv/Dt) - y \cdot (Du/Dt)] \tag{5.49}$$

Where L,M and N denote the sum of all moments in the direction of axes x,y,z respectively, so that:

$L = \Sigma M_x = \int \delta M_x$ is the sum of moments in the direction of axis O_x of frame R_j

$M = \Sigma M_y = \int \delta M_y$ is the sum of moments in the direction of axis O_y of frame R_j

$N = \Sigma M_z = \int \delta M_z$ is the sum of moments in the direction of axis O_z of frame R_j

$$\Sigma M_x = \int \delta m \cdot \begin{Bmatrix} y \cdot [dW/dt - U \cdot q + V \cdot p - z \cdot (p^2 + q^2) + x \cdot (p \cdot r - dq/dt) + y \cdot (q \cdot r + dp/dt)] \\ -z \cdot [dV/dt - W \cdot p + U \cdot r - y \cdot (r^2 + p^2) + z \cdot (q \cdot r - dp/dt) + x \cdot (p \cdot q + dr/dt)] \end{Bmatrix} \tag{5.50}$$

$$\Sigma M_y = \int \delta m \cdot \begin{Bmatrix} z \cdot [dU/dt - V \cdot r + W \cdot q - x \cdot (q^2 + r^2) + y \cdot (p \cdot q - dr/dt) + z \cdot (p \cdot r + dq/dt)] \\ -x \cdot [dW/dt - U \cdot q + V \cdot p - z \cdot (p^2 + q^2) + x \cdot (p \cdot r - dq/dt) + y \cdot (q \cdot r + dp/dt)] \end{Bmatrix} \tag{5.51}$$

$$\Sigma M_z = \int \delta m \cdot \begin{Bmatrix} x \cdot [dV/dt - W \cdot p + U \cdot r - y \cdot (r^2 + p^2) + z \cdot (q \cdot r - dp/dt) + x \cdot (p \cdot q + dr/dt)] \\ -y \cdot [dU/dt - V \cdot r + W \cdot q - x \cdot (q^2 + r^2) + y \cdot (p \cdot q - dr/dt) + z \cdot (p \cdot r + dq/dt)] \end{Bmatrix} \tag{5.52}$$

Furthermore, the following relations apply for the mass and product moments of inertia:

$$I_{xx} = \int (y^2 + z^2) \cdot \delta m \tag{5.53}$$

$$I_{yy} = \int (x^2 + z^2) \cdot \delta m \tag{5.54}$$

$$I_{zz} = \int (x^2 + y^2) \cdot \delta m \tag{5.55}$$

$$I_{yz} = \int y \cdot z \cdot \delta m \tag{5.56}$$

$$I_{zx} = \int z \cdot x \cdot \delta m \tag{5.57}$$

$$I_{xy} = \int x \cdot y \cdot \delta m \tag{5.58}$$

Introducing the definitions of mass and product moments of inertia into the Euler equations yields:

$$\begin{aligned} \Sigma M_x = {} & I_{xx} \cdot (dp/dt) - (I_{yy} - I_{zz}) \cdot q \cdot r + I_{yz} \cdot (r^2 - q^2) - I_{zx} \cdot (p \cdot q + dr/dt) \\ & + I_{xy} \cdot (p \cdot r - dq/dt) + m \cdot y_G \cdot (dW/dt - U \cdot q + V \cdot p) - m \cdot z_G \cdot (dV/dt - W \cdot p + U \cdot r) \end{aligned} \tag{5.59}$$

$$\begin{aligned} \Sigma M_y = {} & I_{yy} \cdot (dq/dt) - (I_{zz} - I_{xx}) \cdot p \cdot r + I_{xz} \cdot (p^2 - r^2) - I_{xy} \cdot (q \cdot r + dp/dt) \\ & + I_{yz} \cdot (q \cdot p - dr/dt) + m \cdot z_G \cdot (dU/dt - V \cdot r + W \cdot q) - m \cdot x_G \cdot (dW/dt - U \cdot q + V \cdot p) \end{aligned} \tag{5.60}$$

$$\begin{aligned} \Sigma M_z = {} & I_{zz} \cdot (dr/dt) - (I_{xx} - I_{yy}) \cdot p \cdot q + I_{xy} \cdot (q^2 - p^2) - I_{yz} \cdot (r \cdot p + dq/dt) \\ & + I_{zx} \cdot (r \cdot q - dp/dt) + m \cdot x_G \cdot (dV/dt - W \cdot p + U \cdot r) - m \cdot y_G \cdot (dU/dt - V \cdot r + W \cdot q) \end{aligned} \tag{5.61}$$

Below, the six generic differential equations of motion obtained by the application of Newton-Euler method are grouped together:

$$\Sigma F_x = m \cdot (dU/dt - V \cdot r + W \cdot q) - m \cdot [x_G \cdot (q^2 + r^2) - y_G \cdot (p \cdot q - dr/dt) - z_G \cdot (p \cdot r + dq/dt)] \tag{5.62}$$

$$\Sigma F_y = m \cdot (dV/dt - W \cdot p + U \cdot r) - m \cdot [y_G \cdot (r^2 + p^2) - z_G \cdot (q \cdot r - dp/dt) - x_G \cdot (p \cdot q + dr/dt)] \tag{5.63}$$

$$\Sigma F_z = m \cdot (dW/dt - U \cdot q + V \cdot p) - m \cdot [z_G \cdot (p^2 + q^2) - x_G \cdot (p \cdot r - dq/dt) - y_G \cdot (q \cdot r + dp/dt)] \tag{5.64}$$

$$\Sigma M_x = I_{xx}\cdot(dp/dt) - (I_{yy} - I_{zz})\cdot q\cdot r + I_{yz}\cdot(r^2 - q^2) - I_{zx}\cdot(p\cdot q + dr/dt) + I_{xy}\cdot(p\cdot r - dq/dt) + m\cdot y_G\cdot(dW/dt - U\cdot q + V\cdot p) - m\cdot z_G\cdot(dV/dt - W\cdot p + U\cdot r) \quad (5.65)$$

$$\Sigma M_y = I_{yy}\cdot(dq/dt) - (I_{zz} - I_{xx})\cdot p\cdot r + I_{xz}\cdot(p^2 - r^2) - I_{xy}\cdot(q\cdot r + dp/dt) + I_{yz}\cdot(q\cdot p - dr/dt) + m\cdot z_G\cdot(dU/dt - V\cdot r + W\cdot q) - m\cdot x_G\cdot(dW/dt - U\cdot q + V\cdot p) \quad (5.66)$$

$$\Sigma M_z = I_{zz}\cdot(dr/dt) - (I_{xx} - I_{yy})\cdot p\cdot q + I_{xy}\cdot(q^2 - p^2) - I_{yz}\cdot(r\cdot p + dq/dt) + I_{zx}\cdot(r\cdot q - dp/dt) + m\cdot x_G\cdot(dV/dt - W\cdot p + U\cdot r) - m\cdot y_G\cdot(dU/dt - V\cdot r + W\cdot q) \quad (5.67)$$

By assuming that the centre of mass of the vehicle coincides with the origin O_j of the frame of reference and also that the vehicle is symmetrical about the plane defined by axes O_jx and O_jz, the above equations can be further simplified.

In this case the following relations apply:

$$x_G = y_G = z_G = 0 \quad (5.68)$$

and

$$I_{xy} = I_{zy} = 0 \quad (5.69)$$

Introducing these relations into the generic equations yields:

$$\Sigma F_x = m\cdot(dU/dt - V\cdot r + W\cdot q) \quad (5.70)$$

$$\Sigma F_y = m\cdot(dV/dt - W\cdot p + U\cdot r) \quad (5.71)$$

$$\Sigma F_z = m\cdot(dW/dt - U\cdot q + V\cdot p) \quad (5.72)$$

$$\Sigma M_x = I_{xx}\cdot(dp/dt) - (I_{yy} - I_{zz})\cdot q\cdot r - I_{zx}\cdot(p\cdot q + dr/dt) \quad (5.73)$$

$$\Sigma M_y = I_{yy}\cdot(dq/dt) - (I_{zz} - I_{xx})\cdot p\cdot r + I_{xz}\cdot(p^2 - r^2) \quad (5.74)$$

$$\Sigma M_z = I_{zz}\cdot(dr/dt) - (I_{xx} - I_{yy})\cdot p\cdot q + I_{zx}\cdot(r\cdot q - dp/dt) \quad (5.75)$$

Many researchers simplify the above equations even further, by reducing the degrees of freedom according to the specific requirements of their studies. For instance, the

equations for the frequently used bicycle model can be obtained by neglecting all degrees of freedom apart from the lateral translation (direction of y axis) and the rotation about the vertical axis (z). The forward speed (U) is also considered to be constant:

Thus, the equations for the bicycle model become:

$$\Sigma F_y = m \cdot (dV/dt + U \cdot r) \tag{5.76}$$

$$\Sigma M_z = I_{zz} \cdot (dr/dt) \tag{5.77}$$

5.4 Introduction of External Forces and Moments

5.4.1 Gravitational Forces and Moments

The gravitational force applies to the centre of mass of the vehicle. It is easy to introduce the effects of a sloped road, by multiplying the gravity vector by the transformation matrix $\mathbf{L}(\Theta, \Phi, \Psi)$, where angle Ψ is equal to zero.

$$\mathbf{G} = \begin{bmatrix} G_x \\ G_y \\ G_z \end{bmatrix} = \begin{bmatrix} (\sin\Psi \cdot \sin\Theta - \cos\Psi \cdot \sin\Phi \cdot \cos\Theta) \cdot m \cdot g \\ (\cos\Psi \cdot \sin\Theta + \sin\Psi \cdot \sin\Phi \cdot \cos\Theta) \cdot m \cdot g \\ \cos\Phi \cdot \cos\Theta \cdot m \cdot g \end{bmatrix} = \mathbf{L}(\Theta, \Phi, \Psi) \cdot \begin{bmatrix} 0 \\ 0 \\ m \cdot g \end{bmatrix} \tag{5.78}$$

The resulting vector G produces three moments as follows:

$$M_{xG} = G_z \cdot y_G \tag{5.79}$$

$$M_{yG} = G_z \cdot x_G \tag{5.80}$$

$$M_{zG} = G_y \cdot x_G - G_x \cdot y_G \tag{5.81}$$

5.4.2 Suspension Forces and Moments

It is assumed that suspension forces act in the vertical direction. In the general case, spring forces are considered as functions of the deflection in the following manner:

$$F = K_{f,r}[\text{deflection}] \tag{5.82}$$

where subscript f denotes front springs, while r denotes rear springs

Such functions may be linear or non-linear, including the effect of bump-stops or non-linear springs.

Considering the general motion of the vehicle and referring to figure 5.2, spring forces can be written as:

$$F_{k1} = -K_f\left[\left(z - |c|\cdot\theta - |a|\cdot\varphi\right)\right] \tag{5.83}$$

$$F_{k2} = -K_f\left[\left(z + |c|\cdot\theta - |a|\cdot\varphi\right)\right] \tag{5.84}$$

$$F_{k3} = -K_r\left[\left(z - |d|\cdot\theta + |b|\cdot\varphi\right)\right] \tag{5.85}$$

$$F_{k4} = -K_r\left[\left(z + |d|\cdot\theta + |b|\cdot\varphi\right)\right] \tag{5.86}$$

The total vertical force generated by the springs is:

$$F_{zk} = \Sigma F_{ki} \tag{5.87}$$

Furthermore, the spring forces result in the development of moments about the axes Ox and Oy:

$$M_{xk} = |c|\cdot\left(-F_{k1} + F_{k2}\right) + |d|\cdot\left(-F_{k3} + F_{k4}\right) \tag{5.88}$$

$$M_{yk} = -|a|\cdot\left(F_{k1} + F_{k2}\right) + |b|\cdot\left(F_{k3} + F_{k4}\right) \tag{5.89}$$

Following the same procedure, the equivalent relations for the dampers are obtained, using a non-linear function for the damping force with respect to velocity.

$$F_{d1} = -D_f\left[\left(W - |c|\cdot p - |a|\cdot q\right)\right] \tag{5.90}$$

$$F_{d2} = -D_f\left[\left(W + |c|\cdot p - |a|\cdot q\right)\right] \tag{5.91}$$

$$F_{d3} = -D_r\left[\left(W - |d|\cdot p + |b|\cdot q\right)\right] \tag{5.92}$$

$$F_{d4} = -D_r\left[\left(W + |d| \cdot p + |b| \cdot q\right)\right] \tag{5.93}$$

The total vertical force developed by dampers is:

$$F_{zd} = \Sigma F_{di} \tag{5.94}$$

Moments developed by dampers are given as:

$$M_{xd} = |c| \cdot \left(-F_{d1} + F_{d2}\right) + |d| \cdot \left(-F_{d3} + F_{d4}\right) \tag{5.95}$$

$$M_{yk} = -|a| \cdot \left(F_{d1} + F_{d2}\right) + |b| \cdot \left(F_{d3} + F_{d4}\right) \tag{5.96}$$

In case the vehicle incorporates anti-roll bars, it is essential to take into account the moments developed about the longitudinal axis of the vehicle, as a result of roll motion during cornering, as:

$$\begin{aligned} M_{x\,f\,roll} &= -K_{f\,roll} \cdot \theta \\ M_{x\,r\,roll} &= -K_{r\,roll} \cdot \theta \end{aligned} \tag{5.97}$$

Total forces and moments produced by springs, dampers and anti-roll bars are, thus:

$$F_{zkd} = F_{zk} + F_{zd} \tag{5.98}$$

$$M_{xkdroll} = M_{xk} + M_{xd} + M_{x\,f\,roll} + M_{x\,r\,roll} \tag{5.99}$$

$$M_{ykd} = M_{yk} + M_{yd} \tag{5.100}$$

5.4.3 Tyre Forces and Moments

Tyre forces and moments are calculated based on the velocity vector at the centre of each of the four wheels, the corresponding linear velocity of rolling and, last but not least, the vertical load at the four corners of the vehicle. The physical tyre models presented in chapters 3 and 4 use directly the aforementioned kinematic quantities and the total vertical load for the calculation of tyre forces and moments. On the contrary, the Magic Formula and other empirical and analytical models make use of the actual

slip values in the form of slip angle and longitudinal slip ratio. In order to maintain compatibility with such models, the interface between the vehicle model and any tyre model is set up in order to provide the following inputs from the vehicle to the tyres:

1. Slip angle
2. Slip ratio
3. Vertical load
4. Camber angle
5. Forward velocity of the centre of the wheel

Tyre models can selectively use the first 4 input quantities (Magic Formula and other semi-empirical and analytical physical models), or all 5 input quantities (Physical numerical models). In particular, the forward velocity is used in conjunction with the slip angle and slip ratio in order to extract the linear velocity of rolling and the lateral velocity of the centre of the wheel which are required by the numerical physical models. This procedure takes place within the tyre model calling functions.

Referring to figure 5.5, the tyre slip angles for the general case of the four-wheel steering are calculated by the following relations:

$$\alpha_1 = \delta_1 - \text{Arctan}\left[\left(V + |a| \cdot r\right)/\left(U + |c| \cdot r\right)\right] \tag{5.101}$$

$$\alpha_2 = \delta_2 - \text{Arctan}\left[\left(V + |a| \cdot r\right)/\left(U - |c| \cdot r\right)\right] \tag{5.102}$$

$$\alpha_3 = \delta_3 - \text{Arctan}\left[\left(V - |b| \cdot r\right)/\left(U + |d| \cdot r\right)\right] \tag{5.103}$$

$$\alpha_4 = \delta_4 - \text{Arctan}\left[\left(V - |b| \cdot r\right)/\left(U - |d| \cdot r\right)\right] \tag{5.104}$$

where α_i denotes the slip angle of the i^{th} wheel and δ_f, δ_r denote the front and rear steering angles respectively.

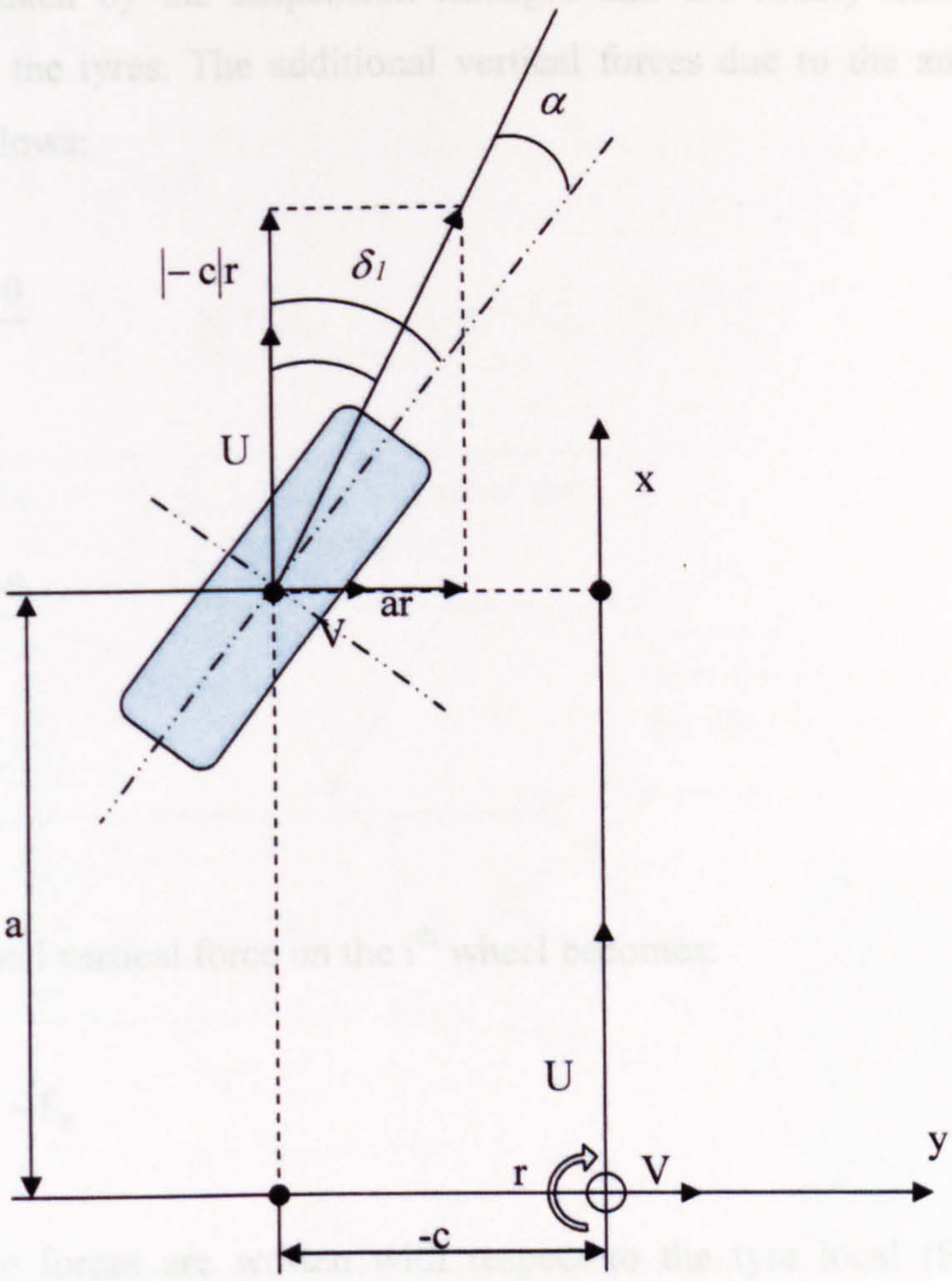

Figure 5. 5 Relation between the slip angle and the kinematic conditions at the wheel centre

The longitudinal slip ratio can be calculated if the rotational dynamics of the wheels are solved simultaneously to the equations of motion of the vehicle, taking also into consideration the tyre force equations, as demonstrated in detail in section 3.3.5.1. Alternatively, a slip ratio value can be imposed as an external stand-alone excitation. Although the rotational motion of the wheel has already been described in equations (3.171)-(3.172), the idea of the inclusion of the wheel dynamics in the vehicle model was abandoned as a source of further complications, such as the need for the definition of wheel braking and/or driving torque functions, not to mention the significant increase in computational time, even under purely cornering manoeuvres.

The vertical forces applied on the wheel hubs can be easily calculated by adding the elastic and damping forces generated by the suspensions at the corresponding points (equations (5.83)-(5.86) and (5.90)-(5.93)). Furthermore, the reactions of the anti-roll

bars are undertaken by the suspension linkages and are finally transferred to the ground through the tyres. The additional vertical forces due to the ant-roll bars are expressed as follows:

$$F_{z1roll} = -\frac{K_{froll} \cdot \theta}{2|c|} \tag{5.105}$$

$$F_{z2roll} = \frac{K_{froll} \cdot \theta}{2|c|} \tag{5.106}$$

$$F_{z3roll} = -\frac{K_{rroll} \cdot \theta}{2|d|} \tag{5.107}$$

$$F_{z4roll} = \frac{K_{rroll} \cdot \theta}{2|d|} \tag{5.108}$$

The resulting total vertical force on the i^{th} wheel becomes:

$$F_{zi} = F_{ziroll} - F_{ki} - F_{di} \tag{5.109}$$

Finally, all tyre forces are written with respect to the tyre local (SAE) frame of reference. Hence, it is essential to project the tyre forces to the vehicle frame of reference (R_j):

$$F_{xityre} = (F_x)_i \cdot \cos\delta_i - (F_y)_i \cdot \sin\delta_i \tag{5.110}$$

$$F_{yityre} = (F_x)_i \cdot \sin\delta_i + (F_y)_i \cdot \cos\delta_i \tag{5.111}$$

The forces determined by relations (5.110) and (5.111) generate moments about the axes of the local frame of reference. The calculation of pitch and yaw moments requires the knowledge of the distance of the origin of the local frame of reference from the ground. Referring to figure 5.6, if the initial vertical displacement of the vehicle body (z_o) is known, then the height of the frame of reference from the ground is equal to $h+z_o-z$. Therefore, the tyre moments about the local frame of reference are written as follows:

$$M_{x\,tyre} = \sum_{i=1}^{4} F_{yi} \cdot (h + z_o - z) \tag{5.112}$$

$$M_{y\,tyre} = \sum_{i=1}^{4} F_{xi} \cdot (h + z_o - z) \tag{5.113}$$

$$M_{z\,tyre} = \sum_{i=1}^{2} F_{yi} \cdot |a| - \sum_{i=3}^{4} F_{yi} \cdot |b| + (F_{x1} - F_{x2}) \cdot |c| + (F_{x3} - F_{x4}) \cdot |d| \tag{5.114}$$

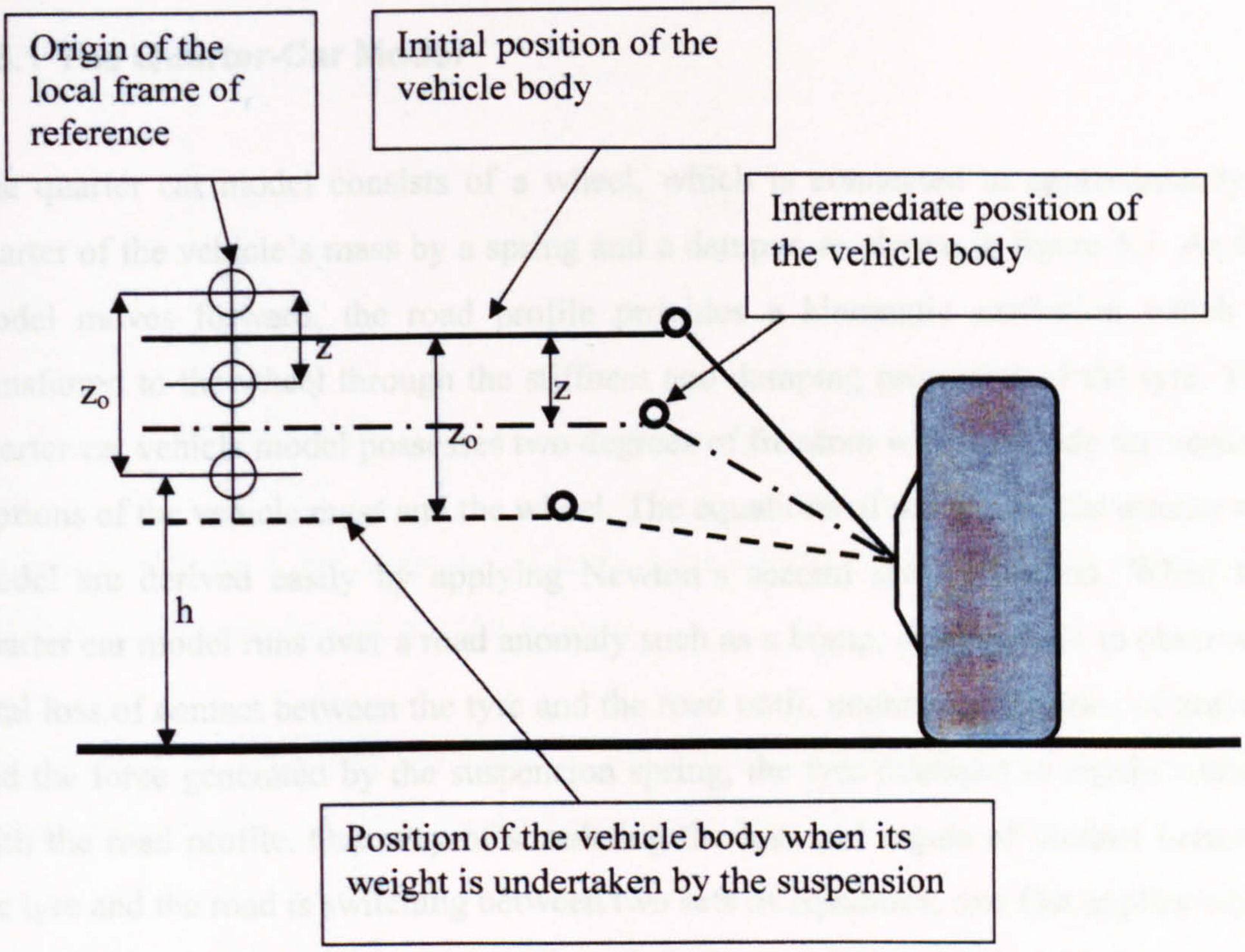

Figure 5. 6 The height of the local frame of reference from the ground

5.5 Enhancement of the Vehicle Model for Combined Ride-Handling Simulations

The present research is focused mainly on the contribution of the pneumatic tyre to the handling characteristics of vehicles. Nevertheless, during the modelling procedure, effort was put into developing a vehicle model as generic as possible, within the pre-specified time schedule. As a result, an additional set of equations was derived, for the inclusion of vertical wheel dynamics. This section describes briefly this approach.

The ride characteristics of a vehicle depend strongly on the unsuspended mass and the vertical stiffness of the tyres. The effects of these factors are overlooked by the 6-degree of freedom model previously described. Therefore, the number of degrees of freedom is increased by adding a vertical motion for each wheel. Prior to the inclusion of the additional 4 degrees of freedom in the original model, the methodology for studying the ride characteristics is demonstrated by presenting the quarter car model.

5.5.1 The Quarter-Car Model

The quarter car model consists of a wheel, which is connected to approximately a quarter of the vehicle's mass by a spring and a damper, as shown in figure 5.7. As the model moves forward, the road profile provides a kinematic excitation which is transferred to the wheel through the stiffness and damping properties of the tyre. The quarter car vehicle model possesses two degrees of freedom which include the vertical motions of the vehicle mass and the wheel. The equations of motion for the quarter car model are derived easily by applying Newton's second law of motion. When the quarter car model runs over a road anomaly such as a bump, it is possible to observe a total loss of contact between the tyre and the road until, under the influence of gravity and the force generated by the suspension spring, the tyre manages to regain contact with the road profile. One way of simulating the loss and regain of contact between the tyre and the road is switching between two sets of equations, one that applies when the tyre is in the air and one that applies when the tyre is in contact with the ground. This switching affects only the equation of motion of the wheel so that in the first case (when the wheel is in the air) the only forces applied on the wheel are those generated by the suspension, as a result of the displacement and velocity of the wheel relative to the vehicle body. When contact between the tyre and the ground surface is established, the wheel is thought to be connected to a second set of spring and damper, which serves as a simple representation of the vertical compliance of the tyre.

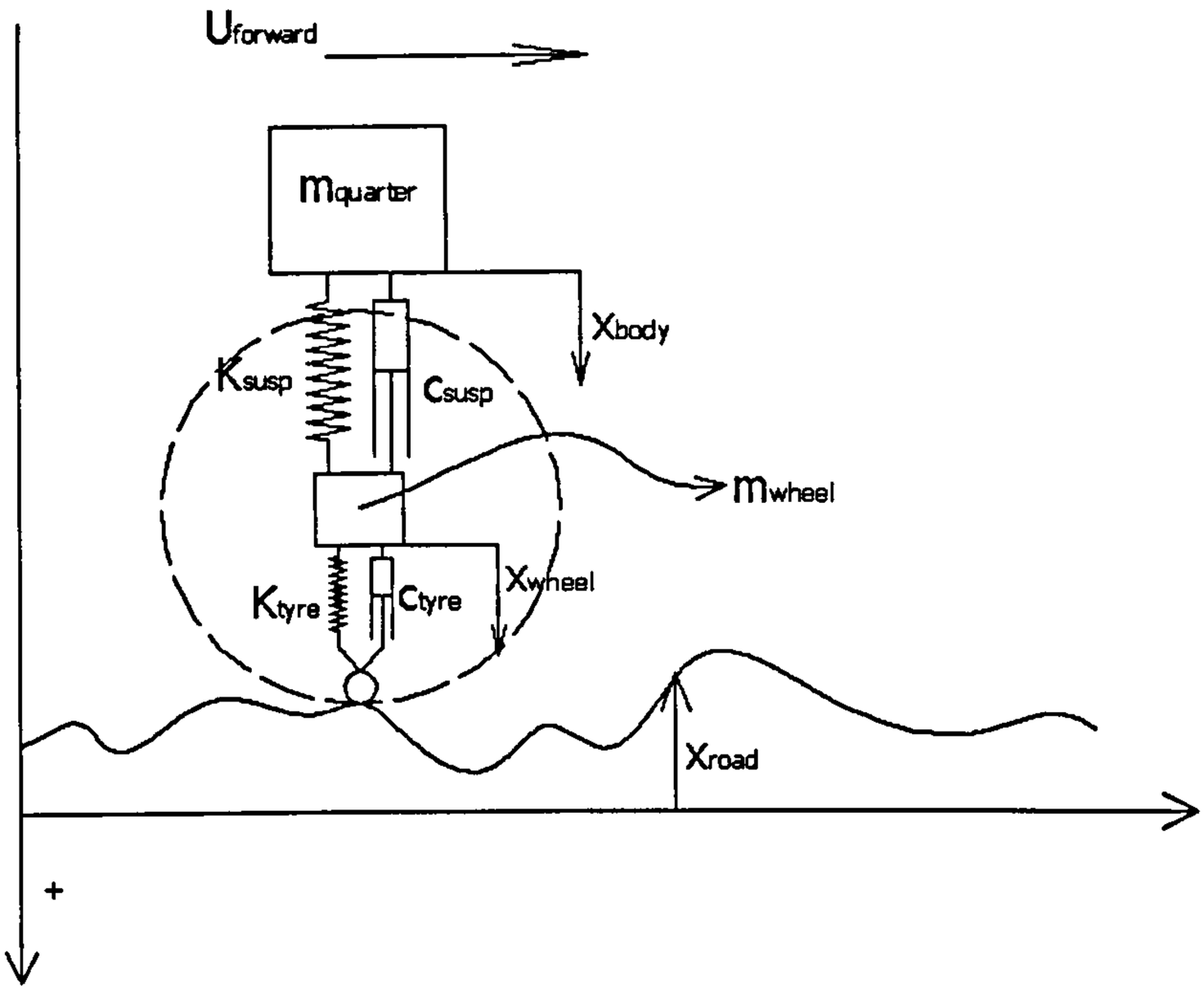

Figure 5. 7 The quarter-car model running over an un-even road

Referring to figure 6, the equations of motion are written first for the case of retaining the contact between the tyre and the ground.

The equation of motion of the wheel is given below, taking into account the elastic and damping forces both from the suspension and the tyre:

$$\begin{aligned} &-k_{tyre}\cdot\left(x_{wheel}-x_{road}\right)-c_{tyre}\cdot\left(\dot{x}_{wheel}-\dot{x}_{road}\right)+m_{wheel}\cdot g-m_{wheel}\cdot\ddot{x}_{wheel}\\ &+k_{susp}\cdot\left(x_{body}-x_{wheel}\right)+c_{susp}\cdot\left(\dot{x}_{body}-\dot{x}_{wheel}\right)=0 \end{aligned} \tag{5.115}$$

Similarly, the equation of motion of the vehicle quarter-body can be easily derived, taking into account the suspension forces. The following equation applies always, irrespective of whether the wheel retains contact or not:

$$-k_{susp}\cdot\left(x_{body}-x_{wheel}\right)-c_{susp}\cdot\left(\dot{x}_{body}-\dot{x}_{wheel}\right)+m_{quarter}\cdot g-m_{quarter}\cdot\ddot{x}_{body}=0 \tag{5.116}$$

The condition that ensures contact between the tyre and the road surface is:

$$k_{tyre}\cdot\left(x_{wheel}-x_{road}\right)+c_{tyre}\cdot\left(\dot{x}_{wheel}-\dot{x}_{road}\right)>0 \tag{5.117}$$

When the contact between the tyre and the road surface is lost, i.e. when equation (5.117) becomes ≤ 0, the following set of equations applies for the wheel and the quarter-body, respectively:

$$m \cdot g - m \cdot \ddot{x}_{wheel} + k_{susp} \cdot (x_{body} - x_{wheel}) + c_{susp} \cdot (\dot{x}_{body} - \dot{x}_{wheel}) = 0 \quad (5.118)$$

$$-k_{susp} \cdot (x_{body} - x_{wheel}) - c_{susp} \cdot (\dot{x}_{body} - \dot{x}_{wheel}) + M \cdot g - M \cdot \ddot{x}_{body} = 0 \quad (5.119)$$

5.5.2 Implementation in the Six Degree of Freedom Model

In order to include the vertical motion of the wheels in the six degree of freedom model, it is essential to add the four equations of motion of the wheels and additionally modify the expressions of the spring, damper and anti-roll bar forces and moments, already written for the vehicle body. The modified equations of motion of the vehicle body remain the same throughout the simulation, while the equations of motion of the wheels switch between two different states according to the loss of contact concept.

The spring and damping forces acting on the vehicle body are modified as follows:

$$F_{k1} = -K_f \left[\left(z - |c| \cdot \theta - |a| \cdot \varphi - x_{wheel1} \right) \right] \quad (5.120)$$

$$F_{k2} = -K_f \left[\left(z + |c| \cdot \theta - |a| \cdot \varphi - x_{wheel2} \right) \right] \quad (5.121)$$

$$F_{k3} = -K_r \left[\left(z - |d| \cdot \theta + |b| \cdot \varphi - x_{wheel3} \right) \right] \quad (5.122)$$

$$F_{k4} = -K_r \left[\left(z + |d| \cdot \theta + |b| \cdot \varphi - x_{wheel4} \right) \right] \quad (5.123)$$

$$F_{d1} = -D_f \left[\left(W - |c| \cdot p - |a| \cdot q - \dot{x}_{wheel1} \right) \right] \quad (5.124)$$

$$F_{d2} = -D_f \left[\left(W + |c| \cdot p - |a| \cdot q - \dot{x}_{wheel2} \right) \right] \quad (5.125)$$

$$F_{d3} = -D_r \left[\left(W - |d| \cdot p + |b| \cdot q - \dot{x}_{wheel3} \right) \right] \quad (5.126)$$

$$F_{d4} = -D_r \left[\left(W + |d| \cdot p + |b| \cdot q - \dot{x}_{wheel4} \right) \right] \quad (5.127)$$

When the vehicle possesses 6 degrees of freedom, roll angle θ is the only variable needed to calculate the moment generated by the anti-roll bars. On the contrary, when

the wheel motions are included, anti-roll bar moments can also be generated by the uneven vertical displacement of the wheels on the opposite sides of the vehicle. For instance, when the front right wheel runs over a road bump the front left wheel remaining levelled, a torsional deflection of the front anti-roll bar is observed. This in turn generates a moment round the longitudinal axis of the vehicle. The effect of the wheel motion on the calculation of the anti-roll moments, can be easily realised by including an additional angle θ_{wheel}, as a result of the uneven displacement of the wheels. Angles $\theta_{wheelf}, \theta_{wheelr}$ for the front and rear anti-roll bars respectively, are written as follows:

$$\frac{x_{wheel1} - x_{wheel2}}{2|c|} = \tan\theta_{wheelf} \Rightarrow$$

$$\theta_{wheelf} = \operatorname{atan}\frac{x_{wheel1} - x_{wheel2}}{2|c|} \tag{5.128}$$

$$\frac{x_{wheel3} - x_{wheel4}}{2|d|} = \tan\theta_{wheelr} \Rightarrow$$

$$\theta_{wheelr} = \operatorname{atan}\frac{x_{wheel3} - x_{wheel4}}{2|d|} \tag{5.129}$$

Consequently, the moments generated by the anti-roll bars are obtained by adding θ_{wheel} to the body roll angle θ, as shown below:

$$\begin{aligned} \mathrm{M_{x\,f\,roll}} &= -\mathrm{K_{f\,roll}} \cdot (\theta + \theta_{\mathrm{wheelf}}) \\ \mathrm{M_{x\,r\,roll}} &= -\mathrm{K_{r\,roll}} \cdot (\theta + \theta_{\mathrm{wheelr}}) \end{aligned} \tag{5.130}$$

It should be noted that the angles $\theta_{wheelf}, \theta_{wheelr}$ may be negative or positive, depending on the relation between right and left-side vertical displacements of the wheels.

The equations of motion of the wheels are given below:

1st Wheel:

Contact condition: $k_{tyre} \cdot (x_{wheel1} - x_{road1}) + c_{tyre} \cdot (\dot{x}_{wheel1} - \dot{x}_{road1}) > 0$ (5.131)

Equation of motion while the tyre retains contact:

$$-k_{tyre1} \cdot (x_{wheel1} - x_{road1}) - c_{tyre1} \cdot (\dot{x}_{wheel1} - \dot{x}_{road1}) + m_{wheel1} \cdot g - m_{wheel1} \cdot \ddot{x}_{wheel1}$$
$$+ K_f \cdot [(z - |c| \cdot \theta - |a| \cdot \varphi - x_{wheel1})] + D_f \cdot [(w - |c| \cdot p - |a| \cdot q - \dot{x}_{wheel1})] \quad (5.132)$$
$$- \frac{K_{froll} \cdot (\theta + \theta_{wheelf})}{2 \cdot c} = 0$$

Equation of motion for loss of contact condition:

$$m_{wheel1} \cdot g - m_{wheel1} \cdot \ddot{x}_{wheel1} + K_f \cdot [(z - |c| \cdot \theta - |a| \cdot \varphi - x_{wheel1})]$$
$$+ D_f \cdot [(w - |c| \cdot p - |a| \cdot q - x_{wheel1})] - \frac{K_{froll} \cdot (\theta + \theta_{wheelf})}{2 \cdot c} = 0 \quad (5.133)$$

2nd Wheel:

Contact condition: $k_{tyre} \cdot (x_{wheel2} - x_{road2}) + c_{tyre} \cdot (\dot{x}_{wheel2} - \dot{x}_{road2}) > 0$ (5.134)

Equation of motion while the tyre retains contact:

$$-k_{tyre2} \cdot (x_{wheel2} - x_{road2}) - c_{tyre2} \cdot (\dot{x}_{wheel2} - \dot{x}_{road2}) + m_{wheel2} \cdot g - m_{wheel2} \cdot \ddot{x}_{wheel2}$$
$$+ K_f \cdot [(z + |c| \cdot \theta - |a| \cdot \varphi - x_{wheel2})] + D_f \cdot [(w + |c| \cdot p - |a| \cdot q - \dot{x}_{wheel2})] \quad (5.135)$$
$$+ \frac{K_{froll} \cdot (\theta + \theta_{wheelf})}{2 \cdot c} = 0$$

Equation of motion for loss of contact condition:

$$m_{wheel2} \cdot g - m_{wheel2} \cdot \ddot{x}_{wheel2} + K_f \cdot [(z + |c| \cdot \theta - |a| \cdot \varphi - x_{wheel2})]$$
$$+ D_f \cdot [(w + |c| \cdot p - |a| \cdot q - \dot{x}_{wheel2})] \quad (5.136)$$
$$+ \frac{K_{froll} \cdot (\theta + \theta_{wheelf})}{2 \cdot c} = 0$$

3rd Wheel:

Contact condition: $k_{tyre} \cdot (x_{wheel\,3} - x_{road\,3}) + c_{tyre} \cdot (\dot{x}_{wheel\,3} - \dot{x}_{road\,3}) > 0$ (5.137)

Equation of motion while the tyre retains contact:

$$\begin{aligned} &- k_{tyre3} \cdot (x_{wheel3} - x_{road3}) - c_{tyre3} \cdot (\dot{x}_{wheel3} - \dot{x}_{road3}) + m_{wheel3} \cdot g - m_{wheel3} \cdot \ddot{x}_{wheel3} \\ &+ K_r \cdot [(z - |d| \cdot \theta + |b| \cdot \varphi - x_{wheel3})] + D_r \cdot [(w - |d| \cdot p + |b| \cdot q - \dot{x}_{wheel3})] \\ &- \frac{K_{rroll} \cdot (\theta + \theta_{wheelr})}{2 \cdot d} = 0 \end{aligned} \quad (5.138)$$

Equation of motion for loss of contact condition:

$$\begin{aligned} &m_{wheel3} \cdot g - m_{wheel3} \cdot \ddot{x}_{wheel3} + K_r \cdot [(z - |d| \cdot \theta + |b| \cdot \varphi - x_{wheel3})] \\ &+ D_r \cdot [(w - |d| \cdot p + |b| \cdot q - \dot{x}_{wheel3})] - \frac{K_{rroll} \cdot (\theta + \theta_{wheelr})}{2 \cdot d} = 0 \end{aligned} \quad (5.139)$$

4th Wheel:

Contact condition: $k_{tyre} \cdot (x_{wheel\,4} - x_{road\,4}) + c_{tyre} \cdot (\dot{x}_{wheel\,4} - \dot{x}_{road\,4}) > 0$ (5.140)

Equation of motion while the tyre retains contact:

$$\begin{aligned} &- k_{tyre4} \cdot (x_{wheel4} - x_{road4}) - c_{tyre4} \cdot (\dot{x}_{wheel4} - \dot{x}_{road4}) + m_{wheel4} \cdot g - m_{wheel4} \cdot \ddot{x}_{wheel4} \\ &+ K_r \cdot [(z + |d| \cdot \theta + |b| \cdot \varphi - x_{wheel4})] + D_r \cdot [(w + |d| \cdot p + |b| \cdot q - \dot{x}_{wheel4})] \\ &+ \frac{K_{rroll} \cdot (\theta + \theta_{wheelr})}{2 \cdot d} = 0 \end{aligned} \quad (5.141)$$

Equation of motion for loss of contact condition:

$$\begin{aligned} &m_{wheel4} \cdot g - m_{wheel4} \cdot \ddot{x}_{wheel4} + K_r \cdot [(z + |d| \cdot \theta + |b| \cdot \varphi - x_{wheel4})] \\ &+ D_r \cdot [(w + |d| \cdot p + |b| \cdot q - \dot{x}_{wheel4})] \\ &+ \frac{K_{rroll} \cdot (\theta + \theta_{wheelr})}{2 \cdot d} = 0 \end{aligned} \quad (5.142)$$

5.6 Steering Geometry

The steer-angles of the front wheels are calculated based on the Ackerman steering geometry [44]. Referring to figure 5.2, the relation between front left (δ_1) and front right (δ_2) steer-angle is given below:

$$\text{cotan}(\delta_1) - \text{cotan}(\delta_2) = \frac{2|c|}{a + |b|} \tag{5.143}$$

5.7 Numerical Procedure

The equations of motion of the vehicle are solved numerically using the 4th order fixed-step Runge Kutta method, or alternatively the Euler-explicit method. It is found that due to the low frequencies involved in vehicle handling dynamics, the simple, single-step Euler method yields identical results to the generally much more accurate Runge Kutta method, for time-steps shorter than 0.01 [s].

The vehicle model operates in combination with a selection of three steady-state tyre models, namely the Magic Formula and the two physical models developed in chapter 3. In transient mode, it interacts with the enhanced generic transient model presented in chapter 4.

When the vehicle model runs in conjunction with a steady-state tyre model, the tyre-force calculating sub-routine is called 4 times (once for each tyre) within each time-step and the corresponding lateral and longitudinal tyre forces are passed to the equations of motion of the vehicle, as external excitations. In the event that the transient tyre model is used in the simulation, this procedure is slightly modified. The discretised tyre model requires a much smaller time-step, lying in the range between 0.0001 and 0.00005 [s]. In order to control the computational effort, the vehicle integrator retains its large time-step (0.01-0.002 [s]), while the tyre model integrator runs internally, performing n time-steps within each external time-step, where n denotes the ratio between vehicle and tyre time-step size. The normal pressure distribution is calculated by the tyre model only once in the beginning of the internal integration procedure, based on the inputs from the vehicle model. At the end of this

procedure the tyre forces corresponding to the n^{th} internal time-step are passed to the vehicle model which, in turn, advances its states and passes them again to the tyre model for a new internal integration session. Obviously, by setting the vehicle time-step size equal to the time-step size used by the tyre integrator, n becomes equal to 1 and the advancing rate of the tyre states coincides with the advancing rate of the vehicle states, with an overall increase in the computational effort required.

5.8 Simulation Results

A number of simulations are carried out with the vehicle running over a flat road surface. The rotational and vertical degrees of freedom of the wheels are disregarded, thus the model is assumed to posses only 6 degrees of freedom. The vehicle parameters correspond to a family saloon car and are shown in table 5.1. The parameters were kindly supplied by the vehicle dynamics laboratory in the Aeronautical and Automotive Engineering department of Loughborough University. The suspension spring, damper and anti-roll bar coefficients included in table 5.1 are assumed to remain constant; hence all suspension components are considered to demonstrate linear behaviour. In addition, it is assumed that the camber angle remains equal to zero for all four wheels during the simulations.

Table 5.1

Vehicle Parameters

Parameter Description	Symbol	Value	Units
Total mass of the vehicle	m	1492	$[Kg]$
Wheelbase	ℓ	2.745	$[m]$
Distance between front axle and origin of the l.f.r.*	a	1.098	$[m]$
Distance between rear axle and origin of the l.f.r.	b	-1.647	$[m]$
Half front track width	c	0.76	$[m]$
Half rear track width	d	0.7635	$[m]$
Height of the origin of the l.f.r. from the ground	h	0.117	$[m]$

Total roll inertia	I_{xx}	513	$[Kg \cdot m^2]$
Total yaw inertia	I_{zz}	2769	$[Kg \cdot m^2]$
Total pitch inertia	I_{yy}	2599	$[Kg \cdot m^2]$
Product of inertia	I_{xy}	1.269	$[Kg \cdot m^2]$
Product of inertia	I_{yz}	0.07266	$[Kg \cdot m^2]$
Product of inertia	I_{zx}	-3.593	$[Kg \cdot m^2]$
Distance of c.g. from the origin of the l.f.r on x-axis	x_G	0	$[m]$
Distance of c.g. from the origin of the l.f.r on y-axis	y_G	0	$[m]$
Distance of c.g. from the origin of the l.f.r on z-axis	z_G	-0.54545	$[m]$
Stiffness coefficient of front suspension	K_f	28880	$[N/m]$
Damping coefficient of front suspension	D_f	3500	$[N \cdot s/m]$
Stiffness coefficient of the rear suspension	K_r	27320	$[N/m]$
Damping coefficient of the rear suspension	D_r	3500	$[N \cdot s/m]$
Front anti-roll bar stiffness coefficient	K_{froll}	1800	$[N \cdot m/rad]$
Rear anti-roll bar stiffness coefficient	K_{rroll}	1800	$[N \cdot m/rad]$

* local frame of reference

5.8.1. Cornering Manoeuvre Using Steady-State Tyre Models

The first simulation involves a step-steer input. The vehicle is considered travelling with an initial forward velocity of 90 km/h (25 m/s) with no traction or braking forces being applied on the wheels (zero longitudinal slip). Figure 5.8 shows the steer angle of the front left wheel, while the angle of the front right wheel is calculated using equation (5.143). Figures 5.9 through 5.22 illustrate various responses, as obtained using the three steady-state tyre models described in chapter 3, namely the Magic Formula, the simple physical model and the advanced physical tyre model. Clearly, the use of different tyre models has yielded large deviations in the handling response of the vehicle. In general, both physical tyre models exhibit a higher force-generating

potential. This is evident directly by comparing graphs 5.17, 5.18 and 5.19, showing the lateral forces generated by each wheel, and indirectly by observing the roll velocity and roll angle, shown in figures 5.11 and 5.14. Also, if one considers the fact that the centre of gravity of the vehicle lies significantly closer to the front axle, it is sensible to expect under-steer behaviour during cornering. The lower lateral forces generated by the Magic Formula tyre model intensify this effect, as observed in figure 5.16, illustrating the path of the vehicle. Two root causes can be identified as responsible for the aforementioned differences in the behaviour of the vehicle. Firstly, the asymptotic values of the tyre forces are velocity dependent for both physical tyre models. Considering the magnitude of the initial velocity (25 m/s) and the additional deceleration due to the projections of the lateral forces on the longitudinal axis, it is easy to realise why the physical tyre models operate under conditions that lie between those shown in figures 3.33 and 3.37, as far as the sliding velocity is concerned. Due to the severity of the manoeuvre, the vehicle operates at high slip angles, where the differences between the forces are larger. The second, more important reason behind the observed differences is related to the load-dependency of tyre friction. The mechanism of the reduction of the coefficient of friction as the vertical load increases is partially explained in section 3.2.3.2. The Magic Formula tyre model accounts for this phenomenon by connecting, through an experimentally identified relation, the coefficient of friction to the actual normal load applied on the tyre (see equations (3.69) and (3.72)). On the contrary, none of the physical models employs a load-dependent coefficient of friction, and results in large deviations observed in the lateral force, as illustrated in figure 3.51. Therefore, as the roll angle increases during the course of the manoeuvre (see figure 5.14), the lateral weight transfer has a negative effect on the grip of the Magic Formula model, leaving the two physical models unaffected.

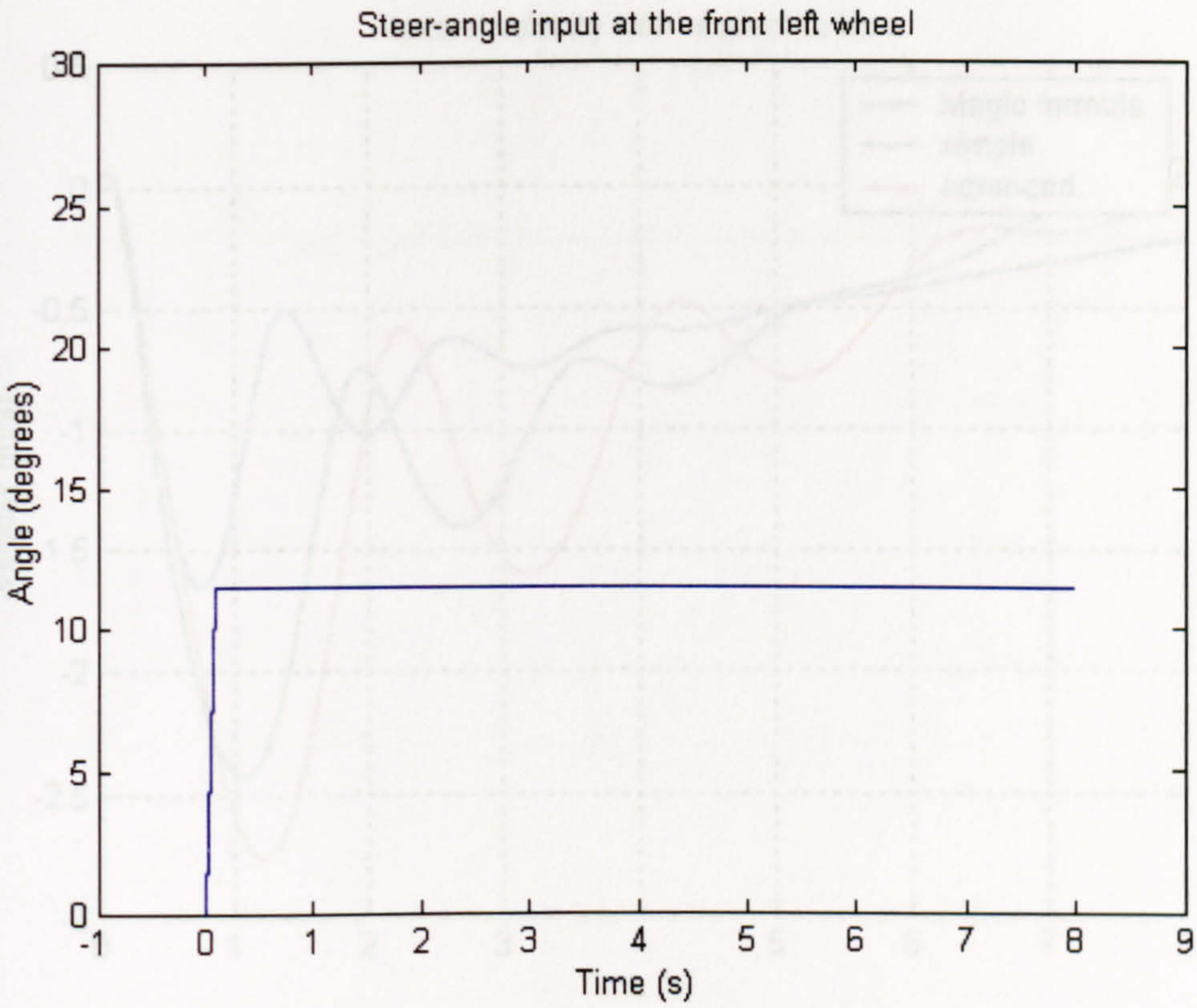

Figure 5. 8 The step-steer input

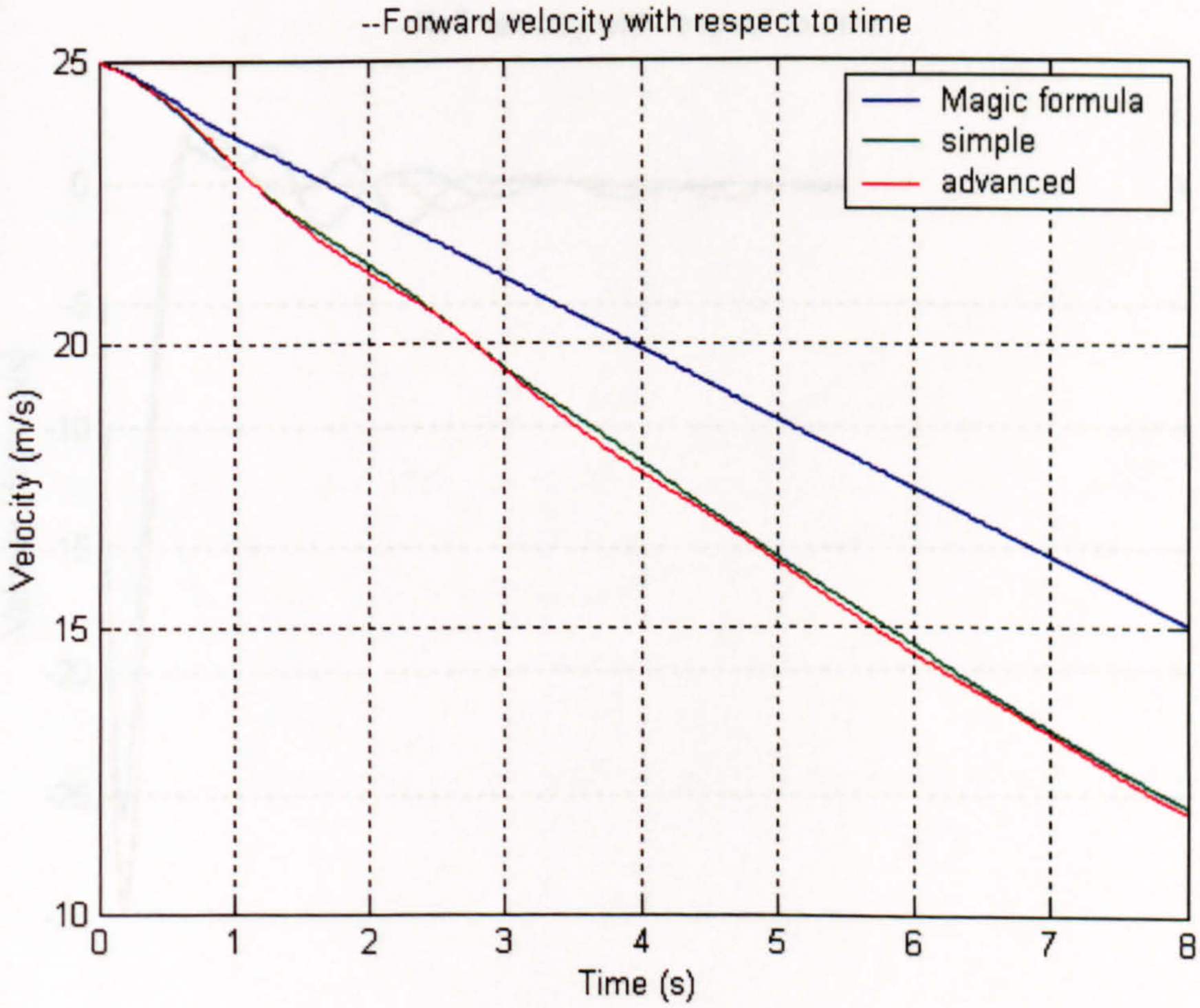

Figure 5. 9 Forward velocity response to a step-steer excitation

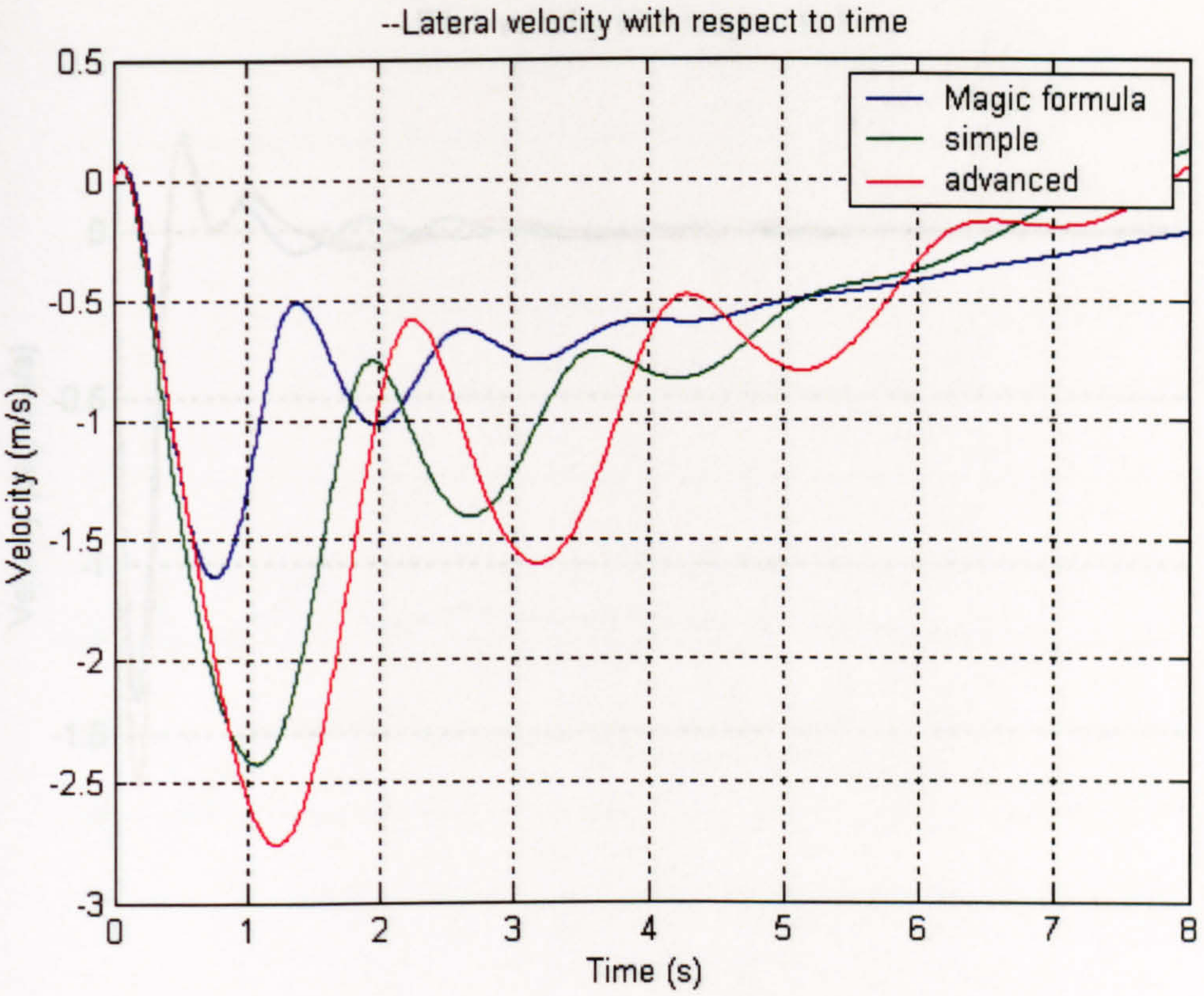

Figure 5. 10 Lateral velocity response to a step-steer excitation

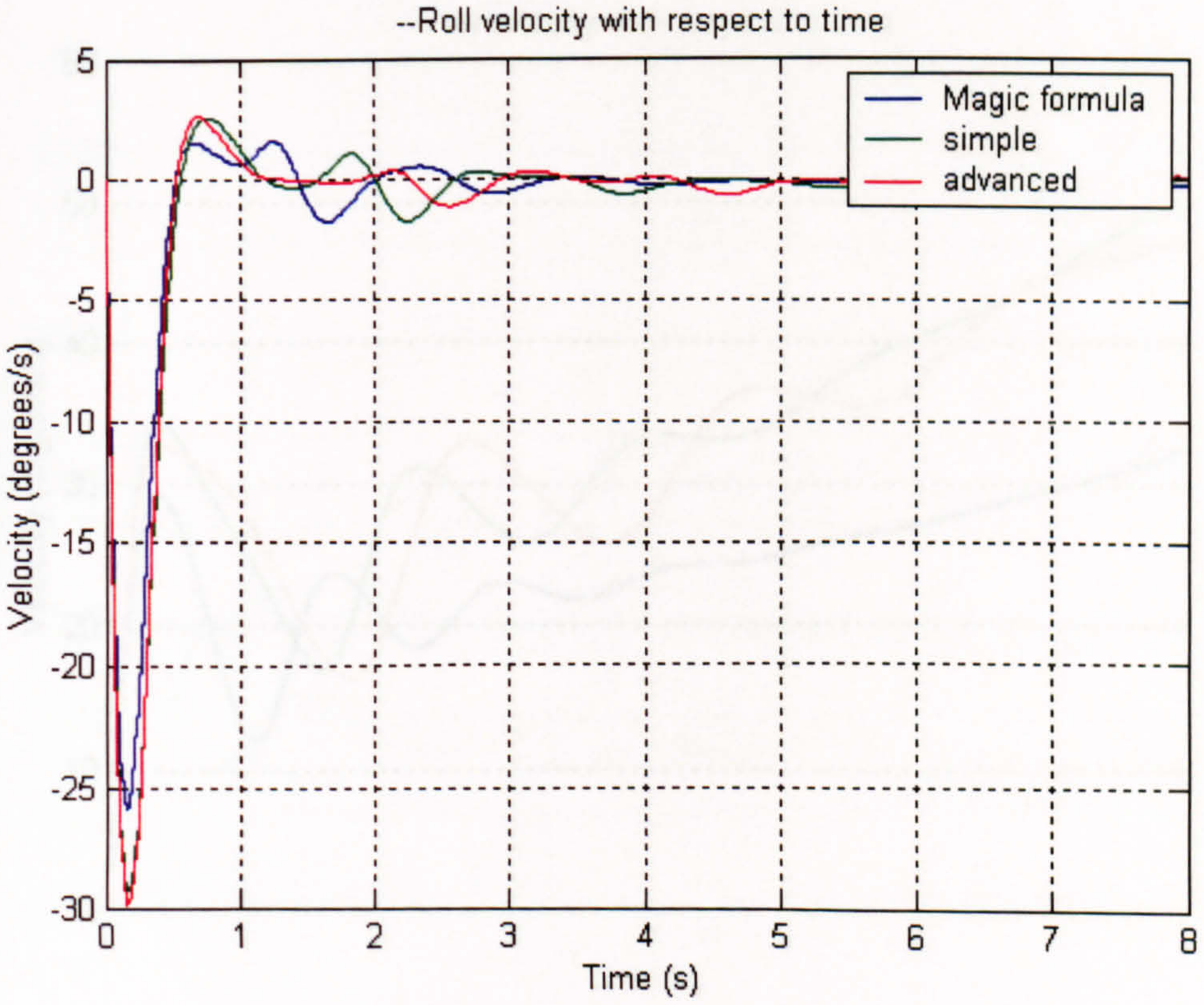

Figure 5. 11 Roll velocity response to a step-steer excitation

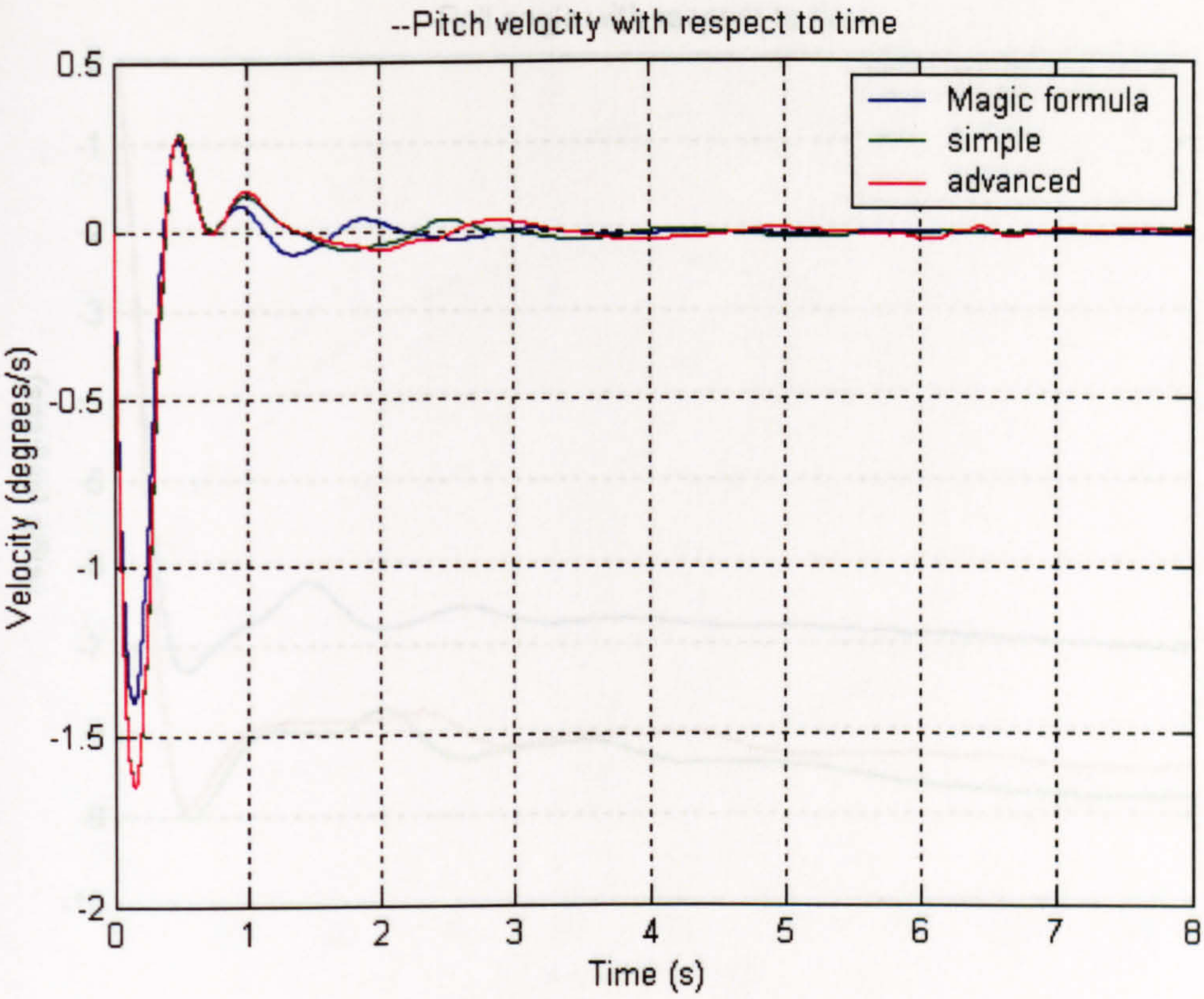

Figure 5. 12 Pitch velocity response to a step-steer excitation

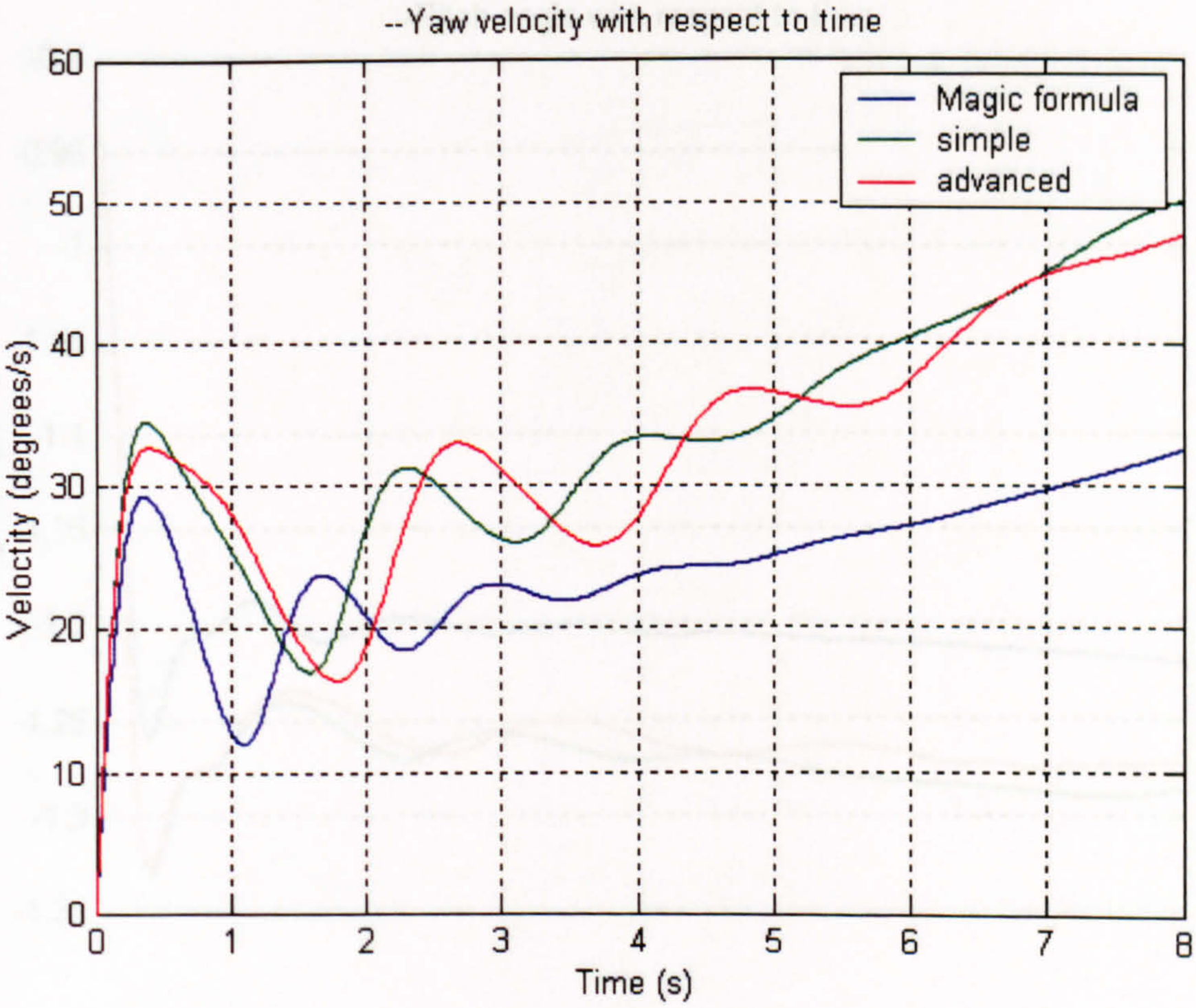

Figure 5. 13 Yaw velocity response to a step-steer excitation

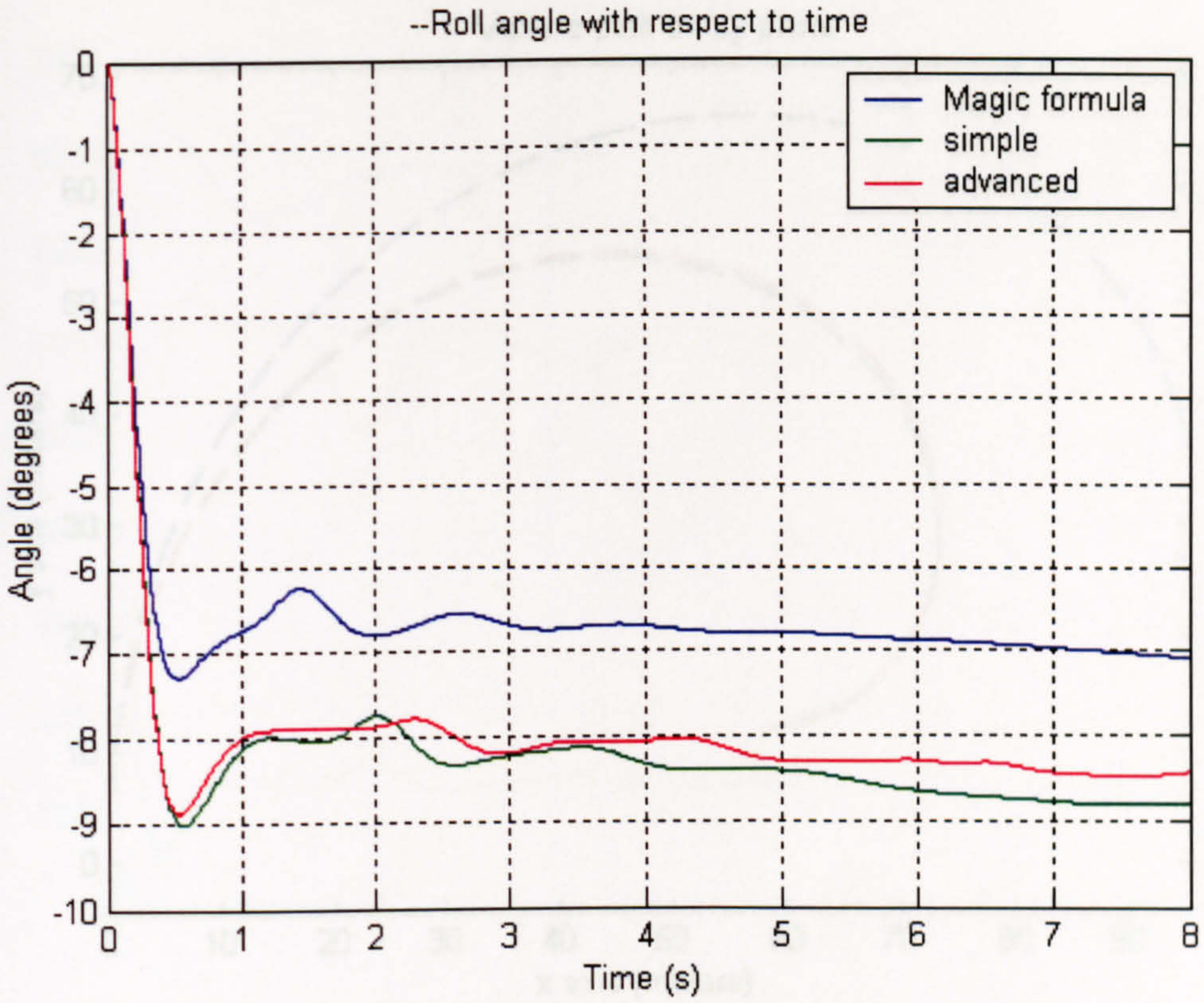

Figure 5. 14 Roll angle response to a step-steer excitation

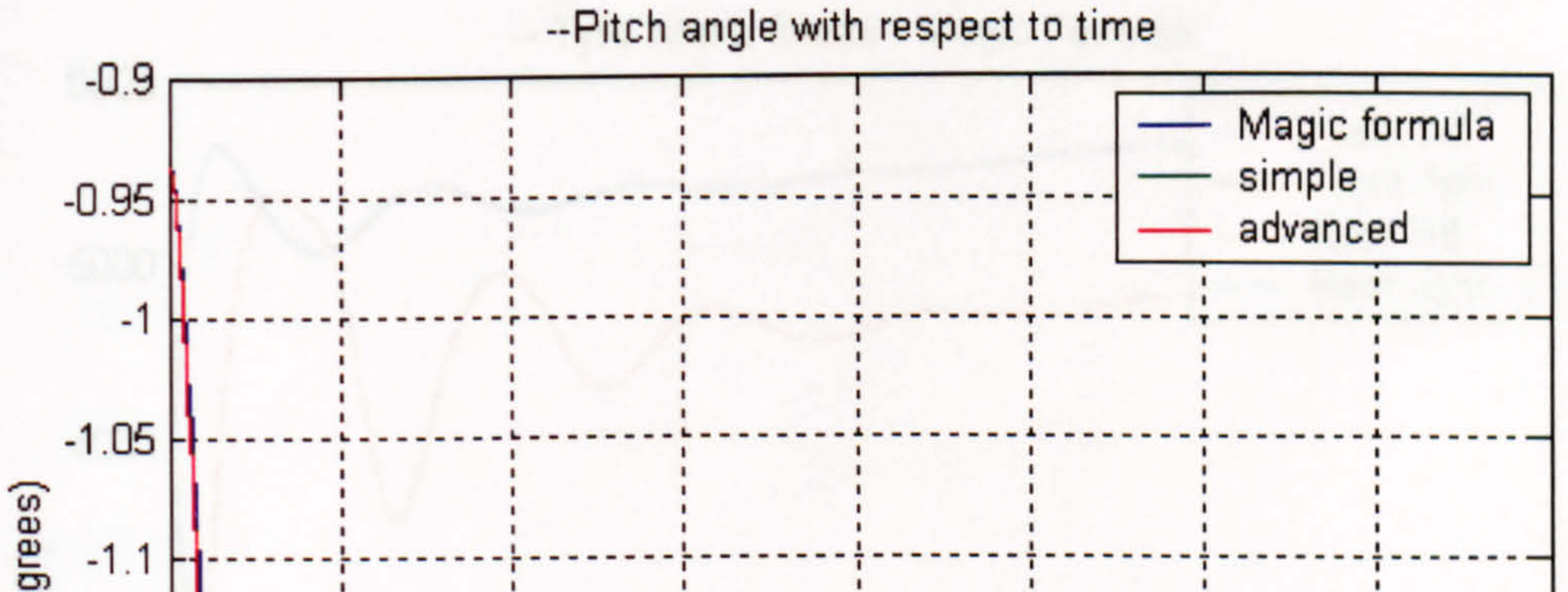

Figure 5. 15 Pitch-angle response to a step-steer excitation

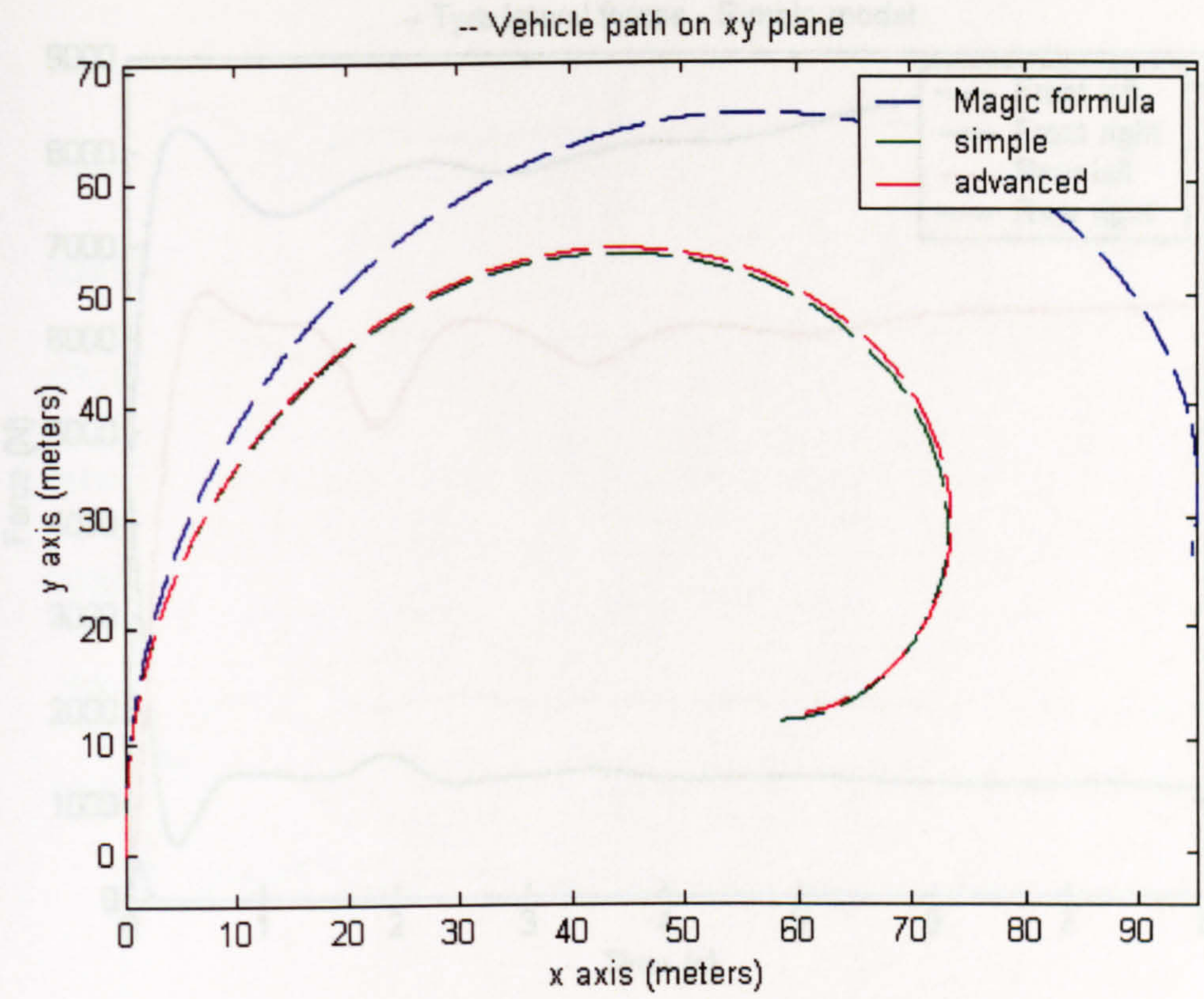

Figure 5. 16 The path of the vehicle under a step-steer manoeuvre

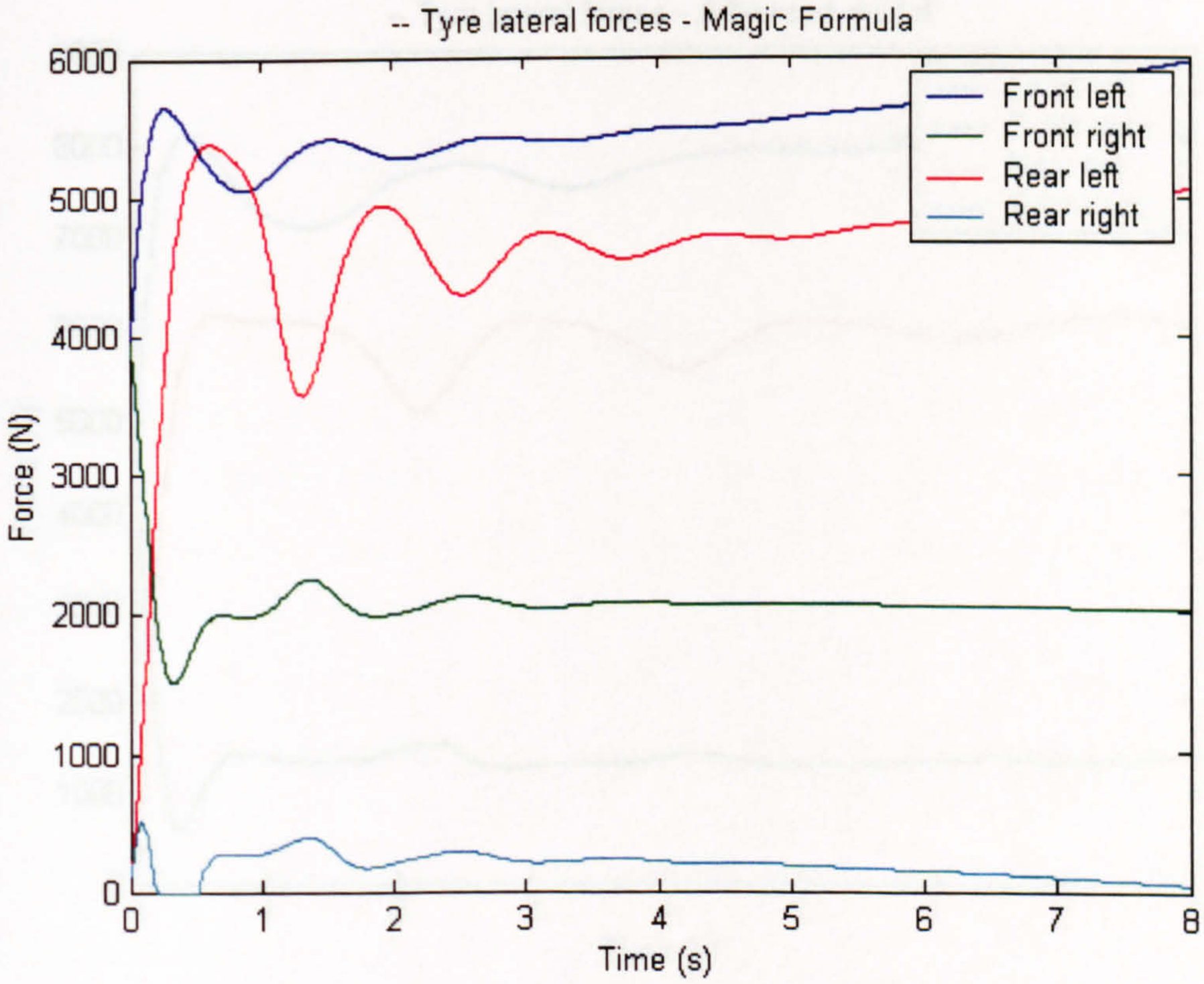

Figure 5. 17Lateral forces on all tyres as generated by the Magic Formula model

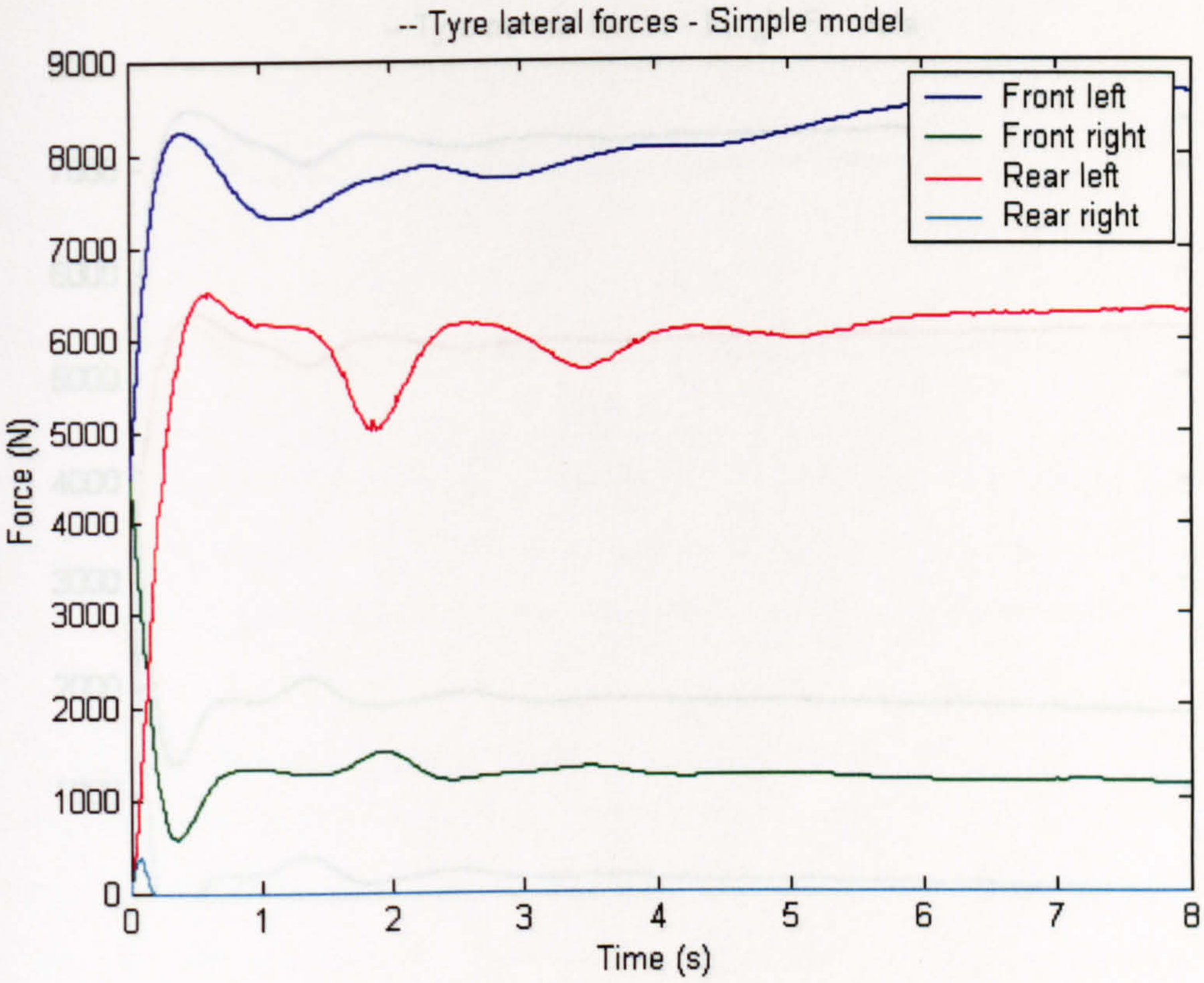

Figure 5. 18 Lateral forces on all tyres as generated by the simple physical tyre model

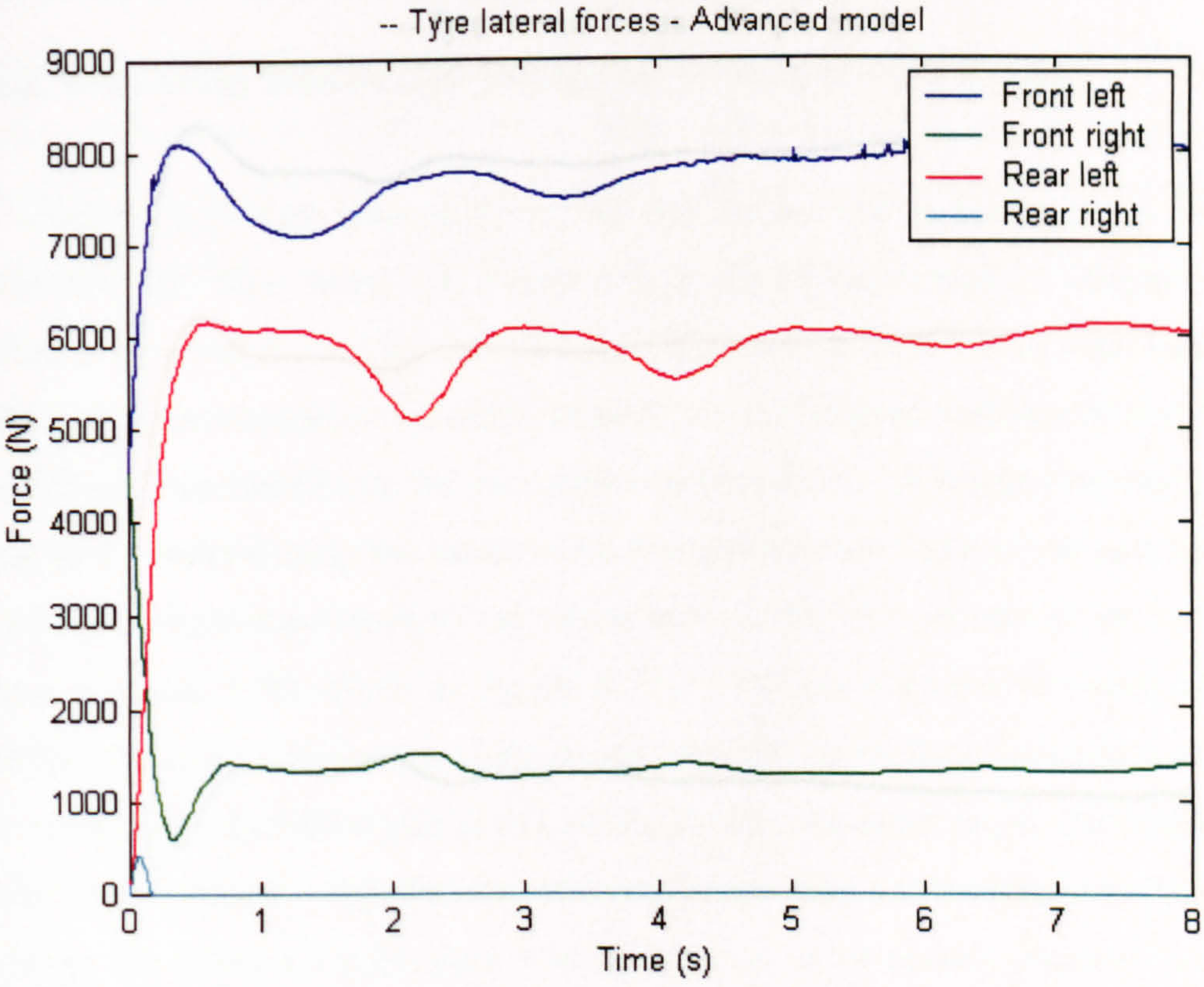

Figure 5. 19 Lateral forces on all tyres as generated by the advanced physical tyre model

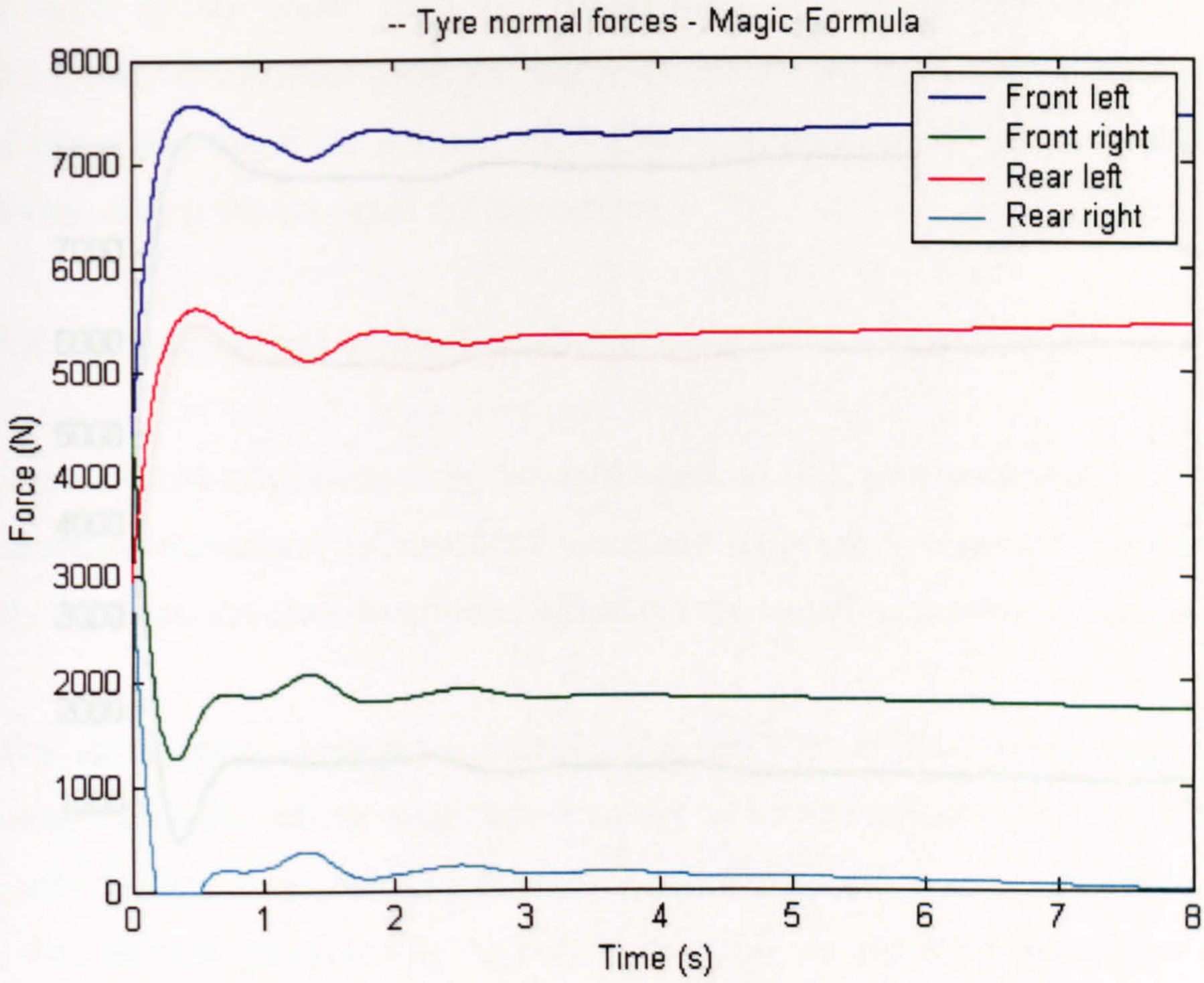

Figure 5. 20 Normal forces generated by the suspension - Magic Formula tyre model

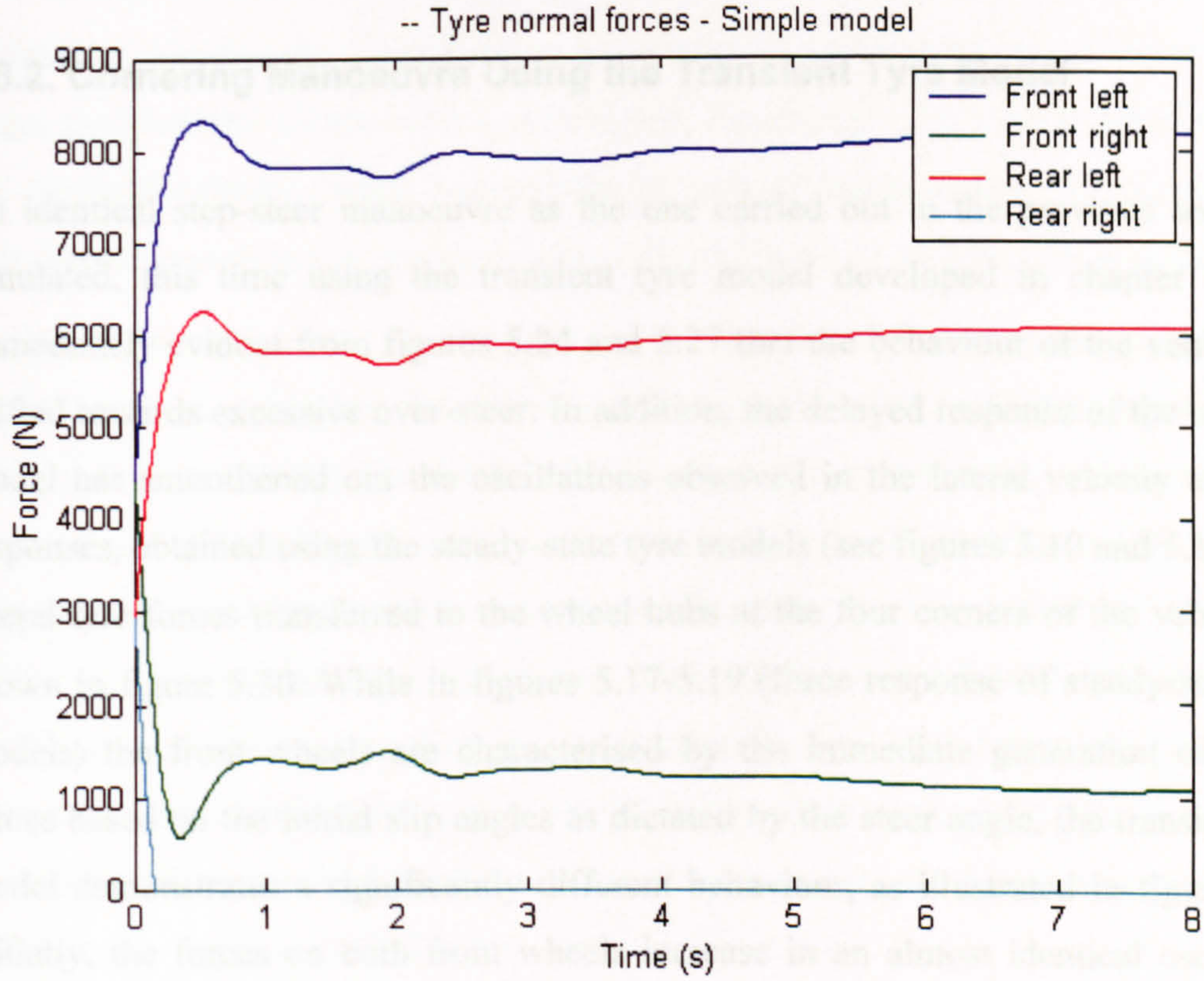

Figure 5. 21 Normal forces generated by the suspension – Simple physical model

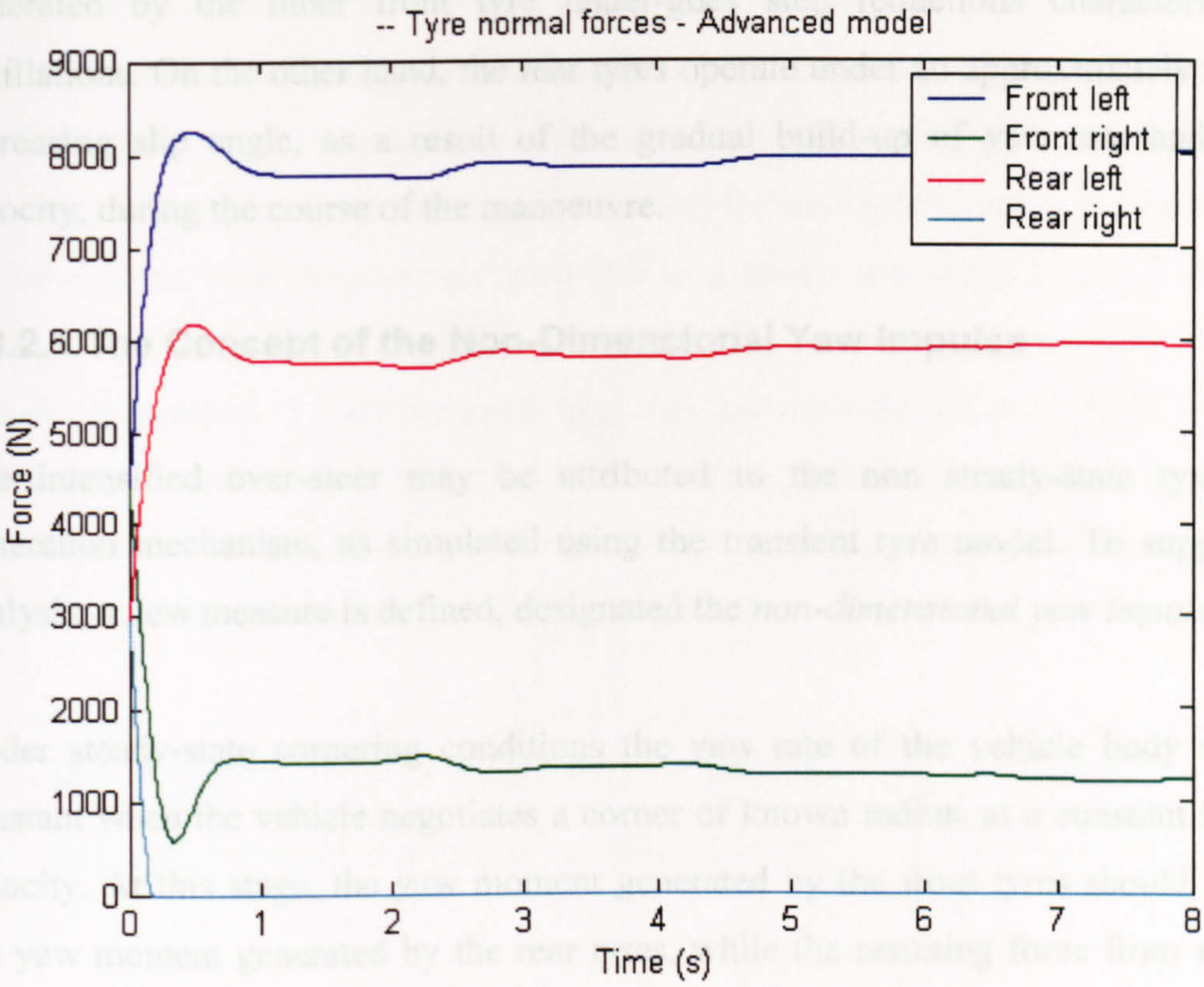

Figure 5. 22 Normal forces generated by the suspension – Advanced physical model

5.8.2. Cornering Manoeuvre Using the Transient Tyre Model

An identical step-steer manoeuvre as the one carried out in the previous section is simulated, this time using the transient tyre model developed in chapter 4. It is immediately evident from figures 5.24 and 5.27 that the behaviour of the vehicle has shifted towards excessive over-steer. In addition, the delayed response of the transient model has smoothened out the oscillations observed in the lateral velocity and yaw responses, obtained using the steady-state tyre models (see figures 5.10 and 5.13). The lateral tyre forces transferred to the wheel hubs at the four corners of the vehicle are shown in figure 5.30. While in figures 5.17-5.19 (force response of steady-state tyre models) the front wheels are characterised by the immediate generation of lateral forces based on the initial slip angles as dictated by the steer angle, the transient tyre model demonstrates a significantly different behaviour, as illustrated in figure 5.30. Initially, the forces on both front wheels increase in an almost identical oscillatory manner, demonstrating significant overshoot. As the effect of vehicle body-roll alters the lateral weight distribution in favour of the outer (left) wheels, the lateral force on the left wheel increases in a step-oscillatory manner. Similarly, the lateral force

generated by the inner front tyre under-goes step reductions characterised by oscillations. On the other hand, the rear tyres operate under an approximately linearly increasing slip angle, as a result of the gradual build-up of yaw rate and lateral velocity, during the course of the manoeuvre.

5.8.2.1 The Concept of the Non-Dimensional Yaw Impulse

The intensified over-steer may be attributed to the non steady-state tyre force generation mechanism, as simulated using the transient tyre model. To support the analysis, a new measure is defined, designated the *non-dimensional yaw impulse*.

Under steady-state cornering conditions the yaw rate of the vehicle body remains constant when the vehicle negotiates a corner of known radius, at a constant forward velocity. At this stage, the yaw moment generated by the front tyres should balance the yaw moment generated by the rear tyres, while the resulting force from all tyres balances the centrifugal inertial force applied on the centre of gravity of the vehicle. This situation holds true irrespective of the inherent handling characteristics of the vehicle i.e. whether the vehicle shows a tendency to under-steer or over-steer. At this stage, the character of the vehicle is revealed, for example, by attempting to increase the forward velocity, while maintaining a path of equal radius of curvature. As indicated in equation 2.4, the steer-angle δ_f will have to increase for a vehicle with under-steering behaviour, or decrease for a vehicle which demonstrates over-steer. Under transient conditions, the definition of under-steer and over-steer appears to be somewhat more ambiguous. Both under-steering and over-steering vehicles tend to increase their yaw rate when subjected to an increase in the steering angle. The yaw moment generated by the front tyres exceeds the yaw moment generated by the rear tyres and this results in a subsequent increase in yaw velocity, until the new equilibrium condition is reached, that is, if equilibrium is achieved at all. In an effort to compare the contribution of non-similar tyre models, such as the steady-state tyre models and the transient model, the non-dimensional yaw impulse is defined as follows:

$$\Gamma = \frac{\left|F_{y1}(t)\cdot\cos(\delta_1(t))+F_{y2}(t)\cdot\cos(\delta_2(t))\right|\mathrm{a}\left|-\right|F_{y3}(t)+F_{y4}(t)\left|\mathrm{b}\right|}{\left|F_{y1}(t)\cdot\cos(\delta_1(t))+F_{y2}(t)\cdot\cos(\delta_2(t))\right|\mathrm{a}\left|+\right|F_{y3}(t)+F_{y4}(t)\left|\mathrm{b}\right|} \tag{5.144}$$

The above non-dimensional quantity indicates the ratio of the resultant yaw moment generated by all tyres (magnitude of the vectorial addition of front and rear moments), divided by the sum of the front and rear yaw moments (scalar addition). In the event that front and rear moments balance each-other, the numerator becomes equal to zero. In the extreme case that the rear tyres fail to generate any force at all, Γ becomes equal to 1, and, finally, if the front tyres generate zero force, Γ equals -1. The term *impulse* is justified if both the numerator and denominator are multiplied by dt, in which case equation (5.144) indicates the ratio of rotational impulses. In order to assess the contribution of the tyre forces in yaw moment generation over a period of time Δt equation (5.144) may be written as follows:

$$\Gamma_{\Delta t} = \frac{|a|\int^{+\Delta t}\left|F_{y1}(t)\cdot\cos(\delta_1(t))+F_{y2}(t)\cdot\cos(\delta_2(t))\right|dt - |b|\int^{+\Delta t}\left|F_{y1}(t)+F_{y2}(t)\right|dt}{|a|\int^{+\Delta t}\left|F_{y1}(t)\cdot\cos(\delta_1(t))+F_{y2}(t)\cdot\cos(\delta_2(t))\right|dt + |b|\int^{+\Delta t}\left|F_{y1}(t)+F_{y2}(t)\right|dt} \quad (5.145)$$

The values of Γ or $\Gamma_{\Delta t}$ are strongly related to the yaw response of a vehicle and provide a comparative measure of the cornering characteristics of a vehicle under transient manoeuvres. It should be noted that these values depend on the interaction between the vehicle and the tyre. For example, when using the Magic Formula tyre model, the load dependency of the tyre characteristics in relation to the various weight transfers may result in different values of Γ and $\Gamma_{\Delta t}$ for a specific vehicle performing a pre-defined manoeuvre on different tyres.

5.8.2.2 Comments on the Non-Dimensional Yaw Impulse

Other measures are often used in order to assess the cornering response of vehicles. In this section, the basic properties of the non-dimensional (normalised) yaw impulse will be discussed briefly, in relation to some of these frequently used measures. Firstly, one may assume that observing the yaw rate alone provides the same insight into the behaviour of the vehicle. The advantages will be shown by considering equation 5.77 which describes the yaw response in the simple case of the bicycle model. For the sake of simplicity a snapshot is considered where the front and rear slip angles are equal to a_f and a_r respectively. It is assumed that the steer-angle is sufficiently small so that the lateral forces are approximately perpendicular to the x-

axis of the vehicle. Furthermore, linear tyres are used in the model. Under these circumstances, equation 5.77 can be re-written as follows, if only the tyre forces are considered:

$$C_{af} \cdot a_f \cdot |a| - C_{ar} \cdot a_r \cdot |b| = I_{zz} \cdot (dr/dt) \tag{5.146}$$

It becomes obvious from equation (5.146) that for a different moment of inertia I_{zz}, different yaw rates would be predicted over a short period of time Δt for which the slip angles are considered to remain constant. Similarly, if the cornering stiffness of both the front and rear tyres is doubled, a twice as high yaw rate is predicted. The increased yaw rate cannot be attributed to an increased contribution from the front tyres or a smaller contribution from the rear tyres. Unlike the yaw rate, the normalised yaw impulse appears to concentrate on the relative contribution of the front and rear tyres. Thus, equation (5.145) results in the same value of $\Gamma_{\Delta t}$ in both the cases examined above. By looking simultaneously at the yaw rate and the normalised yaw impulse, one may arrive to a conclusion as to whether the yaw rate builds up faster due to an alteration in the balance of the vehicle, or due to stiffer – more responsive tyres, both in the front and rear ends. Of course, if the balance is altered by changing the properties of one pair of tyres, front or rear, the normalised yaw impulse would capture the effect.

A similar measure, employed by Milliken and Rice in the Moment Method [116] is the yawing moment coefficient, defined as the total moment about the z-axis divided by the product of the vehicle weight and the wheelbase. It is observed that this measure, although normalised, is not insensitive to changes such as the alteration – by the same factor – of both the front and rear cornering stiffness. In a way, the measure provides an indication of the total yaw moment generated by the tyres, but is unable to reveal whether this yaw moment is due to a substantial contribution by both ends or due to an unequal contribution between the front and rear sets of tyres.

Finally, considering equation (5.144) and assuming a vehicle with provision for rear-wheel steering, it becomes obvious that the normalised yaw impulse equals -1 at the onset of rear-wheel steering. As a conclusion, the normalised yaw impulse may serve

as a clear and simple measure of the transient cornering response of a vehicle. By definition, the measure is sensitive only to the balance between front and rear lateral forces. Off course, this balance is sensitive to a number of other parameters such as the lateral and longitudinal weight transfers which in turn depend on the suspension properties and the position of the centre of mass of the vehicle. All these parameters may vary during the course of a single transient manoeuvre and the normalised yaw impulse is expected to vary as well in a complex, non-linear manner. Nevertheless, if any alterations result in the reduction of $\Gamma_{\Delta t}$ as calculated over a pre-specified period of time, one may be certain that the vehicle has become less over-steering in terms of transient behaviour. A full sensitivity analysis of the normalised yaw impulse to various vehicle and tyre parameters is yet to be undertaken and is expected to reveal the strengths and weaknesses of the proposed measure.

5.8.2.3 Application of the Non-Dimensional Yaw Impulse

In the present work, Γ and $\Gamma_{\Delta t}$ are employed as a rough measure, in order to aid the quantification of the delayed response of the rear tyres in the case of the transient tyre model. While the front tyres also exhibit a delayed response compared to the steady-state tests, it is evident from figure 5.30 that the rate of force generation by the front left tyre is much higher than the corresponding force by the rear left tyre. This effect is quantified in figure 5.32, which shows the non-dimensional yaw impulse with respect to time. $\Gamma_{\Delta t}$ is calculated over a period of 0.6 s from the initiation of the manoeuvre and is found to be equal to 0.2321. The corresponding values of Γ for the vehicle running on the advanced physical tyre model are shown in figure 5.33. As expected, the value of $\Gamma_{\Delta t}$ over the same period of time is significantly lower ($\Gamma_{\Delta t}$=0.1529). It is worth noting that in both figures 5.32 and 5.33, Γ starts from a value of 1, which indicates the sole contribution of the front tyres to the generation of yaw moment.

In general, the aforementioned analysis implies that, when the transient response of the tyres is coupled to the dynamic response of the vehicle a whole, minor delays and phase lags might result in major alterations in its handling behaviour.

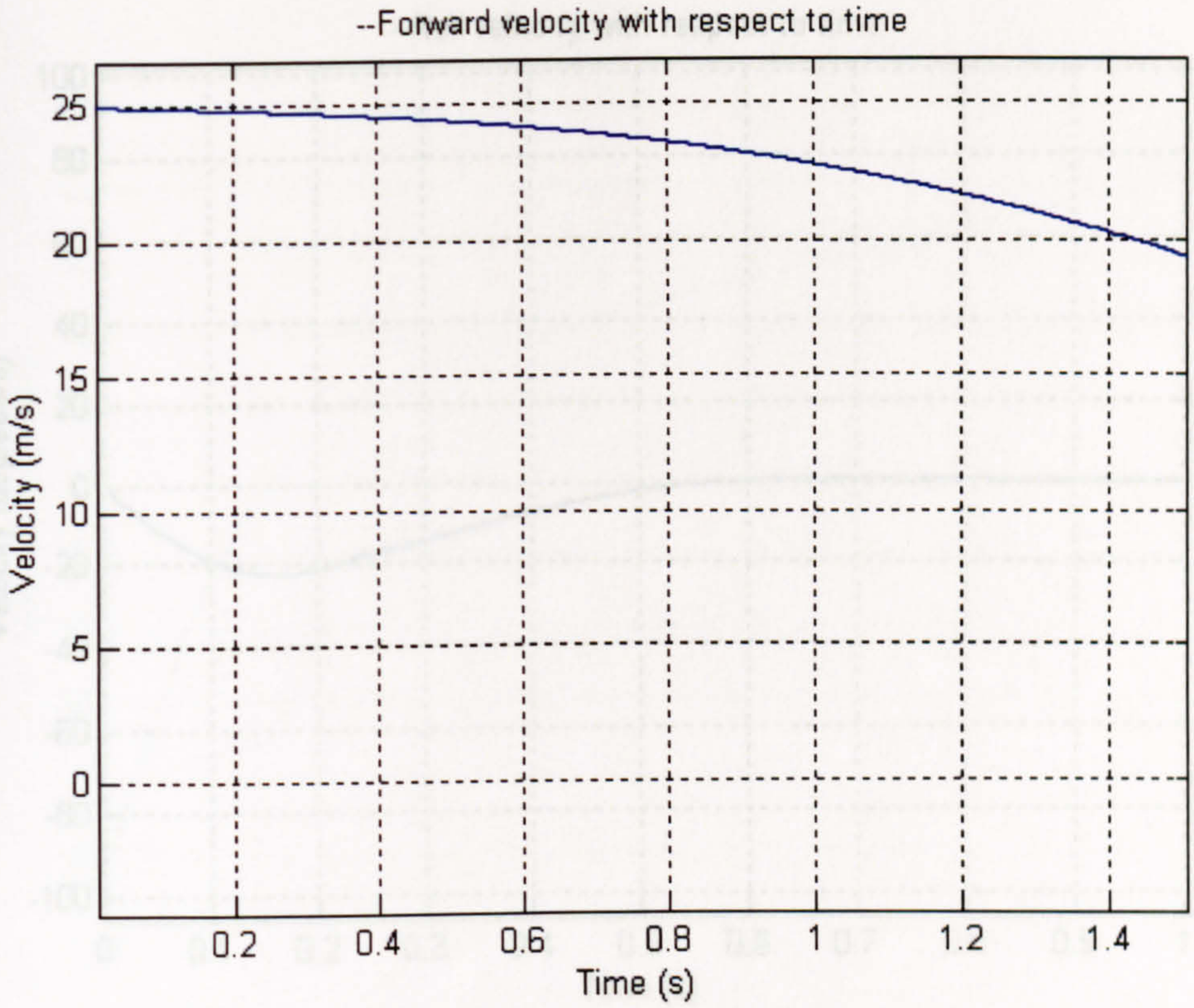

Figure 5. 23 Forward velocity response to a step-steer excitation – Transient tyre model

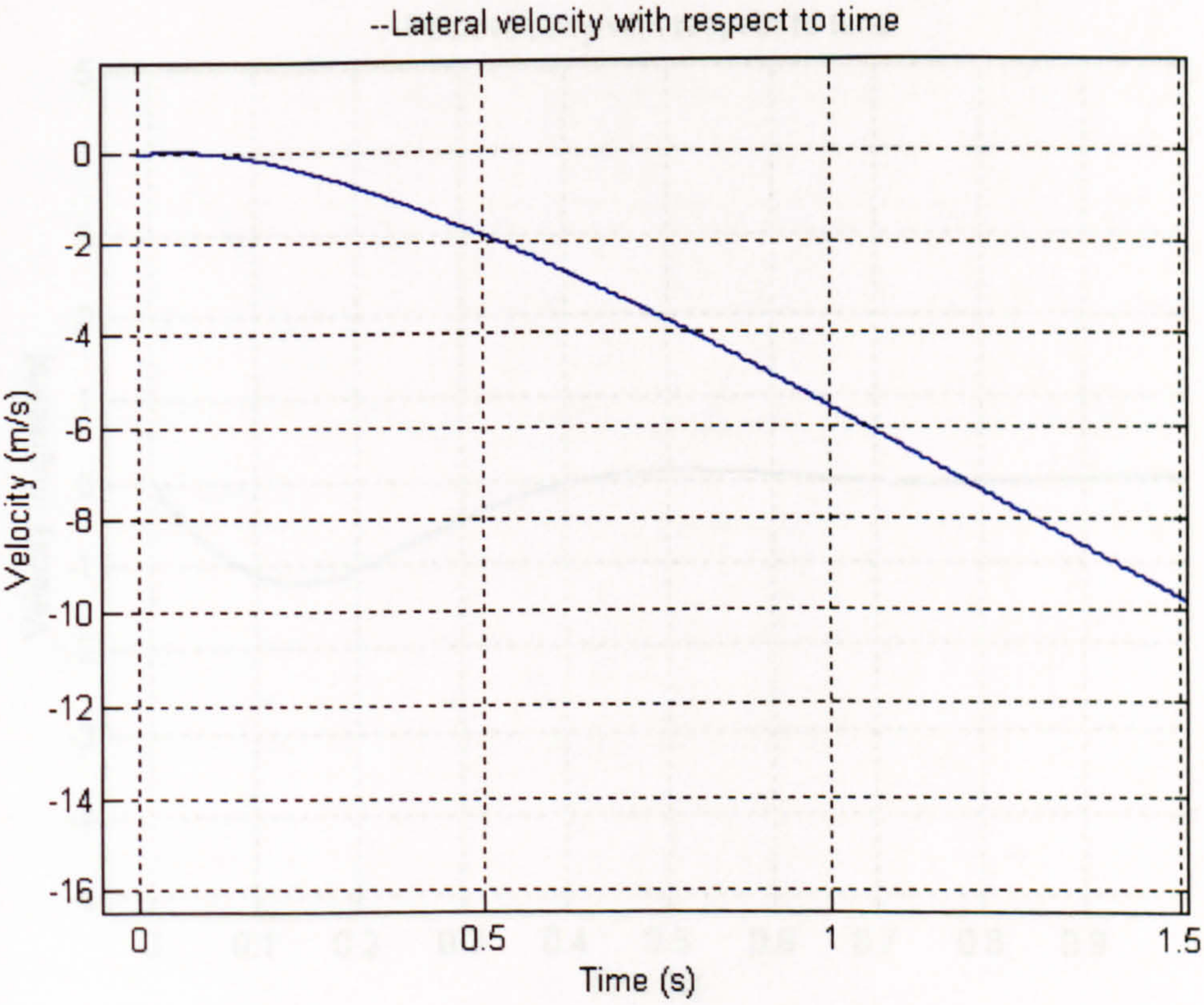

Figure 5. 24 Lateral velocity response to a step-steer excitation – Transient tyre model

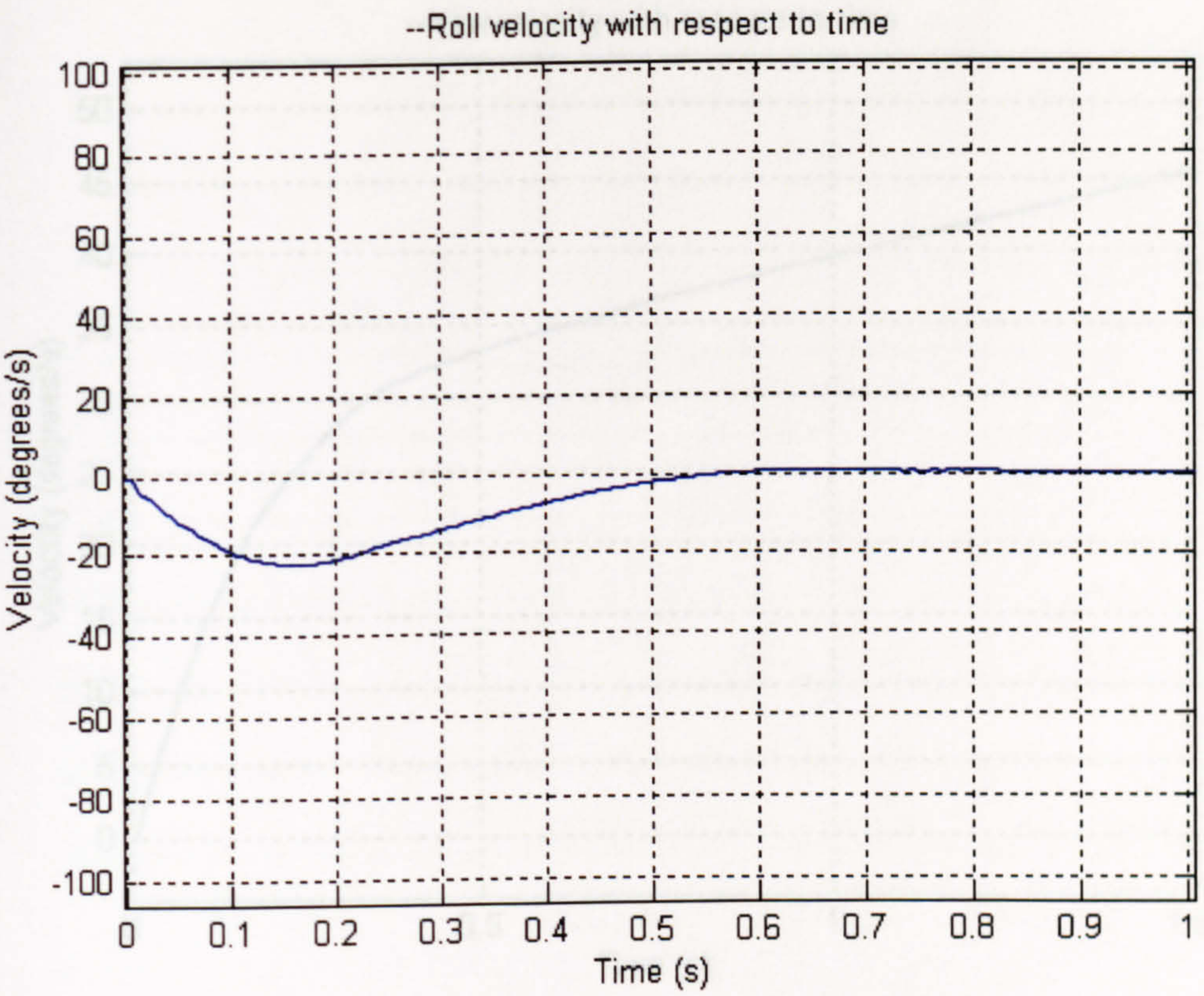

Figure 5. 25 Roll velocity response to a step-steer excitation – Transient tyre model

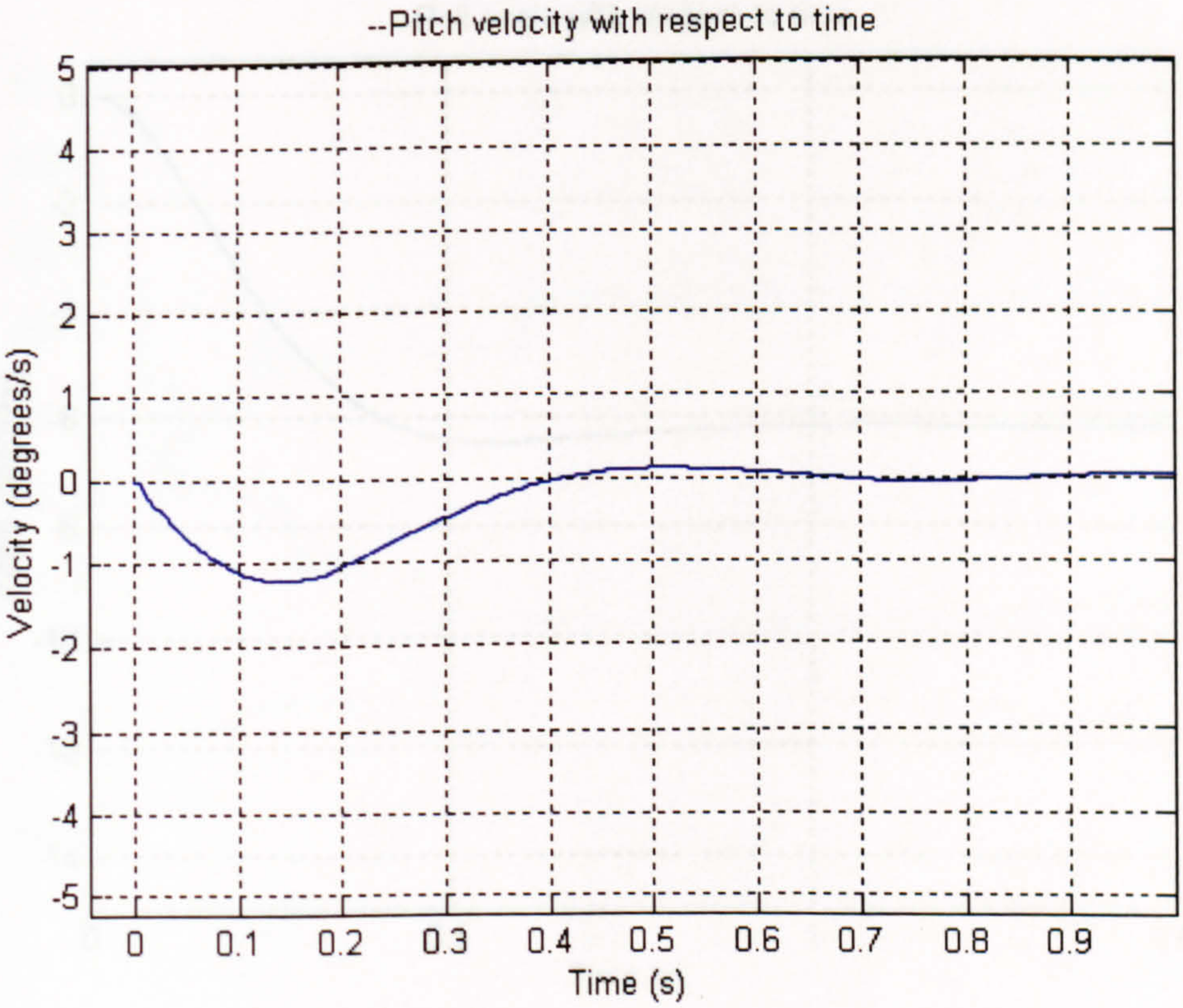

Figure 5. 26 Pitch velocity response to a step-steer excitation – Transient tyre model

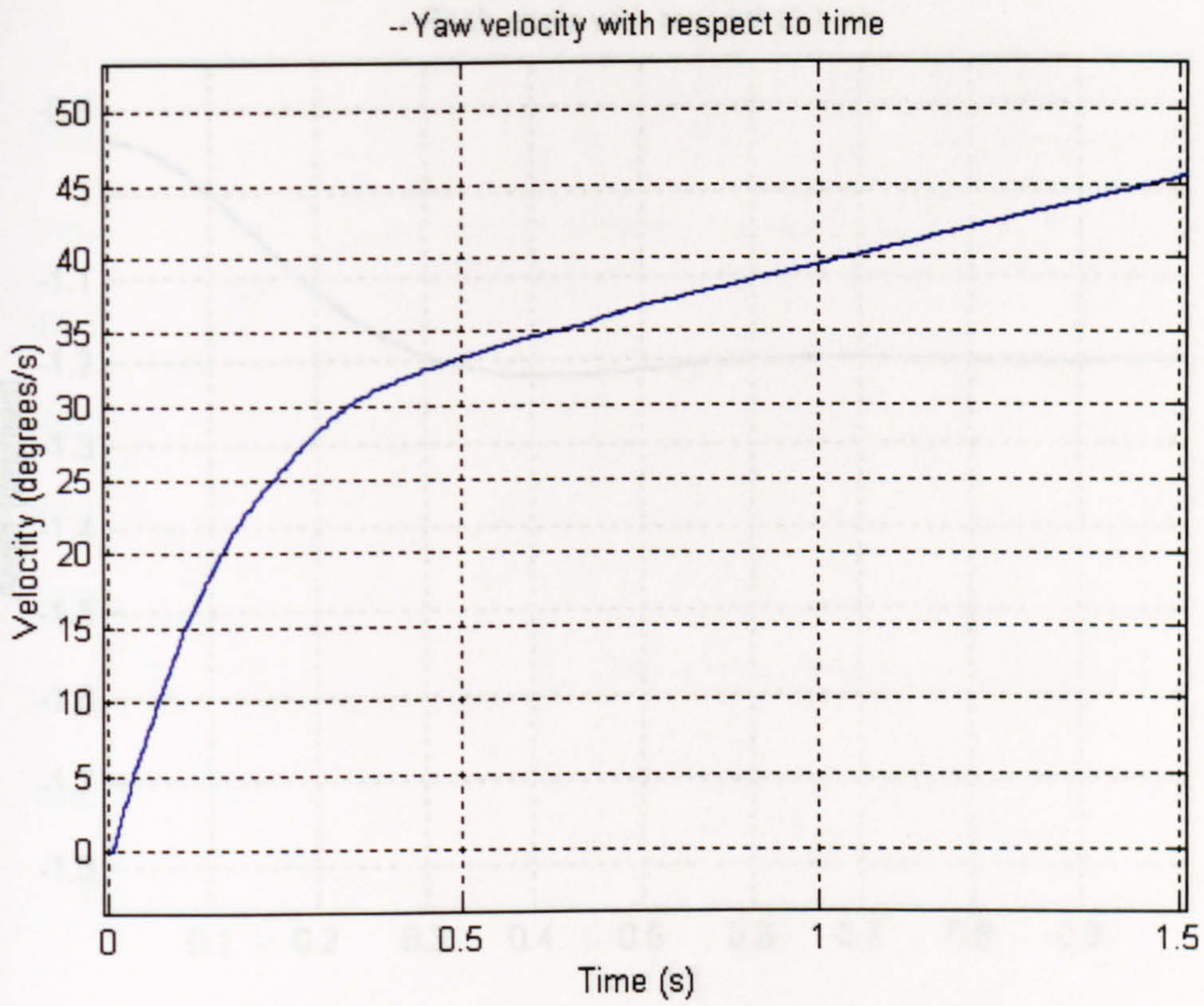

Figure 5. 27 Yaw velocity response to a step-steer excitation – Transient tyre model

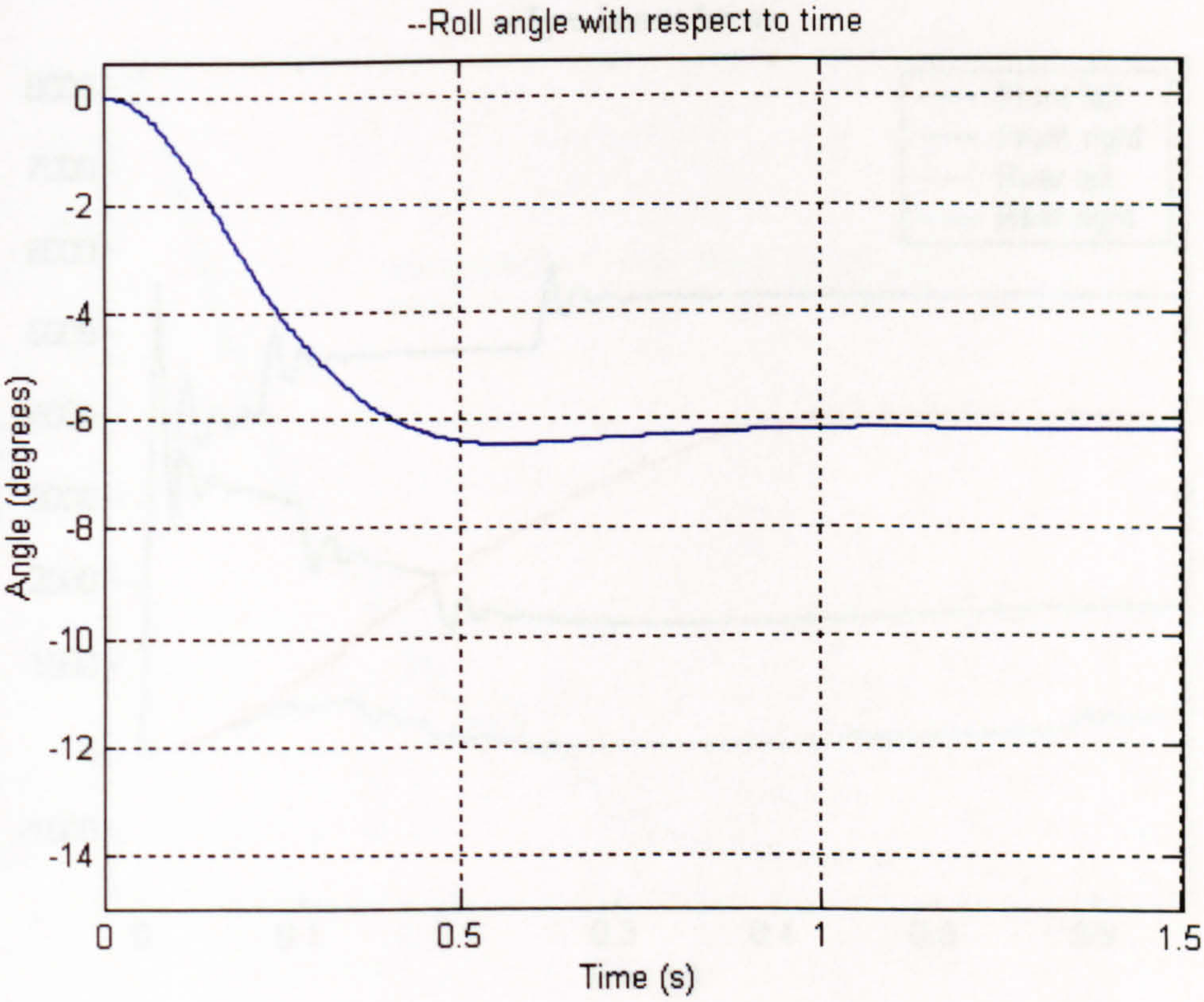

Figure 5. 28 Roll angle response to a step-steer excitation – Transient tyre model

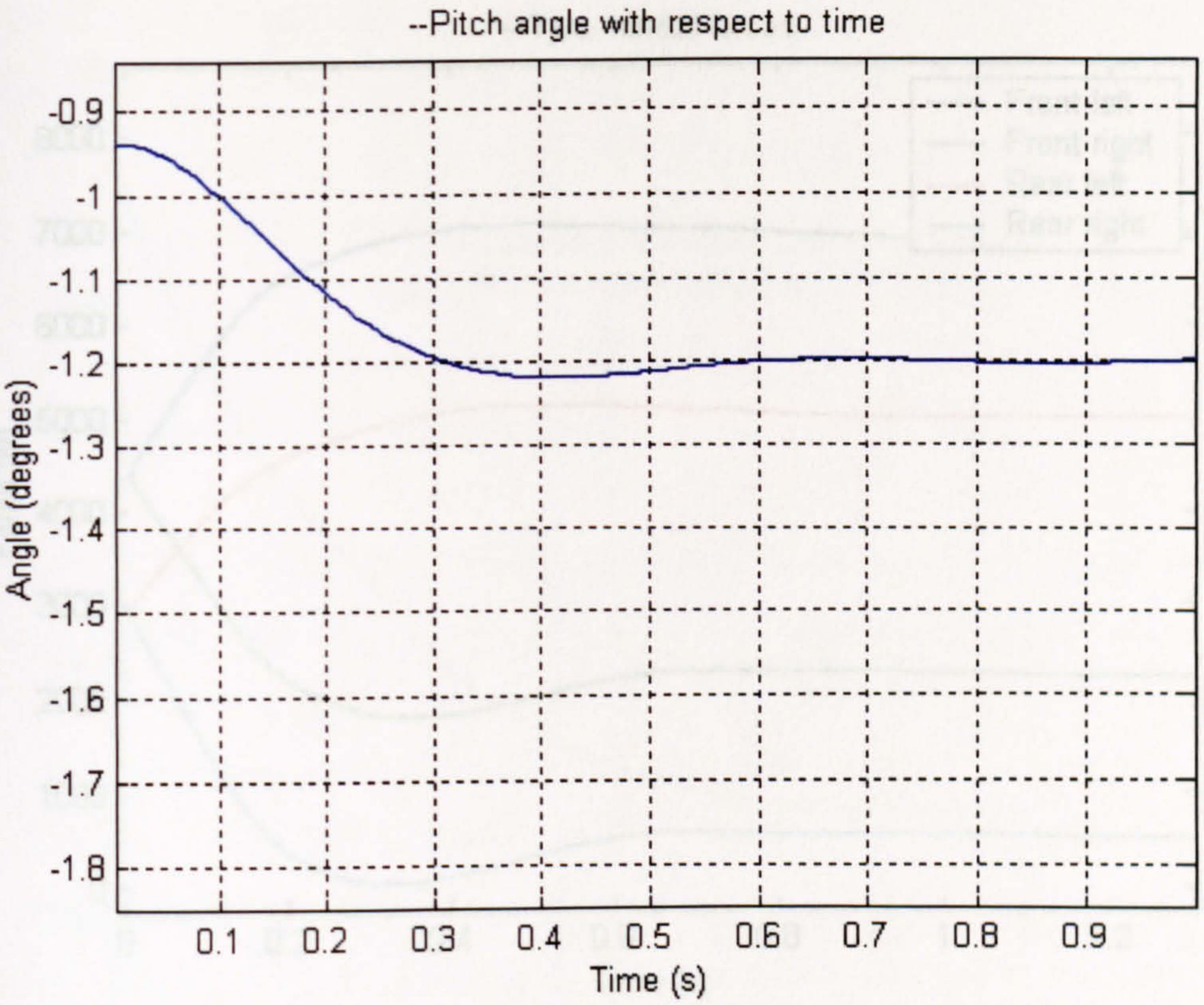

Figure 5. 29 Pitch angle response to a step-steer excitation – Transient tyre model

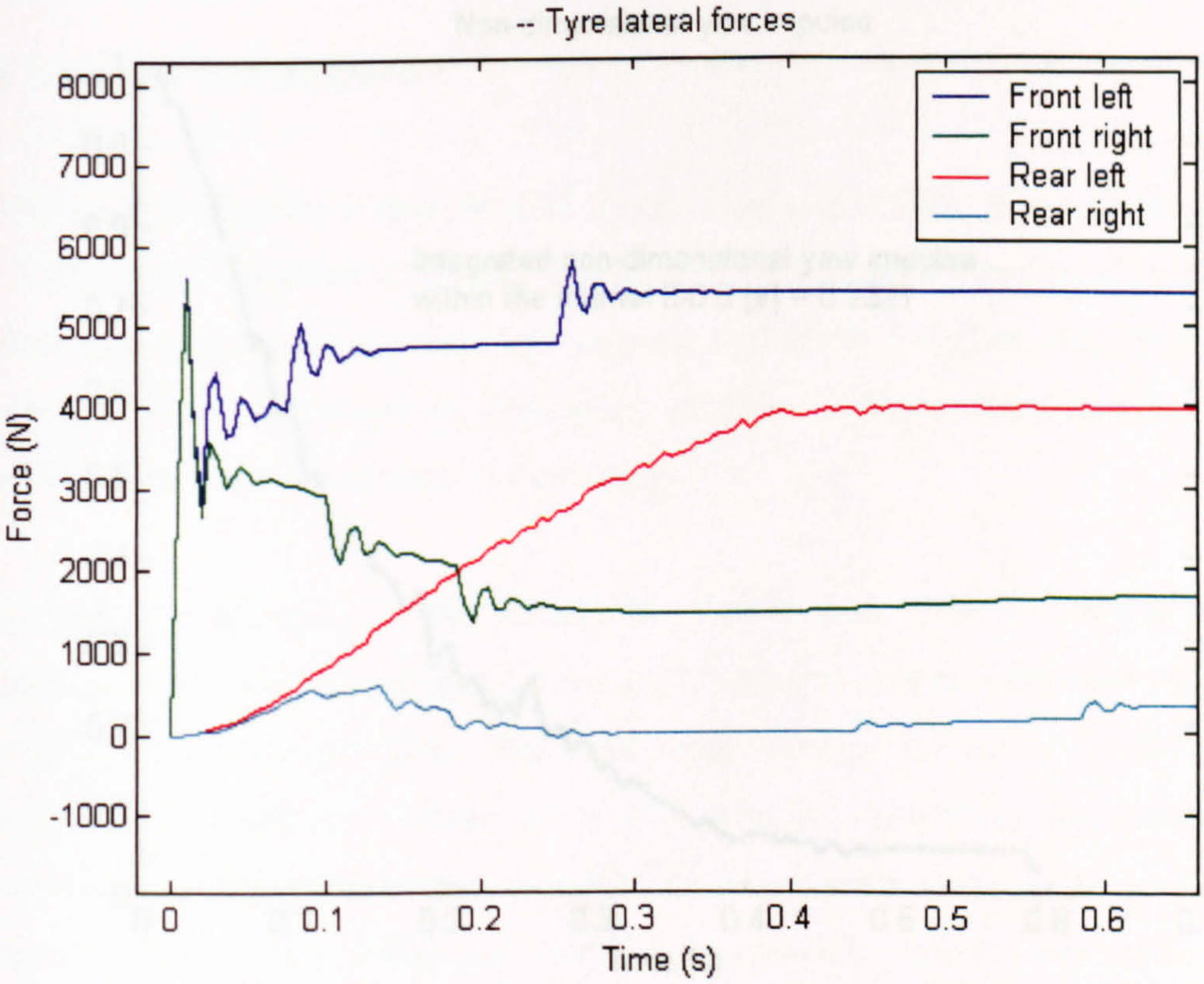

Figure 5. 30 Lateral forces on all tyres as generated by the transient tyre model

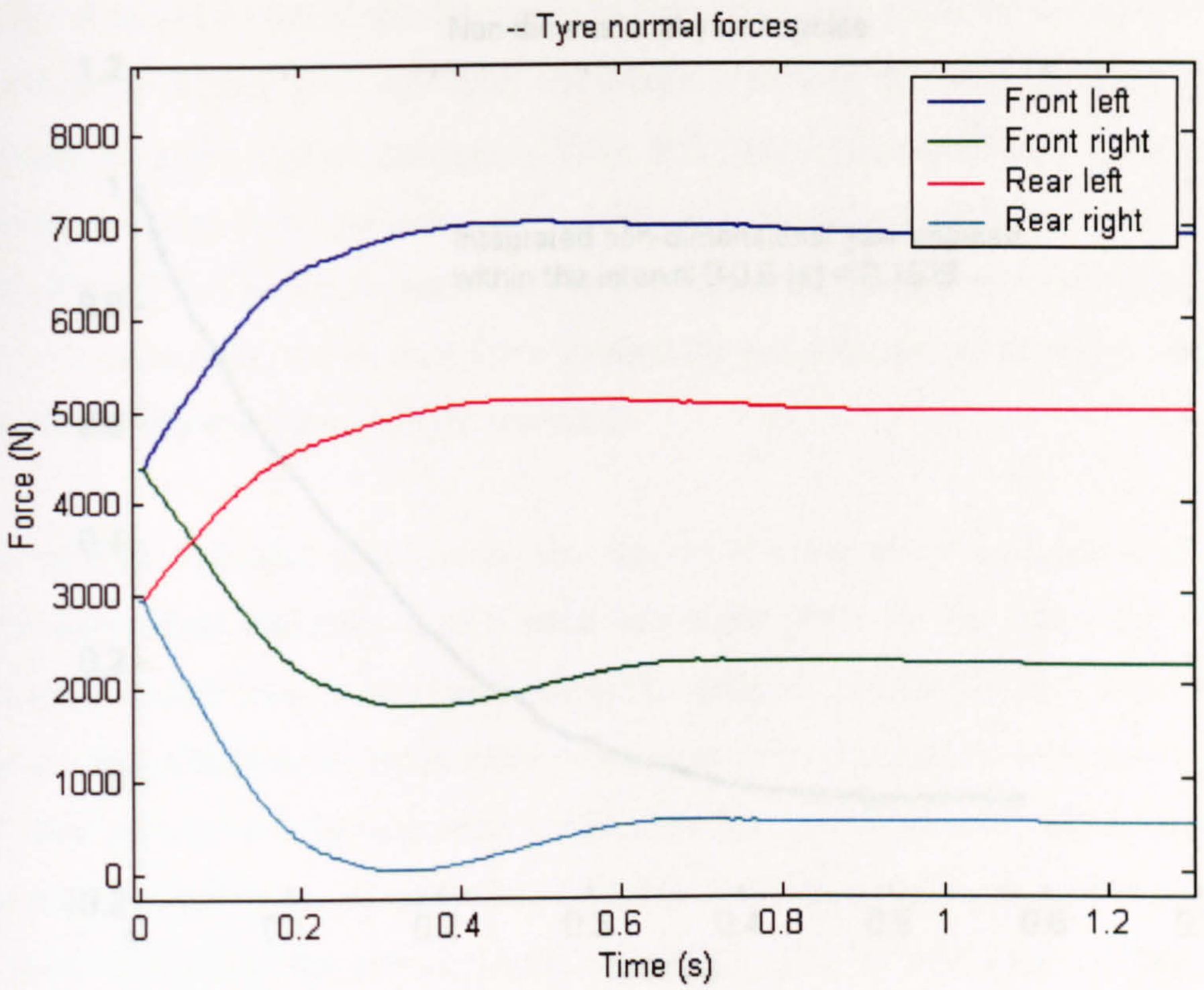

Figure 5. 31 Normal forces generated by the suspension – Transient tyre model

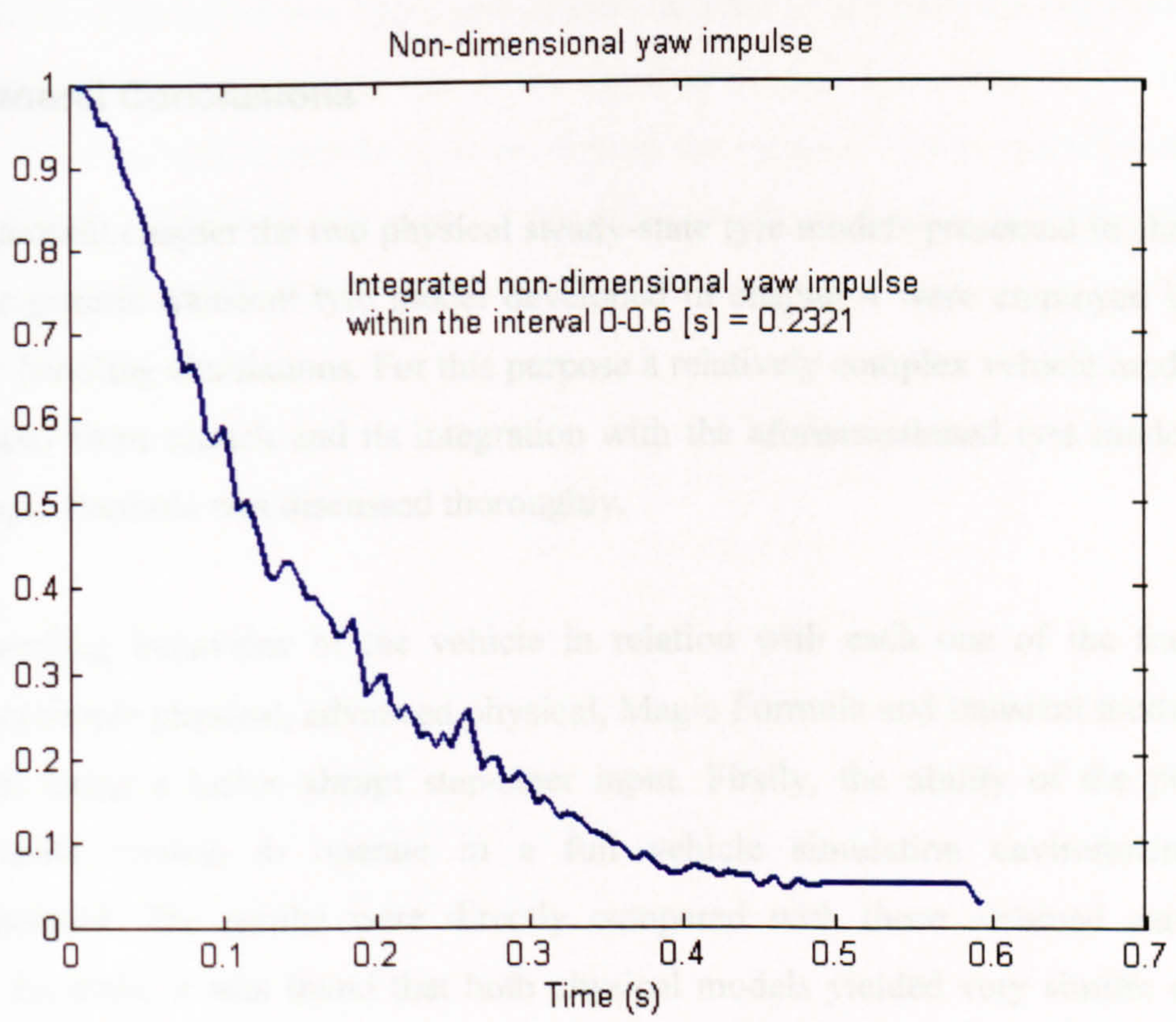

Figure 5. 32 Non-dimensional yaw impulse as generated by the transient tyre model

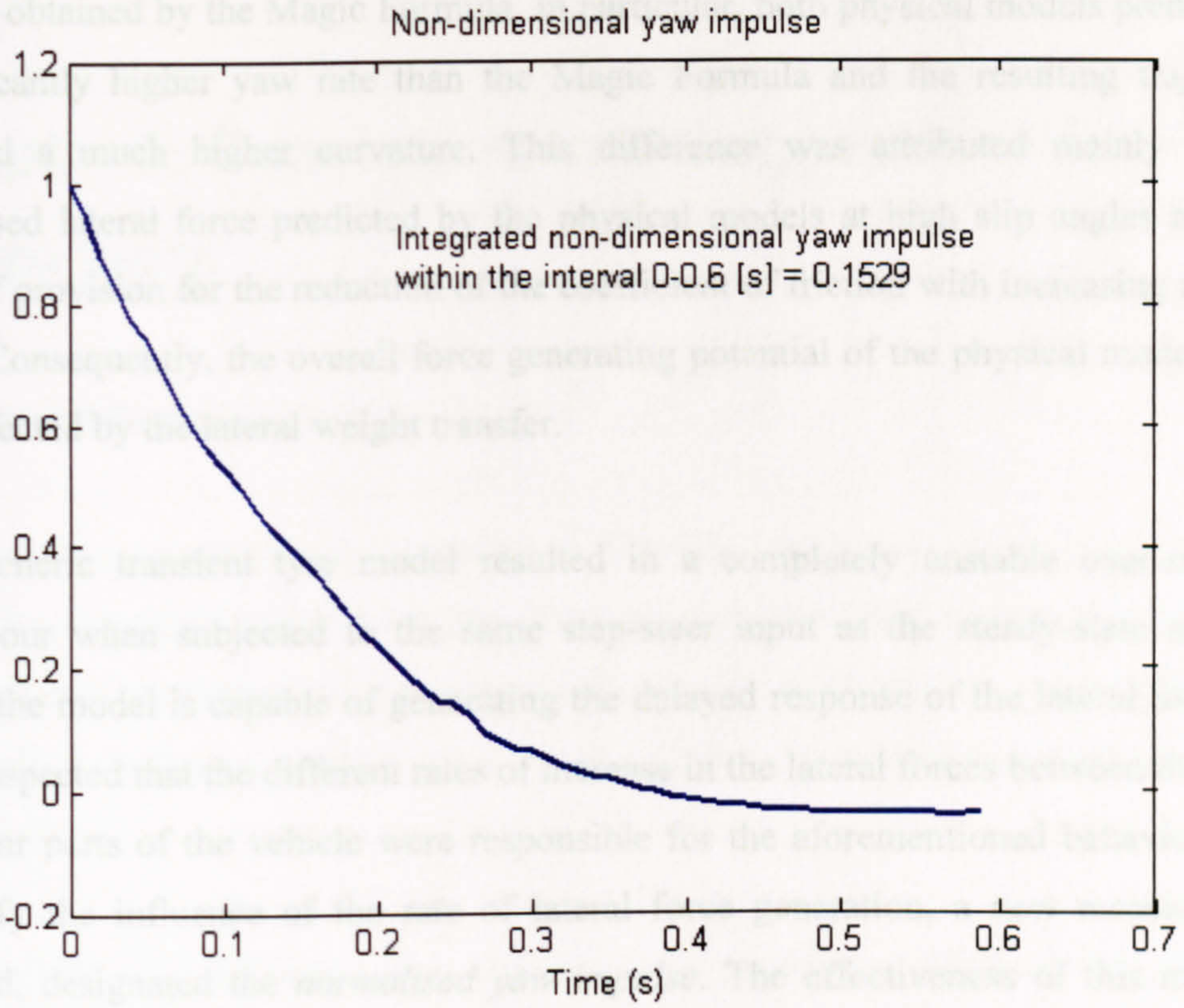

Figure 5. 33 Non-dimensional yaw impulse as generated by the advanced physical tyre model

5.9 General Conclusions

In the present chapter the two physical steady-state tyre models presented in chapter 3 and the generic transient tyre model developed in chapter 4 were employed in full-vehicle handling simulations. For this purpose a relatively complex vehicle model was developed from scratch and its integration with the aforementioned tyre models and the Magic Formula was discussed thoroughly.

The handling behaviour of the vehicle in relation with each one of the four tyre models (simple physical, advanced physical, Magic Formula and transient model) was assessed using a rather abrupt step-steer input. Firstly, the ability of the physical steady-state models to operate in a full vehicle simulation environment was demonstrated. The results were directly compared with those obtained using the Magic Formula. It was found that both physical models yielded very similar results. This was expected since the main difference between the two models lies in the calculation of the self-aligning moment at large slip angles. However, large differences were observed when comparing the results from the physical models to the

results obtained by the Magic Formula. In particular, both physical models predicted a significantly higher yaw rate than the Magic Formula and the resulting trajectory showed a much higher curvature. This difference was attributed mainly to the increased lateral force predicted by the physical models at high slip angles and the lack of provision for the reduction of the coefficient of friction with increasing normal load. Consequently, the overall force generating potential of the physical models was not affected by the lateral weight transfer.

The generic transient tyre model resulted in a completely unstable over-steering behaviour when subjected to the same step-steer input as the steady-state models. Since the model is capable of generating the delayed response of the lateral forces, it was suspected that the different rates of increase in the lateral forces between the front and rear parts of the vehicle were responsible for the aforementioned behaviour. To quantify the influence of the rate of lateral force generation, a new measure was derived, designated the *normalised yaw impulse*. The effectiveness of this measure was discussed briefly and its relation with the yaw rate was analysed to some extent. Finally, the normalised yaw impulse was used in order to compare the response of the advanced physical model with that of the transient model. In the case of the transient model, the normalised yaw impulse confirmed the increased force contribution from the front tyres, while in the case of the steady-state model it was shown that the contribution was better distributed between the front and rear tyres.

Chapter 6: Conclusion and Suggestions for future work

6.1 Overall Conclusion

The present research provides an integrated, detailed picture of the influence of tyre modelling in vehicle handling studies. The main volume of the work is devoted to the mathematical modelling of the pneumatic tyre. In particular, a purely numerical approach is followed, mainly as a result of the computational power available nowadays.

In the field of steady-state tyre analysis, it is found that physical tyre models, possessing a moderate number of parameters with direct physical meaning, can describe the handling behaviour of tyres relatively well. The modelling of the tyre is closely related to the contact mechanics behaviour of rubber in stick-slip, and attention is paid to the velocity dependent friction characteristics. In addition, the successful representation of the longitudinal pressure distribution has been a major concern. It is shown that velocity dependent deviations in pressure distribution largely affect the generation of self-aligning moment, whilst the tyre forces remain unaffected. Numerical analysis has been successfully employed in order to predict, in a physical manner, the effect of viscoelastic friction and hysteresis in the tyre force and moment generation procedure. This approach enables the operation of a tyre model in a wide range of conditions with some confidence that the corresponding condition-dependent properties will change in a way that reflects the undergoing physical phenomena. Despite its generally accepted advantages, the Magic Formula tyre model currently lacks the ability to account for phenomena such as the influence of a velocity dependent normal pressure distribution.

In the area of transient tyre analysis, the significance of accurate prediction of friction is addressed. It is pointed out that the stick-slip behaviour of rubber may be represented by a conventional stick-slip friction law, in combination with the use of a

viscoelastic Kelvin element. In this procedure, the correct choice of simulation parameters such as the time-step and the velocity threshold seems to play an important role. Simulations indicate that abrupt manoeuvres might cause some fluctuations in lateral force characteristics. Still, these preliminary findings need to be refined and compared with carefully designed experiments. Towards the end of the tyre modelling section, findings and approaches from all previous tyre models are combined in order to create a fairly complex discretised generic transient tyre model, which possesses a useful quality, namely a separate fully dynamic representation of the tread with inertial and damping properties. The model seems capable of representing the transience involved in both lateral and longitudinal manoeuvres.

Finally, the ability of the models to operate in a full-vehicle handling simulation environment is demonstrated in chapter 5. By comparing the steady-state tyre models with the magic formula model, it is shown that differences in the characteristics of the tyre model may alter the response of a vehicle significantly. The undoubtedly steep steering input used for the simulations results in the tyres operating at high slip angles and under high vertical loads. Under such conditions, the physical tyre models predict large deviations from the Magic Formula. These deviations lead to a less under-steering behaviour of the vehicle, when running on the physical tyre models. Last, but not least, the use of the generic transient model for the same manoeuvre reveals the significance of the transience in the tyres' responses; in the handling behaviour of the vehicle. It is shown that the tyre forces in the front (steered) wheels increase in a step-oscillatory manner, while the combination of the response lags between front and rear tyres alters the balance between front and rear yaw moment and leads to a completely unstable behaviour of an inherently under-steering vehicle.

6.2 Achievement of Aims

The main objectives of the present research are clearly identified in the first chapter of the thesis. In this section, the level of fulfilment of the 3-year research mission is assessed, with emphasis on the major findings and the novelty of the approaches undertaken.

The research into the steady-state behaviour of the pneumatic tyre has been carried out in conformance with the viscoelastic properties of rubber. The two physical models developed are characterised by a purely dynamic representation of the contact patch, using bristles with inertial and damping properties. Thus, the situation within the contact is described by a couple of second order differential equations for the corresponding degrees of freedom of the bristle, as opposed to the commonly used deformation equations. This quality enables the calculation of the actual sliding velocity of the bristles during the transition between the stick phase and the phase where the bristle has reached the steady-state sliding velocity. The overall behaviour of a Kelvin element with inertia was discussed in relation with the calculation of the transition velocity and the influence of inertia and damping was assessed. It was found that, while inertia is essential for the maintenance of stick-slip, a mass-less Kelvin element is probably a more realistic choice, which still enables the explicit calculation of the transition velocity. In addition, it was pointed out that when both damping and inertia are neglected, i.e. when the bristles are modelled as simple springs (see for example [48] and [56]), the assumption of any sensible transition velocity is justified. In terms of modelling, a new approach is followed for the calculation of the normal pressure distribution. Not only is the vertical deflection calculated dynamically, but also the necessary algebraic constraint equations are formulated and solved simultaneously with the differential equations of motion. This procedure is successfully combined with a non-linear radial stiffness, which accounts for the effect of air-pressure inside the tyre. The effectiveness of the normal pressure calculation procedure was assessed indirectly by calculating the rolling resistance coefficient as a function of rolling velocity. The results showed generally good agreement with experiments; nevertheless the shape of the curves obtained indicates the necessity of incorporating non-linear damping in the calculation of the normal pressure distribution. Finally, the anisotropic, velocity dependent friction together with the anisotropic properties of the bristles in the lateral and longitudinal directions, provide a well defined formulation with direct physical significance for the simulation of combined-slip operating conditions.

The simple physical steady-state model is successfully extended, in order to enable the simulation of transient operating conditions. The integration procedure is modified as required for this purpose and the bristles are also interconnected in an attempt to

achieve a more realistic representation of the tyre tread behaviour. This unique modelling approach is used for the assessment of the role of friction force generation. Subsequently, the requirement for a dynamic tread is integrated in the final generic transient tyre model. Hitherto, this is probably the only numerical model developed, which incorporates a fully dynamic tread with the capability of simulating stick-slip friction. Parallel to the formulation of the equations of motion for the belt and the tread, subtle numerical techniques are employed in order to restrain the tread in the neighbourhood of the contact area and at the same time successfully simulate the rolling motion of the tyre.

A fairly elaborate vehicle model is developed with detailed description of all the intermediate steps, as described in chapter 5. The model is used in handling studies as described in the previous section. Apart from the assessment of the contribution of the tyre models in the overall handling performance of the vehicle, a new measure is devised for the characterisation of the transient response of the vehicle. The *normalised yaw impulse* directly relates the cornering behaviour of the vehicle to the contribution from the tyres. The non-dimensionalisation of this measure to some extent permits a quantitative measure of comparison between the responses of a vehicle using different tyre models, with emphasis on the balance between front and rear tyre forces under transient operating conditions.

6.3 Limitations and Suggestions for Future Work

As is the case in all research activities, the thorough study of a physical phenomenon reveals additional problems to the ones initially perceived. Moreover, one finds that it is impossible to provide full and definitive solutions to a complex problem. Accordingly, the present research has attempted to illuminate certain aspects of tyre handling behaviour using approaches that are characterised by certain limitations.

Firstly, the assumption of a uniform pressure distribution in the lateral direction of the contact patch is clearly not valid due to the geometry of the contacting solids. Large deviations are expected in the presence of camber angle. These deviations might relate to the subsequent drop observed in the cornering stiffness. This phenomenon is accounted for in an empirical manner in the Magic Formula. However, a physical

modelling approach would enhance understanding and increase the level of confidence for use in a wide range of conditions.

Apart from the fact that the presence of camber inclination can alter the normal pressure distribution in the lateral direction and subsequently influence the force generation mechanism, the current formulation of the camber effect neglects the influence of tyre width in the generation of the self-aligning moment.

Additionally, the friction law used in the physical models is independent of the vertical load and this fact leads to inaccurate results under high loads. While it would be simple to adopt an empirical law for the load dependency of friction (such as the one used in the Magic Formula), it is preferable to employ a method, which relates to the viscoelastic nature of rubber friction.

Besides the aforementioned directly identifiable limitations, the potential of the models developed can be increased through a series of improvements. At the same time, an extended range of simulations should be undertaken in combination with carefully conceived experiments.

In terms of modelling, a major improvement would involve the extension of the tyre models from single plane to double or triple-plane models. In this way, the alterations in the shape of the contact and the normal pressure distribution may be simulated adequately for use in vehicle handling studies. The accuracy of the steady-state models would benefit from such an improvement, mainly through the introduction of the effect of tyre width in the self-aligning moment generation due to camber and turn-slip. Nevertheless, these models would be unable to perform at rest. On the contrary, the formulation of the generic transient model permits its use in parking manoeuvres. Under such conditions, the adoption of a multiple-plane model would improve the accuracy in the calculation of the self-aligning moment, by taking into consideration the moment generated by the longitudinal anti-symmetrical deformation of the tyre.

In the experimental field, steady-state tests should be carried out for the accurate determination of the parameters of the physical steady-state models. In addition,

measurements of the size and shape of the normal pressure distribution are required for the identification of the parameters of the advanced steady-state tyre model, affecting the vertical and radial degrees of freedom. Since a direct connection between rolling resistance and normal pressure distribution has been demonstrated, it is possible that measurements of the rolling resistance at different velocities would aid the identification of the parameters involved in the calculation of the normal pressure distribution, avoiding the measurement of the distribution itself. In this procedure, a model incorporating non-linear damping for the simulation of the normal pressure distribution would probably yield better agreement between the experimental and numerical results. In addition, tyre-model oriented transient friction tests are essential for an in-depth investigation of transient friction force generation, ideally in comparison with results obtained by a transient friction tyre model. Finally, appropriate modal tests are required for the estimation of the parameters of the generic transient tyre model.

Based on the aforementioned experimental work, refined versions of all tyre models may be used in extensive handling studies, including combined cornering and braking/traction manoeuvres. The use of the generic transient tyre model may prove valuable in assessing the effectiveness of stability-enhancing control systems in a full-vehicle handling simulation environment. In this context, the concept of *normalised yaw impulse* can be used for the assessment of the transient handling responses of the vehicle. To gain confidence in the use of this measure, a sensitivity analysis is required, using a variety of steady-state and transient models with different properties.

List of References

[1] Daniels, J. *Car Suspension at Work: Theory and practice of Steering, Handling and Roadholding – 2nd Edition*, 1998 (Motor Racing Publications L.t.d), Croydon, England.

[2] Pacejka, H. Simplified Analysis of Steady-State Turning Behaviour of Motor Vehicles. Part 1: Handling diagrams of Simple Systems. *Vehicle System Dynamics*, 1973, **2**, pp. 161-172.

[3] Pacejka, H. Simplified Analysis of Steady-State Turning Behaviour of Motor Vehicles. Part 2: Stability of the Steady State Turn. *Vehicle System Dynamics*, 1973, **2**, pp. 173-183.

[4] Pacejka, H. Simplified Analysis of Steady-State Turning Behaviour of Motor Vehicles. Part 3: More Elaborate Systems. *Vehicle System Dynamics*, 1973, **2**, pp. 185-204.

[5] Dixon J.C. *Tyres, Suspension and Handling*, 1991, (Cambridge University Press).

[6] Pacejka H. B. *Tyre and Vehicle Dynamics*, 2002 (Butterworth Heinemann), Oxford.

[7] Ellis J.R. *Vehicle Handling Dynamics*, 1989, (John R. Ellis).

[8] Milliken, W.F. and **Milliken, D.L.** *Race Car Vehicle Dynamics*, 1995, (SAE).

[9] Rauh, J. Virtual Development of Ride and Handling Characteristics for Advanced Passenger Cars. *Vehicle System Dynamics*, 2003, **40**, Nos. 1-3, pp. 135-155.

[10] Schiehlen, W. Modeling and Analysis of Non-Linear Multibody Systems. *Vehicle System Dynamics*, 1986, **15**, pp. 271-288.

[11] **Rahnejat H.** *Multi-Body Dynamics – Vehicles, Machines and Mechanisms*, 1998, (Professional Engineering Publishing Limited).

[12] **Pacejka H.B.** and **Besselink I.J.** Magic Formula Tyre Model with Transient Properties. *Tyre Models for Vehicle Dynamics Analysis, Supplement to Vehicle System Dynamics*, 1997, **27**, pp. 234-249.

[13] **Pacejka, H.B.** Analysis of the Dynamic Response of a Rolling String-Type Tire Model to Lateral Wheel-Plane Vibrations. *Vehicle System Dynamics*, 1972, **1**, pp. 37-66.

[14] **Maurice, J.P., Berzeri, M.** and **Pacejka H.B.** Pragmatic Tyre Model for Short Wavelength Side Slip Vibrations. *Vehicle System Dynamics*, 1999, **31**, pp. 65-94.

[15] **Zhou, J., Wong, J.Y.** and **Sharp, R.S.** A Multi-Spoke, Three Plane Tyre Model for simulation of Transient Behaviour. *Vehicle System Dynamics*, 1999, **31**, pp.35-45.

[16] **A. van Zanten, Erhardt R.** and **Lutz A.** Measurement and Simulation of Transients in Longitudinal and Lateral Tire Forces. SAE paper 900210, 1990.

[17] **Mastinu, G.** and **Fainello, M.** Study on the Pneumatic tyre Behaviour on Dry and Rigid Road by Finite Element method. *Vehicle System Dynamics*, 1992, **21**, pp. 143-165.

[18] **Mastinu, G., Gaiazzi, S., Montanaro, F.** and **Pirola, D.** A Semi-Analytical Tyre Model for Steady and Transient-State Simulations. *Vehicle System Dynamics Supplement*, 1997, **27**, pp. 2-21.

[19] **Gipser, M.** Ftire, a New Fast Tire Model for Ride Comfort Simulations. From: http://www.ftire.com/free.htm

[20] **Oertel, C.** and **Fandre, A.** Ride Comfort Simulations and Steps Towards Life Time Calculations: RMOD-K and ADAMS. *International Adams Users' Conference*, Berlin 1999.

[21] **Bliman, P. A., Bonald, T. and Sorine, M.** Hysteresis Operators and Tyre Friction Models. Application to Vehicle Dynamic Simulation. Zeitschrift *fuer Angewandte Mathematik und Mechanik*, 1996, **76**(2), pp. 309-312.

[22] **Dahl, P. R.** Solid Friction Damping of Mechanical Vibrations. *AIAA Journal*, 1976, **14**(12), pp. 1675-1682.

[23] **Canudas de Wit, C., Olsson, H., Astrom, K.J. and Lischinsky, P.** A New Model for Control of Systems with Friction. *IEEE transactions on Automatic Control*, 1995, **40**(3), pp. 419-425.

[24] **Deur, J.** Modelling and Analysis of Longitudinal Tire Dynamics Based on the LuGre Friction Model. *Proceedings of the IFAC Conference on Advances in Automotive Control*, 2001, Karlsuhe, Germany, pp. 101-106.

[25] **Canudas-De-Wit C., Tsiotras P., Velenis E., Basset M.** and **Gissenger G.** Dynamic Friction Models for Road/Tire Longitudinal Interaction. *Vehicle System Dynamics*, 2003, **39**, pp. 189-226.

[26] **Braghin, F., Cheli, F.** and **Resta, F.** Friction Law Identification For Rubber Compounds on Rough Surfaces at Medium Sliding Speeds. *3rd AIMETA International Tribology conference*, Salerno, Italy, 18-20 September 2002.

[27] **De Togni, R. S., Eiss, N. S. Jr. and Rorrer, R. A. L.** The Role of System Dynamics on the Behavior of Elastomeric Friction. *Wear and Friction of Elastomers* edited by Denton and Keshavan, ASTM, STP 1145., pp. 30-49.

[28] **Rorrer, R. A. L., Eiss, N. S. Jr. and De Togni, R. S.** Measurement of Frictional Stick-Slip Transitions for Various Elastomeric Materials Sliding against Hard Counterfaces. *Wear and Friction of Elastomers* edited by Denton and Keshavan, ASTM, STP 1145., pp. 50-64.

[29] **Moore D. F.** *The Friction of Pneumatic Tyres*, 1975 (Elsevier Scientific Publishing Company).

[30] **Bird K. D.** and **Martin J. F.** The Calspan Tire Research Facility: Design, Development and Initial Test Results. SAE paper 730582, 1973.

[31] **Lagner W. J.** Development of a Flat Surface Tire Testing Machine. SAE paper 800245, 1980.

[32] **Joy T. J. P., Hartley D. C.** and **Turner D. M.** Tires for High Performance Cars. SAE Transactions, 1956, **64**, pp. 319-333.

[33] **Gough V. E.** Practical Tire Research. SAE Transactions, 1956, **64**, pp. 310-318.

[34] **Robson J. J.** High-Speed Cornering Forces. SAE Transactions, 1956, **64**, pp. 334-337.

[35] **Yap P.** Measurement of Radial Truck Tire Dry Cornering Characteristics. SAE paper 912677 in Johnson E. (Editor), *Tires and Handling,* SAE PT-59.

[36] **Gohring E. C., von Glasner** and **Pflug H.C.** Contribution to the Force Transmission Behavior of Commercial Vehicle Tires. SAE paper 912692 in Johnson E. (Editor), *Tires and Handling,* SAE PT-59.

[37] **Cabrera J. A., Ortiz A., Simon A., Garcia F.** and **Perez de la Blanca A.** A Versatile Flat Track Tire Testing Machine. *Vehicle System Dynamics*, 2003, **40**, pp. 271-284.

[38] **Pottinger M.G., Marshall K. D.** and **Arnold G. A.** Effects of Test Speed and Surface Curvature on Cornering Properties of Tires. SAE paper 760029, 1976.

[39] **Dowson, D.** History of Tribology – 2nd Edition, 1998 (Professional Engineering Publishing), London.

[40] **Bowden, F.P. and Tabor, D.** *The Friction and Lubrication of Solids – Part II,* 1964 (Oxford University Press), London.

[41] **Bakker, E., Pacejka, H.B.** and **Lidner, L.** A New Tyre Model with an Application in Vehicle Dynamics Studies. SAE paper 890087, 1987.

[42] **Pacejka H.B.** and **Sharp R.S.** Shear Force Development by Pneumatic Tyres in Steady-State Condition: A Review of Modelling Aspects. *Vehicle System Dynamics*, 1991, **20**, pp. 121-176.

[43] **R. Hadekel** *The Mechanical Characteristics of Pneumatic Tyres.* S&T Memo No. 10/25. Ministry of Supply, London, England, 1952.

[44] **Wong J. Y.** *Theory of Ground Vehicles*, 2001, (John Wiley & Sons).

[45] **Fiala E.** *Seitencrafte am rollenden luftreifen.* VDI-Zeitschrift, 1954, **96**, pp. 973-979.

[46] **Sakai H.** Theoretical and Experimental Studies on the Dynamic Properties of Tyres, Part 1: Review of theories of Rubber Friction. *Int. J. of Vehicle Design*, 1981, **2**(1), pp. 78-110.

[47] **Sakai H.** Theoretical and Experimental Studies on the Dynamic Properties of Tyres, Part 2: Experimental Investigation of Rubber Friction and deformation of a tyre. *Int. J. of Vehicle Design*, 1981, **2**(2), pp. 182-226.

[48] **Sakai H.** Theoretical and Experimental Studies on the Dynamic Properties of Tyres, Part 3: Calculation of the six components of force and moment of a tyre. *Int. J. of Vehicle Design*, 1981, **2**(3), pp. 335-372.

[49] **Sakai H.** Theoretical and Experimental Studies on the Dynamic Properties of Tyres, Part 4: Investigations of the influences of running conditions by calculation and experiment. *Int. J. of Vehicle Design*, 1982, **3**(3), pp. 333-375.

[50] **Ward, I. M.** *Mechanical Properties of Solid Polymers – 2nd Edition*, 1983 (John Wiley & Sons, L.t.d.).

[51] **Findley W. N., Lai J. S.** and **Onaran K.** *Creep and relaxation of nonlinear viscoelastic materials*, 1976, (North-Holland Publishing Company).

[52] **Gim, G.** and **Nikravesh, P.E.** An analytical model of pneumatic tyres for vehicle dynamic simulations. Part 1: Pure Slips. *Int. J. of Vehicle Design* **11**(6), 1990, pp. 589-618.

[53] **Gim, G.** and **Nikravesh, P.E.** An analytical model of pneumatic tyres for vehicle dynamic simulations. Part 2: Comprehensive Slips. *Int. J. of Vehicle Design* **12**(1), 1991, pp. 19-39.

[54] **Gim, G.** and **Nikravesh, P.E.** An analytical model of pneumatic tyres for vehicle dynamic simulations. Part 3: Validation against experimental data. *Int. J. of Vehicle Design* **12**(2), 1991, pp. 217-228.

[55] **Bernard J.E., Segel L.** and **Wild R.E.** Tyre Shear Force Generation During Combined steering and Braking Maneuvers. SAE paper 770852, 1977.

[56] **Sharp R.S.** and **El-Nashar M.A.** A Generally applicable Digital Computer Based Mathematical Model for the Generation of Shear Forces by Pneumatic Tyres. *Vehicle System Dynamics*, 1986, **15**, pp. 187-209.

[57] **Levin, M.A.** Investigation of features of Tyre Rolling at Non-Small Velocities on the Basis of a Simple Tyre Model with Distributed Mass Periphery. *Vehicle System Dynamics*, 1994, **23**, pp. 441-466.

[58] **Bakker, E.** and **Pacejka, H.B.** Tyre Modeling for Use in Vehicle Dynamics Studies. SAE paper 870421, 1987.

[59] **Schieschke, R. RALPHS.** Ein effizientes Rechenmodell zur Ermittlung von Reifenkraften auf physikalischer Basis. *Automobil-Industrie* (4) 1986.

[60] **Sitchin, A.** Acquisition of Transient Tire Force and Moment Data for Dynamic Vehicle Handling Simulations. SAE paper 831790, 1983.

[61] **Rimondi, R.** and **Gavardi, P. A.** New interpolative model of the mechanical characteristics of the tyre as an input to handling models. *FISITA Congress*, Torino, Italy, 1990, SAE paper 905246.

[62] **Pacejka H.B., Bakker E.** The Magic Formula Tyre Model. *Tyre Models for Vehicle Dynamics Analysis, Suppl. to Vehicle System Dynamics*, 1993, **21**, pp. 1-18.

[63] **Bayle, P., Forrisier, J.F.** and **Lafon, S.** A New Tyre Model for Vehicle Dynamics Simulation. *Automotive Technol. Int.*, 1993, pp. 193-198.

[64] **Oosten, J.J.M. (van)** and **Bakker, E.** Determination of Magic Tyre model Parameters. *Proceedings of 1st Colloquium on Tyre Models for Vehicle Analysis*, ed. H.B. Pacejka, Delft 1991, *Suppl. Vehicle System Dynamics*, **21**, 1993.

[65] **Radt, H.S.** and **Milliken, W.F.** Non-dimensionalising tyre data for vehicle simulation. *Road Vehicle Handling*, Inst. Of Mech. Eng. (C133/83), 1983.

[66] **Pacejka, H.B.** Analysis of the Shimmy Phenomenon. *Proc. Auto. Div. of Inst. Of Mech. Engineers*, 180, (1965-66), part 2A.

[67] **Loeb, J.S., Guenther, D.A., Chen, F.** and **Ellis, J.R.** Lateral stiffness, cornering stiffness and relaxation length of the pneumatic tire. SAE paper 900129, 1990.

[68] **Pacejka, H.B.** In-plane and out-of-plane dynamics of pneumatic tyres. *Vehicle System Dynamics*, 1981, **10**(4-5), pp. 221-251.

[69] **Clover, C.L.** and **Bernard, J.E.** Longitudinal Tire Dynamics. *Vehicle System Dynamics*, 1998, **29**, pp. 231-259.

[70] **Zdobyskaw, J.G.** Selfexcited Vibrations of the Tire. *Vehicle System Dynamics*, 1982, **11**, pp. 345-362.

[71] Bowden, F.P. and Tabor, D. *The Friction and Lubrication of Solids*, 2001 (Oxford University Press), London.

[72] Johnson K. L. *Contact Mechanics*, 1985, (Cambridge University Press).

[73] Archard, J. F. Elastic deformation and the laws of friction. *Proc. Roy. Soc.*, 1957, **A243**, pp. 190-205.

[74] Greenwood, J. A. and Williamson, J. B. P. Contact of nominally flat surfaces. *Proc. Roy. Soc.*, 1966, A295, pp. 300-319.

[75] Whitehouse, D. J. and Archard, J. F. The properties of random surfaces of significance in their contact. *Proc. Roy. Soc.*, 1970, **A316**, pp. 97-121.

[76] Greenwood, J. A. and Wu, J. J. Surface Roughness and Contact: An Apology. *Meccanica*, 2001, **36**, pp. 617-630.

[77] Indian Rubber Institute *Rubber Engineering*, 2000 (McGraw Hill), New York.

[78] Zhang, S.-W. *Tribology of Elastomers,* 2004 (Elsevier), Amsterdam.

[79] Grosh, K. A. The relation between the friction and visco-elastic properties of rubber. *Proceedings of the Royal Society (London),* 1963, **A 274**, pp. 21-39.

[80] Schallamach, A. How Does Rubber Slide? *Wear*, 1971, **17**, pp. 301-312.

[81] Persson, B. N. J. On the theory of rubber friction. *Surface Science*, 1998, **401**, pp. 445-454.

[82] Browne, A., Ludema, K.C. and Clark, S.K. Contact Between the Tyre and Roadway. In: **Clark, S.K. (editor),** *Mechanics of Pneumatic Tyres*, 1981, Washington D.C.

[83] Persson, B. N. J., Albohr, O., Mancosu, F., Peveri, V., Samoilov, V. N. and Sivebaek, I. M. On the nature of static friction, kinetic friction and creep. *Wear*, 2003, **254**, pp. 835-851.

[84] Armstrong-Helouvry B. *Control of Machines with Friction*, 1991 (Kluwer Academic Press), Boston.

[85] Armstrong-Helouvry B. Stick Slip and Control in Low Speed Motion. *Transactions on Automatic Control*, 1993, **38**(10), pp. 1483-1496.

[86] Zegelaar, P.W.A. and **Pacejka, H.B.** Dynamic Tyre Responses to Brake Torque Variations. *Vehicle System Dynamics Supplement*, 1997, **27**, pp. 65-79.

[87] Blundell M. V. The Modelling and Simulation of Vehicle Handling Part 1: Analysis Methods. *Proceedings of the Institution of Mechanical Engineers, Part K: Journal of Multi-body Dynamics*, 1999, **213**(K2), pp. 103-118.

[88] Blundell M. V. The Modelling and Simulation of Vehicle Handling Part 2: Vehicle Modelling. *Proceedings of the Institution of Mechanical Engineers, Part K: Journal of Multi-body Dynamics*, 1999, **213**(K2), pp. 119-134.

[89] Blundell M. V. The Modelling and Simulation of Vehicle Handling Part 3: Tyre Modelling. *Proceedings of the Institution of Mechanical Engineers, Part K: Journal of Multi-body Dynamics*, 1999, **213**(K2), pp. 119-134.

[90] Blundell M. V. The Modelling and Simulation of Vehicle Handling Part 4: Handling Simulation. *Proceedings of the Institution of Mechanical Engineers, Part K: Journal of Multi-body Dynamics*, 2000, **214** (K2), pp. 71-94.

[91] Hegazy, S., Rahnejat, H. and **Hussain, K.** Multi-Body Dynamics in Full-Vehicle Handling Analysis under Transient Manoeuvre. *Vehicle System Dynamics*, 2000, **34**, pp 1-24.

[92] **Allen R.W., Szostak H.T., Rosenthal T.J., Klyde D.H.** and **Owens K.J.** Characteristics Influencing Ground Vehicle Lateral/Directional Dynamic Stability. SAE paper 910234, 1991.

[93] **Rahnejat, H.** Multi-body dynamics: Historical Evolution and Application. *Proceedings of the I mech E, Part C, Journal of Mechanical Engineering Science*, 2000, **214**(1), pp. 149-173.

[94] **Pacejka H. B.** Non-linearities in Road Vehicle Dynamics. *Vehicle System Dynamics*, 1986, **15**, pp. 237-254.

[95] **Pacejka, H. B.** Lateral dynamics of road vehicles. *Proceedings, 3rd Seminar on Advanced Vehicle System Dynamics*, 1986, pp. 75-120.

[96] **Lukowski S.A., Fiedler R.A.** and **Claar P.W.** An Investigation of a Road-Vehicle Directional Behaviour Under Steady-State Conditions. SAE paper 911872, 1991.

[97] **Abe Masato** A Theoretical Analysis on Vehicle Cornering Behaviours in Acceleration and in Braking. *Vehicle System Dynamics*, 1985, **14**, pp. 140-143.

[98] *Vehicle Dynamic Terminology*, SAE J670e, 1976.

[99] **Whitcomb, D.W.** and **Milliken, W.F.** Design implications of a general theory of automobile stability and control. *Proceedings of the Imech E, Auto. Div.*, 1956, pp. 376-391.

[100] **Bickerstaff, D.J.** The handling properties of light trucks. SAE paper 760710, 1976.

[101] **Lee, Yung-Li, Dziuba, J.C. Jr.** and **Lu, Ming-Wei.** Vehicle handling design process using DOE. *International Journal of Vehicle Design*, 1996, **17**(1), pp. 40-54.

[102] Antoun, R.J., Hackert, P.B., O'Leary, M.C. and **Sitchin, A.** Vehicle dynamic handling computer simulation: Model development, correlation and application using ADAMS. SAE paper 860574, 1986.

[103] Hackert, P.B., O'Leary, M.C. and **Sitchin, A.** Dynamic simulation of light truck handling maneuvers using ADAMS. *American Society of Mechanical Engineers, Applied Mechanics Division,* 1986, **80**, pp 277-286.

[104] Naude, Alwyn F. and **Steyn, Jasper L.** Objective evaluation of the simulated handling characteristics of a vehicle in a double lane-change manoeuvre. SAE paper 930826, 1993.

[105] Hegazy Shawky ABD El-Hameed. Multi-Body Dynamic Analysis for Assessment of Vehicle Handling with Aerodynamic Interactions Under Transient Manoeuvres. *PhD Thesis*, 2000, University of Bradford.

[106] Kim S. J. and **Savkoor A. R.** The Contact Problem of In-Plane Rolling of Tires on a Flat Road. *Vehicle System Dynamics Supplement*, 1997, **27**, pp. 189-206.

[107] Gehman, S.D. Rubber Structure and Properties. In: **Clark, S.K. (editor),** *Mechanics of Pneumatic Tyres*, 1981, Washington D.C.

[108] Oertel, C. On Modelling Contact and Friction Calculation of Tyre Response on Uneven Roads. *Vehicle System Dynamics Supplement*, 1997, **27**, pp. 289-302.

[109] Clark, S. K. Brief History of Tyre Rolling Resistance. *Rubber Division Symposia*, 1983, **1**, pp. 1-23.

[110] Halling, J. *Introduction to Tribology,* 1976 (Wykeham publications L.t.d), London.

[111] Thieme, H. van Eldik, Dijks, A.J. and Bobo, S. Measurement of Tire Properties. In: **Clark, S.K. (editor),** *Mechanics of Pneumatic Tyres*, 1981, Washington D.C.

[112] Karnopp D. Computer Simulation of Stick-Slip Friction in Mechanical Dynamic Systems. *Transactions of the ASME – Journal of Dynamic Systems, Measurement and Control*, 1985, **107**, pp. 100-103.

[113] Quarteroni, A., Sacco, R. and Saleri, F. *Numerical mathematics*, 2000, (Springer-Verlag), New York.

[114] Plybon, B.F. *An introduction to applied numerical analysis*, 1992, (PWS-KENT PUBLISHING COMPANY), Boston.

[115] Cavallo, A., Setola, R. and **Vasca F.** *Using Matlab Simulink and Control System Toolbox - A Practical Approach.* 1996, (Prentice Hall).

[116] Milliken, W.F. JR and **Rice, R.S.** Moment Method. C113/83 *Road Vehicle Handling*, Imech E, 1983.

[117] Higuchi, A. and Pacejka, H.B. The Relaxation Length Concept at Large Wheel Slip and Camber. *Vehicle System Dynamics Supplement*, 1997, **27**, pp. 50-64.

Appendix A: Publications

1 **Mavros, G., Rahnejat, H.** and **King, P.D.** Investigation of Steady-State Tyre Force and Moment Generation under Combined Longitudinal and Lateral Slip Conditions. *Vehicle System Dynamics Supplement*, 2004, **41**, pp. 351-360.

2 **Mavros, G., Rahnejat, H.** and **King, P.D.** Transient analysis of tyre friction generation using a brush model with interconnected viscoelastic bristles.

In queue for publication in the Proc. *Instn Mech. Engrs, Part K: J. Multi-body Dynamics*.

3 **Mavros, G., Rahnejat, H.** and **King, P.D.** Analysis of the transient handling properties of a tyre, based on the coupling of a flexible carcass – belt model with a separate tread incorporating transient viscoelastic frictional properties. *3rd International Tyre Colloquium - Tyre Models for Vehicle Dynamics Analysis*, August 30-31, 2004 Vienna, Austria.

Appendix B: Additional figures

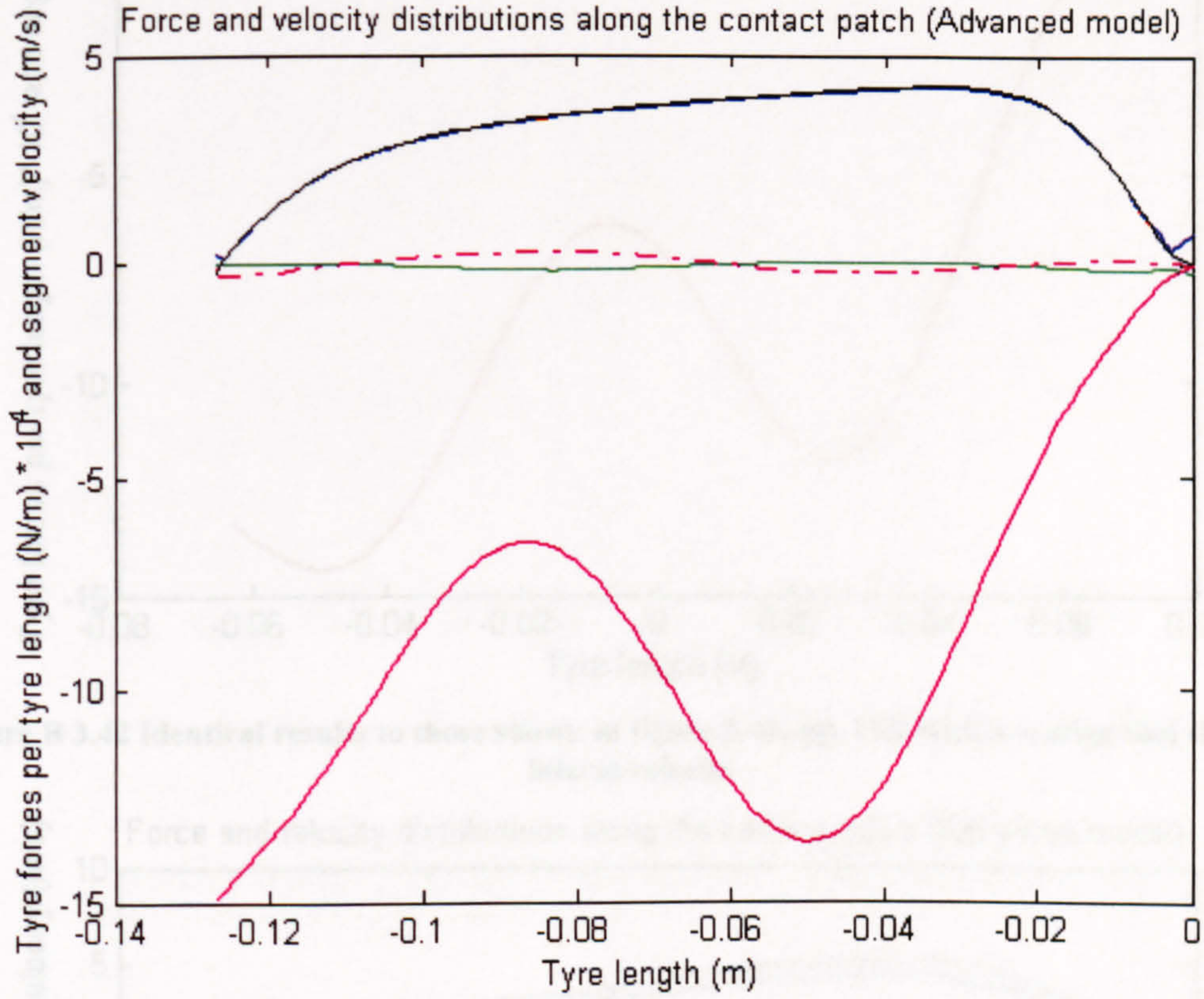

Figure B 3.40 Identical results to those shown in figure 3.40, pp. 152, with a scaling that shows the lateral velocity

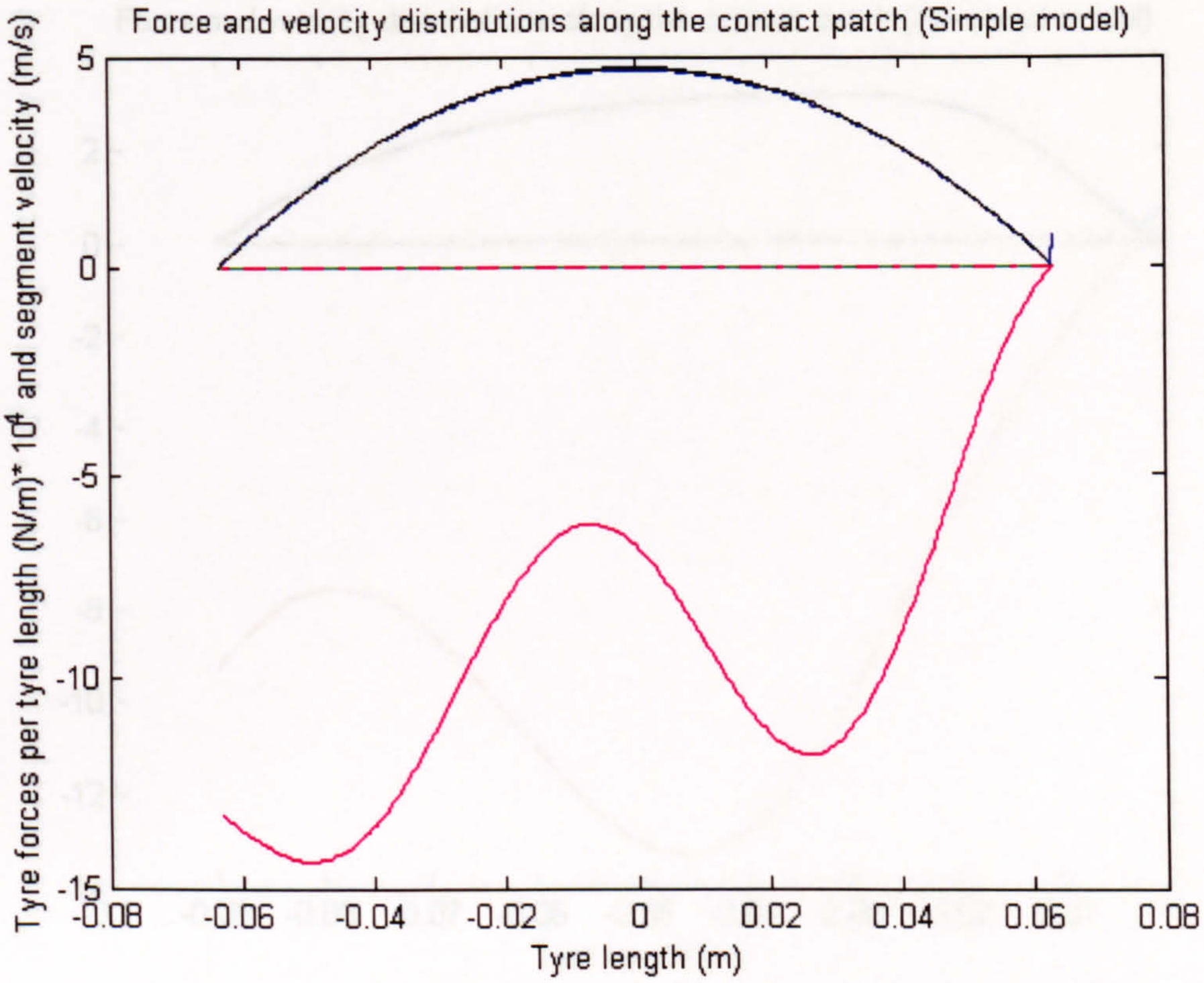

Figure B 3.42 Identical results to those shown in figure 3.42, pp. 153, with a scaling that shows the lateral velocity

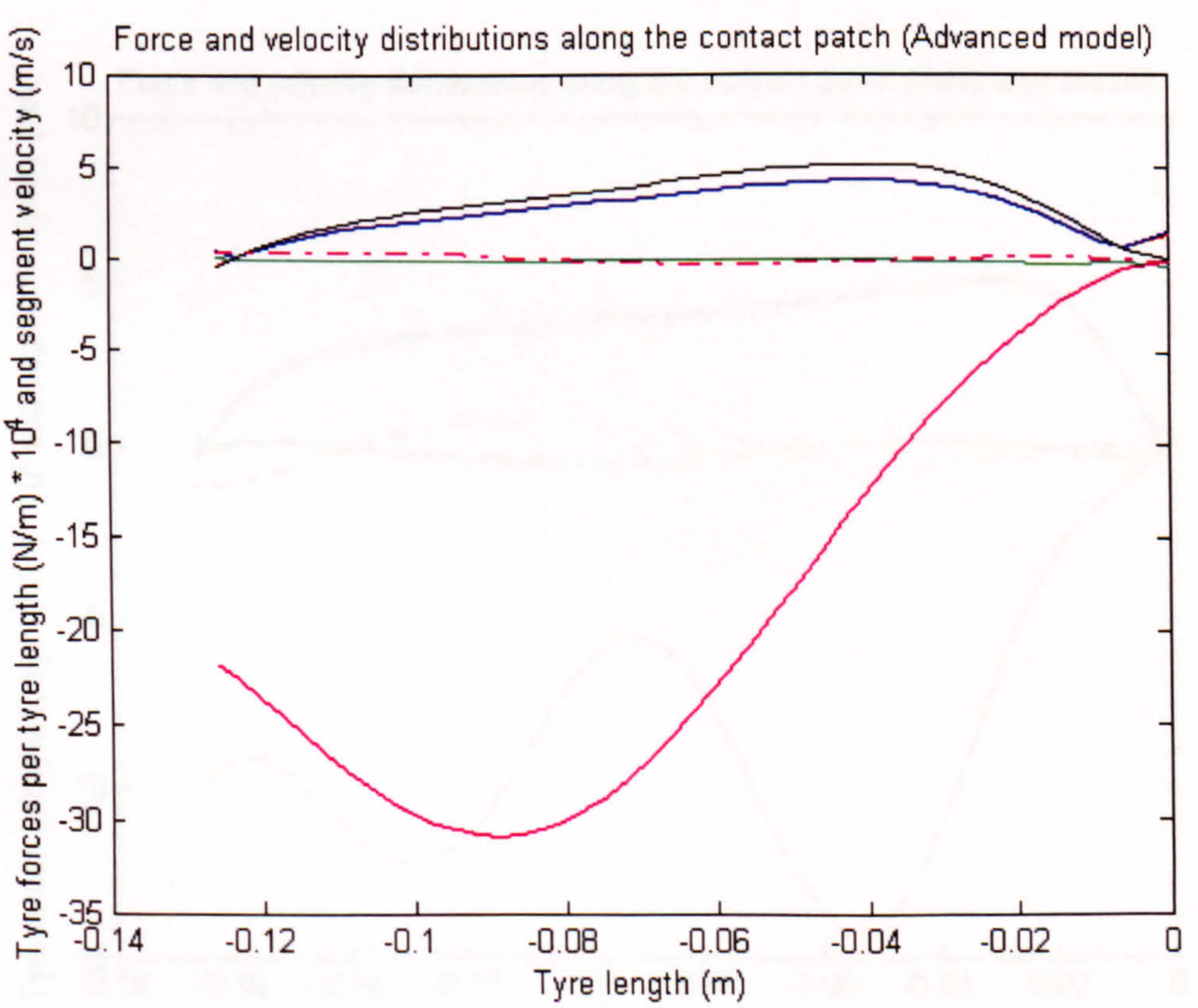

Figure B 3.46 Identical results to those shown in figure 3.46, pp. 155, with a scaling that shows the lateral velocity

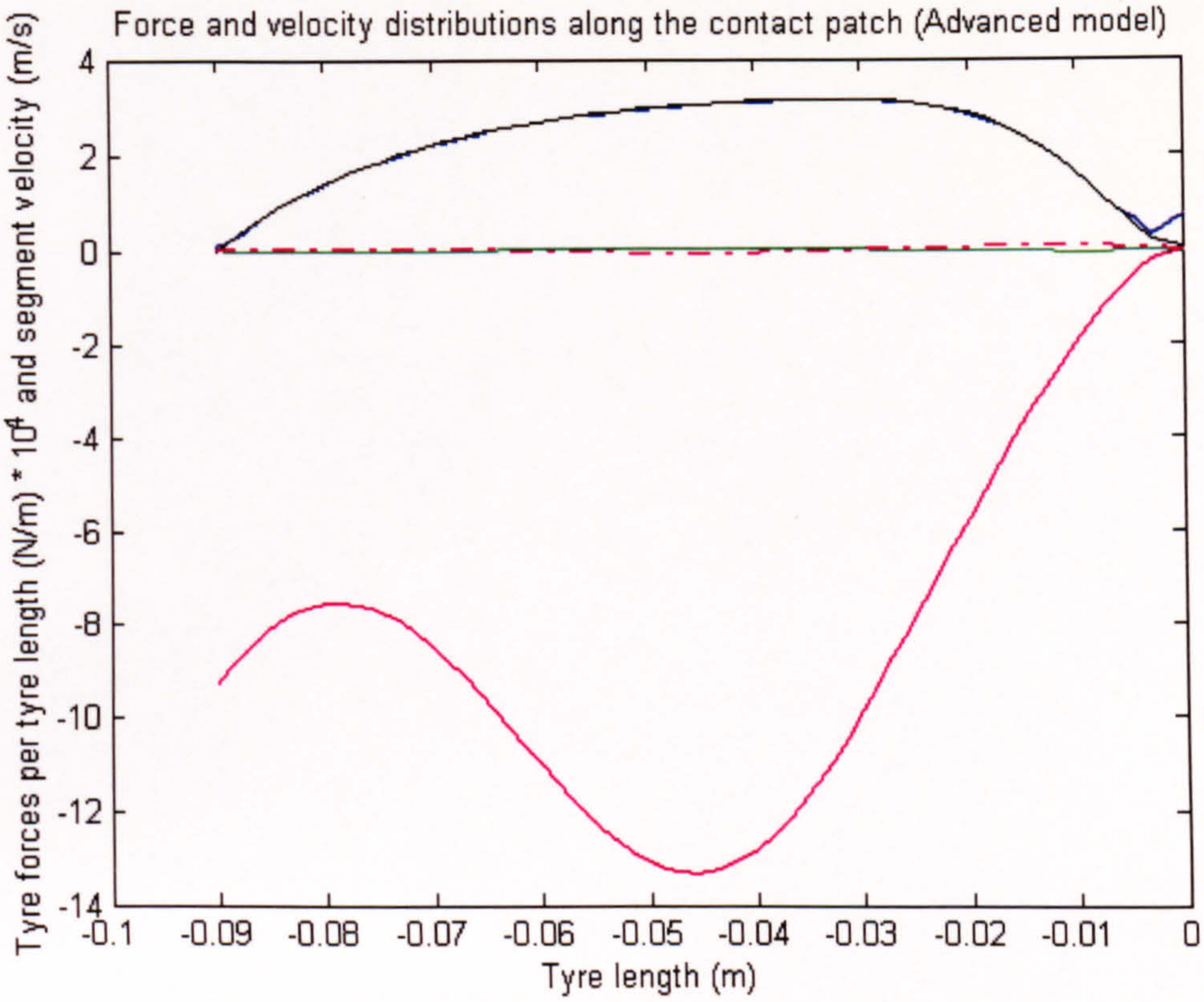

Figure B 3.50 Identical results to those shown in figure 3.50, pp. 157, with a scaling that shows the lateral velocity

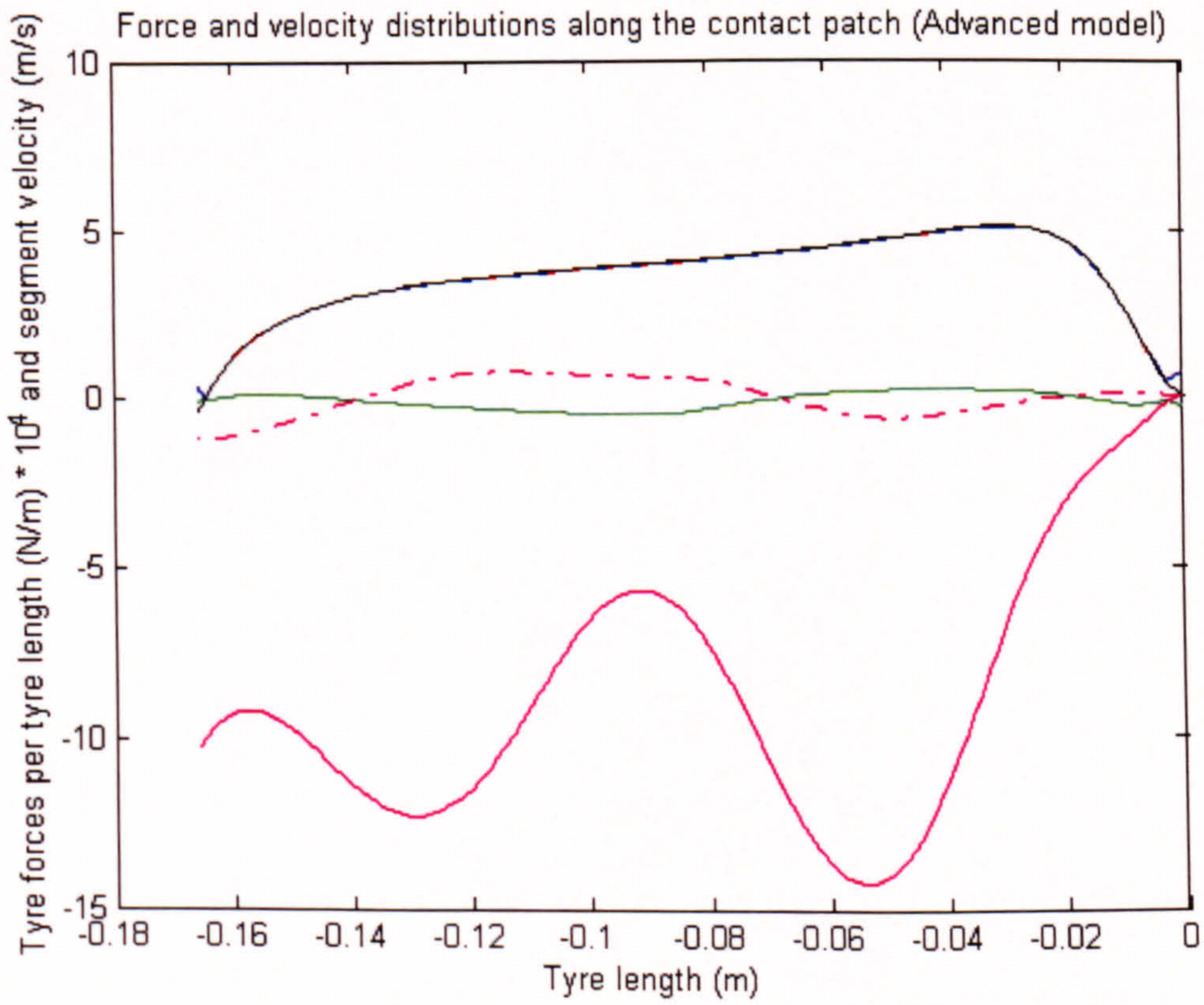

Figure B 3.54 Identical results to those shown in figure 3.54, pp. 159, with a scaling that shows the lateral velocity